EDITED and PUBLISHED quarterly at the offices of The American Society of Mechanical Engineers, United Engineering Center, 345 E. 47th St., New York, N. Y. 10017. Cable address, "Mechaneer," New York. Second-class postage paid at New York, N. Y., and at additional mailing offices.

CHANGES OF ADDRESS must be received at Society headquarters seven weeks before they are to be effective. Please send old label and new address.

PRICES: To members, $25.00, annually; to nonmembers, $50.00. Single copies, $15.00 each. Add $1.50 for postage to countries outside the United States and Canada.

STATEMENT from By-Laws. The Society shall not be responsible for statements or opinions advanced in papers or . . . printed in its publications (B 13, Par. 4).

INDEXED by the Engineering Index, Inc.

transactions of the ASME

Published Quarterly by
The American Society of
Mechanical Engineers
Volume 100 • Number 1
FEBRUARY 1978

journal of heat transfer

(Contents continued on page 24)

CONTENTS (CONTINUED)

R. Siegel

National Aeronautics and Space Administration,
Lewis Research Center,
Cleveland, Ohio

Shape of Two-Dimensional Solidification Interface During Directional Solidification by Continuous Casting

An analysis was made of the two-dimensional solidification of an ingot being cooled and withdrawn vertically downward from a mold consisting of parallel walls of finite length. In some metallurgical solidification processes the liquid metal is maintained superheated so that it transfers heat into the solidification interface as a means of controlling the metal structure during solidification. This energy plus the latent heat of fusion is removed by the coolant along the sides of the ingot. Increasing the ingot withdrawal rate or the heat addition at the solidification interface causes the interface to move downward within the mold and have a nonplanar shape as a result of the curved paths for heat flow into the coolant. This distortion of the interface in the case of directional solidification leads to an undesirable metallic structure. The present heat transfer analysis shows how the flatness of the interface is related to the ingot thickness, the withdrawal rate, the heat addition from the superheated liquid metal, and the temperature difference available for cooling. This provides an understanding of the conditions that will yield a maximum rate of casting while achieving the desired flatness of the interface. The results are interpreted with respect to the conditions for obtaining an aligned eutectic structure by directional solidification. In this process an additional constraint must be included that relates the ingot withdrawal rate and the heat transfer rate from the liquid metal to the solidification interface.

Introduction

This paper is concerned with how the heat transfer conditions effect the two-dimensional shape of the solidification interface during continuous casting of a slab shaped ingot. By proper control of the conditions at the solidification interface, it is possible in some casting processes to obtain an internal metallic structure that has a desirable unidirectional character. The flatness of the interface is important in regulating this directional structure in the solidifying material, and the relation between this flatness and the heat flow conditions will be determined by the analysis. In addition to examining the directional casting process, the present method of solution is of general interest in the area of two-dimensional solidification analysis, as it further illustrates the use that can be made of conformal mapping in this type of problem.

There have been numerous analyses of solidification, for the most part by approximate analytical techniques and numerical methods. The review article in reference [11][1] provides some appreciation of the previous work. Most of the investigations have been for one-dimensional geometries, that is, for interfaces that are planar, cylindrical, or spherical. The increased interest in two and three-dimensional solidification, and the mathematical difficulties involved, are indicated in the conference proceedings in reference [2]. A difficulty with the multi-dimensional problem is that the interface shape and its location are unknown, thereby making it difficult to set up a solution procedure for the heat conduction equation. Three analyses, somewhat related to the present study, are found in references [3], [4], and [5]. In reference [3], the interface shape was determined numerically for a cylindrical crystal being pulled from a melt. In reference [4] continuous casting in an infinitely long mold was analyzed by the heat balance integral method. The effect of convection in the

Contributed by the Heat Transfer Division for publication in the JOURNAL OF HEAT TRANSFER. Manuscript received by the Heat Transfer Division July 15, 1977.

[1] Numbers in brackets designate References at end of paper.

liquid region was investigated in reference [5] using numerical methods combined with conformal mapping. The discussions at the end of reference [3] and the references listed in the three papers also contain several related publications of interest. The present analysis will obtain an analytical solution for a two-dimensional solidification problem arising during continuous casting of a slab-shaped ingot. The physical conditions are described at the beginning of the analysis. For these conditions the shape of the solidification interface is found to depend on a single dimensionless parameter.

The particular problem being studied here arose in connection with the direct formation of composite structures by directional-solidification from a eutectic alloy melt. Composites consisting of a reinforcing phase within a metallic matrix can be formed from molten eutectics by proper control during solidification (references [6] and [7]). One of the requirements of the process is that the solidification interface be kept planar within a given tolerance. A second requirement is that there be a sufficiently high temperature gradient in the molten metal at the interface; the required temperature gradient is related to the rate of casting. This gradient can be maintained by having the molten phase superheated and by having sufficient cooling of the solid phase. The interaction of these heat transfer quantities will be studied here for a continuous casting configuration. For a given heat addition and cooling rate, the maximum casting rate that corresponds to maintaining the solidification interface within a specified tolerance of flatness can be determined. The results are interpreted in relation to the directional solidification of eutectics.

Analysis

Energy Equation and Boundary Conditions. The geometry being analyzed is shown in Fig. 1(*a*). An ingot is being formed by uniform withdrawal at velocity $\bar{u}$ from an insulated mold. In the region below the mold the sides of the ingot are being strongly cooled, such as by forced convection of a liquid metal, and are assumed at uniform temperature t_c. The molten eutectic alloy above the interface is maintained in a superheated condition and consequently transfers heat to the solid-liquid interface. The superheat is necessary to control the crystal structure in the alloy in the process under consideration. It is assumed that there is a uniform heat transfer to the interface either by conduction, $k_l(\partial t_l/\partial n)$, or by convection $h(t_l - t_f)$; in the latter case the approximation is made that the heat transfer coefficient is uniform over the surface of the interface. Since the ingot is being withdrawn at a uniform rate, the latent heat of fusion removed per unit area locally at the interface is $\bar{u}\rho\lambda\,\partial x/\partial s$ where ds is a differential length along the interface. The boundary condition at the interface is then

$$k\left.\frac{\partial t}{\partial n}\right|_s = q(s) = q_l + \bar{u}\rho\lambda\frac{\partial x}{\partial s} \tag{1}$$

where q_l can be by conduction or convection. As will be discussed later in more detail, for purposes of controlling the crystal structure, the conditions of interest are slow withdrawal rates (in the range of several cm/hr) and a large temperature gradient (can be 100°C/cm or more) in the molten alloy adjacent to the interface. Hence, the last term on the right side of equation (1) is usually much smaller than the q_l term. It is also necessary that the interface be kept close to planar. This means that $\partial x/\partial s$ in the last term of equation (1) is approximately unity and does not cause significant variation in $q(s)$. As a result, to a good approximation, for all the conditions of interest here the $q(s)$ can be regarded as constant over the interface and equal to

$$q_s = k\left.\frac{\partial t}{\partial n}\right|_s = q_l + \bar{u}\rho\lambda \tag{2}$$

In the situation of low interface curvature, $\partial x/\partial s \approx 1$ and equation (2) will be a good approximation, even for large $\bar{u}\rho\lambda$. When the interface curvature is large, equation (2) will be a good approximation only when $\bar{u}\rho\lambda \ll q_l$. A second boundary condition along the interface is that the temperature is constant and equal to the fusion temperature,

$$t(s) = t_f \tag{3}$$

The other boundary conditions are that along the insulated mold (see Fig. 1(*a*))

$$\frac{\partial t}{\partial x} = 0 \qquad (x = \pm a,\ y > -b) \tag{4}$$

and along the cooled boundary,

$$t = t_c \qquad (x = \pm a,\ y < -b) \tag{5}$$

The dimension b in Fig. 1(*a*) is unknown and will be found in the solution as a function of the heat transfer quantities.

The ingot is withdrawn slowly at a steady rate, and it is assumed that the energy $\rho\bar{u}C_p\partial t/\partial y$ being transported by the movement is small compared to the heat being conducted. From results such as those found in reference [8], this is a satisfactory assumption if the Peclet number $\bar{u}2a/(k/\rho C_p)$ is less than unity. As will be discussed later, the $\bar{u}$ values of interest here are quite low, in the range of several cm per hr. This yields Peclet numbers that are well below unity. Hence the energy equation to be solved within the solidified material is Laplace's equation,

$$\nabla^2 t = 0 \tag{6}$$

It might seem that the boundary conditions are overspecified since equations (2) and (3) give both the heat flux and temperature at the same boundary. However, it is the shape of the boundary that is un-

Nomenclature

A = physical parameter and dimensionless length = $a/\gamma = (q_l + \bar{u}\rho\lambda)a/k(t_f - t_c)$
a = half-width of ingot
b = distance from center of interface to bottom edge of mold
C_p = specific heat of solid
C_1, C_2, etc = integration constants
c, d = values in mapping along real axis of u-plane
F = ratio, $(\partial t_l/\partial n)_s/\bar{u}$
h = convective heat transfer coefficient
K = complete elliptic integral of the first kind
k = thermal conductivity of solidified metal
k_l = thermal conductivity of liquid metal
l = length of ingot
n = normal to interface, $N = n/\gamma$
Q = heat flow per unit time
q = heat flux
q_l = heat flux from liquid metal to solidification interface
s = distance along interface
t = temperature; $T = (t - t_c)/(t_f - t_c)$
t_l = temperature in liquid metal
u = coordinate in u-plane, $u = \xi + i\eta$
$\bar{u}$ = withdrawal velocity of ingot
V = intermediate plane in mapping
W = potential plane, $W = -T + i\psi$
x,y = coordinates in physical plane, $X = x/\gamma$, $Y = y/\gamma$
z = complex physical plane, $z = x + iy$; $Z = z/\gamma$
α,β = inflection points on solidification interface
γ = length scale parameter, $k(t_f - t_c)/(q_l + \bar{u}\rho\lambda)$
δ = deviation of interface from being flat; $\Delta = \delta/\gamma$
ζ = complex derivative, $-\partial T/\partial X + i\partial T/\partial Y$
θ = argument of ζ-plane
λ = latent heat of fusion per unit mass of solid
ξ, η = coordinates of u-plane
ρ = density of metal
ψ = coordinate along heat flow in W plane
ω = mapping plane, $\log|\zeta| + i\theta$

Subscripts

c = at cooled surface
f = at solidification temperature
l = liquid metal
s = at solidification interface

known and must be found to simultaneously satisfy these two conditions. The solution will be found by using a conformal mapping procedure.

Dimensionless Variables. Before beginning the conformal mapping it is convenient to adopt a system of dimensionless variables. A dimensionless temperature is defined as $T \equiv (t - t_c)/(t_f - t_c)$. To simplify the boundary condition in equation (2), a length scale parameter is defined as

$$\gamma = \frac{k(t_f - t_c)}{q_s} = \frac{k(t_f - t_c)}{q_l + \bar{u}\rho\lambda}$$

and the dimensionless lengths then become $N = n/\gamma$, $X = x/\gamma$, etc. The boundary conditions become

$$\left.\begin{aligned} T &= 1 \\ \frac{\partial T}{\partial N} &= 1 \end{aligned}\right\} \text{ at solidification interface} \tag{7a}$$

$$T = 0 \text{ at cooled surface} \tag{7b}$$

These conditions are shown in Fig. 1(b) which gives the geometry in dimensionless coordinates. The numbers around the boundary will designate corresponding points in the conformal mapping.

Conformal Mapping Procedure. The basic ideas for applying conformal mapping to some types of solidification problems were developed in reference [9]. Since positive heat flow is in the direction of negative temperature gradient, the $-T$ can be taken as a potential function for heat flow, and we can let $-T$ be the real part of an analytic function of a complex variable

$$W = -T + i\psi \tag{8}$$

that satisfies Laplace's equation. The lines of constant T and ψ form an orthogonal net where the constant ψ lines are along the direction of heat flow. Hence, lines $\widehat{23}$ and $\widehat{78}$ in Fig. 1(b) are constant ψ lines as there is no heat flow normal to them because the boundary is insulated. As a result, the solidified region maps into a rectangle bounded by constant T and ψ lines as shown in Fig. 2(a). If this region can be conformally mapped into the physical plane, then the known temperature distribution in Fig. 2(a) (uniformly spaced vertical lines) will give the temperatures at the corresponding points in Fig. 1(b). In the mapping process the normal derivative condition at the interface, $\partial T/\partial N = 1$, will be satisfied.

The potential and physical planes can be related by use of the derivative of equation (8)

$$\frac{dW}{dZ} = \frac{-\partial T}{\partial X} + i\frac{\partial \psi}{\partial X} = \frac{-\partial T}{\partial X} + i\frac{\partial T}{\partial Y} \tag{9}$$

where the last relation on the right was obtained by using one of the Cauchy-Riemann equations. Defining ζ as $\zeta \equiv -\partial T/\partial X + i\,\partial T/\partial Y$, equation (9) can be integrated to yield

$$Z = \int \frac{1}{\zeta} dW + C_1 \tag{10}$$

By carrying out this integration, the physical (Z) plane is related to the potential (W) plane, and the known temperature distribution in Fig. 2(a) can be mapped into Fig. 1(b). Before the integration can be carried out, the ζ has to be related to W. This relation will introduce the temperature derivative boundary conditions that must be satisfied.

The temperature derivatives at the boundaries of the solidified region are used to map the region into the ζ-plane shown in Fig. 2(b). Along the solidification interface $\partial T/\partial N = 1$, so that $(\partial T/\partial X)^2 + (\partial T/\partial Y)^2 = 1$ and this boundary lies along a unit circle. Along the constant temperature cooled surfaces $\partial T/\partial Y = 0$ and along the insulated surfaces $\partial T/\partial X = 0$. The mapping between Fig. 2(b) and Fig. 2(a) which is needed to integrate equation (10) will be done by means of a few intermediate transformations.

First, a logarithmic transformation is used:

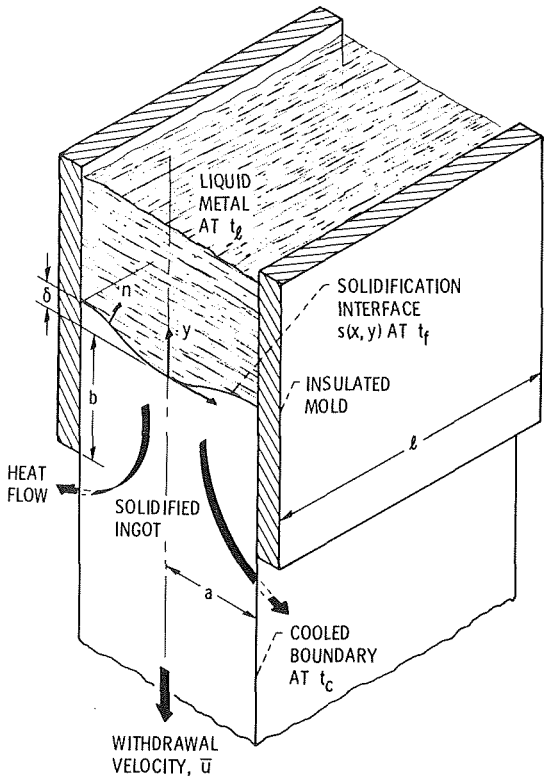

Fig. 1(a) Physical geometry

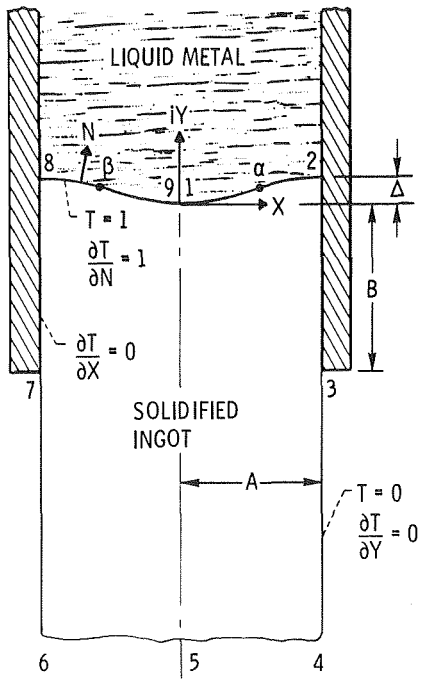

Fig. 1(b) Dimensionless physical plane, $Z = X + iY$

Fig. 1 Ingot being withdrawn continuously from mold

$$\omega = \log \zeta = \log |\zeta| + i\theta \tag{11}$$

where θ is the argument of ζ as shown in Fig. 2(b). Along the unit circle in Fig. 2(b), $\omega = i\theta$, so this becomes a vertical line in Fig. 2(c).

The boundary of Fig. 2(c) can be unfolded along the real axis so that the solidified region occupies the upper half plane. The result of this is shown in Fig. 2(d), and the mapping is accomplished by means of the Schwarz-Christoffel transformation

$$\frac{d\omega}{du} = \frac{C_2(u+d)(u-d)}{(u-1)(u+1)\sqrt{u-c}\sqrt{u+c}} \tag{12}$$

Equation (12) can be integrated to yield

$$\omega = C_2\left[-\frac{1}{2}\log\frac{\sqrt{u^2-c^2}-u}{\sqrt{u^2-c^2}+u} + \frac{(1-d^2)}{2\sqrt{1-c^2}} \times \log\frac{\sqrt{u^2-c^2}-u\sqrt{1-c^2}}{\sqrt{u^2-c^2}+u\sqrt{1-c^2}}\right] + C_3 \tag{13}$$

The corresponding points are matched between the ω and u-planes to evaluate C_2 and C_3, and to find a relation between c and d. Point 1 at $u = 0$ corresponds to $\omega = i\pi/2$, point 2 at $u = c$ must yield $\omega = i\pi/2$, and point 3 at $u = 1$ must correspond to $\omega = \infty + i\pi/2$ or $\infty + i\pi$ depending on whether $u = 1$ is approached from below or above along the real axis. These conditions lead to $C_2 = -1$, $C_3 = i\pi/2$ and $1 - d^2 = \sqrt{1-c^2}$. This last relation will be used later to locate the inflection points (α and β in Fig. 1(b)) along the frozen interface as this corresponds to points $u = \pm d$. With these values ω becomes,

$$\omega = \log\zeta = \frac{1}{2}\log\frac{\sqrt{u^2-c^2}-u}{\sqrt{u^2-c^2}+u} - \frac{1}{2}\log\frac{\sqrt{u^2-c^2}-u\sqrt{1-c^2}}{\sqrt{u^2-c^2}+u\sqrt{1-c^2}} + i\frac{\pi}{2} \tag{14}$$

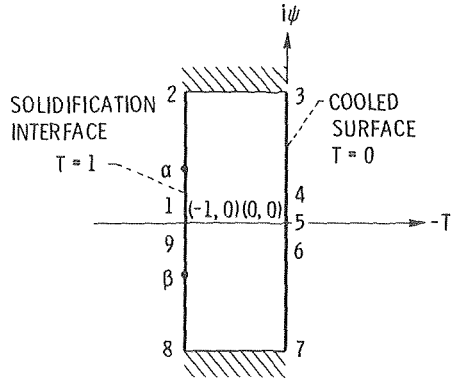

Fig. 2(a) Potential plane, $W = -T + i\psi$

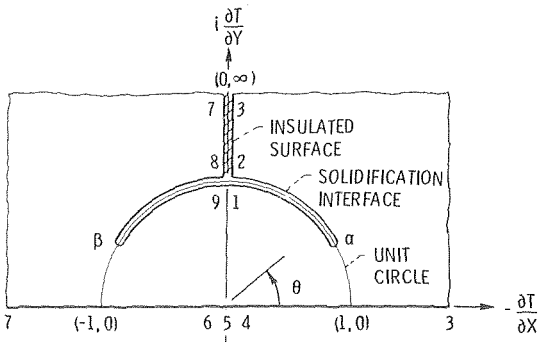

Fig. 2(b) Temperature derivative plane, $\zeta = -\partial T/\partial X + i\partial T/\partial Y$

Continuing the mapping transformations to relate W and ζ, which will be done by means of the intermediate variable u, the real axis of the u-plane is folded into a rectangle in the V-plane shown in Fig. 2(e). The solidified region is inside this rectangle. The mapping between u and V is found from the Schwarz-Christoffel transformation as

$$\frac{dV}{du} = \frac{C_4}{\sqrt{u-c}\sqrt{u+c}\sqrt{u-1}\sqrt{u+1}} \tag{15}$$

Then by rotation and translation the V-plane is transformed into the W-plane to complete the mapping

$$W = -iV - 1 \tag{16}$$

Now return to the integration of equation (10). This is written in the form,

$$Z = \int \frac{1}{\zeta(u)}\frac{dW}{dV}\frac{dV}{du}du + C_1 \tag{17}$$

From equation (14)

$$\frac{1}{\zeta(u)} = e^{-\omega} = \frac{1}{i}\left(\frac{\sqrt{u^2-c^2}+u}{\sqrt{u^2-c^2}-u}\right)^{1/2}\left(\frac{\sqrt{u^2-c^2}-u\sqrt{1-c^2}}{\sqrt{u^2-c^2}+u\sqrt{1-c^2}}\right)^{1/2} \tag{18}$$

Substituting equations (18) and (15), and the derivative of equation (16) yields

$$Z = \int \frac{1}{i}\left(\frac{\sqrt{u^2-c^2}+u}{\sqrt{u^2-c^2}-u}\right)^{1/2}\left(\frac{\sqrt{u^2-c^2}-u\sqrt{1-c^2}}{\sqrt{u^2-c^2}+u\sqrt{1-c^2}}\right)^{1/2}(-i) \times \frac{C_4}{\sqrt{u^2-c^2}\sqrt{u^2-1}}du + C_1 \tag{19}$$

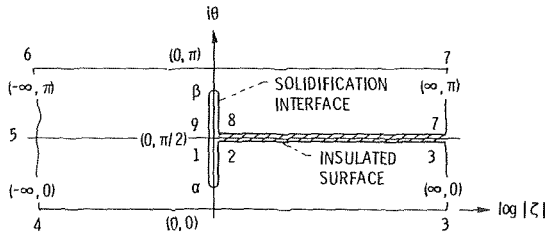

Fig. 2(c) Intermediate ω plane, $\omega = \log|\zeta| + i\theta$

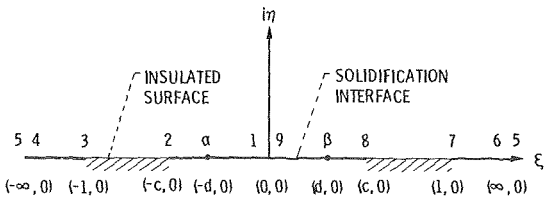

Fig. 2(d) Intermediate u plane, $u = \xi + i\eta$

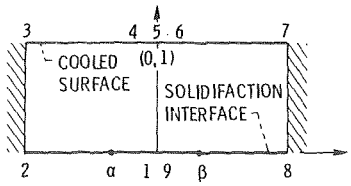

Fig. 2(e) Intermediate V plane

Fig. 2 Planes used in conformal mapping procedure

Equation (19) is integrated to give

$$Z = \frac{-iC_4(1-\sqrt{1-c^2})}{2c^2}\left[\log\frac{\sqrt{u^2-c^2}-u\sqrt{1-c^2}}{\sqrt{u^2-c^2}+u\sqrt{1-c^2}} + \log\frac{\sqrt{u^2-c^2}-u}{\sqrt{u^2-c^2}+u} - \log(u^2-1)\right] + C_1 \quad (20)$$

The constants are evaluated by having the origin $Z = 0$ at $u = 0$ and the width of the ingot be A, which means that the real part of Z must equal $-A$ when $u = 1$. This gives $C_1 = -A/2$ and $C_4 = (-A/\pi)[c^2/(1-\sqrt{1-c^2})]$. Then equation (20) becomes

$$\frac{Z}{A} = \frac{z}{a} = \frac{i}{2\pi}\left[\log\frac{\sqrt{u^2-c^2}-u\sqrt{1-c^2}}{\sqrt{u^2-c^2}+u\sqrt{1-c^2}} + \log\frac{\sqrt{u^2-c^2}-u}{\sqrt{u^2-c^2}+u} - \log(u^2-1)\right] - \frac{1}{2} \quad (21)$$

Equations for Solidification Interface. The interface between points 8 and 9 in Fig. 1(*b*) corresponds to points along the real axis $u = \xi$ in Fig. 2(d) where $0 \le \xi \le c$. Since ξ is less than c, some of the quantities in the square roots in equation (21) will be negative, so that along the interface z/a becomes,

$$\frac{z_s}{a} = \frac{i}{2\pi}\left\{\log\frac{i\sqrt{c^2-\xi^2}-\xi\sqrt{1-c^2}}{i\sqrt{c^2-\xi^2}+\xi\sqrt{1-c^2}} + \log\frac{i\sqrt{c^2-\xi^2}-\xi}{i\sqrt{c^2-\xi^2}+\xi} - \log[-(1-\xi^2)]\right\} - \frac{1}{2}$$

The log of a complex number can be written in terms of the inverse tangent, so this reduces to

$$\frac{z_s}{a} = \frac{1}{\pi}\left[\tan^{-1}\frac{\sqrt{c^2-\xi^2}}{\xi\sqrt{1-c^2}} + \tan^{-1}\frac{\sqrt{c^2-\xi^2}}{\xi} - \pi\right] - \frac{i}{2\pi}\log(1-\xi^2).$$

Separating real and imaginary parts and taking into account the fact that the interface is symmetric about $x = 0$ gives the parametric equations along the interface,

$$\frac{x_s}{a} = \pm\left(1 - \frac{1}{\pi}\tan^{-1}\frac{\sqrt{c^2-\xi^2}}{\xi\sqrt{1-c^2}} - \frac{1}{\pi}\tan^{-1}\frac{\sqrt{c^2-\xi^2}}{\xi}\right) \quad (22a)$$

$$0 \le \xi \le c$$

$$\frac{y_s}{a} = -\frac{1}{2\pi}\log(1-\xi^2) \quad (22b)$$

The value of the height δ in Fig. 1(*a*) is of interest as it shows how far the interface deviates from being planar. Point 2 in Fig. 1(*b*) corresponds to $\xi = -c$ in Fig. 2(*d*), so from equation (21(*b*)) the value of δ/a is

$$\frac{\delta}{a} = -\frac{1}{2\pi}\log(1-c^2) \quad (23)$$

Another quantity of interest is the height b of the interface above the bottom edge of the mold which is at point 7 in Fig. 1(*b*). Point 7 corresponds to $u = 1$ in Fig. 2(*d*) so that from equation (21) $b/a = |\lim_{u\to 1} Im(z/a)|$. This yields

$$\frac{b}{a} = \frac{1}{2\pi}\log\left[\frac{(1-\sqrt{1-c^2})^2}{4(1-c^2)}\right] \quad (24)$$

In Fig. 1(*b*), it is noted that there are inflection points along the interface at points α and β; these correspond to $\xi = \pm d$ in Fig. 2(*d*). In connection with obtaining the constants in equation (14), it was found that $d^2 = 1 - \sqrt{1-c^2}$. If we let $\xi = d$ in equation (22(*a*)) and then substitute $d = (1-\sqrt{1-c^2})^{1/2}$, we obtain

$$\left.\frac{x_s}{a}\right|_{\substack{\text{inflection}\\ \text{point}}} = \pm\left[1 - \frac{1}{\pi}\tan^{-1}\frac{1}{(1-c^2)^{1/4}} - \frac{1}{\pi}\tan^{-1}(1-c^2)^{1/4}\right] = \pm\frac{1}{2} \quad (25a)$$

From equation (22b)

$$\left.\frac{y_s}{a}\right|_{\substack{\text{inflection}\\ \text{point}}} = -\frac{1}{2\pi}\log(1-c^2)^{1/2} = \frac{1}{2}\frac{\delta}{a} \quad (25b)$$

where δ/a is given by equation (23).

Expression for c in Terms of Physical Conditions. The previous results are in terms of the quantity c that has values between 0 and 1, but arises during the conformal mapping without any particular physical significance. The c will now be related to the imposed physical conditions. By fixing points in the physical plane, it was found earlier in connection with equation (20) that $C_4 = -(A/\pi)[c^2/(1-\sqrt{1-c^2})]$. The C_4 can also be determined from the fact that the width of the rectangle in Fig. 2(*a*) is unity as fixed by the specified temperature difference. This gives

$$W(7) - W(8) = 1 = \int_c^1 \frac{dW}{dV}\frac{dV}{du}du$$

Inserting equations (15) and (16)

$$1 = \int_c^1 (-i)\frac{C_4 du}{\sqrt{u^2-c^2}\sqrt{u^2-1}} = -C_4\int_c^1 \frac{du}{\sqrt{u^2-c^2}\sqrt{1-u^2}}$$

The integral is another form of the complete elliptic integral of the first kind

$$K(\sqrt{1-c^2}) = \int_0^{\pi/2}\frac{d\varphi}{\sqrt{1-(1-c^2)\sin^2\varphi}}$$

so that $C_4 = -1/K(\sqrt{1-c^2})$. Equating this to the previously determined value for C_4 gives

$$A = \frac{(q_l + \bar{u}\rho\lambda)a}{k(t_f - t_c)} = \frac{q_s a}{k(t_f - t_c)} = \frac{\pi(1-\sqrt{1-c^2})}{c^2 K(\sqrt{1-c^2})} \quad (26)$$

Thus the c can be determined from the physical inputs that specify the value for $q_s a/k(t_f - t_c)$.

Total Heat Flow to Coolant. A quantity of some interest is the total amount of heat being transferred through the solidification interface and then removed by the coolant. This includes both the heat flow from the superheated liquid metal and the latent heat removed at the interface. When the interface is planar this is $Q = 2alq_s$, but as the interface becomes distorted, the Q increases in proportion to the increased surface area. Since the Q at the interface must exit through the cooled surfaces, the Q can be written as

$$Q = 2l\int_{y(6)}^{y(7)} k\frac{\partial t}{\partial x}dy$$

Putting this in dimensionless form and using the Cauchy-Riemann equation $\partial T/\partial X = -\partial\psi/\partial Y$ yields after integration $Q/2lk(t_f - t_c) = \psi(6) - \psi(7) = \psi(9) - \psi(8) = Im\,[W(9) - W(8)]$. By using equations (15) and (16) this can be written as,

$$-\frac{Q}{2lk(t_f - t_c)} = Im\int_{u=0}^{u=c}\frac{dW}{dV}\frac{dV}{du}du = Im\int_0^c -i\frac{C_4}{\sqrt{u^2-c^2}\sqrt{u^2-1}}du$$

Inserting C_4, and noting that the integration is along the ξ axis of the u-plane with $0 \le \xi \le c < 1$, yields

$$\frac{Q}{2lk(t_f - t_c)} = \frac{1}{K(\sqrt{1-c^2})}\int_0^c \frac{d\xi}{\sqrt{c^2-\xi^2}\sqrt{1-\xi^2}} = \frac{K(c)}{K(\sqrt{1-c^2})} \quad (27)$$

where $K(c)$ is the complete elliptic integral

$$K(c) = \int_0^c \frac{d\xi}{\sqrt{c^2-\xi^2}\sqrt{1-\xi^2}} = \int_0^{\pi/2}\frac{d\varphi}{\sqrt{1-c^2\sin^2\varphi}}$$

Results and Discussion

The solution has been obtained in parametric form in terms of the quantity c which is a quantity in the conformal mapping without direct physical significance. The solution shows that the controlling physical parameter is $q_s a/k(t_f - t_c)$ where q_s is the total amount of

heat carried away from the interface by conduction through the solid. The q_s is equal to the sum of the heat supplied by the molten eutectic alloy to the interface by convection or conduction, plus that due to latent heat. The physical parameter is related to c by equation (26). This equation is used to obtain the c corresponding to a $q_s a/k(t_f - t_c)$ of interest; then this c is used in the other parts of the solution to obtain the interface location and shape, and the total rate of heat removal corresponding to the given $q_s a/k(t_f - t_c)$.

Interface Shape. The interface shape is obtained from equation (22), and the height of the center of the interface above the bottom edge of the mold is obtained from equation (24). From these results, Figs. 3 and 4 are obtained. The interface shape has been normalized in Fig. 4(*c*) by dividing by the length δ, which is the total variation in interface height from centerline to wall.

Fig. 3 shows how the interface moves further up into the mold and becomes more planar as q_s or the width a is decreased, or $k(t_f - t_c)$ is increased. One of the conditions for forming the proper internal structure during directional solidification is that the solidification interface not deviate very far from being planar. As seen in Fig. 3, the tolerance on interface flatness determines how large $A = (q_l + \bar{u}\rho\lambda)a/k(t_f - t_c)$ can be. The deviation from being planar is shown in more detail in Fig. 4(*a*). If the maximum value of A for being within the planar limits is A_{max}, then the maximum withdrawal rate is

$$\bar{u}_{max} = \frac{1}{\rho\lambda}\left[\frac{k(t_f - t_c)}{a} A_{max} - q_l\right] \tag{28}$$

For example, from Fig. 4(*a*), to have an interface flatness such that

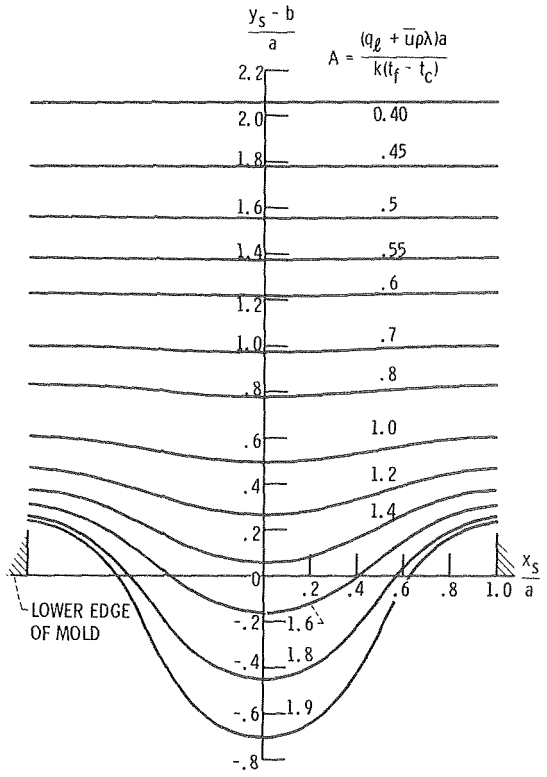

Fig. 3 Location and shape of solidification interface for various values of A

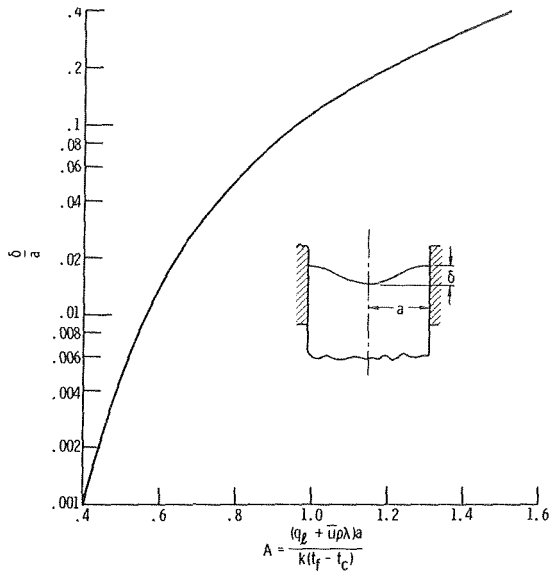

Fig. 4(a) Deviation of interface from being planar

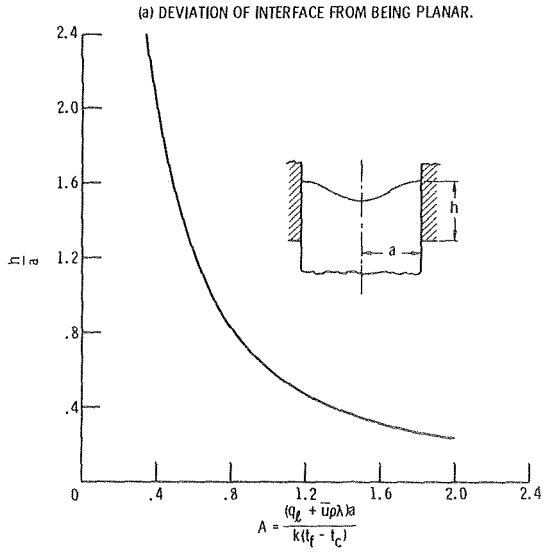

Fig. 4(b) Height of interface above bottom edge of mold

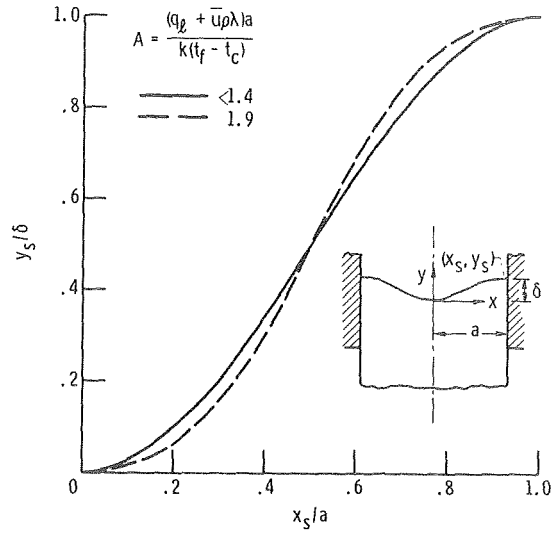

Fig. 4(c) Normalized shape of solidification interface

Fig. 4 Interface characteristics

$\delta/a < 0.05$ requires that the A_{max} be less than 0.8. Fig. 4(*b*) gives detailed information on the interface deviation from flatness and vertical location within the mold.

It was shown in the analysis that the inflection point along the interface is located half way both vertically and horizontally between the ingot centerline and the mold surface (see Fig. 4(*c*)). This means that if the interface is normalized to unit height, the curves for all values of A will pass through a common central point. As shown by Fig. 4(*c*), the normalized profiles are practically the same over the entire range of A values.

Fig. 5 shows how the total heat flow through the ingot varies as a function of the parameter A. For small A, the interface is essentially flat, and $Q = 2al q_s$, hence the curve becomes a line of unit slope. For larger A the interface area becomes curved so there is a greater area for heat transfer and the curve bends upward.

Application to Directional Solidification of Eutectics. By proper control of the solidification process, it is possible to obtain an aligned eutectic structure in an ingot solidified from a molten eutectic alloy. This aligned structure, extending along the length of the ingot, provides desirable strength characteristics. For proper control of the eutectic structure it is necessary to fulfill two conditions (references [10, 11]). The interface must be flat within a certain tolerance. The second condition is that the temperature gradient in the liquid metal at the solidification interface divided by the ingot growth rate must be above a certain value that is determined by the microscopic behavior at the interface during solidification of the eutectic alloy. If this ratio is called F, the parameter A can be rearranged into

$$A = \frac{[k_l(\partial t_l/\partial n)_s/\bar{u} + \rho\lambda]a\bar{u}}{k(t_f - t_c)} = \frac{(k_l F + \rho\lambda)a\bar{u}}{k(t_f - t_c)}$$

The maximum casting rate of the ingot will then correspond to when A has its maximum value corresponding to the required flatness of the interface, and F has its minimum value required by the metallurgical behavior at the solidification interface. Then

$$\bar{u}_{max} = \frac{A_{max}k(t_f - t_c)}{(k_l F_{min} + \rho\lambda)a} \tag{29}$$

To illustrate this relation, it is helpful to have a few numerical examples. The calculations will be made with a nickel base eutectic alloy containing strengthening phases of Ni_3Al and Ni_3Cb, and having the following properties: k of solid = 0.277 *W*/cm °C; k of liquid = 0.152 *W*/cm °C; ρ of solid = 0.00839 Kg/cm^3; λ = 56.2 *W* hr/Kg; t_f = 1250°C.

From practical experience in ingot casting, for a proper internal structure it is desired to have the interface sufficiently flat so that $\delta/a \leq 0.0035$. Then from Fig. 4(*a*) the maximum value of A that can be imposed is $A_{max} = 0.48$. For proper control of the aligned eutectic structure the F_{min} for this eutectic system is 150°C hr/cm^2 (reference [9]). Inserting these values into equation (29) yields,

$$\bar{u}_{max}(\text{cm/hr}) = \frac{(0.48)(0.277)[1250 - t_c(°\text{C})]}{[(0.152)(150) + (0.00839)(56.2)]a(cm)}$$

Some sample results are,

a, cm	$\bar{u}_{max}$, cm/hr	
	t_c = 750°C	t_c = 250°C
0.1	28.6	57.1
0.5	5.71	11.4
1.0	2.86	5.71

These values illustrate how the maximum casting rate can be increased by decreasing t_c or a. The casting configuration analyzed here is concerned with an advanced system in which the ingot is directly cooled in the region below the mold. Current industrial practice usually has the solidifying material entirely contained in a mold that is externally cooled. This provides a lower heat transfer than for the present configuration, and casting rates of 0.6 – 1.0 cm/hr are commonly obtained for turbine blade castings about one to two cm wide.

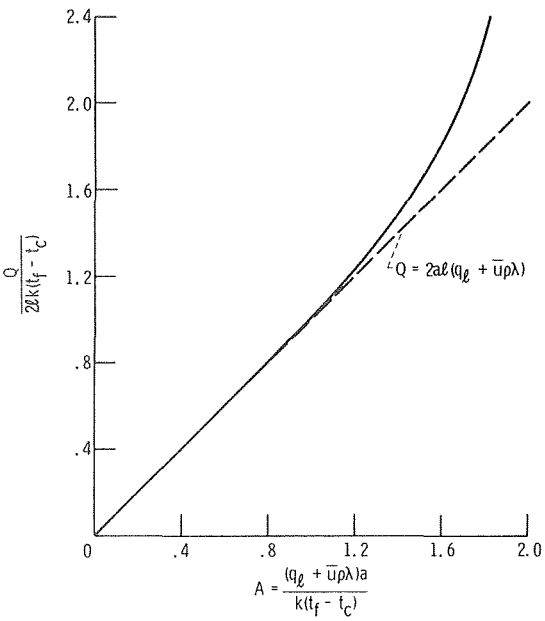

Fig. 5 Total heat flow at the interface as a function of the parameter *A*

These rates are consistent with the present results.

Conclusions

An analytical solution for the solidification of an ingot during continuous casting has been obtained by using a conformal mapping method. The two-dimensional shape of the solidification interface was obtained, and the interface position within the mold was found. The interface shape and position are governed by a single parameter $(q_l + \bar{u}\rho\lambda)/(k/a)(t_f - t_c)$, where the numerator is the total heat flux being conducted away from the interface as a result of heat flow from the superheated liquid metal and the latent heat of fusion. The results show how the flatness of the interface depends on the heat addition to the interface from the superheated liquid metal in contact with it, and on the solidification rate. An increase in either of these two quantities causes the interface to become more curved. Regulating the crystal structure in a eutectic alloy to obtain aligned growth depends on the flatness of the interface and on the ratio of the temperature gradient in the liquid metal at the interface to the solidification rate. For these two quantities specified, according to the requirements for a particular eutectic alloy, the results predict how fast the ingot can be withdrawn from the mold. The withdrawal speed can be increased by decreasing the width of the ingot or by lowering the temperature of the cooled boundary.

Acknowledgment

The author appreciates the helpful suggestions of Coulson M. Scheuermann of the Lewis Research Center.

References

1 Muehlbauer, J. C. and Sunderland, J. E. "Heat Conduction with Freezing or Melting," *Appl. Mech. Rev.*, Vol. 18, Dec. 1965, pp. 951–959.

2 Okendon, J. R. and Hodgkins, W. R., eds., *Moving Boundary Problems in Heat Flow and Diffusion*, Clarendon Press, Oxford, 1975.

3 Wilcox, W. R. and Duty, R. L., "Macroscopic Interface Shape During Solidification," JOURNAL OF HEAT TRANSFER, TRANS. ASME, Series C, Vol. 88, Feb. 1966, pp. 45–51.

4 Sfeir, A. A. and Clumpner, J. A., "Continuous Casting of Cylindrical Ingots," JOURNAL OF HEAT TRANSFER, TRANS. ASME, Series C, Vol. 99, Feb. 1977, pp. 29–34.

5 Kroeger, P. G. and Ostrach, S., "The Solution of a Two-Dimensional Freezing Problem Including Convection Effects in the Liquid Region," *Intl. Jour. of Heat and Mass Transfer*, Vol. 17, no. 10, Oct. 1974, pp. 1191–1207.

6 Mollard, F. R. and Flemings, M. C., "Growth of Composites from the Melt-Part I," *Trans. Metall. Soc. AIME*, Vol. 239, Oct. 1967, pp. 1526–1533.

Mollard, F. R. and Flemings, M. C., "Growth of Composites from the Melt-Part II," *Trans. Metall. Soc. AIME,* Vol. 239, Oct. 1967, pp. 1534–1546.

7 Jackson, K. A. and Hunt, J. D., "Lamellar and Rod Eutectic Growth," *Trans. Metall. Soc. AIME,* Vol. 236, Aug. 1966, pp. 1129–1142.

8 Schneider, P. J., "Effect of Axial Fluid Conduction on Heat Transfer in the Entrance Regions of Parallel Plates and Tubes," TRANS. ASME, Vol. 79, No. 4, May 1957, pp. 765–773.

9 Siegel, R., "Conformal Mapping for Steady Two-Dimensional Solidification on a Cold Surface in Flowing Liquid," NASA TN D-4771, 1968.

10 Flemings, M. C., *Solidification Processing,* McGraw-Hill Book Co., 1974.

11 Scheffler, K. D., et al., "Alloy and Structural Optimization of a Directionally Solidified Lamellar Eutectic Alloy," PWA-5300 (NASA CR-135000), Pratt & Whitney Aircraft Co., 1976.

E. M. Sparrow
R. R. Schmidt
J. W. Ramsey

Department of Mechanical Engineering,
University of Minnesota,
Minneapolis, Minn.

Experiments on the Role of Natural Convection in the Melting of Solids

Experiments are performed whose results convey strong evidence of the dominant role played by natural convection in the melting of a solid due to an embedded heat source. The research encompassed both melting experiments and supplementary natural convection experiments, with a horizontal cylinder as the heat source. For the melting studies, the cylinder was embedded in a solid at its fusion temperature, whereas in the natural convection tests it was situated in the liquid phase of the same solid. A special feature of the experiments was the use of a grid of approximately 100 thermocouples to sense thermal events within the phase change medium. The time history of the heat transfer coefficients for melting was characterized by an initial sharp decrease followed by the attainment of a minimum and then a rise which ultimately led to a steady value. This is in sharp contrast to the monotonic decrease that is predicted by a pure conduction model. The steady state values were found to differ only slightly from those measured for pure natural convection. This finding enables melting coefficients to be taken from results for natural convection. The positions of the solid-liquid interface at successive times during the melting process also demonstrated the strong influence of natural convection. These interfaces showed that melting primarily occurred above the cylinder. In contrast, the interfaces given by the conduction model are concentric circles centered about the cylinder.

Introduction

In this paper, experiments are described which are aimed at illuminating the heat transfer processes which occur when a solid is melted by a heat source embedded within the solid. The currently standard analytical approach to such problems is based on heat conduction as the sole transport mechanism. On the other hand, it can be reasoned that the temperature differences which necessarily exist in the melt region will induce buoyancy forces and these, in turn, will generate natural convection motions. It appears, however, that experiments have not yet been reported which specifically address this issue, aside from those on convective instabilities involved in the melting of horizontal ice layers (e.g., [1])[1] and those presented in [2] subsequent to the submission of this paper ([2] will be elaborated shortly). The need for such experiments has motivated the present work, which is part of a larger study of energy storage via solid/liquid phase change.

Separate experiments on melting and on natural convection were performed to obtain a definitive relation between the heat transfer coefficients for the two cases. In the melting tests, a solid was initially brought to its fusion temperature by external heating. Then, the experiment was initiated when a horizontal heating cylinder embedded in the solid was energized to give a steady rate of heat transfer. The cylinder was instrumented with thermocouples and, in addition, an array of 92 thermocouples was deployed throughout the phase change medium with the aid of a specially designed fixture. The cylinder-mounted thermocouples facilitated the evaluation of instantaneous heat transfer coefficients, while those in the medium enabled the position of the solid-liquid interface to be identified. The data runs encompassed a parametric range of heat fluxes from 1430 to 7870 W/m^2.

These experiments were performed with a eutectic mixture of sodium nitrate and sodium hydroxide, which has a melting temperature of about 244°C (471°F). This substance has been considered for application as an intermediate range thermal storage medium. It has the virtues of being inexpensive, non-corrosive (no corrosion of a steel tank over a period of one year) and non-toxic.

The aim of the second group of experiments was to determine natural convection heat transfer coefficients with the horizontal heating cylinder situated in a purely liquid environment, specifically, in the liquid phase of the aforementioned eutectic. For these experiments, the temperature of the liquid environment was maintained as close to the fusion temperature as possible. The same instrumentation and heat fluxes were employed in the natural convection studies as in the melting experiments.

The heat transfer coefficients for the melting experiments are plotted here as a function of time and their trend, relative to the monotonic timewise decrease of those for pure conduction, provides immediate insight into the nature of the transport processes. The

[1] Numbers in brackets designate References at end of paper.

Contributed by the Heat Transfer Division for publication in the JOURNAL OF HEAT TRANSFER. Manuscript received by the Heat Transfer Division August 2, 1977.

natural convection coefficients are also plotted as a function of time. The steady state coefficients for the two groups of experiments—melting and natural convection—are then compared to provide further evidence about the transport processes. The final evidence is furnished by the shapes of the solid-liquid interface which were deduced from the thermocouple grid in the phase change medium.

The experiments of [2] and those reported here appear to have been concurrent and independent efforts aimed at a common goal. There are both similarities and differences in the two sets of experiments and, most significantly, their qualitative findings are mutually supportive. Quantitative comparisons are difficult to make because of the different media employed and because the results of [2] may have been influenced by subcooling and end losses and were not supplemented by separate natural convection experiments.

The Experiments

Experimental Apparatus. The apparatus that was designed and fabricated for the experiments is shown in a vertical sectional view in Fig. 1. As seen there, it is made up of a test chamber surrounded by a multilayer wall consisting of heating panels and insulation layers. The test chamber is a cubical, mild-steel tank, 33 cm (13 in.) on a side. For the experiments, the test chamber was filled with the phase change material to a height of about 25 cm (10 in.).

The test chamber is equipped with a horizontal heating cylinder which consists of a thin-walled incoloy sheath housing a uniformly wound electrical resistance element. The outside diameter of the sheath is 1.9 cm (¾ in.) and its length is 25.4 cm (10 in.). As seen in Fig. 1, the cylinder is parallel to one pair of side walls and midway between them. Its centerline is about 5.4 cm (2 in.) above the floor of the tank.

Two auxiliary heaters were installed in the test chamber to neutralize potential problems associated with the density change that accompanies solid-liquid phase change. Since the liquid phase occupies a greater volume than the solid phase (for a given mass), it is necessary to provide expansion space. This was accomplished by the use of the so-called vent heater, which passes vertically downward through the phase change material adjacent to one of the walls of the chamber. When actuated, the vent heater opens a vertical channel through the solid phase-change material, and this enables any expansion fluid associated with melting around the horizontal cylinder to escape to the top of the solid.

The second auxiliary heating device is situated in the upper part of the test chamber and is used to help prevent the formation of voids during the freezing of the phase change material which necessarily precedes each melting run. One essential measure in the prevention of voids is to avoid the formation of a solid skin across the top of the freezing mass and, in general, to keep the upper part of the material in the liquid state until the very end of freezing. The accomplishment of these objectives was furthered by the just-mentioned heater. An additional assist in keeping the upper part of the material unfrozen until the end was provided by the heating panel situated above the top of the test chamber.

A copper water-carrying cooling coil affixed to the lower edge of the outside walls of the test chamber was activated during the freezing of the phase change material. Its placement in the lower part of the chamber ensured that freezing would occur from bottom to top. This direction of freezing is another important measure in the avoidance of voids.

The thermocouple instrumentation utilized in the test chamber will now be discussed. All thermocouples were made from separate, but matched rolls of 30-gage teflon-coated chromel and alumel wire.

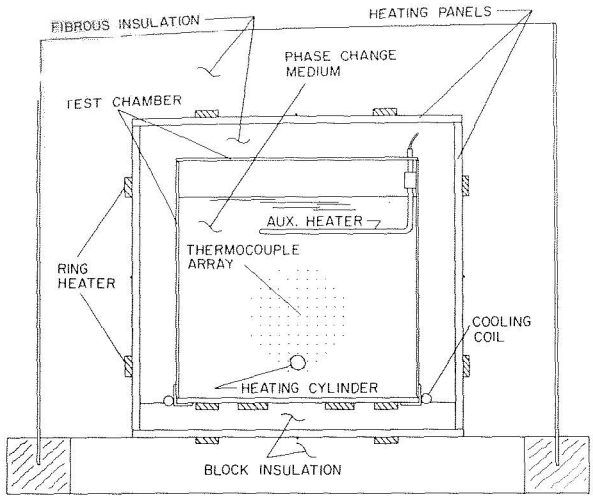

Fig. 1 Vertical sectional view of the experimental apparatus

The choice of teflon as a coating was based on its ability to tolerate temperatures up to about 290°C (550°F). Six thermocouples were spot welded to the horizontal heating tube around a circumference situated mid-way along the length of the tube. The thermocouple junctions were separated by an angular spacing of 60 deg. The chromel and alumel lead wires were stretched tightly along the tube and were brought out at one end.

As was noted earlier, 92 thermocouples were deployed throughout the phase change material. These thermocouples were stretched horizontally between a pair of supporting racks. The racks were respectively positioned at the walls adjacent to the ends of the horizontal cylinder so that the thermocouples were parallel to the cylinder. The thermocouple junctions were situated in a vertical plane that encompassed the mid-length position of the heated cylinder. The chromel wire extended from the junction toward one of the racks and the alumel wire extended from the junction to the other rack. By suitable guides, the leads were brought vertically upward along the side walls of the chamber and were taken out through an access port. Once outside the apparatus, the leads were drawn tightly, via special springs, toward a connector panel. The tension was adjusted so that the horizontally stretched thermocouples in the test chamber would not sag during the experiments.

The test chamber was surrounded by a 5 cm (2 in.) layer of high-temperature spun glass insulation at the sides and top, and by a 3¾ cm (1½ in.) thick layer of calcium silicate block insulation below. External to the insulation, each side, the top, and the bottom were equipped with a heating panel. Each panel consisted of a 0.95 cm (⅜ in.) thick aluminum plate, on the outer face of which was mounted a ring-shaped electric heater. A thermocouple was affixed to the center of each panel. Outside of the heating panels was another layer of insulation, 12½ cm (5 in.) of spun glass at the sides and top, and 7½ cm (3 in.) of calcium silicate at the bottom. At the very outside, the insulation was enclosed in plywood.

The thermocouple emf's were read and recorded by a Doric Digitrend 210 digital millivoltmeter. This instrument can be programmed to read and record thermocouples at preselected intervals, and this feature was employed during the later stages of the data runs.

Nomenclature

h = heat transfer coefficient, equations (1) and (2)
q = heat transfer per unit time and area at cylinder surface
T_w = surface temperature of horizontal cylinder
T_∞ = ambient temperature
T^* = phase change temperature

Experimental Procedure. At the very beginning of the experiments, the constituents of the eutectic, 83.2 percent sodium nitrate and 16.8 percent sodium hydroxide, in granular form, were carefully weighed and placed in the test chamber. These granular solids were melted, and the liquid was well mixed to obtain a homogeneous substance. Freezing was then initiated, making use of the cooling water to freeze from below and the immersion and top panel heaters to keep the upper portion of the material in the liquid phase until the end. At the conclusion of the freezing process, the lower part of the solid was in the 160°C (325°F) range, whereas the upper part was in the 230°C (450°F) range.

The solid was then heated to obtain a temperature close to the fusion value. To this end, the heating panels on all faces (sides, top and bottom) were energized and operated under automatic regulation so as to maintain the temperature at a control point (center of top heating panel) at a fixed value of 260°C (500°F). This heating regime was continued until a thin melt layer (observed through a viewing aperture) appeared on the upper surface of the solid. Normally, about seven days were required to attain this state. From then onward, the control point temperature was gradually reduced, and the temperatures on the horizontal cylinder and in the phase change material were carefully monitored. These manipulations usually encompassed a three-day period.

The solid was regarded as being ready for a data run when it had achieved a mean temperature of 243°C (469.5°F) with spatial variations of ±0.4°C (0.75°F). This temperature is about 1°C (1.5°F) below the fusion value. Attempts to approach closer to fusion would have resulted in an undue amount of melting of the solid.

About an hour before the initiation of a data run, the vent heater was activated. The run itself was begun by actuating the current flow to the horizontal cylinder. At the same time, the power to the vent heater was diminished to about a quarter of its initial value (i.e., to about two watts), and after an hour it was turned off. The heat flow to the horizontal cylinder was maintained constant throughout the data run, at power levels which ranged from 20.6 to 113.6 W (i.e., power densities from 1430 to 7870 W/m^2). Run times ranged from 4 to 26 hours, increasing with lower heating rates. Thermocouple data were collected at one-minute intervals at early times when changes were rather rapid and at lesser frequencies at later times when the temperature variations became gradual.

For the natural convection runs, the phase change material was liquified by appropriate adjustment of the heating panels. Then, the control point temperature was set at about 245°C (474°F), and ample time (two to three days) was allowed for the liquid to attain temperature uniformity at this level. The initiation of a data run involved the application of power to the horizontal cylinder and the activation of the thermocouple reading and recording instrumentation. The data runs were completed in one to two hours.

Results and Discussion

Heat Transfer Coefficients. For the melting experiments, heat transfer coefficients were evaluated from the defining equation

$$h = \frac{q}{T_w - T^*} \tag{1}$$

In this equation, q is the heat flux at the surface of the horizontal cylinder—determined from the electric power input and the area of the heated surface. T_w is the circumferential-average cylinder wall temperature (the mean value of six surface-mounted thermocouples), and T^* is the melting temperature of the eutectic phase change material. During any given data run, both q and T^* were constant, while T_w varied with time, at least during early times. Therefore, equation (1) was evaluated at a succession of times spanning the entire duration of each data run.

The instantaneous heat transfer coefficients from equation (1) are plotted in Fig. 2 as a function of time. An inset at the top of the figure continues the presentation for larger times. The results are parameterized by the surface heat flux q, which ranges from about 1400 to 7900 W/m^2.

Inspection of the figure reveals a characteristic pattern in the results which is common to all of the cases that were investigated. Starting with high values at early times, the heat transfer coefficient decreases sharply and attains a minimum, whereafter it increases and ultimately reaches a steady state value. This behavior, in itself, provides important insights into the transfer processes, especially when compared to that which would occur if only conduction were involved. For pure conduction phase change, the heat transfer coefficient starts from high values at early times and then decreases monotonically with time, never attaining a steady state value.[2] Therefore, the results of Fig. 2 provide clear evidence that transfer mechanisms other than mere conduction are involved.

It appears that conduction is the dominant transport mechanism only at very early times, that is, during the period when the transfer coefficient decreases. Thereafter, natural convection comes into play

[2] There do not appear to be any quantitative heat transfer results in the literature for conduction phase change due to a cylindrical source. The qualitative behavior of the conduction coefficients can be readily deduced by physical reasoning supported by the information given in (3) on the movement of the liquid-solid interface.

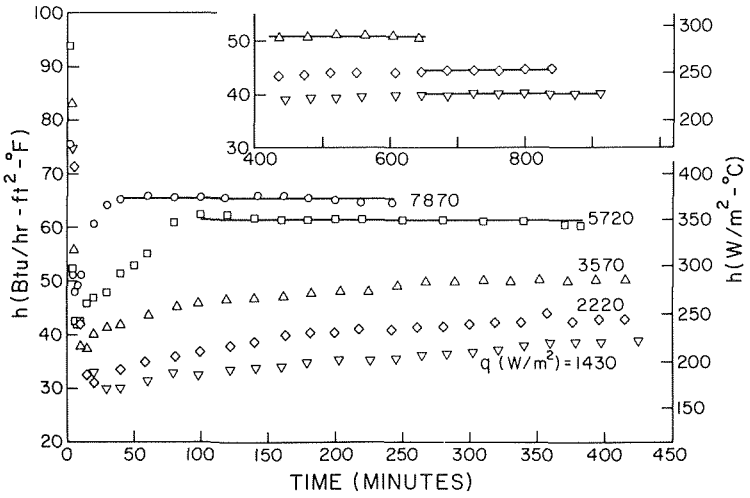

Fig. 2 Heat transfer coefficients for the melting experiments

and finally takes over. It is especially noteworthy that a steady value of h is ultimately attained even though the liquid-solid interface continues to move as melting proceeds. This suggests that in the steady state regime, the processes which occur in the neighborhood of the interface do not contribute significantly to the overall thermal resistance. The steady state value of h for each heating rate is delineated by a horizontal line.

It may also be observed that the onset of natural convection and attainment of the steady state occur at earlier times at higher heating rates. In addition, the higher the heating rate, the larger are the heat transfer coefficients. These trends are reasonable inasmuch as higher heating rates correspond to higher values of the Grashof number (based on either q or $(T_w - T^*)$).

Fig. 1, with the aid of equation (1), also conveys information on the time variation of the cylinder surface temperature. Since both q and T^* were evaluated as constants for a given data run, equation (1) shows that the variation of T_w with time is reciprocal to that of h.

The finding that natural convection is a major contributor to the melting problem motivated the no-phase-change natural convection experiments with the cylinder situated in the liquid eutectic. The heat transfer coefficients for these experiments were evaluated from

$$h = \frac{q}{T_w - T_\infty} \tag{2}$$

The quantities q and T_w have the same meaning as in equation (1). T_∞ represents the average of six thermocouples situated in the liquid and displaced by about 1.3 cm (½ in.) from the surface of the cylinder. These thermocouples were deployed in a vertical plane at the mid-length of the cylinder. They were positioned below and at the sides of the cylinder, so that they were washed by fluid moving toward the boundary layer that flows around the cylinder surface.

The natural convection heat transfer coefficients are plotted as a function of time in Fig. 3. The various runs are parameterized by the surface heat flux, the values of which are identical to those of the melting experiments. The figure shows that after a brief transient period, a steady state heat transfer regime is established. The steady state heat transfer coefficient for each heating rate is indicated by a solid line. The heat transfer coefficients increase with increasing heating rate, as is consistent with the corresponding increase of the Grashof number.

The main relevance of these natural convection heat transfer coefficients is to serve as a basis for comparison with those for the melting problem. The steady state values for the melting and natural convection problems are brought together in Fig. 4, where they are plotted on logarithmic coordinates as a function of the surface heat flux. The natural convection coefficients fall consistently on a straight line and the melting coefficients, aside from a slight scatter, can be regarded as lying on a parallel straight line.

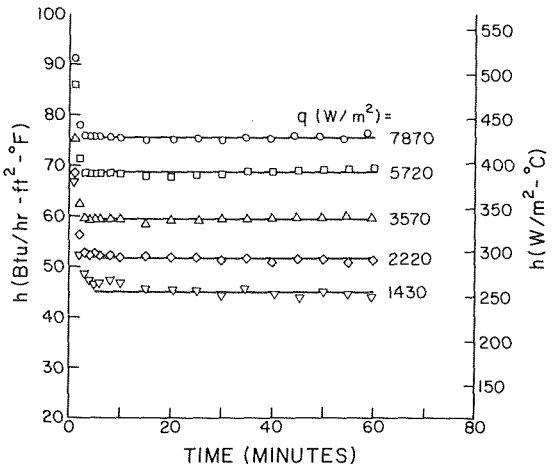

Fig. 3 Heat transfer coefficients for the natural convection experiments

The steady state melting coefficients are about 12 percent smaller than those for pure natural convection. The fact that the two sets of values are so close is a further indication that natural convection plays a dominant role in the heat transfer through the liquid melt. Indeed, the comparison in Fig. 4 gives license for the use of natural convection coefficients for the design of melting systems involving a horizontal embedded heater.

The small differences between the two sets of results can readily be rationalized. As will be illustrated shortly, relatively little melting takes place adjacent to the lower portion of the cylinder, with the result that the melt layer is relatively thin in that region. The thinness of the layer may impose constraints on the natural convection flow pattern which do not exist when the cylinder is situated in a purely liquid environment. Other geometrical differences (size, shape) and thermal differences (stratification) may also play a role. The natural convection coefficients themselves may be affected by the finite height of the test chamber. Notwithstanding all of these possibilities, there are only modest differences in the heat transfer coefficients (Fig. 4).

Liquid-Solid Interfaces. Attention will now be turned to another type of evidence that demonstrates the dominance of natural convection as a transport vehicle in the melting problem. In Figs. 5 and 6, the positions of the solid-liquid interface at a succession of times are plotted, respectively for heat fluxes of 1430 and 5720 W/m². These interfaces were deduced from the temperatures measured in the phase

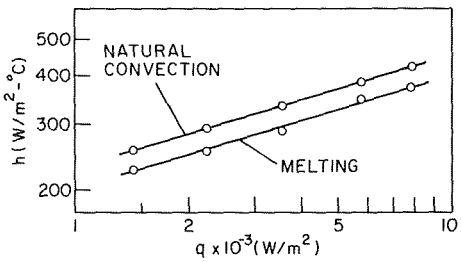

Fig. 4 Steady state heat transfer coefficients for melting and for natural convection

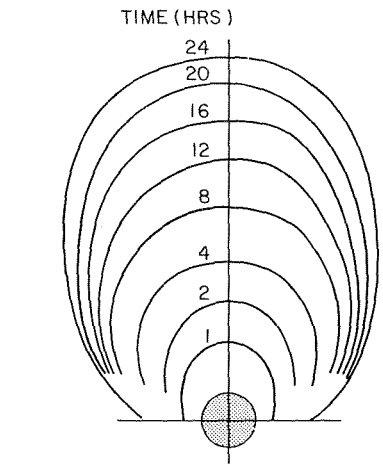

Fig. 5 Positions of the solid-liquid interface at a succession of times, q = 1430 W/m²

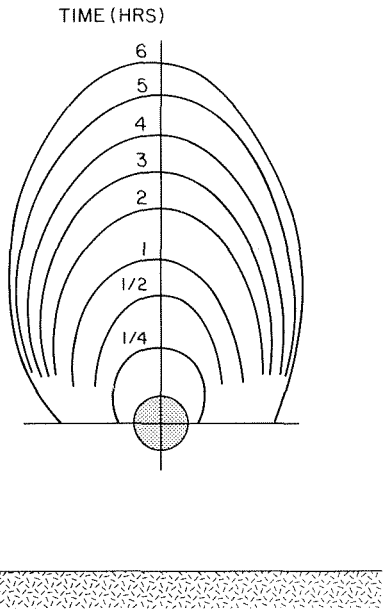

Fig. 6 Positions of the solid-liquid interface at a succession of times, q = 5720 W/m²

change medium via the thermocouple grid. Specifically, by examining the temperature history at any point in the grid, the time at which the melting front passed that point could be identified. Once this information was obtained at all points where melting had occurred, working plots were prepared to facilitate the interpolations needed to draw the position of the interface at any selected instant of time.

Figure 5, which corresponds to the lowest heat flux used in the experiments, shows successive interface positions at times ranging from 1 to 24 hours. The heat flux for Fig. 6 is four times that for Fig. 5 and, correspondingly, the interfaces have been plotted at times that are one-quarter of those of Fig. 5. The horizontal heating cylinder is shown in both of the figures, and the cylinder diameter (1.9 cm, ¾ in.) provides a scale from which all other lengths may be inferred. The floor of the test chamber is also indicated in the figures.

Figures 5 and 6 show that melting primarily takes place above the heated cylinder, with very little melting below. This is in sharp contrast to the melting pattern that would be predicted by a solution based on pure conduction, for which the interfaces would be a succession of concentric circles surrounding the cylinder. The strong upward thrust of the melting zone is caused by natural convection. The primary factor in this thrust is the plume which rises from the top of the heated cylinder. The plume conveys hot liquid to the upper part of the melt region and, in this way, perpetuates the upward movement of the interface.

There is ample evidence that the floor of the test chamber is sufficiently far from the heating cylinder so as not to affect the melting process. Such evidence is provided by photographs presented in [2] and by the authors' own visual observations of the size and shape of the melt region.

A comparison of Figs. 5 and 6 may be made for interfaces that correspond to times in the ratio of a factor of one-fourth (i.e., reciprocal to the heat flux ratio). This comparison shows that the interfaces for the lower heat flux tend to be fuller than those for the higher heat flux. Aside from this, the interface positions at corresponding times tend to be more or less coincident.

It is also of interest to take note of the size of the melt region at the time when the melting heat transfer coefficient approaches a steady value. For example, from Fig. 2, it can be observed that for the 5720 W/m² heat flux, the steady state is approached in the 1½ to 2 hour range. At this time, Fig. 6 shows that the height of the melt region is only three diameters above the top of the heating cylinder.

Other Issues. With regard to the steady state heat transfer coefficients presented in Fig. 4, efforts made to compare them with literature information for natural convection about a horizontal cylinder did not prove fruitful. The main stumbling block was the absence of the thermophysical property values needed to evaluate the literature correlations (e.g., [4], pp. 444–446). In this connection, difficulties were encountered on various fronts. First, property values are not available for the sodium nitrate—sodium hydroxide eutectic. Although the properties of the pure components are tabulated [5], these components are solids at the temperature at which the eutectic mixture is a liquid.[3] Finally, the absence of proven procedures for evaluating properties of liquid mixtures from component properties [6, 7] tended to discourage even *ad hoc* use of the available component data.

While it is regrettable that the aforementioned comparison could not be made, it has not deterred the major findings of the work. In particular, the separate experiments on melting and on natural convection have enabled a quantitative relation between the two sets of heat transfer coefficients to be determined.

When a heating element with a finite heat capacity is employed in a transient experiment, there is some reason for concern about the influence of that heat capacity on the results being sought. The natural convection results presented in Fig. 3 provide some perspective about the time scale of such possible influences. The transient period in evidence there is the result of two factors: (*a*) the actual flow and thermal transients in the fluid, (*b*) the transient due to the heat capacity of the heater. Thus, the duration of the transient that is due to the latter is no greater than that in evidence in Fig. 3. As can be seen in Fig. 2, those duration times are shorter than the times at which natural convection begins to influence the melting process.

Another aspect of the natural convection results which merits brief mention is the possible presence of temperature stratification. The measured temperature distributions in the liquid prior to the initiation of a data run indicated no stratification at that time. After an hour's run, the vertical variation of the temperature in the liquid environment, over the height of the cylinder, was estimated to be 4 to 5 percent of $(T_w - T_\infty)$. In view of this relatively small variation, and also noting that T_∞ was obtained as an average, it can be concluded that stratification was not a factor in the results.

In order to determine the phase change temperature in terms of the specifics of the instrumentation (i.e., thermocouples, millivoltmeter), temperature versus time curves for freezing were generated. The cooling curves give the fusion temperature to be 244.2°C (471.5°F), and this value was used for the evaluation of T^* in equation (1).

Concluding Remarks

The experimental results presented here have conveyed strong evidence of the dominant role played by natural convection in the melting of a solid due to an embedded heat source. There are three distinct aspects of the results which contribute testimony about the importance of natural convection. First, the timewise behavior of the heat transfer coefficient deviates markedly from the monotonic decrease that is characteristic of conduction phase change. The results show that conduction dominates only during the earliest stages of the melting process, whereafter natural convection comes into play and ultimately gives rise to a steady value of the transfer coefficient.

Furthermore, via separate experiments, the steady values of the melting coefficient were shown to differ only slightly from those for pure natural convection. This finding enables melting coefficients to be taken from results for natural convection.

The final piece of evidence is provided by the positions of the liquid-solid interface, which were determined at a succession of times during the melting process. These results showed that melting primarily occurred above the heated cylinder, with very little melting

[3] The eutetic mixture solidifies at a temperature lower than the solidification temperature of any other mixture of the components.

below. This is in contrast to the predictions of the pure conduction model, according to which the moving interface is represented by a succession of concentric circles centered about the horizontal cylinder.

In view of the demonstrated importance of natural convection in melting problems, it appears unreasonable to continue the present practice of neglecting it in the analysis of such problems.

Acknowledgment

This research was performed under the auspices of ERDA grant No. E(11-1)-2595.

References

1 Seki, N., Fukusako, S., and Sugawara, M., "A Criterion of Onset of Free Convection in a Horizontal Melted Water Layer with Free Surface," ASME, JOURNAL OF HEAT TRANSFER, Vol. 99, 1977, pp. 92–98.

2 White, R. D., Bathelt, A. G., Leidenfrost, W., and Viskanta, R., "Study of Heat Transfer and Melting Front From a Cylinder Imbedded in a Phase Change Material," ASME paper 77-HT-42, 17th National Heat Transfer Conference, Salt Lake City, Utah, Aug. 1977.

3 Stephan, K., and Holzknecht, B., "Heat Conduction in Solidification of Geometrically Simple Bodies," Wärme- und Stoffübertragung, Vol. 7, 1974, pp. 200–207.

4 Karlekar, B. V., and Desmond, R. M., *Engineering Heat Transfer*, West Publishing Co., St. Paul, 1977.

5 Janz, G. J., *Molten Salts Handbook*, Academic, New York, 1967.

6 Reid, R. C., and Sherwood, T. K., *The properties of Gases and Liquids*, McGraw-Hill, New York, 1958.

7 Blander, M., ed., *Molten Salt Chemistry*, Interscience, New York, 1964.

J. H. Royal
Senior Engineer,
Union Carbide Corporation,
Linde Division,
Tonawanda, N. Y.
Assoc. Mem. ASME

A. E. Bergles
Professor and Chairman,
Department of Mechanical
Engineering and Engineering
Research Institute,
Iowa State University,
Ames, Iowa
Mem. ASME

Augmentation of Horizontal In-Tube Condensation by Means of Twisted-Tape Inserts and Internally Finned Tubes

Low pressure steam was condensed inside horizontal tubes of different internal geometries to investigate passive heat transfer augmentation techniques. A smooth tube, the smooth tube having two twisted-tape inserts, and four internally finned tubes were tested. The twisted-tape inserts were found to increase average heat transfer coefficients by as much as 30 percent above smooth tube values on a nominal area basis. The best performing internally finned tube increased average heat transfer coefficients by 150 percent above the nominal smooth tube values. Techniques were developed to correlate the improved heat transfer performance of the two twisted-tape inserts and the four internally finned tubes. The equations developed provide a reasonably accurate description of both the sectional and the average heat transfer coefficients. The finned tube correlation was also reasonably successful in predicting the data from the one other investigation of this augmentation technique for which detailed data were available.

Introduction

During filmwise in-tube condensation, vapor condenses at the cooler tube wall, and the condensate coats the tube wall with a continuous film. When the condensate layer is symmetric, with well defined phase segregation, the flow regime is said to be annular. Often, gravitational, shear, and pressure forces redistribute the liquid film and disrupt this well defined phase segregation. Interfacial waves, entrained droplets, stratification, bubbles, and vapor slugs can all be present and can greatly modify the flow field.

If the thermophysical properties of the condensing media are favorable, in-tube film condensation heat transfer coefficients can be quite high. However, many industrially important fluids, such as organic liquids and most fluorocarbon refrigerants, do not have such favorable properties. The condensation heat transfer coefficients for these fluids are often low enough to present a significant heat transfer resistance in a condenser. For such cases, techniques to augment in-tube condensation can be used to reduce the condensing-side thermal resistance to the extent that significant reductions in condenser size may be possible.

A literature survey of the field [1][1] disclosed a surprising number of attempts to augment condensation. However, relatively few of these studies were involved with in-tube condensation.

Cox, et al. [2] experimented with internally grooved and knurled tubes in single and multi-tube tests. The grooved tubes were reported to show an improvement in overall performance of up to ten percent; however, the knurled tubes demonstrated no obvious advantage. These investigators also indicated that spirally corrugated tubes matched the performance of the grooved tubes.

Prince [3] investigated heat transfer surfaces for use in horizontal tube desalination evaporators where condensation occurs inside tubes. He tested corrugated and internally ribbed tubes along with other surfaces. He reported significant increases in overall heat transfer coefficients for the ribbed tubes, but decreases in heat transfer coefficients for the corrugated tubes. The individual heat transfer coefficients from these experiments were not determined.

Reisbig [4] reported on the condensation of Refrigerant-12 inside tubes with internal longitudinal fins. Detailed data are not provided, and no correlations are presented.

Gottzmann and his co-workers [5, 6] condensed hydrocarbons within vertical tubes containing internal longitudinal fins. They noted increased condensation rates, but provided no condensation-side film coefficients.

Vrable, et al. [7–9] reported a study of the condensation of Refrigerant-12 inside tubes with internal longitudinal fins. Inlet reduced pressures for these tests varied from 0.18 to 0.46. Mass fluxes varied from 86.7 to 853 kg/m^{2}s. 26 experiments with two internally finned tubes were reported. These data were correlated by modifying the

[1] Numbers in brackets designate References at end of paper.

Contributed by the Heat Transfer Division for publication in the JOURNAL OF HEAT TRANSFER. Manuscript received by the Heat Transfer Division January 24, 1977.

semi-empirical, smooth tube correlation of Cavallini and Zecchini [10]. This correlation was modified by changing the constant, using as the characteristic length twice the equivalent diameter, and incorporating an additional term to adjust for pressure effects. The equation which correlated the data to within approximately ±30 percent is

$$\bar{h}_c = 0.02 \frac{k_f}{2d_e} \left(\frac{2d_e G_e}{\mu_f} \right)^{0.8} \mathrm{Pr}_f^{0.33} \left(\frac{p}{p_{cr}} \right)^{-0.65} \quad (1)$$

where

$$G_e = \left[\left(\frac{\rho_f}{\rho_v} \right)^{0.5} x + (1 - x) \right] G$$

Recently, Kröger [11] reported on studies of the laminar condensation of Refrigerant-12 inside smooth and internally finned tubes. Significant improvements in heat transfer were observed with internally finned tubes, but at Reynolds numbers well below those of interest here.

The study reported here was undertaken to investigate two potentially useful in-tube condensation augmentation techniques: twisted-tape inserts and internally finned tubes. The techniques were selected because both are basic passive augmentation techniques used extensively for single-phase flow. Twisted tapes are easily fabricated and installed, and internally finned tubes have recently become readily available. The study was designed to obtain a wide range of experimental data and to develop useful correlations of the data.

Experimental Facility and Procedure

Facility. An experimental facility was constructed to test the augmentation techniques and to provide the smooth tube reference data. Condensing steam was the medium selected for the experiment. The facility consisted of appropriate piping and instrumentation designed to test single, in-tube condenser tubes of various diameters, internal geometries, and lengths. Fig. 1 is a schematic of the facility.

For the experiments reported here, the condensing side of the facility was operated in an open-loop configuration. Clean steam was introduced into the dryer through a strainer from a building service steam main. A throttling valve controlled the dry, saturated steam flow rate to the test condenser. Up to 320 kg/hr of steam at eight bar with 0–16°C of superheat was available at the test condenser inlet. The condensate or condensate-vapor mixture exited the test condenser through an adiabatic sight glass section. The condensate-vapor mixture then flowed to the after-condenser to complete the condensation process. The subcooled condensate then passed through the system pressure regulation valves to the condensate flowmeter. The condensate was finally discharged to a floor drain.

Water was used as the test condenser coolant. The coolant entered the test condenser through a flowmeter. After passing through the test condenser, the coolant was discharged through the coolant drain valve. The coolant drain valve was used for coolant flow control to pressurize the coolant side of the test condenser in order to suppress coolant side subcooled boiling.

Test Condenser. Two concentric tubes formed the counterflow test condenser. The test condenser was divided into four, 0.91 m long units to form the test condenser sections. These sections were arranged in series, with the condensing medium uninterruptedly flowing through the test tube, while the coolant was diverted through mixing sections before proceeding to the next section. Thermocouples were

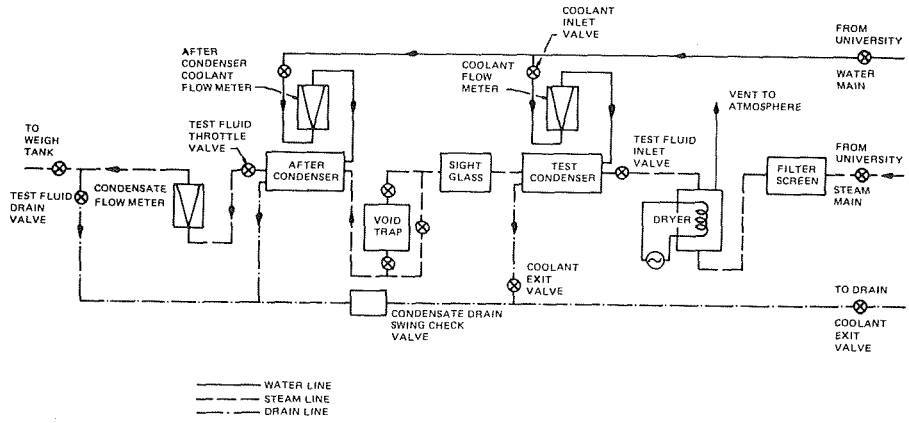

Fig. 1 Schematic of experimental facility

Nomenclature

A = area
b = fin height
c_p = specific heat at constant pressure
d = diameter
f = friction factor
F = factor, equation (6), etc.
G = mass flux
G_e = adjusted mass flux, equation (1)
h = heat transfer coefficient
k = thermal conductivity
L = heat transfer length of tube
m = fin parameter, equation (7)
n = number of fins
p = pressure
p_{cr} = critical pressure
Pr = Prandtl number
q = heat transfer rate
r = radius
Re = Reynolds number
T = temperature
u = velocity
w = interfin spacing
x = quality
y = half-pitch-to-diameter ratio
z = axial coordinate
δ = tape thickness
ζ = fin efficiency
μ = dynamic viscosity
ρ = density

Subscripts

a = axial
c = condensation
e = based on equivalent diameter
f = liquid or friction
i = inside
o = outside
s = saturation
t = tangential
tt = twisted tape
v = vapor
w = wall

Table 1 Selected Geometric Parameters of the Experimental Tubes

Tube Number	A	B	C	D	E	F	G
Type	Smooth	Twisted Tape #1	Twisted Tape #2	Fin #1	Fin #2	Fin #3	Fin #4
Material	Cu	Cu, SS	Cu, SS	Cu	Cu	Cu	Cu
Outside Diameter	1.5875	1.5875	1.5875	1.5875	1.2776	1.2776	1.5900
Inside Diameter	1.3843	1.3843	1.3843	1.4707	1.1811	1.1532	1.3970
Equivalent Diameter	1.3843	0.8252	0.8252	0.8260	0.7602	0.7564	0.6767
Wall Thickness	0.1016	0.1016	0.1016	0.0584	0.0490	0.0622	0.0965
Total Wetted Perimeter	4.3487	7.0419	7.0419	7.8750	5.3310	5.1891	8.1979
Nominal Wetted Perimeter	4.3487	4.3487	4.3487	4.6203	3.7104	3.6228	4.7437
Total Perimeter/ Nominal Perimeter	1.0	1.6193	1.6193	1.7045	1.4368	1.4324	1.7279
Cross-Sectional Area	1.5052	1.4529	1.4529	1.6264	1.0129	0.9648	1.3864
Tape Thickness	n.a.	0.0378	0.0378	n.a.	n.a.	n.a.	n.a.
Fin Height	n.a.	n.a.	n.a.	0.0599	0.1735	0.1631	0.1448
Fin Base Width	n.a.	n.a.	n.a.	0.0475	0.1669	0.1394	0.1245
Fin Tip Width	n.a.	n.a.	n.a.	0.0277	0.0478	0.0434	0.0462
Number of Fins	n.a.	n.a.	n.a.	32	6	6	16
Pitch, cm/180°	n.a.	4.57	9.65	30.48	17.15	straight	27.94

All dimensions in cm or cm^2, as appropriate.
n.a. = not applicable

used to measure coolant temperatures in the mixing sections at the entrance and exit of each condenser section. Pressure taps were provided at the condenser inlet and at the exit from each section to monitor the local pressure of the condensing medium.

Test condenser tube wall temperatures were obtained from 36 copper-constantan thermocouples, spaced axially in groups of three at 0.3 m intervals along the test condenser. At each station, the three thermocouples were distributed circumferentially, with one at the top of the tube and the others at 90 deg and 180 deg.

After completion of the smooth tube experiments, the tube was modified by insertion of a twisted tape. The twisted tapes were sheared from stainless steel sheet stock to a width of 1.339 ± 0.003 cm. Several strips were welded together to form each tape. The tape was then twisted until the desired pitch was obtained.

The twisted tapes were installed in the smooth tube by removing the test condenser end fittings and pulling the tape into the tube. A clearance of 0.22 mm was required for installation; hence, the tape was in only intermittent contact with the tube wall. Dimensions of the tapes are listed in Table 1.

The Forge-Fin Division of Noranda Metal Industries, Inc. supplied the four finned tubes tested during this study. These tubes were seamless tubes with integral longitudinal fins, three of which had spiral fins. Table 1 presents the important dimensions of the tubes.

Procedure. For a particular tube, data were obtained over a range of inlet pressures and condensing fluid mass fluxes. Typically an inlet pressure was established and flow rates were varied within the limitations imposed by the equipment. Quality changes were restricted to approximately 100 percent, and inlet conditions were held near saturation. Ranges of some of the more important dependent variables are listed in Table 2. After the system had stabilized at the selected conditions, the raw data were recorded.

A digital computer was used to process the data. Coolant flow rates and enthalpy changes were used to determine the energy transfers. Three sets of three wall temperatures were averaged to obtain sectional average wall temperatures. Saturation temperatures for each test section were calculated by averaging the local saturation temperatures corresponding to the local pressures. The sectional temperature difference, average saturation temperature minus average wall temperature, was corrected for tube wall thermal resistance and used with the sectional coolant energy gain to calculate the sectional heat transfer coefficient based upon nominal tube dimensions:

Table 2 Experimental Facility Dependent Variable Ranges

Mass Flux	150–583 kg/m^2 s
Heat Flux	220,000–1,400,000 W/m^2
Inlet Vapor Velocity	80–220 m/s
Average Condensing Heat Transfer Coefficient	19,000–110,000 W/m^2 K
Heat Transfer Rate	41,000–200,000 W
Outlet Quality	−0.019 (subcooled)–0.041

$$h_c = \left[\frac{2\pi r_i \Delta z(\overline{T}_s - \overline{T}_w)}{q/A} - \frac{r_i}{k_w}\ln\left(\frac{r_0}{r_i}\right)\right]^{-1} \quad (2)$$

Tube average heat transfer coefficients were obtained in an analogous manner. Additionally, the total energy loss of the condensing medium was calculated from flow rate and enthalpy to obtain the overall heat balance required for data quality control.

Experimental Data

Fig. 2 is representative of the experimental results for all tubes at a common inlet pressure. Curves have been fitted to the data points by linear regression techniques to clarify trends. As can be observed from the figure, the tubes with the twisted-tape inserts, Tubes *B* and *C*, outperform Tube *A*, the smooth tube, by as much as 30 percent. Tube *B*, with the more tightly twisted tape, consistently demonstrates higher heat transfer coefficients than Tube *C*.

The internally finned tubes showed dramatic increases in heat transfer coefficients. For example, Tube *G* out-performed the smooth tube by as much as 150 percent on a nominal area basis. Among the finned tubes, it should be noted that performance improvement is not solely a function of increased heat transfer area. For example, Tube *E*, which has 40 percent more area than a smooth tube and a fin-height-to-radius ratio of 0.3, is a better augmentation device than tube *D*, which has 70 percent more area than a smooth tube and a fin-height-to-radius ratio of 0.08.

Fig. 3 is representative of the experimental pressure drop for all tubes at the same common inlet pressure as Fig. 2. The finned tube data generally follow the same trends as observed with the heat transfer results. Tubes *E* and *G*, with the longest spiral fins have the

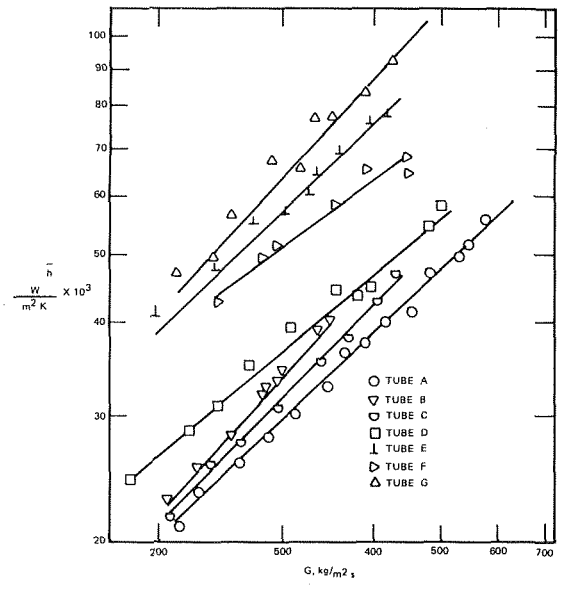

Fig. 2 Experimental average heat transfer coefficients versus mass flux, all tubes, inlet pressure = 4.2 bar

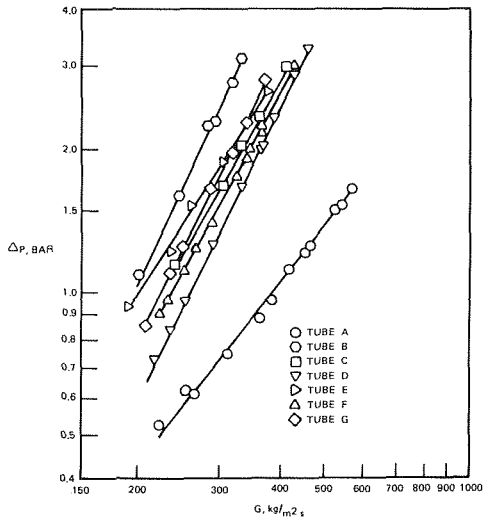

Fig. 3 Experimental total pressure drop versus mass flux, all tubes, inlet pressure = 4.2 bar

highest heat transfer and the highest pressure drop. A comparison of the data for Tube E with the data of Tube F indicates the effects of fin spiral.

The twisted-tape pressure drop data are in contrast to the finned tube data in that the pressure drop results are not analogous to the heat transfer results. Much greater percentage increases in pressure drop than increases in heat transfer are observed.

It is apparent from both of these figures that the twisted tapes are less optimum in-tube condensation augmentation devices than are the internally finned tubes. The most attractive augmentated tube seems to be Tube G.

Additional details of the facility, operating procedures, data reduction, and experimental results are presented elsewhere [1, 12, 13].

Heat Transfer Correlation for Twisted-Tape Inserts

An attempt was made to model the effects of a twisted tape on the in-tube condensation process. The methodology of this analysis was to identify those twisted-tape effects which contributed to the augmentation of condensation heat transfer, and then to model these effects in such a way as to make them compatible with those in-tube condensation correlations which had been found suitable for the smooth tube [1, 12, 13].

Three effects were considered in the twisted-tape analysis: the increase in frictional pressure drop due to the additional wetted surface of the tape, the additional heat transfer area provided due to conduction effects through the tape, and the increase in the vector velocity due to the contribution of the induced tangential velocity component.

Tangential Velocity Effects. The twisted tape induces a tangential component of velocity which is a function of radius. This velocity component, when added vectorially to the axial velocity, yields the increased velocity due to the twisted tape at a given radius. This is the velocity necessary to maintain the mass flow rate through the longer spiral flow path created by the tape.

The tangential velocity component is

$$u_t = u_a \frac{\pi r}{2yr_i} \tag{3}$$

and the magnitude of the resultant velocity is given by

$$u = (u_a{}^2 + u_t{}^2)^{0.5} \tag{4}$$

Substituting equation (3) into equation (4) then yields

$$u = u_a \left[\frac{\pi^2}{4}\left(\frac{r}{yr_i}\right)^2 + 1\right]^{0.5} \tag{5}$$

Since the interfacial shear stress is a function of the velocity near the interface and the interfacial shear is of primary importance to the heat transfer process, it is reasonable to conclude that the vapor velocity should be evaluated at the radius of the interface. The local interfacial radius can be determined from the local quality and the assumptions of a local flow regime and local void fraction. However, for simplicity it is suggested that equation (5) be evaluated at the tube inside radius. By evaluating the total velocity at the wall rather than at the interface, the effect is over-predicted. This is, however, offset by the neglect of the twisted-tape effects on the liquid film, which would also tend to augment the heat transfer.

The following velocity correction factor is thus obtained:

$$F_t = \frac{u}{u_a} = \frac{1}{2y}(\pi^2 + 4y^2)^{0.5} \tag{6}$$

Since F_t characterizes the tangential effect of the twisted tape on velocity, this correction factor is applied to the Reynolds number of interest in a particular correlation.

Fin Effects. A twisted tape in contact with the tube wall increases the active heat transfer surface because the tape behaves as a fin. Therefore, a correction factor should be included to predict the extent of heat transfer augmentation due to the fin effect of the tape.

The twisted tape is assumed to be in good thermal contact with the tube wall, and the wall is assumed to be a good conductor. These tube wall assumptions lead to the conclusion that the temperature at the base of the twisted tape approaches that of the wall far from the fin. Thus, with the twisted-tape base temperature approximately equal to that of the wall, the twisted tape can be modelled as a longitudinal fin of rectangular profile. Assuming the fin to have a length of half the tube inside diameter and to have an insulated tip, the equation for fin effectiveness is

$$\zeta = \frac{2\tanh\left(\frac{md_i}{2}\right)}{md_i} \tag{7}$$

where

$$m = \left(\frac{2h_c}{k_{tt}\delta_{tt}}\right)^{0.5}$$

The total heat transferred per unit length of the tube is the sum of the heat transferred at the unfinned wall, and the heat transferred through the two fins:

$$q = q_w + 2q_{tt} \tag{8}$$

where

$$q_w = h_c L(\pi d_i - 2\delta_{tt})(\overline{T}_s - \overline{T}_w)$$

and

$$q_{tt} = h_c L \zeta r_i (\overline{T}_s - \overline{T}_w)$$

Defining the fin effect correction factor, F_{tt}, as the ratio of total heat transfer to the heat transfer to be expected without the fin effect results in

$$F_{tt} = \frac{q}{\pi d_i L h_c (\overline{T}_s - \overline{T}_w)} \tag{9}$$

Substituting equation (8) into equation (9) yields

$$F_{tt} = \frac{\pi d_i - 2\delta_{tt} + 2r_i\zeta}{\pi d_i} \tag{10}$$

or

$$F_{tt} = 1 + \frac{2}{\pi}\left(\frac{\zeta}{2} - \frac{\delta_{tt}}{d_i}\right) \tag{11}$$

Therefore, by multiplying the empty tube value of the condensation heat transfer coefficient by F_{tt}, the result will be corrected for tape conduction effects.

Wall Shear Effects. The insertion of a twisted tape into the in-tube condensation process radically alters certain basic geometric parameters. The reduction of the cross-sectional area of flow is small for thin tapes such as those under consideration here, but the addition to the wetted surface area is quite large.

The addition of significant wetted surface to that of the smooth tube increases the total wall shear and, hence, the pressure loss. To predict twisted-tape heat transfer coefficients, those smooth tube correlations requiring the explicit inclusion of a friction factor must be supplied with the proper twisted-tape friction factor.

Lopina and Bergles [14] presented a single phase friction factor correction. This correction factor was the ratio between the friction factor of a tube containing a twisted tape and the smooth tube friction factor:

$$F_f = \frac{f_{tt}}{f} = 2.75y^{-0.406} \tag{12}$$

where y is the ratio of tape half-pitch to tube inner diameter.

The alteration in the ratio of cross-sectional area to wetted area must also be incorporated in the correlating procedure for those correlations not explicitly including a friction factor. This can be accomplished by the use of the equivalent diameter in place of the nominal diameter.

Summary. The separate effects considered above are suggested as modifications to smooth in-tube condensation correlations to enable the prediction of in-tube condensation heat transfer coefficients for tubes with twisted-tape inserts. The modifications are summarized as follows:

1 The substitution of the equivalent diameter for the nominal diameter for those correlations not requiring an explicit friction factor.

2 The multiplication of velocity or Reynolds number terms by F_t, the tangential velocity correction factor, equation (6).

3 The multiplication of the resultant heat transfer coefficient by the fin-effect correction factor, F_{tt}, equation (11).

4 The multiplication of the single-phase friction factor, where required, by F_f, the friction factor correction factor, equation (12).

Comparison With Present Experimental Results. The in-tube correlation of Akers, et al. [16] and Soliman, et al. [17] were modified, as suggested above, and used to produce a point-by-point comparison with the experimental data. The correlation of Akers, et al. is an average correlation, providing a value for the tube-averaged heat transfer coefficient. The correlation of Soliman, et al. is a local correlation providing local heat transfer coefficients which must be integrated to determine the tube-averaged heat transfer coefficients.

As modified, the higher mass flux correlation of Akers, et al.[16] becomes

$$\overline{h}_c = 0.0265\frac{k_f}{d_e}\left(\frac{F_t G_e d_e}{\mu_f}\right)^{0.8} \mathrm{Pr}_f^{0.4} F_{tt} \tag{13}$$

where the equivalent diameter

$$d_e = \frac{\pi d_i^2}{\pi d_i + 2(d_i - \delta_{tt})}$$

is used since the original equation does not explicitly contain a friction term, and no explicit correlation for increased wall shear can be made.

The correlation of Soliman, et al. [17] is modified by the multiplication of all Reynolds number terms by F_t, multiplication of the friction shear stress term in equation (36) of reference [16] by F_f, and by multiplying the resultant heat transfer coefficients by F_{tt}. For both correlations, experimental values were used for the various independent parameters required.

The following ranges of the twisted-tape effects were encountered:

F_t: 1.09 – 1.38

F_f: 1.66 – 2.24

F_{tt}: 1.02 – 1.10

The results of the comparisons are shown in Figs. 4–7. As can be observed in Figs. 4 and 5, the tube-averaged data were predicted by the modified correlation of Akers, et al. with errors of less than ±30 percent for nearly the entire data set.

The use of the Soliman correlations to predict the sectional data was somewhat less successful. As can be observed from Figs. 6 and 7, approximately one third of the data fall outside of the 30 percent bands. It should be noted that the data presented in these figures are the sectional heat transfer coefficients, that is heat transfer coefficients averaged over a small quality range. The sectional data exhibited more scatter than the average data [1]. The data from Section 3 of the experimental facility consistently evidenced lower heat transfer coefficients than did the following, lower quality section. Since the Soliman correlation predicts increasing heat transfer coefficients with increasing quality, the data for Section 3 were consistently overpredicted. Further discussion on this point is given in reference [1].

Some error results from the assumption of good thermal contact between tape and tube, which was used in the analysis. It should be noted that the installation procedures did not guarantee good thermal contact. This thermal resistance would reduce the fin effect of the twisted tape. This error was minimized by using thin stainless steel strips for the tapes.

Heat Transfer Correlation for Finned Tubes

Correlation Development. The physics of in-tube condensation is dramatically altered by the presence of internal fins. The fins provide a large increase in active heat transfer area, which contributes to higher heat transfer rates. However, this effect is somewhat offset by the fin-efficiency effects and the decrease in local heat transfer coefficients as the condensate film thickness increases, submerging the fins. Additionally, the fins contribute to higher heat transfer by promoting more turbulent mixing within and between phases.

To account for these effects, a correlation found suitable for the prediction of smooth tube data was modified. The correlation of Akers, et al. [16] was selected for modification because it provided a reasonable correlation of the average smooth tube data obtained during this investigation.

A multiplicative term, based upon a dimensionless combination of geometric parameters was determined. It served to modify the Akers correlation and enabled the modified correlation to predict the experimental data. The modified equation is

$$h_c = 0.0265\frac{k_f}{d_e}\left(\frac{G_e d_e}{\mu_f}\right)^{0.8} \mathrm{Pr}_f^{0.33}\left[160\left(\frac{b^2}{\overline{w}d_e}\right)^{1.91} + 1\right] \tag{14}$$

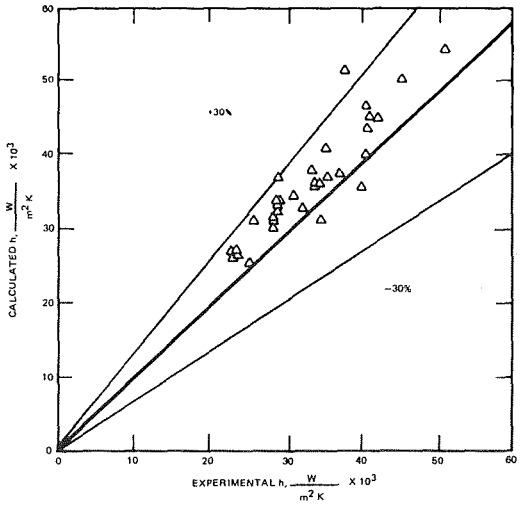

Fig. 4 Calculated average heat transfer coefficients versus experimental average heat transfer coefficients, tube B, modified correlation of Akers, et al. [15]

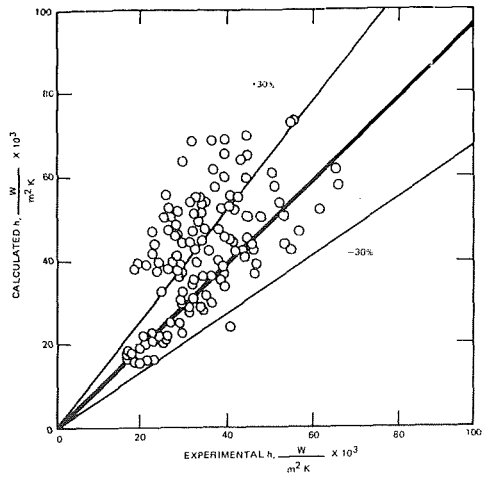

Fig. 6 Calculated sectional heat transfer coefficients versus experimental sectional heat transfer coefficients, tube B, modified correlation of Soliman, et al. [16]

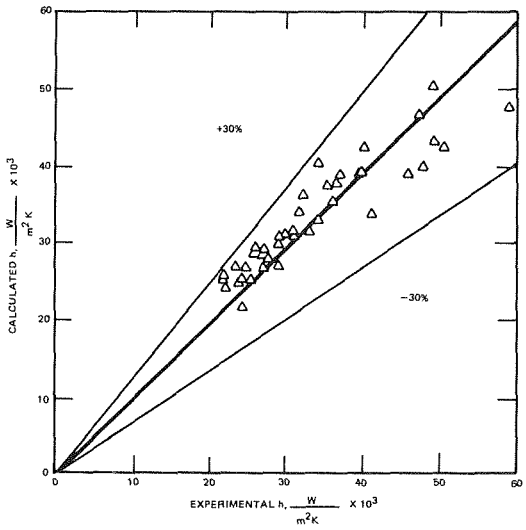

Fig. 5 Calculated average heat transfer coefficients versus experimental average heat transfer coefficients, tube C, modified correlation of Akers, et al. [15]

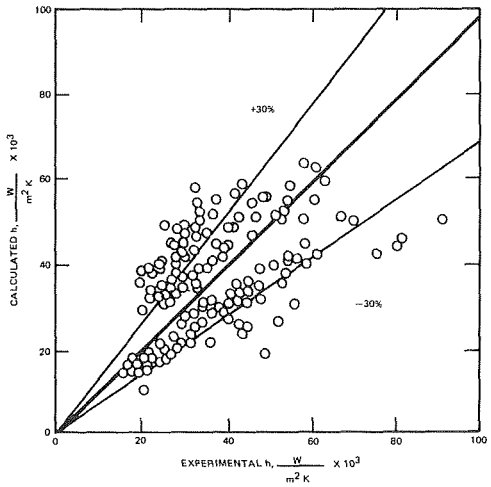

Fig. 7 Calculated sectional heat transfer coefficients versus experimental sectional heat transfer coefficients, tube C, modified correlation of Soliman, et al. [16]

where $\overline{w}$ is the average of the interfin distance at the base and tip of the fins. This equation is strictly empirical, in contrast to the twisted-tape correlation. Fin efficiency, wall shear effects, turbulation, and entrainment are all included in the additional term.

The geometrical factor used in equation (14) differs from other dimensionless geometric parameters which have been used to correlate single-phase data for internally finned tubes. Watkinson, et al. [18] used w/d. Vasil'chenko and Barbaritskaya [19, 20] used b/d, and Ornatskii, et al. [21, 22] used w/b. The reason for the necessity of the b^2 term in the parameter used here seems to be that fin height is more important to heat transfer performance in condensing systems than in single-phase systems. This is perhaps due to interfin-channel flooding considerations.

Comparison With Experimental Results. As shown in Fig. 8, equation (14) correlates the average heat transfer coefficients to within 30 percent for 95 percent of the data.

An attempt was made to use equation (1) to predict the experimental data reported here. This correlation proved to be a very poor predictor of the experimental data, some of the data being overpredicted by a factor of ten. The reason for the gross overprediction seems to be the reduced pressure term. Vrable's data were taken at reduced pressures an order of magnitude greater than the reduced pressures at which the data reported here were taken. With his empirically determined exponent of −0.65, this term gave too great a weighting at lower reduced pressures.

An attempt was made to predict Vrable's Refrigerant-12 data with equation (14). For the tube with 150 percent area increase, equation (14) predicted the data rather well. Most of the calculated values were within 30 percent of the experimental results. A plot of calculated versus experimental data appears as Fig. 9. The correlation failed to predict the data for Vrable's tube which had a 275 percent area increase. It is noted that this tube falls outside the geometrical limits imposed upon equation (14) by its data base, and attempting to predict data obtained from this tube is an unsupportable extrapolation of the equation.

Conclusions and Recommendations

This study has clarified the heat transfer performance of two different augmentation techniques for condensation inside horizontal smooth tubes. Twisted tapes were found to increase average heat

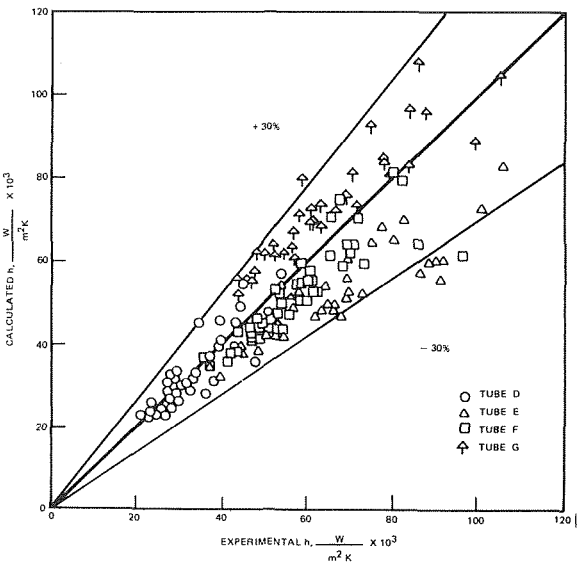

Fig. 8 Calculated average heat transfer coefficients versus experimental average heat transfer coefficients, tubes D–G, equation (14)

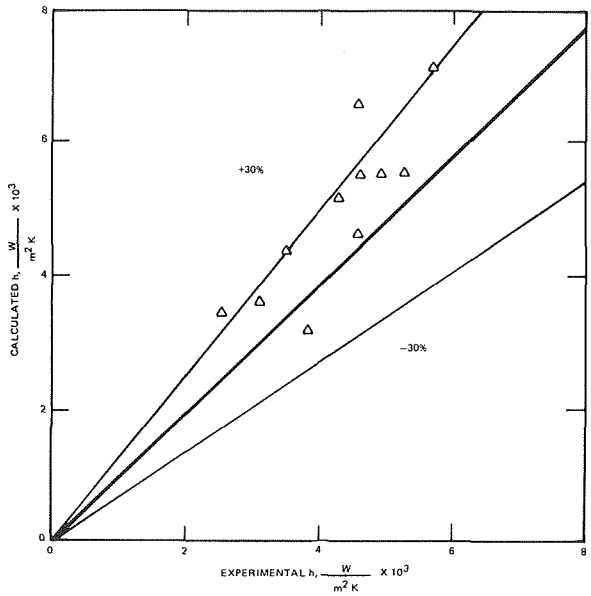

Fig. 9 Calculated average heat transfer coefficients versus experimental average heat transfer coefficients, data of Vrable [7], equation (14)

transfer coefficients of condensing steam by as much as 30 percent above the empty tube values on a nominal area basis. Internally finned tubes were found to increase in-tube condensation heat transfer coefficients by as much as 150 percent above the smooth tube values on a nominal area basis.

A correlation was developed to predict in-tube condensation heat transfer coefficients for tubes equipped with twisted tapes. The technique involved several modifications to existing smooth in-tube condensation correlations. No additional empirical factors are utilized in the correlations. Two modified correlations, one for sectional average coefficients and the other for overall average coefficients, proved to be fairly useful predictors of augmented heat transfer performance. Because no other data appear to be available in the open literature, an independent verification of the correlations could not be performed.

A correlation was also developed for the internally finned tubes. This correlation, equation (14), proved to be a satisfactory predictor of heat transfer coefficients for in-tube condensation inside of the tubes with internal longitudinal fins. The correlation also served to predict satisfactorily the refrigerant data of another investigation where conditions and tube geometries were similar to those tested during this program.

To further understand the augmentation of in-tube condensation, continued testing is necessary. Experiments with other working fluids would be of special importance to the development of a more comprehensive correlation. Experiments designed to investigate the details of heat transfer in the region of flooded fins will also be of interest.

Acknowledgments

This study was sponsored by the Engineering Research Institute, Iowa State University. Honeywell Corporation provided a grant for construction of the experimental facility. The work was performed in the Heat Transfer Laboratory of the Department of Mechanical Engineering at Iowa State University.

References

1 Royal, J. H., "Augmentation of Horizontal In-Tube Condensation of Steam," Ph.D. Thesis, Department of Mechanical Engineering, Iowa State University, 1975.

2 Cox, R. B., Matta, G. A., Pascale, A. S., and Stromber, K. G., "Second Report on Horizontal-Tubes Multiple-Effect Process Pilot Plant Tests and Design," Research and Development Report No. 592, OSW Contract No. 14-01-0001-2247: United States Department of the Interior, May 7, 1970.

3 Prince, W. J., "Enhanced Tubes for Horizontal Evaporator Desalination Process," M.S. Thesis in Engineering, University of California, Los Angeles, 1971.

4 Reisbig, R. L., "Condensing Heat Transfer Augmentation Inside Splined Tubes," ASME Paper 74-HT-7, AIAA/ASME Thermophysics and Heat Transfer Conference, Boston, July, 1974.

5 Milton, R. M., and Gottzmann, C. F., "Liquefied Natural Gas: High Efficiency Reboilers and Condensers," *Chemical Engineering Progress*, Vol. 68, No. 9, 1972, pp. 56–69.

6 Gottzmann, C. F., O'Neill, P. S., and Milton, P. E., "High Efficiency Heat Exchangers," *Chemical Engineering Progress*, Vol. 69, No. 7, 1973, pp. 69–75.

7 Vrable, D. L., "Condensation Heat Transfer Inside Horizontal Tubes With Internal Axial Fins," Ph.D. dissertation, University of Michigan, 1974.

8 Vrable, D. L., Yang, W. J., and Clark, J. A., "Condensation of Refrigerant-12 Inside Horizontal Tubes with Internal Axial Fins," *Heat Transfer 1974, Fifth International Heat Transfer Conference*, Vol. 3, Japan Society of Mechanical Engineers, Tokyo, 1974, pp. 250–254.

9 Yang, W. J., "Equivalent f and j Factors for Condensation Inside Horizontal Smooth and Finned Tubes," *Letters in Heat and Mass Transfer*, Vol. 1, 1974, pp. 127–130.

10 Cavallini, A., and Zecchini, R., "High Velocity Condensation of Organic Refrigerants Inside Tubes," *Proceedings of the XIIIth International Congress of Refrigeration*, International Institute of Refrigeration, Brussels, Belgium, 1971.

11 Kröger, D. G., "Laminar Condensation Heat Transfer Inside Inclined Tubes," Paper No. AIChE-29 presented at the 16th National Heat Transfer Conference, St. Louis, Mo., Aug., 1976.

12 Royal, J. H., and Bergles, A. E., "Augmentation of Horizontal In-Tube Condensation of Steam," Heat Transfer Laboratory Technical Report HTL-9, Engineering Research Institute, Iowa State University, Ames, Iowa, 1975.

13 Royal, J. H., and Bergles, A. E., "Experimental Study of the Augmentation of Horizontal In-Tube Condensation," *ASHRAE Transactions*, Vol. 82, Part 1, 1976, pp. 919–931.

14 Lopina, R. F., and Bergles, A. E., "Heat Transfer and Pressure Drop in Tape-Generated Swirl Flow of Single-Phase Water," JOURNAL OF HEAT TRANSFER, TRANS ASME Vol. 91, 1969, pp. 434–442.

15 Akers, W. W., Deans, H. A., and Crosser, O. K., "Condensing Heat Transfer Within Horizontal Tubes," *Chemical Engineering Progress Symposium Series*, Vol. 55, No. 29, 1959, pp. 171–176.

16 Soliman, J., Schuster, J. R., and Berenson, P. J., "A General Heat Transfer Correlation for Annular Flow Condensation," JOURNAL OF HEAT TRANSFER, TRANS. ASME, Vol. 90, 1968, pp. 267–276.

17 Watkinson, A. P., Miletti, D. L., and Tarasoff, P., "Turbulent Heat Transfer and Pressure Drop in Internally-Finned Tubes," AIChE Preprint No. 10, presented at the Thirteenth National Heat Transfer Conference, Denver, Aug. 6–9, 1972.

18 Vasil'chenko, Yu. A., and Barbaritskaya, M. S., "Resistance With Non-Isothermal Fluid Flow in Tubes With Longitudinal Fins," *Thermal Engineering*, Vol. 16, No. 1, 1969, pp. 28–35.

19 Vasil'chenko, Yu. A., and Barbaritskaya, M. S., "Heat Transfer in Tubes With Longitudinal Fins," *Thermal Engineering*, Vol. 16, No. 5, 1969, pp. 105–109.

20 Ornatskii, A. P., Shcherbakov, V. K., and Semena, M. G., "Investigation of Velocity Distribution in Tubes With Internal Longitudinal Fins," *Thermal Engineering*, Vol. 17, No. 2, 1970, pp. 108-111.

21 Ornatskii, A. P., Shcherbakov, V. K., and Semena, M. G., "Investigation of Heat Transfer in Channels Between Fins of Tubes With Internal Longitudinal Fins," *Thermal Engineering*, Vol. 17, No. 11, 1970, pp. 96-100.

G. H. Junkhan

Department of Mechanical Engineering,
Iowa State University,
Ames, Iowa

Some Effects of Mechanically-Produced Unsteady Boundary Layer Flows on Convective Heat Transfer Augmentation

Tests of experimental results from augmentation of convective heat transfer coefficients at a gas/solid interface by mechanical disruption of the boundary layer are discussed on both an average and a local basis. The averaged data show that the augmentation obtained depends upon the wake effects of the mechanical device used to produce the disturbance and upon the time required to re-establish the boundary layer after the disturbance has occurred. The local data analysis indicates that the amount of augmentation obtained depends on the relative velocity vector of the fluid with respect to the mechanical device and upon the time behavior of this vector.

Introduction

A gas/solid interface is the controlling heat transfer resistance in many heat transfer devices or systems. Recently an effort to augment such convective heat transfer coefficients by means of mechanical scraping of surface boundary layers was reported [1].[1] A heated flat plate, shown in Fig. 1, with air flowing parallel to its surface and a blade rotating in a plane parallel to the plate surface was used as the experimental system. Details of the plate construction are given in reference [2]. Significantly increased convective heat transfer coefficients were obtained for scraper clearances of 0.76 mm (0.030 in.) to 4.06 mm (0.16 in.) and blade rotational speeds of 100 to 2000 rpm over a plate Reynolds number range from 40,000 to 650,000. The measurements reported in [1] were taken at six stations distributed spanwise across the plate at the same distance downstream from the leading edge. The data from these stations were averaged to give a single, local value of Nusselt number based on distance from the leading edge. Improvements in the local Nusselt number were attributed to a turbulent type of flow between the scraper blade and the plate surface; the greatest increases were obtained for flow conditions where a laminar or transitional boundary layer would have existed if the scraper were not present.

This paper presents further analysis of the span-averaged data and discusses local, unaveraged data in an effort to gain further insight into the phenomena responsible for the augmentation obtained.

Span-Averaged Data

Fig. 2 shows typical augmentation obtained for one clearance, together with solid lines representing well-known laminar and turbulent boundary layer heat transfer correlations taken from Kays [3].

The effect of clearance for the range investigated is relatively small as shown in Fig. 3 where the augmentation, expressed as the ratio of scraped to unscraped Nusselt number is plotted as a function of a dimensionless clearance ϕ. The dimensionless clearance is defined by

$$\phi = \frac{\delta}{5x}\sqrt{\mathrm{Re}_x}$$

where δ is the scraper clearance and x is the distance from the leading edge. For laminar boundary layer flow, ϕ is the equivalent of the ratio of scraper clearance to unscraped boundary layer thickness. The

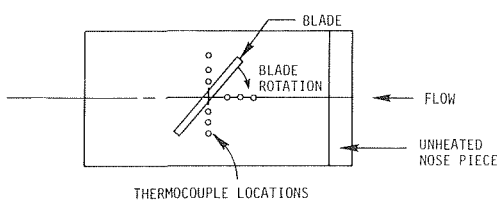

Fig. 1 Plan view of plate

[1] Numbers in brackets designate References at end of paper.

Contributed by the Heat Transfer Division for publication in the JOURNAL OF HEAT TRANSFER. Manuscript received by the Heat Transfer Division May 16, 1977.

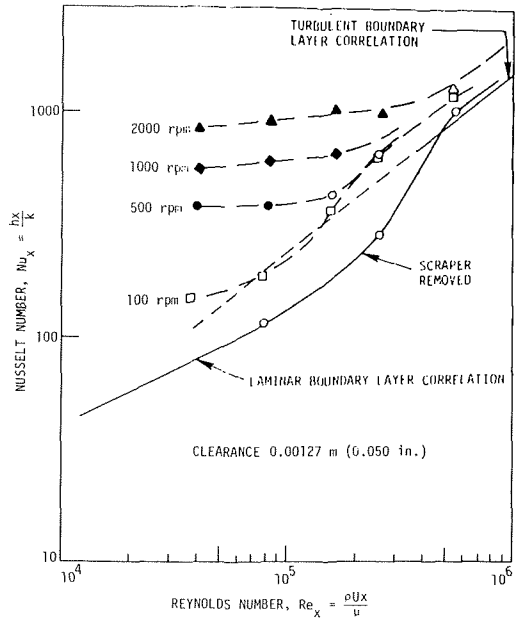

Fig. 2 Span-averaged heat transfer results for 0.00127m (0.050 in.) clearance

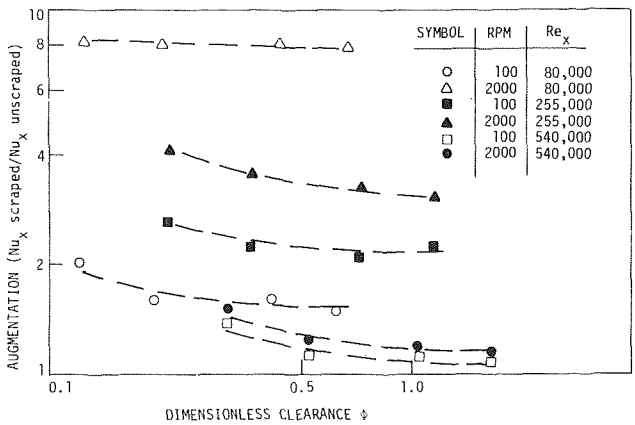

Fig. 3 Clearance effects for span-averaged data

maximum augmentation observed was approximately inversely proportional to the fourth root of the clearance, with much of the data showing even smaller effects.

The span-averaged data in Fig. 2 for 100 rpm rotational speed and Reynolds numbers from 40,000 up to about 180,000 fall close to an extension of the turbulent correlation to lower Reynolds numbers. Data for higher rotational speeds are well above the extended turbulent correlation line in this Reynolds number range, but data for each rotational speed appear to eventually fall into or close to the turbulent correlation as the Reynolds number increases. This behavior suggests that scraping frequency causes the majority of augmentation above the turbulent correlation, with greater improvement obtained for higher scraping frequency.

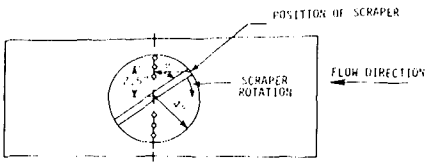

Fig. 4(a) Blade nomenclature for wake shedding

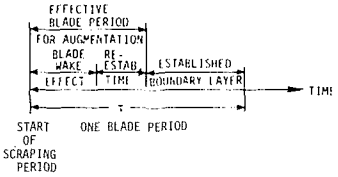

Fig. 4(b) Time diagram for boundary layer disruption events

Fig. 4 Time and blade position sketches for span-averaged data

An objective of boundary layer scraping is to disrupt an established layer, resulting in greater fluid mixing near the surface and a larger heat transfer coefficient. The frequency of scraping is obviously intimately connected with the time that an established boundary layer exists. It is clear that the blade will leave a downstream wake which will affect the boundary layer at the measuring stations located on the span of the plate. The wake will exist as long as the blade is upstream of the measuring station; the effective blade period for augmentation is thus not the same as the blade period based on rotational speed alone.

The length of the effective blade period can be calculated with the aid of the plan view in Fig. 4(a) showing the location of the six spanwise thermocouples, the scraper blade and pertinent dimensions. The scraper blade, rotating in a clockwise direction in Fig. 4(a), will affect the measuring stations from the time it is directly over them until it is no longer in a position where its wake will pass over them. During this time interval, the scraper blade will rotate through the angle indicated as θ. The present apparatus geometry gives an average θ of about 51 deg for the six thermocouples used, or about 28 percent of the blade period based on rotational speed for a two-bladed scraper.

In addition to the time the flow is disturbed by the wake, time is required for the boundary layer to re-establish itself. When the blade

Nomenclature

h = convective heat transfer coefficient
k = thermal conductivity of fluid
U = free stream fluid velocity
V_B = scraper blade velocity
$V_{F/B}$ = relative velocity of fluid with respect to the blade
x = distance from leading edge of plate
δ = scraper clearance above plate surface
θ = angular position of scraper blade
μ = fluid viscosity
ρ = fluid density
τ = blade period

Dimensionless groups

$Nu_x = \frac{hx}{k}$ = Nusselt number based on distance from leading edge

$Re_x = \rho\frac{Ux}{\mu}$ = Reynolds number based on distance from leading edge

$\phi = \frac{\delta}{5x}\sqrt{Re_x}$ = dimensionless blade clearance

$\wedge$ = used over symbol in equations to indicate a vector quantity

Table 1 Calculated effective blade period for span-averaged data. Clearance = 0.00127m (050 in.)

Nominal Reynolds Number Re_x	Blade Speed rpm	Wake Effect Time sec	Re-establishment Time sec	Effective Blade Period sec	Time w/ Established B. Layer %	Augmentation Nu_x Scraped Nu_x Unscraped
40,000	100	0.0840	0.0423	0.1263	58	1.75
80,000	100	0.0840	0.0211	0.1051	65	1.53
160,000	100	0.0840	0.0108	0.0948	68	2.10
260,000	100	0.0840	0.0066	0.0906	70	2.95
530,000	100	0.0840	0.0032	0.0872	71	1.10
40,000	500	0.0168	0.0423	0.0591	1.5	4.36
80,000	500	0.0168	0.0211	0.0379	37	3.14
160,000	500	0.0168	0.0108	0.0276	54	2.49
260,000	500	0.0168	0.0066	0.0234	61	3.00
40,000	1000	0.0084	0.0423	0.0507	- - -	6.48
80,000	1000	0.0084	0.0211	0.0295	1.7	4.90
160,000	1000	0.0084	0.0108	0.0192	36	3.79
40,000	2000	0.0042	0.0423	0.0465	- - -	9.73
80,000	2000	0.0042	0.0211	0.0253	- - -	7.31
160,000	2000	0.0042	0.0108	0.0150	- - -	6.13
260,000	2000	0.0042	0.0066	0.0108	28	4.55
530,000	2000	0.0042	0.0032	0.0074	51	1.10

tip is in a position where it will no longer influence the measuring station with its wake, there is a fixed distance from the blade tip to the measuring station. Assuming a developed boundary layer exists upstream of the blade, and that the boundary layer re-establishes itself at the same speed as the free stream velocity, the time required for re-establishment can be estimated.

The effective blade period for augmentation is then the total time consumed for the wake effect and boundary layer re-establishment; these time increments are shown in the diagram in Fig. 4(b). For the remainder of the blade period an established boundary layer exists over the measuring station.

Re-establishment time varies with the free stream velocity, independent of scraper rotational speed. If the sum of the wake effect time and the re-establishment time is large enough, little or no established boundary layer will ever exist at the measurement station and a larger increase in span-averaged heat transfer coefficient should be observed.

Calculations of wake effect time, re-establishment time, effective blade period, and percent time with established boundary layer were made for all span-averaged data. Results for the 1.27 mm clearance are given in Table 1. The last column in Table 1 contains values of the augmentation obtained, defined as for Fig. 3. The augmentation shown in Table 1 is plotted in Fig. 5 as a function of the percent of time an established boundary layer existed. The augmentation range for points for which no established boundary layer existed is shown on the ordinate and is well above the augmentation obtained for points with even partially-established boundary layers. The improvement indicated in Fig. 5 is typical of the other clearances used.

If the data of Table 1 are applied to Fig. 2, those points for which an established boundary layer could not exist are all significantly above the extended turbulent boundary layer correlation; even those data with short established boundary layer times (say 50 percent or less) show considerable improvement. The improvement is indicated in Fig. 2 by the filled points, all of which had an established boundary layer for 50 percent of the time or less.

Local Effects of Blade Motion. The above analysis of span-averaged data for re-establishment of the boundary layer does not include effects of the direction of blade motion with respect to the flow because the data were averaged. Local data for the same measurement stations have subsequently been examined and regular differences from one side of the plate to the other were found. Fig. 6 shows typical local behavior; blade motion opposite to the free stream flow direction results in Nusselt numbers as much as 65 percent higher than when the blade motion is generally in the same direction as the free

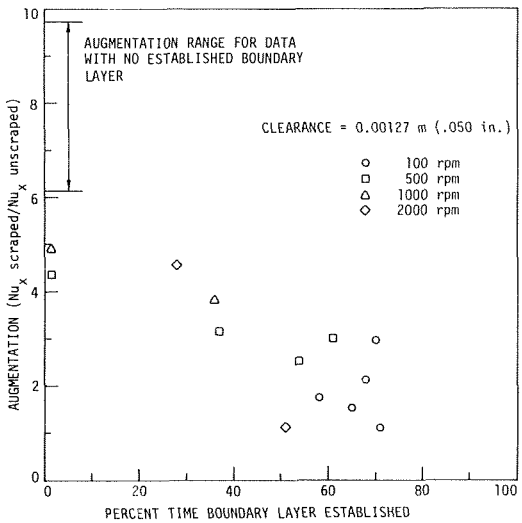

Fig. 5 Effect of boundary layer establishment time on augmentation

stream.

Such behavior suggests that differences in boundary layer disturbance occur because non-uniform blade wakes are shed due to variable relative motion between the fluid and the blade. Even though both fluid velocity and blade speed are constant, the relative velocity vector of the fluid with respect to the blade changes continuously as the blade rotates; the continuously varying angle between the absolute blade velocity vector and the absolute fluid velocity vector results in several different relative motion cases. These relative motion cases can be obtained using the vector equation

$$\hat{V}_{F/B} = \hat{U} - \hat{V}_B$$

where $V_{F/B}$ is the relative velocity, U is the free stream velocity and V_B is the blade velocity at a given radius.

The first of these cases is shown in Fig. 7(a) where the blade motion ω is in a direction generally opposite to the main fluid flow velocity U. For $0 < \theta < 90$, a wake will be shed downstream of the blade because the relative velocity vector $V_{F/B}$ will always have a downstream component for any blade position.

The second case is shown in Fig. 7(b) where the blade moves gen-

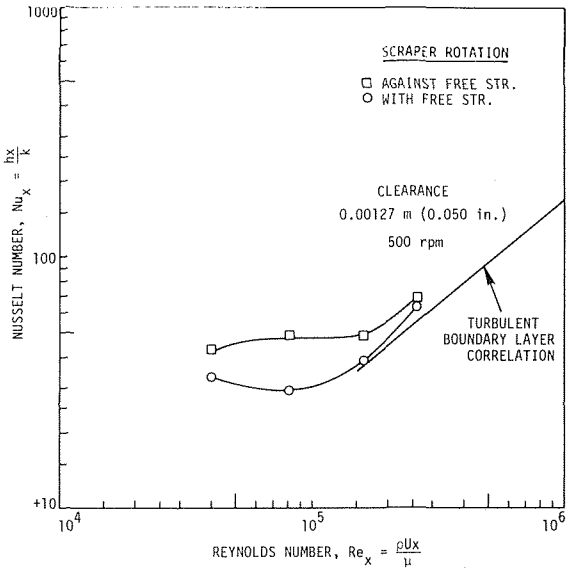

Fig. 6 Local heat transfer results for 0.00127m (0.050 in.) clearance

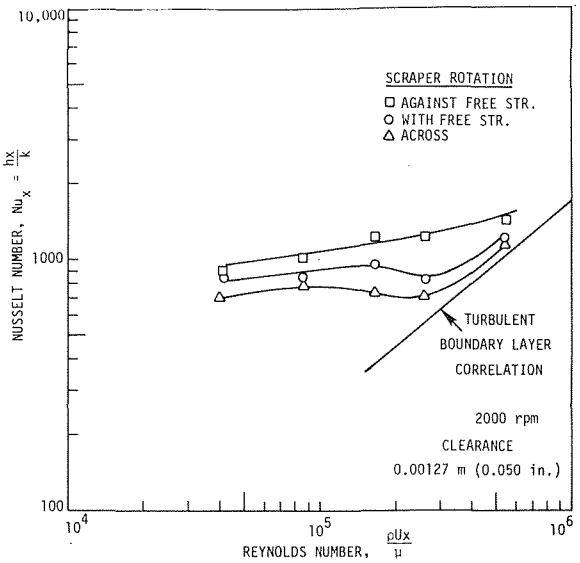

Fig. 8 Local results for 2000 rpm and 0.00127m (0.050 in.) clearance

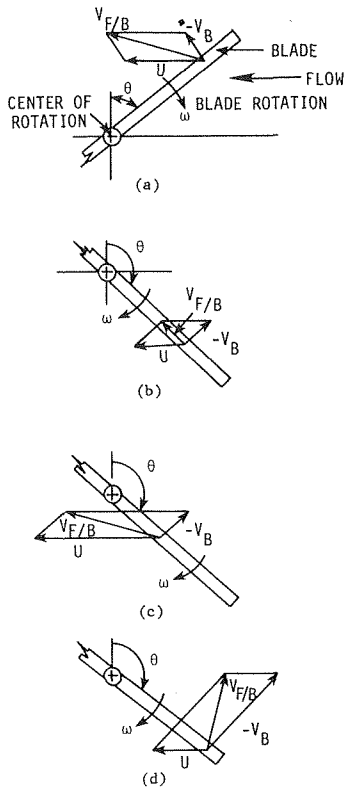

Fig. 7 Velocity diagram for local results with different blade speed and position cases

erally in the same direction as the flow; for this case no wake will be shed since $V_{F/B}$ lies along the blade. Boundary layer re-establishment will occur quickly because little or no wake is shed.

The third case, shown in Fig. 7(c), results in a blade wake since the $V_{F/B}$ vector is ahead of the moving blade; the boundary layer is disturbed much as in Fig. 7(a), but with less time for the wake to cover the measurement station and probably a shorter time is required for boundary layer re-establishment since relatively undisturbed fluid will immediately follow the blade.

A fourth case, depicted in Fig. 7(d), exists when the blade moves generally in the same direction as the flow but sufficiently faster so that the wake is shed behind the moving blade; no wake will affect the measuring station prior to the arrival of the blade for this case.

The last three cases can occur at different positions along the length of the blade at the same time, since blade velocity increases with distance from the center of rotation. Calculations of $V_{F/B}$ for various positions on the blade at constant free stream velocity U and blade angle θ show that with the proper magnitudes of U and V_B, the $V_{F/B}$ vector will leave a wake behind the blade near the tip and ahead of the blade closer to the center of rotation. Between these two positions, $V_{F/B}$ lies along the blade, so that no wake is shed at that location. As the blade rotates to a new θ position, the angle between V_B and U changes; the position for which no wake is shed then moves along the blade as it rotates. The reduced Nusselt number observed in Fig. 6 for Re_x = 81,000 and blade motion generally in the free stream direction would be caused by such a phenomenon; similar results are found for other blade rotational speeds and clearances where the free stream and blade velocities tested have relative velocity vectors that behave in the same manner.

Further evidence is found from additional data taken upstream of the center of blade rotation; the blade motion is *across* the free stream direction as it passes over these measuring positions. Typical data for this location should be lower than either of the other two locales because the relative velocity vector is nearly parallel to the blade except for very high blade velocity; in addition, the re-establishment time is very short. Typical data from these locations is shown in Fig. 8 where the upstream measuring station augmentation is considerably below the other measuring positions.

Conclusions

An analysis of heat transfer data taken on a flat plate when the boundary layer was disturbed by a moving blade has shown that considerable heat transfer augmentation may be obtained for normally laminar or transitional boundary layers. The span-averaged data analysis shows that the effective augmentation period depends on the wake behind the blade and the time required to re-establish the boundary layer. In addition, these data have indicated that the augmentation obtained is inversely related to the amount of time that an established boundary layer exists over the surface.

The local data analysis has shown that the amount of augmentation obtained is dependent on the direction of the blade with respect to the main flow. Moreover, the simple fluid/blade vector model has shown that the effect of the blade depends greatly on both the mag-

nitude and direction of the relative velocity vector and the time that this vector remains in a particular orientation with respect to the flow; the relative velocity vector thus affects not only the blade wake effect time, but the re-establishment time as well.

The results obtained suggest that, at least for laminar or transitional boundary layers, regularly unsteady flow in the region normally ascribed to boundary layer flow will result in considerable augmentation of convective heat transfer coefficients.

Acknowledgment

The Iowa State University Engineering Research Institute has partially supported this work.

References

1 Hagge, J. K., and Junkhan, G. H., "Mechanical Augmentation of Convective Heat Transfer," JOURNAL OF HEAT TRANSFER, Vol. 97, Nov. 1975, pp. 516–520.

2 Hagge, J. K., and Junkhan, G. H., "Experimental Study of a Method of Mechanical Augmentation of Convective Heat Transfer Coefficients in Air," Technical Report HTL-3/ISU-ERI-Ames-74158, Nov. 1974, Engineering Research Institute, Iowa State University, Ames, Iowa.

3 Kays, W. M., *Convective Heat and Mass Transfer,* McGraw-Hill Book Co., New York, 1966.

J. C. Chato
Professor,
Department of Mechanical and Industrial Engineering,
University of Illinois at Urbana-Champaign
Urbana, Ill.

R. S. Abdulhadi
Assistant Professor,
Department of Mechanical Engineering,
University of Jordan,
Amman, Jordan

Flow and Heat Transfer in Convectively Cooled Underground Electric Cable Systems: Part 1—Velocity Distributions and Pressure Drop Correlations

Velocity distributions and pressure drop correlations have been obtained experimentally for a wide range of physical, flow, and thermal parameters in three models of oil-cooled underground electric cable systems. The flow can be considered as consisting of several, interconnected, parallel channels. If one of these is significantly larger in cross section, it will dominate the behavior of the entire system with velocities up to an order of magnitude greater than in the other channels. Laminar, fully developed flow exists at a dimensionless entrance length as low as $x/D_H = 100$. *The turbulent velocity profiles are essentially uniform in the larger, main channel, but not in the small channels with lower velocities. Laminar friction factors can be correlated with an equivalent Reynolds number, based on the main flow channel alone, as* $f_e \cdot Re_e = 30$. *Turbulent friction factors increase with increasing skid wire roughness ratios and approach the asymptotic values of 0.013 and 0.021 for roughness ratios 0.0216 and 0.0293, respectively. Cable heating had no noticeable effect on the friction factor correlations.*

Introduction

At the present time, about 3,200 km (2,000 miles) or less than one percent of the total electrical transmission lines in the United States are underground. The largest of these cable systems has a capacity of approximately 500 MW at 345 kV. Although it is generally agreed that the present technology of underground transmission is not capable of both efficiently and economically meeting anticipated requirements, basic design improvements of oil-cooled underground cable systems are needed until new and different techniques are developed.

The current carrying capacity of underground cables is limited by the maximum allowable temperature of the electrical insulation that is required for long life and high reliability. This limiting temperature is about 85°C (185°F) and occurs at the inner diameter of the insulation in contact with the electrical conductor. This temperature depends primarily on the rate at which heat generated within the system (due to conductor losses, magnetic effects, and other factors) can be transferred to the surrounding earth or some other cooling medium. In forced-cooled systems for oil filled, pipe-type cable circuits, chilled oil is circulated through the pipe and most of the heat generated in the cable and insulation is absorbed by the oil. The heat is then transferred from the oil to the environment at refrigeration stations located at predetermined intervals along the transmission line.

By use of a forced-cooled system, the power capacity of underground cables can be economically increased. In such systems, the heat generated within the conductor is transferred by conduction through the cable insulation to the surface of the cable. This heat is then transferred to the oil by a combination of forced and natural convection. Forced convection is established by the flow of the oil in the pipe; natural convection is set up by the temperature difference between the cable surface and the oil.

The flow in a cable-pipe is characterized by the irregular surfaces and cross sections resulting from the particular configurations of the cables inside the pipe and the repeated roughness of cable surfaces due to the skid wires wound helically around the cables.

The heat transfer and friction characteristics of surfaces having different types of roughness and flow geometries became the subject of extensive analytical and experimental investigation as a result of their increasing application in the fuel element design for both gas and water-cooled reactors as well as liquid-metal, fast breeder nuclear reactor systems. More recently, these surfaces became of increasing

Contributed by the Heat Transfer Division and presented at the Winter Annual Meeting, New York, N. Y., December 5–10, 1976. Revised manuscript received by the Heat Transfer Division August 20, 1976. Paper No. 76-WA/HT-45.

concern to investigators involved in the design and construction of oil-filled, pipe-type underground electrical cable systems.

Several investigations of rod bundles with helically wrapped wire spacers were reported [1–4][1]. It was concluded from most of these investigations that both the friction factors and Nusselt numbers of rod bundles with wire spacers increase with increasing roughness ratios and decreasing distance between wire wraps.

Detailed experimental data and correlations of the fluid mechanics and heat transfer characteristics of oil-filled, pipe-type cable systems are scarce. Published results do not cover the entire range of flow and thermal conditions applicable in the design and operation of such systems. An experimental investigation of the forced cooling for a model pipe-type cable system was reported in 1970 [5]. Temperature profiles from the cable surface to the pipe wall were measured and used to calculate the oil film thermal resistance. Our calculations, based on reported system dimensions and flow velocities, indicate that most of these tests were conducted under laminar flow conditions with Reynolds numbers below 500.

Beckenbach, et al. [6] presented a theoretical approach for the prediction of the friction factor as a function of the Reynolds number for a pipe-type cable system. Their predicted values were compared with experimental results obtained under isothermal conditions with oil and water used as working fluids in order to cover a wide range of flow Reynolds numbers. Correlations for friction factors are presented in references [7–10]. Other related works were further discussed in references [11, 12].

The purpose of our work is to understand more fully the flow and thermal characteristics of underground cable systems. In this article, we are reporting on the velocity distributions and pressure drops obtained for a wide range of parameters. The temperature distributions and heat transfer results are reported in a companion article [13]. Dimensionless correlations were developed for application in the design of full-scale underground cable systems.

The Experimental Setup

Geometrical parameters of the three different models ((1) large cables in large pipe, (2) small cables in small pipe, and (3) small cables in large pipe) used in this investigation are presented in Table 1 and the different cable configurations referred to in the table are shown in Fig. 1. The schematic diagram of the experimental setup is shown in Fig. 2. Details of the construction and instrumentation are given in references [11, 12].

One test section was made of 140 mm I.D. plexiglass pipe in order to facilitate visual observation of the flow. The second test section consisted of a 45 mm I.D. steel pipe with 3.2 mm thick walls. A heating strip was wrapped around the steel portion of this test section in order to simulate the heat generated within the outer pipe as a result of the electromagnetic eddy currents that exist in an actual cable system.

One set of simulated cables was made up of three, 38 mm O.D. thin wall steel tubes. Sixteen-gauge copper wires (1.3 mm dia) were wound around each of the tubes to simulate the actual skid wire arrangement in a real system. Electric resistance heaters were inserted along the axis in each of the cables to provide the required heat flux rates. Thermocouples were soldered to the cable surface at 1.22 m intervals, and the thermocouple leads were pulled through the inside of the tubes to avoid disturbing the flow.

Another set of simulated cables was made up of three, 13 mm O.D. steel tubes. The skid wires were simulated by 30-gauge Teflon-insulated wires (0.53 mm O.D.), and the heater installation was the same as that in the larger cables. Two thermocouple junctions were soldered to each of the three tubes at 2 m and 8.4 m from the test section inlet. Fig. 3 shows typical sections from an actual cable and the two simu-

Table 1 Physical parameters of three test models

	Model 1			Model 2			Model 3
Configuration	1	2	3	1	2	3	1
D_p, mm	140	140	140	45	45	45	140
D_c, mm	38	38	38	13	13	13	13
D_e, mm	59.7* = D_H	93.5	102.7	18.1* = D_H	28.5	31.5	107.0* = D_H
D_s, mm	1.29	1.29	1.29	0.53	0.53	0.53	0.53
S_1, mm	23.0	2.6	2.6	6.5	1.1	1.1	6.5
S_2, mm	11.0	1.3	1.3	5.0	0.5	0.5	119.0
A_e/A_p	0.776	0.745	0.758	0.754	0.725	0.743	0.975
D_s/D_e	0.0216	0.0138	0.0126	0.0293	0.0187	0.0168	0.00495

Pitch/$D_s \simeq$ 10 and 17; wire helix angles $\simeq$ 83 deg and 52 deg; test section length = 9.14 m
*A_c = overall flow area in configuration 1 for each model.

[1] Numbers in brackets designate References at end of paper.

Nomenclature

A_e = effective or main flow cross-sectional area as shown in Fig. 1
A_p = pipe cross-sectional area
d = distance between cable surface and inside pipe wall in any radial traverse
D_c = cable outside diameter
D_e = hydraulic diameter based on A_e
D_H = hydraulic diameter based on overall flow area
D_p = pipe inside diameter
D_s = skid wire height
$f = D_H \Delta P/2L\rho U^2$, friction factor based on overall flow area
$f_e = D_e \Delta P/2L\rho U_e^2$, friction factor based on A_e
L = axial distance between pressure taps
ΔP = pressure drop between two axial locations
q_c = heat flux rate from the cable surface to the oil
q_w = heat flux rate from pipe wall to the oil
Re = UD_H/ν, Reynolds number based on overall flow area
$\mathrm{Re}_e = U_e D_e/\nu$, Reynolds number based on A_e
S_1 = distance between two adjacent cables
S_2 = distance between cable and pipe wall
u = axial velocity in radial traverse
u_{max} = maximum velocity in a radial traverse
U = mean velocity based on overall flow area
U_e = mean velocity based on A_e
x = axial distance from inlet of test section
y = radial distance from a cable surface
ρ = density
ν = kinematic viscosity

lated cables used in this investigation.

Oil flow rates through the test section, heat exchanger, and calibration devices were measured with a combination of calibrated venturi and rotameter systems.

Pressure drops between different points along the test section were measured with U-tube manometers connected between the pressure taps.

Oil temperatures at the inlet, outlet, and intermediate stations along the test section, as well as surface temperatures of the cables and outer pipe, were measured by 24-gauge copper-constantan thermocouples.

Local oil velocities and corresponding temperatures were measured with a hot-film sensor which was connected to a constant-temperature anemometer through a temperature switching circuit. A screw-type traversing mechanism was designed and used to move the sensor between the cables and outer pipe in any radial direction.

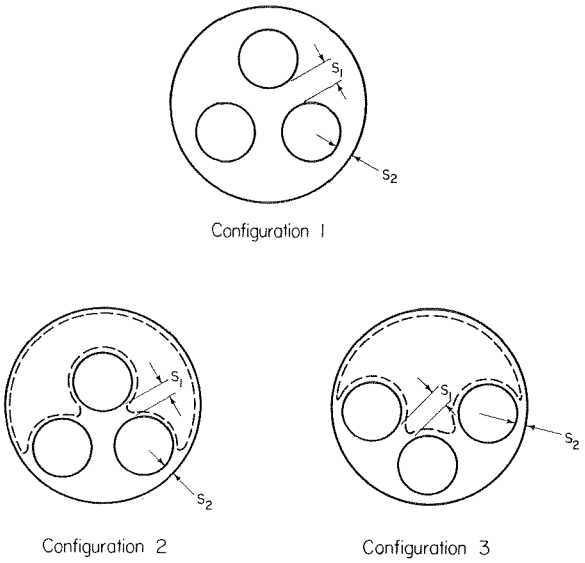

Fig. 1 Cross sections of three cable configurations. Effective flow areas are within dashed lines. In configuration 1, effective and total flow areas are the same

Discussion of the Results

Axial Velocity Distributions. Typical isothermal velocity distributions in the vertical plane of symmetry measured at three different axial locations for laminar flow conditions in Model 1 are shown in Fig. 4. Our velocity and pressure drop results indicate that the flow was virtually fully developed at $x/D_H = 117$.

Fig. 5 shows a set of typical isothermal axial velocity distributions at different flow rates for cable configuration 3 in Model 2. These profiles indicate a shift in the position of the point at which maximum local velocity occurs toward the smooth wall of the outer pipe with increasing Reynolds numbers. This is in agreement with the results of previous experimental investigations of flow in annular passages with the inner surface being rough and the outer surface smooth. It is also obvious from these results that the turbulent velocity profiles (Re = 2406) are flatter than those in the laminar range.

The maximum local velocity, u_{max}, and the total radial distance, d, between a cable and the pipe wall were used to obtain good dimensionless correlation of all velocity data. Fig. 6 shows this correlation applied to the results of Fig. 5 as well as for the velocity distributions for cases involving heated cables at $x/D_H = 473$.

Velocities in the small restricted triangular channel bounded by the two bottom cables and the outer pipe wall in configuration 2 in Model 1 were measured at different flow rates in order to determine their magnitudes relative to the corresponding velocities in the main

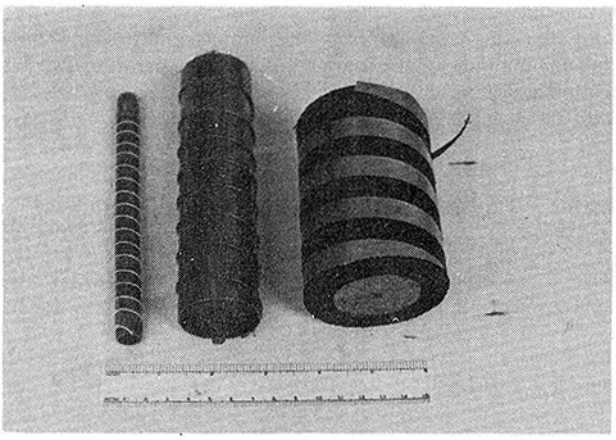

Fig. 3 Typical sections of actual (right) and simulated cables (actual cable is shown here without skid wires)

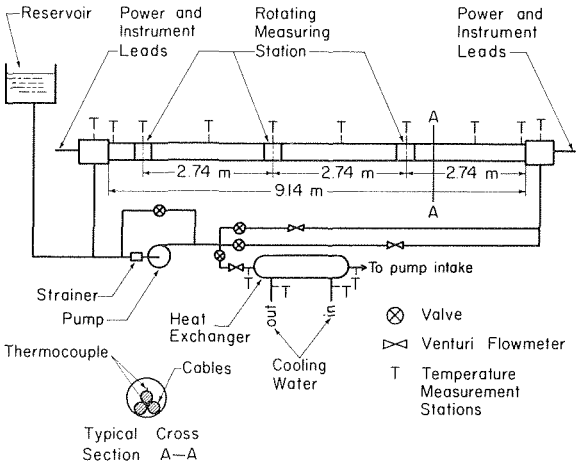

Fig. 2 Schematic diagram of experimental setup for Models 1 and 3. For Model 2 rotating measuring stations were at 2 m and 8.4 m from the inlet of the test section, pressure taps were at 0.9 m intervals, and temperatures could be measured at 2, 6, and 8.5 m from the inlet

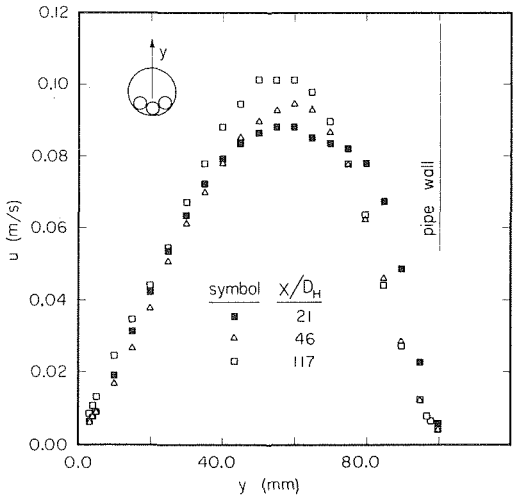

Fig. 4 Local axial velocity distributions for configuration 3 in Model 1 at Re ≈ 244, $q_c = 0$

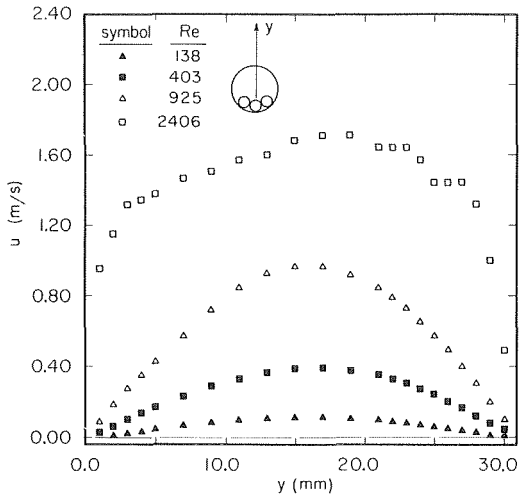

Fig. 5 **Axial velocity distributions for configuration 3 in Model 2 at x/D_H = 473, q_c = 0**

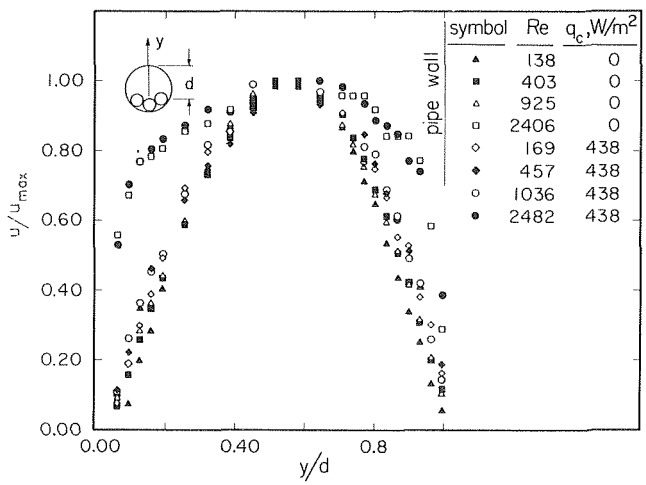

Fig. 6 **Dimensionless axial velocity distributions for configuration 3 in Model 2 at x/D_H = 473**

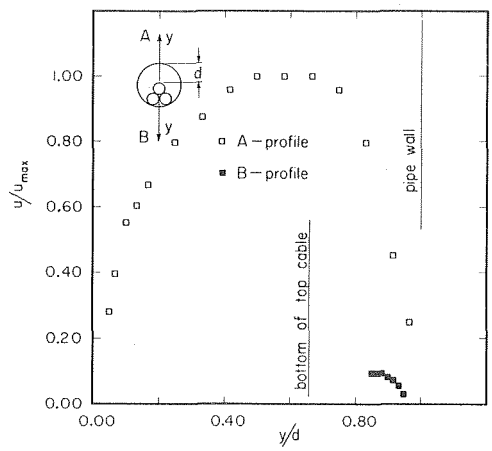

Fig. 7 **Dimensionless velocity distributions for configuration 2 in Model 1 at x/D_H = 94, Re = 1647, q_c = 0**

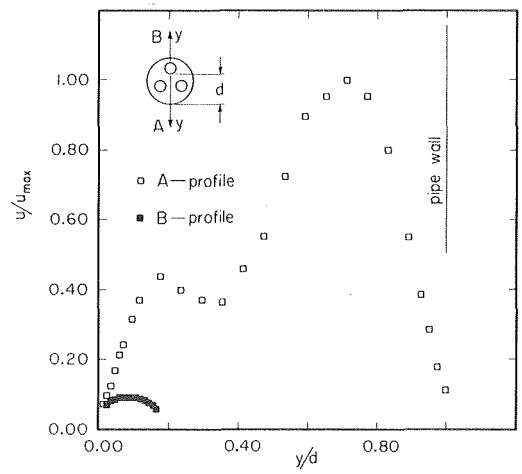

Fig. 8 **Dimensionless velocity distributions for configuration 1 in Model 1 at x/D_H = 142, Re = 180, q_c = 400 W/m²**

flow channel. The velocities in the restricted channel were found to be approximately one order of magnitude lower than the corresponding main flow velocities for the entire laminar flow range. The relative magnitudes increased, however, as transition into turbulence occurred. One typical comparison of these velocities is presented in Fig. 7.

A similar phenomenon was found to exist for configuration 1 in both Models 1 and 2 as shown in Fig. 8 which clearly indicates that for low Reynolds numbers (Re = 180) in the laminar range, the velocity in the secondary flow region between the cable and pipe wall is no more than ten percent of the maximum velocity in the main flow channel. Other results, not shown here but reported in references [11, 12], show that this ratio is a strong function of the flow Reynolds number and increased to about 80 percent for Re = 6600.

Pressure Drop Results and Correlations. Pressure drops were measured for different cable configurations under laminar, transitional, and turbulent flow conditions for both isothermal and non-isothermal cases. The correlation of the friction factor, f, against the usual Reynolds number, Re, based on the entire flow cross section produced quite different curves for the three configurations. In the laminar range for Model 2 the values of f.Re were 30, 12, and 8 for configurations 1, 2 and 3 respectively. The transition to turbulence started around Re $\simeq$ 600 for configuration 1 and Re $\simeq$ 1200 for configurations 2 and 3. In the turbulent range at Re $\simeq$ 5000, the friction factor was 0.023 for configuration 1 and 0.012 for the other two configurations with a skid wire roughness ratio of 0.0293.

A better correlation of these results was obtained by using an effective hydraulic diameter, D_e, based on the actual main flow area and wetted perimeter for each case (neglecting small channels between the cables and the pipe wall) as shown in Fig. 9. However, while the latter method gives a better correlation of the results, the former is more practical because it eliminates the need to guess the actual cable configuration in any particular section of a cable pipe.

In the laminar range, $\mathrm{Re}_e < 1{,}000$, the best correlation is

$$f_e \cdot \mathrm{Re}_e = 30 \tag{1}$$

However, a more conservative design value may be

$$f_e \cdot \mathrm{Re}_e = 35 \tag{2}$$

In the transition and turbulent range, $1{,}000 < \mathrm{Re}_e < 20{,}000$, Rehme's correlation [7] based on equation (1) can be written as

$$\sqrt{\frac{2}{f_e}} + 2.13\,\ell n\sqrt{\frac{2}{f_e}} = 2.13\,\ell n\,\mathrm{Re}_e - 1.664 \tag{3}$$

The left hand side of equation (3) is virtually a straight line in the range of interest $8 < \sqrt{2/f_e} < 14$. Introducing a linear relation, which fits the actual function within two percent, allows the simplification

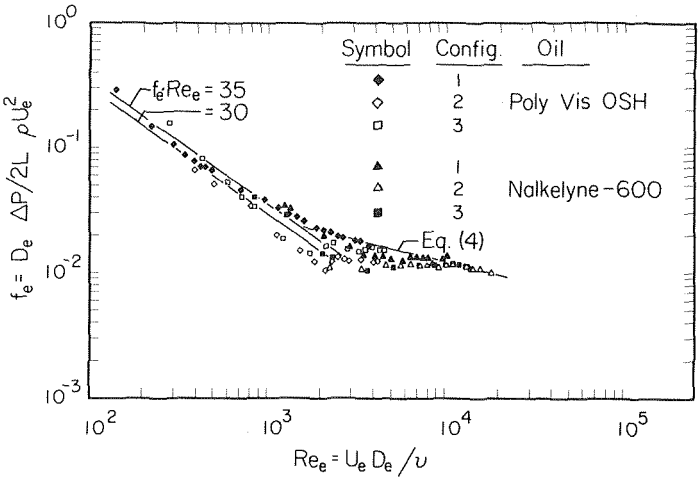

Fig. 9 Friction factor results based on effective hydraulic diameter in Model 1 at $x/D_H = 120$, $L = 2.87$ m, $q_c = 400$ W/m^2

of equation (3) to

$$f_e = \frac{2}{(1.783\ \ell n\ \mathrm{Re}_e - 3.858)^2} \tag{4}$$

The curve in Fig. 9 shows that this correlation fits the upper limits of the data quite well for $D_s/D_H = 0.0216$. However, as shown in Fig. 10, increasing D_s/D_H to 0.0293 decreased the transition Reynolds number and increased the turbulent friction factor from 0.013 to 0.021, without affecting the laminar friction factor. Thus, Rehme's correlation seems to work only for small roughness ratios with configuration 1.

Friction factor results for a wide range of flow and thermal parameters are shown in Fig. 11. These results indicate that cable heating had no noticeable effect on the friction factor correlations and that fully developed flow conditions existed as low as $x/D_H = 100$. Our results for configuration 1 are in good agreement with those given in reference [9]. However, with the other two configurations, we measured considerably higher transition Reynolds numbers, whereas reference [9] found no substantial differences among the three configurations. Changing the pitch-to-height ratio of the skid wire from 10 to 17 by changing the helix angle of the wire from approximately 83 deg to 52 deg did not affect the results noticeably.

Reference [10] indicates that the influence of the round skid wire extends to a total distance of 8 times the wire diameter. Therefore the 10:1 pitch to diameter ratio used can be considered small enough to insure that the entire cable surface is influenced by the skid wires with virtually no unaffected surface.

Conclusions

Examination of the above results suggests the following conclusions:

1 The flow in a cable pipe becomes hydrodynamically fully developed at $x/D_H = 100$. Shorter entrance length would be sufficient for the flow to become fully developed in the lower range of laminar Reynolds numbers.

2 Fully developed laminar, axial velocity profiles are similar for both isothermal and non-isothermal cases. Under turbulent conditions, the profiles become flatter and indicate that the point at which the maximum velocity occurs tends to shift slightly toward the smooth wall of the outer pipe. The local maximum velocity and the distance between the cable surface and the pipe wall are sufficient to correlate the velocity distribution results.

3 The axial velocity in the restricted flow channels between three cables or two cables and the pipe wall is approximately one order of magnitude lower than the maximum velocity in the main flow channel for the entire laminar flow range. Very little mixing seems to take place between the separate flow channels. However, both mixing and flow velocities in the restricted channels increase with increasing Reynolds numbers in the transitional and turbulent regimes.

4 Transition to turbulence for configurations 2 and 3 starts around $\mathrm{Re}_e = 2000$. In the transition region, the friction factors increase with

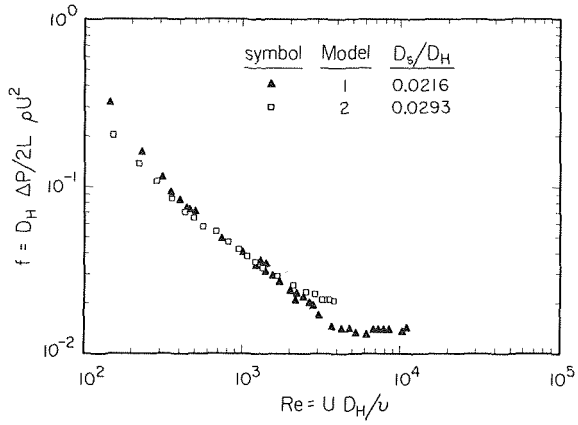

Fig. 10 Friction factor results for cable configuration 1 in two different Models (After reference [10]). Re = Re_e, $f = f_e$

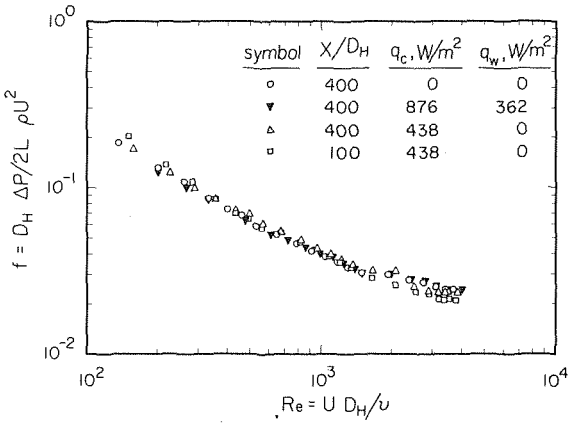

Fig. 11 Friction factor results for configuration 1 in Model 2. Re = Re_e, $f = f_e$

increasing Reynolds numbers and approach an asymptotic value under fully turbulent flow conditions. The transition for configuration 1 is gradual and seems to start at around $Re_e = 600$. The skid wire roughness ratio for any cable configuration has a strong influence on the transition Reynolds number. In addition, the turbulent friction factors increase with increasing roughness ratios.

5 Friction factors can be best correlated by the use of an equivalent Reynolds number, Re_e. Laminar friction factors are independent of the skid wire roughness ratio and can be calculated from equations (1) or (2). Turbulent friction factors can be correlated by equation (4) for relatively low roughness ratios (<.0216) but they increase considerably with higher roughness ratios. Asymptotic values for turbulent friction factors were 0.013 and 0.021 corresponding to skid wire roughness ratios of 0.0216 and 0.0293 respectively.

These results are applicable for a cable to pipe diameter ratio in the range of $0.2 < D_c/D_p < 0.36$. For $D_c/D_p < 0.2$ the friction factors will converge on the smooth pipe data. For $0.36 < D_c/D_p <$ maximum = 0.464 all flow cross sections have about the same dimensions and the equivalent area must be taken as the total flow area for all configurations. The transition to turbulence, as well as the magnitude of the turbulent friction factor, may be influenced not only by the roughness ratio, as shown in this study, but also by the relative size of the rough surface. These parameters should be further investigated in the ranges not covered in this report.

Acknowledgments

This work was supported in part by Contract No. E(49-18)-1568, (RP 7821-1) from the Electric Power Research Institute and the U. S. Energy Research and Development Administration. Oils were furnished by the Chevron, Conoco, and Sun Oil Companies.

References

1 Hoffman, H. J., Miller, C. W., Sozzi, G. L., and Sutherland, W. A., "Heat Transfer in Seven-Rod Clusters—Influence of Linear and Spacer Geometry on Superheat Fuel Performance," GEAP-5289 General Electric Co., San Jose, Cal., Oct. 1966.

2 Shimazaki, T. T., and Freede, W. F., "Heat Transfer and Hydraulic Characteristics of the SRE Fuel Element," Book 1, p. 273, Reactor Heat Transfer Conference, 1956.

3 Waters, E. D., "Fluid Mixing Experiments with a Wire-Wrapped Seven-Rod Fuel Assembly," HW-70178 Rev., Hanford Atomic Products Operation, Richland, Wash., Nov. 1963.

4 Kattchee, N., and Machewicz, M. V., "Heat Transfer and Fluid Friction Characteristics of Tube Clusters with Boundary-Layer Turbulence Promoters," ASME Paper 63-HT-1, ASME-AIChE Heat Transfer Conference, Boston, Mass., Aug. 1963.

5 Zanona, A., and Williams, J. L., "Forced-Cooling Model Tests," *IEEE Trans.*, Vol. PAS-89, No. 3, 1970, pp. 491–503.

6 Beckenbach, J. W., Glicksman, L. R., and Rohsenow, W. M., "The Prediction of Friction Factors in Turbulent Flow for an Underground Forced-Cooled Pipe-Type Electrical Transmission Cable System," Heat Transfer Laboratory Report No. 80619-89, MIT, 1974.

7 Rehme, K., "Simple Method of Predicting Friction Factors of Turbulent Flow in Non-Circular Channels," *International Journal Heat Mass Transfer*, Vol. 16, 1973, pp. 933–950.

8 Lewis, M. J., "Optimising the Thermohydraulic Performance of Rough Surfaces," *International Journal Heat Mass Transfer*, Vol. 18, 1975, pp. 1243–1248.

9 Slutz, R. A., Glicksman, L. R., Rohsenow, W. M., and Buckweitz, M. D., "Measurement of Fluid Flow Resistance for Forced Cooled Underground Transmission Lines," *IEEE Trans.*, Vol. PAS-94, No. 5, 1975, pp. 1831–1834.

10 Abdulhadi, R. S., and Chato, J. C., "Combined Natural and Forced Convective Cooling of Underground Electric Cables," *IEEE Trans.*, Vol. PAS-96, No. 1, 1977, pp. 1–8.

11 Abdulhadi, R. S., "Natural and Forced Convective Cooling of Underground Electric Cables," Ph.D. Thesis, Department of Mechanical and Industrial Engineering, University of Illinois at Urbana-Champaign, Dec. 1975.

12 Abdulhadi, R. S., and Chato, J. C., "Natural and Forced Convective Cooling of Underground Electric Cables," Technical Report No. ME-TR-609, UILU-ENG 75-4003, Department of Mechanical and Industrial Engineering, University of Illinois at Urbana-Champaign, Dec. 1975.

13 Abdulhadi, R. S., and Chato, J. C., "Flow and Heat Transfer in Convectively Cooled Underground Electric Cable Systems: Part 2—Temperature Distributions and Heat Transfer Correlations," ASME JOURNAL OF HEAT TRANSFER, Feb. 1978, pp. 36–40.

R. S. Abdulhadi
Assistant Professor,
Department of Mechanical Engineering,
University of Jordan,
Amman, Jordan

J. C. Chato
Professor,
Department of Mechanical
and Industrial Engineering,
University of Illinois at Urbana-Champaign,
Urbana, Ill.

Flow and Heat Transfer in Convectively Cooled Underground Electric Cable Systems: Part 2—Temperature Distributions and Heat Transfer Correlations

Temperature distributions and heat transfer correlations have been obtained experimentally for a wide range of physical, flow and thermal parameters in three models of oil-cooled underground electric cable systems. The results show that in the laminar range, with the oils used, the thermal boundary layer thickness around the heated cables is only of the order of 2-3 mm over the entire length of the test section. Consequently, the best correlation of the heat transfer results is obtained if the Nusselt number, based on the cable diameter, is plotted against $Re \cdot Pr^{0.4}$, where the Reynolds number is based on the overall hydraulic diameter of the cross section of the flow. For laminar flows, the oil temperatures in the restricted flow channels between three cables or two cables and the pipe wall are about 11 °C higher than corresponding bulk temperatures. As the flow becomes turbulent, the thermal boundary layer tends to vanish and the oil temperature becomes uniform over the entire flow cross section. Laminar Nusselt numbers are independent of the skid wire roughness ratio and the flow Reynolds number, but increase with increasing Rayleigh number and axial distance from the inlet, indicating significant natural convection effect. The range of laminar Nusselt numbers was 5–16. Turbulent Nusselt numbers increase with increasing roughness ratios. The Nusselt numbers at Re = 3000 are 30 and 60 for roughness ratios of 0.0216 and 0.0293, respectively.

Introduction

The current carrying capacity of underground cables is limited by the maximum allowable electrical insulation temperature required for long life and high reliability. This limiting temperature is about 85 °C (185 °F) and occurs at the inner diameter of the insulation in contact with the electrical conductor. This temperature depends primarily on the rate at which heat generated within the system due to conductor losses, magnetic effects, and other factors can be transfered to the surrounding earth or some other cooling medium. In forced cooled systems for oil filled, pipe-type cable circuits, chilled oil is circulated through the pipe and most of the heat generated in the cable and insulation is absorbed by the oil. The heat is then transferred from the oil to the environment at refrigeration stations located at predetermined intervals along the transmission line.

The purpose of our work is to understand more fully the flow and thermal characteristics of underground cable systems. The velocity distributions and pressure drop correlations have been discussed in a companion article [1].[1] A detailed description of the experimental setup and range of parameters covered in the investigation are also reported in the above article and in references [2] and [3]. References [4–12] are selected works on heat transfer results related to this investigation.

Three cable configurations were used: (1) Open triangular, (2) close-packed triangular, and (3) cradled. The three models used were (1) large cables (38 mm OD) in large pipe (140 mm ID), (2) small cables

Contributed by the Heat Transfer Division and presented at the Winter Annual Meeting, New York, N. Y., December 5–10, 1976. Revised manuscript received by the Heat Transfer Division August 20, 1976. Paper No. 76-WA/HT-42.

[1] Numbers in brackets designate References at end of paper.

(13 mm OD) in small pipe (45 mm ID) and (3) small cables in large pipe. The cables had "skid wires" wrapped around them (1.29 mm and 0.53 mm OD respectively for the large and small cables).

In this paper, we are reporting on the temperature distributions and heat transfer results we obtained for a wide range of parameters. Dimensionless correlations are developed for application in the design of full-scale underground cable systems for the prediction of their thermal behavior.

Discussion of the Results

Temperature Distributions. Oil and surface temperatures were measured for a wide range of physical and flow parameters in order to determine temperature distributions and to calculate average heat transfer coefficients at various cross sections along the cable pipe. Oil temperatures in the restricted flow channels between three cables or between two cables and the pipe wall were also measured for all flow conditions to determine the maximum oil temperatures in the system.

Cable surface temperatures were found to be essentially uniform around the perimeter of each cable at any cross section for both laminar and turbulent flow conditions.

Fig. 1 shows typical temperature distributions in the vertical plane of symmetry for configuration 2 in model 2 at different flow rates. The choice of the measured minimum oil temperature to correlate the results is arbitrary and was based on the fact that this temperature was usually very close to the oil bulk temperature as calculated from the flow rate, inlet temperature, and heat input to the system.

Fig. 2 shows typical temperature distributions measured in a horizontal plane on both sides of the top cable of configuration 2 in model 2. These profiles indicate relatively uniform temperatures throughout the flow region between the cable and pipe wall, as well as similarity of the temperature distributions on both sides of the cable.

Examination of both vertical and horizontal temperature profiles seems to indicate that upward natural convection currents exist along the vertical center line of the pipe, while secondary currents exist in a narrow region near the pipe wall. This observation is in agreement with analytical predictions of natural convection currents in cable pipes [13].

The effect of natural convection currents prevailed for the entire laminar flow regime as shown clearly by the results of Fig. 1. The intensity of natural convection currents and their augmenting influence on the overall thermal performance of the cable system are increasing functions of the difference between cable and oil temperatures. The results of a special experiment, which was conducted to determine

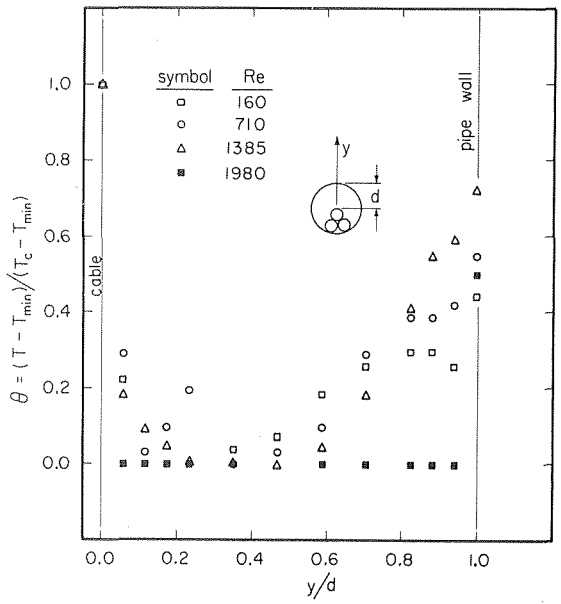

Fig. 1 Dimensionless temperature distributions for configuration 2 in model 2 at $x/D_H = 473$, $q_c = 438$ W/m², $q_w = 174$ W/m²

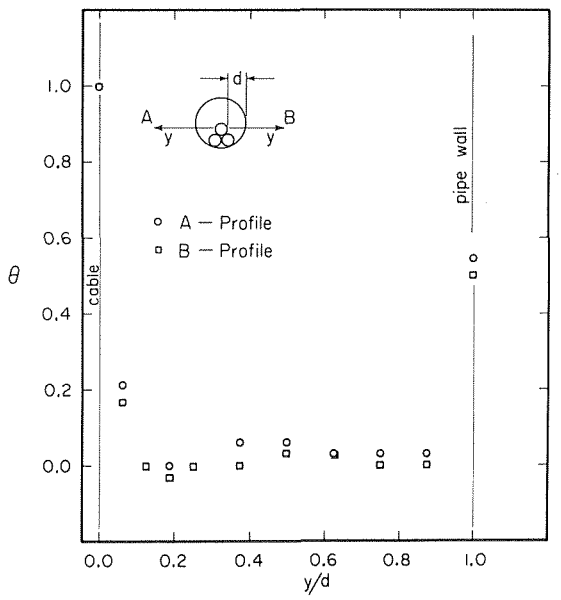

Fig. 2 Dimensionless horizontal temperature distributions for configuration 2 in model 2 at $x/D_H = 473$, Re = 160, $q_c = 438$ W/m², $q_w = 174$ W/m²

Nomenclature

c_p = specific heat of oil
D_c = cable outside diameter
D_H = hydraulic diameter based on overall flow area
D_p = pipe inside diameter
D_s = skid wire height
d = distance between cable surface and inside pipe wall in any radial traverse
$\mathrm{Gr} = g\beta(T_c - T_b)\, D_c{}^3/\nu^2$, Grashof number
g = gravitational acceleration
h = heat transfer coefficient between a heated surface and surrounding oil
k = thermal conductivity of oil
$\mathrm{Nu} = hD_c/k$, Nusselt number
P = axial distance between skid wires
$\mathrm{Pr} = \mu c_p/k$, Prandtl number
q_c = heat flux rate from the cable surface to the oil
q_w = heat flux rate from inside pipe wall to the oil
$R = \mathrm{Ra}\,\mathrm{Pr}^{0.4}$
Ra = Gr·Pr, Rayleigh number
$\mathrm{Re} = UD_H/\nu$, Reynolds number
T = local oil temperature
T_b = oil bulk temperature
T_c = cable surface temperature
T_{max} = maximum oil temperature in restricted subchannels
T_{min} = minimum oil temperature at any cross section
U = oil mean velocity based on overall flow area
x = axial distance from inlet of test section
y = radial distance from a cable surface
β = coefficient of thermal expansion
ρ = oil density
μ = dynamic viscosity of oil
ν = kinematic viscosity of oil
$\theta = (T - T_{min})/(T_c - T_{min})$, dimensionless temperature

this relationship, will be discussed later.

Fig. 3 shows typical temperature distributions in the entrance region and at the end of the test section. The uniform temperature distribution at $x/D_H = 124$ indicates that the effects of natural convection are relatively insignificant in the entrance region of the cable pipe. However, as the oil flows downstream extracting thermal energy from the heated cables and pipe, the effects of natural convection are enhanced resulting in elevated oil temperatures near the top of the pipe at $x/D_H = 473$.

Oil temperatures in the flow sub-channels, bounded by three cables or two cables and the pipe wall, were measured under different flow conditions in order to determine the maximum oil temperatures in the system. Fig. 4 shows that the sub-channel temperatures were higher than the bulk temperatures for the entire laminar region, but became nearly equal as the flow became turbulent.

The thickness of the thermal boundary layer around the cables was of the order of 2–3 mm throughout most of the laminar flow range. Under turbulent conditions, the thermal boundary layer diminished as the cable surface temperature approached that of the oil bulk.

Heat Transfer Results and Correlations. A total of 36 forced convective heat transfer runs were performed under different flow and thermal conditions and the results were correlated in terms of dimensionless parameters. The effects of the following parameters were investigated: Re, Ra, Pr, P/D_s, x/D_H, y/d, skid wire helix angle, and three typical configurations. Other parameters, in particular D_s/D_c and D_c/D_p, were fixed at values which are typical in current practice with underground cable systems. Among these variables, changing P/D_s from ~10 to ~17 by changing the helix angle from 83 deg to 52 deg had no detectable effect on the results.

In order to correlate the results of all the heat transfer experiments in dimensionless form, the Nusselt number, Nu, for each flow rate was calculated and plotted as a function of the flow Reynolds number, Re, and the oil Prandtl number, Pr.

Two different characteristic lengths were used in attempting to define a Nusselt number. In one case, the Nusselt number, Nu, was defined in terms of the hydraulic diameter, D_H, of the entire flow area. No satisfactory correlation was obtained by using D_H as the characteristic length.

Another correlation of the same results was obtained by substituting the cable diameter, D_c, for the hydraulic diameter, D_H, in the definition of the Nusselt number. The correlations based on this definition are presented in Fig. 5. These curves suggest that the choice of the cable diameter as the characteristic length in the definition of the Nusselt number gives a better correlation of all the data obtained in test models having significantly diverse geometrical parameters. The physical explanation of the above observation is assumed to be the following:

1 The thermal boundary layer thickness around the cable was found to be very small, of the order of only 2–3 mm. Since the heat transfer coefficient for forced convection is a function of the difference between the cable surface temperature and the oil bulk temperature outside the thermal boundary layer, it can be reasonably assumed that the spacing between the cable and pipe wall, represented by the hydraulic diameter, has little influence as long as the thermal boundary layer is much smaller than D_H.

2 On the other hand, the buoyancy effect, which is the driving force for natural convection, is proportional to the third power of the characteristic length of the heated surface. Based on the above observation, it is reasonable to assume that each cable behaves like a heated surface in an infinite environment and its diameter represents the characteristic length.

The index for the buoyancy force in natural convection is the Rayleigh number, which was defined as:

$$\mathrm{Ra} = \left(\frac{g\beta(T_c - T_b){D_c}^3}{\nu^2}\right) \times \left(\frac{\mu c_p}{k}\right) \tag{1}$$

Fig. 5 indicates that while the Nusselt number in the laminar region was independent of both the flow Reynolds number and the skid wire roughness ratio, it increased with increasing Rayleigh numbers. This

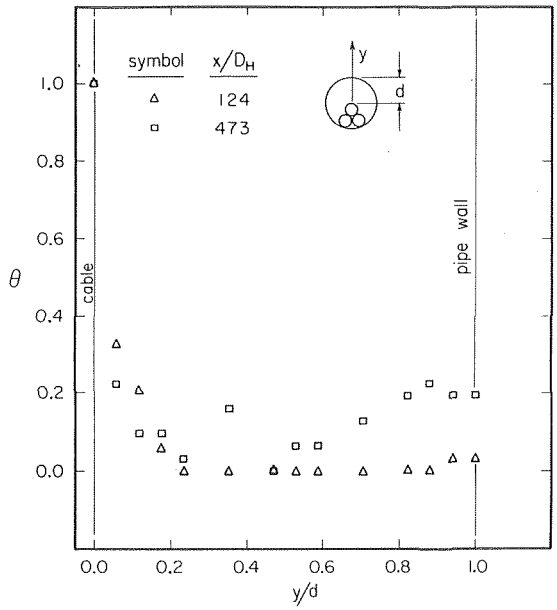

Fig. 3 Dimensionless temperature distributions for configuration 2 in model 2 at Re = 696, q_c = 438 W/m², q_w = 0

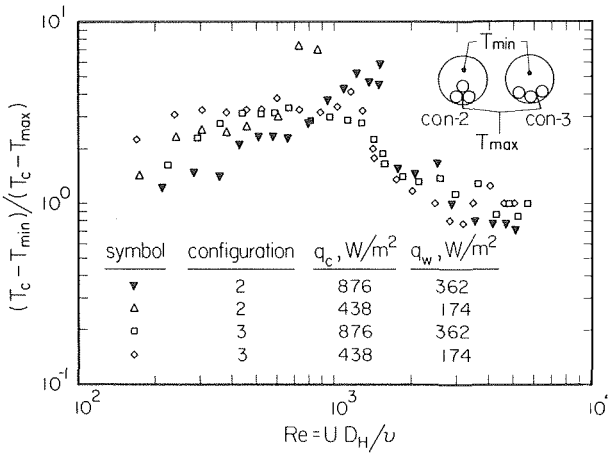

Fig. 4 Dimensionless maximum oil temperatures in model 2

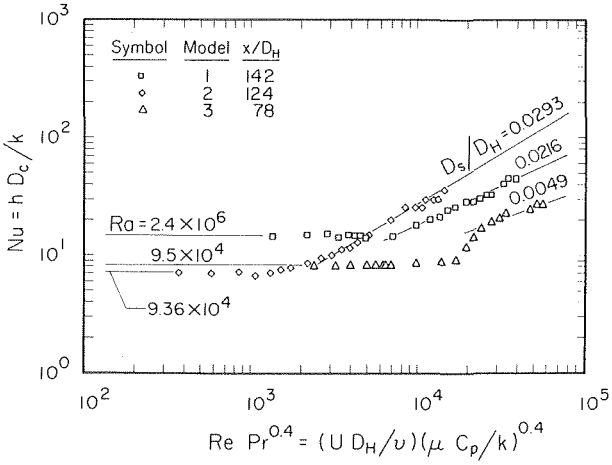

Fig. 5 Nusselt number results, based on cable diameter, for configuration 1 in three different models

relationship is also illustrated in more detail by the results of Fig. 6. If the natural convection dominates the heat transfer, we can assume that

$$\mathrm{Nu} = a \cdot \mathrm{Ra}^{0.25} \tag{2}$$

where the constant, a, ranges from 0.36 to 0.46 for configuration 1 (Fig. 5). These values are slightly less than those in the literature for free cylinders or the values reported in reference [9]. The constant for configuration 3 (Fig. 6) is 0.364. Since the cables interfere thermally with each other, a reduction in the proportionality constant, a, can be expected.

Fig. 5 also shows the effect of the skid wire roughness ratio, D_s/D_H, on both the transition Reynolds number and the turbulent Nusselt numbers. It is obvious that the transition Reynolds number of model 3, which had the lowest roughness ratio ($D_s/D_H = 0.0049$), was almost one order of magnitude higher than that for model 2 ($D_s/D_H = 0.0293$). It is also seen from these results that in the transition and turbulent flow regimes the Nusselt number as well as the slope of its line increase with increasing skid wire roughness ratio. We have insufficient information to give generalized correlations. The best fit curves through the data points in the transition-turbulent regimes can be expressed as follows.

For $D_s/D_H = 0.0293$, $1.5 \times 10^3 < R < 2 \times 10^4$

$$\mathrm{Nu} = 0.011\, R^{0.85} \tag{3}$$

For $D_s/D_H = 0.0216$, $7 \times 10^3 < \mathrm{R} < 4 \times 10^4$

$$\mathrm{Nu} = 0.042\, R^{0.66} \tag{4}$$

For $D_s/D_H = 0.0049$, $2 \times 10^4 < R < 6 \times 10^4$

$$\mathrm{Nu} = 0.127\, R^{0.49} \tag{5}$$

where $R \equiv \mathrm{Re}\ \mathrm{Pr}^{0.4}$

The magnitudes of the heat fluxes on the cables or on the pipe wall had no significant effect on the results.

Fig. 7 shows the results of six sets of heat transfer experiments for configuration 3 in model 2 with three different kinds of cable oils. Since the transition from laminar to turbulent conditions depends largely on the conditions in the main flow channel, one correlation was tried by plotting the Nusselt number, based on the cable diameter, against the flow Reynolds number, based on the pipe hydraulic diameter. However, the pattern of the scatter in the transition and turbulent regimes indicated a dependence on the physical properties of the different oils and suggested the necessity to include the Prandtl number as a correlating parameter. Fig. 7 shows that satisfactory correlation of the heat transfer results was obtained when the Nusselt number, based on the cable diameter, was plotted against the quantity $\mathrm{Re}\cdot\mathrm{Pr}^{0.4}$, where the Reynolds number was based on the hydraulic diameter of the entire cross section, D_H.

Correlations of the heat transfer results for cable configuration 2 in model 2 are shown in Fig. 8. In reference to Figs. 5–8, the following observations are made:

1 The Nusselt number, based on cable diameter, in the laminar flow regime depends primarily on the Rayleigh number as expressed in equation (2). The effect of the Reynolds number is very slight. Thus, natural convection effects are significant in this region and mixed convection is the dominant mechanism of heat transfer.

2 The transition from laminar to turbulent flow starts at $\mathrm{Re} \simeq 400$ for configuration 1, and at $\mathrm{Re} \simeq 1400$ for configurations 2 and 3. The onset of transition for the latter two configurations was actually observed as a sudden drop in the temperature of the cable surface, as well as in the oil temperature in the restricted subchannels. Other indications of turbulence were an instantaneous increase in pressure drop and an increase in mean velocity fluctuations.

3 Configuration 1 had the largest wetted, rough perimeter of all three configurations and, therefore, represented the largest rough surface area under all flow conditions. At relatively low velocities, $\mathrm{Re} < 400$, the Nusselt number was almost constant and natural convection was the dominant mode of heat transfer. Beyond this point, the Nusselt number gradually increased with increasing Reynolds numbers due to the development of turbulence.

4 Correlations of Nusselt number results were in good agreement for Reynolds numbers below 400 and above 1400. The higher Nusselt

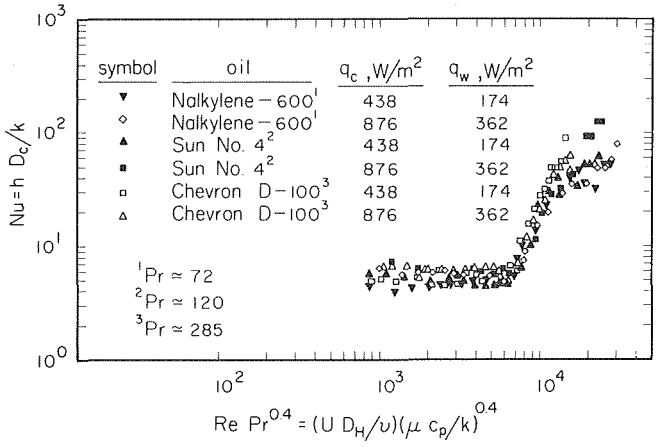

Fig. 7 Nusselt number results for cable configuration 3 in model 2 at $x/D_H = 473$. (After reference [12])

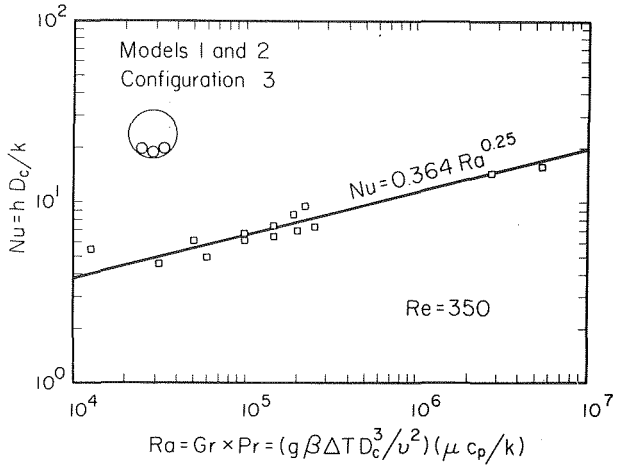

Fig. 6 Variation of the Nusselt number with Rayleigh number in the laminar region for configuration 3

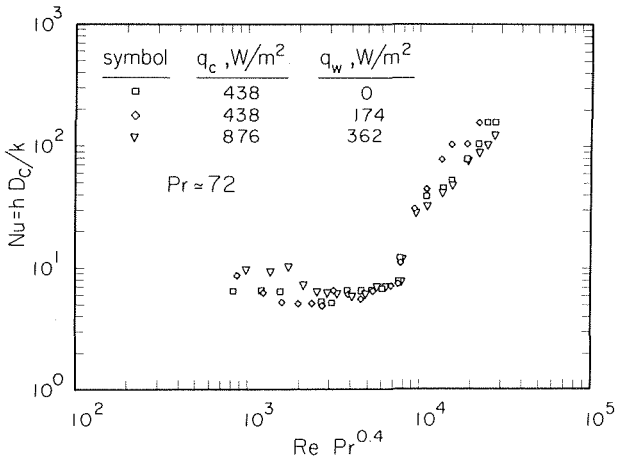

Fig. 8 Nusselt number results for cable configuration 2 in model 2 at $x/D_H = 473$

numbers for configuration 1 in comparison to those for 2 and 3 in the range $400 < Re < 1400$ were primarily due to an increased level of turbulence produced as a result of the larger exposure of the skid wires to the main flow. The skid wires act as turbulence promoters.

5 In the higher turbulence regime, the difference between cable surface and oil temperatures was often less than 0.5 °C. Any temperature fluctuations in this range resulted in the relatively large measurement errors, which explain the scatter of the results in this region.

A special experiment was conducted to study the effects of natural convection currents in the laminar range. Heat transfer parameters were measured for a wide range of Rayleigh numbers by increasing the heat flux rate from 0 – 110 W/m^2, while maintaining steady laminar flow conditions. The results show that in the laminar range, the Nusselt numbers near the entrance ($x/D_H = 124$) were slightly lower than those near the exit ($x/D_H = 473$) for all cases where Ra > 50,000. At lower Rayleigh numbers, the entrance Nusselt numbers were equal to or slightly higher than those near the exit. Thus, at the higher Rayleigh numbers the development of the natural convective circulation compensates for the thickening of the boundary layer in the axial direction.

Heat transfer to the pipe wall has been correlated on the basis of the Nusselt number formed by the hydraulic diameter of the entire pipe, as shown in Fig. 9. The orders of magnitude of these Nusselt numbers are the same as the ones for the cables based on the cable diameter in Figs. 7 and 8. The early transition to turbulence with configuration 1 is clearly indicated by the increase of Nusselt numbers starting at $R = 2000$.

Conclusions

1 Temperature profiles indicate that the thermal boundary layer thickness around a heated cable is approximately 2–3 mm at any axial location. Vertical profiles also indicate that oil temperatures are essentially uniform in the entrance region, and that higher temperatures develop near the top of the pipe with increasing axial downstream distance indicating the development of natural convection effects.

2 The dominant mode of heat transfer in the laminar range is mixed (natural and forced) convection, and the Nusselt number throughout this range is an increasing function of the Rayleigh number, but is independent of the flow Reynolds number and the skid wire roughness ratio. In addition, the results indicate that the Nusselt number increases along the axial distance downstream from the inlet, for Ra > 50,000, in contrast to the previously held assumption that the Nusselt number near the end of a cable pipe would be much smaller than that in the entrance region.

3 The skid wire roughness ratio for any cable configuration has a strong influence on the transition Reynolds number. In addition, the turbulent Nusselt numbers increase with increasing roughness ratios.

4 The best correlations of the heat transfer results are obtained if the Nusselt numbers are plotted against the quantity $Re \cdot Pr^{0.4}$, where the Reynolds number is based on the overall hydraulic diameter of the entire cross section. For heat transfer to the cables, the Nusselt number should be based on the cable diameter; whereas, for heat transfer to the pipe wall, the overall hydraulic diameter should be used in the Nusselt number. Based on these correlations, the Nusselt numbers in the laminar region ($Re < \sim 1000$) were between 5–16, depending on the Rayleigh number. In the low turbulence region ($Re \simeq 3000$), the Nusselt numbers for the cables were between 30–80, depending mainly on the skid wire roughness ratio; whereas, the Nusselt numbers for the pipe wall were between 60 and 200.

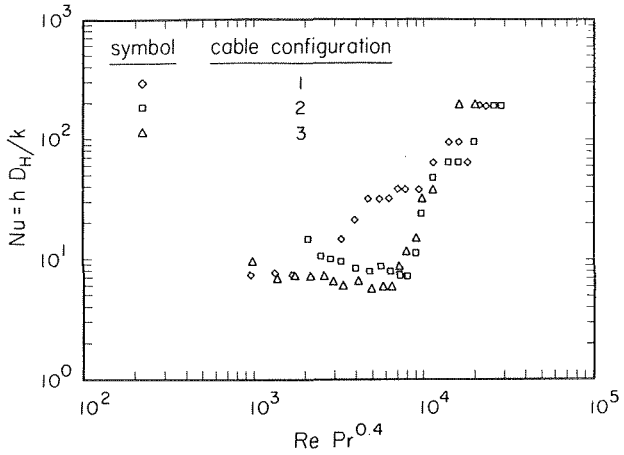

Fig. 9 Nusselt number results for pipe wall at $x/D_H = 473$, $q_c = 876$ W/m^2, $q_w = 362$ W/m^2 (After reference [12])

Acknowledgments

This work was supported in part by Contract No. E(49-18)-1568, (RP 7821-1) from the Electric Power Research Institute and the U. S. Energy Research and Development Administration. Oils were furnished by Chevron, Conoco and Sun Oil Companies.

References

1 Chato, J. C. and Abdulhadi, R. S., "Flow and Heat Transfer in Convectively Cooled Underground Electric Cable Systems: Part 1—Velocity Distributions and Pressure Drop Correlations," ASME JOURNAL OF HEAT TRANSFER, Feb. 1978, pp. 30–35.

2 Abdulhadi, R. S., "Natural and Forced Convective Cooling of underground Electric Cables," Ph.D. Thesis, Department of Mechnical and Industrial Engineering, University of Illinois at Urbana-Champaign, Dec. 1975.

3 Abdulhadi, R. S. and Chato, J. C., "Natural and Forced Convective Cooling of Underground Electric Cables," Technical Report Number ME-TR-609, UILU-ENG 75-4003, Dec. 1975, Department of Mechnical and Industrial Engineering, University of Illinois at Urbana-Champaign, Urbana, Ill.

4 Neher, J. H., and McGrath, M. H., "The Calculation of the Temperature Rise and Load Capability of Cable Systems," *AIEE Trans.*, Vol. 76, 1954, pp. 752–772.

5 Buller, F. H., "Artificial Cooling of Power Cables," *AIEE Trans.*, Vol. 71, 1952, pp. 634–641.

6 Sheriff, N., and Gumley, P., "Heat-Transfer and Friction Properties of Surfaces with Discrete Roughnesses," *International Journal Heat Mass Transfer*, Vol. 9, 1966, pp. 1297–1320.

7 Notaro, J., and Webster, D. J., "Thermal Analysis of Forced-Cooled Cables," Paper 70 TP 518-PWR., IEEE Summer Meeting at Los Angeles, Calif., July 1970.

8 Zanona, A., and Williams, J. L., "Forced-Cooling Model Tests," *IEEE Trans.*, Vol. PAS-89, No. 3, 1970, pp. 491–503.

9 Slutz, R. A., Orchard, W. P., Glicksman, L. R., and Rohsenow, M. W., "Cooling of Underground Transmission Lines: Heat Transfer Measurements," Heat Transfer Laboratory Report No. 80619-87, 1974, Massachusetts Institute of Technology, Cambridge, Mass.

10 Webb, R. L., Eckert, E. R., and Goldstein, R. J., "Heat Transfer and Friction in Tubes with Repeated-Rib Roughness," *International Journal Heat Mass Transfer*, Vol. 14, 1971, pp. 601–617.

11 Bahder, G., Eager, G. S., Jr., Silver, D. A. and Turner, S. E., "550 kV and 765 kV High Pressure Oil Filled Pipe Cable System," *IEEE Trans.*, Vol. PAS-95, No. 2, 1976, pp. 478–488.

12 Abdulhadi, R. S. and Chato, J. C., "Combined Natural and Forced Convective Cooling of Underground Electric Cables," *IEEE Trans.*, Vol. PAS-96, No. 1, 1977, pp. 1–8.

13 Chern, S. Y. and Chato, J. C., "Numerical Analysis of Convective Cooling of Pipe-Type Electric Cables," Technical Report No. ME-TR-712, UILU-ENG 76-4006, Department of Mechnical and Industrial Engineering, University of Illinois at Urbana-Champaign, 1976.

T. G. Theofanous
T. H. Bohrer
M. C. Chang
P. D. Patel

Purdue University,
West Lafayette, Ind.

Experiments and Universal Growth Relations for Vapor Bubbles With Microlayers

Solutions for bubble growth rates including the effects of inertia, heat transfer, and microlayer evaporation were obtained in generalized coordinates. Experimental growth rate data, covering a wide range of superheats, were obtained under precisely controlled conditions. The theoretical development appears to provide a satisfactory a priori prediction of these data. In particular, the Γ-effect predicted earlier is fully corroborated by these data which are the first to cover an extended range of this parameter.

Introduction

The initial impetus for this work was to provide experimental verification of the universal representation of bubble growth rates reported recently [1].[1] Of particular interest is the range of conditions for which inertia effects cannot be neglected, and the characteristic vapor density ratio, Γ [1], is large (especially relevant to liquid metal boiling and/or liquids subjected to rapid depressurization). The latter condition implies high initial superheats. This, in turn, promotes inertia limitations which, however, can also be achieved, more simply, by imposing low ambient pressures (low vapor densities). This independent requirement for high superheats has led to a choice of experimental conditions and techniques which stimulated consideration of the additional problem of microlayer effects.

Microlayer development is typical when a bubble grows in the immediate vicinity of a solid wall. This situation arises, for example, in nucleate boiling, and it has received considerable attention in the past decade. Depending on the conditions, microlayer evaporation due to its own stored superheat, or due to heat transfer from the adjacent wall, can significantly influence the bubble growth rates. Many theoretical studies have attempted to sort out these contributions for the most common heat transfer-limited growth regime. Some have also considered inertia limitations. Good surveys have been presented by Cooper and Vijuk [2] and Dwyer [3]. However, the lack of definitive experimental data does not facilitate a choice among these theories or provide guidance for additional analytical efforts. Although a few experimentalists have looked at such details as space/time variations in microlayer thickness [4], including the formation of a dry-patch [5], most data were obtained under typical nucleate boiling conditions [6]. The ambiguities in comparisons referred to above are due to the nonuniformity and nonstationarity of the temperature field under these experimental conditions. The situation is even less definitive when inertia contributions become significant [7].

Within the context of the present work, microlayer effects first arose in the somewhat different topology of thin wire probes. These probes were necessary to produce a predictable (both in space and time) single nucleation event in the energetically neutral way of a simple touching. Since the successful operation of this system did not allow an unlimited reduction of the probe diameter, it became necessary to theoretically establish the limit of negligible microlayer interference. This was accomplished by a simple extension of the analysis presented earlier [1], which also produced a universal representation of bubble growth in terms of an appropriately normalized wire-probe radius. At this point, only straightforward extensions in the experimental and analytical tools were required to consider the problem for microlayers typical of nucleate boiling (plane wall geometry). This latter extension is not meant to address the complete problem of microlayer contributions to nucleate boiling. It is rather intended as a first step, providing analytical insight and clear experimental verification for an idealized but relevant system.

Experimental

Apparatus and Procedure. The basic experimental goal was to predictably nucleate and record the growth of a single vapor bubble in a highly metastable (superheated) liquid. To avoid ambiguities in local conditions associated with the transient heating and/or depressurization techniques the "wetting" Freon (11 and 113)/glass pair was chosen. With special cleansing, loading, and deactivation procedures [8, 9] superheats up to 60°C were attainable for indefinite durations. A 2000-ml Pyrex flask, fitted with an optical window, was utilized as the experimental vessel. A layer of glycerol was employed to "seal" the liquid Freon in this flask. Slow depressurization and isolation at room temperature yielded the corresponding metastable state. The pressure was measured with a mercury manometer. Room

[1] Numbers in brackets designate References at the end of paper.

Contributed by the Heat Transfer Division for publication in the JOURNAL OF HEAT TRANSFER. Manuscript received by the Heat Transfer Division November 29, 1976.

and glycerol temperatures were measured by means of a mercury thermometer and copper-constantan thermocouple respectively. Any thermal gradients whatsoever were absent prior to nucleation.

It was determined that predictable nucleation in this system may be achieved by simply touching two solid surfaces within the superheated liquid. This procedure is advantageous because it results in a minimum disturbance of local conditions and initiates a bubble in a most "natural" manner. For the spherically symmetric bubble experiments, the two stainless steel wire probes, shown in Fig. 1, were utilized for this purpose. By placing their horizontal segments at right angles (forming a cross) and about 0.5 mm apart, only a slight, electromagnetically driven, vertical travel was required for bubble nucleation at the point of contact (coincident also with the flask center). Three different probe sizes were utilized with diameters of 0.25 mm, 0.51 mm, and 0.81 mm. For the hemispherical bubble experiments, a small glass disk immersed in the center of the Freon volume, and a thin (0.61 mm dia) stainless steel wire, its one end sharpened to a point, were utilized. By placing the wire at a position normal to the disk, at its center, and about 0.5 mm apart, only a slight, electromagnetically released, vertical travel was required for the sharpened wire end to make contact with the disk and thus produce a nucleation event. Fig. 2 illustrates this mechanism, within the context of the overall experimental setup.

Photographic records were obtained at 9000 fps using either a Dynafax model 326 high-speed framing camera or a Hycam model K2004 16 mm high-speed motion picture camera. A schematic of the overall arrangement is shown in Fig. 3. Complete details are given by Bohrer [8] and Chang [9].

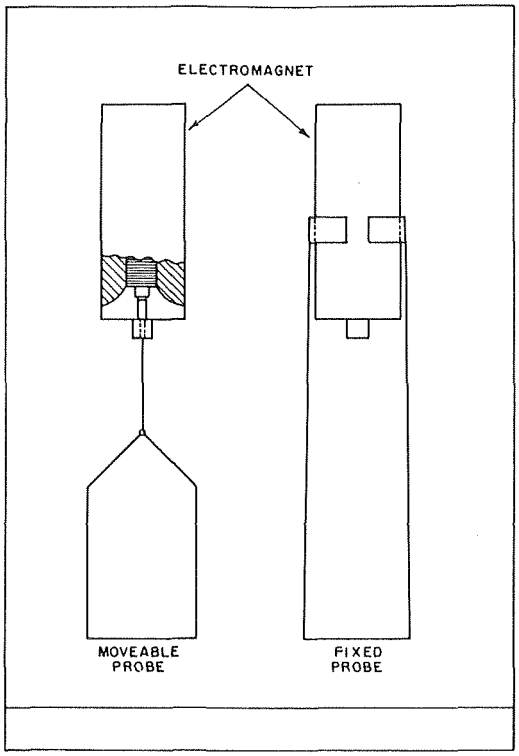

Fig. 1 Schematic diagram of the nucleation probes

Data Reduction. Smooth-walled spherical (and hemispherical) bubbles were observed in all experiments. Two typical growth sequences are presented in Figs. 4 and 5. Considerable agitation and entrainment was noted only when the wall of the spherical bubbles encountered the vertical segments of the two nucleation probes. For the spherical bubbles, the diameters along two orthogonal axis never differed by more than 15 percent, except in the very early stages of growth when the bubble and the probe diameters were of the same magnitude. The hemispherical bubbles exhibited similarly small distortions. Under such conditions a simple arithmetic averaging is sufficient to express vapor volume content. Further, a probe volume correction, important only for the very early stages at growth, was applied to determine the true vapor volume.

The time origin was determined by extrapolation to zero radius. The only factor that may interfere with this extrapolation technique is the delay time due to surface tension effects. For the conditions of interest here this time was determined by numerical methods [10] and was found to be less than 0.003 ms. A conservative (upper bound) estimate of the uncertainty in time origin was determined for some of the experiments, as follows. Physically realistic upper and lower bounds were calculated for the time needed to reach the size of the first bubble detected on the film. The Rayleigh solution, for inertia-controlled growth, provides the lower bound. An upper bound is obtained from the complete numerical simulation [10] with an artificially degraded growth rate by utilizing a vaporization coefficient of 0.1 (all comparisons with these Freon data indicate a coefficient of unity). Each data point was then represented by a horizontal bar, its length reflecting the total uncertainty in time origin. Clearly, as the framing rate increases, the probability of recording an earlier instance of the growth sequence increases. This leads to a decrease in total time-origin uncertainty. Other relevant uncertainty limits were established as follows: length, ±0.0025 cm; frame separation, 0.5 percent; superheat, 2 percent.

Nomenclature

A_* = a parameter, $\left(\frac{2}{3}\frac{P^*(T_\infty) - P_\infty}{\rho_\ell}\right)^{1/2}$

B = a parameter, $\left(\frac{12}{\pi}\alpha_\ell\right)^{1/2}\left(\frac{\rho_\ell c_\ell (T_\infty - T^*(P_\infty))}{\lambda \rho_v^*(P_\infty)}\right)$

c = specific heat

Ja = Jakob number, $\frac{\rho_\ell c_\ell (T_\infty - T^*(P_\infty))}{\lambda \rho_v^*(P_\infty)}$

k = thermal conductivity

n = number of probe segments (from bubble center to its wall)

P = pressure

Pr = Prandtl number

$P^*(T)$ = saturation pressure at temperature T

Q_p = heat conducted to microlayer surface in time t

r = probe radius

r^* = dimensionless probe radius, $\frac{A_*}{B^2} r$

R = bubble radius

R^* = dimensionless bubble radius, $\frac{A_*}{B^2} R$

T = temperature

$T^*(P)$ = saturation temperature at pressure P

t = time from growth initiation

t^* = dimensionless time, $\frac{A_*^2}{B^2} t$

α = thermal diffusivity

Γ = a parameter, $\frac{\rho_v^*(T_\infty)}{\rho_v^*(P_\infty)}$

λ = latent heat of evaporation

ρ = density

$\rho^*(P)$ = saturation density at pressure P

$\rho^*(T)$ = saturation density at temperature T

ϕ = a parameter, $\frac{T_v - T^*(P_\infty)}{T_\infty - T^*(P_\infty)}$

θ = a parameter, defined by equation (7).

Subscripts

ℓ = liquid

s = solid

v = vapor

∞ = conditions far away from the bubble

Range of Experimentation. The range of parameters covered in the present work is compared in Table 1 with those of the experiments in Dergarabedian [11], Florschuetz, et al. [12], Board and Duffey [13], and Lien [14]. The parameters compared are the Jakob number Ja, the superheat ΔT, and the characteristic vapor density ratio Γ.

Though experiments involving liquids besides water have also been performed by some of the cited authors, the parameter values of these are similar to those shown in Table 1.

Analytical

Bubbles With Probe Microlayers. For generality let us consider $n/2$ cylindrical probes of radius r arranged with an "effective" common intersection. A bubble nucleating at this point will grow in a spherically symmetric fashion with its wall remaining perpendicular to each probe's axis. A smooth liquid microlayer is left behind the advancing wall. Counting from the common origin up to the bubble wall, there are n probe segments each of length $R(t)$. The formulation for this case is the same as that presented earlier [1] with the exception that the heat balance equation (over the bubble) will now be augmented by the probe contributions.[2] For this calculation the microlayer is considered "thick" compared to the thermal wave penetration distance (see Appendix). Furthermore each microlayer element is assumed to be "deposited" with a *uniform* temperature of T_∞. Assuming thermodynamic equilibrium at all liquid-vapor interfaces, the temperature driving force for heat conduction in the microlayer is $(T_\infty - T_v(t))$. The total heat conducted to the microlayer surface up to time t is:

$$Q_p = \frac{2\sqrt{\pi} rnk_\ell}{\sqrt{\alpha_\ell}} \int_0^t \frac{(T_\infty - T_v)}{(t-\tau)^{1/2}} \left(\frac{dR}{d\tau}\right) d\tau \tag{1}$$

With this result the heat balance equation now yields:

$$\frac{dR}{dt} = \left(\frac{12}{\pi}\alpha_\ell\right)^{1/2} \frac{\rho_\ell c_\ell}{\lambda \rho_v} \frac{(T_\infty - T_v(t))}{2\sqrt{t}} + \frac{2\sqrt{\pi} rnk_\ell}{\sqrt{\alpha_\ell}\lambda\rho_v(4\pi R^2)} \int_0^t \frac{(T_\infty - T_v)}{(t-\tau)^{1/2}} \left(\frac{dR}{d\tau}\right) d\tau \tag{2}$$

Together with the simplified form of the momentum equation and the definitions and notations of [1] the final system in dimensionless form is:

$$\frac{dR^*}{dt^*} = \phi \qquad \text{with } R^*(0) = 0 \tag{3}$$

$$(\Gamma - 1)\phi^3 + \frac{1}{2\sqrt{t^*}}\phi^2 + \phi - \frac{1}{2\sqrt{t^*}} - \left(\frac{1}{48}\right)^{1/2} nr^* \int_0^{t^*} \frac{\phi - \phi^3}{\sqrt{t^* - \tau}} d\tau \left\{\int_0^{t^*} \phi d\tau\right\}^{-2} = 0 \tag{4}$$

The function $\phi = \phi(t^*; \Gamma, nr^*)$ is obtained for various combinations of the parameters by means of a successive approximation scheme applied to equation (4). An initial variation of ϕ with t^* is assumed. The integrals of the last term in equation (4) are evaluated for several times and the resulting cubic is solved for the same times. This new set of ϕ values is similarly utilized to generate yet another set of results from the solution of the cubic. The process is repeated until convergence is achieved. Even with a gross initial guess of $\phi = 1$ (true only at $t^* = 0$), only a few iterations are required for convergence. Equation (3) is finally integrated to obtain $R^* = R^*(t^*; \Gamma, nr^*)$. The results are presented as universal plots in Figs. 6 and 7 for the range of parameters relevant to the conditions of the experimental program.

For clarity of presentation, the results for this two-parameter family of curves are presented only over the physically interesting range of the parameter Γ. Similarly a corresponding range of the nr^* parameter was chosen. In so far as the probe contribution to the bubble growth rate is concerned, a geometric and a transport effect are discerned. Since the microlayer area increases as dR, while the bubble surface area increases as RdR, the geometry favors a continuous decline in microlayer importance. As seen in Figs. 6 and 7, by the time R^* becomes of order nr^* the solution becomes parallel to that of a microlayer-free bubble ($nr^* = 0$). What is left, however, is a relatively strong memory effect of the probe-augmented early growth. The transport effect is related to the degree of inertia limitations present, and hence differences in thermal gradients between the bubble wall and the microlayer. As inertial limitations increase, all thermal gradients diminish and so does the microlayer role. This effect may be observed in terms of the differences in probe contributions between solutions in the range of non-negligible inertia limitation $t^* < 1$ and those in the range of heat-transfer-controlled growth, $t^* > 10$. Over the duration of a particular growth event, heat transfer limitations increase in significance with time. The above discussion indicates (and Figs. 6 and 7 show) that the correspondingly increased role of microlayer contribution can only be felt if the bubble size is not large enough compared to the probe size for the geometric effect to overshadow the transport effect.

Bubbles With Wall (Planar) Microlayers. Except for geometry differences, the derivation here parallels the one just given. The microlayer now has the shape of a disk with a diameter equal to that of the bubble. As above, for nonmetallic fluids, for the times of interest the microlayer may be considered, as far as conduction is concerned,

[2] In this formulation, the well known solutions for the asymptotic inertia (Raleigh) and heat transfer (Birkhoff, et al., Scriven) regimes are coupled by assuming that both remain valid even as actual control is shifting (with growth) from the former to the latter, provided the driving forces in each one are adjusted to reflect actual conditions. In addition, here, we assume negligible wall shear and surface tension effects.

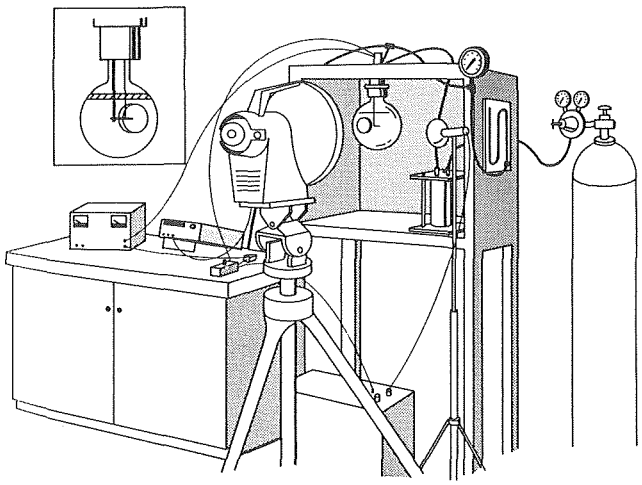

Fig. 2 Isometric view of the experimental apparatus

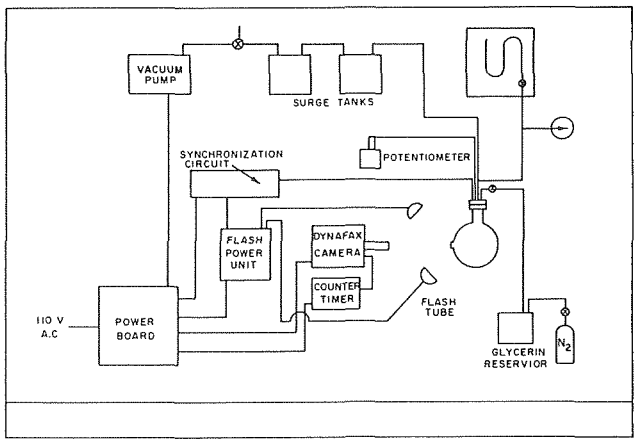

Fig. 3 Schematic diagram of the experimental apparatus (Dynafax system)

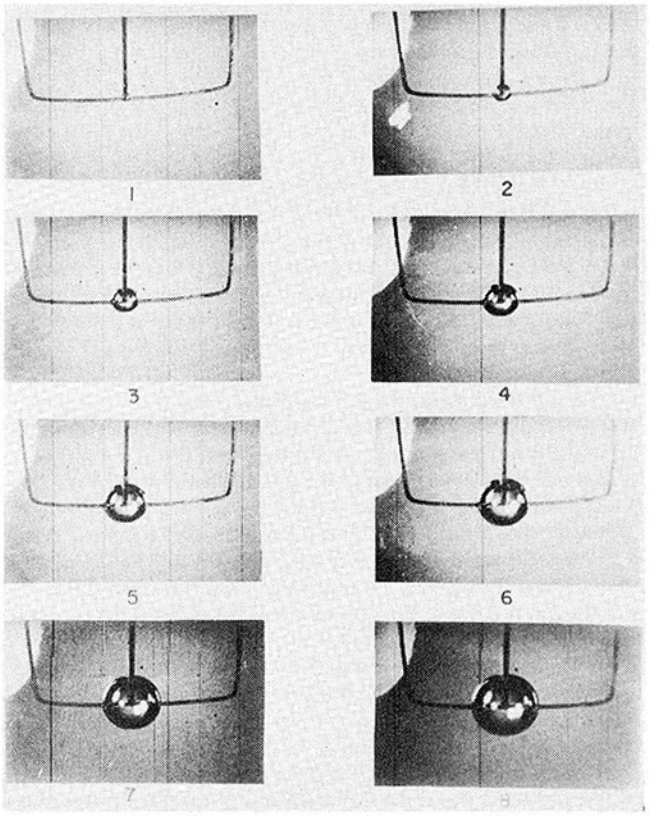

Fig. 4(*a*)

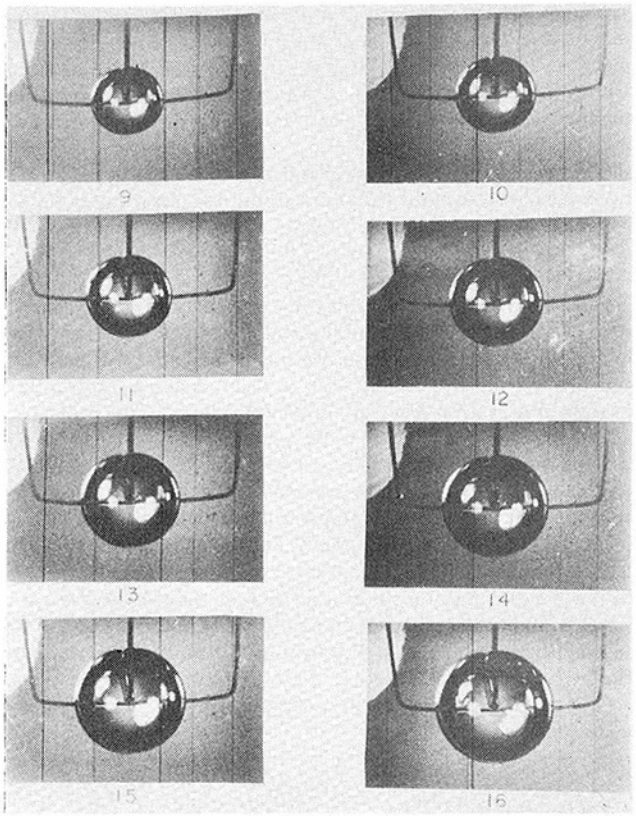

Fig. 4(*b*)

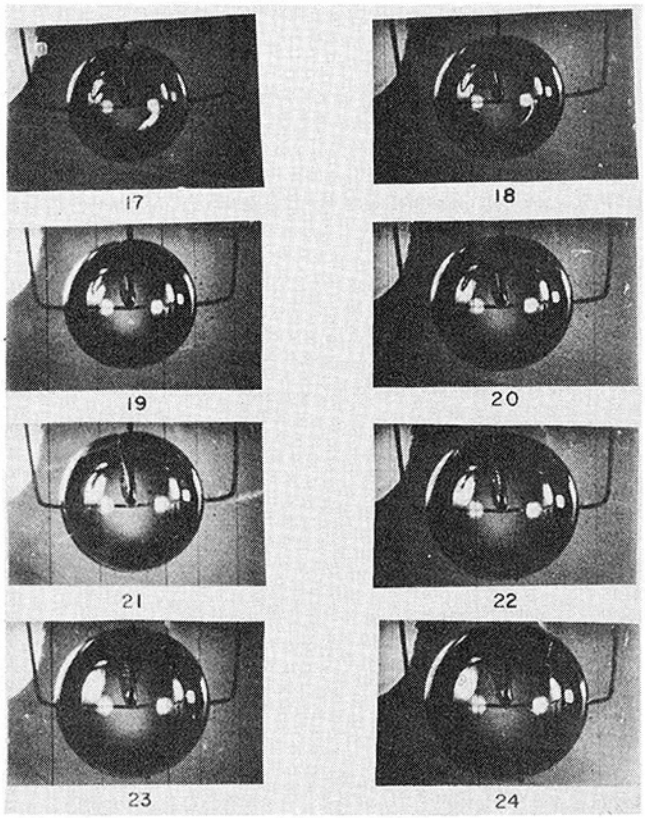

Fig. 4(*c*)

Fig. 4 Typical frames from spherical bubble growth photographic results. (Freon-113, superheat = 50.8°C, T_∞ = 22.2°C, probe diameter = 0.51 mm, frame separation = 0.224 ms)

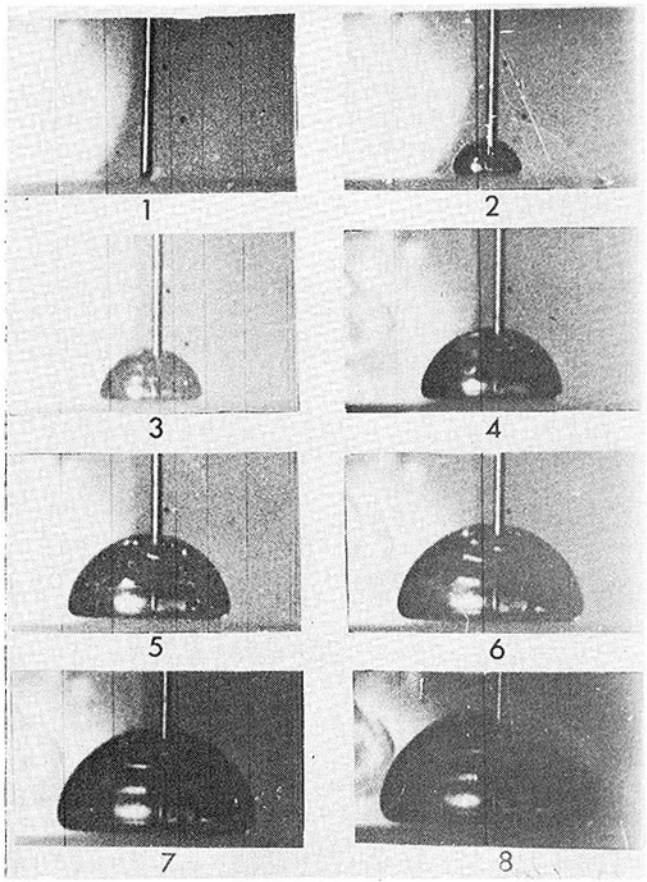

Fig. 5 Typical frames from hemispherical bubble growth photographic results. (Freon-113, superheat = 18.6°C, T_∞ = 22°C, probe diameter = 0.61 mm, frame separation = 1.332 ms)

Table 1 A comparison of the range of experimentation by various authors

Experiments of	Liquid	Maximum Superheat °C	Maximum Γ	Maximum Jakob No. Ja
Florschuetz, et al. [12]	Water	3.9	1.14	11.7
Dergarabedian [11]	Water	5.3	1.19	15.9
Board and Duffey [13]	Water	20.3	2.14	173.0
Lien [14]	Water	15.7	2.54	2690
Present work	Freon-113 and 11	59.4	18.45	3195

as semi-infinite (see Appendix). The case of an extremely well-conducting microlayer can also be included by simply using the thermal-transport properties of the wall instead of those of the fluid. The final system of equation is:

$$\frac{dR^*}{dt^*} = \phi; \qquad R^*(0) = 0 \tag{5}$$

$$(\Gamma - 1)\phi^3 + \phi + \frac{\phi^2}{2\sqrt{t^*}} - \frac{1}{2\sqrt{t^*}} - \frac{\theta}{12}\left\{\int_0^{t^*} \phi d\tau\right\}^{-2} \times \int_0^{t^*}\int_0^{\tau} \phi(u)du \frac{[\phi(\tau) - \phi^3(\tau)]}{\sqrt{t^* - \tau}} d\tau = 0 \tag{6}$$

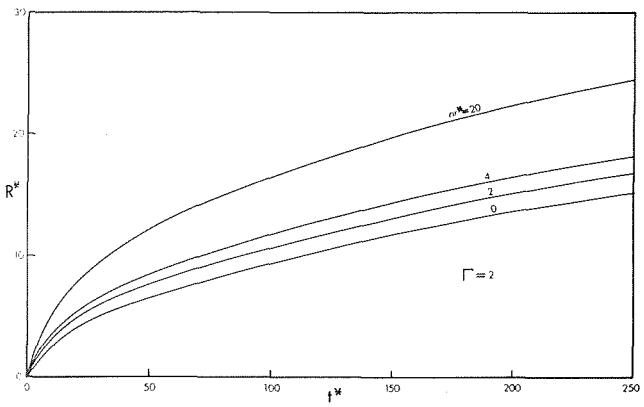

Fig. 6 Universal plot of the spherical bubble radius versus time for different probe parameter nr^* ($\Gamma = 2$)

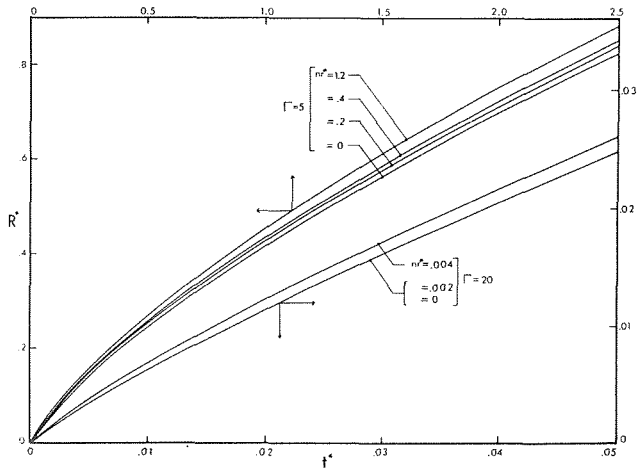

Fig. 7 Universal plot of the spherical bubble radius versus time for different probe parameter nr^* ($\Gamma = 5, 20$)

where:

$$\theta = \begin{cases} \dfrac{\rho_s c_s}{\rho_\ell c_\ell}\left(\dfrac{\alpha_s}{\alpha_\ell}\right)^{1/2} & \text{for liquid metal/solid system} \\ 1 & \text{for ordinary liquid/solid system} \end{cases} \tag{7}$$

The function $\phi = \phi(t^*; \Gamma, \theta)$ was obtained for various combinations of the parameters by solving equation (6) in a fashion similar to that employed for the solution of equation (4). The function $R^* = R^*(t^*; \Gamma, \theta)$ was obtained by numerically integrating equation (5). The results are presented as universal plots in Figs. 8 and 9 for an extensive range of Γ and θ values.

The net effect of the microlayer contribution may be found by comparing the results of Fig. 8 with those of [1]. For illustration, the solution for microlayer-free bubbles (no plate) is included for $\Gamma = 20$. Contrary to the results for probe microlayers, a continuously increasing microlayer contribution with time is observed here. This is favored by both the geometric and transport effects mentioned before. Now the bubble surface area increases at the same rate as the microlayer surface area. This behavior does not produce a cancellation of

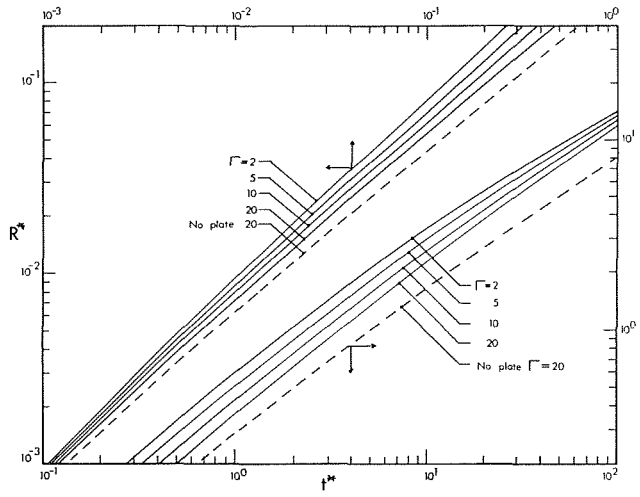

Fig. 8 Universal plot of the hemispherical bubble radius versus time compared with the no-plate results for $\Gamma = 20$. Here, $\theta = 1$

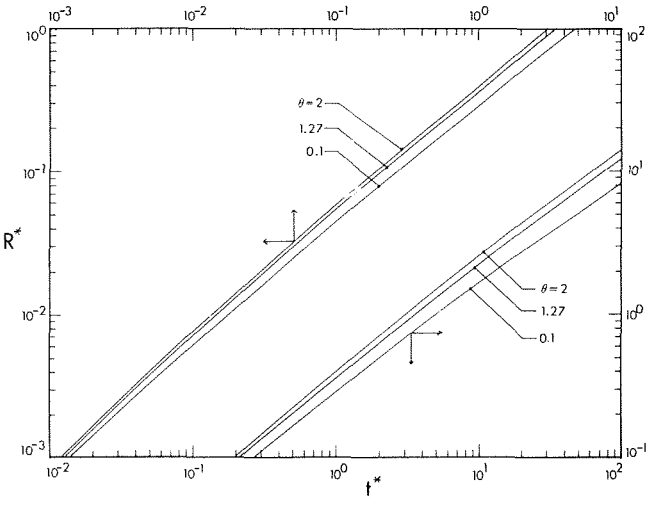

Fig. 9 Universal plot of the hemispherical bubble radius versus time for different parameter θ. $\theta = 1.27$ corresponds to a liquid sodium-stainless steel system

the transport effect as it did for the probe microlayers. Hence for small values of t^*, where the growth is predominantly inertia controlled, i.e., $R^* = t^*$, the contribution of the microlayer, as expected, is minimal. At $t^* \sim 10^{-2}$ a difference of only 10 percent is observed. For intermediate values of t^* (i.e., $t^* \sim 1$) the growth is by a combination of inertia and thermal limitations, and the microlayer contribution increases. For $t^* = 1$ this contribution is about 25 percent. From this point on thermal effects become increasingly important and the microlayer contribution correspondingly increases. For $t^* = 100$ the microlayer contributes an increase of 50 percent in bubble size. Similar trends are found for other values of the parameter Γ. These results are in excellent agreement with the previously available solutions for this (heat transfer control) asymptotic regime of Sernas and Hooper [6] and van Ouwerkerk [5].

The effect of the parameter θ is shown in Fig. 9. The value $\theta = 1.27$ corresponds to the liquid sodium-stainless steel system which is of current interest in nuclear applications.

Results and Discussion

A set of typical spherical bubble growth results (with probe microlayers) are presented in Figs. 10–13. Fig. 10 represents the highest superheat run and clearly confirms the Γ-effect predicted previously [1]. It also demonstrates the excellent agreement between the experimental data and the present solutions for this case of negligible microlayer effects. Fig. 11 shows a similarly good comparison between

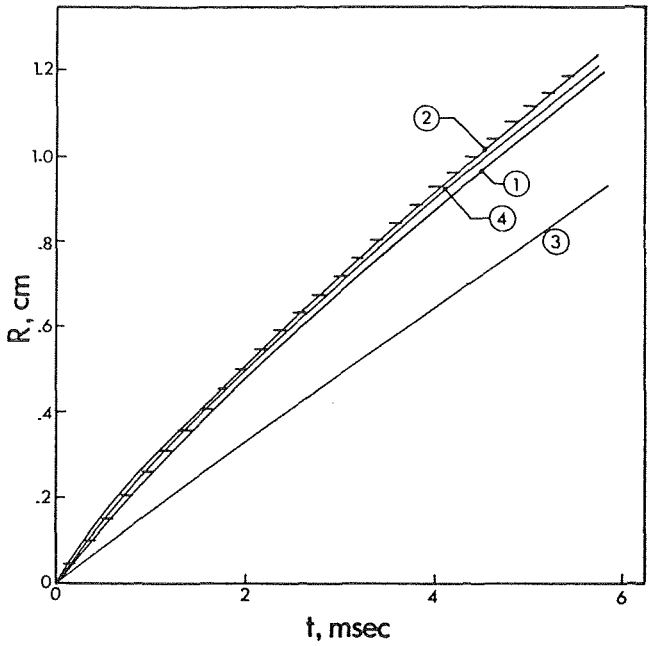

Fig. 10 A comparison of the theoretical results with experimental data for a spherical bubble: (1) numerical solution [10]; (2) solution with the probes accounted for; (3) solution of [16]; (4) present solution without considering the probe effects. (Freon-113, superheat = 59.4°C, T_∞ = 22.8°C, probe diameter = 0.25 mm)

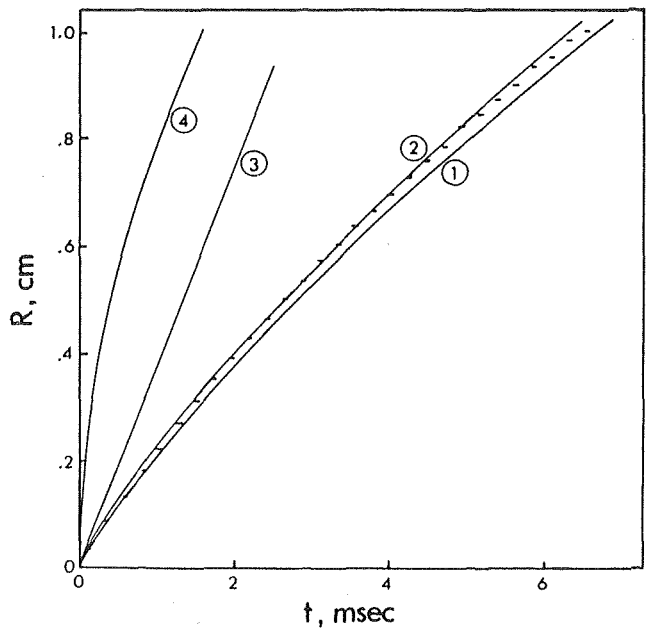

Fig. 11 A comparison of the theoretical results with experimental data for a spherical bubble: (1) numerical solution [10]; (2) solution with the probes accounted for; (3) "inertia"; (4) "heat-transfer" solution. (Freon-113, superheat = 34.1°C, T_∞ = 22.8°C, probe diameter = 0.25 mm)

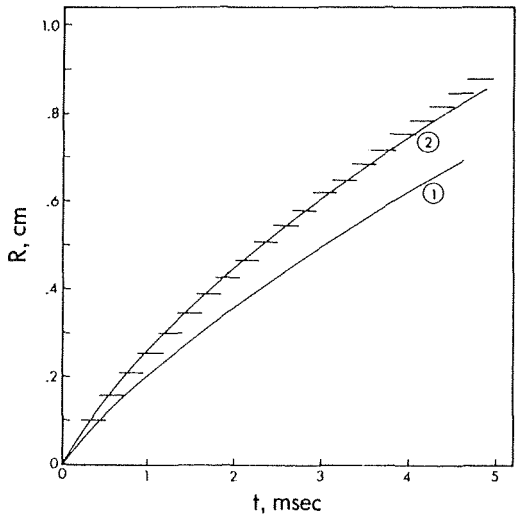

Fig. 12 A comparison of the theoretical results with experimental data for a spherical bubble: (1) numerical solution [10]; (2) solution with the probes accounted for. (Freon-113, superheat = 31.9°C, T_∞ = 24.7°C, probe diameter = 0.81 mm)

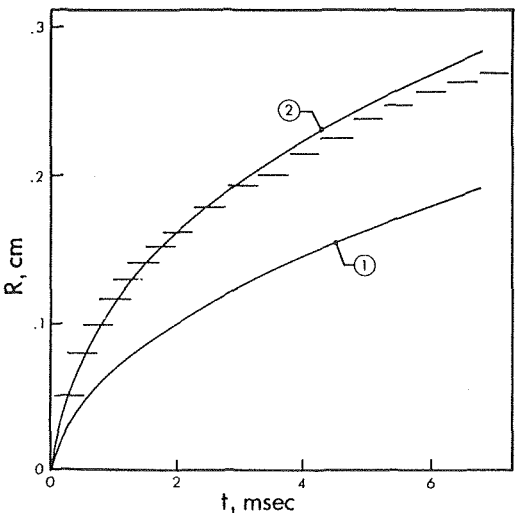

Fig. 13 A comparison of the theoretical results with experimental data for a spherical bubble: (1) numerical solution [10]; (2) solution with the probes accounted for. (Freon-11 superheat = 17.8°C, T_∞ = 21.7°C, probe diameter = 0.51 mm)

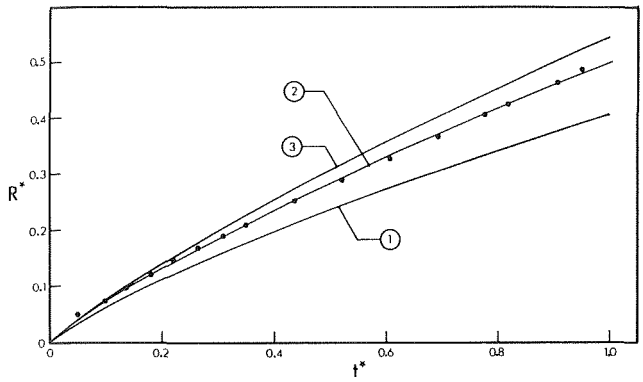

Fig. 14 A comparison of the theoretical results with experimental data for a hemispherical bubble: (1) solution without plate, $\Gamma = 5.09$; (2) solution with plate, $\Gamma = 5.09$; (3) solution with plate, $\Gamma = 3.58$ (Freon-113, superheat = 36.7°C, T_∞ = 22°C, probe diameter = 0.61 mm)

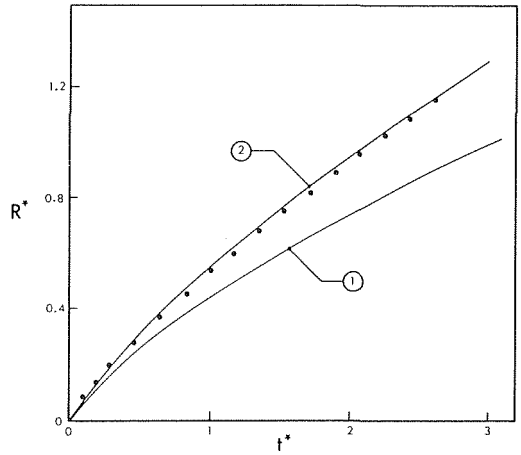

Fig. 15 A comparison of the theoretical results with experimental data for a hemispherical bubble: (1) solution without plate, $\Gamma = 3.58$; (2) solution with plate, $\Gamma = 3.58$. (Freon-113, superheat = 29.4°C, T_∞ = 21°C, probe diameter = 0.61 mm)

experiment and predictions, for a set of conditions for which both the "inertia" and the "heat transfer" solutions greatly overpredict the data. Figs. 12 and 13 demonstrate the predictive capability under conditions for which microlayer effects become of increasing importance, i.e., larger probe diameters and lower superheats. It has been shown [1] that only slight differences exist between the approximate analytical technique utilized here and the numerical solution (with a vaporization coefficient of unity) [10] which may be taken as the "exact" one. In the comparison presented before, we have avoided even these slight differences by adding the probe contributions to the bubble size as predicted by the present work to the results of the numerical simulation. The results of reference [15] were utilized to estimate the microlayer thickness. The probe surface area utilized in these calculations includes an increase due to the microlayer. For the case of Fig. 13 the result is sensitive to this thickness. However, the hydrodynamic displacement thickness, commonly utilized for microlayer thickness estimation in nucleate boiling, is of the same magnitude. For the other cases some differences between the two methods are obtained but the results are not sensitive to such changes.

A set of typical hemispherical bubble growth results (with plane-wall microlayers) are presented in Figs. 14–16. These results are presented in terms of the dimensionless quantities R^* and t^* and all analytical predictions are based on the solution of equations (5) and (6) (neglecting the small contribution of the microlayer left on the vertical nucleation probe, in comparison to that of the microlayer at the base of the bubble, on the wall). Due to their small magnitude, as seen from the comparisons already presented, uncertainties in time origin have not been included. Fig. 14 illustrates a case of combined (inertia and heat transfer) growth control, and a significant microlayer influence. The sensitivity to the parameter Γ is also indicated. Excellent agreement is also indicated by the comparison of Fig. 15 for a lower Γ-value (and superheat). However, for the lowest superheat results of Fig. 16, the agreement is good only up to $t^* = 5$. Beyond this time, the data very quickly develop a trend indicating negligible microlayer contribution. To confirm this departure an additional experiment was run under similar conditions. Reproducibility was excellent. Since the t^*-range covered in all three figures corresponds to similar real time (5–8 ms), this difference cannot be attributed to variations in exposure times for the microlayer. On the other hand it is interesting to note that the good agreement observed in Figs. 14 and 15 is also in the range of $t^* < 5$. As discussed in the Appendix the "thick microlayer" assumption cannot be responsible for this discrepancy since it would cause a deviation in the *wrong direction*. Although the mechanism is not clear at this time, this discrepancy appears to indicate an unexpected microlayer behavior at low superheats (and bubble growth rates), or perhaps high t^* values, which could be particularly relevant in considering microlayer effects in nucleate boiling.

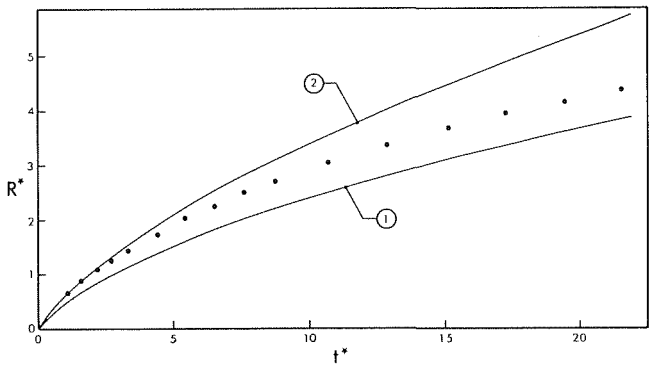

Fig. 16 A comparison of the theoretical results with experimental data for a hemispherical bubble: (1) solution without plate, $\Gamma = 2.14$; (2) solution with plate, $\Gamma = 2.14$. (Freon-113, superheat = 18.6°C, T_∞ = 22°C, probe diameter = 0.61 mm)

Conclusions

Solutions for bubble growth rates including the effects of inertia, heat transfer, and microlayer evaporation were obtained in generalized coordinates. Experimental growth rate data were obtained under precisely controlled conditions, covering a wide range of superheats, and encompassing the complete range of t^* characterizing the relative importance of inertia versus heat transfer as control mechanisms. The theoretical development appears to provide a satisfactory a priori prediction of these data. In particular, the Γ-effect predicted earlier is fully corroborated by these data which are the first to cover an extended range of this parameter.

These results also indicate that kinetic effects (nonequilibrium at the vapor-liquid interface) for Freon-11 and -113 and the range of experimental conditions covered are negligible. The microlayer effects are precisely predictable except for an anomalous behavior observed for $t^* > 5$ (i.e., low superheat, low Γ-values). This behavior may be of importance in considerations of nucleate boiling.

References

1 Theofanous, T. G., and Patel, P. D., "Universal Relations for Bubble Growth," *Int. J. Heat Mass Transfer*, Vol. 19, 1976, p. 425.

2 Cooper, M. G., and Vijuk, R. M., "Bubble Growth in Nucleate Pool Boiling," Paper B2.1, 4th Int. Heat Transfer Conference, Paris 1970.

3 Dwyer, O. E., *Boiling Liquid Metal Heat Transfer*, American Nuclear Society, 1976.

4 Jawurek, H. H., "Simultaneous Determination of Microlayer Geometry and Bubble Growth in Nucleate Boiling," *Int. J. Heat Mass Transfer,* Vol. 12, 1969, p. 843.
5 van Ouwerkerk, H. J., "The Rapid Growth of a Vapor Bubble at a Liquid-Solid Interface," *Int. J. Heat Mass Transfer,* Vol. 14, 1971, p. 1415.
6 Sernas, V., and Hooper, F. C., "The Initial Vapor Bubble Growth on a Heated Wall During Nucleate Boiling," *Int. J. Heat Mass Transfer,* Vol. 12, 1969, p. 1627.
7 Stewart, J. K., and Cole, R., "Bubble Growth Rates During Nucleate Boiling at High Jacob Numbers," *Int. J. Heat Mass Transfer,* Vol. 15, 1972, p. 665.
8 Bohrer, T. H., "Bubble Growth in Highly Superheated Liquids," MS thesis, Purdue University, May, 1973.
9 Chang, M. C., "A Study of Bubble Growth in Trichlorotrifluoro Ethane," MS thesis, Purdue University, May, 1974.
10 Theofanous, T. G., Biasi, L., Isbin, H. S., and Fauske, H. K., "Vapor Bubble Growth in Constant and Time Dependent Pressure Fields," *Chem. Engng. Sci.,* Vol. 24, 1969, p. 885.
11 Dergarabedian, P., "Observations on Bubble Growths in Various Superheated Liquids," *J. Fluid Mech.,* Vol. 9, 1960, p. 39.
12 Florschuetz, L. W., Henry, C. L., and Rashid Khan, A., "Growth Rates of Free Vapor Bubbles in Liquids at Uniform Superheats Under Normal and Zero Gravity Conditions," *Int. J. Heat Mass Transfer,* Vol. 12, 1969, p. 1465.
13 Board, S. J., and Duffey, R. B., "Spherical Vapour Bubble Growth in Superheated Liquids," *Chem. Engng. Sci.,* Vol. 26, 1971, p. 263.
14 Lien, Y. C., "Bubble Growth Rates at Reduced Pressure," DSc thesis, MIT Feb. 1969.
15 Carroll, B. J., and Lucassen, J., "Capillarity-Controlled Entrainment of Liquid by a Thin Cylindrical Filament Moving Through an Interface," *Chem. Engng. Sci.,* Vol. 28, 1973, p. 23.
16 Mikic, B. B., Rosenhow, W. M., and Griffith, P., "On Bubble Growth Rates," *Int. J. Heat Mass Transfer,* Vol. 13, 1970, p. 657.
17 Cooper, M. G., and Lloyd, A. J., "The Microlayer in Nucleate Pool Boiling," *Int. J. Heat Mass Transfer,* Vol. 12, 1969, p. 895.

APPENDIX

The Thick Microlayer Assumption

There are several papers that discuss heat transfer mechanisms in the microlayer at the base of a growing bubble. The most comprehensive discussion has been presented by van Ouwerkerk [5]. He concludes that although the microlayer evaporates during growth, in fact to such an extent that a substantial dry patch develops and grows at the expense of the microlayer, the "thick microlayer" assumption is adequate for bubble growth calculations in nonmetallic fluids of sufficiently high Prandtl number. There can be some question concerning the accuracy of van Ouwerkerk's calculation to nucleate boiling; however, it is very well suited for our experimental conditions. Specifically, under nucleate boiling conditions, and especially in subcooled boiling, bubbles may start out with $R \propto t$ and continue with $R \propto \sqrt{t}$ (at low superheats the first regime is negligible) but ultimately the growth law is strongly affected by the non-uniformity of the temperature field. The initial growth may slow down faster than the square-root law dictates and van Ouwerkerk's theory will break down. However, for an initially uniform temperature field, as has been the case for all our experiments, we expect (and observe) an asymptotic $R \propto \sqrt{t}$ behavior developing from an initial $R \propto t$ growth. It is easy to see that as the time exponent increases above the asymptotic 1/2 value the thick microlayer approximation improves. Hence *conservative* limits of the applicability of our model to our experiments may be obtained utilizing van Ouwerkerk's theory.

Van Ouwerkerk has considered analytically the *complete* problem of microlayer heat transfer and *evaporation* taking into account conduction within the wall. Two parameters are important in affecting the accuracy of the thick microlayer approximation: $MH^{-1/2} = (k_s\rho_s c_s/k_\ell\rho_\ell c_\ell)^{1/2}$ and $2\mathrm{Pr}\, Z_b{}^2$. Here Z_b is the growth constant of the microlayer thickness, $\delta(t)$, i.e., $\delta(t) = Z_b\sqrt{2\nu_\ell}$ (ν_ℓ is the kinematic viscosity of the liquid). The growth constant has been determined theoretically as $Z_b = 0.9$. Based on his experimental results van Ouwerkerk recommends a value of $Z_b = 0.6$. This is also supported by the values measured by Cooper and Lloyd (0.4–0.7) [17]. Fig. 3 of van Ouwerkerk can be utilized to precisely evaluate the limitations of the "thick microlayer" assumption for any particular set of conditions. *Since this analysis was based on the asymptotic regime of heat transfer controlled growth the error would be overestimated by Fig. 3 for cases with non-negligible inertial effects (i.e., $t^* < 10$).* As expected the results of Fig. 3 also indicate that when $MH^{-1/2} > 1$ that the "thick microlayer" assumption will always cause an *underestimation* of the bubble growth rate.

When the solid-liquid pair is such that $MH^{-1/2} \sim 1$ the "thick microlayer" assumption causes negligible error. In many practical applications, in fact, $MH^{-1/2}$ is not much greater than 1, (i.e., 1.3 for n-heptane on Perspex, 3.3 for n-heptane or benzene on Pyrex, 4.2 for carbon tetrachloride on PYREX(/ For the present experiment $MH^{-1/2} = 4.4$ and $\mathrm{Pr} = 7$. Even with a value of $Z_b = 0.5$, as Fig. 3 indicates, the "thick microlayer" assumption is excellent, (i.e., *less* than 7 percent error in bubble growth rate and *less* than 20 percent in microlayer evaporation rate).

H. S. Fath
Graduate Student

R. L. Judd
Associate Professor
Department of Mechanical Engineering,
McMaster University,
Hamilton, Ontario, Canada

Influence of System Pressure on Microlayer Evaporation Heat Transfer

Evaporation of the microlayer underlying a bubble during nucleate boiling heat transfer is experimentally investigated by boiling dichloromethane (methylene chloride) on an oxide coated glass surface using laser interferometry and high speed photography. The influence of system pressure (51.5 kN/m^2—101.3 kN/m^2) and heat flux (17 kW/m^2—65 kW/m^2) upon the active site density, frequency of bubble emission, bubble departure radius and the volume of the microlayer evaporated have been studied. The results of the present investigation indicate that the microlayer evaporation phenomenon is a significant heat transfer mechanism, especially at low pressure, since up to 40 percent of the total heat transport is accounted for by microlayer evaporation. This contribution to the overall heat transfer decreases with increasing system pressure and decreasing heat flux. The results obtained were used to support the model propounded by Hwang and Judd for predicting boiling heat flux incorporating microlayer evaporation, natural convection and transient thermal conduction mechanisms.

Introduction

In recent years, boiling heat transfer has achieved worldwide interest, primarily because of its application in nuclear reactors, jet aircraft engines and rockets. The heat transfer achieved by phase change is very high and as a consequence, boiling is used to cool devices requiring high heat transfer rates.

Much research concerning nucleate boiling during the past several years has been conducted in order to determine the mechanisms associated with bubble formation that are responsible for producing the high heat fluxes. In recent years, the mechanism known as microlayer evaporation, in which energy is transferred away from the heating surface into the bubbles by evaporation of a thin layer of superheated liquid underneath them, has assumed prominence as one possible explanation of nucleate boiling heat transfer. Snyder and Edwards [1][1] were the first to suggest that evaporation might occur at the base of a bubble from a thin liquid film or "microlayer" left on the surface during bubble formation. Rapid evaporation from the base would have the effect of drawing large amounts of heat directly out of the boiling surface during bubble growth. The temperature of the surface underneath such a film would be expected to drop significantly after evaporation had begun.

Moore and Mesler [2] investigated boiling on a thermocouple which could measure the average temperature within a small local area and had a microsecond response time. During nucleate boiling, these authors observed that the surface temperature fluctuated with time. The fluctuation was such that periodically the surface temperature would drop rapidly and then return to its previous level. Moore and Mesler did not know whether these drops occurred with the same frequency as bubble formation, nor did they have any indication of when the temperature drops began with respect to bubble growth. However, the rapidity of cooling immediately suggested an evaporation phenomenon and gave support to Snyder and Edwards's hypothesis.

The first indirect evidence of the microlayer was obtained by Hendricks and Sharp [3], who used high speed photographic data correlated with the surface temperature-time profiles underneath large discrete bubbles in order to determine when the local fluctuation of surface temperature occurred in the bubble growth and departure cycle. The results of their experiment indicated that the rapid temperature decrease was associated with bubble growth, which suggested that the rapid temperature decrease was due to microlayer evaporation rather than surface quenching.

Sharp [4] reported two experiments involving direct observation of the microlayer by two different optical techniques involving interference of monochromatic light and reflection of polarized light examined through a flat plate over the growing bubbles. As a result of these experiments, the microlayer was proven to exist.

Cooper and Lloyd [5] continued the work using high speed photography synchronized with the output of several rapidly responding surface thermometers located on the surface of a glass plate during

[1] Numbers in brackets designate References at end of paper.

Contributed by the Heat Transfer Division for publication in the JOURNAL OF HEAT TRANSFER. Manuscript received by the Heat Transfer Division May 20, 1977

the growth and departure of individual vapor bubbles of toluene in pool boiling at low pressure. The results obtained lent support to the microlayer theory of boiling heat transfer. Furthermore, these authors discussed the hydrodynamics of formation of the microlayer and the effect of evaporation of the microlayer upon the growth of the bubbles.

Further direct measurements of the microlayer thickness were obtained by Jawurek [6] who used an optical technique which permitted the simultaneous determination of microlayer geometry and the bubble profile in nucleate boiling.

The purpose of the present investigation is to present an experimental study on the influence of system pressure and heat flux upon the microlayer evaporation phenomenon and its relative significance and contribution to the total heat transfer rate, using interferometry and high speed photography.

Experimental Investigation

Similar to the investigation reported by Voutsinos and Judd [7] and Hwang and Judd [8], dichloromethane (methylene chloride) was boiled on a borosilicate glass heating surface coated with a half wave length thickness of stannic oxide which conducted electric current and generated heat, causing the liquid to boil. Detailed description of the experimental apparatus assembled to carry out this investigation can be found in reference [9].

A sectional view of the test assembly is shown in Fig. 1. The test assembly was comprised of a piece of stainless steel pipe closed by a base plate and cover plate resting on gaskets. A glass specimen heating surface was arranged within the test assembly in the base plate of the vessel. The oxide coating on the heating surface was in contact with the dichloromethane where the boiling took place. The test vessel was partially filled with one litre of dichloromethane so that the level of liquid was located 25 mm above the heating surface. The same charge of dichloromethane was used throughout the whole test period.

The research investigation requirements dictated that system pressure should be varied. The required levels of system pressure were obtained by evacuating the test vessel with a vacuum pump whose pressure could be controlled by a manually adjusted needle valve bleeding atmospheric air. Transfer of vapor from the test vessel to the vacuum pump was minimized by the use of a suitably located reflux condenser.

The two temperature measurements required were the bulk liquid temperature and the heating surface temperature. The sensing junction of the thermocouple used to measure the heating surface temperature was epoxied on the underside of the heating surface, and, based upon appropriate calculations, it was assumed that the temperature measured represented the heating surface temperature. The output signal of this thermocouple was directed to a recorder so that the temperature could be recorded during the test period and a time average could be obtained. The sensing junction of each of the three thermocouples used to measure the bulk liquid temperature was located at a different level in the bulk liquid. The output signals of these thermocouples were averaged to obtain a representative measurement. The approximate locations of the thermocouples measuring the heating surface temperature and the bulk liquid temperature are indicated in Fig. 1 by the symbols T_w and T_∞, respectively.

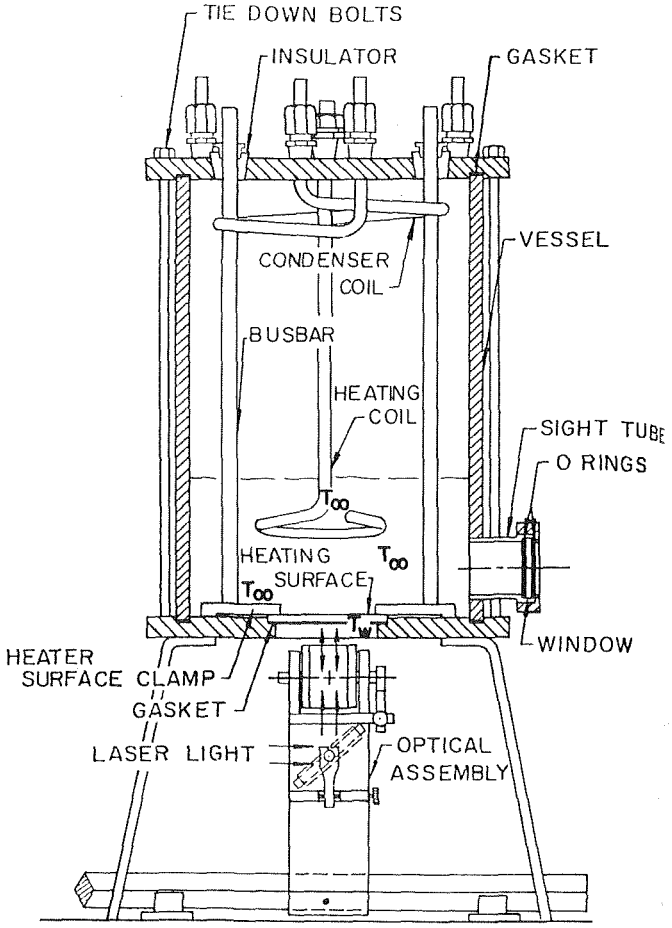

Fig. 1 Test assembly

At the commencement of each test, the cooling water valve controlling the flow to the condenser was fully opened. The barometric pressure was measured and the vacuum pressure desired was calculated using the vapor pressure curve for dichloromethane. Then the vacuum pump was started and the pressure inside the test vessel was reduced to the desired value by manual operation of the pressure control valve. The direct current power supply was adjusted until the potential level desired was achieved. At the same time, the power input to the heating coil was adjusted so that the bulk temperature attained the saturation temperature according to the pressure established.

During the period of time in which steady state boiling conditions were being established, the camera was loaded with film, the camera power supply was adjusted to give the required framing rate and the timing mark generator was switched on. Finally, the surface heating power dissipation was measured. The attainment of thermal equi-

Nomenclature

A_T = heating surface area
C = fluid specific heat
C_0 = constant in equation (1)
C_1 = constant in equation (4)
C_2 = constant in equation (8)
$\bar{f}$ = frequency of bubble emission
h_{fg} = latent heat
k_ℓ = fluid thermal conductivity
K = constant for area of influence relationship
N/A_T = active site density
P_{sat} = system pressure
q_m/A_T = measured heat flux
q_{ME}/A_T = microlayer evaporation heat flux
q_{NB}/A_T = nucleate boiling heat flux
q_{NC}/A_T = natural convection heat flux
q_p/A_T = predicted heat flux
R_b = bubble departure radius
t = time
T = temperature
T_w = wall temperature
T_{sat} = saturation temperature
T_∞ = bulk temperature
V_{ME} = volume of microlayer evaporated
α_ℓ = fluid thermal diffusivity
ρ_ℓ = fluid density

librium was indicated when the heating surface thermocouple output remained invariant within ±0.5°C and when the manometer measuring the system pressure appeared visually unchanged. When these conditions were fulfilled, the bulk temperature was measured and the high speed camera was activated.

It was found that the best framing rate for the high speed camera was 3900 frames per second which gave the clearest pictures. Lower speed led to unclear interference fringes, especially at high pressures, due to the rapid microlayer evaporation. Higher speed gave clear pictures, but the period of time available to record the phenomenon was not sufficient for the analysis of bubble formation and departure. For each value of system pressure, the heat flux was changed in six increments starting from the highest value down to the lowest. Each film obtained for the nucleate boiling tests (4 system pressure levels by 3 levels of heat flux) was later analyzed to determine the active nucleation site density, the frequency of vapour bubble emission, the bubble departure radius and the volume of microlayer evaporated.

Table 1 Data organization for photographic tests

	System Pressure P_{sat}(kN m^2)			
	51.5 (~0.50 Atm)	64.7 (~0.65 Atm)	80.2 (~0.80 Atm)	101.3 (1.00 Atm)
Heat Flux	64.11	—	56.56	—
$\frac{q_m}{A_T}$	44.65	44.98	38.46	46.63
	28.70	27.81	24.26	29.83
(kW/m^2)	—	19.71	—	17.51
	21.1	26.6	32.2	39.4
	Saturation Temperature T_{sat} (°C)			

Results and Discussion

The results obtained for dichloromethane boiling on a glass heating surface at a pressure of one atmosphere and lower show that the decrease in system pressure gives a higher superheat ΔT_{sup} for a given heat flux q_m/A_T, as seen in Fig. 2.

The natural convection heat transfer relationship was found to follow:

$$q_{NC}/A_T = C_o\,(T_w - T_{sat})^{4/3} \tag{1}$$

where the constant C_o varied with the system pressure. The value of C_o at P_{sat} = 51.5 kN/m^2 (approximately one half atmosphere) is equal to 184, which is exactly the same value given by Hwang and Judd [8]. The value of C_o increases with increasing system pressure.

The relationship between the nucleate boiling heat flux q_m/A_T and the superheat ΔT_{sup} can be expressed as:

$$q_m/A_T \alpha\ \Delta T_{sup}{}^n \tag{2}$$

The value of n at P_{sat} = 101.3 kN/m^2 (atmospheric pressure) is equal to 7.5, and it increases with decreasing system pressure.

The results presented in Fig. 3 relating to the active site density N/A_T demonstrate the influence of heat flux and system pressure upon this parameter. It can be seen that increasing the heat flux causes an increase in the site density to facilitate the transfer of additional heat. Moreover, the curves shown in this figure seem to be parallel with a slope of about m = 0.58 which more or less agrees with the correlations which advocate that the heat flux is proportional to the square root of the active site density.

Three active site density correlations are presented for comparison with the results of the present investigation, including the correlation of Hwang and Judd [8] for dichloromethane boiling at 51.5 kN/m^2, Kirby and Westwater [10] for carbon tetrachloride boiling at 101.3 kN/m^2, and Judd [11] for Freon 113 boiling at 155.9 kN/m^2. All three of these correlations were based upon results obtained by photographing the boiling phenomenon through a glass heating surface. The

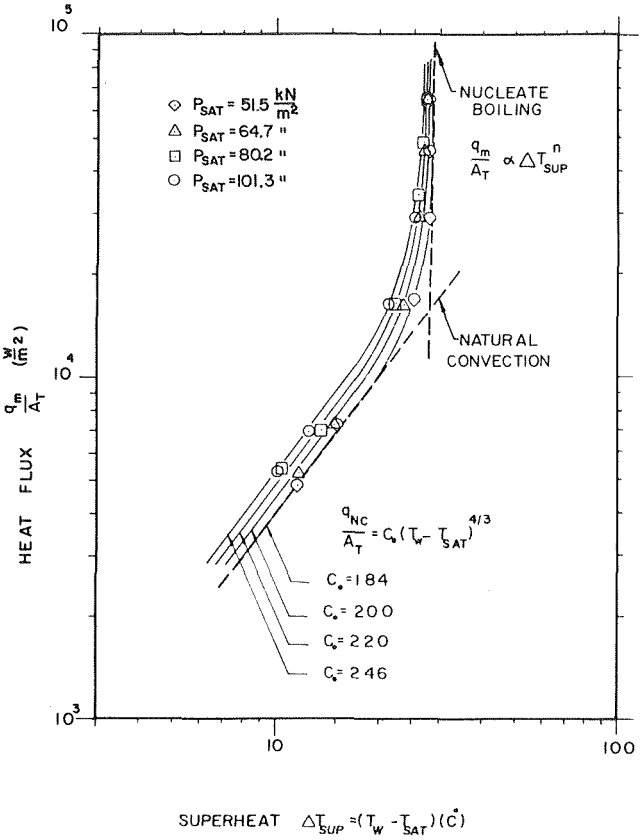

Fig. 2 Boiling characteristic curve

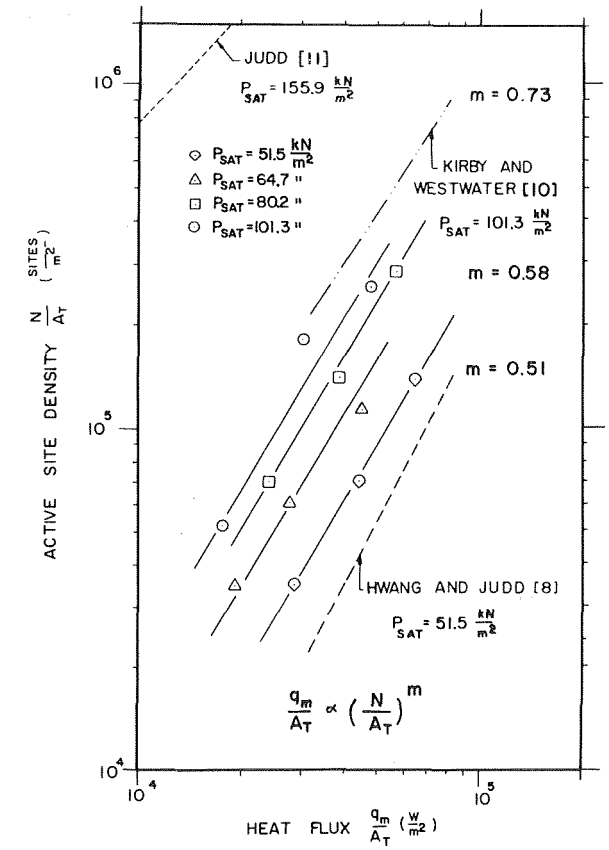

Fig. 3 Active site density results

difference between the correlation for dichloromethane boiling at 51.5 kN/m^2 obtained in the present investigation and that obtained by Judd and Hwang is most likely the result of differences in the glass heating surfaces used.

The influence of heat flux and system pressure upon the frequency of bubble emission $\bar{f}$ is presented in Fig. 4. The curves presented show that the frequency of bubble emission varies directly with heat flux and that bubble frequency increases with pressure until a maximum value has been obtained after which bubble frequency decreases.

In terms of average values, the bubble flux density Φ was calculated from the active site density and bubble frequency by the relationship:

$$\begin{bmatrix}\text{Bubble Flux}\\ \text{Density}\end{bmatrix}(\Phi) = \begin{bmatrix}\text{Active Site}\\ \text{Density}\end{bmatrix}\left(\frac{N}{A}\right) * \begin{bmatrix}\text{Bubble}\\ \text{Frequency}\end{bmatrix}(\bar{f}) \tag{3}$$

From Fig. 5 it can be seen that increasing the heat flux and system pressure increases the bubble flux density. The bubble flux density agrees very well with the results of Hwang and Judd [8] as shown in the same figure.

The effect of heat flux and system pressure upon the maximum bubble radius R_b is presented in Fig. 6, which shows that increasing the heat flux decreases the maximum bubble radius. This finding agrees with the results presented by Hwang and Judd [8]. Although at each level of heat flux various bubble sizes were observed, the average bubble size changed significantly with heat flux.

The average volume of microlayer evaporated $\overline{V}_{ME}$ was obtained by averaging the results for a number of bubbles selected from each of the active sites on the boiling surface within the field of view of the high speed camera. The volume of the microlayer evaporated $\overline{V}_{ME}$ depends upon the initial microlayer thickness and the bubble departure radius. Since both of these parameters decrease with increasing heat flux and system pressure, it is not unreasonable to observe that an increase in heat flux and system pressure leads to a decrease in volume of the microlayer evaporated as indicated in Fig. 7. The results of the present investigation at $P_{\text{sat}} = 51.5$ kN/m^2 were compared with those presented by Hwang and Judd [8] and Voutsinos and Judd [7] in Fig. 7 as well. The comparison shows little difference between the results, presumably because the way in which the analysis was performed yielded comparable values.

In the determination of bubble emission frequency, bubble flux density, maximum bubble radius and volume of microlayer evaporated, it is necessary to consider many individual bubbles originating from numerous active nucleation sites located within the field of view of the high speed camera. Consequently, averages must be used to

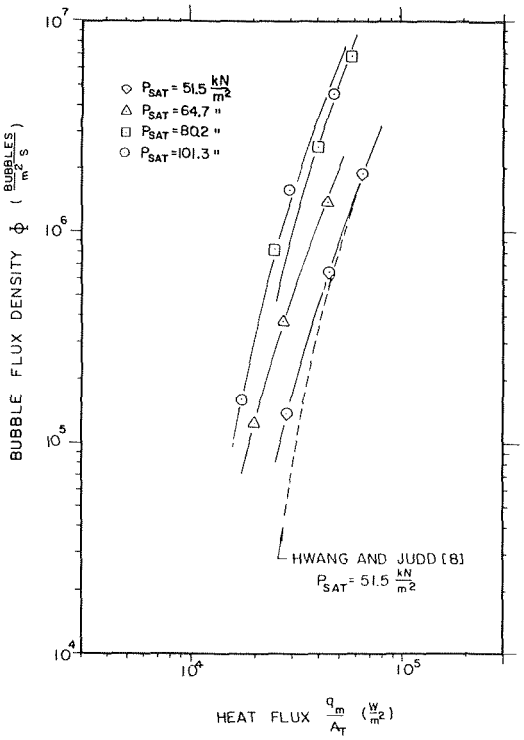

Fig. 5 Bubble flux density results

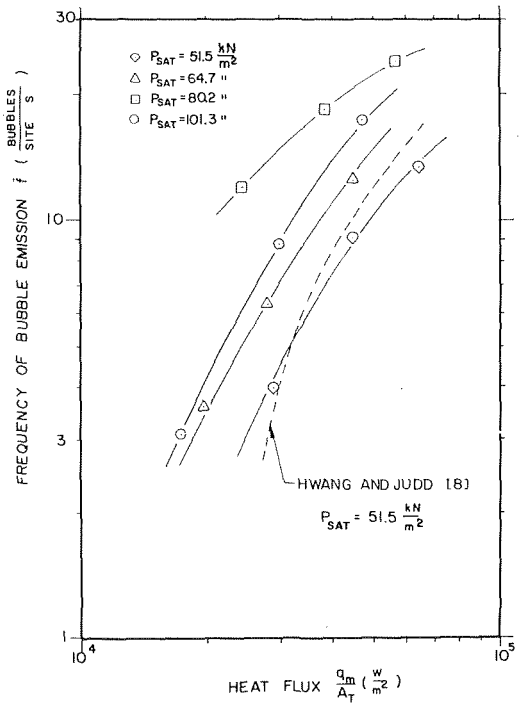

Fig. 4 Bubble frequency results

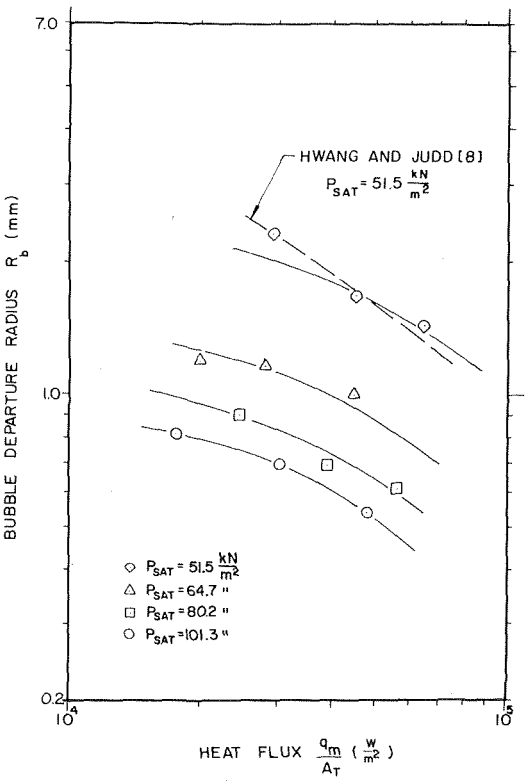

Fig. 6 Bubble departure radius results

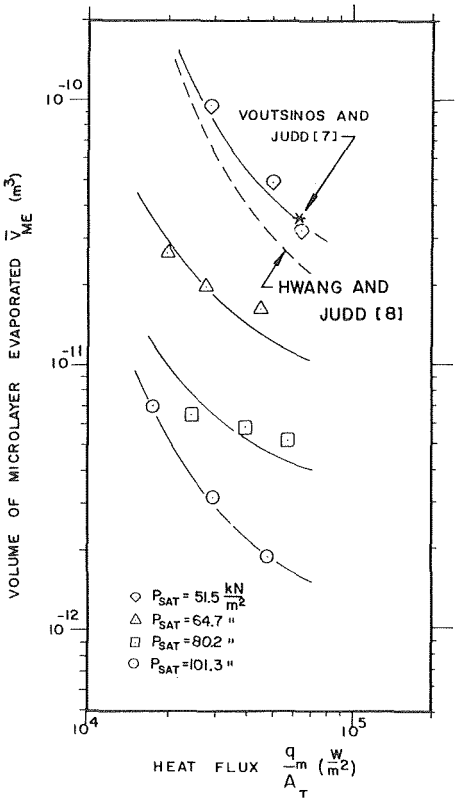

Fig. 7 Volume of microlayer evaporated per bubble

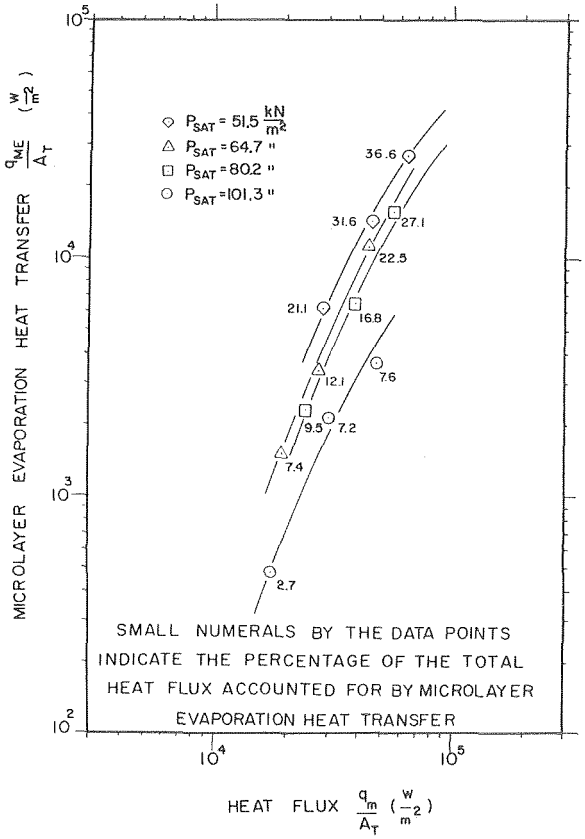

Fig. 8 Microlayer evaporation heat transfer results

represent these parameters, particularly since considerable variation is frequently observed within the data sample. Although it is not appropriate to discuss the variability of the results used in the determination of the values plotted in the preceding graphs because of space limitations, this matter has been investigated and reported in reference [9].

The rate of heat transfer by microlayer evaporation q_{ME}/A_T, obtained by multiplying the average energy transferred per bubble due to microlayer evaporation $\rho_\ell h_{fg} \overline{V}_{ME}$ by the bubble flux density Φ can be computed by the relationship:

$$q_{ME}/A_T = \rho_\ell h_{fg} \overline{V}_{ME} \Phi = \rho_\ell h_{fg} \overline{V}_{ME} \frac{N}{A_T} \bar{f} = C_1 \overline{V}_{ME} \Phi \qquad (4)$$

where $C_1 = \rho_\ell h_{fg}$ is a fluid property constant. The results predicted by equation (4) are plotted in Fig. 8 as a function of the measured heat flux and system pressure.

From equation (4) it is obvious that the microlayer heat transfer depends upon the fluid properties, the average volume of the microlayer evaporated and the bubble flux density. All these parameters are functions of both the system pressure and the heat flux. At constant pressure (C_1 = constant), the average volume of the microlayer evaporated decreases and the bubble flux density increases with increasing heat flux. From the results obtained, the increase in the bubble flux density is much greater than the decrease in the average volume of microlayer evaporated so that $\overline{V}_{ME}\Phi$ appears to increase with increasing heat flux.

The effect of system pressure upon microlayer heat transfer depends upon how much each of the parameters on the right hand side of equation (4) varies with pressure. The bubble flux density Φ increases with increasing system pressure. On the other hand, the fluid density ρ_ℓ, the latent heat h_{fg} and the average volume of microlayer evaporated $\overline{V}_{ME}$ decrease with increasing system pressure. The reduction of the average energy transferred per bubble due to microlayer evaporation $\rho_\ell h_{fg} \overline{V}_{ME}$ is greater than the increase in the bubble flux density Φ, so that the energy transferred by the microlayer evaporation q_{ME}/A_T decreases with the increase of system pressure.

The microlayer evaporation phenomenon is definitely a significant heat transfer mechanism at atmospheric pressure and may be significant at pressures above atmospheric pressure depending upon the heat flux. The percentage values obtained by the present results range up to 40 percent of the measured heat flux. Such high percentages give support to the microlayer evaporation phenomenon as an important heat transfer mechanism. This importance, however, decreases with increasing system pressure and decreasing heat flux.

Heat Transfer Considerations

Although there are many models proposed to explain the nucleate boiling phenomenon, none of these models can adequately predict nucleate boiling heat transfer under all the parameters of heat flux, subcooling and pressure for different combinations of surface and fluid conditions. Also, in the models which exist in the literature, little attention has been given to the existence of microlayer evaporation heat transfer mechanism as a significant contributor to the total heat transfer. The boiling heat transfer model which is discussed below is that proposed by Hwang and Judd [8]. This proposed model gives an indication of the significance of the microlayer heat transfer to the total boiling heat transfer process at various levels of heat flux and system pressure.

Hwang and Judd considered the predicted heat flux q_p/A_T to be comprised of three components, microlayer evaporation q_{ME}/A_T, transient conduction to the superheated layer (nucleate boiling) q_{NB}/A_T and natural convection q_{NC}/A_T. The natural convection component occurs in the regions uninvolved in bubble nucleation, whereas the microlayer evaporation component as well as the transient conduction to the superheated layer component occur in the same region of influence. However, the heat transfer associated with the displacement of the superheated layer occurs in the departure period, whereas the heat transfer associated with microlayer evaporation occurs in the growth period, and so the two mechanisms complement each other.

The natural convection component q_{NC}/A_T can be predicted by multiplying the heat transfer by the natural convection q_{NC}/A_{NC} expressed by equation (1) by a ratio representing the portion of the surface not involved in nucleate boiling and microlayer evaporation $[1 - K\pi R_b{}^2(N/A_T)]$ so that:

$$q_{NC}/A_T = \left(\frac{q_{NC}}{A_{NC}}\right)\left(\frac{A_{NC}}{A_T}\right) = C_0(T_w - T_{sat})^{4/3}\left[1 - K\pi R_b{}^2\left(\frac{N}{A_T}\right)\right] \tag{5}$$

The transient conduction to the superheated layer (nucleate boiling) component is obtained by multiplying the average heat flux resulting from the extraction of energy from the heating surface to form the superheated layer $(q/A)_{av}$ by a ratio representing the portion of the surface involved in the nucleate boiling and microlayer evaporation $K\pi R_b{}^2(N/A_T)$. Assuming only pure conduction in the liquid in the area of influence, this part of the problem is modeled as conduction to semi-infinite body (the liquid here) with a step change in temperature ($\Delta T = T_w - T_{sat}$) at the surface. From any conduction text the solution for this case is given:

$$q/A = \frac{k_\ell \Delta T}{\sqrt{\pi \alpha_\ell t}} \tag{6}$$

The superheated layer is replaced with a frequency $\bar{f}$ where $\bar{f}$ is the frequency of bubble emission. Hence, the average heat flux over the area of influence would be:

$$(q/A)_{av} = \bar{f}\int_0^{1/\bar{f}} q/A\, dt = 2k_\ell \Delta T\sqrt{\frac{\bar{f}}{\pi\alpha_\ell}} \tag{7}$$

The nucleate boiling component q_{NB}/A_T will be predicted by:

$$q_{NB}/A_T = (q/A)_{av}\left[K\pi R_b{}^2\left(\frac{N}{A_T}\right)\right]$$

$$= 2\sqrt{\pi\rho_\ell C_\ell k_\ell}\, K R_b{}^2\sqrt{\bar{f}}\left(\frac{N}{A_T}\right)(T_w - T_{sat})$$

$$= C_2 K R_b{}^2\sqrt{\bar{f}}\left(\frac{N}{A_T}\right)(T_w - T_{sat}) \tag{8}$$

where $C_2 = 2\sqrt{\pi\rho_\ell C_\ell k_\ell}$ is a fluid property constant which is primarily dependent upon temperature and only slightly dependent upon pressure.

In each of the equations representing the components q_{NC}/A_T and q_{NB}/A_T, K is a parameter greater than unity relating the area of influence around a nucleation site from which energy is transported by nucleate boiling to the projected bubble area at departure. If the entire energy content within an area of influence twice the departure diameter were transported by the departing bubble as claimed by Han and Griffith [12], then the value of K would be four. This could be considered to be the upper limit of K. However, it should not be expected that the whole energy content within the area of influence would be transported by the departure of bubble. The value of K which best fits the present experimental results was $K = 1.8$.

Summing equations (4), (5) and (8) yields the relationship:

$$q_p/A_T = C_0(T_w - T_{sat})^{4/3}\left[1 - K\pi R_b{}^2\left(\frac{N}{A_T}\right)\right] + C_1\bar{V}_{ME}\Phi + C_2 K R_b{}^2\sqrt{\bar{f}}\left(\frac{N}{A_T}\right)(T_w - T_{sat}) \tag{9}$$

All the parameters have been obtained by experimental measurements. Fig. 9 presents the verification of equation (9) above using the measurements reported in the previous section for the value of $K = 1.8$. The various dashed lines seen in the figure serve to indicate the contributions of microlayer evaporation, natural convection and nucleate boiling at each level of heat flux and system pressure, whereas the heavy solid line represents the contribution of all three mechanisms. At each level of system pressure, the sum of the three components representing the predicted heat flux q_p/A_T closely approaches the measured heat flux q_m/A_T with a discrepancy of the order of ±15 percent. This agreement does not necessarily establish the general validity of the model, since K is an empirical constant. However, it has been demonstrated that in the range of parameters investigated, microlayer evaporation heat transfer is an essential component of the overall heat transfer phenomenon.

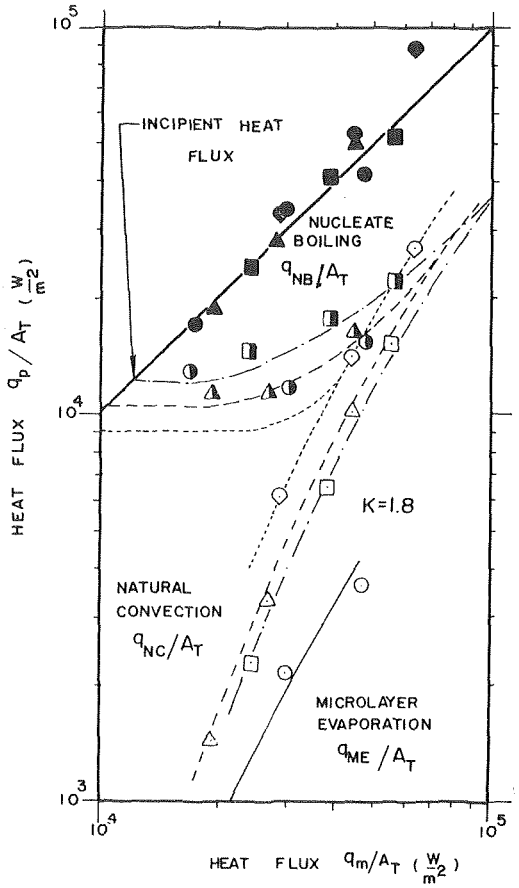

Fig. 9 Verification of heat transfer model. Symbols correspond to the levels of pressure identified in the preceding graphs. The open symbols represent the contribution of microlayer evaporation, the half darkened symbols represent the contribution of microlayer evaporation and natural convection, and the fully darkened symbols represent the contribution of microlayer evaporation, natural convection and nucleate boiling.

Conclusions

The results obtained through this research work can be summarized as follows:

1 The investigation presents a set of measurements for saturated nucleate boiling of dichloromethane (methylene chloride) on an oxide coated glass heating surface for various combinations of heat flux varying from 17 kW/m^2 to 65 kW/m^2 and system pressure varying from 51.5 kN/m^2 to 101.3 kN/m^2.

2 The calculated results showed that the microlayer evaporation phenomenon is definitely a significant heat transfer mechanism, especially at lower pressure, since it contributed up to 40 percent of the measured heat flux. The importance of microlayer evaporation decreases with increasing system pressure, and it is expected that at somewhat higher pressures than those investigated in the present study the contribution of microlayer evaporation will become entirely insignificant at all levels of heat flux. Consequently, the microlayer evaporation phenomenon is unlikely to be of any consequence in devices such as pressurized boiling water reactors.

3 The model for predicting the nucleate boiling heat flux proposed by Hwang and Judd was evaluated by the present measurements. The results of this analysis indicated that the experimental data were in agreement with the proposed model.

Acknowledgment

The authors wish to acknowledge the support of the National Research Council of Canada through grant A4362.

References

1 Snyder, N. R., and Edwards, D. K., "Summary of Conference on Bubble Dynamics and Boiling Heat Transfer," Memo 20-137, Jet Prop. Lab., June 14-15, 1956.

2 Moore, F. D., and Mesler, R. B., "The Measurement of Rapid Surface Temperature Fluctuations During Nucleate Boiling of Water," *AICHE J.*, Vol. 7, 1961, pp. 620–624.

3 Hendricks, R. C., and Sharp, R. R., "Initiation of Cooling Due to Bubble Growth on a Heating Surface," NASA TN D2290, 1964.

4 Sharp, R. R., "The Nature of Liquid Film Evaporation During Nucleate Boiling," NASA TN D1997, 1964.

5 Cooper, M. G., and Lloyd, A. J., "The Microlayer in Nucleate Pool Boiling," *Int. JHMT*, Vol. 12, 1969.

6 Jawurek, H. H., "Simultaneous Determination of Microlayer Geometry and Bubble Growth in Nucleate Boiling," *Int. JHMT*, Vol. 12, 1969.

7 Voutsinos, C. M. and Judd, R. L., "Laser Interferometric Investigation of the Microlayer Evaporation Phenomenon," JOURNAL OF HEAT TRANSFER, TRANS. ASME, Vol. 97, Series C, No. 2, 1975.

8 Judd, R. L., and Hwang, K. S., "A Comprehensive Model for Nucleate Pool Boiling Heat Transfer Including Microlayer Evaporation," JOURNAL OF HEAT TRANSFER TRANS. ASME, Vol. 98, Series C, No. 4, Nov. 1976.

9 Fath, H., "Laser Interferometric Investigation of Microlayer Evaporation for Various Levels of Pressure and Heat Flux," M. Eng. thesis, McMaster University, 1977.

10 Kirby, D. B., and Westwater, J. W., "Bubble and Vapour Behaviour on a Heated Horizontal Plate During Pool Boiling Near Burnout," *Chem. Eng. Progress Symposium Series*, Vol. 61, 1061, pp. 241.

11 Judd, R. L., "Influence of Acceleration on Subcooled Nucleate Boiling," Doctoral Dissertation, University of Michigan, 1968.

12 Han, C. Y., and Griffith, P., "The Mechanism of Heat Transfer in Nucleate Pool Boiling," *Int. JHMT*, Vol. 8, 1965.

M. Sultan
Graduate Student

R. L. Judd
Associate Professor

Mechanical Engineering Department,
McMaster University,
Hamilton, Ontario, Canada

Spatial Distribution of Active Sites and Bubble Flux Density

An experimental investigation is presented concerning the boiling of water at atmospheric pressure on a single copper surface in which the spatial distribution of active nucleation sites was investigated at different levels of heat flux and subcooling. The results obtained indicated that the active sites were located randomly on the heating surface, since the distribution of active sites followed the Poisson relationship. Changes in heat flux and subcooling did not affect the distribution of active nucleation sites although additional active sites formed among the sites which had already been activated when heat flux was increased. The frequency of vapor bubble emission and the bubble flux density have been studied as well. The results obtained showed that the heat flux had a great effect on the vapor bubble emission frequency although the influence of subcooling was of lesser significance. However, the bubble flux density was found to be non-uniformly distributed over the heating surface contrary to what had been expected.

Introduction

In the last few years, interest in boiling heat transfer has initiated considerable research in order to study the mechanism of boiling heat transfer and to meet the design requirements of devices such as nuclear power plant reactors. Many different aspects of boiling heat transfer have been investigated, but one feature which has not received sufficient attention to the present time is the role of the surface in nucleate boiling. It is known that when the surface temperature exceeds the saturation temperature of the liquid sufficiently, vapor bubbles will form at specific locations on the heating surface termed "nucleation sites" which are pits, scratches, and grooves that have the ability to trap vapor. The heating surface contains many such potentially active nucleation sites that have trapped small amounts of vapor which are not necessarily active nucleation sites. According to the heat flux applied, a number of potentially active nucleation sites will be active and the number of active nucleation sites will increase as the heat flux increases until the entire surface becomes "vapor blanketted" at high rates of heat flux. However, the mechanism determining the manner in which potentially active nucleation sites become active under specified operating conditions is not understood very well. It is to this end that the research reported herein is directed in an attempt to relate the spatial distribution of active nucleation sites to heat flux, superheat, and subcooling for boiling on a single heating surface.

Jakob [1][1] was the first to demonstrate that the rate of heat transfer was dependent upon the surface roughness. Corty and Foust [2] obtained results which showed that both the slope and position of the boiling curve changed with changes in surface roughness. Kurihara and Myers [3] studied boiling with different surface finishes and found that the number of active nucleation sites increased with increased roughness. Hsu and Schmidt [4] also showed that heat transfer increased with increasing surface roughness for a polished stainless steel surface. Berenson [5] investigated the effect of surface roughness using different surface materials prepared by lapping and by emery paper. The results which he obtained indicated that heat transfer was greater in the case of the lapped surface than in the case of the emery paper finished surface. Thus, heat transfer decreased with an apparent increase in surface roughness, contrary to the findings of the previous investigators.

Vachon, Tanger, Davis and Nix [6] studied pool boiling on polished and chemically etched stainless steel surfaces with a variety of different surface roughnesses at atmospheric pressure using distilled water, and came to the same conclusion as Berenson [5], that is, that an increase in roughness does not necessarily mean an increase in heat transfer. Shoukri and Judd [7] studied pool boiling of distilled, degassed water at atmospheric pressure on a single copper surface with different surface finishes, and showed that decreasing surface roughness shifted the boiling curve to higher superheat for the same heat flux. Nishikawa [8] observed the formation of bubbles from a horizontal surface and observed a greater number of bubble columns on a rough surface than on a smooth one.

From this survey of the effect of surface condition on nucleate boiling, it may be concluded that surface roughness cannot be used in the characterization of boiling surfaces because such a measurement represents the macroroughness of the surface which is only related to the distribution of active cavities in a very indirect manner. However, surface roughness measurements may be useful for comparison purposes when using the same technique for the preparation of boiling

[1] Numbers in brackets designate References at end of paper.

Contributed by the Heat Transfer Division for publication in the JOURNAL OF HEAT TRANSFER. Manuscript received by the Heat Transfer Division May 31, 1977.

surfaces from the same material.

In 1960, Gaertner and Westwater [9] reported a method to determine the distribution of active nucleation sites. The method was based on an electroplating phenomena by which an impressed current resulted in a nickel film being plated on the surface. This technique identified the location of the active sites since, during the electroplating, vapor bubbles originating at the active nucleation sites would push the plating solution away from the surface so that very little metal could be plated at that location. High contrast photographs were taken of the plated surface to permit counting of the pinholes representing the active sites.

In 1967, Heled and Orell [10] proposed another technique which greatly facilitated the identification and location of active sites. This technique was based on the observation of scale deposits which formed on a surface first polished to a high degree and then electroplated with either chrome or nickel. The tap water or distilled water which was boiled contained soluble salts which formed ring shaped deposits during nucleate boiling.

In 1970, Yoshihiro Iida and Kiyosi Kobayasi [11] experimentally determined the active site density, the distribution of time average void fraction in three boiling regimes, and the thickness of superheated liquid layer on a single horizontal heating surface in saturated pool boiling of water by the use of an electric probe. Yoshihiro, et al. [11] obtained good agreement between the active site density results and the results obtained by Gaertner, et al. [9], and presented a distribution map of void fraction in a vertical plane which showed that the domain of high void fraction lies above the superheated liquid layer.

In 1974, Nail, Vachon and Morehouse [12] studied pool boiling on a cold rolled stainless steel test specimen. Power was controlled so that the first 12 to 20 bubbles formed on the surface remained on the surface sufficiently long to allow a bubble locator to be positioned over the center of origin of the selected bubbles. The positions of all the centers were recorded, thus enabling the distribution of active nucleation sites to be determined.

In the present investigation, which was carried out at low heat flux levels in the isolated bubble regime, an electrical resistance probe technique was used to study the distribution of active nucleation sites and to measure the frequency of bubble emission at each site as will be explained below. This technique proved quite satisfactory, except that it was not possible to obtain active nucleation site distributions when the active site density was extremely large, since the probe could not easily distinguish active nucleation sites when the distance between sites decreased to the order of one bubble diameter. However, for those conditions which permitted the resistance probe technique to be used, the nature of the technique was such that the number of bubbles emitted per unit area per unit time, termed the "bubble flux density," could be determined as well.

It is desirable to know how the bubble flux density varies over a heating surface in order to understand the mechanism of nucleate boiling heat transfer. The fact that very little bubble flux density data exists may be due to the fact that knowledge of the frequency of vapor bubble emission is not well established. Voutsinos [13] studied the influence of heat flux and subcooling upon the bubble flux density. For dichloromethane boiling on a glass surface, Voutsinos showed that the bubble flux density increases with increasing heat flux and decreases with increasing subcooling. More recently, Judd and Hwang [14] studied the influence of heat flux and subcooling on the bubble flux density as well. For the same surface/fluid combination, Hwang and Judd obtained results in agreement with the effect of heat flux but contrary to the effect of subcooling when the results obtained were compared with those obtained by Voutsinos [13]. The different subcooling effect may be due to different methods of computing the average frequency of vapor bubble emission, or due to different surface characteristics. In addition to the study of spatial distribution of active nucleation sites described above, the frequency of vapor bubble emission and the spatial distribution of bubble flux density over the heating surface are reported in the research described herein.

Experimental Apparatus And Procedure

At the commencement of the research, an experimental apparatus constructed by Wiebe [15] in 1970 to measure temperature profiles near the heating surface already existed. However, the operating criteria for the present investigation were considerably changed from the previous requirements and consequently the apparatus described below is essentially a modified design.

A sectional view of the complete boiler assembly is presented in Fig. 1. The vessel was made from schedule 40 stainless steel pipe. Two stainless steel flanges were welded on the outside diameter at both ends of the pipe and a stainless steel cover plate was attached to the flange at the top of the vessel with eight cap screws which compressed a rubber gasket between the flange and the cover plate. Two circular sight glass windows were located diametrically opposite at a level which permitted observation of the bubbles at the probe location. The heater block was made from a copper cylinder. Thirteen cartridge

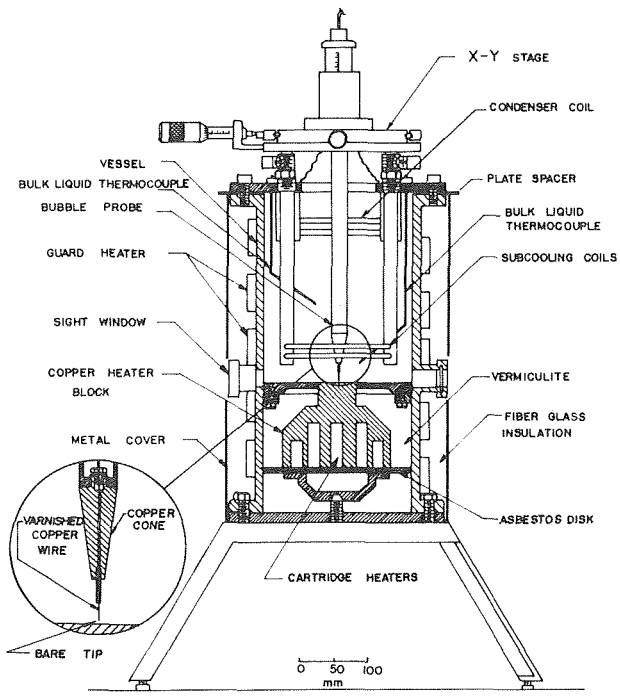

Fig. 1 Section of boiler vessel

Nomenclature

A = heating surface area
a = local surface area
Q/A = heat flux
T_∞ = bulk liquid temperature
T_w = heating surface temperature
T_s = liquid saturation temperature
N/A = active site density
Na = actual population of active sites in local area "a"
$\overline{Na}$ = expected population of active sites in local area "a"
$P(Na)$ = probability that a random local area "a" has a population "Na"
Z_{Na} = number of local areas having a population "Na"
f = surface average vapor bubble frequency

heaters were installed in symmetrically located holes in the base of the heater block. A stainless steel skirt was brazed flush with the top of the copper block to provide a continuous extension of the boiling surface. The boiling surface was machine-finished after the skirt was brazed before the heater block assembly was installed in the vessel. The heating surface was initially prepared with a fine slow speed lathe cut. In final finishing, the heater block assembly was rotated at a higher speed in the lathe chuck and the heating surface was polished using a group of "Diamond Grit" papers with numbers 200, 400, 600, respectively. The root mean square surface roughness was measured in ten different directions by means of a Talysurf profilometer, giving a 10 μ in. average value of mean square roughness for the heating surface.

The present investigation required that the subcooling in the bulk liquid be varied. This condition was satisfied by the use of a single pass heat exchanger comprised of eight stainless steel tubes, semi-circular in shape, brazed between two stainless steel pipes and located approximately 25 mm above the skirt to provide the bulk subcooling. To condense the vapor which formed at the free surface of water, a single pass vapor condenser comprised of two stainless steel tubes arranged in a semi-circular form between two stainless steel pipes was positioned approximately 25 mm below the cover plate. The cooling water flow rate through the heat exchanger and vapor condenser was controlled by the use of needle valves.

An $X - Y$ stage provided with two micrometers capable of reading $\pm 2.54 \times 10^{-3}$ mm was fixed to the cover plate on four supports. The stage provided a controlled and accurate travel of the bubble probe in two normal directions. The bubble probe depicted in Fig. 1 was mounted on an adjustable support to control the vertical distance between the probe tip and the heating surface. This distance was approximately 0.2 mm in the lower and intermediate heat flux cases and 0.1 mm in the higher heat flux case and was chosen to optimize the strength of the signal observed on the oscilloscope screen.

Reference [16] reported that electrical probes are widely used for obtaining information on the flow structure in two-phase gas-liquid flows. It was claimed that conductance probes, which depend for their operation on the fact that the electrical conductivity of a two phase mixture is strongly dependent on the phase distribution, can be used for flow regime detection, void fraction measurement, bubble and drop size determination and film thickness measurement. This concept was used in the present investigation to determine the locations of the active sites on the heating surface and also the frequency of vapor bubble emission.

The conductance probe output voltage gave an indication of the conductance of the water or the vapor between the bubble detection probe and the heating surface. Fig. 2(a) which represents the probe response at some considerable distance from the nucleation site, shows that there was a bridge of water between the bubble detection probe and the heating surface since the signal was invariant during the sampling period. The conductance of the medium within the probe tip-heating surface gap decreases whenever vapor is generated and thus the output voltage signal decreases intermittently. Fig. 2(b) shows the probe response at a horizontal distance of approximately 0.25 mm from the nucleation site where the signal shown in Fig. 2(c) was obtained. The observation of "strong" fluctuations indicated the location of the active site. These fluctuations also made possible the computation of frequency of vapor bubble emission.

The heat flux was obtained in the present investigation by two methods. The first method considered the rate of heat transfer in the neck of the heater block to be determined by one-dimensional heat conduction. The second method obtained the rate of heat flux by accounting for the total heat loss from the system to the surroundings, which was subtracted from the total electric heat input to the system. The greatest difference was 2.37 percent, which is most likely due to the assumption of one-dimensional heat conduction in the first method. The second method values were used to represent the value of the rate of heat transfer throughout.

The vessel was filled to a depth of approximately 150 mm with deionized distilled water containing 0.1 gm of salt/litre. Then the $X—Y$ stage was manipulated to move the bubble probe in different

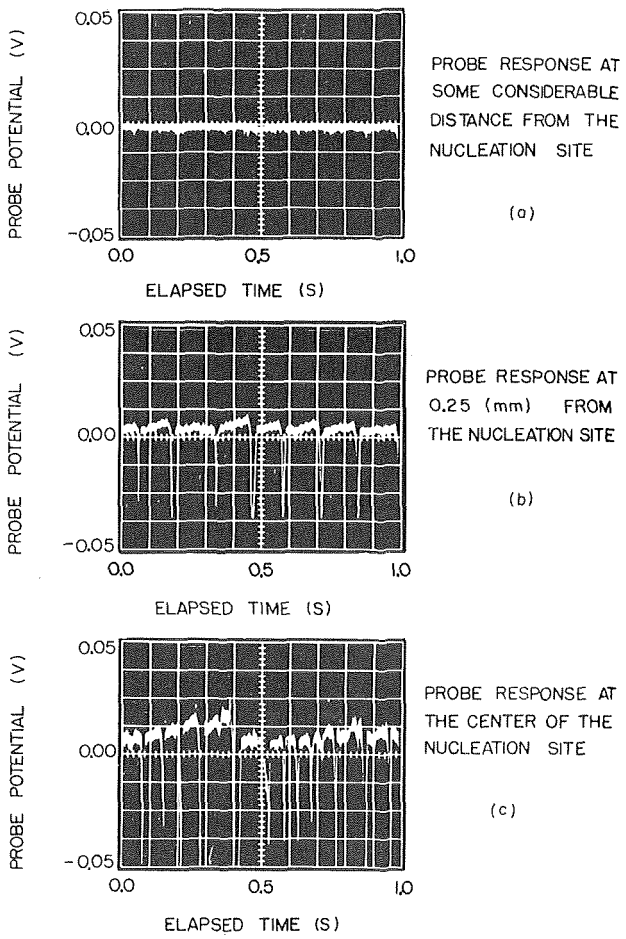

Fig. 2 Influence of probe displacement from nucleation site

directions to check that there was no contact between the probe and the heating surface, after which the copper block heaters and guard heaters were turned on. A copper block heater setting of approximately 475 kW/m^2 was established to heat up the boiler assembly quickly. A heat up time of approximately two hours was allowed to elapse in order to achieve steady state conditions and to ensure that the nucleation sites were properly activated at the beginning of each test, after which the heat input was reduced to the desired level; two hours were required for the system to regain steady state whenever any change in heat flux or subcooling took place. The readings of all the thermocouples were displayed by means of a recording potentiometer, and, in addition, the thermocouple signals were measured individually by means of a manually balanced potentiometer. All the thermocouple locations were identified in reference [17].

The $X—Y$ stage was adjusted to place the bubble detection probe in the zero reference position. The Y micrometer was fixed at its zero reference position and the X micrometer was moved very slowly until a significant deflection in the voltage appeared on the oscilloscope screen. Then X and Y micrometers were moved very small increments in both directions until a strong signal appeared. The reading of X and Y micrometer was recorded on a data sheet and the location so identified was deemed to represent the position of the particular active site.

Each deflection of the oscilloscope beam represented a bubble emitted at that time and consequently the number of deflections observed on the oscilloscope screen over a fixed time interval could be interpreted as the bubble emission frequency. Ten readings of the signal from each active site were taken and averaged to obtain the bubble emission frequency at that site. Afterward, the Y micrometer was returned to its original setting and the X micrometer was moved

once again. The same procedure described above was continued through a 25.4 mm scan. Afterward the Y micrometer was moved 0.635 mm and the X micrometer was moved through another 25.4 mm scan. These steps were repeated through a 25.4 mm scan in the Y direction. At the conclusion of the scanning procedure, an area 25.4 mm $\times$ 25.4 mm square had been examined by the bubble detection probe and the locations of all the active sites detected had been recorded. At the end of the test, all the thermocouple signals were measured once again using the manually balanced potentiometer. The ambient temperature was measured using a mercury in glass thermometer and a reading of the barometric pressure was obtained in order to compute the saturation temperature of the water corresponding to the atmospheric pressure.

An error analysis associated with the experimental work is presented in reference [17].

Results and Discussion

The characteristic boiling curve represents the relationship between the wall superheat ($T_w - T_s$) and the heat flux Q/A. Previous investigations of the effect of surface condition on the surface superheat have shown that it is not possible to predict whether roughening a surface will produce smaller or larger values of superheat for the same rate of heat flux as discussed previously. Not only might the position of the boiling curve change with the change of surface roughness, but the slope of the boiling curve might change as well. Consequently, it is important to know the heat flux/superheat relationship for each surface/fluid combination. Fig. 3 shows the characteristic boiling curve for the present study. The experimental data obtained by Wiebe [15] and Gaertner [18] were plotted on the same graph to compare with the results of the present work. Subcooling has a slight effect on the superheat at constant heat flux as illustrated in Fig. 4. Increasing subcooling first causes the superheat to increase slightly and then causes the superheat to decrease. The value of subcooling corresponding to the maximum value of superheat increases with increasing heat flux. This type of behavior is in qualitative agreement with the observations of Wiebe [15] and Judd [19].

Fig. 5 presents the distribution of the active nucleation site population over the heating surface for test $B1$. The distribution of active sites within a 25 square array and a 100 square array can be seen at a glance. Fig. 6 presents the distribution of bubble flux density within the same 100 square array. In accordance with the practice followed in the present study, the bubbles forming at an active site on a grid line were considered to originate within the right hand sector. For instance, one active site lies on the line $X = 0.8$ between $Y = 0.8$ and $Y = 0.9$; the bubbles originating from this active site were considered to originate in the sector 0.8×0.8.

The active site density observed in the present investigation for the three levels of heat flux were plotted on the same graph with the data which had been observed by Kurihara and Myers [3] and Westwater and Gaertner [9] as shown in Fig. 7 for the sake of comparison. The present results indicate that the active site density observed increases with the increase of heat flux in the same manner as that observed by Kurihara and Myers and Westwater and Gaertner. The present results indicate a greater value of active site density than the comparable

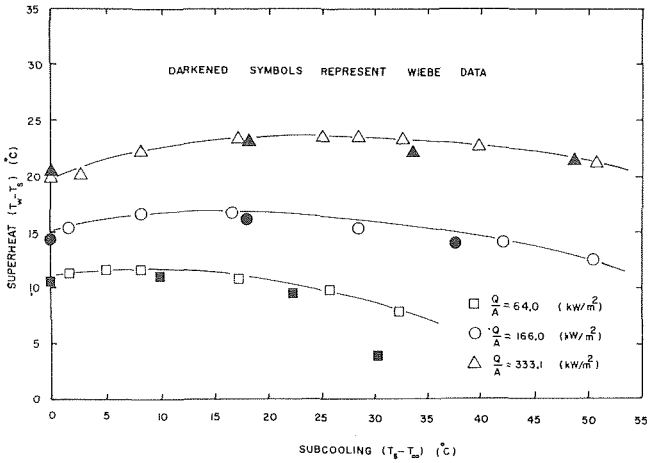

Fig. 4 Variation of surface superheat with bulk subcooling

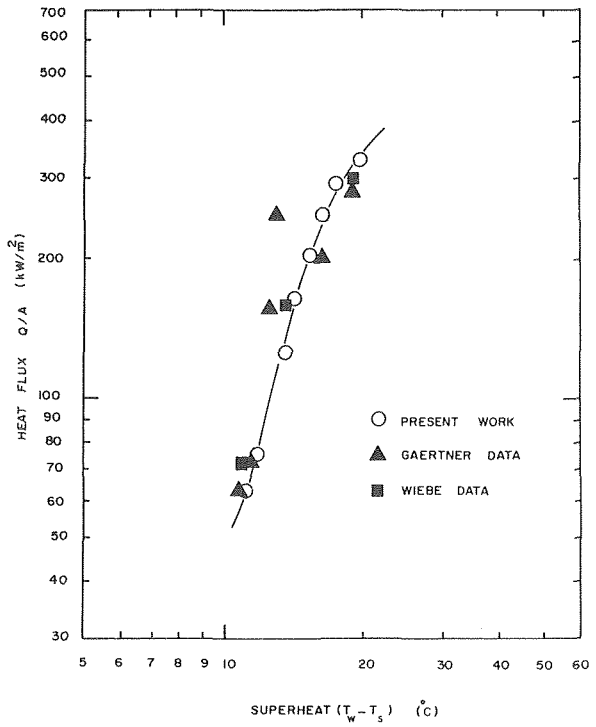

Fig. 3 Characteristic boiling curve for present investigation

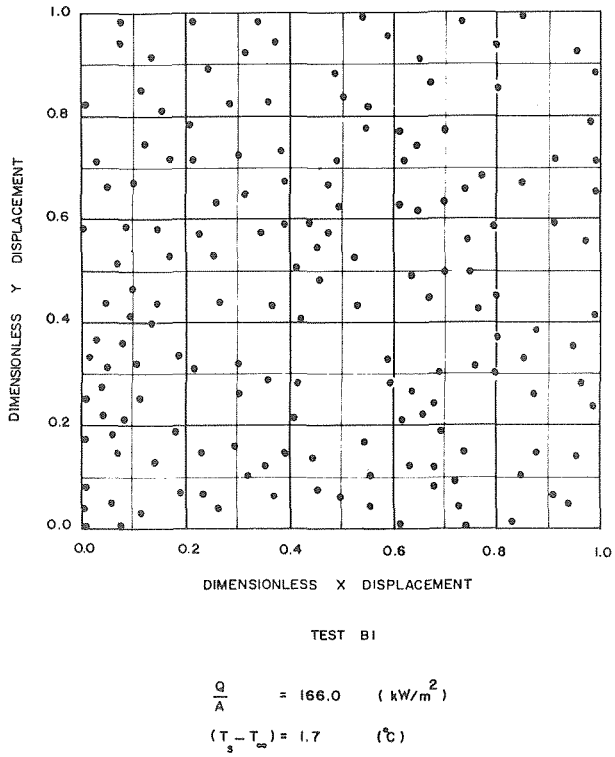

Fig. 5 Distribution of active nucleation sites

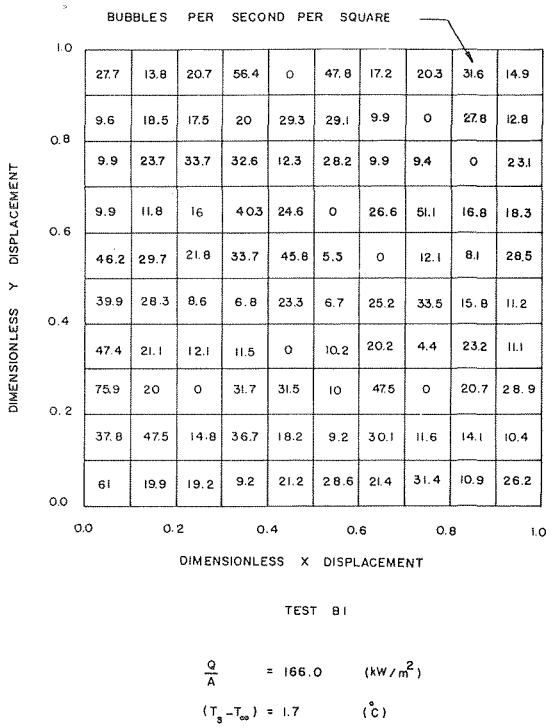

Fig. 6 Distribution of bubble flux density

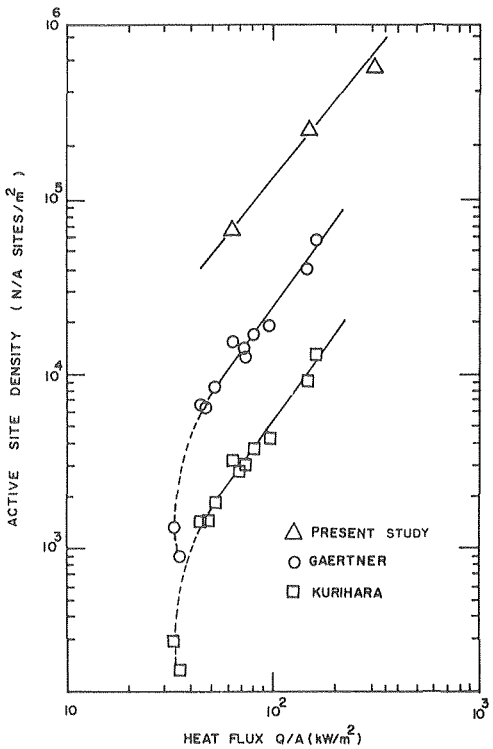

Fig. 7 Active site density versus heat flux

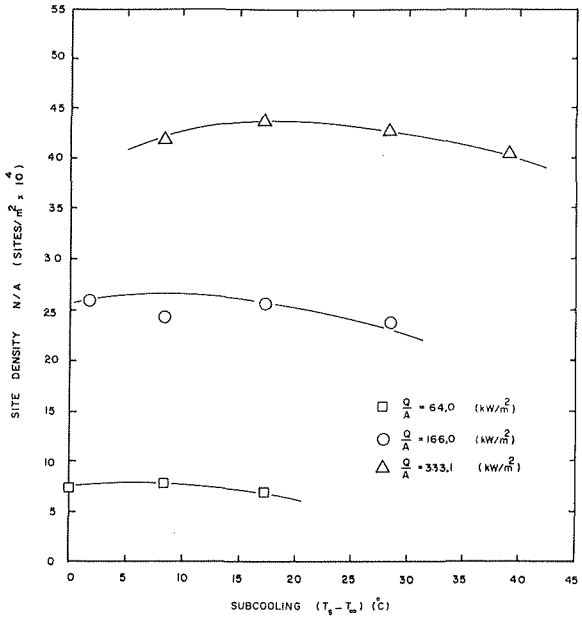

Fig. 8 Variation of active site density with bulk subcooling

results for the three different levels of heat flux which may be due to a difference in the heating surface microroughness. The results of the present investigation in Fig. 8 indicate that subcooling has much less influence on active site density than heat flux. There are no comparable results known for the water/copper combination which would enable the observed variation in the active site density to be corroborated, but some similar work has been done by Judd [19] with the Freon 113 glass/surface combination which has the same trend as the present investigation.

Any study of the boiling heat transfer process occurring on a heating surface should involve the spatial distribution of the local active site population in order to properly account for the mechanisms of boiling heat transfer. Many natural processes involving spatial distributions are described by the Poisson equation

$$P(X) = \frac{e^{-U}U^X}{X!} \tag{1}$$

where

$P(X)$ = probability of event X occurring
U = expected value of event X

Only one study exists which treats the distribution of active sites on the heating surface. Gaertner [20] determined that for three different levels of heat flux, the spatial distribution of the local active site population followed the Poisson distribution. The implication of the agreement found between the data and the Poisson distribution is that the active sites were distributed randomly on the heating surface.

The spatial distribution of the active sites on the heating surface has been studied in the present investigation at three different heat flux levels and various levels of subcooling as well. The heating surface was divided into a number of small squares of area "a" so that the probability of the local population within a square having the value "Na" could be as calculated according to

$$P(Na) = \frac{a}{A} Z_{Na} = \frac{e^{-\overline{Na}}(\overline{Na})^{Na}}{(Na)!} \tag{2}$$

where

$P(Na)$ = probability of finding "Na" active sites in area "a"
Na = actual number of active sites in area "a"
$\overline{Na}$ = expected number of active sites in area "a"
A = heating surface area
a = local surface area
Z_{Na} = number of small areas having a local population Na

The probability distributions obtained showed that agreement with the Poisson distribution was better when the heating surface was divided into a 25 square array than when it was divided into 100

square array although satisfactory agreement was found in both cases. Consequently, the probability of finding the local population "Na" in area "a" from both theoretical and experimental considerations was calculated by equation [2] considering $a/A = 1/25$. The probability distribution in Fig. 9 shows a good fit with the Poisson distribution and this conclusion is confirmed by the results of a χ^2 test. The findings of the present investigation are consistent with those of Gaertner's investigation so far as the randomness of the active nucleation site distribution is concerned.

Fig. 10 shows the effect of subcooling on the surface average frequency of vapor bubble emission for three different levels of heat flux. The results indicate that the frequency first increases with increase of subcooling and then decreases again with further increase of subcooling. The degree of subcooling corresponding to the maximum bubble frequency increases with increasing heat flux levels. The present investigation considers the distribution of bubble flux density within a 100 square array representing the entire heating surface. Fig. 11 shows the percentage cumulative bubble flux density versus the percentage cumulative area of the heating surface. It is seen that the effect of subcooling is negligible but that the effect of heat flux is very significant. As the heat flux is increased, the number of active sites increases and the bubble frequency increases as well. Consequently, there is a tendency for the bubble flux density distribution to become uniform at high heat flux, in which case ten percent of the area would contribute ten percent of the bubble flux density, for instance.

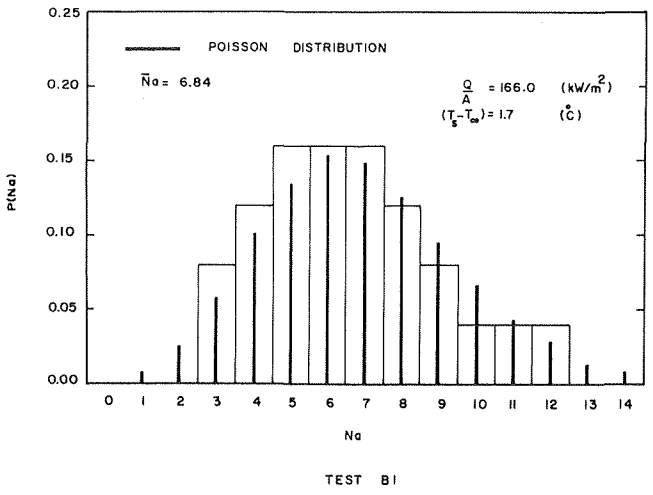

Fig. 9 Local active site distribution

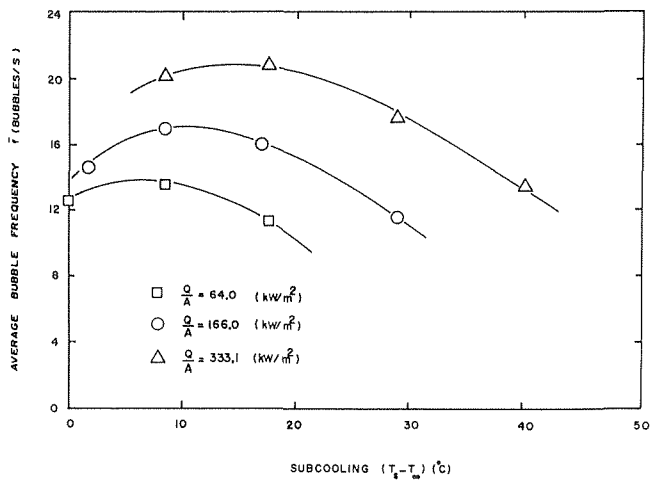

Fig. 10 Variation of average bubble frequency with bulk subcooling

Finally, the influence of heat flux and subcooling on the pattern of the active nucleation sites was studied in the present investigation. An area 5.0 mm × 5.0 mm square was selected from the 25.4 mm × 25.4 mm square area to examine the change in the pattern of the active nucleation sites with changing heat flux and subcooling during a single experimental test. As heat flux was increased at constant subcooling, bubbles continued to originate from the nucleation sites already activated and some nucleation sites appeared due to the increase of heat flux. As the subcooling was increased at constant heat flux, the active nucleation site pattern hardly changed at all, except for one additional active nucleation site which appeared, perhaps as the result of the slight increase of superheat with increasing subcooling indicated in Fig. 4.

Conclusions

1 The results of the present investigation for water boiling on a single copper surface at atmospheric pressure indicated that the active nucleation sites were randomly located and that their spatial distribution followed the Poisson distribution in agreement with Gaertner's findings.

2 Bubble flux density was observed to be non-uniformly distributed even though it was thought that the heat flux was uniform over the heating surface so that one might have expected the bubble flux to be uniformly distributed as well.

3 Changes in heat flux and subcooling did not affect the pattern of active nucleation sites. Although increasing heat flux caused more active sites to be activated, the additional active sites formed among the sites which have been already activated. Subcooling appeared to have hardly any effect at all.

References

1 Jakob, M., *Heat Transfer*, Vol. 1, Wiley, New York, (1949).

2 Corty, C. and Foust, A. S., "Surface Variables in Nucleate Boiling," *Chemical Engineering Progress Symposium* Series, Vol. 51, No. 17, (1955).

3 Kurihara, H. M., and Myers, J. E., "The Effects of Superheat and Surface Roughness on Boiling Coefficients," *AIChE Journal*, Vol. 6, No. 1, (1960).

4 Hsu, S. T., and Schmidt, F. W., "Measured Variations in Local Surface Temperatures in Pool Boiling of Water," ASME JOURNAL OF HEAT TRANSFER, (1961).

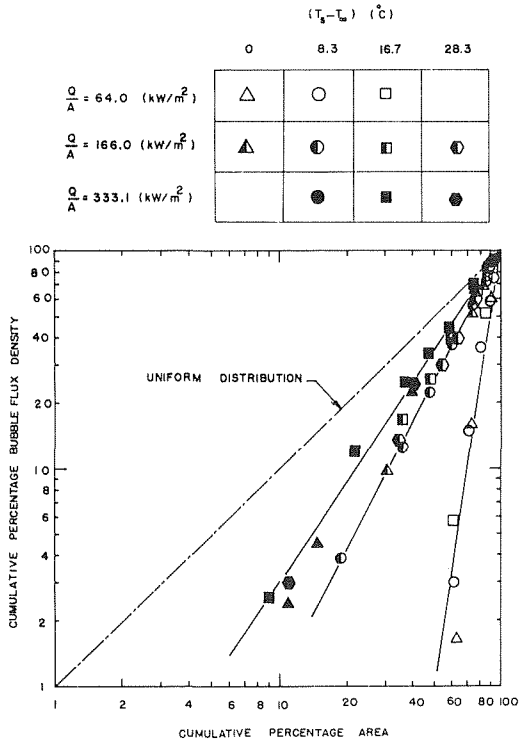

Fig. 11 Cumulative percentage bubble flux density versus cumulative percentage area

5 Berenson, P. J., "Experiments on Pool Boiling Heat Transfer," *International Journal of Heat and Mass Transfer,* Vol. 5, (1962).

6 Vachon, R. I., Tanger, G. E., Davis, D. L., and Nix, G. H., "Pool Boiling on Polished and Chemically Etched Stainless-Steel Surface," ASME JOURNAL OF HEAT TRANSFER, Vol. 90, No. 2, (1968).

7 Shoukri, M., and Judd, R. L., "Nucleation Site Activation in Saturated Boiling," ASME JOURNAL OF HEAT TRANSFER, Vol. 97, No. 1, (1975).

8 Nishikawa, K., *Transfer Society Mechanical Engineers,* Japan, No. 20, (1954).

9 Westwater and Gaertner, "Population of Active Sites in Nucleate Boiling Heat Transfer," *Chemical Engineering Progress Symposium,* Series 30, No. 56, (1960).

10 Heled, Y., and Orell, A., "Characteristic of Active Nucleation Sites in Pool Boiling," *Journal Heat and Mass Transfer,* Vol. 10, pp. 553–554, (1967).

11 Yoshihiro Iida, and Kiyosi Kobayasi, "An Experimental Investigation of the Mechanism of Pool Boiling Phenomena by a Probe Method," Fourth International Heat Transfer Conference, Paris—Versailles, (1970).

12 Nail, J. P., Vachon, R. A., and Morehouse, J., "An SEM Study of Nucleate Sites in Pool Boiling from 304 Stainless-Steel," ASME JOURNAL OF HEAT TRANSFER, Vol. 96, No. 2, (1974).

13 Voutsinos, C. M., "Laser Interferometric Investigation of Microlayer Evaporation for Various Levels of Subcooling and Heat Flux," M. Eng. thesis, Mechanical Engineering Department, McMaster University, Canada, (1976).

14 Judd, R. L., and Hwang, K. S., "A Comprehensive Model for Nucleate Pool Boiling Heat Transfer," ASME JOURNAL OF HEAT TRANSFER, Vol. 98, No. 1, (1976).

15 Wiebe, J. R., "Temperature Profiles in Subcooled Nucleate Boiling," M. Eng. thesis, Mechanical Engineering Department, McMaster University, Canada, (1970).

16 ASME Heat Transfer Division, "Two Phase Flow Instrumentation," Aug. (1969).

17 Sultan, M., "Spatial Distribution of Active Sites and Bubble Flux Density," M. Eng. thesis, McMaster University, Hamilton, Canada, 1977.

18 Gaertner, R. F., "Photographic Study of Nucleate Pool Boiling on a Horizontal Surface," ASME JOURNAL OF HEAT TRANSFER, No. 1, (1965).

19 Judd, R. L., "Influence of Acceleration on Subcooled Nucleate Boiling," Ph.D. thesis, University of Michigan, Mich., 1968.

20 Gaertner, R. F., "Distribution of Active Sites in Nucleate Boiling of Liquids," Chemical Engineering Progress Symposium Service, Vol. 59, No. 41, (1963).

S. V. Patankar
S. Ramadhyani
E. M. Sparrow

Department of Mechanical Engineering,
University of Minnesota,
Minneapolis, Minn.

Effect of Circumferentially Nonuniform Heating on Laminar Combined Convection in a Horizontal Tube

An analytical study has been made of how the circumferential distribution of the wall heat flux affects the forced/natural convection flow and heat transfer in a horizontal tube. Two heating conditions were investigated, one in which the tube was uniformly heated over the top half and insulated over the bottom, and the other in which the heated and insulated portions were reversed. The results were obtained numerically for a wide range of the governing buoyancy parameter and for Prandtl numbers of 0.7 and 5. It was found that bottom heating gives rise to a vigorous buoyancy-induced secondary flow, with the result that the average Nusselt numbers are much higher than those for pure forced convection, while the local Nusselt numbers are nearly circumferentially uniform. A less vigorous secondary flow is induced in the case of top heating because of temperature stratification, with average Nusselt numbers that are substantially lower than those for bottom heating and with large circumferential variations of the local Nusselt number. The friction factor is also increased by the secondary flow, but much less than the average heat transfer coefficient. It was also demonstrated that the buoyancy effects are governed solely by a modified Grashof number, without regard for the Reynolds number of the forced convection flow.

Introduction

It is well established that the heat transfer characteristics of horizontal and inclined laminar forced convection pipe flows can be significantly affected by secondary fluid motions induced by buoyancy. In the extensive literature dealing with this subject (to be summarized shortly), primary attention has been focused on problems characterized by uniform addition of heat per unit axial length. Another characteristic common to the entire available body of literature is that only circumferentially uniform thermal boundary conditions have been considered. These have included circumferentially uniform (albeit axially variable) wall temperature and circumferentially uniform wall heat flux.

In practice, there are applications where thermal circumferential uniformity may not be attained. For instance, the heat flux incident on the absorber tube of a line-focus solar collector is concentrated on only a portion of the tube circumference. Similarly, the fluid-carrying tubes of a flat plate solar collector receive a circumferentially nonuniform heat flux. The buoyancy forces are sensitive to the circumferential positioning of the portions of the tube wall that are more strongly and less strongly heated. Therefore, it can be expected that the induced secondary flows will be significantly affected by the imposed circumferential nonuniformities, as will the heat transfer parameters (e.g., Nusselt numbers). Recent experiments [1][1] have demonstrated that even a low-Reynolds-number turbulent flow in a horizontal pipe is sensitive to nonuniformities in circumferential heating, thereby heightening the expectation of their importance in a laminar flow.

The foregoing considerations have served to motivate the present investigation. A study is made of fully developed, buoyancy-affected laminar flow in a horizontal tube subjected to two limiting heating conditions. In one case, the tube is heated uniformly over a 180 deg arc encompassing the upper half of its circumference, while the lower portion of the tube is adiabatic. For the second case, uniform heating is applied over the lower half of the tube and the upper part is adiabatic. In both cases, the heat addition per unit length is uniform.

The highly complex flow fields induced by buoyancy preclude an analytical solution of the problem. Since solutions will be sought for

[1] Numbers in brackets designate References at end of paper.

Contributed by the Heat Transfer Division for publication in the JOURNAL OF HEAT TRANSFER. Manuscript received by the Heat Transfer Division April 22, 1977.

conditions where the natural convection is a first-order effect rather than a perturbation of the forced convection, numerical techniques are required. The difference equations were derived and solved by adapting the formulation of Patankar and Spalding [2], which incorporates Spalding's scheme [3] for dealing with the issues of central versus upwind differences. Solutions were obtained over a wide range of values of the governing buoyancy parameter, such that very large natural convection effects were encountered at the high end of the range. The Prandtl number, which appears as a parameter in the equations, was assigned values of 0.7 and 5 (e.g., air and water). The results obtained from these solutions include average Nusselt numbers, friction factors, circumferential Nusselt number distributions, and isotherm and streamline maps. The presentation of the results will be made with a view to illuminating the differences between the top heated and bottom heated cases.

From a careful search of the literature, the authors were unable to find any prior work on laminar mixed convection (i.e., combined forced and natural convection) in a tube with circumferentially nonuniform thermal boundary conditions. However, as noted earlier, the circumferentially uniform case has been treated extensively. Analyses have been performed via finite differences [4–6], as perturbations of the forced convection solution [7–11], and via a boundary layer model at high values of the buoyancy parameter [12, 13]. These references encompass studies of inclined tubes as well as of horizontal tubes. Numerous experiments designed to model circumferentially uniform boundary conditions have also been reported [14–24].

It is relevant to comment on a recurring viewpoint expressed in many of the aforementioned analytical studies of fully developed laminar mixed convection in a horizontal pipe. In those papers, the results were parameterized by the group ReRa, where Re is the conventional pipe Reynolds number and Ra is Rayleigh number based on the axial temperature gradient $\partial T/\partial z$, that is

$$\mathrm{Re} = \overline{w}D/\nu, \quad \mathrm{Ra} = g\beta(\partial T/\partial z)R^4/\alpha\nu \tag{1}$$

Since the departures from pure forced convection were found to increase with increasing ReRa, it appeared that the relative importance of buoyancy was magnified at larger values of Re—a finding that is contrary to intuition.

To clarify this matter, it may first be noted that $\partial T/\partial z$ is not a true measure of the cross sectional temperature differences that give rise to the buoyancy effects. This is because $\partial T/\partial z$ is not only related to the heating rate, but also to the mean velocity of the forced convection flow. Rather, the rate of heat transfer per unit length Q', which is a realistically prescribable thermal input parameter, is a true measure of the cross sectional temperature differences. If a modified Grashof number Gr^+ based on Q' is defined as

$$\mathrm{Gr}^+ = g\beta Q'R^3/k\nu^2 \tag{2}$$

then it is easily shown that

$$\mathrm{ReRa} = (2/\pi)\mathrm{Gr}^+ \tag{3}$$

Since buoyancy-induced departures from pure forced convection have been found to depend on ReRa, it is now seen that a buoyancy parameter Gr^+ is a measure of these effects. It is especially interesting to note that it is the magnitude of Gr^+ alone, without reference to any forced convection parameters, which governs the heat transfer results. From this, it follows that the Nusselt numbers for fully developed laminar mixed convection in a horizontal pipe flow are independent of the Reynolds number, as is also the case for fully developed laminar forced convection in tubes.

Analysis and Solutions

The starting point of the analysis is the equations expressing conservation of mass, momentum, and energy, all expressed in cylindrical coordinates. The first task in the specialization of these equations to fully developed, laminar mixed convection in a horizontal tube is the formulation of the buoyancy terms.

If attention is first focused on the radial momentum equation, then the corresponding buoyancy term can be deduced from pressure and body forces that appear therein,

$$-\partial p/\partial r - \rho g \sin\theta \tag{4}$$

where the r, θ coordinates are illustrated in the insets of Fig. 1. The density appearing in (4) can be related to the temperature via the Boussinesq model, according to which density variations are considered only insofar as they contribute to buoyancy, but are otherwise neglected. If T_b and ρ_b are the bulk temperature and the corresponding bulk density at any axial station in the fully developed regime, then, according to the Boussinesq approach

$$\rho = \rho_b - \rho_b\beta(T - T_b) \tag{5}$$

The bulk state is a logical reference state in problems where the heat input is prescribed, as in the present problem. Furthermore, if

$$p^* = p + \rho_b g r \sin\theta \tag{6}$$

then (4) becomes

$$-\partial p^*/\partial r + \rho_b g\beta(T - T_b)\sin\theta \tag{7}$$

The last term in (7) is the buoyancy force. A similar manipulation of the pressure and body forces in the tangential momentum equation yields

$$(-\partial p^*/\partial\theta)/r + \rho_b g\beta(T - T_b)\cos\theta \tag{8}$$

To further adapt the conservation equations, the constant property assumption is introduced and the subscript b is deleted from ρ_b in (7)

Nomenclature

c_p = specific heat at constant pressure
D = tube diameter
f = friction factor, equation (21)
Gr^+ = modified Grashof number, $g\beta Q'R^3/k\nu^2$
g = acceleration of gravity
h = local heat transfer coefficient, $q/(T_w - T_b)$
$\overline{h}$ = average heat transfer coefficient, $q/(\overline{T}_w - T_b)$
k = thermal conductivity
Nu = local Nusselt number, hD/k
$\overline{\mathrm{Nu}}$ = average Nusselt number, $\overline{h}D/k$
Nu_0 = forced convection value of $\overline{\mathrm{Nu}}$
P = dimensionless pressure, equation (10b)
p = pressure
p^* = reduced pressure, equation (6)
Q' = rate of heat transfer per unit length
q = rate of heat transfer per unit area
R = tube radius
Re = Reynolds number, $\overline{w}D/\nu$
r = radial coordinate
T = temperature
T_w = local wall temperature
$\overline{T}_w$ = average wall temperature, equation (18)
U, V, W = dimensionless velocities, equation (10a)
u, v, w = velocity components in r, θ, z
$\overline{W}$ = mean value of W
$\overline{w}$ = mean axial velocity
α = thermal diffusivity
β = thermal expansion coefficient
η = dimensionless radial coordinate, r/R
θ = angular coordinate
μ = viscosity
ν = kinematic viscosity
ρ = density
Φ = dimensionless temperature, $(T - T_b)/(Q'/k)$
ψ = stream function

Subscript

b = bulk property

and (8). The fully developed condition is implemented by setting

$$\partial u/\partial z = \partial v/\partial z = \partial w/\partial z = 0, \quad \partial p/\partial z = dp/dz \tag{9a}$$

$$\partial T/\partial z = dT_b/dz = Q'/\rho c_p \pi R^2 \overline{w} \tag{9b}$$

in which Q' is the rate of heat transfer to the fluid per unit axial length. In the present problem, Q' is a constant. Viscous dissipation and compression work are deleted from the energy equation, as is appropriate for typical laminar flows.

As a final step, dimensionless variables are introduced as follows

$$U = \frac{u}{\nu/R}, \quad V = \frac{v}{\nu/R}, \quad W = \frac{w}{(-dp/dz)(R^2/\mu)} \tag{10a}$$

$$\eta = \frac{r}{R}, \quad \Phi = \frac{T - T_b}{(Q'/k)}, \quad P = \frac{p^*}{\rho(\nu/R)^2} \tag{10b}$$

With these inputs, the equations expressing conservation of mass, of r, θ, and z momentum, and of energy become

$$\partial(\eta U)/\partial\eta + \partial V/\partial\theta = 0 \tag{11}$$

$$U\frac{\partial U}{\partial \eta} + \frac{V}{\eta}\frac{\partial U}{\partial \theta} - \frac{V^2}{\eta} = \frac{\partial P}{\partial \eta} + \nabla^2 U - \frac{U}{\eta^2} - \frac{2}{\eta^2}\frac{\partial V}{\partial \theta} + \mathrm{Gr}^+\Phi \sin\theta \tag{12}$$

$$U\frac{\partial V}{\partial \eta} + \frac{V}{\eta}\frac{\partial V}{\partial \theta} + \frac{UV}{\eta} = -\frac{1}{\eta}\frac{\partial P}{\partial \theta} + \nabla^2 V + \frac{2}{\eta^2}\frac{\partial u}{\partial \theta} - \frac{V}{\eta^2} + \mathrm{Gr}^+\Phi \cos\theta \tag{13}$$

$$U\frac{\partial W}{\partial \eta} + \frac{V}{\eta}\frac{\partial W}{\partial \theta} = 1 + \nabla^2 W \tag{14}$$

$$U\frac{\partial \Phi}{\partial \eta} + \frac{V}{\eta}\frac{\partial \Phi}{\partial \theta} + \frac{(W/\overline{W})}{\pi Pr} = \frac{1}{\mathrm{Pr}}\nabla^2\Phi \tag{15}$$

where ∇^2 is the Laplace operator in polar coordinates. The parameter Gr^+ has already been defined in equation (2) and $\overline{W}$ is the cross sectional average value of W. Pr is the Prandtl number. The equations thus contain two independent parameters, Gr^+ and Pr.

As was noted earlier, consideration will be given to two heating conditions. These are illustrated in the insets of Fig. 1. In the top heating case, there is a uniform heat flux q on the upper half of the tube wall, while the lower half is insulated. In the bottom heating case, the uniform heat flux is applied along the lower half of the tube and the upper half is insulated. These boundary conditions are symmetric about the vertical diameter of the tube. Owing to this symmetry, the solution domain can be confined to half of the tube cross section and, for concreteness, the region $-\pi/2 \le \theta \le \pi/2$ is selected.

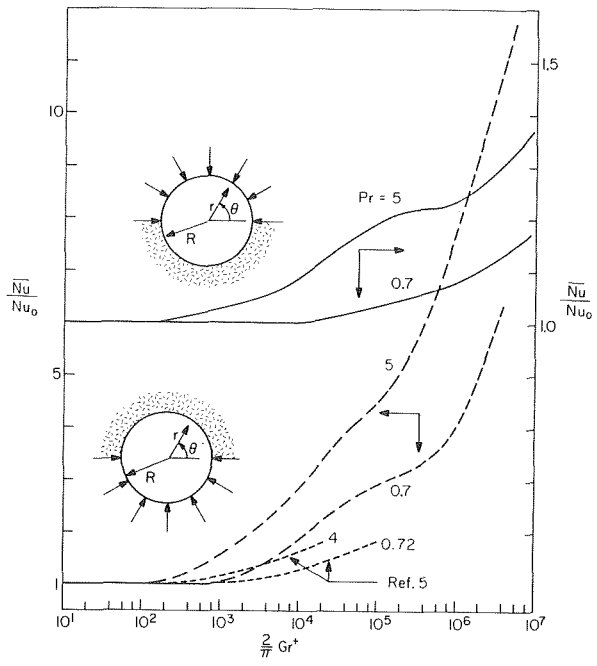

Fig. 1 Circumferential average Nusselt numbers

When the heat flux boundary conditions are expressed in terms of the variables of the analysis, there results

$$\frac{\partial \Phi}{\partial \eta} = \frac{1}{\pi} \text{ for } 0 \le \theta \le \frac{\pi}{2}, \quad \frac{\partial \Phi}{\partial \eta} = 0 \text{ for } -\frac{\pi}{2} \le \theta \le 0 \tag{16a}$$

for top heating, and

$$\frac{\partial \Phi}{\partial \eta} = 0 \text{ for } 0 \le \theta \le \frac{\pi}{2}, \quad \frac{\partial \Phi}{\partial \eta} = \frac{1}{\pi} \text{ for } -\frac{\pi}{2} \le \theta \le 0 \tag{16b}$$

for bottom heating. The factor $1/\pi$ appearing in equations (16a) and (16b) stems from the fact that $Q' = \pi R q$. The other boundary conditions on the tube wall and those on the symmetry line are conventional and need not be stated explicitly here.

In addition to satisfying the governing equations and boundary conditions, the solution must be compatible with the definition of the bulk temperature, the dimensionless form of which is

$$\int\int \Phi W \eta d\eta d\theta = 0 \tag{17}$$

where the integration is extended over the solution domain.

The differential equations (11) through (15) and their boundary conditions comprise a highly coupled system involving the five variables U, V, W, P, and Φ. The numerical scheme empolyed to solve these equations is an adaptation of that of [2], which is a finite difference procedure for three-dimensional parabolic flows. It involves marching in the streamwise direction while solving a two-dimensional elliptic problem at each marching station. The removal of all reference to the marching direction gives rise to a procedure for two-dimensional elliptic situations, and this was one of the adaptive actions taken here. A second adaptation involved the reformulation of the difference equations, which had been derived in [2] for rectangular coordinates, to accommodate r, θ polar coordinates.

In recognition of the fact that the conventional central difference approximation can yield unrealistic results at high flow rates, the discretization performed in [2] was based on the so-called Spalding difference scheme [3] (SDS). The SDS makes use of central differences for grid Peclet numbers (based on the local velocity and grid dimension) in the range $-2 \le \mathrm{Pe} \le 2$. For Peclet numbers outside this range, the diffusion terms are dropped and the convection terms are evaluated by the upwind difference scheme. In actuality, the SDS is a computationally inexpensive approximation of a smooth Peclet-number-weighted superposition of the central difference and upwind difference representations [3]. The true weighting function involves computationally expensive exponentials. In order to attain greater accuracy in the present solutions, the SDS was replaced by a power-law representation which closely approximates the true weighting function. The increment in computational time associated with the use of the power-law representation is negligible.

On the basis of computational experiments, it was found that solutions of high accuracy would be obtained with a 28×28 grid. For most of the cases, the grid points were distributed uniformly throughout the solution domain. At high values of Gr^+, where more complex flow patterns are encountered, and where for top heating there are sharp variations of wall temperature, supplemental solutions were obtained using a nonuniform grid. These solutions were essentially the same as those for the uniform grid.

The solution method was iterative in nature, and the computational time required to obtain convergence was found to increase markedly with Gr^+. In this connection, it was advantageous to proceed from lower to higher Gr^+ and to extrapolate the converged solutions for two values of Gr^+ to obtain starting values for the next Gr^+.

For each of the two thermal boundary conditions investigated, solutions were obtained for Gr^+ ranging from 10 to approximately 10^7. The Prandtl number was assigned values of 0.7 and 5, which, re-

spectively, typify fluids such as air and water.

Results and Discussion

In the presentation that follows, initial consideration will be given to those quantities that are of most direct relevance to applications—the circumferential average Nusselt number and the friction factor. The circumferential distributions of the local Nusselt number will then be presented. Finally, information about the flow and temperature fields will be provided via streamline and isotherm maps.

Circumferential Average Nusselt Numbers. Since only a portion of the tube wall is heated, an average heat transfer coefficient will be evaluated such that it pertains specifically to that portion of the wall. An average wall temperature $\overline{T}_w$ may be defined by integrating over the heated arc

$$\overline{T}_w = (1/\pi)\int_0^{\pi} T_w d\theta, \quad \overline{T}_w = (1/\pi)\int_{\pi}^{2\pi} T_w d\theta \tag{18}$$

respectively for top heating and bottom heating. The average heat flux on the heated arc is q (= constant). With these, the average coefficient and the corresponding Nusselt number may be defined as

$$\overline{h} = q/(\overline{T}_w - T_b), \quad \overline{\mathrm{Nu}} = \overline{h}D/k \tag{19}$$

It is relevant to compare the values of $\overline{\mathrm{Nu}}$ for mixed convection with that for a pure forced convection flow having the same thermal boundary condition (i.e., partially heated wall). For the latter case, an analytical solution in the form of a series can be obtained, from which a heat transfer coefficient and Nusselt number can be evaluated in accordance with equation (19) (e.g., [25]). If that Nusselt number is denoted by Nu_0, then

$$\mathrm{Nu}_0 = 3.058 \tag{20}$$

independent of both the Reynolds and Prandtl numbers, as is customary for fully developed, forced convection laminar pipe flows.

The results for $\overline{\mathrm{Nu}}/\mathrm{Nu}_0$ are plotted as a function of the modified Grashof number Gr^+ in Fig. 1. The curves in the upper part of the figure are for top heating and are referred to the right-hand ordinate. The long-dash curves in the lower part of the figure correspond to bottom heating and are keyed to the left-hand ordinate.

The figure shows that the Nusselt number increases with increasing values of Gr^+ in accordance with the expected strengthening of the buoyancy-induced secondary flow. The extent of the Nusselt number increase is markedly different for the two heating arrangements as witnessed by the distinctly different ranges of the right- and left-hand ordinate scales. In the top heated case, the values of $\overline{\mathrm{Nu}}/\mathrm{Nu}_0$ are well below 1.5 over the entire range investigated. On the other hand, for bottom heating, the $\overline{\mathrm{Nu}}/\mathrm{Nu}_0$ curves soar to values as high as 6 and 12, respectively, for $\mathrm{Pr} = 0.7$ and 5.

This remarkable difference is explained by the fact that the top heated case is a relatively stable configuration in which the secondary flows are weak. Conduction is still the dominant mechanism of heat transfer and, hence, the Nusselt number values do not differ appreciably from the buoyancy-free prediction. In the bottom heated case, the configuration is much less stable. The secondary flow velocities are an order of magnitude higher, and natural convection is the dominant heat transfer mechanism.

It is also seen from the figure that the Nusselt number is quite sensitive to the Prandtl number, increasing as the Prandtl number increases. This trend is in accord with that for natural convection flows in general. It is also interesting to note that the impact of the Prandtl number is somewhat different for the two heating arrangements. In particular, if the bottom heated results were to be replotted with $\mathrm{Gr}^+\mathrm{Pr}$ as abscissa variable, the curves for the two Pr values would lie quite close to each other except in the region where they tend to be wavy. On the other hand, a similar replotting of the results for the top heated case still leaves a substantial gap between the curves.

The aforementioned waviness of the curves reflects a change in the structure of the secondary flow. At low values of Gr^+, the secondary flow consists of a single eddy in each vertical half of the tube. At higher Gr^+, this simple structure breaks down into a more complex pattern consisting of multiple eddies. The levelling off of the curves at the onset of the waviness corresponds to the end of the single eddy mode, and the subsequent formation of the multiple eddies leads to a renewal of the increasing trend of the Nusselt number.

It appears that there are threshold values of Gr^+ that have to be exceeded before the buoyancy effects cause a detectable change in the Nusselt number relative to that for pure forced convection. For $\mathrm{Pr} = 5$, the threshold value of $(2/\pi)\mathrm{Gr}^+$ is about 100 for both bottom heating and top heating. On the other hand, for $\mathrm{Pr} = 0.7$, the respective threshold values for bottom heating and top heating are about 700 and 10,000. Thus, for bottom heating, the two threshold values can be represented as $(2/\pi)\mathrm{Gr}^+\mathrm{Pr} \cong 500$. The threshold values for top heating do not appear to be correlated by a Grashof-Prandtl product.

In addition to the results of the present analysis, Fig. 1 contains a pair of short-dashed lines taken from [5]. These results correspond to mixed convection in a tube with circumferentially uniform wall temperature and uniform heat addition per unit axial length (the Nu_0 value for these conditions is 4.36). It is seen that these $\overline{\mathrm{Nu}}/\mathrm{Nu}_0$ curves fall below the present curves for the bottom heated case, and it can be verified that they fall above the curves for the top heated case. This qualitative relationship appears to be physically reasonable.

Friction Factor. The buoyancy-induced secondary flow gives rise to an increase of the axial pressure gradient and its dimensionless counterpart, the friction factor f. When the definition of the friction factor

$$f = \frac{(-dp/dz)D}{{}^1/_2\rho\overline{w}^2} \tag{21}$$

is rephrased in terms of the variables of the analysis, there follows

$$f\mathrm{Re} = 8/\overline{W} \tag{22}$$

where Re is the conventional pipe Reynolds number given by equation (1). A direct assessment of the effects of buoyancy can be obtained from the values of the ratio $f\mathrm{Re}/(f\mathrm{Re})_0$, in which $(f\mathrm{Re})_0$ is the forced convection value (equal to 64). This ratio is plotted in Fig. 2 as a function of Gr^+, both for top heating and for bottom heating.

It may be seen from the figure that the increase of $f\mathrm{Re}$ due to buoyancy is much greater for bottom heating than for top heating, as was also true for the Nusselt number. In general, the increases in $f\mathrm{Re}$ are substantially smaller than the corresponding increases in $\overline{\mathrm{Nu}}$. It is also interesting to note that whereas greater increases in $\overline{\mathrm{Nu}}$ were sustained by fluids of higher Prandtl number, the opposite trend is in evidence for $f\mathrm{Re}$. The diminished influence of buoyancy on $f\mathrm{Re}$ for

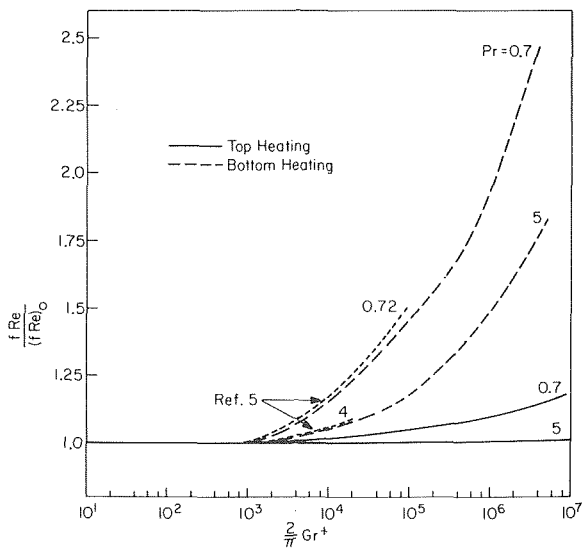

Fig. 2 Friction factors

fluids of higher Prandtl number may be attributed to the dampening of the secondary flow velocities owing to the higher viscosities of such fluids.

Fig. 2 also contains curves which depict the analytical results of [5]. These curves, which correspond to circumferentially uniform wall temperature, fall in close proximity to those for the present bottom heating case.

Circumferential Nusselt Number Distributions. The local Nusselt number at any circumferential location on the heated arc was evaluated from

$$\mathrm{Nu} = hD/k, \quad h = q/(T_w - T_b) \tag{23}$$

where T_w is the local wall temperature. To facilitate comparisons of the circumferential distributions of the Nusselt number for various cases, it is convenient to employ the ratio $\mathrm{Nu}/\overline{\mathrm{Nu}}$, as in Figs. 3 through 5.

Each of these figures contains a comparison of the circumferential distributions of $\mathrm{Nu}/\overline{\mathrm{Nu}}$ for top heating and for bottom heating. The successive figures, which are arranged in the order of increasing values of Gr^+, illustrate how the Nusselt number distributions for the two heating conditions evolve as the buoyancy effects grow progressively more important. The respective values of $(2/\pi)\mathrm{Gr}^+$ for Figs. 3–5 are 10^2, $\sim 10^5$, and $\sim 0.5 \times 10^7$ to 10^7. The slight lack of coincidence of the Gr^+ values in Fig. 5 has no effect on the qualitative comparison of the distributions for top and bottom heating, which is the main concern of this figure as well as of Figs. 3 and 4.

The cause of this slight mismatch is historical. When the analysis of the present problem was first undertaken, the choice of the dimensionless variables was influenced by those of [5]. With those variables, the resulting dimensionless buoyancy parameter is the product of a dimensionless pressure gradient and the Rayleigh number of equation (1). It was this parameter to which values were assigned as input to the numerical solutions. Subsequently, when it was discovered that Gr^+ was a more appropriate index of the buoyancy effects, its values were deduced from those of the aforementioned pressure gradient—Rayleigh number product in conjunction with the $f\mathrm{Re}/(f\mathrm{Re})_0$ results. Whereas the same set of input parameters had been assigned for all heating conditions and Prandtl numbers, the values of $f\mathrm{Re}/(f\mathrm{Re})_0$ differ among the various cases (Fig. 2). This gives rise to the moderate differences among the Gr^+ values which are in evidence at the higher Gr^+.

The angular coordinates θ and θ' which appear on the abscissa of Figs. 3–5 are defined on the inset of Fig. 3. The θ coordinate is used for the top heating case and the θ' coordinate for the bottom heating case. The definitions of the solid and dashed curves, as given in Fig. 3, are common to all three figures.

From an examination of Fig. 3, it is seen that for $\mathrm{Gr}^+ \sim 10^2$, the Nusselt number distributions for top heating and bottom heating are only slightly different, thereby confirming the small influence of buoyancy. The Nusselt numbers vary by a factor of about 2½ along the heated arc, with the highest values in the neighborhood of the junction of the heated and adiabatic portions of the tube, i.e., near θ and $\theta' = 0$. This is a plausible result since fluid passing through the unheated portion of the tube assists in transporting heat away from the adjacent portions of the heated arc.

As the buoyancy effects become stronger, the Nusselt number distributions for the two heating arrangements evolve in different ways. As can be seen in Fig. 4 ($\mathrm{Gr}^+ \sim 10^5$), the Nusselt numbers along the bottom heated arc are very nearly uniform, whereas those along the top heated arc exhibit a markedly greater variation than that for pure forced convection. The trend toward uniformity for bottom heating is the result of the vigorous secondary flow caused by the instability inherent in heating from below. On the other hand, for top heating, increases in Gr^+ lead to an increasingly stratified temperature field which gives rise to large circumferential variations.

The effects of increasing buoyancy on the Nusselt number distributions are further confirmed by Fig. 5 ($\mathrm{Gr}^+ \sim 10^7$). In addition, there is evidence of a change in the flow pattern for the bottom heated case, as witnessed by the peaks and troughs in the distribution curves. As will be demonstrated shortly, these undulations result from the presence of a localized recirculation zone situated near the bottom of the tube.

The Nu/Nu distributions for bottom heating are relatively insensitive to the Prandtl number. For top heating, the effects of Prandtl number are accentuated with increasing Gr^+ and are most significant in the neighborhood of the junction between the heated and adiabatic portions of the tube. Overall, the variations are larger at higher Prandtl numbers. This behavior is reasonable since a lower Prandtl number fluid has a relatively high thermal conductivity which pro-

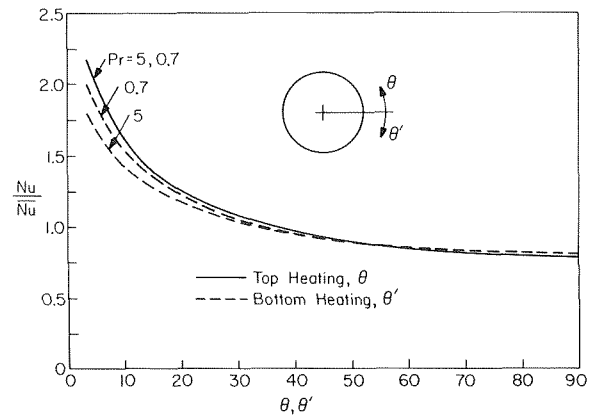

Fig. 3 Circumferential Nusselt number distributions, $(2/\pi)\mathrm{Gr}^+ = 10^2$

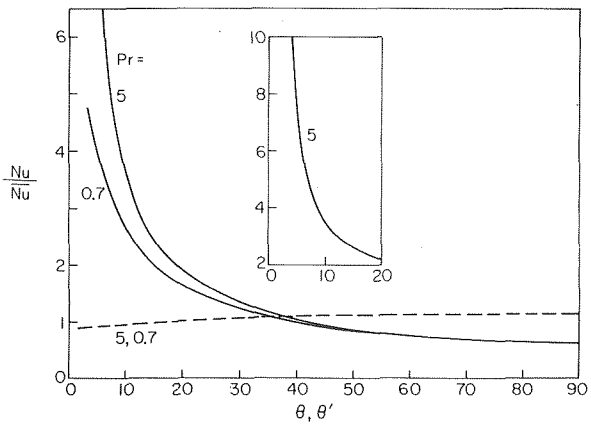

Fig. 4 Circumferential Nusselt number distributions, $(2/\pi)\mathrm{Gr}^+ \sim 10^5$

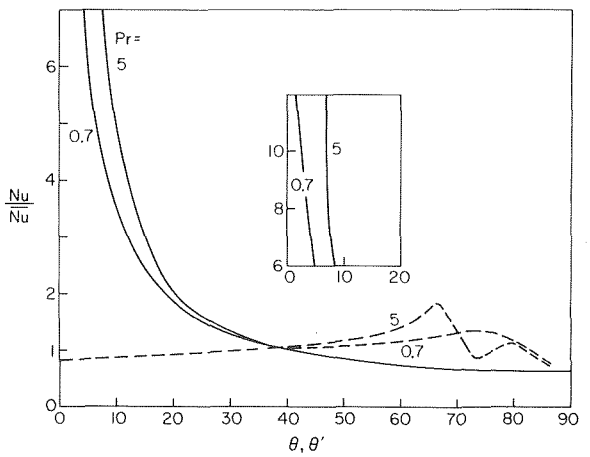

Fig. 5 Circumferential Nusselt number distributions. Top heating results are for $(2/\pi)\mathrm{Gr}^+ \sim 10^7$; bottom heating results are for $(2/\pi)\mathrm{Gr}^+ \sim 0.4 - 0.5 \times 10^7$

motes circumferential conduction and thereby reduces the variations.

Isotherm and Streamline Maps. Information about the temperature field and the secondary flow pattern will now be presented by means of isotherm and streamline maps. The isotherms are expressed in terms of the dimensionless temperature

$$(T - T_b)/(\overline{T}_w - T_b) \tag{23}$$

The stream function was deduced from the velocity field solutions by evaluating the integral

$$\psi/\nu = -\int_0^\eta V d\eta \tag{24}$$

along lines θ = constant, with $\psi = 0$ at $r = 0$.

The isotherms and streamlines are presented in Figs. 6–8. Each of these figures contains several representations of the tube cross-section showing the isotherms and streamlines for a group of related cases. In each of the cross-sectional representations, the isotherms are plotted in the left half and the streamlines in the right half. Both the isotherms and streamlines are symmetric about the vertical diameter of the tube.

Fig. 6 is for top heating and for a Prandtl number of five. The successive cross-sectional representations correspond to increasing values of Gr^+ as indicated in the figure caption. The isotherms reflect an increasing degree of stratification as Gr^+ increases. At the lowest value of Gr^+, the isotherms show some tendency to conform to the circular contour of the wall, but at higher Gr^+ they become nearly horizontal. The streamlines confirm the expected presence of a secondary flow. The rather regular single eddy in evidence at the lowest Gr^+ tends to become distorted as Gr^+ increases and then breaks up into a multiple eddy structure. To the knowledge of the authors, such a mulitple eddy array has not been previously reported for mixed convection in a horizontal tube.

The results for bottom heating and Pr = 5 are presented in Fig. 7, with the successive diagrams arranged in order of increasing Gr^+. At the lowest value of Gr^+, heating from below produces a pattern of isotherms and streamlines that is similar to that for heating from above (note that the isotherms in Fig. 7(a) are reversed relative to those of Fig. 6(a)). A major difference, however, is that the secondary flow velocities are an order of magnitude higher in the bottom heated case.

As Gr^+ increases, the isotherms in the near-wall region tend to follow the contour of the tube, so that the wall temperature becomes more uniform. The secondary flow continues to be characterized by a regular, single-eddy pattern at intermediate Gr^+. At the highest value of Gr^+, a relatively small counterrotating eddy is in evidence at the bottom of the tube. Its presence is the cause of the undulations in the $Nu/\overline{Nu}$ curve for Pr = 5 in Fig. 5. The upflow leg of this eddy is believed to be similar to a thermal.[2] In general, as witnessed by the values of ψ/ν, the secondary flow for bottom heating is much more vigorous than that for top heating.

It is appropriate to remark here that the flow and temperature fields were assumed to be *steady* via the governing equations and the so-

[2] A thermal is a buoyant mass which rises from a discrete location on a horizontal heated surface.

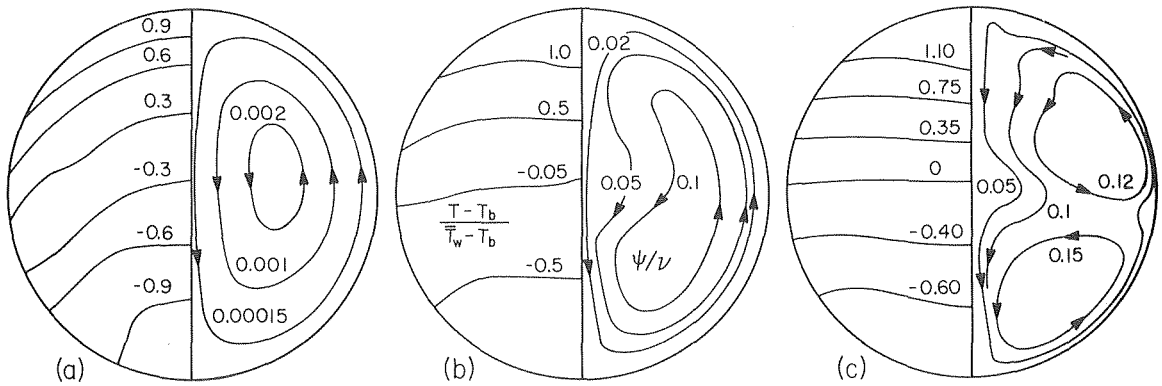

Fig. 6 Isotherm and streamline maps for top heating and Pr = 5. Parametric values of $(2/\pi)Gr^+$: (a) 10, (b) 10^4, (c) 10^6

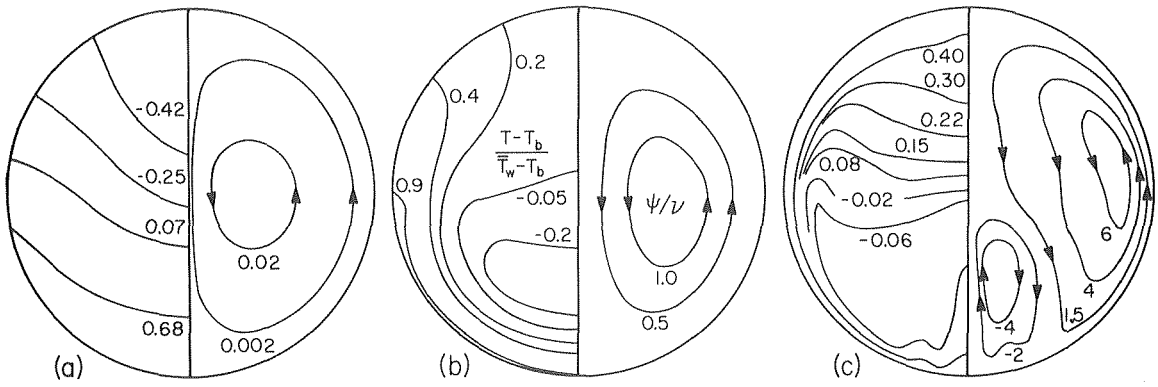

Fig. 7 Isotherm and streamline maps for bottom heating and Pr = 5. Parametric values of $(2/\pi)Gr^+$: (a) 10, (b) 10^4, (c) 0.5×10^7

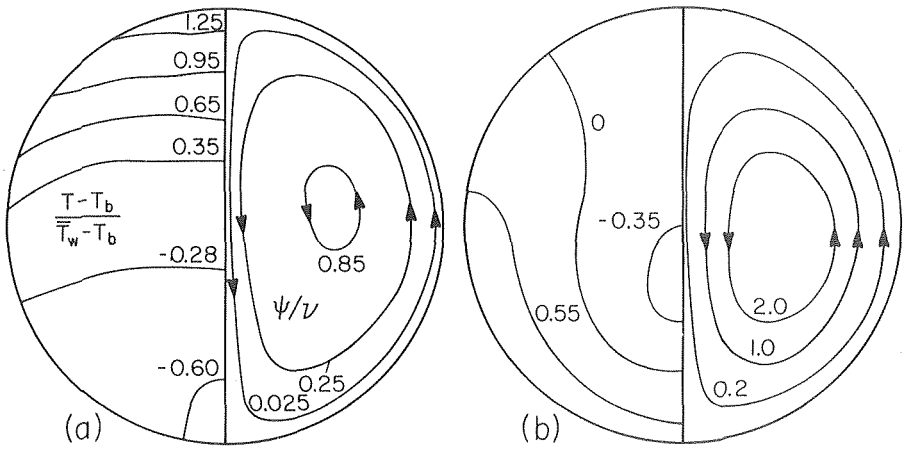

Fig. 8 Isotherm and streamline maps for Pr = 0.7 and $(2/\pi)Gr^+ = 10^4$. (*a*) top heating, (*b*) bottom heating

lution method. When the resulting flow field is as complex as in Fig. 7(*c*), it is possible that in reality the flow exhibits a steady-periodic behavior rather than a totally time-invariant one. An examination of this matter, however, is beyond the scope of the present work; some form of stability analysis will be required to resolve the question.

Representative results for Pr = 0.7 are presented in Fig. 8 in order to permit a comparison with corresponding cases (i.e., same Gr^+) for Pr = 5 in Figs. 6 and 7. In general, the shapes of the isotherms and streamlines are similar for the two Prandtl numbers, although there are certain differences of detail.

Concluding Remarks

The results of this investigation have demonstrated that the effects of buoyancy on laminar forced convection in a horizontal tube depend markedly on the circumferential distribution of the wall heat flux. When heat is added along the bottom half of the tube while the top half is insulated, a vigorous secondary flow is induced which gives rise to a significant increase in the average Nusselt number relative to that for pure forced convection. The increases in Nusselt number are greater at higher Prandtl numbers. The vigorous secondary flow is also instrumental in bringing about a relatively uniform distribution of the local Nusselt number along the heated arc.

When the top half of the tube is heated with the bottom half insulated, temperature stratification ensues and the induced secondary flow is much weaker than that corresponding to the bottom heated case. As a consequence, the buoyancy-related increase of the Nusselt number is also smaller. On the other hand, the stratification creates large circumferential variations of the local Nusselt number.

The secondary flow increases the friction factor relative to its forced convection value, but the increases are substantially smaller than those sustained by the average Nusselt number. In common with the Nusselt number, the friction factor is more affected by bottom heating than by top heating.

It was also demonstrated that the buoyancy effects are governed solely by the modified Grashof number Gr^+, without regard to the Reynolds number of the forced convection flow. It is the opinion of the authors that Gr^+ is a more apt measure of the buoyancy effects than the ReRa product (equation (1)) that has been employed frequently in the past.

Acknowledgment

This research was performed under the auspices of NSF Grant ENG-7518141.

References

1 Schmidt, R., "Experiments on Buoyancy-Affected and Buoyancy-Unaffected Turbulent Heat Transfer for Water in a Tube with Circumferentially Non-uniform Heating," Ph.D. thesis, Department of Mechanical Engineering, University of Minnesota, 1977.

2 Patankar, S. V., and Spalding, D. B., "A Calculation Procedure for Heat, Mass, and Momentum Transfer in Three-Dimensional Parabolic Flows," *International Journal of Heat and Mass Transfer,* Vol. 15, 1972, pp. 1787–1806.

3 Spalding, D. B., "A Novel Finite-Difference Formulation for Differential Expressions Involving Both First and Second Derivatives," *International Journal for Numerical Methods in Engineering,* Vol. 4, 1972, pp. 551–559.

4 Cheng, K. C., and Hong, S. W., "Combined Free and Forced Laminar Convection in Inclined Tubes," *Applied Scientific Research,* Vol. 27, 1972, pp. 19–38.

5 Hwang, G. J., and Cheng, K. C., "Boundary Vorticity Method for Convective Heat Transfer with Secondary Flow—Application to the Combined Free and Forced Laminar Convection in Horizontal Tubes," *Heat Transfer, Vol. 4,* 1970, Paper No. NC3.5, Elsevier Publishing Company, Amsterdam, 1970.

6 Newell, P. H., and Bergles, A. E., "Analysis of Combined Free and Forced Convection for Fully Developed Laminar Flow in Horizontal Tubes," ASME JOURNAL OF HEAT TRANSFER, Vol. 90, 1970, pp. 83–93.

7 Faris, G. N., and Viskanta, R., "An Analysis of Laminar Combined Forced and Free Convection Heat Transfer in a Horizontal Tube," *International Journal of Heat and Mass Transfer,* Vol. 12, 1969, pp. 1295-1309.

8 Iqbal, M., and Stachiewicz, J. W., "Variable Density Effects in Combined Free and Forced Convection in Inclined Tubes," *International Journal of Heat and Mass Transfer,* Vol. 10, 1967, pp. 1625–1629.

9 Iqbal, M., and Stachiewicz, J. W., "Influence of Tube Orientation on Combined Free and Forced Laminar Convection Heat Transfer," ASME JOURNAL OF HEAT TRANSFER, Vol. 88, 1966, pp. 410–420.

10 Del Casal, E., and Gill, W. N., "A Note on Natural Convection Effects in Fully Developed Horizontal Tube Flow," *AIChE Journal,* Vol. 8, 1962, pp. 570–574.

11 Morton, B. R., "Laminar Convection in Uniformly Heated Horizontal Pipes at Low Rayleigh Numbers," *Quarterly Journal of Mechanics and Applied Mathematics,* Vol. 12, 1959, pp. 410–420.

12 Siegwarth, D. P., Mikesell, R. D., Readal, T. C., and Hanratty, T. J., "Effect of Secondary Flow on the Temperature Field and Primary Flow in a Heated Horizontal Tube," *International Journal of Heat and Mass Transfer,* Vol. 12, 1969, pp. 1535–1552.

13 Mori, Y., and Futagami, K., "Forced Convective Heat Transfer in Uniformly Heated Horizontal Tubes," *International Journal of Heat and Mass Transfer,* Vol. 10, 1967, pp. 1801–1813.

14 Sabbagh, J. A., Aziz, A., El-Ariny, A. S., and Hamad, G., "Combined Free and Forced Convection in Circular Tubes," ASME JOURNAL OF HEAT TRANSFER, Vol. 98, 1976, pp. 322–324.

15 Bergles, A. E., and Simonds, R. R., "Combined Forced and Free Convection for Laminar Flow in Horizontal Tubes with Uniform Heat Flux," *International Journal of Heat and Mass Transfer,* Vol. 14, 1971, pp. 1989–2000.

16 Hussain, N. A., and McComas, S. T., "Experimental Investigation of Combined Convection in a Horizontal Circular Tube with Uniform Heat Flux," *Heat Transfer,* Vol. 4, 1970, Paper No. NC3.4, Elsevier Publishing Company, Amsterdam, 1970.

17 Petukhov, B. S., Polyakov, A. F., and Strigin, B. K., "Heat Transfer in Tubes with Viscous-Gravity Flow," *Heat Transfer—Soviet Research,* Vol. 1, 1969, pp. 24–31.

18 Shannon, R. L., and Depew, C. A., "Combined Free and Forced Laminar Convection in a Horizontal Tube with Uniform Heat Flux," ASME JOURNAL OF HEAT TRANSFER, Vol. 90, 1968, pp. 353–357.

19 Petukhov, B. S., and Polyakov, A. F., "Experimental Investigation of Viscogravitational Fluid Flow in a Horizontal Tube," *High Temperature*, Vol. 5, 1967, pp. 75–81.

20 Petukhov, B. S., and Polyakov, A. F., "Effect of Free Convection on Heat Transfer During Forced Flow in a Horizontal Pipe," *High Temperature*, Vol. 5, 1967, pp. 348–351.

21 Mori, Y., Futagami, K., Tokuda, S., and Nakamura, M., "Forced Convective Heat Transfer in Uniformly Heated Horizontal Tubes, 1st Report—Experimental Study on the Effect of Buoyancy," *International Journal of Heat and Mass Transfer*, Vol. 9, 1966, pp. 453–463.

22 McComas, S. T., and Eckert, E. R. G., "Combined Free and Forced Convection in a Horizontal Circular Tube," JOURNAL OF HEAT TRANSFER, TRANS. ASME, Series C, Vol. 88, 1966, pp. 147–153.

23 Iqbal, M., "Free Convection Effects Inside Tubes of Flat-Plate Solar Collectors," *Solar Energy*, Vol. 10, 1966, pp. 207–211.

24 Ede, A. J., "The Heat Transfer Coefficient for Flow in a Pipe," *International Journal of Heat and Mass Transfer*, Vol. 4, 1961, pp. 105–110.

25 Reynolds, W. C., "Heat Transfer to Fully Developed Laminar Flow in a Circular Tube with Arbitrary Circumferential Heat Flux," JOURNAL OF HEAT TRANSFER, TRANS. ASME, Series C, Vol. 82, 1960, pp. 108–112.

R. R. Gilpin
H. Imura[1]
K. C. Cheng

Department of Mechanical Engineering,
University of Alberta,
Edmonton, Alberta, Canada

Experiments on the Onset of Longitudinal Vortices in Horizontal Blasius Flow Heated from Below

Experiments were performed to confirm the occurrence and growth of longitudinal vortices in a laminar boundary layer developing in water over a heated horizontal flat plate with uniform surface temperature. Photographs of the vortices, measurements of the conditions of their onset, and measurements of their wavelength are presented. Comparisons are made with theoretical instability results for the critical Grashof number and wavelength. Temperature profiles across the boundary layer were measured for flows with and without vortices to show qualitatively the effect that the longitudinal vortices have on the heat transfer rate at the plate. Under conditions of thermal instability the longitudinal vortices were found to be the first stage of the laminar-turbulent transition process in a boundary layer heated from below.

Introduction

The temperature profile in a laminar boundary layer flow over a flat plate with a constant wall temperature has been extensively analyzed since the publication of Pohlhausen's first solution [1].[2] It does not appear, however, that the conditions for the onset of thermal instability in this flow have been critically investigated. Physically when a boundary layer is heated from below or cooled from above a potentially unstable top-heavy situation exists due to the variation of fluid density with temperature. The problem is apparently analogous to the case of a laminar boundary layer flowing along concave wall where an instability due to the centrifugal force exists [2–4]. In the case of the concave wall the instability (Görtler instability) manifests itself in the form of vortex rolls aligned longitudinally with the flow. Due to these vortex rolls the flow field develops a three-dimensional character which alters the wall heat transfer.

Calculations have been made, for example, by Mori [5], Sparrow and Minkowycz [6], and Chen, Sparrow, and Mucoglu [7], of the effect of the buoyancy term on the laminar boundary layer profile on an isothermally heated, horizontal, flat plate. These calculations of mixed convection suggest that the relative importance of free and forced convection can be represented by the physical parameter $Gr_x/Re_x^{5/2}$. A perplexing practical question arises, however, as to the limit of validity of the two-dimensional free and forced convection formulation in view of the fact that the flow may be unstable. Recently, Wu and Cheng [8] have obtained theoretical results which suggest that for Grashof numbers beyond a critical value, the flow is unstable with respect to small disturbances in the longitudinal vortex mode. This analysis employed a nonparallel flow model in which a linearization was made about the basic Blasius velocity and Pohlhausen temperature profiles.

The present experimental investigation was initiated to confirm the onset of longitudinal vortex rolls in a horizontal Blasius flow of water over a flat plate with constant wall temperature and to assess its practical significance. However, from flow visualization studies it became evident that one can clearly identify, in addition to the initial onset of the instability in the form of vortex rolls, a subsequent amplification of the disturbances and a transition to regimes of more disordered secondary flow. The effects of thermal instability on the temperature field in this postcritical regime were also investigated. It is of interest to note that Sparrow and Husar's experiments [9] on longitudinal vortices in natural convection flow along an inclined plate, apparently demonstrate a similar sequence of events even though the nature of the basic flow is quite different. This suggest that some analogy exists between the present problem and that of Sparrow and Husar [9] as well as Lloyd and Sparrow [10]. These experiments have apparently motivated subsequent theoretical studies of this problem [11–14].

For completeness, it should be mentioned that for the case of horizontal plane Poiseuille flow heated from below, longitudinal vortex rolls also exist. This thermal instability problem has been studied both theoretically and experimentally in the thermal entrance region [15–18] and the fully developed region [19–20].

The hydrodynamic stability of a Blasius flow has been studied very extensively in the past; however, as has been pointed out, little in-

[1] On leave from the Department of Mechanical Engineering, Kumamoto University, Japan.

[2] Numbers in brackets designate References at end of paper.

Contributed by the Heat Transfer Division for publication in the JOURNAL OF HEAT TRANSFER. Manuscript received by the Heat Transfer Division May 23, 1977.

formation is available for the thermal instability of this flow. Since the laminar boundary layer flow over a flat plate with a constant wall temperature is very basic to the study of forced convection heat transfer the present thermal instability problem is of considerable theoretical and practical interest.

2 Experimental Apparatus and Procedure

2.1 **Water Tunnel.** An existing closed loop water tunnel, shown in Fig. 1, was used as the basic flow facility for the experiments. This facility consists essentially of a circulation pump, a heat exchanger, and the associated piping for transporting the water around a closed loop. The heat exchanger is connected to a refrigeration system so that the water in the tunnel can be controlled at any temperature between room temperature and 0°C. The water tunnel has two test sections. The dimensions of the small test section are 25.4 × 45.7 × 213.4 cm, width by height by length, and those of the large one are 64.0 × 91.4 × 182.9 cm. The contraction ratio between the large and small test sections is 5 to 1. These test sections have windows made of acrylic resin plates in order to permit a visual investigation of the flow. The circulation pump of the water tunnel is driven by a variable speed d-c drive which is capable of producing a steady water velocity in the small test section between 0.02 and 5 m/s.

2.2 **The Isothermal Heating Plate Assembly.** The present experiment was performed over a horizontal heating plate which was installed in the small working section. The leading edge of the plate was located near the end of the converging section. The heating plate and the other attached equipment are shown in Fig. 2. The test surface utilized in the experiments was fabricated from copper plate with dimensions 6.35 mm × 152.4 cm × 24.1 cm, thickness by length by width. The plate was designed to provide an isothermal surface to the boundary layer flow which could be either heated or cooled from the bottom surface by circulating water from a controllable, constant temperature bath.

In order to make the main flow parallel to the plate it was necessary to accelerate the flow under the plate. This was done using a pump to suck a small amount of water from under the plate near its leading edge and reinjecting it further downstream. It was, however, difficult to obtain a flow which was perfectly parallel to the plate at its leading edge. To avoid a separation bubble from forming at the leading edge it was found that the flow had to be directed slightly downward onto the plate in this region generating a somewhat wedge-type flow. Varying the amount of water bypassed under the plate and thus the angle of the flow at the leading edge appeared, however, to have a negligible effect on the results if the flow was confined to small deviations from parallel flow. A sharp unheated tail plate with a length of 15.2 cm was attached to the trailing edge of the plate to minimize the disturbances caused by the wake flow behind the plate.

2.3 **Temperature Measurements.** The temperatures of the heating water were measured at the inlet of the suction pipe in the tank and at the inlet and the outlet of the heating plate by copper-constantan thermcouples, T.C. 1 to 3 (Fig. 2). Temperatures in the water tunnel were measured 23 cm upstream from the leading edge and also 40 cm downstream from the trailing edge by copper-constantan thermocouples T.C. 4 and 5. In order to measure the temperature profiles across the boundary layer, copper-constantan thermocouples formed in a loop (Fig. 2 insert) were used. The plane of the loop was aligned perpendicular to the flow and the thermocouple was positioned using a traversing mechanism that could be read with an accuracy of 1/500 mm.

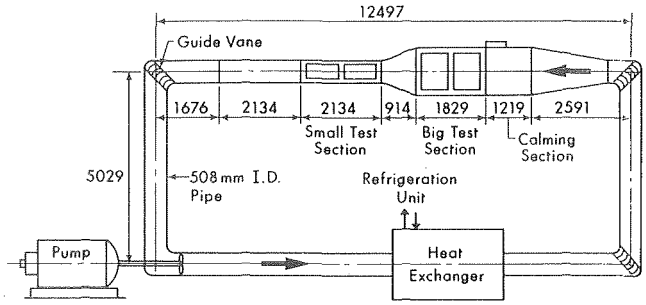

Fig. 1 Schematic diagram of the water tunnel facility

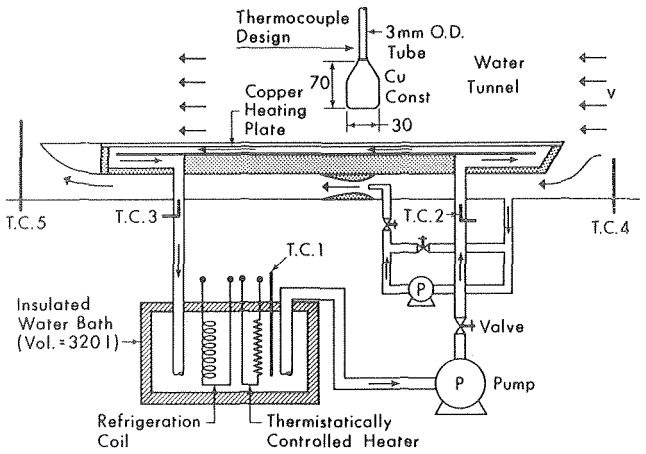

Fig. 2 Diagram of the constant temperature plate and auxiliary equipment

To check whether the thermocouple wire was actually perturbing the boundary layer flow, three wire diameters, 127, 76, and 25 μ were tried. The hot junctions of the 127 and 76 μ thermocouples were made by butt welding the copper and constantan wires together thus producing a very small junction volume. To obtain a successful weld of the 25 μ wires it was found that an overlapping of the wires was required. This produced an effective junction diameter of 50 μ. The velocities outside the boundary layer were normally measured using a 3 mm OD Pitot tube. The very low velocities were also determined by measuring the time required for a floating dust particle to pass between two lines 50 cm apart.

2.4 **The Flow Visualization Technique.** An electrochemical technique similar to that described by Sparrow and Husar [9] was employed to facilitate direct visual observation of longitudinal vortices. In the present experiments, Phenolphthalein was used as a pH indicator instead of Thymol blue [9]. The plate surface itself served as the negative electrode and the positive electrode was provided by a pair of copper sheets situated on the side walls of the test section. When a small d-c voltage (10–20 volts) is impressed between the two electrodes, ionization at the plate surface generates the tracer fluid

Nomenclature

Gr_x, Gr_{x_c} = Grashof numbers, $g\beta(\Delta T)x^3/\nu^2$ and $g\beta(\Delta T)x_c^3/\nu^2$
g = gravitational acceleration
Pr = Prandtl number
Re_x, Re_{x_c} = Reynolds numbers, $(U_\infty x/\nu)$ and $(U_\infty x_c/\nu)$
T, T_w, T_∞ = fluid, wall, and free stream temperatures
U_∞ = free stream velocity
x, y = distance from leading edge and normal distance from plate surface
x_c = distance from leading edge to onset point of instability
β = coefficient of thermal expansion
η = similarity variable, $y(U_\infty/\nu x)^{1/2}$
θ = dimensionless temperature difference, $(T - T_\infty)/\Delta T$
λ = wavelength of vortex rolls
ν = kinematic viscosity
ΔT = temperature difference, $(T_w - T_\infty)$
ΔT_{max} = maximum peak to peak amplitude of temperature fluctuation

showing the pink indicator color. Photography of the motion of this indicator dye then gave an indication of flow patterns in the boundary layer adjacent to the plate. The application of the present flow visualization method is restricted to relatively low velocity range (0–15 cm/s). Further details of the method can be found in [9].

3 Experimental Results and Discussion

3.1 **The Basic Flow and Temperature Fields for Stable Case.** The free stream velocity above the plate was first checked for uniformity. When the horizontal laminar boundary layer is cooled from below, the layer is stable since the density of water decreases upward from the plate surface. For a stable flow case, the temperature above the plate was found to be uniform within ±0.2°C throughout the water with the exception of the boundary layers of the order of 1–10 mm thick on the side walls and the plate. Measurements of the velocities showed that the free stream velocities were also very uniform being within ±0.5 percent of the mean value. Due to the growth of side wall and plate boundary layers, the free stream flow accelerated slightly, about 15 percent, in passing through the test section. No direct measurements of the turbulence level were made in the test section; however, by observing the deviation of the paths of suspended particles from straight lines the estimated turbulence level would appear to be less than 5 percent.

In order to obtain an isothermal surface over the entire plate, a high rate of flow of the fluid circulated from the constant temperature bath was maintained. As a result, the temperatures at the three locations, T.C. 1, 2, and 3 shown in Fig. 2, were almost identical. Since the installation of a permanent thermocouple at the plate surface would disturb the uniform temperature condition required, the surface temperatures were obtained by lowering one of the free stream thermocouples from above the plate until it touched the surface. The results of these measurements were usually within 0.2°C of the temperature of the circulating fluid below the plate. A maximum difference of 0.6°C was obtained with a high flow velocity when the temperature difference between the plate and the free stream was 16°C. An average of the temperature obtained from the thermocouple touching the plate and the water bath temperature was finally used for the surface temperature, T_w, since it appeared to represent a good estimate of the plate surface temperature.

In order to confirm the Pohlhausen temperature profiles for stable basic flow, a number of temperature profiles were measured with the plate cooled below the free stream temperature. Measurements made of the profile are shown in Fig. 3 along with the theoretical profile for Pr = 7. The curve for Pr = 10 was given for reference only. It can be seen that the results obtained with the 76 and 25 μ wires agreed while those obtained with the 127 μ wire were somewhat lower. The measurements with the smaller thermocouples were at the most 10 percent below the theoretical profile for Pr = 7, where the property values were evaluated at the free stream temperature T_∞. For the present investigations, this level of agreement between theory and experiment was considered as adequate.

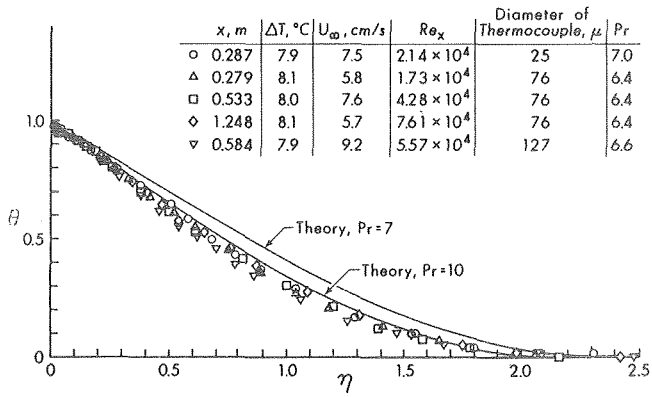

Fig. 3 Stable boundary layer temperature profiles produced in the case of cooling from below

Table 1 Range of parameters for experiments

ΔT,°C	T_∞,°C	U_∞,cm/s
1.8–2.0	25.5–21.7	2.7–15.2
3.5–4.1	7.8–24.0	2.9–7.3
7.7–8.2	7.7–8.1	3.0–20.2
11.6–12.0	7.8–8.3	2.9–16.4
15.6–15.9	8.2–8.5	3.3–17.2

3.2 **Flow Visualization Studies for the Unstable Case of Heating from Below.** The ranges of parameters of the present experiments for the case of heating from below are listed in Table 1. Temperature differences between the plate and free stream were varied in the range ΔT = 2–16°C and velocities of the main flow were in the range U_∞ = 2.7–20 cm/s. The corresponding Reynolds numbers, Re_ℓ, on the plate are in the range 10^3–10^5, which is within the hydrodynamically stable region for isothermal flows.

Insight into the qualitative nature of the formation and development of longitudinal vortices is gained by direct visual observation of flow patterns made visible by the electrochemical technique. Three representative series of photographs of the flow field are presented in Figs. 4(*a*), (*b*), and (*c*) where the top and side views of the vortices are shown. The top views of the onset and growth of the longitudinal vortices show a remarkable resemblance to those shown in Fig. 1 of Sparrow and Husar [9] for the case of longitudinal vortices in natural convection flow on inclined plates. This observation would suggest that the structure and the physical process for the onset and growth of the longitudinal vortices in the present experiments are similar to those observed by Sparrow and Husar [9] even though the nature of the main flow is different. If the flow field were two-dimensional (basic flow without longitudinal vortices), the plate would be blanketed by a thin and uniform film of tracer fluid moving parallel to the surface [9]. Observations of the stable flow over a cooled plate confirmed this flow pattern of the dye. Also the photographs in Fig. 4 showed the existence of a stable two-dimensional laminar flow (Blasius flow) in the region near the leading edge.

An inspection of the top view in Fig. 4(*a*) reveals that an array of more or less regularly spaced lines, oriented parallel to the main flow, appears at a certain distance (roughly 1.7 ft or 0.5 m) from the leading edge. This indicates the onset of longitudinal vortices. As noted by Sparrow and Husar [9], the presence of the discrete lines is indicative of spanwise motions of a cellular nature. The lines of tracer fluid correspond to regions of upward motion between counter-rotating vortex rolls. The foregoing observation is confirmed by an inspection of the side views. Examining Fig. 4(*a*), it can be seen that at roughly the same point in the side view of the plate corresponding to the occurrence of parallel lines in the top view, the tracer dye can be seen rising off the plate. This is dye that is being lifted off the plate by the upflow between vortex rolls. These dye patterns were never observed for a stable flow.

The density difference term, $\beta\Delta T$, in the Grashof number is 3×10^{-4} for Fig. 4(*a*). For Fig. 4(*b*), $\beta\Delta T$ is increased to 5.1×10^{-4} while the main stream velocity is the same. As a result, the flow became more susceptible to instability and the onset point has moved forward to approximately the 1 ft (0.3 m) point. In this case it can also be seen that further down the plate the regular longitudinal vortices begin to break up into a highly disordered flow pattern. In Fig. 4(*c*), with the main stream velocity decreased, this succession of the flow patterns shifts toward the leading edge of the plate. This indicates that the low Reynolds number flow is more susceptible to thermal instability. Physically, one could anticipate this behavior in that at high Reynolds number, the buoyancy effects would tend to be washed out. The succession from stable two-dimensional laminar flow through the development of secondary flow to disordered flow represents the first stages of the laminar to turbulent transition process. It is apparently characteristic of similar unstable flows, for example, the natural convection flow on an inclined plate [9, 10].

3.3 **Instability Onset Point and Wavelength of Longitudinal Vortex Rolls.** For a given experimental condition, the distance along

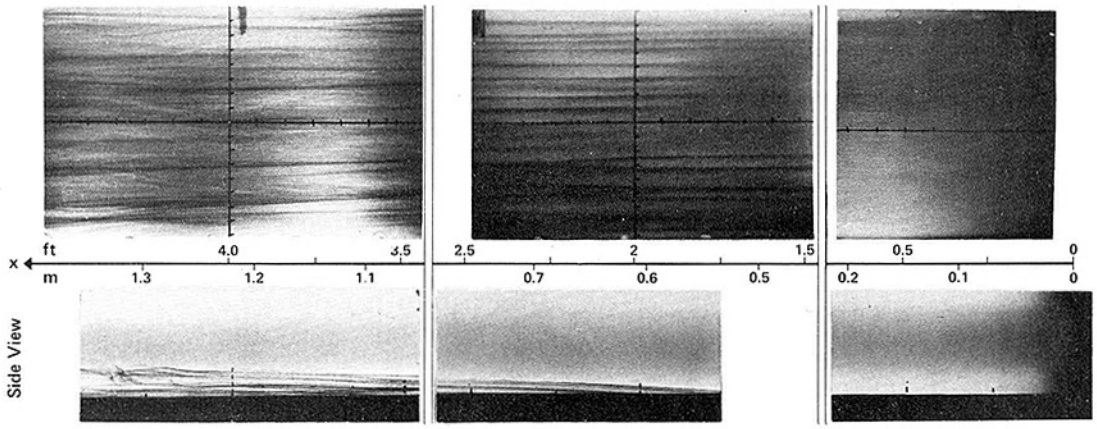

Fig. 4(*a*) Photographs of dye pattern on the heating plate for $U_\infty = 7.3$ cm/s, $T_\infty = 8°C$, $\Delta T = 7.8°C$, and $\beta\Delta T = 3.0 \times 10^{-4}$

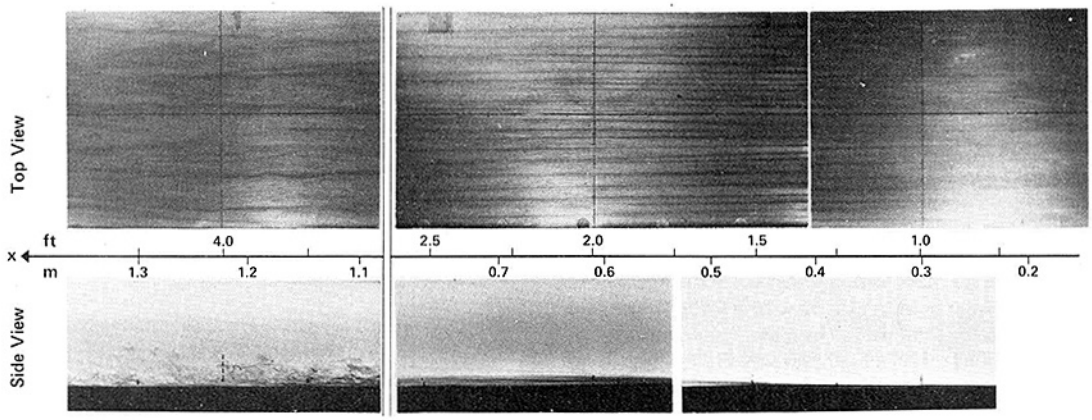

Fig. 4(*b*) Photographs of dye pattern on the heating plate for $U_\infty = 7.6$ cm/s, $T_\infty = 24°C$, $\Delta T = 4.1°C$, and $\beta\Delta T = 5.1 \times 10^{-4}$

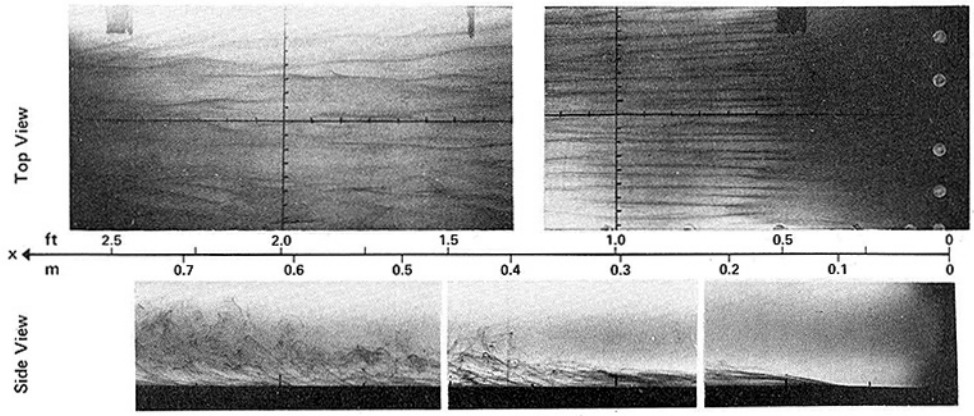

Fig. 4(*c*) Photographs of dye pattern on the heating plate for $U_\infty = 2.9$ cm/s, $T_\infty = 8°C$, $\Delta T = 11.5°C$, and $\beta\Delta T = 4.4 \times 10^{-4}$

the plate at which vortices could be first observed is not a precisely definable quantity. As can be seen from the photographs in Fig. 4, the position varies somewhat across the plate. It also fluctuated in time. In a given situation, however, there are positions where there are never any vortices and similarly positions where there are always vortices. The zone of uncertainty between these positions is typically of the order of 20 percent of the distance from the leading edge.

Linear stability theory [8] suggests that the onset points for instability can be correlated using the Reynolds and Grashof numbers where the critical length x_c is the distance from the leading edge to the onset point. Fig. 5 shows the observed onset points correlated in this fashion where the open points indicate positions at which vortices were only occasionally observed and the solid points indicate positions where vortices always existed. The property values of water used in Fig. 5 were evaluated at the free stream temperature T_∞. A study by Seban [21] suggests that this may not be unreasonable for a variable

property fluid with a high Prandtl number since the thermal boundary layer in that case is much thinner than the velocity boundary layer.

The measured onset points using free stream property values were found to be correlated by

$$\mathrm{Gr}_{x_c} = c_1 \mathrm{Re}_{x_c}^{3/2} \tag{1}$$

where c_1 was between 46 and 110. When properties calculated at the film temperature were used a wider scatter in the experimental results occurred. The correlation of the results by equation (1) using film temperature properties resulted in c_1 being between 30 and 200.

From a count of the number of lines aligned in the streamwise direction distributed across the width of the plate, the average wavelength of the longitudinal vortices can be determined. One wavelength corresponds to two counter-rotating vortices. Results for x_c/λ versus Re_{x_c} are shown in Fig. 6. The data can be correlated by

$$x_c/\lambda = c_2 \mathrm{Re}_{x_c}^{1/2} \text{ (or } x_c/\lambda = (0.035\text{–}0.070)\mathrm{Gr}_{x_c}^{1/3}) \tag{2}$$

where $c_2 = 0.16$ and 0.31 bounded the data.

3.4 **Comparison Between Theory and Experiment for Instability Results.** Instability results from linear stability analysis [8] are also plotted in Figs. 5 and 6 for comparison. The theoretical values for c_1 in equation (1) are 100 for Pr = 7 and 75 for Pr = 10. As mentioned previously, the uncertainty in the measurement of the onset point was approximately 20 percent. Taking into consideration possible uncertainties in the temperature and velocity measurements would result in an estimated uncertainty in c_1 of approximately 50 percent. Within the accuracy of the measurements the measured values of c_1 of 46 to 110 are therefore seen to agree with the theory.

The value of c_2 in equation (2) calculated from the theory is 0.28 and is not very sensitive to variations in Pr. The scatter in the experimental results was quite large for this measurement; however, the experimental values of c_2 between 0.16 and 0.31 are of the right order of magnitude.

The level of agreement between theory and experiment is rather surprising and unexpected in view of the known order of magnitude of difference between theory and experiment for the onset of longitudinal vortices in natural convection boundary layers along inclined plates [10–14] and in the thermal entrance region of horizontal plane Poiseuille flow [15, 16, 18] both with heating from below. Normally one would expect the theoretically predicted onset point to fall below that observed in the experiments since the instability must grow to a finite amplitude before it can be observed.

Another factor that may influence the onset of instability is the strong variation of the properties of water (in particular its viscosity) with temperature. The theory in reference [8] pretains strictly to the case of constant fluid properties and in the experiments variations through the boundary layer of up to 40 percent in viscosity existed for some tests. The onset points were observed to be correlated adequately using fluid properties based on the free stream temperature; however, some of the remaining scatter in the results may be due to the effects of variable properties.

The circumstances under which the theory and experiment agree are already under investigation [22]; however, due to the complex nature of the problem it may be some time before the situation can be clarified. Normally, in the engineering literature the agreement between theory and experiment is taken to confirm the theoretical prediction. However, in this particular instance one is cautioned against such immediate conclusion. Notwithstanding the foregoing remark, the results shown in Figs. 5 and 6 would suggest that the theoretical predictions are at least qualitatively correct.

3.5 **Temperature Measurements in the Postcritical Regime.** Further insight into the character of the unstable flow is obtained by examining the temperatures that exist in the boundary layer. The temperature profiles in Figs. 7(*a*), (*b*), and (*c*) correspond to the conditions in the respective photographs Figs. 4(*a*), (*b*), and (*c*). These temperature profiles were measured at fixed positions along the center line of the plate. As mentioned previously, the vortices on the plate constantly shifted from side to side across the flow direction; thus, by averaging the temperature over a period of time at a fixed position, an approximate spanwise average of the temperature was obtained. Several profiles measured off the center line showed that the mean profiles thus obtained were essentially constant across the plate. The qualitative behavior observed in these temperature profiles will be illustrated using Fig. 7(*b*). In Fig. 7(*b*) the measurement of the mean temperature profile upstream of the onset of vortices, profile number (1), gives a result that is the same as that obtained from the case of cooling from below (stable case) and is only slightly below the theory. At positions (2) and (3) which are in the postcritical regime with longitudinal vortices, it can be seen that the profile has changed significantly. Both the temperature gradient at the wall and total thermal boundary layer thickness have increased above that for the Pohlhausen profile.

Fig. 8(*b*) shows the peak to peak amplitude ΔT_{max} of the temperature fluctuation in the boundary layer normalized by the tempera-

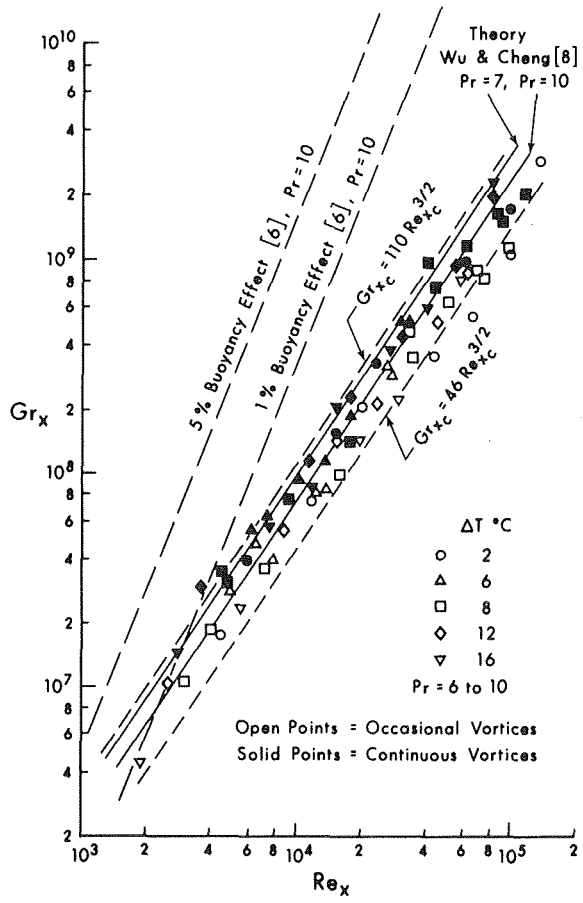

Fig. 5 Correlations for the point of onset of longitudinal vortices in a plane Blasius flow heated from below

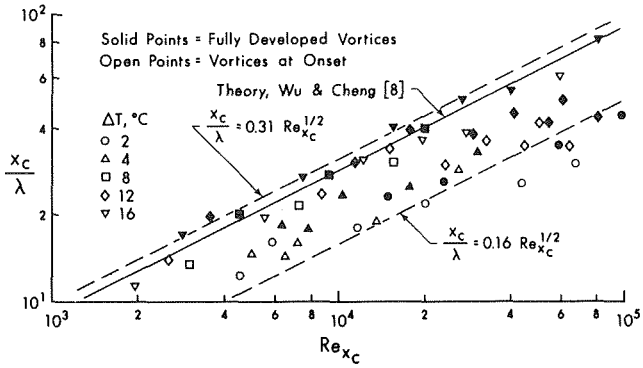

Fig. 6 Correlations for the typical wavelength of the longitudinal vortices

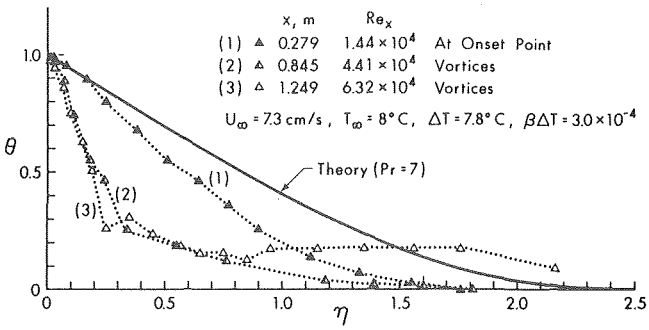

Fig. 7(a) Mean temperature profiles for conditions in Fig. 4(a)

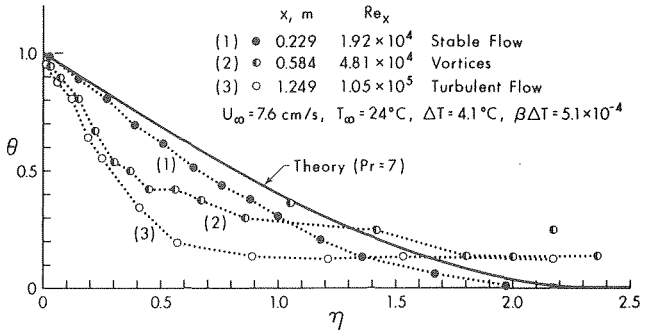

Fig. 7(b) Mean temperature profiles for conditions in Fig. 4(b)

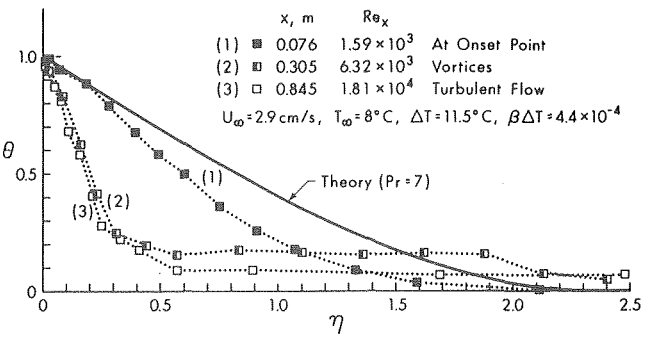

Fig. 7(c) Mean temperature profiles for conditions in Fig. 4(c)

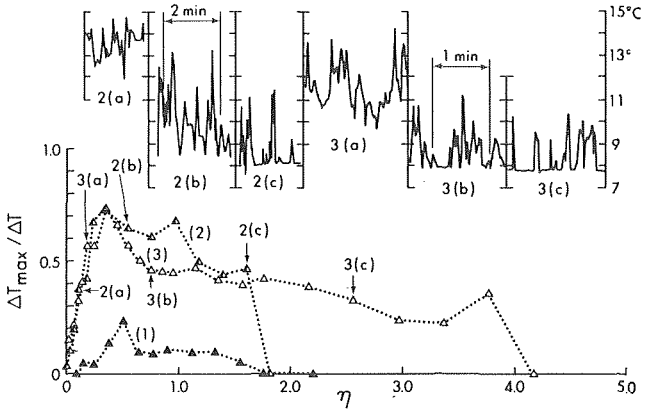

Fig. 8(a) Peak-to-peak temperature fluctuation profiles of positions indicated in Fig. 7(a)

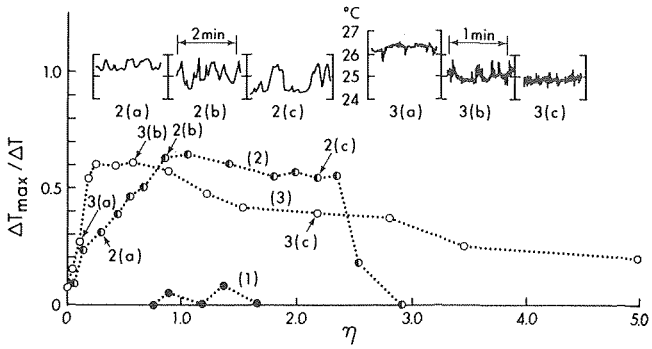

Fig. 8(b) Peak-to-peak temperature fluctuation profiles at positions indicated in Fig. 7(b)

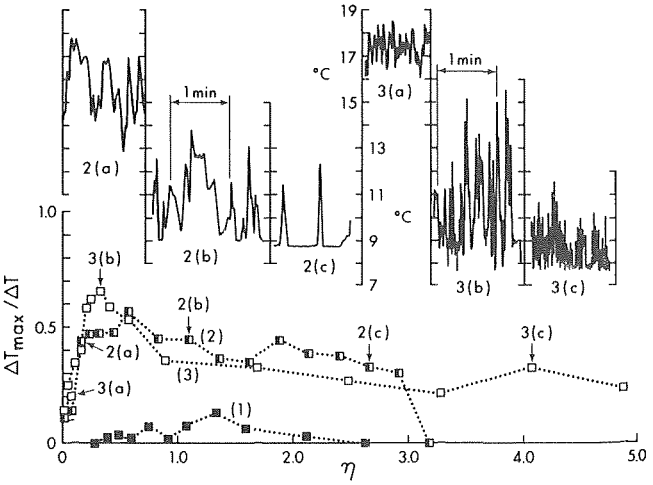

Fig. 8(c) Peak-to-peak temperature fluctuation profiles at positions indicated in Fig. 7(c)

ture difference ΔT between the plate surface and the free stream. It can be seen that upstream of the observed onset point there is very little (less than 10 percent) temperature fluctuation in the boundary layer. However, after the onset of vortices the amplitude of the fluctuations is up to 60 percent of ΔT. Examining the inserts which show samples of the temperature records at various points in the profile, it can be seen that at position (2) which is immediately downstream from the onset point the temperature fluctuations have a relatively long period ranging 10 to 60 s. The fluctuations at this point were observed to be coincident with the slow but steady shifting and swaying of the vortices in a direction perpendicular to the main flow. Further downstream at position (3) the amplitude of the fluctuations remains the same; however, they are of a higher frequency indicating a more highly disordered flow. This occurs due to a breakdown of the regular vortices setting the stage for a turbulent flow. Further temperature measurement results shown in Figs. 7(a), (c) and Figs. 8(a), (c) confirm these qualitative observations at other flow conditions.

3.6 **Practical Implications for Forced Convection.** *Heat Transfer on a Horizontal Plate.* It would be anticipated that the existence of longitudinal vortices in the laminar boundary layer could affect the heat transfer rate through the layer. This effect was confirmed from the measurements of temperature profiles through the boundary layer. As noted previously, the development of vortices was accompanied by an increase in the mean temperature gradient at wall. Thus, the conventional heat transfer calculations neglecting the existence of longitudinal vortices may be in serious error in the postcritical regime. The unstable conditions occur when heating from below or cooling from above exists and the value of the parameter $Gr_{x_c}Re_{x_c}^{-3/2}$ exceeds some critical value, c_1. For practical purposes a value of c_1 of 100 would be suggested on the basis of the present experiments. In this connection, it is also of practical interest to compare the present instability results with Sparrow and Minkowycz's

results [6] for 1 and 5 percent increase in local heat transfer rate due to the buoyancy effect on a forced convection flow. The results from [6] are also plotted in Fig. 5 for reference. Comparing these results with the condition for the onset of instability it would appear that the development of longitudinal vortex rolls will be the dominant effect of the buoyancy force.

4 Concluding Remarks

The present experiments confirm that thermal instability in a Blasius flow on a horizontal plate heated from below results in the formation of cellular secondary flows in the form of longitudinal vortices. Further, flow visualization studies have shown that a succession of flow regimes exist in a thermally unstable Blasius flow on a flat plate. These regimes include a stable two-dimensional laminar flow regime near the leading edge of the plate, followed by the onset of instability and growth of longitudinal vortices, and finally, the break-up of these vortices into a turbulent flow. Thus, as was observed by Sparrow and Husar [9] for a natural convection flow on an inclined plate, the longitudinal vortices are seen as the first stage of the laminar to turbulent transition process for a thermally unstable flow.

In the present study the position of the onset of instability was observed to depend on both the free stream velocity and the temperature difference across the boundary layer. The condition for thermal instability, $Gr_{x_c}Re_{x_c}^{-3/2} > 100$, was studied in the Reynolds number range 2×10^3 to 10^5 and the corresponding Grashof number range 4×10^6 to 3×10^9. The thermal instability is therefore occurring at much lower Reynolds numbers than that for which hydrodynamic instability occurs in a Blasius flow. In that case, where thermal effects are absent, Tollmien-Schlichting waves constitute the first stage of transition at a Reynolds number around 5×10^5. Heating and cooling are known to have an effect on this stability limit [24, 25]. Thermal effects would also appear to influence the onset of Görtler vortices on a concave wall [26]. Another limiting case is that of no free stream velocity ($Re_x = 0$) which corresponds to natural convection above an upward facing horizontal heating surface. The onset of instability in this case has been studied by Pera and Gebhart [23]. The present experimental results can be seen as further defining the boundary and mechanism of instability in the flow regime between the two limiting cases of Re = 0, i.e., pure natural convection, and Gr = 0, i.e., pure forced convection.

It will be noted, however, that as yet the entire range of instability conditions has not been explored. In particular, for the flow regime with high Reynolds and high Grashof numbers one may anticipate that two instability modes, thermal and hydrodynamic, could coexist. This flow regime remains, however, as a subject of further research.

Acknowledgment

The authors wish to acknowledge the contributions of Dr. G. S. H. Lock in the conception and planning of the Water Tunnel Facility and of Mr. Boochoon in its construction and operation. The construction of the Water Tunnel Facility and work on this project were funded by the National Research Council of Canada. The second author, Mr. Imura, wishes to thank Professor T. Fujii, Kyushu University, Japan, for his encouragement to carry out this research.

References

1 Pohlhausen, E., "Der Wärmeaustausch zwischen festen Körpern und Flüssigkeiten mit kleiner Reibung und Kleiner Wärmeleitung," *Zeitschrift für angewandte Mathematik und Mechanik,* Vol. 1, 1921, pp. 115–120.

2 Görtler, H., "Über eine Analogie zwischen den Instabilitäten laminarer Grenzschichtströmungen an konkaven Wänden und an erwärmten Wänden," *Ingenieur-Archiv,* Vol. 28, 1959, pp. 71–78.

3 Tani, I., "Production of Longitudinal Vortices in the Boundary Layer along a Concave Wall," *J. Geophys. Res.,* Vol. 67, 1962, pp. 3075–3080.

4 Bippes, H., and Görtler, H., "Dreidimensionale Störungen in der Grenzschicht an einer konkaven Wand," *Acta Mechanica,* Vol. 14, 1972, pp. 251–267.

5 Mori, Y., "Buoyancy Effects in Forced Laminar Convection Flow over a Horizontal Flat Plate," JOURNAL OF HEAT TRANSFER, TRANS. ASME, Series C, Vol. 83, 1961, pp. 479–482.

6 Sparrow, E. M., and Minkowycz, W. J., "Buoyancy Effects on Horizontal Boundary Layer Flow and Heat Transfer," *International Journal of Heat and Mass Transfer,* Vol. 5, 1962, pp. 505–511.

7 Chen, T. S., Sparrow, E. M., and Mucoglu, A., "Mixed Convection in Boundary Layer Flow on a Horizontal Plate," JOURNAL OF HEAT TRANSFER, TRANS. ASME, Series C, Vol. 99, 1977, pp. 66–71.

8 Wu, R. S., and Cheng, K. C., "Thermal Instability of Blasius Flow along Horizontal Plates," *International Journal of Heat and Mass Transfer,* Vol. 19, 1976, pp. 907–913.

9 Sparrow, E. M., and Husar, R. B., "Longitudinal Vortices in Natural Convection Flow on Inclined Plates," *Journal of Fluid Mechanics,* Vol. 37, 1969, pp. 251–255.

10 Lloyd, J. R., and Sparrow, E. M., "On the Instability of Natural Convection Flow on Inclined Plates," *Journal of Fluid Mechanics,* Vol. 42, 1970, pp. 465–470.

11 Haaland, S. E., and Sparrow, E. M., "Vortex Instability of Natural Convection Flow and Inclined Surfaces," *International Journal of Heat and Mass Transfer,* Vol. 16, 1973, pp. 2355–2367.

12 Hwang, G. J., and Cheng, K. C., "Thermal Instability of Laminar Natural Convection Flow on Inclined Isothermal Plates," *Canadian Journal of Chemical Engineering,* Vol. 51, 1973, pp. 659–666.

13 Lee, J. B., and Lock, G. S. H., "Instability in Boundary-Layer Free Convection along an Inclined Plate," *Trans. Canadian Society for Mechanical Engineering,* Vol. 1, 1972, pp. 197–203.

14 Kahawita, R. A., and Meroney, R. N., "The Vortex Mode of Instability in Natural Convection Flow along Inclined Plates," *International Journal of Heat and Mass Transfer,* Vol. 17, 1974, pp. 541–548.

15 Hwang, G. J., and Cheng, K. C., "Convective Instability in the Thermal Entrance Region of a Horizontal Parallel-Plate Channel Heated from Below," JOURNAL OF HEAT TRANSFER, TRANS. ASME, Series C, Vol. 95, 1973, pp. 72–77.

16 Kamotani, Y., and Ostrach, S., "Effect of Thermal Instability on Thermally Developing Laminar Channel Flow," JOURNAL OF HEAT TRANSFER, TRANS. ASME, Series C, Vol. 98, 1976, pp. 62–66.

17 Cheng, K. C., and Wu, R. S., "Axial Heat Conduction Effects on Thermal Instability of Horizontal Plane Poiseuille Flows Heated From Below," JOURNAL OF HEAT TRANSFER, TRANS. ASME, Series C, Vol. 98, 1976, pp. 564–569.

18 Hwang, G. J., and Liu, C. L., "An Experimental Study of Convective Instability in the Thermal Entrance Region of a Horizontal Parallel-Plate Channel Heated from Below," *Canadian Journal of Chemical Engineering,* Vol. 54, 1976, pp. 521–525.

19 Nakayama, W., Hwang, G. J., and Cheng, K. C., "Thermal Instability in Plane Poiseuille Flow," JOURNAL OF HEAT TRANSFER, TRANS. ASME, Series C, Vol. 92, 1970, pp. 61–68.

20 Akiyama, M., Hwang, G. J., and Cheng, K. C., "Experiments on the Onset of Longitudinal Vortices in Laminar Forced Convection Between Horizontal Plates," JOURNAL OF HEAT TRANSFER, TRANS. ASME, Series C, Vol. 93, 1971, pp. 335–341.

21 Seban, R. A., *The Laminar Boundary Layer of a Liquid with Variable Viscosity, Heat Transfer Thermodynamics and Education,* Boelter Anniversary Volume, Johnson, H. A., Ed., McGraw-Hill, 1964, pp. 319–329.

22 Chen, T. S., private communication, 1976.

23 Pera, L., and Gebhart, B., "On the Stability of Natural Convection Boundary Layer Flow over Horizontal and Slightly Inclined Surfaces," *International Journal of Heat and Mass Transfer,* Vol. 16, 1973, pp. 1147–1163.

24 Wazzan, A. R., Okamura, T. T., and Smith, A. M. O., "The Stability of Water Flow over Heated and Cooled Flat Plates," JOURNAL OF HEAT TRANSFER, TRANS. ASME, Vol. 90, 1968, pp. 109–114.

25 Strazisar, A. J., Prahl, J. M., and Reshotko, E., "Experimental Study of the Stability of Heated Laminar Boundary Layers in Water," Report FTAS/TR-75-113, Case Western Reserve University, Dept. of Mechanical Engineering and Aerospace Engineering, 1975.

26 Kahawita, R. A., and Meroney, R. N., "The Influence of Heating on the Stability of Laminar Boundary Layers along Concave, Curved Walls," ASME *Journal of Applied Mechanics,* Vol. 99, 1977, pp. 11–17.

S. J. Rhee
Research Assistant

V. K. Dhir
Assistant Professor,
Mem. ASME

I. Catton
Professor,
Mem. ASME

Chemical, Nuclear, and Thermal Engineering Department,
School of Engineering and Applied Science,
University of California, Los Angeles,
Los Angeles, Calif.

Natural Convection Heat Transfer in Beds of Inductively Heated Particles[1]

Experimental observations of the onset of convective motion in beds of inductively heated particles have been made. Data for the heat transfer coefficient were obtained from water-cooled beds of steel particles. The particulate beds were formed in a 10.4 cm dia glass jar, insulated at the bottom and on the sides. The free surface of a layer of water overlying the bed was maintained at a constant temperature by a copper plate cooled with tap water. In the experiments, the depths of the particulate bed and the overlying layer were varied.

The observations showed that increasing the depth of the liquid layer over the bed tended to lower the critical internal Rayleigh number at which the onset of convection occurred. For overlying liquid layer-to-bed depth ratios of one or more, natural convection was observed to begin at $R_1 \simeq 11.5$. The heat transfer data for $R_I > 11.5$ are correlated with $Nu = 0.190\ R_I^{0.69}$ However, with no liquid layer on top of the bed, natural convection was observed to occur at $R_I \simeq 46$, which is slightly higher than observed in earlier studies made with Joule heating.

Introduction

In recent years, considerable research has been done on the onset of convection and heat transfer behavior in volumetrically heated layers of liquid or particulate beds, because of its applications to certain hypothetical accident situations in nuclear reactors. In this paper, the convective transfer of heat from volumetrically heated particulate beds covered with a finite layer of liquid is studied.

The earliest theoretical study of the occurrence of natural convection in porous media filled with liquid was made by Horton and Rogers [1],[2] who were interested in the distribution of sodium chloride in subterranean sand layers. A similar problem was solved later by Lapwood [2], and he obtained the same result as Horton and Rogers did for the onset of convection in a porous medium heated from below and bounded at top and bottom with rigid conducting boundaries. Lapwood's criterion for the onset of convection is:

$$R_{E'} \equiv \frac{g\beta_f \Delta T L P}{\alpha_f \nu_f} = 4\pi^2 \tag{1}$$

In equation (1), P is the permeability of the bed and is assumed to be based on Ergun's equation [3]. However, the subsequent experimental results of Morrison, Rogers, and Horton [4] did not agree with their own or Lapwood's prediction. The basic reason given at that time for the discrepancy between experimental and theoretical results was that the experiments were performed under unsteady conditions. Later, Katto and Masuoka [5] studied, both theoretically and experimentally, the onset of convection in a porous medium subjected to a linear temperature gradient. From their theoretical model they derived the same criterion as that of Horton et al. and Lapwood for the occurrence of convection; but they suggested that the thermal diffusivity of the mixture, used in the Rayleigh number in equation 11], should be defined as the thermal conductivity of the porous medium divided by the specific heat and density of the fluid. Thus, their modified criterion for the onset of convection is:

$$R_E \equiv \frac{k_f g\beta_f \Delta T L P}{k_m \alpha_f \nu_f} \simeq 4\pi^2 \tag{2}$$

The data for the critical Rayleigh number obtained for particle diameter-to-bed depth ratios varying from 0.04 to about 1, and using glass, steel, and aluminum spheres, were found to correlate well with equation (2).

Analysis of heat transfer across a porous layer bounded between two rigid walls was made by Gupta and Joseph [6]. The theoretical curve maximizing the Nusselt number as a function of the Rayleigh number was computed numerically. The results of this numerical analysis were shown to agree very well with the experimental results of Buretta and Berman [7]. Natural convective heat transfer data of

[1] This work was supported by the Reactor Safety Research Division of the U.S. Nuclear Regulatory Commission under Agreement No. AT(04-3)-34P.A.223 Mod. 1.

[2] Numbers in brackets designate References at end of paper.

Contributed by the Heat Transfer Division for publication in the JOURNAL OF HEAT TRANSFER and presented at the Winter Annual Meeting, Atlanta, Nov. 27–Dec. 2, 1977. Manuscript received by the Heat Transfer Division August 19, 1977.

Buretta and Berman for a porous layer heated from below indicated a critical Rayleigh number of 33, with a transition in the nature of the convective heat transfer at a Rayleigh number between 200 and 300. The onset of instability in a porous bed with an overlying layer of liquid has been studied both theoretically and experimentally by Sun [8]. The porous bed and the overlying liquid layer were bounded at top and bottom with rigid conducting walls. The bed was heated from below while the liquid layer was cooled from above. Using perturbation theory, Sun predicted the Rayleigh number for onset of convection in terms of varying ratios, η, of the liquid layer depth to the particulate bed depth. Sun's experimental observations of the critical Rayleigh number, for the range of $\eta = 0$ to 0.21, compared very favorably with the data. His experimental data show that the critical external Rayleigh number for the bed decreased with η, whereas the critical external Rayleigh number for the overlying layer increased with η. Sun also observed that for a fixed value of the external Rayleigh number for the bed, the Nusselt number increased as η was increased.

The thermal instability of a volumetrically heated liquid layer with an initially stabilizing or destabilizing temperature profile in the layer was analyzed by Sparrow, Goldstein, and Jonsson [9]. From their analysis, Sparrow et al. concluded that as the volumetric heating rate is increased, a volumetrically heated liquid layer becomes more susceptible to instability, and the convective motion initiates at smaller Rayleigh numbers. Experimental observations of heat transfer, as well as the initiation of instability, in a Joule heated layer of electrolyte bounded horizontally between two rigid plates held at constant and equal temperatures were made by Kulacki and Goldstein [10]. Kulacki and Goldstein's experimental data indicated that the critical external Rayleigh number, based on half the layer thickness, was 620 ± 30, whereas the value predicted by linear stability theory was 560. The heat transfer data for the upper and lower boundaries with R_I' varying from 580 to 3.78×10^5 and Pr varying from 5.76 to 6.35 were correlated as

$$Nu_I = 0.756\ R_I'^{0.25} \tag{3}$$

and

$$Nu_0 = 2.006\ R_I'^{0.1} \tag{4}$$

The observations of Kulacki and Goldstein have subsequently been confirmed by the experimental work of Jahn and Reineke [11]. The problem of upward and downward heat transfer from a volumetrically heated horizontal layer with a destabilizing temperature difference at the upper and lower boundaries has been analyzed by Suo-Anttila and Catton [12]. Their results are in general agreement with those of Kulacki and Goldstein, but their magnitudes for the heat transfer at the boundaries are different from Kulacki and Goldstein's observations, where the bounding surfaces were held at the same temperature.

Experimental observations of the onset of natural convection and heat transfer in volumetrically heated porous layers with rigid bounding walls have been made by Buretta and Berman [7] and Sun [8]. In both of these studies, the porous layer contained glass particles and volumetric heating was accomplished by the Joule heating of water containing 0.01 mole percent of $CuSO_4$. The bottom of the bed was an adiabatic surface, whereas the top rigid wall was held at a constant temperature. For these boundary conditions, natural convection was observed to occur at

$$R_{Ic} \simeq 33. \tag{5}$$

In Buretta and Berman's data, a discontinuity in Nusselt number at about $R_I = 70$ for 3 mm dia particles and at about $R_I = 200$ for 6 mm dia particles was observed. No experimental reason for this anomalous behavior was given, and it was postulated that bifurcation was probably caused by the presence of two different unstable modes. The data on the lower branch, covering the range $30 < R_I < 70$ for 3 mm dia particles and $30 < R_I < 200$ for 6 mm dia particles, were found to correlate with

$$\log (Nu \pm 0.034) = 0.237 \log R_I - 0.356; \tag{6a}$$

while the data in the upper branch, covering the ranges $70 < R_I < 900$ for 3 mm dia particles and $200 < R_I < 900$ for 6 mm dia particles, were found to correlate with

$$\log (Nu \pm 0.070) = 0.553 \log R_I - 0.871 \tag{6b}$$

Sun did not observe any such discontinuity in his data and also did not make an attempt to correlate his data. But a curve faired through Sun's data would indicate that the heat transfer could be correlated by

$$Nu = 0.116\ R_I^{0.573} \tag{6c}$$

The correlation equation (6c) suggests the critical Rayleigh number is about 45. This value is higher than Sun's reported value of 33 and the difference can be attributed to variability in data and error resulting from personal judgment in drawing a best line through the data. The heat transfer predicted by equations (6b) and (6c) differ from each other by only a few percent.

Analysis for the onset of natural convection in a porous medium

Nomenclature

c_{ps}, c_{pf} = the specific heats of the particulate material and the liquid, respectively
D = the inner diameter of the glass jar
d = the diameter of the spherical particles
f = frequency
g = the acceleration of gravity
k_s, k_f, k_m = thermal conductivity of the particles, the liquid, and volume averaged thermal conductivity of the porous medium filled with liquid, $\epsilon k_f + (1 - \epsilon)k_s$, respectively.
L, L_f = the depths of the particulate bed and the overlying layer of liquid, respectively
m_s, m_f = the masses of the particles and the liquid in the particulate bed, respectively
Nu = the Nusselt number for the porous layer, as defined in equation [7]
Nu_I = the Nusselt number for the overlying layer of liquid, as defined in equation [9]
P = the permeability of the porous medium, $\epsilon^3 d^2/150\ (1 - \epsilon)^2$
Q_v = the heat generation rate per unit volume of the particulate bed, $[(m_s c_{ps} + m_f c_{pf})\text{-}dT/dt]/V$
R_E = the external Rayleigh number for the particulate bed, as defined in equation [2]
R_f = the Rayleigh number for the overlying layer of liquid, $g\beta_f(T_m - T_T)L_f^3/\alpha_f\nu_f$
R_I = the internal Rayleigh number for the particulate bed, as defined in equation [8]
R_{Ic} = critical internal Rayleigh number
R_I = the internal Rayleigh number for a volumetrically heated liquid layer of depth L, $g\beta_f Q_v L^5/32k_f\alpha_f\nu_f$
T = temperature
T_B, T_M, T_T = the temperatures of the bottom of the bed, the particulate bed-liquid layer interface, and the copper plate, respectively
T_{max} = the maximum temperature in the bed
t = time
V = the total volume of the particulate bed, $(\pi/4)D^2L$
z = distance from the bottom of the test cell
α_f = the thermal diffusivity of the liquid
β_f = the coefficient of thermal expansion of the liquid
ΔT = the temperature difference between any two bounding surfaces
ϵ = the porosity of the particulate bed
η = the ratio of the liquid layer depth to the particulate bed depth, L_f/L
ν_f = the kinematic viscosity of the liquid

Subscript

c = at the center line of the test cell

with internal heat generation has recently been made by Gasser and Kazimi [13]. In their model, the top of the particulate bed is assumed to be a free surface. For bottom surface temperatures greater or less than the free surface temperatures, Gasser and Kazimi have obtained a relationship between the critical internal Rayleigh number and the external Rayleigh number. More recently, Hardee and Nilson [14] have made experimental observations similar to those of Sun. Their experimental results, obtained with electrolytically heated, sodium chloride-saturated beds of sand, agree quite well with Sun's data.

The primary purpose of the present work is to experimentally determine the criteria for the onset of convection and the magnitude of convective heat transfer in a volumetrically heated particulate bed when a liquid layer exists over the bed. This configuration is more general than those studied previously, and is closer to situations that may occur in practice, such as during the cooling of a fuel bed after a hypothetical core disruptive accident in a liquid metal fast breeder reactor. In the present experiments, induction heating is employed so that the heat is generated in the metallic particles rather than in the coolant. The bottom surface of the bed is insulated, while the top surface of the liquid layer is maintained at a constant temperature.

Experimental Measurements

In this work, distilled water was chosen as the test liquid. Preliminary experiments with 800–1,000 mμ particles showed that at one atmosphere system pressure, it was very difficult to attain the onset of convection prior to the incipience of boiling in the bed. Thus, to reduce the resistance of the bed, larger particles were required. In all of the experiments reported in this paper, 304 stainless steel balls 6.35 mm in diameter and having a sphericity of 5.08 mμ were used. Data for the onset of convection and convective heat transfer were obtained for particulate bed depths of 26 mm ($d/L \simeq 0.244$) and 52 mm ($d/L \simeq 0.122$), while the depth of the liquid layer overlying the bed was varied parametrically from 0 to 209 mm.

Apparatus and Procedure. A schematic diagram of the test cell used in this study is shown in Fig. 1. The particulate bed was formed in a 104 mm ID pyrex glass jar. The pyrex jar was insulated on the outside with a thick layer of ginned cotton. Five 2.5 mm dia holes, equally spaced along the diameter, were drilled in the base of the jar. Thirty-gauge chromel-alumel thermocouples were passed through these holes and pasted to the bottom surface of the jar with epoxy resin. The glass jar was supported on a 20 mm thick plexiglas block. Induction heating of the particles was achieved by placing a 10 turn, 210 mm ID work coil around the jar, and connecting the coil to a 10 kW, 453 kHz radio frequency generator. The work coil was made of a 4.75 mm OD copper tube. In order to obtain uniform heating of the particulate bed, constant clearance ($\simeq$2 mm) was maintained between different turns of the coil by holding it in a plexiglas fixture.

The surface of the liquid layer overlying the bed was maintained at a constant temperature by a 6 mm thick copper plate, forming the base of a cylindrical chamber 103 mm in diameter and 40 mm in height. Tap water was circulated through this chamber. The surface of the copper plate touching the layer of liquid was finely polished, while the chamber side surface had fins to increase the heat transfer area between the plate and the cooling water. Six 30 gauge chromel-alumel thermocouples were embedded on the surface of the cooling plate at different radii and angular positions. These thermocouples, together with three other similar thermocouples used to determine the temperature at the interface between the particulate bed and the liquid layer, were carried through three sleeves passing through the cooling chamber. The thermocouple outputs, after passing through a selector switch and a filter to eliminate radio-frequency noise [15], were read on a Houston X-Y recorder.

Prior to each experiment, the particles and the glass jar were thoroughly washed with acetone. The jar and particles were then dried, the glass jar weighed, and the particles were added to the desired depth in the jar. The glass jar was weighed again, and the weight and depth information were used to determine the porosity of the bed. The porosity of all particulate beds studied in this work was about 0.39, and the maximum error in determining the porosity is expected to be less than ±2.5 percent. Calibration of the rate of heat generation in the particulate bed as a function of the fractional power output of the radio frequency generator was made for each bed depth. For the calibration runs, the particulate bed was saturated with distilled water; starting with the bed at an equilibrium reference temperature and a certain power input to the work coil, the temperature at one of the locations in the bed was recorded until the water started to boil. Knowing the rate of temperature increase, the thermal capacity, and the volume of the bed (particles and water), the heat generation rate per unit volume of the bed could be determined. The rate of temperature increase at various locations in the bed did not show a dif-

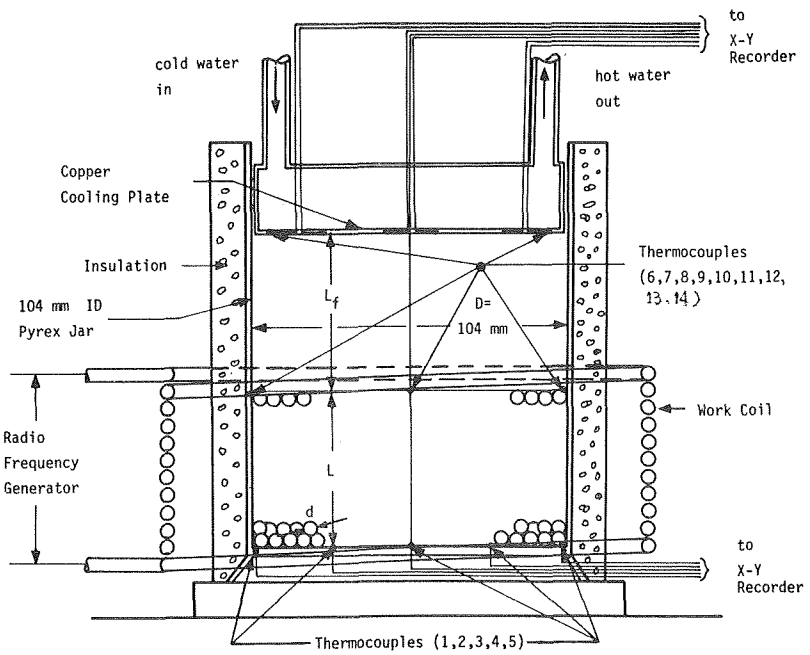

Fig. 1 A schematic diagram of the experimental set-up

ference of more than ±5 percent. In calculating the volumetric heating rate, a mean value of three horizontal and two vertical locations was taken. Complete experimental details are given by Rhee [16].

After the calibration, more distilled water was added to make an overlying liquid layer of about the desired depth. The work coil was then energized and the water was deaerated by boiling it for more than 20 min. Deaeration of the water was done to preclude the possibility of any air pockets in the bed. thereafter, the power was turned off, and the particulate bed and overlying layer were allowed to cool. The cooling chamber was then lowered into the glass jar and gently pressed against the top of the particulate bed to smooth out the interface, which might have been disturbed during deaeration. Thereafter, the cooling chamber was moved to the desired height and firmly fixed with clamps. Finally, the positions of the thermocouples at the interface between the particulate bed and the liquid layer were adjusted, and the particulate bed and liquid layer were allowed to attain thermal equilibrium.

Starting with the bed in a static equilibrium state, the radio frequency generator was switched on and a desired power applied to the work coil. The temperature of one of the thermocouples at the base of the particulate bed was recorded on the X-Y recorder. Initially, the temperature was found to increase linearly, but later the rate of temperature increase started to fall off asymptotically as steady state was approached. If the heat generation rate in the bed was such that the internal Rayleigh number was greater than the critical Rayleigh number, the temperature in the asymptotic range started to fluctuate with time. These fluctuations were an indication that fluid motion within the bed had begun. Usually, temperature at one of the locations at the base of the particulate bed was monitored for about 15 minutes to insure that pseudo-steady state had been established. Thereafter, temperature at other locations at the base of the particulate bed, at the particulate bed-liquid layer-interface and at the cooling plate were monitored one at a time for a span of about five minutes. The fluctuations in the pseudo-steady state temperatures possessed a certain characteristic frequency and amplitude. Overall it took one to three hours to reach steady state in the porous layer after the work coil was energized. This time is of the same order as reported earlier by Kulacki and Goldstein [10]. When the heat generation rate in the bed was such that heat was transferred by pure conduction, no oscillations in temperature were observed when a steady state was achieved.

After noting the steady state temperature shapes at various locations, the power was turned off, the system was allowed to come to a static equilibrium state, and the above procedure was repeated for different power inputs and/or for different depths of the overlying liquid layer.

Data Reduction. Generally, a five-minute time-averaged temperature was obtained from the temperature-time traces. These temperatures were then used to calculate a mean temperature for the surface of interest. For the average temperatures of bottom and interface, an area-weighted temperature of different thermocouples placed symmetrically about the axis was taken. However, for the cooling plate, an arithmetically averaged temperature was chosen as the mean temperature, because the maximum temperature difference between extreme observations was relatively small. Also, as the thermocouples on the cooling plate were placed at different radii and angular positions, the extra effort needed to obtain area-averaged temperatures was not seen to yield any significantly better information. For the most severe conditions studied in the present experiments, when the maximum temperature in the particulate bed was only a few degrees below the saturation temperature, the maximum deviation in the cooling plate temperatures was +3.6, −4.1 K, while similar values for the interface and bottom surface were +9.8, −7.5 K and +8.3, −4.8 K, respectively.

For the thermophysical properties required to evaluate the Nusselt and Rayleigh numbers of the overlying liquid layer, the mean of the top cooling plate and the particulate bed-liquid layer interface temperatures was chosen as a reference temperature. For the particulate bed, the average of the bottom and the interface temperatures was chosen as the reference temperature.

Results

A total of 27 observations for convective heat transfer in volumetrically heated particulate beds with nearly insulated boundaries, and with an overlying layer of liquid cooled at the top, were made. Out of these, five observations fell within the region where conduction was the sole mechanism of heat transfer in the porous layer. Data for the overlying liquid layer depth-to-particulate bed depth ratios, η, of 0, 0.21, 1.0, and 3.38 were taken, where the bed depth was 54 mm (L/D = 0.5), while data for η = 8.04 were taken with a bed depth of 26 mm (L/D = 0.25). These data are tabulated in reference [16].

The dimensionless rate of heat transfer from the bed was based on the temperature difference between the bottom of the bed and the particulate bed-liquid layer interface, and is defined as:

$$\mathrm{Nu} \equiv \frac{Q_v L^2}{2k_m(T_B - T_M)} \tag{7}$$

In equation (7) the conductivity, k_m, of the mixture is based on the volume-averaged conductivity of the steel and water in the particulate bed. The internal Rayleigh number in the bed is defined as:

$$\mathrm{R}_I \equiv \frac{k_f g \beta_f Q_v L^3 P}{2k_m{}^2 \alpha_f \nu_f} \tag{8}$$

while the external Rayleigh number, R_E, is defined in the same manner as suggested by Katto and Masuoka [5] and given by equation (2). The Nusselt number for the liquid layer is based on the temperature difference between the particulate bed-liquid layer interface and the copper plate, and is defined as:

$$\mathrm{Nu}_f \equiv \frac{Q_v L L_f}{k_f(T_M - T_T)} \tag{9}$$

The Rayleigh number for the liquid layer is defined in the conventional manner. The uncertainties in the evaluation of the Nusselt and the internal Rayleigh numbers for the bed are within ±7.1 percent and ±10.5 percent, respectively. Similar values for the Nusselt and Rayleigh numbers for the liquid layer are ±6.2 percent and ±6.1 percent, respectively.

Onset of Natural Convection and Heat Transfer. Fig. 2 shows the dependence of the dimensionless heat transfer on the internal Rayleigh number of the bed for different values of η. The data for η = 0 are about 5–10 percent lower than Sun's [8] and Buretta and Berman's [7] heat transfer correlation, equations (6b) and (6c). This is within the uncertainty of the present data as well as those of Sun, and Buretta and Berman. However, the dependence of the Nusselt number on the internal Rayleigh number is about the same as reported by Hardee and Nilson [14], Sun, and Buretta and Berman. The critical Rayleigh number, obtained by noting the intercept on the abscissa (Nu = 1) of a straight line drawn through the data points, shows the critical Rayleigh number to be about 46. The values of R_{Ic} in references [7, 8, 14], where Joule heating of the liquid in the presence of glass or sand particles was employed, were reported to be about

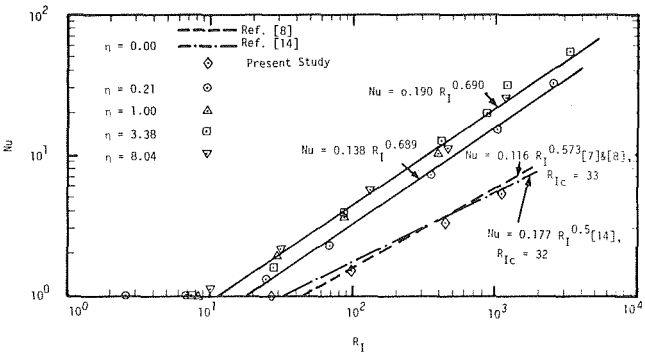

Fig. 2 Dependence of particulate bed heat transfer on internal Rayleigh number and dimensionless liquid layer depth

33. The higher value of R_{Ic} obtained from extrapolation of the present data is not thought to be due to the bottom surface of the test cell not acting as a perfectly insulated surface. The maximum heat loss from the bottom of the test cell is expected to be less than 0.7 watts or 0.3 percent of the heat generated in the particulate bed. The conductance of the bottom of the cell is calculated to be 1 $W/m^2 - K$ (Biot number $\simeq$ 10), which is too small to be of any significance. However, the probable cause of the higher R_{Ic} could be the additional resistance to transfer of heat from the particles to the coolant. The thermal conductivity of steel particles is about 20 times higher than that of water; the steel particles thus can be considered to be isothermal relative to a water layer of depth equal to the diameter of the sphere. For a given temperature drop across the liquid layer, local heat transfer from the particles to the thermal layer would depend on the nature of flow around the particles. Use of volume averaged thermal conductivity is justified when there is no fluid motion in the particulate bed, however at the onset of convection, the thermal resistance at the surface of the particles may result in a slightly higher temperature drop across the bed. In all of the Joule heating studies [7, 8, 14], the thermal conductivity of the glass or sand particles used was about the same as that of the coolant. The particles thus acted only as hydraulic resistances and were thermally inactive. The volume-averaged thermal conductivity of these porous layers under conditions of simple conduction would not differ much from natural convection conditions. The data of Katto and Masuoka [5] for the onset of convection in bottom heated particulate beds also indicate that the critical Rayleigh number with steel and aluminum balls was invariably higher than with glass balls. Thus, it would seem that dependent on the relative conductivities of the coolant and the particles, some variations in R_{Ic} are possible when the critical Rayleigh number is obtained by extrapolating the natural convection data.

For a volumetrically heated particulate bed having upper boundary as a free surface and the lower boundary as a rigid surface, Gasser and Kazimi's [13] analysis showed that for external Rayleigh number less than 40, the critical internal Rayleigh number could be a double valued function of R_E. The higher value of critical internal Rayleigh number occurred when the free surface temperature was greater than the bottom temperature. In the present work, the boundary conditions are different than those treated in reference [13] and external Rayleigh number cannot be varied independently of internal Rayleigh number and vice versa. By definition of Nusselt number, the external and internal Rayleigh number are equal at the onset of convection. Although obtained under different boundary conditions, it is surprising to note that for no liquid layer at the top and particulate bed bottom temperature greater than the free surface temperature, the critical internal Rayleigh number given in reference [13] is about 40 when the external Rayleigh number is also about 40.

The heat transfer is seen to increase by about threefold when a liquid layer of about one fifth of the bed depth lies over the particulate bed. The rate at which the heat transfer increases with R_I also increases as the depth of the liquid layer increases. As η increases to one, further improvement in heat transfer is observed. But the data for η = 3.38 and 8.04 merely overlap the data for η = 1. This means that no further improvement in heat transfer is realized for η greater than one. The heat transfer data for η = 0.21 is correlated within ±10 percent as:

$$\mathrm{Nu} = 0.138\ \mathrm{R}_I{}^{0.689} \qquad \text{for } \eta = 0.21 \tag{10}$$

while the data for all other values of η are correlated within ±26 percent as:

$$\mathrm{Nu} = 0.190\ \mathrm{R}_I{}^{0.690} \qquad \text{for } \eta \geq 1. \tag{11}$$

The heat transfer given by equation (11) is about four times higher than the heat transfer observed by Sun and Buretta and Berman when no liquid layer is present over the bed. In other words, the convective motion in the overlying liquid helps to remove more heat from the bed. Later on we will discuss the liquid layer heat transfer further.

The critical internal Rayleigh number is plotted as a function of η in Fig. 3. It is noted that the Rayleigh number at the onset of convective motion in the bed decreases rapidly as η is increased to one. Thereafter, no further reduction is observed and the critical Rayleigh number reaches an asymptotic value of about 12; i.e.,

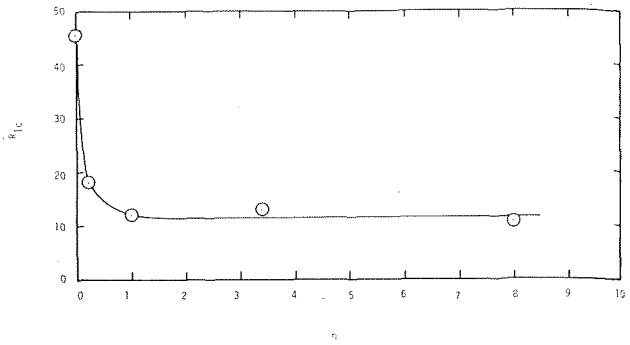

Fig. 3 Influence of η on internal Rayleigh number at the onset of convection in the bed

$$R_{Ic} \simeq 12 \qquad \text{for } \eta \geq 1. \tag{12}$$

These results indicate that the convective motion in the overlying layer of liquid tends to destabilize the fluid in the bed at lower volumetric heat generation rates than are required for destabilization without the layer.

The Nusselt number of the overlying liquid layer is plotted in Fig. 4 as a function of the liquid layer Rayleigh number, R_f. In this Fig., the general correlation of Hollands, et al. [17], for natural convection between two parallel plates, is also plotted. It is observed that the present data for the liquid layer, in which the boundary layer at the particulate bed-liquid layer interface is disrupted because of the inflow and outflow of liquid to and from the porous bed, is about 2.5 to 3 times higher than for a liquid layer bounded between two rigid walls. However, the functional dependence of the Nusselt number on the Rayleigh number is about the same as for Bénard convection between two parallel plates. The heat transfer data for the liquid layer can be divided into two groups. For the laminar range ($10^4 < R_f < 4.0 \times 10^6$), the heat transfer data are correlated within ±28 percent by:

$$\mathrm{Nu}_f = 0.715\ R_f{}^{0.248} \qquad \text{for } 10^4 < R_f < 4.0 \times 10^6 \tag{13}$$

In the turbulent region the data are, within ±33 percent, represented by:

$$\mathrm{Nu}_f = 0.234\ R_f{}^{0.307} \qquad \text{for } 5 \times 10^7 < R_f < 3.5 \times 10^{10} \tag{14}$$

The region of transition from laminar to tubulent flow is seen to lie between the Rayleigh numbers of 4×10^6 and 5×10^7. The transition region is, again, about the same as has been observed for natural convection between two parallel plates [18].

The coupling of the heat transfer across the layer of liquid with the internal heat generation rate in the particulate bed is shown in Fig. 5. Here, the Nusselt number of the layer is plotted as a function of R_I for different values of η. For η = 0.21 and 1.0, the convective motion in the liquid layer is laminar, and in transition region and heat transfer is seen to increase as $R_I{}^{0.2}$. The Rayleigh number of the layer for η = 3.38 is in the turbulent range, and the heat transfer is seen to increase as $R_I{}^{0.25}$. The data for η = 8.04, also in the turbulent range, show a slightly higher dependence ($R_I{}^{0.26}$) on R_I. The higher slope for η = 8.04 arises because of the low value of Nu_f observed at $R_I \simeq 10$. This Rayleigh number is close to the onset of convection in the bed; also, the particulate bed is much shallower for η = 8.04 (d/L = 0.244). It is possible that initially the flow is affected by the proximity of the rigid wall to the liquid layer-particulate bed interface. For all of the data plotted in Fig. 5, it is observed that the cooling plate temperature remains nearly constant (289 ± 4 K). This implies that the particulate bed interface temperature increases as $Q_v{}^{4/5}$ or $Q_v{}^{3/4}$, depending on whether the flow in the upper layer is laminar or turbulent, respectively.

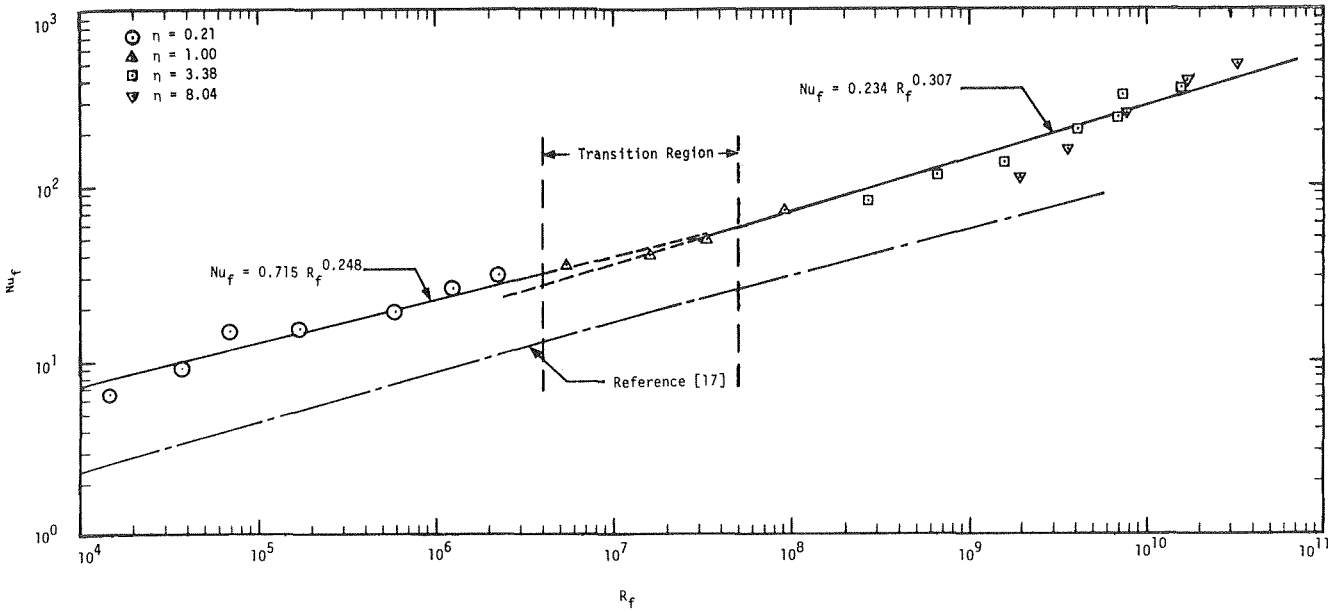

Fig. 4 Correlation of overlying liquid layer heat transfer data

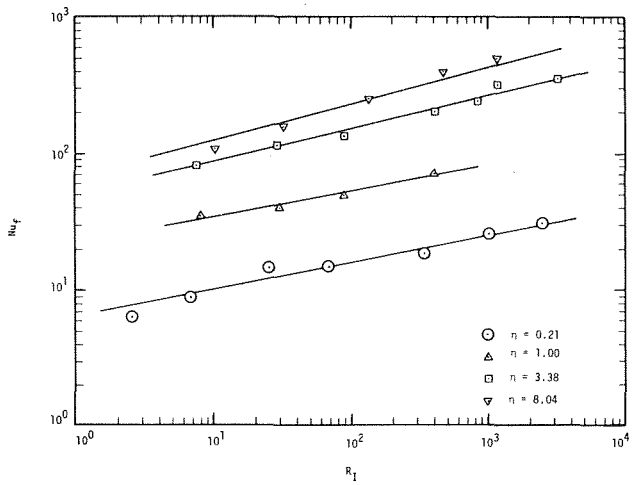

Fig. 5 Dependence of liquid layer heat transfer on internal Rayleigh number of the bed

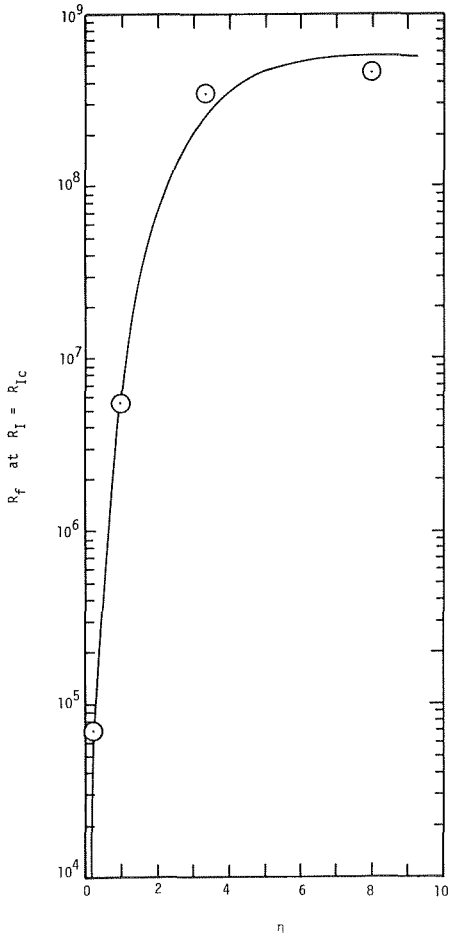

Fig. 6 Variation of overlying liquid layer Rayleigh number with η at the time of onset of convection in the bed

Knowing the Nusselt number of the liquid layer at R_{Ic} from Fig. 5, the Rayleigh number of the liquid layer at the onset of convection in the particulate bed is obtained from Fig. 4. These data are plotted in Fig. 6 as a function of η. The liquid layer Rayleigh number at the incipience of convection in the bed increases very sharply as η is increased from zero to two, but thereafter R_f reaches an asymptotic value of about 5.5×10^8. Fig. 6 shows that for all of the values of η studied in the present work, convective motion already exists in the liquid layer while conduction is still the mechanism of heat transfer in the particulate bed. As the overlying liquid layer has access to the particulate bed, the convective motion in the overlying layer tends to induce motion in the fluid saturating the pores of the particulate bed. The motion of the fluid in the overlying layer becomes more vigorous as η is increased and will tend to destabilize the liquid at lower heat generation rates; it will also tend to enhance the heat removal from the bed. This is exactly the trend observed in Fig. 2 and 3. As η is increased to about two, R_f corresponds to a fully developed turbulent convective motion in the liquid layer, and no further advantage either in terms of a reduction in R_{Ic} or an increase in the Nusselt number of the bed is realized by increasing η further. The asymptotic nature of R_f at the onset of convection in the bed is consistent with the similar behavior of R_{Ic} as η is increased beyond one.

Fluid Flow Pattern and the Temperature Distribution in the Particulate Bed. The thermocouple readings for the temperatures across the particulate bed-liquid layer interface and at the bottom of the particulate bed indicate that liquid generally enters the bed on the sides and exits from the central portion of the bed. However, in two observations for $\eta = 0.21$ and 3.38, when the heat generation rate in the particulate bed was such that R_I was close to R_{Ic}, the thermocouple readings indicated that the liquid entered on one side of the bed and left from the other side. As the volumetric heating of the bed was increased, the one-cell mode of convection shifted to a two-cell mode. These observations still need to be confirmed with visual observations.

As pointed out earlier, the steady state temperature at a particular location in the bed or the overlying liquid layer fluctuated with time. These fluctuations were quite regular and slow at the base plate of the particulate bed, but were random and faster at the particulate bed-liquid layer interface and the top cooling plate. The frequency of the oscillations in temperature at the center of the particulate bed base plate is listed in Table 1 for various values of η and R_I. It is observed that the frequency tends to increase with R_I and η. This is indicative of the close relationship between the vigor of the fluid motion in the bed and the oscillations in the local temperatures. The temperature distribution at the centerline of the particulate bed and the liquid layer when $\eta = 1$, the depth of the particulate bed is 52 mm, $R_I = 403$, and $R_f = 9.3 \times 10^7$, is shown in Fig. 7. The upper and lower bounds observed for the local temperature during a time period of five min are also marked in Fig. 7. The bottom of the particulate bed is observed to behave as an insulated surface, whereas the maximum temperature occurs near the middle of the bed. The thermal boundary layers at the particulate bed-liquid layer interface and at the cooling plate are quite thin, though precise temperature profiles in the boundary layers were not determined because better instrumentation would be needed to measure at the small distances involved. The temperature in the bulk of the liquid layer is observed to remain fairly constant.

The dimensionless maximum temperatures in the particulate bed, noted from temperature profiles at the centerline of the test cell (similar to the one shown in Fig. 7), are plotted in Fig. 8 for various values of η and R_I. The data of Fig. 8 show that for $\eta = 0.21$ and 1.0, when the motion in the overlying layer of liquid is laminar in nature, an increase in R_I causes the maximum temperature in the bed to increase also. However, for $\eta = 3.38$, an increase in R_I is seen to result in a slightly lower maximum temperature. It is postulated that the highly turbulent nature of the overlying layer of liquid for $\eta \geq 3.38$ and $R_I > R_{Ic}$ tends to induce motion deep enough into the particulate bed to lower the maximum temperature.

Conclusions

- The onset of natural convection and heat transfer in volumetrically heated particulate beds having finite overlying liquid layers has been observed.
- The presence of an overlying liquid layer tends to destabilize the fluid in the particulate bed at lower heat generation rates than would be required to destabilize a bed without liquid above it. For liquid layer depth-to-bed depth ratios, η, greater than one, natural convection is observed to occur at

$$R_{Ic} \simeq 12 \qquad \text{for } \eta \geq 1$$

- The presence of an overlying layer of liquid tends to enhance the transfer of heat from the particulate bed. The heat transfer data for $\eta \geq 1$ are correlated by

$$\text{Nu} = 0.190\, R_I^{0.690} \qquad \text{for } \eta \geq 1$$

- The heat transfer capacity of the overlying layer of liquid is considerably enhanced because of the inflow and outflow of liquid to and from the particulate bed. The heat transfer data for the liquid layer when an inductively heated porous bed, of permeability 4.2×10^{-2} mm^2, lies underneath, are correlated by

$$\text{Nu}_f = 0.715\, R_f^{0.248} \qquad \text{for laminar flow}$$

and

$$\text{Nu}_f = 0.234\, R_f^{0.307} \qquad \text{for turbulent flow.}$$

The transition from laminar to turbulent flow was observed to occur for R_f of between 4×10^6 and 5×10^7.

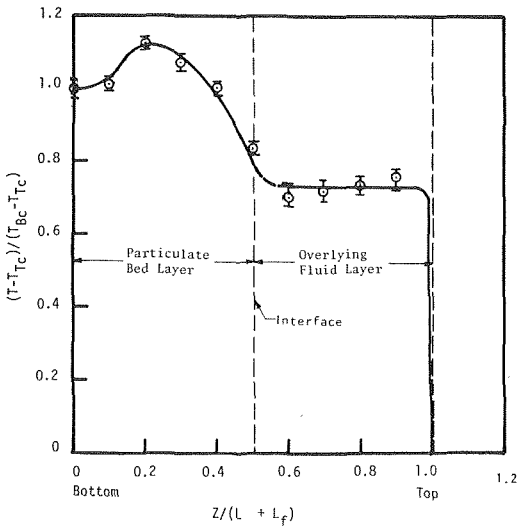

Fig. 7 Temperature profile at the center line of test cell for $\eta = 1$ and $Q_v = 0.4447$ W/cm^3, $R_f = 9.3 \times 10^8$, $R_I = 403$

Table 1 Frequency of oscillations in the temperature at the center of the base of the particulate bed

η	R_I	f (Hz $\times 10^3$)
0.21	69	1.667
	347	2.381
	1,030	3.849
	2,510	7.680
1.00	89	1.922
	403	3.333
3.38	89	3.030
	410	4.762
	1,200	6.173
	3,250	8.333
8.04	32	3.333
	134	5.051
	468	9.804
	1,180	11.905

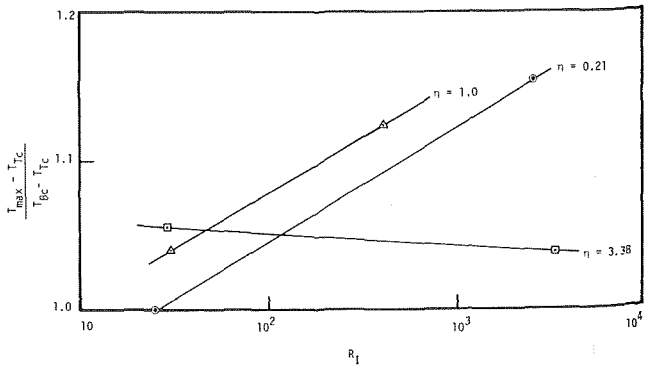

Fig. 8 Dependence of maximum temperature at the center of the test cell on R_I and η

References

1 Horton, C. W., and Rogers, Jr., F. T., "Convective Currents in a Porous Medium," *Journal Applied Physics*, Vol. 16, 1945, pp. 367–370.

2 Lapwood, E. R., "Convection of Fluid in a Porous Medium," *Proc. Camb. Phil. Soc.*, Vol. 44, 1948, pp. 508–521.

3 Leva, M., *Fluidization*, McGraw-Hill, New York, 1959.

4 Morrison, H. L., Rogers, F. T., and Horton, C. W., "Convective Currents in Porous Media, II: Observations of Conditions at Onset of Convections," *Journal Applied Physics*, Vol. 20, 1949, pp. 1027–1029.

5 Katto, Y., and Masuoka, T., "Criterion for the Onset of Convective Flow in a Fluid in a Porous Medium," *International Journal Heat Mass Transfer*, Vol. 10, 1967, pp. 297–309.

6 Gupta, V. P., and Joseph, D. D., "Bounds for Heat Transport in a Porous Layer," *Journal Fluid Mech.*, Vol. 57, Part 3, 1973, pp. 491–514.

7 Buretta, R. J., and Berman, A. S., "Convective Heat Transfer in a Liquid Saturated Porous Layer," ASME *Journal of Applied Mechanics*, Vol. 43, No. 2, 1976.

8 Sun, W. J., "Convective Instability in Superposed Porous and Free Layers," Ph.D. Dissertation, University of Minnesota, 1973.

9 Sparrow, E. M., Goldstein, R. J., and Jonsson, V. K., "Thermal Instability in a Horizontal Fluid Layer: Effect of Boundary Conditions and Non-Linear Temperature Profile," *Journal Fluid Mechanics*, Vol. 18, 1969, pp. 513–528.

10 Kulacki, F. A., and Goldstein, R. J., "Thermal Convection in a Horizontal Fluid Layer with Uniform Volumetric Energy Sources," *Journal Fluid Mechanics*, Vol. 55, Part 2, 1972, pp. 271–287.

11 Jahn, M., and Reineke, H., "Free Convection Heat Transfer with Internal Heat Sources—Calculations and Measurements," *Proceedings 5th International Heat Transfer Conference*, Vol. III, Nos. 2–8, Tokyo, 1974.

12 Suo-Anttila, A. J., and Catton, I., "The Effect of Stabilizing Temperature Gradient on Heat Transfer from a Molten Fuel Layer with Volumetric Heating," ASME Paper No. 74 WA/HT-45, 1974.

13 Gasser, R. D., and Kazimi, M. S., "Onset of Convection in a Porous Medium with Internal Heat Generation," ASME JOURNAL OF HEAT TRANSFER, Vol. 98, No. 1, 1976, pp. 49–54.

14 Hardee, H. C., and Nilson, R. H., "Heat Transfer Regimes and Dryout in a Porous Bed of Fuel Debris," *Nuclear Science and Engineering*, Vol. 63, No. 2, 1977.

15 Dhir, V. K., and Catton, I., "Dryout Heat Fluxes for Inductively Heated Particulate Beds," ASME JOURNAL OF HEAT TRANSFER, Vol. 99, No. 2, 1977.

16 Rhee, S. J., "Convective Heat Transfer in Beds of Inductively Heated Particles," M.S. in Engineering, University of California, Los Angeles, June 1977.

17 Hollands, K. G. T., Raithby, G. D., and Konicek, L., "Correlation Equations for Free Convection Heat Transfer in Horizontal Layers of Air and Water," *Internal Journal Heat Mass Transfer*, Vol. 18, Nos. 7–8, 1975, pp. 879–884.

18 Catton, I., "Natural Convection in Horizontal Liquid Layers," *Physics of Fluids*, Vol. 19, 1966, pp. 2522–2522.

R. Greif

Department of Mechanical Engineering,
University of California,
Berkeley, Calif.

An Experimental and Theoretical Study of Heat Transfer in Vertical Tube Flows

An experimental and theoretical study was carried out for the heat transfer in laminar and turbulent tube flows with air and argon. Radial temperature profiles were measured at a location 108 tube diameters from the inlet of the vertical, electrically heated test section. The temperature of the tube wall was also measured. The experimental data were in good agreement with the results obtained from numerical solutions of the conservation equations and from simplified, fully developed solutions. For turbulent flows the Reynolds numbers varied from 10,000 to 19,500; for laminar flows the Reynolds numbers varied from 1850 to 2100 while the Rayleigh numbers varied from 70 to 80.

Introduction

The present work is a study of the heat transfer to a gas flowing in a vertical tube (cf. Donovan [15][1]). Measurements have been made with air and argon in both turbulent flow and in laminar flow. Theoretical results have been obtained from numerical solutions of the conservation equations as well as from solutions of simplified formulations for both turbulent and laminar flows.

The determination of the heat transfer in turbulent pipe flows has been the subject of many investigations and comprehensive reviews and bibliographies are available which provide a summary of results. The present work on turbulent flows therefore serves as a check on the experimental system and also gives a basis for appraising models for turbulent transport by direct comparison with the measured gas temperature profiles. Experimental results were obtained over a range of Reynolds numbers varying from about 10,000 to 19,500.

Measurements of gas temperature profiles were also made in laminar flows for Reynolds numbers varying from 1850 to 2100 and for Rayleigh numbers varying from 70 to 80. Comparisons with theoretical predictions were made and over the range of conditions tested the importance of natural convection was clearly demonstrated.

Basic Equations

The flows investigated in this study are two dimensional, steady and take place in a tube that is electrically heated and suspended in the vertical direction. The governing equations for the conservation of momentum in the axial (vertical) direction and the conservation of energy are given by

$$\rho u \frac{\partial u}{\partial X} + \rho v \frac{\partial u}{\partial r} = \frac{1}{r}\frac{\partial}{\partial r}\left[r\mu_{eff}\frac{\partial u}{\partial r}\right] - \rho g - \frac{dP}{dX} \tag{1a}$$

$$\rho u \frac{\partial H}{\partial X} + \rho v \frac{\partial H}{\partial r} = \frac{1}{r}\frac{\partial}{\partial r}\left\{\frac{r\mu_{eff}}{\mathrm{Pr}_{eff}}\left[\frac{\partial H}{\partial r} + (\mathrm{Pr}_{eff} - 1)u^2\right]\right\} \tag{1b}$$

These equations are valid for laminar or turbulent flow; in the former case the subscript, *eff*, is dropped and the resulting variables then correspond to the usual molecular transport quantities (cf. equations (2) and (4)). The conserva tion equations, including the conservation of mass, were solved numerically using the method of Spalding and Patankar [1]. The particular program used in this study is specified in detail by Mason [2] (cf. Donovan [15]) and will not be repeated here. For completeness it is noted that H is the total enthalpy.

For turbulent flow we take

$$\mu_{eff} = \mu + \mu_T = \mu + \rho\ell^2\left|\frac{\partial u}{\partial r}\right| \tag{2}$$

in conjunction with the following relations for the mixing length:

$$\ell' = K(r_0 - r) \quad \text{for} \quad K(r_0 - r) < \lambda r_0 \tag{3a}$$

$$\ell' = \lambda r_0 \quad \text{for} \quad K(r_0 - r) > \lambda r_0, \tag{3b}$$

along with the van Driest damping factor [3] given by

$$\ell = \ell'[1 - \exp\{-(r_0 - r)(\tau_w/\rho)^{1/2}/\nu A^*\}] \tag{3c}$$

with $K = 0.44$, $\lambda = 0.09$, and $A^* = 26$. For the effective thermal conductivity we similarly take $k_{eff} = k + k_T$ so that

$$\mathrm{Pr}_{eff} \equiv \frac{\mu_{eff}c_p}{k_{eff}} = \frac{(\mu_{eff}/\mu)\mathrm{Pr}}{1 + \left(\frac{\mu_{eff}}{\mu} - 1\right)\frac{\mathrm{Pr}}{\mathrm{Pr}_T}} \tag{4}$$

In our calculations the turbulent Prandtl number, Pr_T, has been set equal to 0.9.

[1] Numbers in brackets designate References at end of paper.

Contributed by the Heat Transfer Division for publication in the JOURNAL OF HEAT TRANSFER. Manuscript received by the Heat Transfer Division January 3, 1977.

For the turbulent flow calculations the initial condition for the axial velocity was specified as being uniform from the center of the pipe to the position $r = 0.9\, r_0$. Over the interval $0.9\, r_0 \leq r \leq r_0$ a parabolic velocity profile was used. The numerical values for the initial velocity profile were chosen to agree with the measured mass flow rate according to the relation:

$$\dot{m} = 2\pi\rho_0 \int_0^{r_0} urdr \tag{5}$$

The inlet density, ρ_0, was obtained from the inlet temperature, T_0, and the inlet pressure, P_0. The boundary condition at the tube wall was that of zero velocity and specified heat flux.

For the laminar flow problem the turbulent transport terms were omitted. The only other change is that the initial velocity profile was taken to be a parabola consistent with the measured values of the mass flow rate.

In addition to the numerical solutions of the complete basic equations, that is, equations (1*a*) and (1*b*), simplified analyses and results have also been used for both the turbulent flow and laminar flow problems. In turbulent flow, the well-known results of Deissler and Eian [4] for fully developed conditions provide a simple, direct basis for comparison with both the experimental data and the more complete calculations, and will be discussed in a later section. A simplified theoretical determination of the heat transfer may also be made for internal laminar forced flows with buoyancy effects (cf. Ostrach [5], Hallman [6], Tao [7], and Morton [8]). In these problems the buoyant force, which results from variations in the density, causes a fundamental coupling between the velocity and temperature fields. This coupling requires that the solution for the velocity and temperature fields be carried out simultaneously. References [5–8] simplify the internal laminar convection problem in the vertical direction by assuming a fully developed flow with constant properties except for the density variation in the body force term. The resulting momentum and energy equations are then given by:

$$-\left(\frac{1}{\rho_w}\frac{dp}{dX} + g\right) + \frac{\nu}{r}\frac{d}{dr}\left(\frac{rdu}{dr}\right) - \beta g(T_w - T) = 0 \tag{6a}$$

$$u\frac{\partial T}{\partial X} = \frac{\alpha}{r}\frac{\partial}{\partial r}\left(\frac{r\partial T}{\partial r}\right) \tag{6b}$$

where the subscript, w, refers to wall conditions. Solutions have been obtained for the constant heat flux condition and these results are discussed in a later section.

For completeness we also note the important developing flow studies carried out by Zeldin and Schmidt in air [9] and by Lawrence and Chato in water [10]. These included both experimental and theoretical results. The measurements in air [9] were carried out at a Reynolds number of 500 in a vertical, isothermal tube. A comparison of the experimental and theoretical velocity distributions showed substantial agreement. However, the experimental temperature distributions showed larger radial temperature gradients than were predicted. The measurements in water [10] were carried out at Reynolds numbers varying from 616 to 1232 in a vertical tube with uniform wall heat flux. Good agreement was obtained between the experimental measurements and the theoretical solutions. However, the authors found that the velocity and temperature profiles never became "fully developed" and attributed this to the nonlinear variation of density and viscosity on temperature.

Experimental Apparatus

The experimental test section (cf. Figs. 1 and 2) consists of a vertical inconel steel tube which is 22 ft (6.7 m) long, 0.049 in. (0.124 cm) thick, and 2 in. (5.08 cm) outside diameter. The tube is electrically heated with a 3 phase 440V power supply which is attached to electrodes on both ends. The tube is surrounded by two radiation shields, 10 and 12 in. (25.4 and 30.5 cm) in diameter, which are enclosed in a casing approximately 16 in. (40.6 cm) in diameter. The casing exterior is covered with fiber glass insulation which is 2 in. (5.08 cm) thick. To reduce convection losses from the exterior of the 2 in. (5.08 cm) stainless steel tube, a vacuum pump is used to maintain the casing interior pressure at a value less than 0.1 in. (0.25 cm) of Hg.

Thermocouples are tack welded to the exterior of the test tube at various axial locations (cf. Fig. 2). Several thermocouples are also attached to the exterior of the radiation shields at the test location, $X = 108D$. A thermocouple probe, placed in a 0.125 in. (0.32 cm) OD stainless steel tube and silver soldered to the outside of a 0.75 in. (1.91 cm) OD stainless steel tube is inserted from the upper end of the apparatus to a location 108 diameters from the start of the heated section.[2] This probe may be rotated so that the thermocouple may pass from the pipe center line to the region close to the wall. A perforated radiation shield surrounds the thermocouple. A detailed description of the probe is available [11, 12].

Mass Flow Rate

Laminar Flow. To measure the mass flow rate in laminar flow, the gas line is disconnected from the entrance to the experimental apparatus and connected to a wet test meter. Since the change in head loss caused by disconnecting the gas line from the experimental apparatus and connecting it to the wet test meter is small in comparison to the pressure drop across the needle valves and pressure regulators "upstream," the flow rate may be determined from the relation:

$$\dot{m} = \rho Q \tag{7}$$

The density is evaluated at the ambient temperature and pressure

[2] Inserting and securing the probe a distance of approximately 2.5 ft (0.8 m) from the upper end of the apparatus resulted in a test location $X/D = 108$. This location corresponds to fully developed flow conditions.

Nomenclature

c_p = specific heat
D = diameter
f = friction factor
h = heat transfer coefficient
hD/k = dimensionless heat transfer coefficient, Nusselt number
H = total enthalpy
k = thermal conductivity
ℓ = mixing length
$\dot{m}$ = mass flux
p = pressure
Pr = Prandtl number
q = heat flux
q_{loss} = heat loss from tube
Q = volume flow rate
r = radial coordinate
r_0 = tube radius
r_s = shield radius
$R(T_w)$ = resistance per unit of length
Ra = Rayleigh number = $\beta g r_0^4 (dT_w/dX)/\alpha\nu$
Re = Reynolds number
T = temperature
T^+ = dimensionless temperature = $(T_w - T)c_p\sqrt{\tau_w\rho_w}/q_w$
u = velocity in axial direction
v = velocity in radial direction
X = axial coordinate
y^+ = dimensionless radial coordinate = $(r_0 - r)\sqrt{\tau_w/\rho_w}/\nu_w$
α = thermal diffusivity
β = coefficient of thermal expansion
ϵ = emissivity
ρ = density
τ = shear stress
μ = viscosity

Subscripts

b = bulk condition
eff = molecular plus turbulent
0 = inlet conditions
s = shield
T = turbulent or eddy
w = wall
$108D$ = evaluated at $X/D = 108$

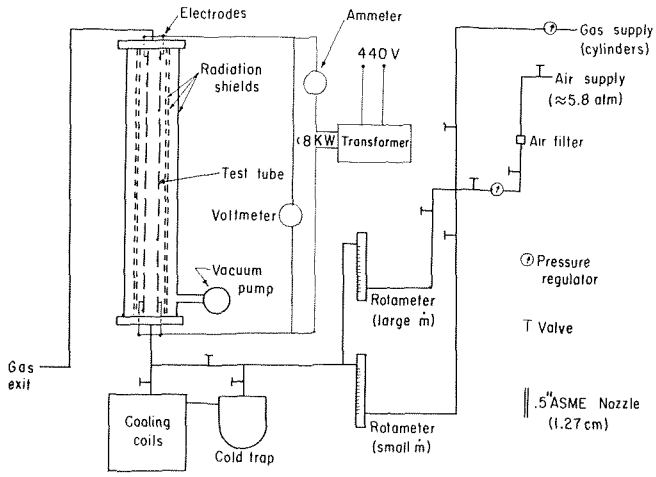

Fig. 1 Experimental apparatus

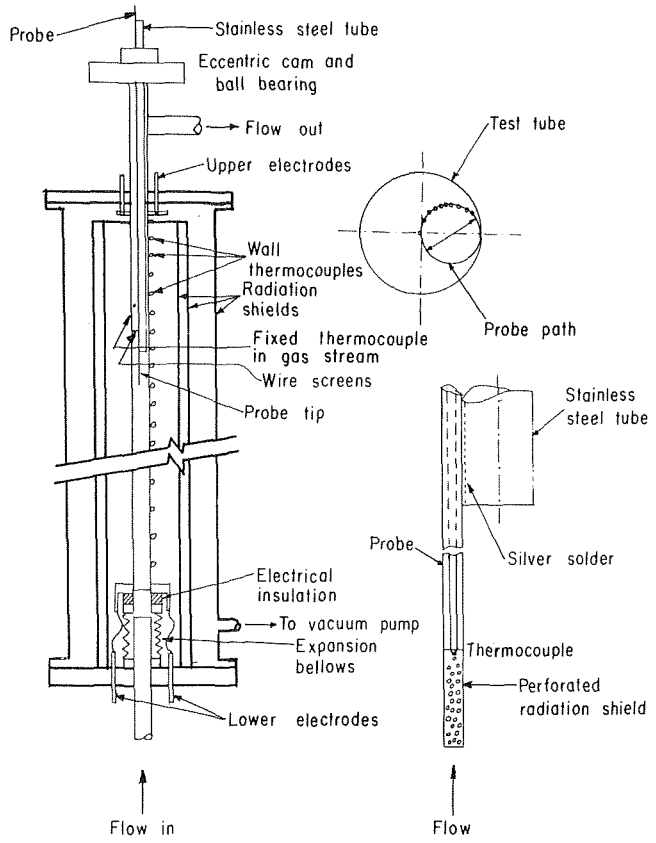

Fig. 2 Test section

since these values are close to the measured values at the inlet to the apparatus.

Turbulent Flow. A standard ASME 0.5 in. (1.27 cm) radius nozzle was used to measure the mass flow rate for the turbulent flow experiments. The static pressure upstream of the orifice was measured with a mercury filled U tube manometer. The temperature upstream of the orifice is measured with a thermocouple in the gas stream. The orifice static pressure drop is measured with a water filled U tube manometer attached to ports in the gas line wall located upstream and downstream of the flow nozzle. The temperature of the gas upstream of the flow nozzle is measured with a thermocouple. These measurements along with the knowledge of the nozzle geometry allow the flow rate to be determined with the use of standard ASME tables [13].

For experiments with air, compressed air is available from a storage tank maintained at 85 psig by a compressor. Other gases, stored in pressurized cylinders, discharge into a manifold connected to a regulator which maintains a constant exit pressure to the gas line at a value between 40 and 60 psig. This line connects with the system upstream of the nozzle in the same manner as the air supply.

Heat Flux. All calculations were made using the constant heat flux boundary condition [15]. The value of the heat flux was obtained experimentally in the following manner. The radiative heat loss from the test section to the adjacent radiation shield was calculated according to the following equation:

$$q_{\text{loss}} = \frac{\sigma(T_w{}^4 - T_s{}^4)}{\frac{1}{\epsilon_w} + \left(\frac{1}{\epsilon_s} - 1\right)\frac{r_0}{r_s}} \tag{8}$$

where the wall and shield temperatures, T_w and T_s, were measured. An energy balance on the tube wall at the test section yields the following equation for the heat flux to the gas:

$$\pi D q_w = [I^2 R(T_w) - \pi D q_{\text{loss}}] \tag{9}$$

The electrical current, I, is measured with a standard a-c ammeter and the electrical resistance of the test section per unit of length, $R(T_w)$, is evaluated at the measured wall temperature.

Bulk Temperature. The bulk temperature, T_b, at the test location, $X/D = 108$, was obtained in the following manner. The measured temperature profile and the theoretical velocity profile were used to calculate the test section bulk temperature, $(T_b)_{108D}$, according to:

$$(T_b)_{108D} = \left.\frac{\int_0^{r_0} \rho u T r dr}{\int_0^{r_0} \rho u r dr}\right|_{108D} \tag{10}$$

The nondimensional heat transfer coefficient, $(hD/K)_{108D}$, is evaluated based upon this value of the bulk temperature according to:

$$\left(\frac{hD}{K}\right)_{108D} = \left.\frac{q_w D}{K(T_w - T_b)}\right|_{108D} \tag{11}$$

An inlet bulk temperature, $(T_b)_0$, is used in the numerical calculation and was determined from the following energy balance:

$$Q_{gen} - Q_{\text{loss}} = \dot{m} c_p [(T_b)_{108D} - (T_b)_0] \tag{12}$$

where

$$Q_{gen} = \int_0^{108D} I^2 R(T_w) dX \tag{12a}$$

and

$$Q_{\text{loss}} = \pi D \int_0^{108D} q_{\text{loss}} dX \tag{12b}$$

Use of this value for the inlet bulk temperature in the calculations insures the equality of the experimental and the theoretical bulk temperatures at the test location.

Results and Discussion

Turbulent Flow

Wall Temperatures. The theoretical wall temperature variation (T_w versus X/D) obtained from the complete numerical calculations using the method of Spalding and Patankar [1] (cf. Mason [2]) is shown in Fig. 3 for several cases which are summarized in Table 1. The excellent agreement between the theoretical and the experimental results for the wall temperature confirms the validity of the constant heat flux assumption that was used in the numerical calculations (cf. Donovan [15]).

Radial Temperature Profiles. Typical radial temperature profiles for both air and argon are presented in Fig. 4. The overall agreement between the theoretical and the experimental results, including the values at the wall, is seen to be very good. Near the center

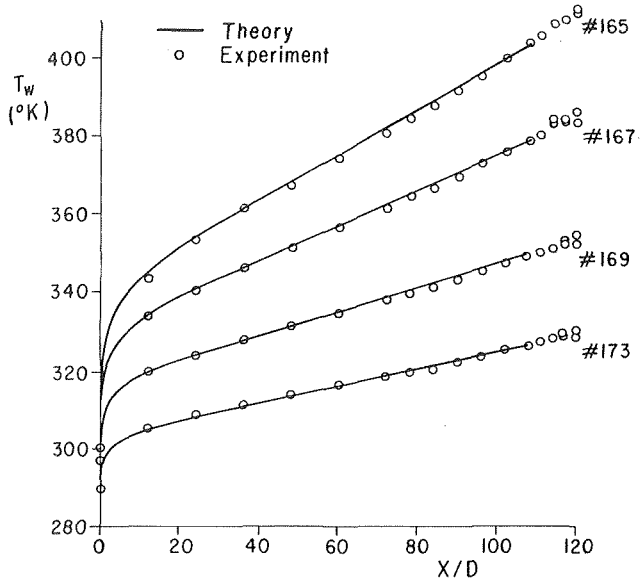

Fig. 3 Experimental and theoretical wall temperatures, turbulent flow (cf. Table 1)

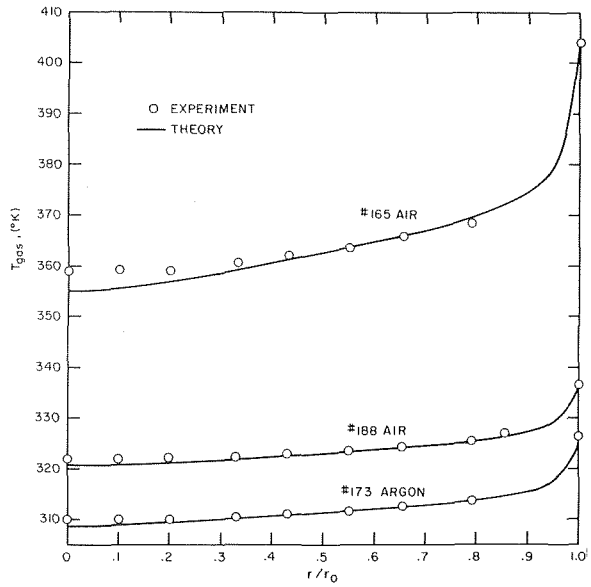

Fig. 4 Temperature profiles in turbulent flow (Runs 165, 173, and 188, cf. Table 1)

line, however, the theoretical temperature profile is not as "flat" as the experimental profile. This is most noticeable in the higher heat flux runs (cf. Fig. 4, run 165) and is believed to be caused by the limitations of the mixing length formulation in this region; i.e., $\mu_T \to 0$ (cf. equation (2)).

The nondimensional temperature profiles resulting from the numerical calculations are also compared in Figs. 5 and 6 with the fully developed, constant property calculations of Deissler and Eian [4] and also with their experimental data. Since the temperature differences are small the constant property assumption should be valid. It can be seen that their data at a Reynolds number of 19,000 are in excellent agreement with the results from the complete numerical calculations except in the region near the pipe center line. This is also consistent with the results of the present experiment as discussed herein.

Of further interest are the data of Deissler and Eian at lower Reynolds numbers (cf. Fig. 6 for a Reynolds number of 10,000). The data no longer agree with the complete numerical calculations. This is in contrast to the present experimental data which are in good

Table 1 Turbulent flow, numerical calculations

Run	Gas	Re	$(hD/k)_{108D}$	Pr	(q_w) (w/m²)
165	Air	17,110	47.9	0.69	1190
167	Air	15,340	44.5	0.69	780
169	Air	19,520	53.0	0.70	630
171	Air	16,510	47.3	0.70	410
172	Air	17,000	48.5	0.70	270
173	Argon	18,490	49.3	0.68	260
185	Air	14,690	43.6	0.70	340
188	Air	9,750	32.8	0.70	230

agreement with the calculations for this same value of the Reynolds number as shown in Fig. 4, run 188. The discrepancy at this Reynolds number between the data of Deissler and Eian and the present data (and with the complete numerical calculations) is probably due to the value they used for the wall shear stress, τ_w. The wall shear stress is required in the determination of the nondimensional variables y^+, T^+, and u^+. The experimental values presented for τ_w, or the friction factor, were obtained from pressure drop measurements which may have been inaccurate at low flow rates [4, p. 37]. For completeness, it is noted that the *calculated* values for the friction factor, both from the present study and from Deissler and Eian, are in good agreement (cf. Fig. 8).

Heat Transfer and Friction Factor. Nondimensional heat transfer coefficients for air calculated for the present experiments are presented in Fig. 7 for various Reynolds numbers. The theoretical results of Deissler and Eian are also presented. The agreement between their results and the present calculations is excellent and this is somewhat surprising in view of the disagreement between the two

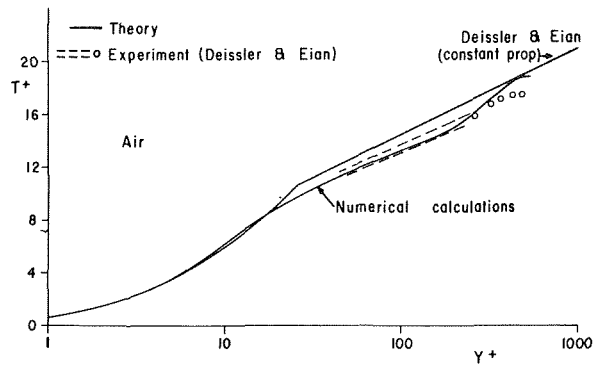

Fig. 5 Nondimensional temperature profile in turbulent flow (Re = 19,000)

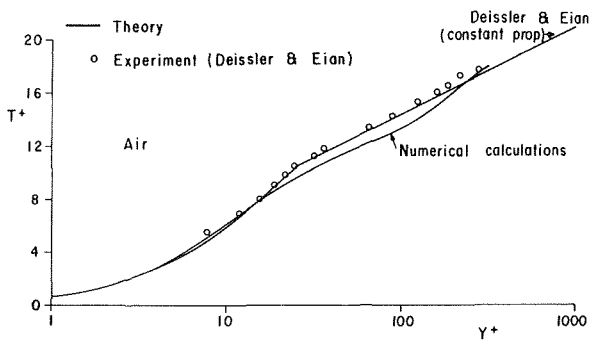

Fig. 6 Nondimensional temperature profile in turbulent flow (Re = 10,000)

theoretical nondimensional temperature profiles (cf. Figs. 5 and 6). The calculated friction factors are given in Fig. 8 along with the theoretical constant property calculations from Deissler and Eian. The agreement is seen to be good as was previously noted. A summary of conditions is presented in Table 1. The maximum value of the ratio of the heat loss to the energy generated is 0.14.

Laminar Flow

Wall Temperatures. Theoretical wall temperature variations obtained from the numerical calculations are shown in Fig. 9 along with the experimental data. The values of the wall temperatures resulting from the calculations are slightly higher than the experimental values. This is because the calculated wall to bulk temperature difference, $T_w - T_b$, is slightly higher than the experimental value. (Recall that the theoretical bulk temperature at the test location, $X = 108D$, is required to be equal to the experimental value.) Note that the experimental and the theoretical wall temperature gradients over the range $60 < X/D < 108$, are in good agreement, thereby giving confidence to the constant heat flux calculation and to the attainment of the fully developed conditions which are part of the simplified analyses (cf. Donovan [15]).

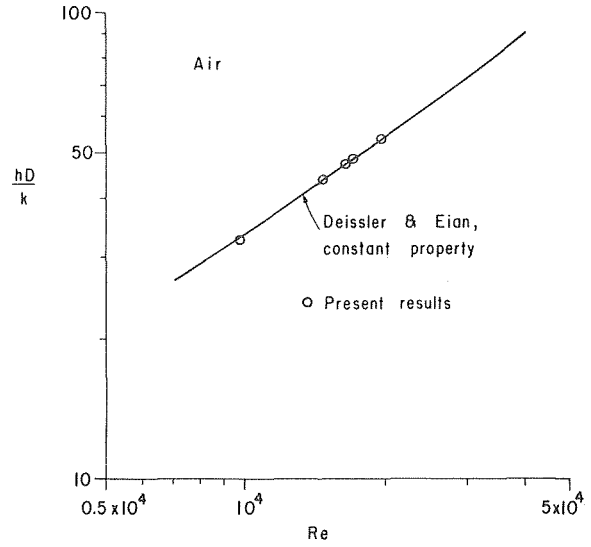

Fig. 7 Nusselt number ($X/D = 108$) versus Reynolds number

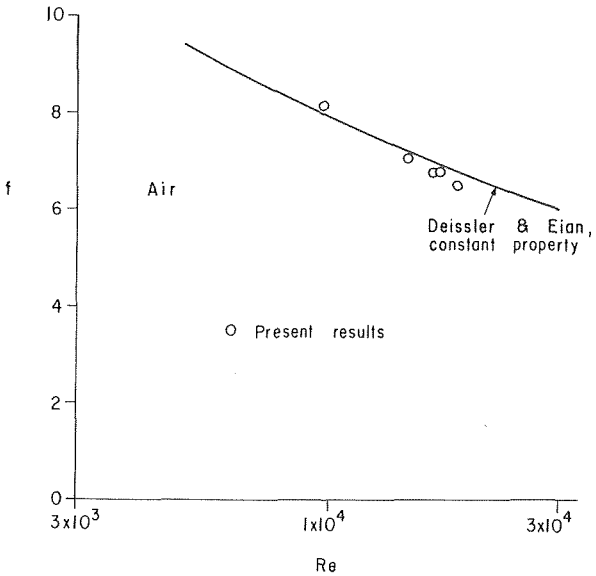

Fig. 8 Friction factor ($X/D = 108$) versus Reynolds number

Simplified Analysis and Complete Numerical Calculations. Typical radial temperature profiles resulting from the simplified analysis and the complete numerical calculations are given in Fig. 10 along with the experimentally measured values. The agreement between the two theoretical calculations is seen to be excellent. It is pointed out that the latter approach includes such effects as variable properties, flow development, and flow acceleration. In the simplified analysis, all transport properties are evaluated at the wall temperature while the numerical calculations do not make this simplification. Variable property effects are small due to the small temperature differences. Tables 2 and 3 contain a summary of results obtained from both methods. The maximum value of the ratio of the heat loss to the energy generated is 0.41.

Typical radial temperature profiles, $T_w - T$, resulting from the simplified analysis[3] are presented in Figs. 11 and 12 along with the experimental data for air and argon. The agreement between the experimental data and the theoretical results is excellent. For com-

[3] It is emphasized again that the theoretical results obtained from both the simplified analysis and the more complete numerical calculations are in excellent agreement.

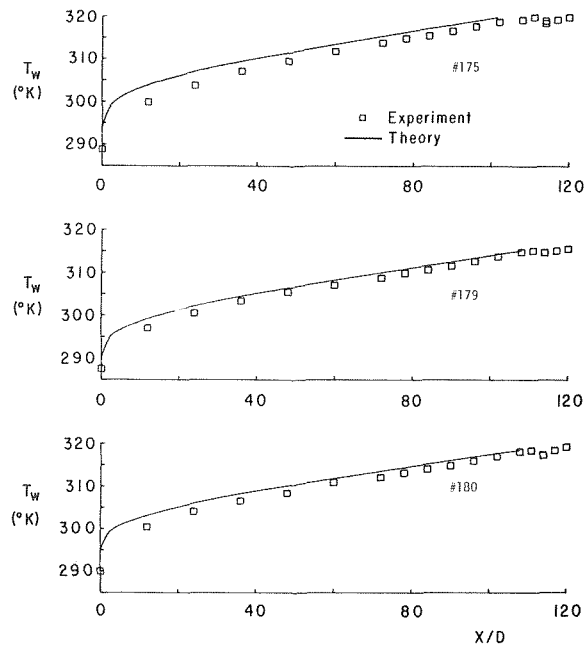

Fig. 9 Experimental and theoretical wall temperatures, laminar flow (cf. Table 2)

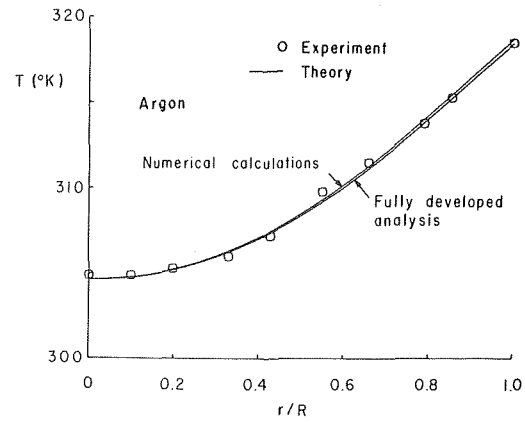

Fig. 10 Temperature profile in laminar flow (Run 180, cf. Tables 2 and 3)

Table 2 Laminar flow, numerical calculations

Run	Gas	Re	$(hD/k)_{108D}$	$Ra^{1/4}$	(q_w) (w/m^2)
174	Air	1910	5.19	2.93	30.4
175	Air	1930	5.19	2.94	29.1
177	Air	2080	5.14	2.90	27.6
179	Air	1880	5.21	2.96	26.4
180	Argon	1870	5.18	3.01	16.2

Table 3 Laminar flow, simplified analysis

Run	Gas	Re	$(hD/k)_{108D}$	$Ra^{1/4}$	(q_w) (w/m^2)
174	Air	1880	5.22	2.89	30.4
175	Air	1910	5.25	2.92	29.1
177	Air	2050	5.25	2.91	27.6
179	Air	1850	5.23	2.92	26.4
180	Argon	1850	5.31	3.01	16.2

pleteness the forced convection, nonbuoyant results are also presented. The increased transport due to buoyancy results in the flatter temperature profiles shown. Recall the value of 4.364 for hD/k [14] for the nonbuoyant constant property calculation which is about 16 percent[4] less than the values with buoyancy present.

Conclusions

Turbulent Flow. Numerical calculations using the method of Spalding and Patankar [1] (cf. Mason [2]) employing a Prandtl mixing length model with van Driest damping yields temperature profiles which are in good agreement with the experimental data for air and argon, although significant differences near the center line are noted. The Reynolds numbers varied from 10,000 to 19,500 and the corresponding values of the Nusselt numbers varied from 33 to 53. The measurements were carried out in an electrically heated tube, 2 in. (5.08 cm) in diameter, which was supported in the vertical direction.

Laminar Flow. A simplified theoretical determination of the heat transfer in internal forced flows with buoyancy present (cf. [5–8]) gave good agreement with measured temperature profiles in air and argon and with more complete numerical calculations. Values of the Reynolds numbers varied from 1850 to 2100 while the Rayleigh numbers varied from 70 to 80. Over this range of conditions, omitting the effects of buoyancy results in a 16 percent error in the Nusselt number.

Acknowledgment

The author is grateful to the National Science Foundation for support of this research.

References

1 Patankar, S. V., and Spalding, D B., *Heat and Mass Transfer in Boundary Layers*, Intertext Books, London, 2nd edition, 1970.

2 Mason, H. B., "Numerical Computation of Steady Natural Convective Flows with Rotation and Stratification," PhD dissertation, Dept. of Mechanical Engineering, University of California, Berkeley, Calif., 1971.

3 van Driest, E. R., "On Turbulent Flow Near a Wall," *Journal Aeronautical Sci.*, Nov., 1956, pp. 1007–1011.

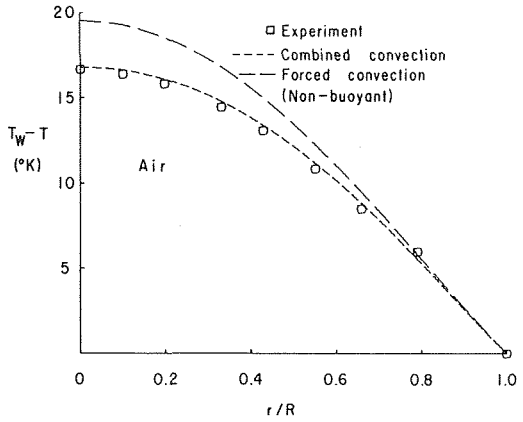

Fig. 11 Temperature profile in laminar flow (Run 174, cf. Tables 2 and 3)

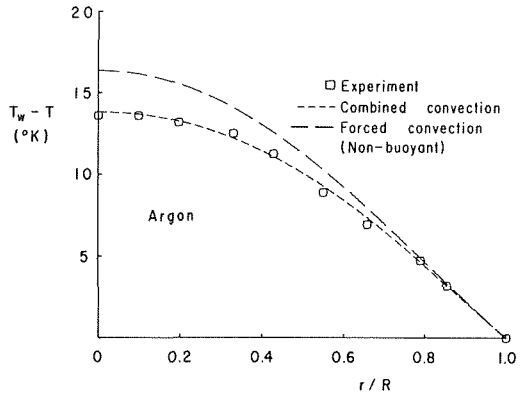

Fig. 12 Temperature profile in laminar flow (Run 180, cf. Tables 2 and 3)

4 Deissler, R. G., and Eian, C. S., "Analytic and Experimental Investigation of Fully Developed Turbulent Flow of Air in a Smooth Tube with Heat Transfer with Variable Fluid Properties," NACA Tech. Note 2629, Feb. 1952.

5 Ostrach, S., "Combined Natural and Forced Convection Laminar Flow and Heat Transfer of Fluids with and without Heat Sources in Channels with Linearly Varying Wall Temperatures," NACA TN 3141, Apr. 1954.

6 Hallman, T. M., "Combined Forced and Free Convection in a Vertical Tube," PhD thesis in Mechanical Engineering, Purdue University, Lafayette, Indiana, 1958.

7 Tao, L. N., "On Combined Free and Forced Convection in Channels," JOURNAL OF HEAT TRANSFER, TRANS. ASME, Series C, Vol. 82, No. 3, Aug., 1960, pp. 233–238.

8 Morton, B. R., "Laminar Convection in Uniformly Heated Vertical Pipes," *Journal of Fluid Mechanics*, Vol. 8, 1960, p. 227.

9 Zeldin, B., and Schmidt, F. W., "Developing Flow with Combined Forced-Free Convection in an Isothermal Vertical Tube," JOURNAL OF HEAT TRANSFER, TRANS. ASME, Series C, Vol. 92, 1972, pp. 211–223.

10 Lawrence, W. T., and Chato, J. C., "Heat-Transfer Effects on the Developing Laminar Flow Inside Vertical Tubes," JOURNAL OF HEAT TRANSFER, TRANS. ASME, Series C, Vol. 88, No. 2, May 1966, pp. 214–222.

11 Habib, I. S., "Heat Transfer to a Radiating Gas Flowing Turbulently in a Tube: An Experimental and Theoretical Study," PhD dissertation, University of California, Berkeley, Calif., 1968.

12 Habib, I. S., and Greif, R., "Heat Transfer to a Flowing Nongray Radiating Gas: An Experimental and Theoretical Study," *International Journal of Heat and Mass Transfer*, Vol. 13, 1970, pp. 1571–1582.

13 *Fluid Meters*, ASME, 6th edition, 1971.

14 Kays, W. M., *Convective Heat and Mass Transfer*, McGraw-Hill, New York, 1966.

15 Donovan, T. E., "Heat Transfer in Internal Flows Including Buoyancy and Thermal Radiation," PhD dissertation, University of California, Berkeley, Calif., Dec. 1975.

[4] It is noted that [1 − (4.36/5.19)]100 = 16 percent.

B. T. F. Chung
L. C. Thomas
Y. Pang[1]

Department of Mechanical Engineering,
The University of Akron,
Akron, Ohio

A Surface Rejuvenation Model for Turbulent Heat Transfer in Annular Flow With High Prandtl Numbers

Heat transfer for high Prandtl number fluids flowing turbulently in a concentric circular tube annulus with prescribed wall heat flux is investigated analytically. This surface rejuvenation based analysis is restricted to thermally and hydrodynamically fully developed flow with constant properties and negligible viscous dissipation.

This formulation leads to predictions for the Nusselt Number that are in basic agreement with predictions obtained on the basis of earlier eddy diffusivity models for $30 \leq Pr \leq 1000$ *and* $10^4 \leq Re \leq 10^6$.

Introduction

Theoretical analyses of turbulent heat transfer in concentric annuli has been the subject of many recent studies. Among them, Kays and Leung [1][2] have obtained solutions for the heat transfer coefficient for turbulent annular flow with constant heat fluxes at walls for a wide range of radius ratios, Prandtl numbers and Reynolds numbers. Using the same classical approach, except with different expressions for velocity distribution and eddy diffusivity, Wilson and Medwell [2] and Michiyoshi and Nakajima [3] resolved the same problem and obtained results in good agreement with those reported by Kays and Leung. Recently, Chung and Thomas [4] analyzed the same problem based on a different modeling concept known as the principle of surface renewal. The strength of this approach lies in the fact that modeling parameters, such as the mean residence time, $\bar{\tau}$, are utilized which have physical significance and are measurable. Predictions for Nusselt number at both the inner and outer wall, based on both approaches, have been found to be in good agreement with the experimental data for air [1].

Whereas the classical approach also has been applied to the high Prandtl number region, the surface renewal analysis of reference [4] is confined to moderate Prandtl number fluids because of the use of the simplifying assumption that turbulent eddies move into direct contact with the surface. Because of the lack of experimental data for high values of Pr, it is felt that the supplementation of previous predictions based on the classical approach by surface renewal-based predictions would be useful. Therefore, attention now is turned to the formulation of a surface renewal-based analysis for turbulent annular flow of high Prandtl number fluids. In this analysis, a more general form of the surface renewal and penetration model known as the surface rejuvenation model will be employed. This model accounts for the effect of the unreplenished layer of fluid that has been reported to reside at the surface.

The surface rejuvenation model was first proposed by Harriott [5] for interfacial mass transfer. This model is based on the hypotheses that 1) eddies intermittently come to within various small distances H of the surface, and 2) unsteady molecular transport controls during their brief residency at the wall. The major difference between the elementary surface renewal model and the surface rejuvenation model is that the former is based on the assumption that the approach distance, H, for each eddy is zero, while the latter accounts for the effect of the thermal resistance of the unreplenished layer of the fluid near the wall region. This effect has been shown to be of negligible significance for moderate to low Prandtl number fluids but of primary concern for large Prandtl number fluids [6].

Early adaptations of the surface rejuvenation model [6–7] to turbulent momentum and heat transfer for tube flow were found to be extremely time consuming. A more efficient computational procedure recently has been proposed by Bullin and Dukler [8]. This stochastic approach has been adapted to turbulent tube flow by Rajagopal and Thomas [9]. In the present study, a stochastic formulation of the surface rejuvenation model will be developed for turbulent heat transfer in a concentric annulus, with emphasis on high Prandtl number fluids.

Analysis

Consideration is now given to a fully developed turbulent annulus flow with constant heat fluxes at the inner and/or outer surfaces of $q_{1\omega}$ and $q_{2\omega}$, respectively. Eddies from the bulk stream are assumed to arrive continuously at random distances H from the wall, remaining

[1] Present address: Department of Mechanical Engineering, Stanford University, Palo Alto, California.

[2] Numbers in brackets designate References at end of Paper.

Contributed by the Heat Transfer Division for publication in the JOURNAL OF HEAT TRANSFER. Manuscript received by the Heat Transfer Division July 19, 1977.

for various lengths of time τ.

Heat Transfer. Based on the surface rejuvenation concept, the following system of equations may be written for the instantaneous energy transport associated with an individual rejuvenation cycle:

$$\frac{\partial T}{\partial \theta} = \alpha \frac{\partial^2 T}{\partial y^2} \quad \theta > 0,\ 0 \le y < \infty \tag{1}$$

$$-k \frac{\partial T}{\partial y} = q_w \text{ at } y = 0 \tag{2}$$

$$T = T_b \text{ as } y \to \infty \tag{3}$$

$$\begin{aligned} T &= f(y) \text{ for } 0 \le y \le H \\ &= T_b \quad \text{for } y > H \end{aligned} \quad \text{at } \theta = 0 \tag{4}$$

$q_w = q_{1w}$ for the inner surface and $q_w = q_{2w}$ for the outer surface, y is the distance from either inner or outer wall extending into the fluid, θ is the instantaneous contact time, and $f(y)$ represents the temperature profiles within the wall region at the first instant of rejuvenation. In the present analysis the viscous dissipation has not been taken into account, which becomes significant only when Brinkman number is large.

As can be seen from the above governing equations, the temperature of the eddy at the first instant of rejuvenation is assumed to be uniform and equal to the bulk stream temperature and the curvature effect is assumed to be negligibly small. The first assumption is realistic for high Prandtl number fluids since the temperature drop is concentrated in the wall region. The second assumption is reasonable because the residence time of the fluid element is short and the penetration depth is shallow for the fully turbulent flow. A recent study by Kakarala [10] has indicated that the curvature effect is important only when flow is in laminar and transition regions. Since equations (1-4) are linear and nonhomogeneous, they can be solved using super-position technique and the standard Fourier integral transform method. This gives rise to an instantaneous temperature profile of the form

$$\begin{aligned} T_b - T(y, \theta) = -q_w\sqrt{\alpha}/k\ [2\sqrt{\theta/\pi}\exp(-y^2/4\alpha\theta) - y/\sqrt{\alpha}\,\text{erfc} \\ (y/2\sqrt{\alpha\theta}) + 1/\sqrt{4\pi\alpha\theta}\int_0^H [T_b - f(\xi)]\left\{\exp\left[-\frac{(y+\xi)^2}{4\alpha\theta}\right]\right. \\ \left. + \exp\left[-\frac{(y-\xi)^2}{4\alpha\theta}\right]\right\} d\xi \end{aligned} \tag{5}$$

With θ set equal to τ, this equation provides a relationship for the temperature profile at the end of the residence time, i.e., the initial condition for $0 \le y \le H$ encountered by the next incoming eddy.

Following Bullin and Dukler [8], expressions can be written for the mean initial temperature profile $T(y, \bar{\tau})$ and the mean temperature profile $\overline{T}(y, \bar{\tau})$ as

$$\begin{aligned} T_b - T(y, \bar{\tau}) = \int_0^\infty P_\tau(\tau) \int_0^\infty P_H(H) \int_0^\infty P_f(f) \\ \times [T_b - T(y, \tau)]\, df\, dH\, d\tau \end{aligned} \tag{6}$$

and

$$\begin{aligned} T_b - \overline{T}(y, \bar{\tau}) = \int_0^\infty P_\theta(\theta) \int_0^\infty P_H(H) \int_0^\infty P_f(f) \\ \times [T_b - T(y, \theta)]\, df\, dH\, d\theta \end{aligned} \tag{7}$$

$\bar{\tau}$ is the mean residence time, $P_\theta(\theta)$, $P_\tau(\tau)$, $P_H(H)$ and $P_f(f)$ are the probabilistic functions for contact time, residence time, approach distance and initial profile, respectively. In this work, Danckwerts' random distribution function is employed for τ and H, [11] i.e.,

$$P_\tau = \frac{1}{\bar{\tau}} \exp\left(-\frac{\tau}{\bar{\tau}}\right) \tag{8}$$

$$P_H = \frac{1}{\overline{H}} \exp\left(-\frac{H}{\overline{H}}\right) \tag{9}$$

where $\overline{H}$ is the mean approach distance. An expression will be developed momentarily for $\bar{\tau}$. From the relation (12)

$$P_\tau(\theta) = -\bar{\tau} \frac{dP_\theta(\theta)}{d\theta} \tag{10}$$

there is obtained

$$P_\theta(\theta) = \frac{1}{\bar{\tau}} \exp\left(-\frac{\theta}{\bar{\tau}}\right) \tag{11}$$

Substituting equations (5) and (8)−(11) into equations (6) and (7) yields an identical expression for $\overline{T}(y, \bar{\tau})$ and $T(y, \bar{\tau})$ which is given by

$$\begin{aligned} T_b - T(y, \bar{\tau}) = T_b - \overline{T}(y, \bar{\tau}) \\ = -(q_w\sqrt{\alpha\bar{\tau}}/k)\exp(-y/\sqrt{\alpha\bar{\tau}}) + 1/2\sqrt{\alpha\bar{\tau}}\int_0^\infty \frac{1}{\overline{H}}\exp \\ \left(-\frac{H}{\overline{H}}\right)\int_0^H [T_b - \bar{f}(\xi)]\left[\exp\left(-\frac{y+\xi}{\sqrt{\alpha\bar{\tau}}}\right)\right. \\ \left. + \exp\left(-\frac{|y-\xi|}{\sqrt{\alpha\bar{\tau}}}\right)\right] d\xi\, dH \end{aligned} \tag{12}$$

Nomenclature

$A = \sqrt{\text{Pr}/\nu\bar{\tau}}\,\overline{H}$

f_r = Fanning friction factor
$f(y)$ = truncated curve for temperature
$g(y)$ = truncated curve for velocity
$\overline{H}$ = mean approach distance
$\overline{H}^+$ = dimensionless mean approach distance, $\overline{H}u^*/\nu$
k = conductivity of fluid
Nu = Nusselt number, $2h(R_2 - R_1)/k$
p = pressure
P_θ = probabilistic function for contact time
P_τ = probabilistic function for residence time
P_H = probabilistic function for approach distance
P_f = probabilistic function for initial profile
Pr = Prandtl number, ν/α
q_ω = wall heat flux
R = radius
R_m = radius of maximum velocity of the flow
r^* = R_1/R_2
Re = Reynolds number, $2U_b(R_2 - R_1)/\nu$
s_m = R_m/R_2
T_b = bulk temperature of the flow
T = instantaneous temperature profile
$\overline{T}$ = mean temperature profile
u = instantaneous velocity profile
$\overline{u}$ = mean velocity profile
U^* = friction velocity, $\sqrt{g_c\sigma_w/\rho}$
U_b = bulk stream velocity
v = $\xi/\overline{H}$
y = distance from either inner or outer wall extending into fluid
z = $H/\overline{H}$
α = thermal diffusivity
ρ = density
μ = dynamic viscosity
ν = kinematic viscosity
τ = residence time
$\bar{\tau}$ = mean residence time
θ = contact time
σ = shear stress
ϵ_m = eddy diffusivity for momentum
ϵ_h = eddy diffusivity for heat
η = $y/\overline{H}$

Subscripts

w = condition at wall
b = bulk stream condition
1 = at inner wall
2 = at outer wall

$\bar{f}(\xi)$ in the above integral is defined as

$$\bar{f}(\xi) = \int_0^\infty P_f(f)\, f(\xi)\, df$$

That the mean initial temperature profile $T(y, \bar{\tau})$ and the mean temperature profile, $\overline{T}(y, \bar{\tau})$ are identical is independent of the boundary conditions involved. The key point is the use of random contact time distribution function which yields the same type of distribution function for residence time, consequently the same expression for mean initial and mean temperature profiles is obtained.

Non-dimensionalizing the above expression and after some algebraic manipulations, we obtain the following integral equations for the temperature profiles within the vicinity of the inner wall

$$\frac{\overline{T}_1(\eta) - T_b}{\dfrac{2q_{1w}R_1}{k}} = \frac{\overline{H}_1{}^+}{A_1\mathrm{Re}}\frac{1-r^*}{r^*}\sqrt{\frac{2}{f_{r_1}}}\exp(-A_1\eta) + \frac{A_1}{2}\int_0^\infty \exp(-z)\int_0^z \frac{T_1(\upsilon) - T_b}{\dfrac{2q_{1w}R_1}{k}}\{\exp[-A_1(\eta+\upsilon)] + \exp[1-A_1|\eta-\upsilon|]\}\, d\upsilon\, dz \quad (13a)$$

and the outer wall region

$$\frac{\overline{T}_2(\eta) - T_b}{\dfrac{2q_{2w}R_2}{k}} = \frac{\overline{H}_2{}^+}{A_2\mathrm{Re}}(1-r^*)\sqrt{\frac{2}{f_{r_2}}}\exp(-A_2\eta) + \frac{A_2}{2}\int_0^\infty \exp(-z)\int_0^z \frac{T_2(\upsilon) - T_b}{\dfrac{2q_{2w}R_2}{k}}\{\exp(-A_2(\eta+\upsilon)] + \exp[-A_2|\eta-\upsilon|]\}\, d\upsilon\, dz \quad (13b)$$

where $A_1 = (\sqrt{\mathrm{Pr}}/\sqrt{\nu\bar{\tau}_1})\,\overline{H}_1$, $A_2 = (\sqrt{\mathrm{Pr}}/\sqrt{\nu\bar{\tau}_2})\,\overline{H}_2$, $r^* = R_1/R_2$, $\eta = y/\overline{H}$, $z = H/\overline{H}$, $\upsilon = \xi/\overline{H}$ with $H = H_1$, $\overline{H} = \overline{H}_1$ for the inner wall region and $H = H_2$, $\overline{H} = \overline{H}_2$ for the outer wall region.

The Fanning friction factor at inner and outer wall can be expressed in term of total friction factor, f_r, [3] as

$$f_{r_1} = \frac{s_m{}^2 - r^{*2}}{r^*(1-r^*)} f_r \quad (14a)$$

$$f_{r_2} = \frac{1 - s_m{}^2}{1-r^*} f_r \quad (14b)$$

where s_m is the ratio of maximum velocity radius to outer radius. The expression of s_m proposed by Kays and Leung [1] is employed here:

$$s_m = \frac{r^* + r^{*0.343}}{1 + r^{*0.343}} \quad (15a)$$

This formula has been supported by various experimental data and some theoretical predictions [2]. The total friction factor, f_r, in a smooth concentric annuli, can be obtained from the following familiar empirical formula

$$\frac{1}{\sqrt{f_r}} = 4\log_{10}(\mathrm{Re}\sqrt{f_r}) - 0.4$$

Substituting equation (14) into (13) and setting η equal to zero gives expressions for the wall temperatures at the inner and outer surfaces in terms of the mean residence time $\bar{\tau}$ of the forms

$$\frac{T_{1w} - T_b}{\dfrac{2q_{1w}R_1}{k}} = \frac{\overline{H}_1{}^+}{A_1\mathrm{Re}}\sqrt{\frac{2(1-r^*)^3}{r^* f_r(s_m{}^2 - r^{*2})}} + A_1\int_0^\infty \exp(-z)\int_0^z \frac{T_1(\upsilon) - T_b}{\dfrac{2q_{1w}R_1}{k}}\exp(-A_1\upsilon)\, d\upsilon\, dz \quad (16a)$$

$$\frac{T_{2w} - T_b}{\dfrac{2q_{2w}R_2}{k}} = \frac{\overline{H}_2{}^+}{A_2\mathrm{Re}}\sqrt{\frac{2(1-r^*)^3}{f_r(1-s_m{}^2)}} + A_2\int_0^\infty \exp(-z)\int_0^z \frac{T_2(\upsilon) - T_b}{\dfrac{2q_{2w}R_2}{k}}\exp(-A_2\upsilon)\, d\upsilon\, dz \quad (16b)$$

The Nusselt numbers at the inner and outer surfaces are expressed in terms of equation (16) as

$$\mathrm{Nu}_1 = \frac{1}{\dfrac{T_{1w} - T_b}{\dfrac{2q_{1w}R_1}{k}}}\frac{1-r^*}{r^*} \quad (17a)$$

$$\mathrm{Nu}_2 = \frac{1}{\dfrac{T_{2w} - T_b}{\left(\dfrac{2q_{2w}R_2}{k}\right)}}(1-r^*) \quad (17b)$$

A relationship for $\bar{\tau}$ now will be developed in terms of momentum transfer given below. As will be seen, the momentum and energy solutions are coupled through the mean residence time.

Momentum Transfer. The governing equations for the instantaneous momentum transfer associated with an individual surface rejuvenation cycle are

$$\frac{\partial u}{\partial\theta} = \nu\frac{\partial^2 u}{\partial y^2} - \frac{1}{\rho}\frac{dp}{dx} \quad (18)$$

$$u = 0 \text{ at } y = 0 \quad (19)$$

$$u = \text{finite as } y \to \infty \quad (20)$$

$$\left.\begin{aligned} u &= g(y) \text{ for } 0 \le y \le H \\ &= U_b \quad \text{for } y > H \end{aligned}\right\} \text{ at } \theta = 0 \quad (21)$$

where $g(y)$ is the truncated curve. The pressure gradient in equation (18) may be expressed in terms of inner and outer wall shear stresses as

$$-\frac{dp}{dx} = \frac{2\sigma_{1w}R_1}{R_m{}^2 - R_1{}^2} \text{ or } -\frac{dp}{dx} = \frac{2\sigma_{2w}R_2}{R_2{}^2 - R_m{}^2} \quad (22)$$

By definition

$$\sigma_{1w} = \frac{1}{2}\rho U_b{}^2 f_{r_1}, \qquad \sigma_{2w} = \frac{1}{2}\rho U_b{}^2 f_{r_2} \quad (23)$$

where f_{r_1} and f_{r_2} have been given by equation (14). The coupling of the solution of equations (18–21) with equations (22) and (23) and with the stochastic process mentioned earlier leads to the following integral equations for the velocity profiles within the vicinities of the inner and outer walls:

$$\frac{U_b - \bar{u}_1(\eta)}{U_b} = \exp\left(-\frac{\overline{H}_1}{\sqrt{\nu\bar{\tau}_1}}\eta\right) + \frac{4\overline{H}_1{}^{+2}}{\mathrm{Re}\left(\dfrac{\overline{H}_1}{\sqrt{\nu\bar{\tau}_1}}\right)^2}\frac{r^*(1-r^*)}{(s_m{}^2 - r^{*2})} \times\left[\exp\left(-\frac{\overline{H}_1}{\sqrt{\nu\bar{\tau}_1}}\eta\right) - 1\right] + \frac{1}{2}\frac{\overline{H}_1}{\sqrt{\nu\bar{\tau}_1}}\int_0^\infty \exp(-z)\times\int_0^z \frac{U_b - \bar{u}_1(\upsilon)}{U_b}\left\{\exp\left[-\frac{\overline{H}_1}{\sqrt{\nu\bar{\tau}_1}}|\upsilon-\eta|\right] - \exp\left[-\frac{\overline{H}_1}{\sqrt{\nu\bar{\tau}_1}}(\upsilon+\eta)\right]\right\} d\upsilon\, dz \quad (24a)$$

$$\frac{U_b - \bar{u}_2(\eta)}{U_b} = \exp\left(-\frac{\overline{H}_2}{\sqrt{\nu\bar{\tau}_2}}\eta\right) + \frac{4\overline{H}_2{}^{+2}}{\mathrm{Re}\left(\dfrac{\overline{H}_2}{\sqrt{\nu\bar{\tau}_2}}\right)^2}\frac{1-r^*}{1-s_m{}^2} \times\left[\exp\left(-\frac{\overline{H}_2}{\sqrt{\nu\bar{\tau}_2}}\eta\right) - 1\right] + \frac{1}{2}\frac{\overline{H}_2}{\sqrt{\nu\bar{\tau}_2}}\int_0^\infty \exp(-z)\int_0^z \frac{U_b - \bar{u}_2(\upsilon)}{U_b}$$

$$\times \left\{ \exp\left[-\frac{\overline{H}_2}{\sqrt{\nu\overline{\tau}_2}} |v - \eta| \right] - \exp\left[-\frac{\overline{H}_2}{\sqrt{\nu\overline{\tau}_2}} (v + \eta) \right] \right\} dv\, dz \quad (24b)$$

These results give rise to the expressions for the dimensionless mean wall shear stresses at inner and outer surfaces of the forms

$$\overline{H}_1{}^+ \sqrt{\frac{s_m{}^2 - r^{*2}}{r^*(1 - r^*)} \frac{f_r}{2}} = \frac{\overline{H}_1}{\sqrt{\nu\overline{\tau}_1}} + \frac{4\overline{H}_1{}^{+2}}{\mathrm{Re}\left(\frac{\overline{H}_1}{\sqrt{\nu\overline{\tau}_1}}\right)} \frac{r^*(1 - r^*)}{s_m{}^2 - r^{*2}}$$

$$- \left(\frac{\overline{H}_1}{\sqrt{\nu\overline{\tau}_1}}\right)^2 \int_0^\infty \exp(-z) \int_0^z \frac{U_b - \overline{u}_1(v)}{U_b} \times \exp\left(-\frac{\overline{H}_1}{\sqrt{\nu\overline{\tau}_1}} v\right) dv\, dz \quad (25a)$$

$$\overline{H}_2{}^+ \sqrt{\frac{1 - s_m{}^2}{1 - r^*} \frac{f_r}{2}} = \frac{\overline{H}_2}{\sqrt{\nu\overline{\tau}_2}} + \frac{4\overline{H}_2{}^{+2}}{\mathrm{Re}\left(\frac{\overline{H}_2}{\sqrt{\nu\overline{\tau}_2}}\right)} \frac{1 - r^*}{1 - s_m{}^2}$$

$$- \left(\frac{\overline{H}_2}{\sqrt{\nu\overline{\tau}_2}}\right)^2 \int_0^\infty \exp(-z) \int_0^z \frac{U_b - \overline{u}_2(v)}{U_b} \times \exp\left(-\frac{\overline{H}_2}{\sqrt{\nu\overline{\tau}_2}} v\right) dv\, dz \quad (25b)$$

In the present computation, the numerical value for $\overline{H}^+{}_1$ and $\overline{H}^+{}_2$ are assumed to be 5. This assumption is based on the experimental observation with a pipe by Popovich and Hummel [13]. Their results have shown that adjacent to the wall there exists a layer of small thickness $y^+ = 1.6 \pm 0.4$ in which a linear velocity gradient occurs at virtually all times, but within which the slope of gradient changes with time. This finding is basically in agreement with the surface rejuvenation concept. The mean approach distance associated with strong eddies reported by these workers was $H^+ = 5.05$. Since the experimental data for the velocity profiles in the sublayer region at both inner and outer surfaces are almost the same, the assumption of $\overline{H}^+{}_1 = \overline{H}^+{}_2$ appears to be reasonable. Therefore, the left hand side of equation (25) is known if the Reynolds number and the dimensions of the annulus are fixed. The parameter $\overline{H}/\sqrt{\nu\overline{\tau}}$ can be solved from equations (24) and (25) simultaneously by iteration. Once $\overline{\tau}$ is established, the Nusselt number can be solved from equation (17).

The iterative procedure involved in computing the temperature profile includes 1) the assumption of a value of $\overline{H}/\sqrt{\nu\overline{\tau}}$, 2) the iterative computation for $(U_b - \overline{u})/U_b$ in the vicinity of the inner and outer walls from equation (24) (the first two terms of the right hand side of equation (24) are used as an initial guess), 3) a comparison of the wall shear stress obtained by the substitution of $(U_b - \overline{u})/U_b$ into equation (25) with the exact value of wall shear stress which is obtained directly from equations (14) for the specified Reynolds number, 4) the selection of a new estimate for $H/\sqrt{\nu\overline{\tau}}$ by solving the third order (in $\overline{H}/\sqrt{\nu\overline{\tau}}$) algebraic equation, equation (25) (note that the left hand side of equation (25) is given), 5) the computation of a second approximation for $(U_b - \overline{u})/U_b$ by the substitution of the improved value of $\overline{H}/\sqrt{\nu\overline{\tau}}$ into equation (24). (These computational steps are repeated until the wall shear stress converges to within 1 percent of the correct value), and 6) the substitution of the final value of $\overline{H}/\sqrt{\nu\overline{\tau}}$ into equation (13) and the iterative solution of this equation for the mean temperature profile (the first two terms of the right hand side of equation (13) are used as the initial guess). In evaluating double integrations in equations (13), (24) and (25), the methods of Gaussian and Gaussian-Laguerre quardrature are employed. It is found that the numerical technique employed in the present analysis converges rapidly. The computer program involving the details of calculation mentioned above is available in reference [14].

Results and Discussion

The numerical solution of equations (24) and (25) for $H/\sqrt{\nu\overline{\tau}}$ are tabulated in [14] for different values of radius ratio and Reynolds number. It is found that for given Re and r^*, the mean residence time of eddies in the inner wall region is always shorter than that in the outer wall region. As a consequence, the Nusselt number at the inner surface is expected to be larger.

Based on the values of $\overline{H}/\sqrt{\nu\overline{\tau}}$, the Nusselt numbers computed from equation (17) are presented graphically in Figs. 1–6. Nusselt numbers at both inner and outer surfaces are plotted against Reynolds number ranging from 10^4 to 10^6, with Prandtl number as a parameter varying from 30 to 1000. The radius ratios are chosen as 0.2, 0.5 and 0.8. As expected, the Nusselt number at the inner surface is greater than that at the outer surface. Unfortunately, no experimental data

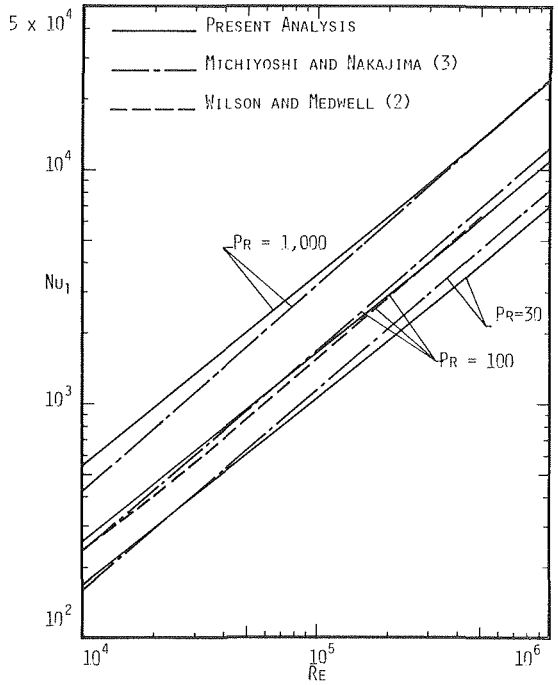

Fig. 1 Nusselt number at the inner surface of an annulus with uniform wall heat flux and $r^* = 0.2$

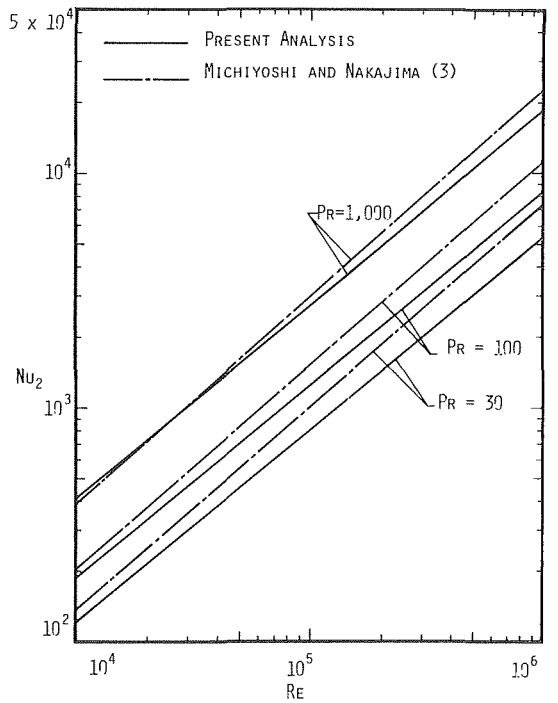

Fig. 2 Nusselt number at the outer surface of an annulus with uniform wall heat flux and $r^* = 0.2$

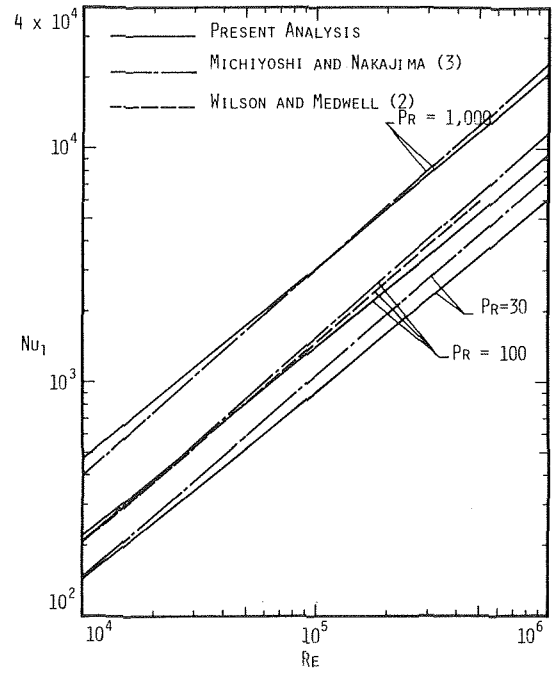

Fig. 3 Nusselt number at the inner surface of an annulus with uniform wall heat flux and $r^* = 0.5$

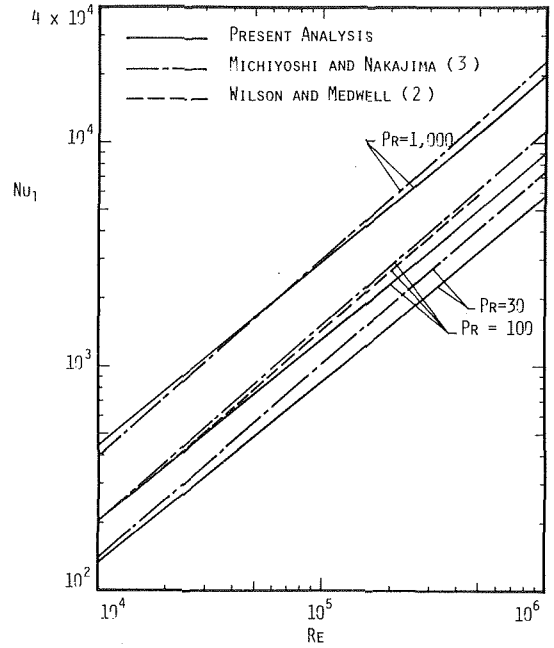

Fig. 5 Nusselt number at the inner surface of an annulus with uniform wall heat flux and $r^* = 0.8$

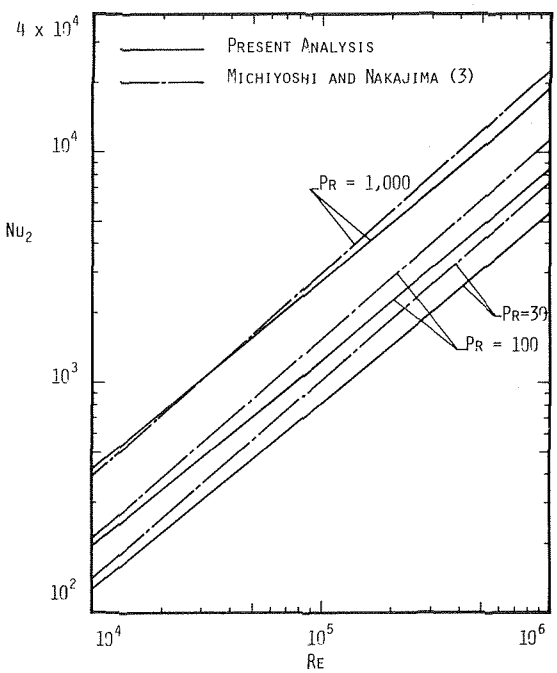

Fig. 4 Nusselt number at the outer surface of an annulus with uniform wall heat flux and $r^* = 0.5$

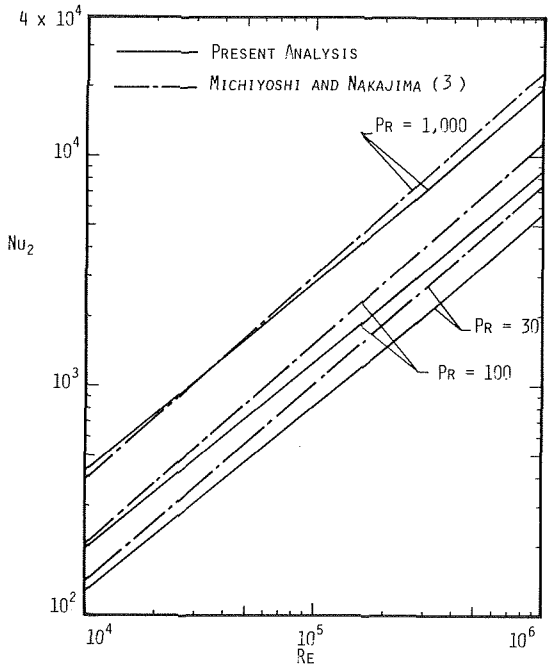

Fig. 6 Nusselt number at the outer surface of an annulus with uniform wall heat flux and $r^* = 0.8$

for Nusselt number in turbulent annular flow for high Prandtl number exist in the open literature; nor is any simple heat transfer correlation in terms of Pr, Re and r^* available. However, theoretical solutions based on the classical eddy diffusivity model [1–3] have been available. The recent results of Michiyoshi and Nakajima [3] which do not differ much from those of Kays and Leung [1] are included in Figs. 1–6. Nusselt numbers at the inner surface predicted by Wilson and Medwell [2] are available for certain values of Re, Pr and r^* only. They are included here for the purpose of comparison. It is found that the present analysis is in reasonable agreement with that of reference [3]. The results of Wilson and Medwell fall between the present results and those of [3].

The numerical results of two limiting cases for $r^* = 0$ and $r^* = 1.0$, which correspond to the cases of circular pipe and two parallel plates flows, respectively, are also computed. These limiting solutions compared well with the previous theoretical works [1, 3]. Comparisons show that the present solutions with $r^* = 0$ agree with the experimental data compiled in [15] within at least 10 percent for a wide range of Prandtl and Reynolds numbers.

As pointed out by Schlichting, at this stage of development the

turbulent flow problem must be solved by a semi-empirical theory. Just as other turbulence models do, the present analysis involves certain empirical constants. They are $\overline{H}^+{}_1$, $\overline{H}^+{}_2$ (in the analysis we assume $\overline{H}^+{}_1 = \overline{H}^+{}_2 = 5$), the radius of maximum velocity and friction factor correlation. Note that in this work, the mean residence times $\overline{\tau}_1$ and $\overline{\tau}_2$ are obtained from the application of surface rejuvenation model to momentum transfer plus the information of radius of maximum velocity, s_m and the friction factor f_r. If the experimental data for $\overline{\tau}_1$ and $\overline{\tau}_2$ are available, it would be unnecessary to use s_m and f_r.

To date, the techniques for measuring $\overline{\tau}$ and $\overline{H}$ are available for pipe flow. Popovich and Hummel [13] applied a flash photolysis method for non-disturbing turbulent flow to measure the approach distance of the eddies. Meek and Baer [16] and Thomas and Greene [17] used flush mounted anemometer probes for measuring the mean bursting period. It is anticipated that the same measurement techniques can be applied to turbulent annular flow. It should be pointed out that the predicted $\overline{\tau}$ and velocity profile based on the surface rejuvenation model agree reasonably well with the measurement of [16] and [17]. The comparison was presented in an earlier paper [7] which was based on Harriott's model instead of the more efficient stochastic approach of Bullin and Duckler [8].

A comparison between the surface rejuvenation and the elementary surface renewal models associated with flow in an annulus is illustrated in Fig. 7. The simple surface renewal model is a limiting case of surface rejuvenation model with $H^+ \equiv 0$, which implies that all eddies are directly in contact with the wall. Obviously, the model is not appropriate for flow with high Prandtl numbers for which the major thermal resistance is concentrated in the wall layer. It is seen from Fig. 7 that for moderate Prandtl number, the Nusselt number predicted by the two surface renewal type models is in good agreement; however, as the Prandtl number increases, the elementary surface renewal model appears to over-predict the heat transfer rate. This is due to the thermal resistance effect of the unreplenished layer, which becomes significant for the high Prandtl number fluids. The numerical results show that the surface renewal model yields a relation of $\mathrm{Nu} \propto \mathrm{Pr}^{1/2}$ while the surface rejuvenation model predicts $\mathrm{Nu} \propto \mathrm{Pr}^{1/3}$.

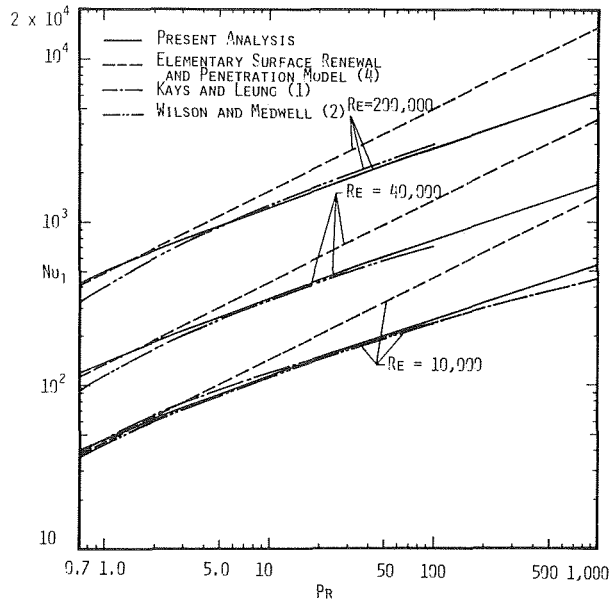

Fig. 7 Comparison of present analysis with elementary surface renewal and penetration model and eddy diffusivity model for the inner-surface Nusselt number of an annulus with uniform wall heat flux and $r^* = 0.2$

Conclusion

An analysis has been presented to estimate heat transfer characteristics for turbulent fully developed annular flow, with emphasis on high Prandtl number fluids. The predicted Nusselt numbers are graphically presented for a wide range of Reynolds numbers, Prandtl numbers, and radius ratios. The same problem has been attacked earlier, using the eddy diffusivity approach which involves analogical relationship for ϵ_h/ϵ_m in terms of Pr and an empirical assumption regarding the variation of ϵ_m/ν near the wall region. In the present approach, predictions of Nusselt number are made in terms of $\overline{\tau}$ and $\overline{H}$ which are directly measurable. The alternative to measuring $\overline{\tau}$ directly is to predict $\overline{\tau}$ from easily measured wall shear stress or friction factor. (Note that the eddy diffusivity models also rely upon the informations of s_m and f_r). Although this provides an analogical relationship between Nusselt number and friction factor, the important point is that a physically meaningful parameter, $\overline{\tau}$, provides the basis for this analogy. It appears that the present model gives a clear picture in describing the exchange mechanism between a turbulent fluid and its boundary. This mechanism is consistent with the previous experimental observations of Fage and Townsend [18], Lin et al. [19], and Popovich and Hummel [13].

Acknowledgment

This study was supported in part by the National Science Foundation under grant GK-35883.

References

1 Kays, W. M., and Leung, E. Y., "Heat Transfer in Annular Passages—Hydrodynamically Developed Turbulent Flow With Arbitrarily Prescribed Heat Flux," *International Journal of Heat and Mass Transfer,* Vol. 6, No. 7, (1963), pp. 537–557.

2 Wilson, N. W., and Medwell, J. O., "An Analysis of Heat Transfer for Fully Developed Turbulent Flow in Concentric Annuli," ASME, JOURNAL OF HEAT TRANSFER, Vol. 90, No. 1, 1968, pp. 43–50.

3 Michiyoshi, I., and Nakajima, T., "Heat Transfer in Turbulent Flow With Internal Heat Generation in Concentric Annulus (I) Fully Developed Thermal Situation," *Journal of Nuclear Science and Technology,* Vol. 5, No. 9, 1968, pp. 476–484.

4 Chung, B. T. F., and Thomas, L. C., "An Analysis of Heat Transfer In Turbulent Annular Flow," *Proceedings 10th Southeastern Seminar on Thermal Sciences,* New Orleans, 1974, pp. 78–94.

5 Harriott, P., "A Random Eddy Modification of the Penetration Theory," *Chemical Engineering Science,* Vol. 17, No. 3, 1962, pp. 149–154.

6 Thomas, L. C., Chung, B. T. F., and Mahaldar, S. K., "Temperature Profiles for Turbulent Flow of High Prandtl Number Fluids," *International Journal Heat and Mass Transfer,* Vol. 14, No. 9, 1971, pp. 1465–1471.

7 Thomas, L. C., Chung, B. T. F., and Mahaldar, S. K., "Adaptation of the Surface Rejuvenation Model and Turbulent Momentum Transfer," *Proceedings of 8th Southeastern Seminar on Thermal Sciences,* Nashville, TN., 1972, pp. 139–162.

8 Bullin, J. A. and Dukler, A. E., "Random Eddy Models for Surface Renewal, Formulation as a Stochastic Process," *Chemical Engineering Science,* Vol. 27, 1972, pp. 439–442.

9 Rajagopal, R., and Thomas, L. C., "Adaptation of the Stochastic Formulation of the Surface Rejuvenation Model to Turbulent Convective Heat Transfer," *Chemical Engineering Science,* Vol. 29, No. 7, 1974, pp. 1639–1644.

10 Kakarala, C. R., Ph.D. Dissertation, Department of Mechanical Engineering, University of Akron, Akron, Ohio (1976).

11 Danckwerts, P. V., "Significance of Liquid Film Coefficients in Gas Absorption," *I&EC,* Vol. 43, No. 6, 1951, pp. 1460–1467.

12 Zwieterling, T. N., "The Degree of Mixing in Continuous Flow Systems," *Chemical Engineering Science,* Vol. 2, No. 1, 1959, pp. 1–15.

13 Popovich, A. T., and Hummel, R. L., "Experimental Study of the Viscous Sublayer in Turbulent Pipe Flow," *AIChE Journal,* Vol. 13, No. 5, 1967, pp. 854–860.

14 Pang, Y., M.S. Thesis, Department of Mechanical Engineering, University of Akron, Akron, Ohio (1977).

15 Hubbard, D. W., and Lightfoot, E. N., "Correlation of Heat and Mass Transfer Data for High Schmidt and Reynlds Numbers," *I&EC Fundamentals,* Vol. 5, No. 3, 1966, pp. 370–379.

16 Meek, R. l., and Baer, A. D., "The Periodic Viscous Sublayer in Turbulent Flow," *AIChE Journal,* Vol. 16, No. 5, 1970, pp. 841–848.

17 Thomas, L. C., and Greene, H. L., "An Experimental and Theoretical Study of the Viscous Sublayer for Turbulent Tube Flow," *Symposium on Turbulence in Liquids,* The University of Missouri, Rolla, Mo., (1973).

18 Fage, A., and Townsend, H. C. H., "Examination of Turbulent Flow with Ultramiscroscope," *Proceedings of Royal Society Series A,* Vol. 135, 1932, pp. 656–662.

19 Lin, C. S., Moulton, R. N., and Putnam, C. T. L., "Mass Transfer Between Solid Wall and Fluid Streams," *I&EC,* Vol. 45, No. 3, 1953, pp. 636–646.

J. A. Roux
Project Engineer

A. M. Smith
Research Supervisor

AEDC Division,
ARO, Inc.,
Arnold Air Force Station, Tenn.

Combined Conductive and Radiative Heat Transfer in an Absorbing and Scattering Infinite Slab

Simultaneous radiation and conduction heat transfer results are presented for an absorbing and isotropically scattering medium having negligible emission. The radiatively participating medium is assumed to be one-dimensional and bounded by an opaque substrate and by a semi-transparent top interface. The boundary interfaces are assumed to reflect and transmit radiation in accordance with Fresnel's equations and Snell's law, respectively. A diffuse radiative flux, along with a conductive flux, is assumed incident upon the participating medium at the top interface. The Chandrasekhar solution to the transport equation is employed, then the solution of the governing energy equation is formulated for the radiatively participating medium. Heat transfer to the substrate is presented as a function of the governing parameters: albedo, optical thickness, and substrate and medium refractive indices. Finally, dimensionless temperature profiles are shown. Solutions for a convective boundary condition are also derived.

Introduction

The transfer of heat simultaneously by conduction and radiation occurs in many materials such as foams, fibers, powders, and other semi-transparent materials of practical engineering importance. The problem considered here is for negligible emission. Negligible emission can even occur in the analysis of reentry heat shields where "severe environments" [1][1] are encountered, i.e., where the imposed (incident) radiation is much more intense than that which is internally emitted. Here it is important to determine not only the heat flux but also the temperature profile, in order to compute the thermal stresses induced across the medium. In addition to these applications, the analysis presented here is also important for its application to cryodeposits formed in thermal vacuum chambers, formed upon cryogenically-cooled optics, and formed upon cryogenically-cooled storage tanks used in outer space. Here the cryodeposit emission is negligible, but part of the incident radiant energy is radiatively scattered and transmitted to the substrate, while the absorbed portion is conducted to the substrate. It is important to be able to determine the temperature profile because at certain temperature levels cryodeposits are expected to undergo structural phase changes [2] which are known to affect the reflectance (due to increased internal scattering) and thus affect the transport of heat to the substrate. Having a means of predicting the temperature profile would permit a better estimation of when this phase change and hence reflectance change will occur.

Most of the work done for combined conduction and radiation has been for a medium bounded by two constant temperature plates with diffuse boundaries, [3, 4, 5]. An extensive bibliography of related problems dealing with simultaneous conduction and radiation heat transfer in a radiatively participating medium is given by Viskanta and Grosh [6]. In spite of the work that has been done, most of the solutions have been given in terms of integral equations, or solutions have been performed for mathematically simplified approaches to the transport equation, such as that of Kubelka-Munk [7] as used in [8]. Little has been done toward using the Chandrasekhar [9] solution to the transport equation in connection with the energy equation to solve the coupled conduction and radiation problem. In this work, the Chandrasekhar solution to the transport equation is used in conjunction with the energy equation to provide a solution which is easy to employ.

Statement of Problem

The geometry and coordinate system associated with the simultaneous conduction and radiation of heat to the substrate are shown in Fig. 1. The nomenclature employed in Fig. 1 is essentially the same as that used in [10] and [11]; regions 1, 2, and 3, respectively, represent air, radiatively-participating medium, and opaque substrate. I_0 is the incident radiant intensity which is taken to be diffusely distributed. The dielectric coating is partially transparent and the opaque substrate is considered to be either a conductor or dielectric having negligible emission. The air-coating interface is assumed to reflect

[1] Numbers in brackets designate References at end of paper.

Contributed by the Heat Transfer Division and presented at the AIChE-ASME Heat Transfer Conference, Salt Lake City, Utah, August 15–17, 1977.
Revised manuscript received at ASME Headquarters October 6, 1977. Paper No. 77-HT-50.

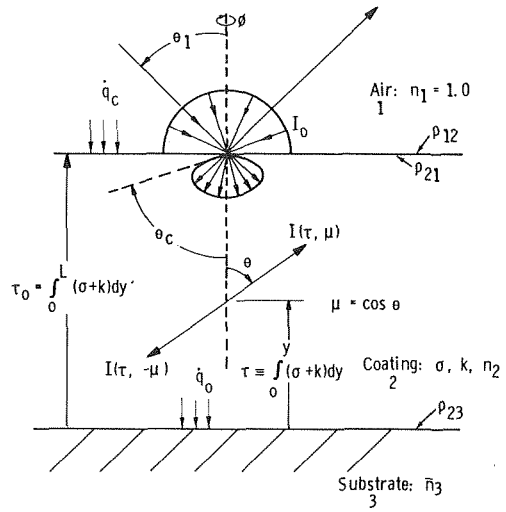

Fig. 1 Coordinate system and geometry

and transmit radiant intensity according to Fresnel's equations and Snell's law, respectively; the substrate is a Fresnel reflector. The external and internal reflectances of the top interface are designated as ρ_{12} and ρ_{21}, respectively. Also, the reflectance of the coating-substrate interface is designated ρ_{23}.

The interior of the radiatively-participating coating is considered to be absorbing and isotropically scattering. Emission is considered to be negligible either due to the substrate being cryogenically cooled or due to the radiation incident upon the top interface being that characterized by a "severe environment" [1] (e.g., radiation emitted from an entry probe gas cap at 20,000 K diffusely incident on a material at 1000 K). The medium is considered to be non-gray with respect to radiative transport and the radiative intensity field is assumed to be axisymmetric. A specified conductive heat load, $\dot{q}_c$, is also assumed to be incident upon the top interface; this heat load may be considered as either positive (heat added) or negative (heat withdrawn) from the coating (see Appendix for the case where this heat load is due to convection). The total heat load to the substrate is designated by $\dot{q}_0$ and also may be positive or negative.

Analysis

The monochromatic radiative transport equation subject to the above assumptions is

$$\frac{di(\tau,\mu)}{d\tau} = \frac{-i(\tau,\mu)}{\mu} + \frac{W}{2\mu}\int_{-1}^{1} i(\tau,\mu')d\mu' \tag{1}$$

where $i(\tau,\mu)$ is the local radiant intensity, $I(\tau,\mu)$, nondimensionalized by the diffusely incident intensity I_0 (Fig. 1); μ is the cosine of the internal polar angle θ defining the direction of $I(\tau,\mu)$; $W = \sigma/(\sigma+k)$ is the albedo parameter, and τ is the local optical depth which is related to the position coordinate y by

$$\tau = \int_0^y (\sigma+k)dy' \tag{2}$$

with σ and k being the scattering and absorption coefficients, respectively. Regular Fresnel reflection and refraction are assumed at the coating boundaries. Mathematically these boundary conditions are expressed as

$$i(\tau_0,-\mu) = \rho_{21}(\mu)i(\tau_0,\mu) + [1-\rho_{12}(\mu')]n_2^2 \tag{3}$$

for the coating-air interface and

$$i(0,\mu) = \rho_{23}(\mu)i(0,-\mu) \tag{4}$$

for the coating-substrate interface where n_2 is the refractive index of the coating and μ' is the $\cos\theta_1$ with θ_1 being the external polar angle (Fig. 1). The directions μ' and μ are related by Snell's law

$$\mu' = [1-(1-\mu^2)n_2^2]^{1/2} \tag{5}$$

and $\tau_0 = \tau(y = L)$ where L is the coating geometrical thickness.

The solution to the transport equation, equation (1), is accomplished by the method of Chandrasekhar. The objective of the Chandrasekhar method is computation of the eigenvalues and eigenvectors of the coefficient matrix associated with the system of simultaneous differential equations resulting from the use of discrete coordinates. Once the eigenvalues and eigenvectors are determined, the homogeneous solution is known; the integration constants are then evaluated from the boundary conditions.

Before the eigenvalues and eigenvectors can be computed, the transport equation, equation (1), together with the boundary conditions, equations (3) and (4), must first be rewritten in terms of the discrete ordinates. This consists of replacing the integral term in equation (1) by a Gaussian quadrature of the form

$$\int_{-1}^{1} f(x)dx = \sum_{j=1}^{p} a_j f(x_j) \tag{6}$$

where x_j are the quadrature points (discrete ordinates), a_j are the quadrature weights, and p (which is an even integer) is the order of the quadrature approximation. Replacing the integral term in equation (1) by equation (6) yields a system of p simultaneous differential equations

Nomenclature

a_i, a_j, a_k = quadrature weights
c_j, c_{p+1-j} = integration constants in equation (11)
h = convective heat-transfer coefficient
I = local monochromatic radiant intensity in coating
I_0 = incident radiant intensity on coating; monochromatic for non-gray coating, total for gray coating
$i = I/I_0$, dimensionless monochromatic intensity
K = thermal conductivity of coating
k = absorption coefficient of coating
L = geometrical thickness of coating
N = conduction-radiation parameter
$n_1, n_2, \bar{n}_3$ = refractive indices of air, coating, and substrate, respectively
p = order of quadrature
$\dot{q}_c$ = conductive heat flux incident on coating top interface
$\dot{q}_0$ = total heat transfer to substrate
$\dot{q}_R$ = monochromatic radiative flux
$\dot{q}_{CS}$ = conductive heat transfer to substrate
$\dot{q}_{RS}$ = total radiative heat transfer to substrate
T, T_S = coating temperature and substrate temperature, respectively
T_{aw} = adiabatic wall temperature
W = scatter albedo of coating
y = position coordinate in coating
θ = internal polar angle (see Fig. 1)
θ_1 = external polar angle (see Fig. 1)
θ_c = internal critical angle (see Fig. 1)
λ, λ_j = eigenvalues
μ, μ' = $\cos\theta$ and $\cos\theta_1$, respectively
$\mu_i, \mu_j, \mu_k, \mu_\ell, \mu_\ell'$ = quadrature points (discrete ordinates)
ν = radiation frequency
ρ_{12}, ρ_{21} = external and internal reflectances, respectively, of coating top interface
ρ_{23} = reflectance of coating-substrate interface
σ = scattering coefficient of coating
τ, τ_0 = local optical depth and coating optical thickness, respectively
ϕ = azimuthal angle (see Fig. 1)

$$\frac{di(\tau, \mu_\ell)}{d\tau} = \frac{-i(\tau, \mu_\ell)}{\mu_\ell} + \frac{W}{2\mu_\ell} \sum_{j=1}^{p} a_j i(\tau, \mu_j), \ \ell = 1, \ldots, p \quad (7)$$

with boundary conditions

$$i(\tau_0, -\mu_\ell) = \rho_{21}(\mu_\ell) i(\tau_0, \mu_\ell) + [1 - \rho_{12}(\mu_\ell')] n_2^2, \quad \ell = 1, \ldots, p/2 \quad (8)$$

and

$$i(0, \mu_\ell) = \rho_{23}(\mu_\ell) i(0, -\mu_\ell), \ \ell = 1, \ldots, p/2 \quad (9)$$

It has been shown [12] that the eigenvalues of equation (7) are the values of λ which satisfy

$$\sum_{j=1}^{p/2} \frac{a_j \mu_j{}^2 \lambda^2}{(1 - \lambda^2 \mu_j{}^2)} = \frac{1}{W} - 1 \quad (10)$$

The eigenvalues of equation (10) occur in plus and minus pairs and are bounded such that $0 \le \lambda_1{}^2 \le 1/\mu_1{}^2 < \lambda_2{}^2 \le 1/\mu_2{}^2 < \ldots < \lambda_p{}^2/2 \le 1/\mu_p{}^2/2$. Thus all the roots (eigenvalues) λ^2 have individual bounds. Using these bounds, the numerical solution for the roots of equation (10) converges very rapidly. The solution of equation (7) for $W \neq 1.0$ is given by

$$i(\tau, \mu_\ell) = \sum_{j=1}^{p/2} \frac{1 - \lambda_j \mu_j}{1 - \lambda_j{}^2 \mu_\ell{}^2} [c_j (1 - \lambda_j \mu_\ell) e^{\lambda_j \tau} + c_{p+1-j}(1 + \lambda_j \mu_\ell) e^{-\lambda_j \tau}], \ \ell = 1, \ldots, p \quad (11)$$

(The solution for $W = 1.0$ is presented in [9], but is not considered here since the radiative and conductive heat transport become uncoupled.)

The values c_j and $c_{p+1-j}[j = 1, \ldots, p/2]$ in equation (11) are the p integration constants determined from the boundary conditions. Substitution of equation (11) into equations (8) and (9) yields a system of p nonhomogeneous linear algebraic equations to be solved for the p values of c; use of the Gauss-Jordan method, Cholesky [13] method, or other computer library routines readily allows determination of the integration constants. Thus the solution of equation (7) is given by equation (11) which only requires the determination of the eigenvalues λ from equation (10) since the eigenvectors are explicitly expressed in equation (11); then the integration constants are easily found via standard techniques for solving systems of nonhomogeneous linear algebraic equations. The results presented in this paper were obtained using a 48 ($p = 48$) point single Gaussian quadrature. However, it should be noted that higher or lower quadrature orders may be used and also different types of quadrature formulas may be used such as the double Gaussian quadrature.

Now it is necessary to derive an expression for the spectral radiative flux, $\dot{q}_R$. Consistent with the axisymmetric assumption, the dimensionless radiative flux at optical depth τ in the coating may be expressed in terms of the Gaussian quadrature as

$$\frac{\dot{q}_R(\tau)}{\pi I_0} = 2 \sum_{i=1}^{p} i(\tau, \mu_i) \mu_i a_i \quad (12)$$

Substitution of equation (11) into equation (12) and rearranging yields

$$\frac{\dot{q}_R(\tau)}{\pi I_0} = 2 \sum_{j=1}^{p/2} (1 - \lambda_j \mu_j) \left(c_j e^{\lambda_j \tau} \sum_{i=1}^{p} \frac{a_i \mu_i}{1 + \lambda_j \mu_i} + c_{p+1-j} e^{-\lambda_j \tau} \sum_{i=1}^{p} \frac{a_i \mu_i}{1 - \lambda_j \mu_i} \right) \quad (13)$$

The summations over index i in equation (13) can be simplified so as to yield

$$\frac{\dot{q}_R(\tau)}{\pi I_0} = -4 \frac{(1 - W)}{W} \sum_{j=1}^{p/2} \frac{(1 - \lambda_j \mu_j)}{\lambda_j} (c_j e^{\lambda_j \tau} - c_{p+1-j} e^{-\lambda_j \tau}) \quad (14)$$

Having an expression for the spectral radiative flux, the solution to the problem of combined conduction and radiation can be formulated. The energy equation may be written [14] as

$$\frac{d}{dy}\left(-K \frac{dT}{dy}\right) + \frac{d}{dy}\left(\int_0^\infty \dot{q}_R(y) d\nu\right) = 0 \quad (15)$$

where K is the thermal conductivity of the coating, T is the temperature at depth y in the coating (Fig. 1), and ν is the radiation frequency which ranges from 0 to ∞. The boundary conditions for equation (15) are

$$T(0) = T_S \text{ at } y = 0 \quad (16)$$

where T_S is the temperature of the substrate, and performing an energy balance at the top interface yields

$$K \left.\frac{dT}{dy}\right|_L = \dot{q}_c \text{ at } y = L \quad (17)$$

Integration of equation (15) yields

$$T = T_S + \frac{1}{K} \int_0^\infty \left(\int_0^y \dot{q}_R(y') dy' - \dot{q}_R(y = L) y \right) d\nu + \dot{q}_c \frac{y}{K} \quad (18)$$

where K has been assumed constant and the boundary conditions in equations (16) and (17) employed. Further assuming that σ and k are independent of temperature and position, equation (18) along with equation (14) allows the development of an explicit expression for the temperature profile in the medium,

$$T = T_S + \frac{4\pi}{K} \int_0^\infty \frac{I_0}{(\sigma + K)} \frac{(1 - W)}{W} \sum_{j=1}^{p/2} \frac{(1 - \lambda_j \mu_j)}{\lambda_j{}^2} \times [c_j (1 - e^{\lambda_j \tau}) + c_{p+1-j}(1 - e^{-\lambda_j \tau})] d\nu + \frac{y}{K} \left[\dot{q}_c + 4\pi \int_0^\infty I_0 \frac{(1 - W)}{W} \times \sum_{j=1}^{p/2} \frac{(1 - \lambda_j \mu_j)}{\lambda_j} (c_j e^{\lambda_j \tau_0} - c_{p+1-j} e^{-\lambda_j \tau_0}) d\nu \right] \quad (19)$$

where $\tau = (\sigma + k)y$ and $\tau_0 = (\sigma + k)L$.

The expression for the heat transferred to the substrate is the sum of the heat transferred by conduction and radiation. The heat conducted to the substrate is given by

$$\dot{q}_{CS} = K \left.\frac{dT}{dy}\right|_{y=0} = \dot{q}_c + 4\pi \int_0^\infty I_0 \frac{(1 - W)}{W} \sum_{j=1}^{p/2} \frac{(1 - \lambda_j \mu_j)}{\lambda_j} \times [c_j (e^{\lambda_j \tau_0} - 1) + c_{p+1-j}(1 - e^{-\lambda_j \tau_0})] d\nu \quad (20)$$

and the radiative flux absorbed by the substrate is given by

$$\dot{q}_{RS} = 2 \int_0^\infty \int_0^1 i(0, -\mu)[1 - \rho_{23}(\mu)] \mu d\mu d\nu = - \int_0^\infty \dot{q}_R(0) d\nu \quad (21)$$

which, by means of equation (14) can be expressed as

$$\dot{q}_{RS} = 4\pi \int_0^\infty I_0 \frac{(1 - W)}{W} \sum_{j=1}^{p/2} \frac{(1 - \lambda_j \mu_j)}{\lambda_j} [c_j - c_{p+1-j}] d\nu \quad (22)$$

The total heat transferred to the substrate is given by

$$\dot{q}_0 = \dot{q}_{CS} + \dot{q}_{RS} \quad (23)$$

which, from equations (20) and (22), can be written as

$$\dot{q}_0 = \dot{q}_c + 4\pi \int_0^\infty I_0 \frac{(1 - W)}{W} \sum_{j=1}^{p/2} \frac{(1 - \lambda_j \mu_j)}{\lambda_j} (c_j e^{\lambda_j \tau_0} - c_{p+1-j} e^{-\lambda_j \tau_0}) d\nu \quad (24)$$

From equations (19), (20), (22), and (24), the temperature profile and the conductive, radiative, and total heat transfer to the substrate can be respectively calculated provided the spectral optical properties of the non-gray medium and substrate, σ, k, n_2, and $\overline{n}_3$, are known. For such a non-gray situation, the integration with respect to frequency could be numerically performed using the standard technique of subdividing the total frequency interval into a finite number of sub-intervals. However, for the purposes of obtaining analytical results and illustrating the effects of the pertinent dimensionless pa-

rameters, the medium and substrate optical properties will be assumed gray. This yields much simpler analytical expressions for the temperature profile and conductive, radiative, and total heat transfer to the substrate,

$$\frac{T}{T_S} = 1 + \frac{(1-W)}{WN}\sum_{j=1}^{p/2}\frac{(1-\lambda_j\mu_j)}{\lambda_j{}^2}[c_j(1-e^{\lambda_j\tau}) + c_{p+1-j}(1-e^{-\lambda_j\tau})] + \tau\left(\frac{1}{4N}\frac{\dot{q}_c}{\pi I_0} + \frac{(1-W)}{WN}\sum_{j=1}^{p/2}\frac{(1-\lambda_j\mu_j)}{\lambda_j}[c_j e^{\lambda_j\tau_0} - c_{p+1-j}e^{-\lambda_j\tau_0}]\right) \quad (25)$$

$$\frac{\dot{q}_{CS}}{\pi I_0} = \frac{\dot{q}_c}{\pi I_0} + \frac{4(1-W)}{W}\sum_{j=1}^{p/2}\frac{(1-\lambda_j\mu_j)}{\lambda_j} \times [c_j(e^{\lambda_j\tau_0}-1) + c_{p+1-j}(1-e^{-\lambda_j\tau_0})] \quad (26)$$

$$\frac{\dot{q}_{RS}}{\pi I_0} = \frac{4(1-W)}{W}\sum_{j=1}^{p/2}\frac{(1-\lambda_j\mu_j)}{\lambda_j}[c_j - c_{p+1-j}] \quad (27)$$

$$\frac{\dot{q}_0}{\pi I_0} = \frac{\dot{q}_c}{\pi I_0} + \frac{4(1-W)}{W}\sum_{j=1}^{p/2}\frac{(1-\lambda_j\mu_j)}{\lambda_j} \times [c_j e^{\lambda_j\tau_0} - c_{p+1-j}e^{-\lambda_j\tau_0}] \quad (28)$$

where $N = K(\sigma + k)T_S/4\pi I_0$ with I_0 for the gray case (equations (25–28)) related to I_0 for the non-gray case (equations (19, 20, 22, 24)) by

$$I_0(\text{gray}) = \int_0^\infty I_0(\text{non-gray})d\nu \quad (29)$$

From equation (19) or (25) it is seen that when the radiation is uncoupled from the conduction ($W = 1.0$) the temperature profile is linear. If in addition to being uncoupled, $\dot{q}_c = 0$, then the temperature of the coating is a constant and is equal to the substrate temperature. It is the radiation terms in equation (19) or (25) which give rise to non-linear-temperature behavior. From equation (19) or (25) it is also seen that for a very high thermal conductivity ($N \to \infty$) the temperature across the coating also approaches T_S. However, from equation (20) or (26) it is seen that the thermal conductivity does not effect the conductive heat transfer. This is because of the assumption that the coating was nonemitting. The beauty of equations (25), (26), (27) and (28) is that they are simple to evaluate.

Results

The primary analytical results are given by equations (25), (26), (27), and (28). The results based on these equations are now shown in the form of temperature profiles (equation (25)) and total heat transfer to the substrate (equation (28)). The temperature profiles as a function of N and W are shown in Fig. 2. Since N represents the importance of conduction to radiation heat transfer, it is seen for a given substrate temperature that as N increases the temperature level is decreased. This is important when a given threshold temperature indicates the onset of melting or a crystalline structure change which can affect the structural characteristics of the coating. As stated earlier, N has no effect upon heat transfer to the substrate; thus the thermal conductivity of the coating becomes important in determining structural effects without influencing heat transfer. Also in Fig. 2 it is seen that as W increases, the temperature level within the coating is likewise reduced for a fixed N. This is because larger W values correspond to more scattering; more scattering means that more radiation is scattered out of the coating and less energy is absorbed, thus causing the temperature increase to be less. Also when the coating is conductively cooled on top, the temperature level may be significantly reduced. The radiation terms in equation (25) cause the profiles to deviate from the linear profiles which would be expected for pure conduction.

In Fig. 3 the total heat transfer to the substrate is shown as a function of optical thickness with coating refractive index and albedo taken as parameters. Since the conductive heat load $\dot{q}_c/\pi I_0$ will cause the heat transfer results to be shifted by a constant amount (see equation (28)), results will only be shown for $\dot{q}_c = 0.0$. Results for a nonzero conductive heat load can easily be obtained by addition or subtraction of the value of $\dot{q}_c/\pi I_0$. Fig. 3 shows that for low albedo ($W = 0.10$) the heat transfer to the substrate is essentially independent of optical thickness because the coating is highly absorbing and conducts the absorbed heat to the substrate, which in this case is a low reflector (black paint). The absorption is so strong for the low albedo coating that significantly increasing optical thickness does not appreciably increase the absorption of the incident radiation. For high albedo ($W = 0.99$), the effect of increasing the optical thickness is to cause a large reduction in the amount of heat transfer to the substrate.

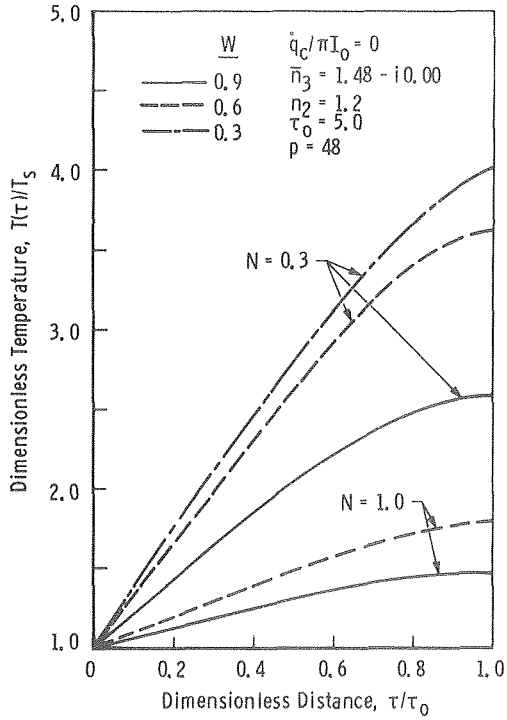

Fig. 2 Nondimensional temperature profile as a function of dimensionless distance for various values of N and W

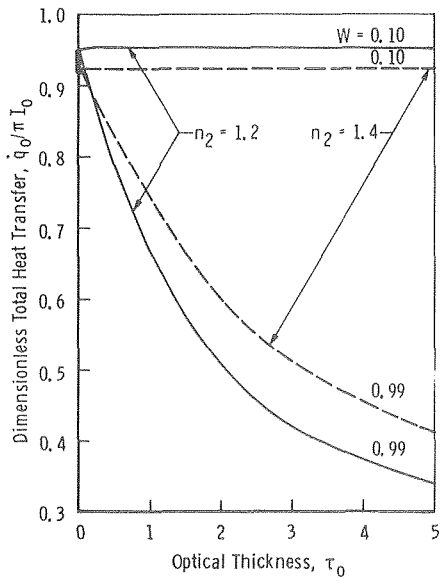

Fig. 3 Heat transfer as a function of optical thickness of various values of n_2 and W; $\bar{n}_3 = 1.48 - i0.00$ and $\dot{q}_c/\pi I_0 = 0.0$

As the optical thickness increases, the coating scattering allows less energy to penetrate to the absorbing substrate. Scattering results in reflecting much of the incident radiation out of the coating. Also shown in Fig. 3 is the effect of refractive index. A coating with a small refractive index ($n_2 = 1.2$) will absorb more heat at small albedo values because of the small top interface reflectance as compared to that of a coating with a higher refractive index ($n_2 = 1.4$). For high albedo values ($W = 0.99$) the higher refractive index coating ($n_2 = 1.4$) is seen to cause more heat transfer to the substrate. This is because the larger refractive index coating has a smaller critical angle which results in the trapping of internally scattered radiation. Radiation incident at the top interface at an angle greater than the critical angle is totally internally reflected, resulting in the substrate having another opportunity to absorb this radiation. The increase in the heat transfer to the substrate observed for very small optical thicknesses as compared to that for the bare substrate is denoted by the broadened line width on the vertical axis of Fig. 3, and is due to the relative refractive index change [11] at the substrate-coating interface. For $W = 0.99$ the two curves are seen to cross at approximately $\tau_0 = 0.25$; below this optical thickness value the heat transfer appears to be dominated by the top-interface reflectance, and above this value the heat transfer is dominated by internal scattering. The albedo and refractive index values of $W = 0.99$, $n_2 = 1.2$ and $W = 0.99$, $n_2 = 1.4$ are characteristic, respectively, of solid H_2O and solid CO_2 in the visible wavelength range.

Illustrated in Fig. 4 is the total heat transfer to the substrate as a function of optical thickness with n_2 and W taken as parameters, but as opposed to Fig. 3, the results are for a bare substrate hemispherical reflectance of about 0.58 (which corresponds to the reflectance calculated from Fresnel's equations for metals using a refractive index characteristic of stainless steel in the visible wavelength range $\bar{n}_3 = 2.48 - i3.43$). Here the heat transfer to the substrate for the low albedo coating increases until it becomes independent of τ_0. Also at very small optical thicknesses slightly more heat is transferred to the substrate for the larger refractive index coating due to the larger relative refractive index change. As in Fig. 3, the increase in heat transfer to the substrate for very small optical thicknesses is denoted by the broadened line width on the vertical axis. At larger optical thicknesses for the lower refractive index and albedo coating ($n_2 = 1.2$, $W = 0.1$), the heat transfer increases because now the top-interface reflectance is the determining factor and the lower refractive index corresponds to a lower interface reflectance [$\rho_{12}(\mu')$]. The high albedo coating shows the heat transfer to have a maximum. This phenomenon is analogous to a critical thickness of high albedo insulation. This heat transfer maximum is due to the trapping of internally scattered radiation as explained in detail in [11]. Similar to Fig. 3 ($W = 0.99$), higher heat transfer to the substrate is observed for the higher refractive index coating. Fig. 5 presents the heat transfer to a highly absorbing substrate as a function of albedo with n_2 and τ_0 taken as parameters. As the albedo approaches zero ($W \to 0.0$) the results are independent of optical thickness. For a given refractive index, the heat transfer is significantly reduced as the albedo increases because of the greater scattering of the incident radiation. For a given optical thickness, the curves for the two refractive indices cross at $W \approx 0.6$. Below $W \approx 0.6$ the substrate absorbs less heat for the higher refractive index coating because of the greater top interface reflectance. At albedo values above $W \approx 0.6$, greater heat transfer occurs for the higher refractive index coating because of the increased trapping of internally scattered radiation.

Shown in Fig. 6 is the heat transfer to the substrate as a function of n_2 with W and $\bar{n}_3$ taken as parameters. For the low and intermediate albedo values ($W = 0.10, 0.70$) the results appear to be independent of the substrate reflectance due to the large value of optical thickness ($\tau_0 = 5.0$). At large W ($W = 0.99$) a small substrate reflectance effect was noticeable. It is interesting to note that for low W ($W = 0.10$) the heat transfer decreases as n_2 increases. Due to the increased top interface reflectance, less radiation enters the highly absorbing coating. For the high albedo ($W = 0.99$) coating the heat transfer is seen to increase as n_2 increases; this is due to the increased trapping of internally scattered radiation. As n_2 increases, the critical angle decreases resulting in more trapping of radiation scattered into directions greater than the critical angle. At the intermediate value of W ($W = 0.7$), the heat transfer is seen to obtain a maximum at about $n_2 = 1.7$. For $n_2 < 1.7$ the heat transfer increases with increasing n_2 indicating internal trapping to be dominant. For $n_2 > 1.7$ the heat transfer decreases with increasing n_2. indicating the top interface reflectance phenomena to be dominant.

Fig. 7 depicts the same parameters as Fig. 6 except for a small value of $\tau_0(\tau_0 = 0.5)$. Here the substrate reflectance is seen to have a significant effect on the heat transfer for all values of W with reduced heat transfer corresponding to the higher reflecting substrate. For the moderate reflecting substrate ($\bar{n}_3 = 2.48 - i3.43$) the heat transfer is seen to increase as n_2 increases for $W = 0.99$, to decrease as n_2 in-

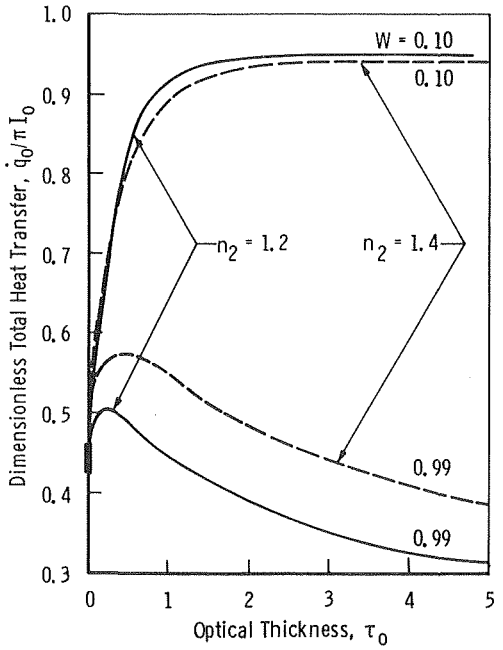

Fig. 4 Heat transfer as a function of optical thickness for various values of n_2 and W; $\bar{n}_3 = 2.48 - i3.43$ and $\dot{q}_c/\pi I_0 = 0.0$

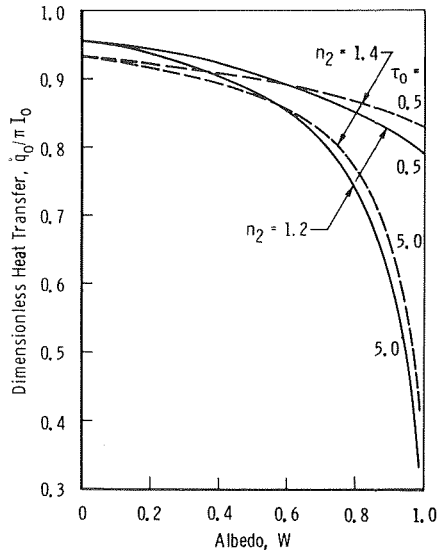

Fig. 5 Heat transfer as a function of albedo for various values of n_2 and τ_0; $\bar{n}_3 = 1.48 - i0.00$ and $\dot{q}_c/\pi I_0 = 0.0$

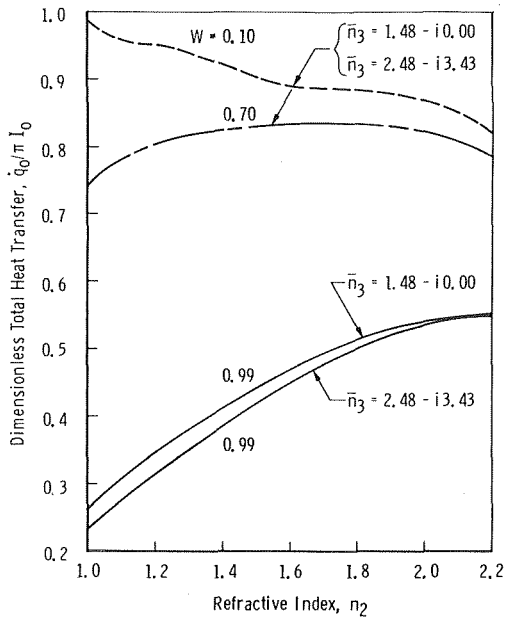

Fig. 6 Heat transfer as a function of coating refractive index for various values of $\bar{n}_3$ and W; $\tau_0 = 5.0$ and $\dot{q}_c/\pi I_0 = 0.0$

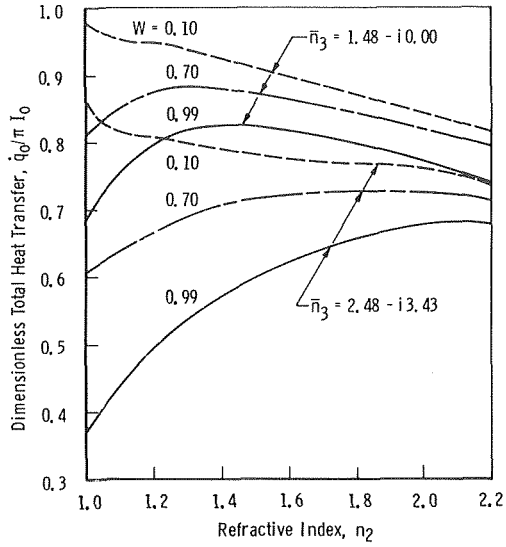

Fig. 7 Heat transfer as a function of coating refractive index for various values of $\bar{n}_3$ and W; $\tau_0 = 0.5$ and $\dot{q}_c/\pi I_0 = 0.0$

creases for $W = 0.10$, and to reach a maximum for $W = 0.70$. For the low reflecting substrate ($\bar{n}_3 = 1.48 - i0.00$) the heat transfer is seen to decrease as n_2 increases for $W = 0.10$ due to the increased top interface reflectance. The heat transfer is seen to attain a maximum for $W = 0.99$ and $W = 0.70$; at low n_2, internal scattering causes the reduction in the heat transfer and at high n_2 the top interface reflectance causes the reduction in the heat transfer.

Summary and Conclusions

A solution to the problem of combined conduction and radiation has been presented for both nongray and gray media having either a conductive or convective boundary condition at the top interface. The temperature profile and heat transfer have been expressed in terms of the Chandrasekhar solution to the radiative transport equation and are presented in equations (19), (20), (22), and (24) for a nongray medium, and in equations (25–28) for a gray medium. These equations were shown to be easy to evaluate for the gray medium, requiring only the simple solution of equation (10) and requiring the use of a library computer routine for solving systems of simultaneous linear nonhomogeneous algebraic equations for the determination of the integration constants $c_i[i = 1, \ldots, p]$. Results were obtained employing a 48-point ($p = 48$) single Gaussian quadrature. High values of W and N were shown to reduce the temperature level of the temperature profile, which can be of importance in determining if the temperature in a given medium is approaching a critical temperature level. Heat transfer to the substrate for media where emission is negligible was shown to be independent of N. The heat transfer to the substrate was shown to be a strong function of n_2, W, τ_0, and bare substrate reflectance. Effects of top interface reflectance and internal scattering dominated the heat transfer behavior. Also, for a moderately reflecting substrate (hemispherical reflectance = 0.58), the heat transfer was shown to have a maximum with respect to optical thickness. This indicates there is a critical thickness of high albedo insulation.

Acknowledgments

The research reported herein was conducted for the Arnold Engineering Development Center (AEDC), Air Force Systems Command (AFSC), by ARO, Inc., a Sverdrup Corporation Company, operating contractor for the AEDC.

References

1 Howe, J. T., and Green, M. J., "Analysis of Sublimation-Cooled Coated Mirrors in Convective and Radiative Environments," *AIAA Journal*, Vol. 11, No. 1, Jan. 1973, pp. 80–87.

2 Wood, B. E., Smith, A. M., Roux, J. A., and Seiber, B. A., "Spectral Infrared Reflectance of H_2O Condensed on LN_2-Cooled Surfaces in Vacuum," *AIAA Journal*, Vol. 9, No. 9, Sept. 1971, pp. 1836–1842.

3 Viskanta, R., "Heat Transfer by Conduction and Radiation in Absorbing and Scattering Materials," ASME JOURNAL OF HEAT TRANSFER, Vol. 87, No. 1, Feb. 1965, pp. 143–150.

4 Weston, K. C., and Hauth, J. L., "Unsteady, Combined Radiation and Conduction in an Absorbing, Scattering, and Emitting Medium," ASME JOURNAL OF HEAT TRANSFER, Vol. 95, No. 3, Aug. 1973, pp. 357–364.

5 Doornink, D. G., and Hering, R. G., "Transient Combined Conductive and Radiative Heat Transfer," ASME JOURNAL OF HEAT TRANSFER, Vol. 94, No. 4, Nov. 1972, pp. 473–478.

6 Viskanta, R., and Grosh, R. J., "Recent Advances in Radiant Heat Transfer," *Appl. Mech. Revs.*, Vol. 17, 1964, pp. 91–100.

7 Steele, F. A., "The Optical Characteristics of Paper," *Paper Trade Journal*, Vol. 100, No. 37, Mar. 1935.

8 Weston, K. C., Howe, J. T., and Green, M. J., "Approximate temperature Distribution for a Diffuse, Highly Reflecting Material," *AIAA Journal*, Vol. 10, No. 9, Sept. 1972, pp. 1252–1254.

9 Chandrasekhar, S., *Radiative Transfer*, Dover, New York, 1960,

10 Merriam, R. L., and Viskanta, R., "Radiative Characteristics of Absorbing, Emitting, and Scattering Media on Opaque Substrates," *Journal of Spacecraft and Rockets*, Vol. 5, No. 10, 1968, pp. 1210–1215.

11 Roux, J. A., Smith, A. M., Shakrokhi, F., "Radiative Transfer Properties of High Albedo CO_2 and H_2O Cryodeposits," *AIAA Progress in Astronautics and Aeronautics: Thermal Control and Radiation*, Vol. 31, C. L. Tien, ed., MIT Press, Cambridge, Mass., 1973, pp. 369–388.

12 Roux, J. A., Todd, D. C., and Smith, A. M., "Eigenvalues and Eigenvectors for Solutions to the Radiative Transport Equation," *AIAA Journal*, Vol. 10, No. 7, July 1972, pp. 973–976.

13 Franklin, J. R., *Matrix Theory*. Prentice-Hall, Englewood Cliffs, New Jersey, 1968, p. 203.

14 Sparrow, E. M., and Cess, R. D., *Radiation Heat Transfer*, Belmont, California, Brooks/Cole Publishing Company, 1966.

APPENDIX

Solution for Convective Boundary Condition

If the heat load $\dot{q}_c$ at the top interface is a result of convective heating, the boundary condition given by equation (17) must be replaced by

$$K\frac{dT}{dy}\bigg|_L = h[T_{aw} - T(y = L)] \text{ at } y = L \tag{A-1}$$

where h and T_{aw} are the specified convective heat-transfer coefficient and adiabatic wall temperature, respectively, and $T(y = L)$ is the medium surface temperature, which is not specified. Then solving equations (15), (16) and (A-1) by employing the same general procedure and assumptions used to obtain equation (19) yields the following explicit expression for the temperature profile in the medium:

$$T(y) = T_S + \frac{(T_{aw} - T_S)\, hy/K}{(1 + hL/K)} - \frac{hy/K}{1 + hL/K}\frac{4\pi}{K}\int_0^\infty \frac{I_0}{(\sigma + k)}\frac{(1 - W)}{W}\sum_{j=1}^{p/2}\frac{(1 - \lambda_j\mu_j)}{\lambda_j{}^2} \times [c_j(1 - e^{\lambda_j \tau_0}) + c_{p+1-j}(1 - e^{-\lambda_j \tau_0})]\, d\nu + \frac{4\pi}{K}\int_0^\infty \frac{I_0}{(\sigma + k)} \times \frac{(1 - W)}{W}\sum_{j=1}^{p/2}\frac{(1 - \lambda_j\mu_j)}{\lambda_j{}^2}[c_j(1 - e^{\lambda_j \tau}) + c_{p+1-j}(1 - e^{-\lambda_j \tau})]\, d\nu + \frac{y}{1 + hL/K}\frac{4\pi}{K}\int_0^\infty I_0\frac{(1 - W)}{W}\sum_{j=1}^{p/2}\frac{(1 - \lambda_j\mu_j)}{\lambda_j} \times [c_j e^{\lambda_j \tau_0} - c_{p+1-j}e^{-\lambda_j \tau_0}]\, d\nu \tag{A-2}$$

The expression for the heat conducted to the substrate becomes

$$\dot{q}_{CS} = \frac{h(T_{aw} - T_S)}{1 + hL/K} - \frac{(h/K)4\pi}{1 + hL/K}\int_0^\infty \frac{I_0}{(\sigma + k)}\frac{(1 - W)}{W}\sum_{j=1}^{p/2} \times \frac{(1 - \lambda_j\mu_j)}{\lambda_j{}^2}[c_j(1 - e^{\lambda_j \tau_0}) + c_{p+1-j}(1 - e^{-\lambda_j \tau_0})]\, d\nu + \frac{4\pi}{1 + hL/K}\int_0^\infty I_0\frac{(1 - W)}{W}\sum_{j=1}^{p/2}\frac{(1 - \lambda_j\mu_j)}{\lambda_j} \times [c_j e^{\lambda_j \tau_0} - c_{p+1-j}e^{-\lambda_j \tau_0}]\, d\nu - 4\pi\int_0^\infty I_0\frac{(1 - W)}{W}\sum_{j=1}^{p/2}\frac{(1 - \lambda_j\mu_j)}{\lambda_j}(c_j - c_{p+1-j})\, d\nu \tag{A-3}$$

while the expression for the radiation flux absorbed by the substrate $\dot{q}_{RS}$ is unchanged and thus equal to equation (22). Finally, the expression for the total heat transfer to the substrate takes the form

$$\dot{q}_0 = \frac{h(T_{aw} - T_S)}{1 + hL/K} - \frac{(h/K)4\pi}{1 + hL/K}\int_0^\infty \frac{I_0}{(\sigma + k)}\frac{(1 - W)}{W}\sum_{j=1}^{p/2}\frac{(1 - \lambda_j\mu_j)}{\lambda_j{}^2} \times [c_j(1 - e^{\lambda_j \tau_0}) + c_{p+1-j}(1 - e^{-\lambda_j \tau_0})]\, d\nu + \frac{4\pi}{1 + hL/K}\int_0^\infty I_0 \times \frac{(1 - W)}{W}\sum_{j=1}^{p/2}\frac{(1 - \lambda_j\mu_j)}{\lambda_j}[c_j e^{\lambda_j \tau_0} - c_{p+1-j}e^{-\lambda_j \tau_0}]\, d\nu \tag{A-4}$$

Equations (A-2), (A-3), and (A-4) can be applied to a medium and substrate with gray optical properties by employing the same procedure used to obtain equations (25), (26), and (28) from equations (19), (20), and (24).

J. L. Krazinski
Graduate Student,
Department of Aeronautical
and Astronautical Engineering

R. O. Buckius
Assistant Professor,
Department of Mechanical
and Industrial Engineering, Assoc. Mem. ASME

H. Krier
Associate Professor,
Department of Aeronautical
and Astronautical Engineering

University of Illinois at Urbana-Champaign,
Urbana, Ill.

A Model for Flame Propagation in Low Volatile Coal Dust-Air Mixtures

A model describing steady, laminar flame propagation in low volatile coal dust-air mixtures is presented. The model includes radiative transport, a two-phase energy equation, and heterogeneous carbon gasification of the coal particles. The differential approximation (or method of spherical harmonics) was used to represent the one-dimensional radiant energy transport. The equations were numerically integrated and predictions of flame structure and the adiabatic flame speed are presented. The effects of radiation properties and coal particle size are presented and discussed. The influence on the temperature profiles of heat released in the solid phase is also described.

Introduction

Coal mine explosions have been a problem for hundreds of years. The projected need for coal as an energy source will demand increased subsurface mining which will, in turn, require improved techniques for the prevention of dust explosions. Preventive procedures, however, must rely on fundamental knowledge concerning the behavior of coal dust combustion. To this end, a mathematical model of flame propagation through coal dust-air mixtures has been developed. The model has been used to predict burning velocities and to study the structure of coal dust-air flames.

Analysis

Assumptions. Coal particles burn in a very complicated manner. The combustion process includes heterogeneous surface reactions, devolatilization and subsequent reaction of the volatile components, swelling, cracking, and other physiochemical changes to the particles. In addition, it is well known that coal particles do not always burn simply as shrinking spheres but can burn internally and form cenospheres (hollow spheres) as well [1, 2].[1] The composition of the volatiles released and the combustion itself depend upon the rate of heating in a flame, thereby making analytical description of the process extremely difficult.

Therefore, in order to obtain a tractable model of the combustion behavior of coal particles, assumptions must be made. Here it is assumed that the particles burn only at the surface according to the irreversible, heterogeneous reaction $C(s) + O_2 \rightarrow CO_2$. Swelling and cenosphere formation are not considered. Volatiles combustion is not included and hence the model is strictly applicable only to low volatile coals. A list of additional assumptions used in developing the theory is given in Table 1.

Two-Phase Reactive Flow. The governing equations for the model are those for steady, laminar flow in a two-phase system. These equations are simplified forms of the general, multiphase flow equations given in the text by Soo [3].

Table 1 Model assumptions

1	The flow is low speed, one-dimensional, and steady. The flow is area-averaged to represent a laminar two-phase system.
2	Body forces are neglected.
3	Viscous forces within the gas phase are neglected.
4	The velocities of the two phases are equal.
5	Pressure in the gas phase is constant while the solid phase pressure is assumed to be zero.
6	Radiative heat transfer to the gas phase is neglected.
7	The Dufour effect (heat flux produced by concentration gradients) is neglected.
8	The Soret effect (mass transfer due to temperature gradients) is neglected.
9	The molecular weight of the gas and the specific heats of the phases are taken as constant.
10	Although actual coal particles are irregular in shape, they are treated here as equivalent spheres by using a sphericity factor. Their density remains constant. They are of uniform size and uniform temperature.
11	Volatiles combustion is not considered.
12	The frequency of inter-particle collisions is assumed to be negligible.
13	Molecular diffusion in the gas phase is not influenced by the presence of coal particles.

[1] Numbers in brackets designate References at end of paper.

Contributed by the Heat Transfer Division of THE AMERICAN SOCIETY OF MECHANICAL ENGINEERS and presented at the AIChE—ASME Heat Transfer Conference, Salt Lake City, Utah, August 15-17, 1977. Manuscript received by the Heat Transfer Division May 2, 1977. Paper No. 77-HT-18.

In a two-phase system, there are three sets of equations—a set for each of the two species and the overall mixture equations. Since the balance equations for the species must add up to the respective mixture equations, only two of these sets are independent. Here the equations for the solid phase and for the mixture are used. The resulting equations are:

Mass Balances.

$$\rho_m U = M = \text{constant} \tag{1}$$

$$\frac{dZ}{dx} = \frac{\Gamma_c}{M} = \frac{-3\rho_m Z \dot{R}_c}{r_c M} \tag{2}$$

$$\frac{d}{dx}[(1-Z)\rho_m U Y_{CO_2}] = \frac{d}{dx}\left[D_{CO_2}(1-Z)\rho_m \frac{dY_{CO_2}}{dx}\right] - \frac{11}{3}\Gamma_c \tag{3}$$

Energy Balances

$$M\frac{d}{dx}[ZC_{p_c}(T_c - T_0) + (1-Z)C_{p_g}(T_g - T_0)] = \frac{d}{dx}\left(\lambda_g \frac{dT_g}{dx}\right) + \Gamma_c H_{CHEM} - \frac{dq_r}{dx} \tag{4}$$

$$M\frac{d}{dx}[ZC_{p_c}(T_c - T_0)] = F_{gc}(T_g - T_c) - \frac{dq_r}{dx} - \Gamma_c H_{COAL} \tag{5}$$

Radiation Equations.

$$\frac{dq_r}{dx} + aG = 4a\sigma T_c^4 \tag{6}$$

$$\frac{dG}{dx} = -3(K - \sigma_s f_1)q_r \tag{7}$$

Auxiliary Equations.

$$\rho_g T_g = \frac{P_g(MW)_g}{R} = \text{constant} \tag{8}$$

$$Y_{O_2} + Y_{N_2} + Y_{CO_2} = 1 \tag{9}$$

$$\rho_m = \frac{\rho_c \rho_g}{Z\rho_g + (1-Z)\rho_c} \tag{10}$$

Here the diffusion coefficient, D_{CO_2}, and the thermal conductivity, λ_g, are assumed to vary with temperature according to

$$D_{CO_2} = (D_{CO_2})_0 \left(\frac{T_g}{T_0}\right)^{1.75} \tag{11}$$

$$\lambda_g = (\lambda_g)_0 \left(\frac{T_g}{T_0}\right)^{0.75} \tag{12}$$

For laminar flow with $U_c = U_g$ the Nusselt number for spherical particles is 2. In this case F_{gc}, the heat transfer lag coefficient, becomes

$$F_{gc} = \frac{3Z\lambda_g \rho_m}{r_c{}^2 \rho_c} \tag{13}$$

Reaction Kinetics. In order to evaluate Γ_c, a functional form must be found for the regression rate, $\dot{R}_c$. Here an expression for $\dot{R}_c$ was obtained by applying Essenhigh's burning time expression [1]. Then $\dot{R}_c$ becomes

$$\dot{R}_c = \frac{1}{8F_D K_D r_c + 2F_{CH}K_{CH}} \tag{14}$$

The factors F_D and F_{CH} are functions of excess air, which account for the progressive vitiation of oxygen in flames. These factors have been set equal to one for present calculations, the disappearance of oxygen being accounted for in the parameters K_D and K_{CH}. These parameters are as given by Essenhigh [1] except that here the mole fraction of oxygen (X_{O_2}) varies throughout the flame.

$$K_D = \frac{\rho_c}{3\rho_{g_0}(D_{O_2})_0 X_{O_2}\left(\frac{T_g}{T_0}\right)^{0.75}} \tag{15}$$

$$K_{CH} = \frac{\left(\frac{4\rho_c}{3}\right)\left[\frac{2\pi R T_c}{(MW_g)}\right]^{0.5}}{X_{O_2}P_g \exp(-E_1/RT_c)} \tag{16}$$

The temperature in the thermal boundary layer surrounding the particles is taken to be T_g.

Notice that the reaction term Γ_c is not as simple as the expressions used for gas-phase, homogeneous reactions. For particle combustion,

Nomenclature

a = absorption coefficient (m^{-1})
C_{p_c} = specific heat of coal (1.794×10^3 J/kg-K)
C_{p_g} = specific heat of gas (1.14×10^3 J/kg-K)
d_c = coal particle dia (m)
D_{O_2} = diffusion coefficient for O_2 in air (1.81×10^{-5} m^2/s at 298 K)
D_{CO_2} = diffusion coefficient for CO_2 in N_2 (1.65×10^{-5} m^2/s at 298 K)
E_1 = activation energy of adsorption used in reaction rate (54.34 MJ/mole)
f_1 = anisotropic scattering parameter
F_{gc} = heat transfer lag coefficient (W/m^3 - K)
F_D = oxygen vitiation factor for reaction under diffusional control
F_{CH} = oxygen vitiation factor for reaction under chemical control
G = average intensity (W/m^2)
H_{CHEM} = heat of reaction of coal (-2.32×10^7 J/kg of coal)
H_{COAL} = energy released in solid phase (J/kg)
K_D = burning parameter for reaction under diffusional control (s/m^2)
K_{CH} = burning parameter for reaction under chemical control (s/m^1)
K = extinction coefficient (m^{-1})
M = mass flux (kg/m^2 – s)
$(MW)_g$ = gas molecular weight (28.86 kg/mole)
n = number density (m^{-3})
P_g = gas pressure (1.013×10^5 Pa)
q_r = radiative heat flux (W/m^2)
Q_{abs} = absorption efficiency (0.84)
Q_{sca} = scattering efficiency (0.16)
r_c = coal particle radius (m)
R = universal gas constant (8314 J/mole-K)
$\dot{R}_c$ = surface regression rate of coal particles (m/s)
T = temperature (T_0 is 298 K)
U = velocity (m/s)
x = distance (m)
X_{O_2} = mole fraction of oxygen
Y_{O_2}, Y_{CO_2}, Y_{N_2} = mass fractions of oxygen, carbon dioxide, and nitrogen, respectively (Y_{O_2} is initially 0.235 in the stoichiometric case).
Z = mass fraction of coal (Z_0 for the stoichiometric case is 8.112×10^{-2} which corresponds to 0.104 kg/m^3)
$\alpha = 2\pi r_c/\lambda$
Γ_c = coal mass depletion rate per unit volume of mixture (kg/m^3-s)
λ = wavelength (m)
λ_g = thermal conductivity of gas (2.52×10^{-2} W/m-K at 298 K)
ρ = density (ρ_c was taken to be 1.25×10^3 kg/m^3)
σ = Stefan-Boltzmann constant (5.669×10^{-8} W/m^2-K^4)
σ_s = scattering coefficient (m^{-1})
Φ = scattering phase function
ω = solid angle
μ = cosine of polar angle

Subscripts

a = adiabatic
c = coal
g = gas
m = mixture
o = conditions at cold end
f = conditions at hot end

the reaction rate includes two terms. The parameter K_D accounts for reactions which are controlled by the rate of oxygen diffusion to the particle surface. The factor K_{CH} accounts for reactions which are controlled by the rate of chemical reaction at the particle surface. For completeness, both types of rate control are included in Γ_c.

Radiation Properties. An approximate formulation of the radiative transfer is employed which is referred to as the differential approximation. The governing expressions given in equations (6) and (7) are obtained by appropriate averages of the one-dimensional gray equation of transfer. The scattering phase function has been represented in the linear anisotropic form

$$\Phi(\mu',\mu) = 1 + 3f_1\mu\mu', -\frac{1}{3} < f_1 < \frac{1}{3} \tag{17}$$

and the gas has been assumed to be transparent to radiation. The averaging required to obtain equations (6) and (7) can be obtained either by the spherical harmonics method [4, 5] or the moment method [5]. For a one-dimensional geometry this method has been shown to be quite accurate [6, 7].

It remains to quantify the radiative properties for coal dust. This requires knowledge of the optical constants of the particle material, the scattering phase function of the coal particle, the size distribution, and the coal concentration. The real and imaginary parts of the index of refraction for coals, carbons, and soot have been reported [8–10]. The spectral characteristics throughout the visible and infrared regions show marked differences between carbon and coal both in magnitude and spectral variation. These values also depend upon the type of coal considered. The spectral variations of coal in the near infrared are not great, so that constant values were used in this work. The real part of the index of refraction used is 1.75 and the imaginary part is 0.35.

The absorption and scattering coefficients for a monodisperse coal dust cloud are defined as

$$a = n\pi r_c{}^2 Q_{abs}(\alpha) \tag{18}$$

$$\sigma_s = n\pi r_c{}^2 Q_{sca}(\alpha) \tag{19}$$

where n is the number of particles per unit mixture volume, Q_{abs} the absorption efficiency, Q_{sca} the scattering efficiency, and $\alpha = 2\pi r/\lambda$, with λ representing wavelength. For steady flow with a monodisperse suspension, n can be calculated from

$$nU = n_0 U_0. \tag{20}$$

The coal dust particles treated here are typically larger than 10 μm in radius. With temperatures of the order of 1500 K and larger, the efficiencies in the large particle limit (α large) can be used. Thus, for constant optical properties, the absorption and scattering efficiencies are constant with respect to wavelength (i.e., gray behavior). The resulting absorption coefficient, using the optical constants given above, is

$$a = 0.84 n\pi r_c{}^2. \tag{21}$$

The radiative transfer includes the effects of scattering through the scattering coefficient and the scattering phase function. In the large particle limit, the diffracted components and the reflected components can be separated. The diffracted portion is concentrated into a small solid angle about the direction of propagation of the incident beam [11, 12] and, in this work, is not separated from the transmitted energy incident on the particle. The reflected portion of the scattered radiation for an opaque particle is a surface phenomenon. The coal particle surface is very rough so that the phase function is assumed to be that of a diffuse, opaque sphere. The dominant scattering direction is back into the incident direction. This is represented as

$$\Phi(\mu) = 1 - \mu\mu' \tag{22}$$

i.e., $f_1 = -(1/3)$. Since the scattering is represented as a surface phenomenon, the scattering coefficient is

$$\sigma_s = 0.16\, n\pi r_c{}^2 \tag{23}$$

for the coal properties given above.

Boundary Conditions. The nine unknowns in this problem are the coal mass fraction (Z), the temperatures of the phases (T_c, T_g), the gas mass fractions (Y_{O_2}, Y_{CO_2}), the variables describing the radiation field (q_r, G), the gas density (ρ_g) and the velocity (U). The nine equations which must be solved are the mixture continuity equation, equation (1), the coal mass balance equation, equation (2), the CO_2 mass balance equation, equation (3), the mixture and coal energy equations, equations (4) and (5), the radiation equations, equations (6) and (7), a state equation, equation (8), and the gas-phase mass conservation equation, equation (9).

The boundary conditions are given at $\pm\infty$. At $-\infty$ there is a mixture of coal dust and air in equilibrium at

$$T_c = T_g = 298 \text{ K}. \tag{24}$$

The initial values of Z and Y_{O_2} are known. The velocity at $-\infty$, U_0, is an unknown parameter. For zero heat loss, it is the adiabatic burning velocity and is dependent only on the initial conditions of the mixture. Since particles are present at $-\infty$, the adiabatic conditions on the radiation field are

$$q_r(-\infty) = 0 \tag{25}$$

$$G(-\infty) = 4\sigma T_0{}^4(-\infty) \tag{26}$$

At $+\infty$, for stoichiometric burning, Z and Y_{O_2} are zero. In addition, the temperatures are given by

$$T_c = T_g = T_{fa} \tag{27}$$

where T_{fa} is the (known) adiabatic flame temperature for zero heat loss. The adiabatic radiation boundary condition is

$$q_r(+\infty) = 0 \tag{28}$$

since the particles absorb all the energy at $x = +\infty$ (the particles disappear only as $x \to +\infty$).

Solution Techniques. This is a two-point boundary value problem with conditions being given at $\pm\infty$. Of course, one cannot integrate the equations over an infinite distance; thus, some approximations must be made to solve the problem. Here the two-point boundary value problem was converted into an initial value problem in which the integration is started from some point $x = 0$ assumed to be "far" from the region of maximum combustion. It is assumed that chemical reaction in the region $x = -\infty$ to $x = 0$ can be neglected. In order to insure that the reaction rate, Γ_c, is zero at $x = 0$, the term (E_1/RT_c) is replaced by

$$\left(\frac{E_1}{RT_f}\right)\left(\frac{T_f - T_0}{T_c - T_0}\right)$$

in Γ_c, as was suggested by Friedman and Burke [13]. This makes Γ_c zero at $x = 0$ where $T_c = T_g = T_0$, but approximates (E_1/RT_c) at the hot end where $T_c \simeq T_f$.

Because of diffusion, the value of Y_{CO_2} at $x = 0$ will not be exactly zero but is given by

$$U_o(Y_{CO_2})_o = D_{CO_2}\left.\frac{dY_{CO_2}}{dx}\right|_{x=0}. \tag{29}$$

Also, the values of $\lambda_g(dT_g/dx)$ and q_r at $x = 0$ will not, in general, be known. Physically, these quantities represent conductive and radiative heat losses from the system. This is similar to the concept of a flameholder used by Hirschfelder et al. [14]. This heat loss can be calculated from the heat balance between $x = 0$ and $x = +\infty$:

$$\lambda_g \left.\frac{dT_g}{dx}\right|_{x=0} - q_r\Big|_{x=0} = M[C_{p_c}Z_\infty + C_{p_g}(1 - Z_\infty)] \cdot (T_{fa} - T_f) \tag{30}$$

where Z_∞ is the mass fraction of coal at $x = +\infty$. The parameter T_f is fixed for each problem and as $T_f \to T_{fa}$, U_0 becomes equivalent to the adiabatic burning velocity.

The radiation boundary condition must also be modified for use at $x = 0$. All radiation arriving at $x = 0$ is assumed to be absorbed (the back scattered portion was found to be negligible); thus, the point x

= 0 is treated as if it is a black wall. In this case, the boundary condition becomes

$$2aq_r(0) = \left.\frac{dq_r}{dx}\right|_{x=0} \tag{31}$$

In order to start the integration at $x = 0$, one must, in general, know the initial values of Y_{CO_2}, dT_g/dx, and q_r. In addition, the burning velocity, U_0, is unknown. Since $dT_g/dx|_{x=0}$, $q_r(0)$, and U_0 are related by equation (30), three values would have to be assumed in order to start the integration. One would then have to iterate on these values until the boundary conditions for the combustion products were satisfied at a given location (the hot end). In practice, due to the expected long preheat zones (discussed further in the next section), the heat loss by conduction is very small and all gradients are initially very low. Hence, Y_{CO_2} and dT_g/dx are assumed to be zero at $x = 0$. Then the solution procedure involves assuming a value of U_0 and calculating $q_r(0)$ from equation (30) with $dT_g/dx|_{x=0} = 0$. The equations are solved by iterating on U_0 until the boundary conditions at the hot end are satisfied. The iteration was terminated when convergence on U_0 to within 2 percent had been achieved.

Because of the relatively short reaction zone and long thermal relaxation region, the set of differential equations forms a stiff system which is difficult to integrate. The equations were solved using the subroutine DIFSUB and developed by C. W. Gear [15]. This subroutine uses a predictor-corrector method with an option for integrating stiff systems. It features an automatic step size selection which allows the integrator to take the longest step possible while satisfying the prescribed error criterion.

Calculated Results

Flame Structure and Velocity. Prior to the introduction of the differential approximation for radiative transport, calculations provided the classical, premixed, flame structures of relatively thin flames and low propagation speeds. For example, using the expression for Γ_c discussed previously, the flame speed was predicted to be 2.8×10^{-3} m/s with a conductive heat loss of only 12.55 W/m^2 at the cold end. Extrapolating the speed from other calculations at higher heat loss, a stoichiometric mixture of coal dust (0.104 kg/m^3) with particles of 50 μm in diameter results in an adiabatic flame speed of 2.82×10^{-3} m/s.

Such low speeds were originally thought to be the result of the limiting reaction kinetics as given by the functional form of Γ_c, an expression derived from burning experiments of single coal particles [1]. However, even at gasification rates of $100 \times \Gamma_c$, the adiabatic flame speed was predicted to be only 2.1×10^{-2} m/s.

A typical profile of the temperatures of the gas and coal particles and of the coal mass fraction, for the case *without* radiative transport, is shown in Fig. 1. Here the flame is fairly thin, approximately 0.1 m in length for the predicted adiabatic speed of 2.82×10^{-3} m/s. Notice also that the coal particle temperature equilibrates very rapidly to that of the gas. The assumed thermodynamic and chemical parameters specified for the coal dust flame calculations are given in the nomenclature.

With the differential approximation utilized to represent the expected strong contribution of radiative transport, the flame speeds and flame thicknesses increase dramatically For a stoichiometric mixture of small coal particles ($d_{c_0} = 30$ μm), the adiabatic flame speed is predicted to be 0.716 m/s. The flame thickness here grows to proportions of several meters. Fig. 2 shows the predicted coal particle and gas temperature profiles as well as the fairly thick reaction zone. The heterogeneous reaction rate term has a long tail caused by the diffusion-controlled rate term in Γ_c. In addition, the radiative transport provides a temperature over-shoot near the end of the reaction zone as well as a long (10 m) relaxation zone in which the coal particle and gas temperatures equilibrate. A required heat loss, by radiation only, was 2.8×10^3 W/m^2 at the cold end.

Burning velocities of this order have been observed experimentally in large enclosed furnaces [16–18] and in small furnaces with heated walls [19, 20]. Structure of this large scale has also been observed experimentally [16–18]. These results should be compared with those obtained from small scale burners [21, 22]. In these latter experiments, the burning velocities are lower and the flames are much thinner than those observed in the larger more adiabatic furnaces [16].

Fig. 3 illustrates additional flame structure for the case shown in Fig. 2. Here the coal mass fraction and particle size variation are given. Notice that the predicted variation of d_c/d_{c_0} is *not* a linear function of the distance, x. A variation of $d_c/d_{c_0} = 1 + bx$ was assumed by Bhaduri and Bandyopadhyay [23] as input to their model. This, of course, over specifies the problem if an energy equation and species conservation equations are being solved additionally.

For all of the results discussed above, it has been assumed that the energy released during reaction was liberated in the gas phase only. In general, however, a fraction of the energy may be released on the particle surface. This effect would be included in the term containing

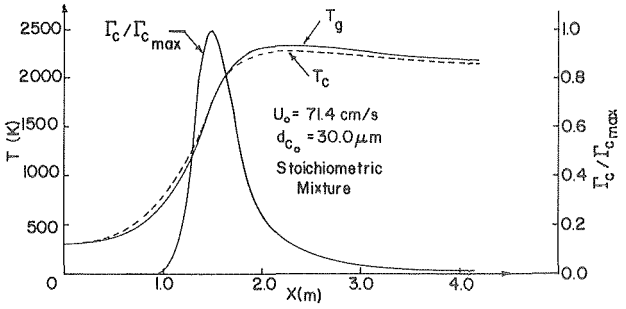

Fig. 2 Temperature and reaction zone profiles predicted *with* radiation transport. (U_0 = 0.714 m/s)

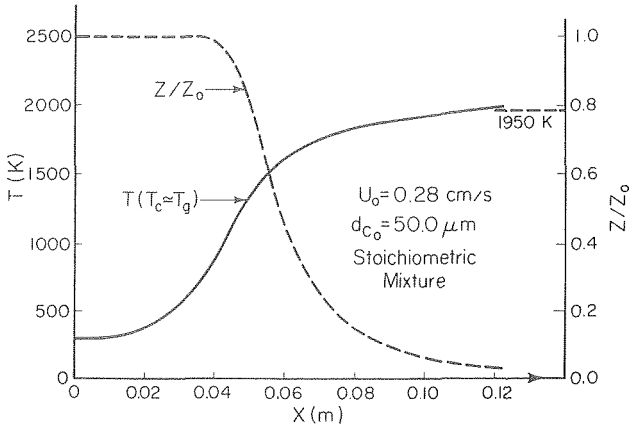

Fig. 1 Temperature and coal mass fraction profiles predicted *without* radiation transport. (U_o = 0.0028 m/s)

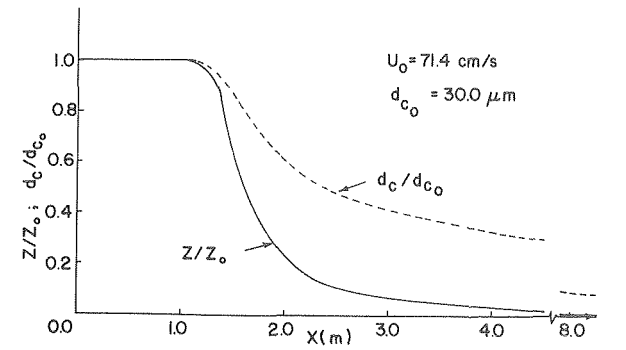

Fig. 3 Coal mass fraction and particle diameter variation, complementary to profiles shown in Fig. 2

H_{COAL} in the coal energy balance equation, equation (5). Based on their calculations, Baum and Street have assumed that approximately 30 percent of the energy is released in the solid phase [24].

In order to assess the effect on flame structure of this solid phase heat release, a calculation was made assuming 50 percent of the heat release was in the coal. The resultant changes in the temperature differences between the phases are illustrated in Fig. 4. Initially, there is an increase in the coal temperature over the gas temperature since the particles are being heated by radiation. Then, for the case of 50 percent of the energy released in the coal (dashed line), there is a further increase in the particle temperature due to the heat release. After the maxima there is a decrease because chemical reaction is releasing heat in the gas and also because the particles are losing appreciable amounts of energy by radiation. As the particles continue to lose energy, their temperature slowly relaxes to the adiabatic flame temperature.

It should be emphasized here that even though the difference ($T_c - T_g$) is greater in the second case, the absolute value of T_c is smaller. In fact, the maximum value of T_c for the case of 50 percent heat release in the solid was some 30 K less than its maximum value for the case of 100 percent heat release in the gas. This was probably due to the fact that even though the chemical reaction was releasing energy in the coal, the particles were also losing more energy and the net result was a decrease in the maximum value of T_c. It was also found that with 50 percent of the energy released in the solid phase, the burning velocity increased only 4.8 percent from 0.707 m/s to 0.741 m/s.

Heat Loss Versus Flame Speed. The adiabatic problem is defined for a region of infinite dimensions in which as $x \to -\infty$ there is no energy lost by either conduction or radiation so that as $x \to +\infty$ the temperatures approach the adiabatic flame temperature. The solution procedure, of course, is an initial value problem in which a small but finite energy is lost at some given point assumed far from the region of maximum combustion.

With radiation included, the preheat zones are very large when compared to classical analyses of gaseous, premixed laminar flames. For such large distances, the heat lost by conduction is very small because the temperature gradients are very low. Therefore, to determine the effect of heat loss (in the direction of propagation), it is assumed that there is only a radiation loss of $-q_r$ at $x = 0$, the cold end.

Fig. 5 presents the prediction of flame speed as a function of radiation losses. The adiabatic flame speed is determined by extrapolating to zero q_r, on the curve of q_r versus U_0. Calculations have been made for flames in which the temperature difference is only 3 K from the adiabatic value of 1953 K. This is shown in the figure. The heat losses at the cold end were small, averaging less than 2.1×10^3 W/m^2. But for cases where the final temperature was about 100 K lower than the adiabatic temperature, the required radiation energy losses exceed 8.4×10^4 W/m^2.

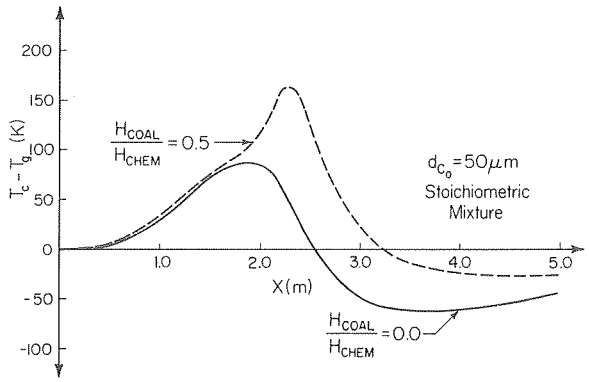

Fig. 4 Difference in coal particle and gas temperatures as a function of the distance in a flame for two cases of solid-phase energy release

As one moves to larger assumed heat losses (and hence lower final temperatures at the hot end), the preheat zone begins to shrink. At a temperature difference exceeding 200 K, the preheat zone is $1/20$ of the length predicted for the 3 K loss. Solutions are then impossible unless one begins to assume that a heat conduction loss also becomes important. Note, too, that for the case of the 200 K loss ($T_f \simeq 1750$ K), the average flame speed is less than 0.50 m/s, while the adiabatic speed is about 0.70 m/s.

The effect of radiative transfer approximations is shown by the three curves in Fig. 5. Curve A includes absorption and anisotropic scattering. This represents an absorption efficiency of 0.84 and a predominant back scattering phase function which most accurately describes coal particles. Curve B assumes that the coal particle is black and thus there is no scattering. The remaining curve C includes the realistic absorption efficiency of 0.84 and neglects scattering. Alternately, curve C can be interpreted as including scattering as if the scattered energy were concentrated into a small solid angle in the forward direction and, therefore, impossible to distinguish from the incident energy on a particle. It is seen that the maximum difference between these approximations for the adiabatic flame velocity is 11 percent, with the most realistic (curve A) being the lowest.

The differential approximation being used here reduces to the correct limiting expressions in the optically thin emission dominated case and the optically thick case. Yet, if either of these limiting solutions are employed, the resulting predictions would be quite different. For the optically thin case, the high temperature region will radiate energy in both directions. Since the media emits and does not absorb, there is a heat loss as $x \to +\infty$ and the temperature profiles would decay with increasing x. Thus, the adiabatic solution could not be obtained. For the optically thick case, the profiles will be similar to the conduction solution (Fig. 1) due to the diffusion type dependence of the optically thick solution. The profiles would be broader and the flame speeds higher than those obtained for the conduction solution. Similar results relating to shock structure have been presented by Scala and Sampson [25]. Therefore, for the optical depths encountered here, neither limiting solution would accurately describe the problem.

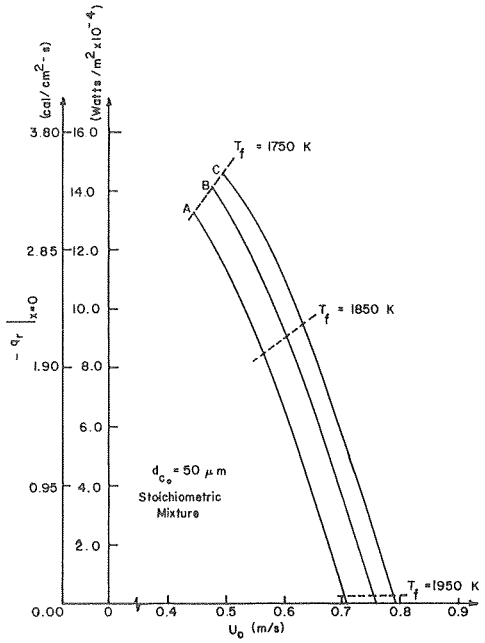

Fig. 5 Laminar flame speed as a function of heat loss by radiation at the cold end

Curve A: absorption and back scattering
Curve B: black particles and no scattering
Curve C: absorption and strong forward scattering

Flame Speed Versus Particle Size. Fig. 6 presents the predicted adiabatic flame speeds as a function of coal particle size. From a standpoint of specific surface (S/V ratio), large particles provide less specific surface for a given fixed mixture ratio. Therefore, they show a lower reaction rate at any given position and, hence, a reduction in flame speed. Previous calculations without radiation showed a marked variation in U_0 as d_{c_o} was decreased, with U_0 increasing 43 percent from 2.8×10^{-3} m/s to 4.0×10^{-3} m/s as d_{c_o} decreased from 50 μm to 25 μm.

However with radiation included and for our coal depletion rate term, the reduction in flame speed with size is only slight, as shown in Fig. 6. Decreasing the magnitude of Γ_c (by multiplying the reaction rate by 0.4) lowered the burning velocities, but still showed the same relative variation of U_0 with particle size. Burning velocities measured by Hattori using 60 μm to 140 μm particles also decreased with particle size although his velocities were in the 0.1 to 0.2 m/s range [26]. Grumer and Bruszak [27] have found a slight increase in flame speed with a decrease in particle size for particles in the 1 to 44 μm range.

The shape of these curves may be due to the combined effects of combustion and radiative heat transfer. From a kinetics point of view, increasing the particle size will decrease Γ_c. Thus a decrease in burning velocity with increased particle size (as was seen in the cases without radiative transport) would be expected. The absorption coefficient for radiation given by equation (18) also varies inversely with particle size for a fixed loading (fixed Z_o). Decreasing d_c would increase the absorption coefficient, effectively making the flame optically thicker. Such a flame would supply less energy to the particles in the preheat zone and a lower burning velocity would be expected. Therefore, the variation of U_0 with particle size would depend on both these opposing factors.

The reduction in flame speed with particle radius (even though slight) is in direct conflict with the predictions of the model presented by Ozerova and Stepanov [28]. Their results are shown as the dotted line in Fig. 6. Because there is too little information given in reference [28] on the kinetic rate parameters, heats of reaction, and other thermodynamic variables, our values cannot be directly compared. However, it appears that in order to predict such a large increase in U_0 with d_{c_o}, either the rate of heterogeneous gasification must be larger than the one being used or additional gas-phase (devolatilization) reactions must be added. Since Ozerova and Stepanov considered carbon combustion only, they did not include devolatilization reactions.

At any rate, it does not appear that flame speeds of the order of 1 m/s would show such a strong increase in speed for the range of particle size shown in Fig. 6. Increasing the rate to 10 or 50 Γ_c will increase the slope, but it will also give much higher values of U_0 than are obtained experimentally.

Concluding Remarks

Utilizing several simplifying assumptions for the steady flame propagation of coal dust-air mixtures, a model has been developed and solutions have been carried out for the flame structure and flame speed. The flame speeds and structure predicted agree with experimental data [16]. The model has used the differential approximation for radiation which represents the transport behavior of such mixtures quite well. The model by Ozerova and Stepanov [28] used a similar but simpler form of the differential approximation.

The predicted dimensions for the flame zones include very long preheat zones and large relaxation zones in which the solid and gas phase temperatures equilibrate. It appears that additional experimental confirmation of this will require careful testing in large scale systems where total energy losses are kept to a minimum. Examples of such systems are those used by Howard and Essenhigh [17] and by Palmer and Tonkin [29], where heat losses to the surroundings were minimized because of the scale of the experiments.

This model can, of course, be made more descriptive of the physiochemical processes of coal dust burning by including a description of the complexities not taken into account. Some of these effects include polydisperse mixtures, two-dimensional heat transport, and devolatilization kinetics. In summary, however, a model has been presented that describes many of the fundamental features of coal dust-air flames and provides a foundation for incorporation of future modeling modifications.

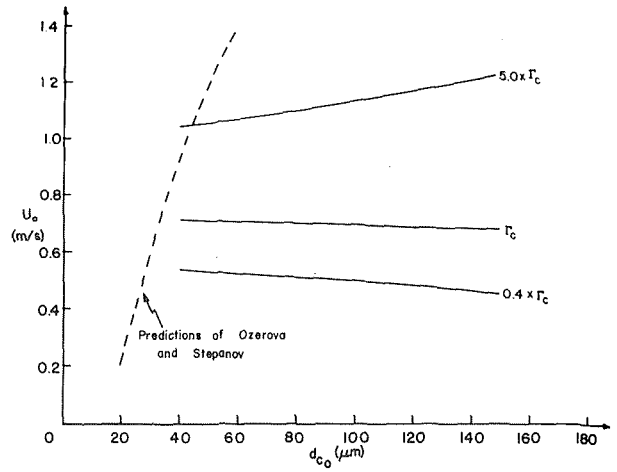

Fig. 6 Predictions of the adiabatic flame speed as a function of coal particle size for three different coal mass depletion rates

References

1 Essenhigh, R. H., "Predicted Burning Times of Solid Particles in an Idealized Dust Flame," *Journal of the Institute of Fuel*, Vol. 34, 1961, pp. 239–244.

2 Brookes, F. R , "The Combustion of Single Captive Particles of Silkstone Coal," *Fuel*, Vol. 48, 1969, pp. 139–149.

3 Soo, S. L., *Fluid Dynamics of Multiphase Systems*, Blaisdell Publishing Co., Waltham, Mass., 1967.

4 Ozisik, M. N., *Radiative Transfer*, John Wiley and Sons, New York, 1973.

5 Cheng, P., "Two-dimensional Radiating Gas Flow by a Moment Method," *AIAA Journal*, Vol. 2, No. 9, 1964, pp. 1662–1664.

6 Cess, R., "On the Differential Approximation in Radiative Transfer," *Zeitschrift fur Angewette Mathematik und Physik*, Vol. 17, 1966, pp. 776–781.

7 Cheng, P., "Study of the Flow of a Radiating Gas by a Differential Approximation," Ph.D. Thesis in Engineering, Stanford University, 1965.

8 Foster, P. J., and Howarth, C. R., "Optical Constants of Carbons and Coals in the Infrared," *Carbon*, Vol. 16, 1968, pp. 719–729.

9 Stull, V. R. and Plass, G. N., "Emissivity of Dispersed Carbon Particles," *Journal of the Optical Society of America*, Vol. 50, 1960, pp. 121–129.

10 Dalzell, W. H. and Sarofim, A. F., "Optical Constants of Soot and their Application to Heat-flux Calculations," ASME, JOURNAL OF HEAT TRANSFER, Vol. 91, 1969, pp. 100–104.

11 Hottel, H. C. and Sarofim, A. F., *Radiative Transfer*, McGraw-Hill, New York, 1967.

12 Blokh, A. G., M. L. Modzalevskaya, and M. N. Galitskaya, "Scattering of Thermal Radiation by Carbon Particles in Flames," *Teploenergetika*, Vol. 19, 1972, pp. 29–31.

13 Friedman, R. and E. Burke, "A Theoretical Model of a Gaseous Combustion Wave Governed by a First Order Reaction," *Journal of Chemical Physics*, Vol. 21, 1953, pp. 710–714.

14 Hirschfelder, J., C. Curtiss, and D. Campbell, "The Theory of Flames and Detonations," *Fourth Symposium (International) on Combustion*, The Williams and Wilkins Co., Baltimore, Md., 1952, pp. 190–211.

15 Gear, C. W., "The Automatic Integration of Ordinary Differential Equations," *Comm. ACM*, Vol. 14, 1971, pp. 176–179 and 185–190.

16 Essenhigh, R. H., "Combustion and Flame Propagation in Coal Systems: A Review," *Sixteenth Symposium (International) on Combustion*, Academic Press, New York, 1976, pp. 353–374.

17 Howard, J. B. and R. H. Essenhigh, "Mechanism of Solid Particle Combustion with Simultaneous Gas-Phase Volatiles Combustion," *Eleventh Symposium (International) on Combustion*, Academic Press, New York, 1967, pp. 399–408.

18 Csaba, J., "Flame Propagation in a Fully Dispersed Coal Dust Suspension," Ph.D. Thesis, Department of Fuel Tech. and Chem. Eng., University of Sheffield (England), 1962.

19 Ghosh, B., D. Basu, and N. K. Roy, "Studies of Pulverized Coal Flames," *Sixth Symposium (International) on Combustion*, Reinhold Publishing Corp., New York, 1956, pp. 595–602.

20 Ghosh, B. and A. A. Orning, "Influence of Physical Factors in Igniting Pulverized Coal," *Industrial and Engineering Chemistry*, Vol. 47, 1955, pp. 117–121.

21 Horton, M. D., Goodson, F. P., and Smoot, L. D., "Characteristics of Flat,

Laminar Coal Dust Flames," *Combustion and Flame*, Vol. 28, 1977, pp. 187–195.

22 Smoot, L. D., Horton, M. D., and Williams, G. A., "Propagation of Laminar Pulverized Coal-Air Flames," *Sixteenth Symposium (International) on Combustion*, Academic Press, New York, 1976, pp. 375–387.

23 Bhaduri, D. and Bandyopadhyay, S., "Combustion in Coal Dust Flames," *Combustion and Flame*, Vol. 17, 1971, pp. 15–24.

24 Baum, M. M. and Street, P. J., "Predicting the Combustion Behavior of Coal Particles," *Combustion Science and Technology*, Vol. 3, 1971, pp. 231–243.

25 Scala, S. M. and Sampson, P. H., "Heat Transfer in Hypersonic Flow with Radiation and Chemical Reaction," *Supersonic Flow Chemical Processes and Radiative Transfer*, edited by Olfe, D. B., and Zahkay, V., The MacMillan Co., New York, 1964, pp. 319–354.

26 Hattori, H., "Flame Propagation in Pulverized Coal-Air Mixtures," Sixth Symposium (International) on Combustion, Reinhold Publishing Corp., New York, 1956, pp. 590–595.

27 Grumer, J. and Bruszak, A. E., "Inhibition of Coal Dust-Air Flames," Bureau of Mines Report of Investigations 7552, U. S. Department of the Interior, Aug. 1971.

28 Ozerova, G. E. and Stepanov, A. M., "Effect of Radiation on Flame Propagation through a Gas Suspension of Solid Fuel Particles," *Combustion, Explosion, and Shock Waves*, Vol. 9, 1973, pp. 543–549.

29 Palmer, K. N. and Tonkin, P. S., "Coal Dust Explosions in a Large-Scale Vertical Tube Apparatus," *Combustion and Flame*, Vol. 17, 1971, pp. 159–170.

T. Ahmad
G. M. Faeth

Mechanical Engineering Department,
The Pennsylvania State University,
University Park, Pa.

An Investigation of the Laminar Overfire Region Along Upright Surfaces

Numerical calculations are presented for the laminar overfire region along an upright burning surface under natural convection conditions. The process was also examined experimentally, using wicks soaked with methanol, ethanol, and propanol to simulate the burning portion of the surface. Predicted flame shapes and wall heat fluxes were within 15–20 percent of the measurements, for various wall inclination angles, except near the tip of the flame where the reaction is quenched by the cold wall. The wall heat flux is nearly constant in the region where the flame is present, but declines beyond the tip of the flame. Shadowgraphs were employed to determine the position of onset of turbulence. For transition beyond the tip of the flame, the flow was laminar for $Gr_x' < .5 - 2 \times 10^8$*, although transition is not completely described by this parameter and effects of fuel type, presence or absence of combustion, distance, and wall angle were also observed.*

Introduction

A fire burning on an upright surface can be divided into two regions: (1) a pyrolysis region, where the wall material is gasified and partly burned in the gas phase adjacent to the surface; (2) the overfire region, where the combustion process is completed and the thermal plume generated by the fire decays by mixing with the ambient gas and heat loss to the surface. The boundary between these two regions is not precisely defined in natural fires, since the rate of pyrolysis at the wall varies in a continuous manner. Pyrolysis rates are strongly dependent upon temperature, however, and a narrow range of temperature (and a correspondingly short distance) separates locations where surface pyrolysis is negligible from points where the surface is generating substantial combustible gases.

Heat transfer between the hot gases and the surface in the overfire region governs heating of the wall material. Eventually, temperatures are reached where pyrolysis is significant. In this manner, the overfire region plays a fundamental role in the mechanism of upward flame spread on surfaces.

The laminar pyrolysis region of a wall fire has been investigated by Kosdon, et al. [1],[1] and Kim, et al. [2]. A variable property solution of the boundary layer equations was developed in similarity variables. The studies assumed a one-step reaction with an infinitely thin diffusion flame, no gaseous radiation, values of unity for the Chapman and Lewis numbers, equal molecular weights, specific heats, and binary diffusivities, etc. Burning rate measurements agreed reasonably well with predictions, particularly for fuels with low molecular weights, where fuel properties most nearly corresponded to the assumptions of the variable property model [2].

Using an integral model proposed by Yang [3], Pagni and Shih [4] investigated the overfire region of wall fires, basing initial conditions on the pyrolysis zone results [2]. Predictions of fuel consumption and flame shape in the overfire region are reported for a wide range of fuels. This model is also capable of providing other quantities as well, e.g., temperatures, velocities, concentrations, etc. [4].

The present investigation extends the work of [4], undertaking more exact theoretical treatment of the laminar portion of the overfire region and giving greater emphasis to heat transfer between the plume and the surface. Unlike the pyrolysis zone, the flow in the overfire region is not similar, and a numerical procedure developed by Hayday, et al. [5] was employed to solve the governing equations. The assumptions of the present analysis were similar to those used during the earlier investigations of the pyrolysis zone [1, 2].

Experiments were conducted to assess the predictions. The pyrolysis zone was simulated by burning fuel-soaked wicks, following the method used by Kim, et al. [6] and Blackshear and Murty [7]. The heat flux to the wall was determined by a transient heating technique. Flame shape was determined from dark field photographs. Shadowgraphs were employed to determine the point of transition to turbulence, so that the measurements could be limited to laminar flow.

Experimental Apparatus and Procedure

Only a brief description of the apparatus is given here. Ahmad [8] provides a more complete discussion. A sketch of the test arrangement is illustrated in Fig. 1. The dimensions of the test walls are summarized in Table 1.

[1] Numbers in brackets designate References at end of paper.

Contributed by the Heat Transfer Division of THE AMERICAN SOCIETY OF MECHANICAL ENGINEERS and presented at the AIChE-ASME Heat Transfer Conference, Salt Lake City, Utah, August 15–17, 1977. Manuscript received at ASME Headquarters November 29, 1977. Paper No. 77-HT-68.

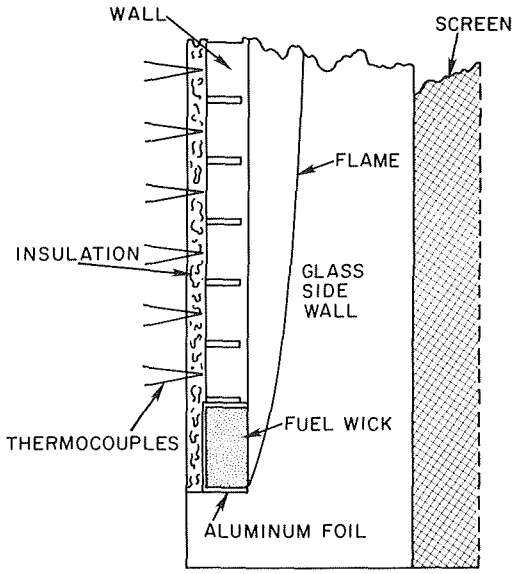

Fig. 1 Test wall assembly

Table 1 Test walls[a]

Wall material	Copper	Steel
Wall height	381	76
Wall width	127	37
Wall thickness	9.5	2.4
Block height	11	3.2
Side wall width	38	19
Screen to wall distance	70	40

[a] All distances in mm.

Pyrolysis Zone. The pyrolysis zone was simulated by igniting the front surface of a fuel-soaked wick [6, 7]. Burning was limited to the front surface by shielding the remaining sides with aluminum foil. Wicks were constructed from various porous furnace bricks and insulating materials; the type of material had no apparent effect on the measurements. The fuel burning rate was measured by weighing the wick before and after combustion over a timed interval. Methanol, ethanol, and propanol were used as test fuels, since they provide a wide variation of properties while minimizing observation difficulties and radiation due to soot formation.

Test Wall. Transient heating of the wall was used to measure the heat flux in the overfire region. In order to obtain the variation of heat flux with position, the wall was segmented into blocks. Three columns of blocks extended along the wall; only the center column was used for the measurements. The dimensions of the blocks are given in Table 1. Measuring the rate of change of temperature of the blocks yields the heat flux to the wall, given the thermal capacity of the blocks. For the heat flux values encountered during the tests, calculations indicated that block temperatures were essentially uniform at each instant of time (the Biot modulus at all conditions was less than 0.001); therefore, copper-constantan thermocouples were mounted on the rear surface of the wall. The thermocouple wires were passed along the wall and covered with insulation in order to reduce errors resulting from the fin-effect of the wires. The temperature of each block was continuously recorded to indicate its heating rate. The thermal capacity of the wall materials was verified by calorimetry.

Condensed material was observed on the wall in the region near the end of the pyrolysis zone. The condensate disappeared, however, early in the wall heating process so that heat flux measurements, which were not influenced by this effect, could be made.

Glass side walls were used to help maintain two-dimensional flow near the center of the wall, and still provide a means of observing the flame. One layer of screening (2 mm spacing, 0.5 mm diameter wire) was mounted across the outer edge of the side walls to reduce disturbances from the room.

Flame Observations. The flames were photographed in a darkened room with a 4 × 5 Super Graflex Camera at a magnification of approximately unity, using Polaroid film (ASA 3000).

The onset of turbulence was determined by a shadowgraph, which employed a mercury arc source collimated with a 180 mm diameter, 1230 mm focal length, front surface parabolic reflector. The shadowgraph was projected on a screen 4 m from the test wall in order to provide high sensitivity.

Experimental Accuracy. The burning rate measurements are averages of three tests at a given condition. The repeatability of these measurements was within ten percent of the mean.

The heat flux measurements were obtained by averaging two tests at a given condition. These measurements were reproducible within 15 percent, with the greatest differences encountered near the point of transition to turbulent flow.

A typical flame photograph is illustrated in Fig. 2. To the eye, the flame zone appeared as a thin bright blue region, surrounded by a duller glowing zone. It was difficult to resolve this detail on the pho-

Nomenclature

B = mass transfer driving potential, equation (18)
C_p = specific heat at constant pressure
F = buoyancy parameter, equation (20)
f = dimensionless stream function
Gr_x^* = modified Grashof number, $Lg \cos \phi x^3/4\, C_p T_\infty \nu_\infty^2$
Gr_x' = modified Grashof number, $g \cos \phi x^3/\nu_\infty^2$
g = acceleration of gravity
h = enthalpy
h_i^0 = enthalpy of formation of i
L = effective heat of vaporization
M_i = molecular weight of i
$\dot{m}''$ = wall mass flux
Pr = Prandtl number
Q = heat of combustion per ν_F' moles of fuel
$\dot{q}''$ = wall heat flux
r = stoichiometry parameter, equation (18)
T = temperature
u = velocity parallel to wall
v = velocity normal to wall
$\dot{w}$ = normalized reaction rate, equation (6)
$\dot{w}_i$ = reaction rate of species i
x = distance along wall
x_0 = end of pyrolysis zone
y = distance normal to wall
Y_i = mass fraction of species i
Y_{FT} = fuel mass fraction in transferred gas
η = dimensionless distance normal to wall, equation (15)
ξ = dimensionless distance along wall, x/x_0
θ_i = Shvab-Zeldovich variables, equation (13)
λ = thermal conductivity
μ = dynamic viscosity
ν = kinematic viscosity
ν_i', ν_i'' = stoichiometric coefficients
ρ = density
τ_0 = dimensionless wall enthalpy, h_{w_0}/L
τ_1 = dimensionless wall enthalpy, h_w/L
ϕ = angle of wall from vertical
ψ = stream function

Subscripts

avg = average value
f = flame
F = fuel
O = oxygen
P = products of combustion
w = wall above pyrolysis zone
w_0 = wall in pyrolysis zone
∞ = ambient

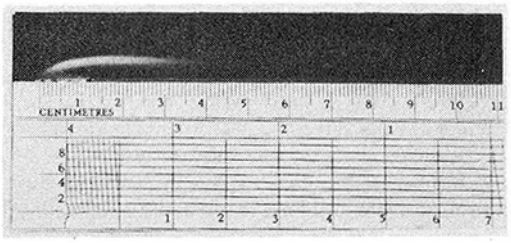

Fig. 2 Photograph of a methanol wall fire, x_0 = 11.1 mm

tographs, and the center of the luminous region was taken as the position of the flame. Measurements were limited to conditions, where the glowing zone extended only ±20 percent of the distance between the center position and the wall.

Analysis

The analysis considers a smooth flat wall at an angle ϕ from the vertical, with a region of length x_0 undergoing pyrolysis at the base of the wall. The flame is overventilated, and when fuel consumption is complete the flame returns to the wall at $x_f > x_0$ under the assumption of a thin diffusion flame. The combusting plume region lies between x_0 and x_f; a thermal plume region is at distances greater than x_f.

The similarity solutions for the pyrolysis zone [1, 2] provide initial conditions for the overfire region. In order to make maximum use of these results, the assumptions and much of the notation of [2] have been employed in the present study.

The assumptions of the analysis are as follows: the flow is laminar, two-dimensional, and steady; the boundary layer approximations apply; the temperature and composition of the ambient gas are constant; viscous dissipation and radiation are negligible; the combustion process is represented by an infinitely thin diffusion flame with no oxygen present between the wall and the flame and no fuel present outside the flame; the flow is an ideal gas mixture with constant and equal specific heats, equal binary diffusion coefficients, unity Lewis number, and constant values of $\rho\mu$ and $\rho\lambda$ (which implies constant Pr); the surface temperature and energy of gasification within the pyrolysis zone is constant. Calculations described in the Appendix indicated that radiation provided no more than 12 percent of the heat flux to the wall for the present tests. The validity of the remaining assumptions is discussed in [1] and [2].

The pyrolysis zone is assumed to be well-defined, with no pyrolysis occurring in the overfire region. These conditions are satisifed by the experiment; for a natural fire, this behavior would require a large activation energy of pyrolysis so that the zone where the pyrolysis rate develops to its full value would be narrow.

Employing these assumptions, the conservation equations are [9]:

$$\frac{\partial \rho u}{\partial x} + \frac{\partial \rho v}{\partial y} = 0 \tag{1}$$

$$\rho\left(u\frac{\partial u}{\partial x} + v\frac{\partial u}{\partial y}\right) = g\cos\phi(\rho_\infty - \rho) + \frac{\partial}{\partial y}\left(\mu\frac{\partial u}{\partial y}\right) \tag{2}$$

$$\rho\left(u\frac{\partial h}{\partial x} + v\frac{\partial h}{\partial y}\right) = \frac{\partial}{\partial y}\left(\frac{\lambda}{C_p}\frac{\partial h}{\partial y}\right) - \sum_i \dot{w}_i h_i^0 \tag{3}$$

$$\rho\left(u\frac{\partial Y_i}{\partial x} + v\frac{\partial Y_i}{\partial y}\right) = \frac{\partial}{\partial y}\left(\frac{\lambda}{C_p}\frac{\partial Y_i}{\partial y}\right) + \dot{w}_i \tag{4}$$

where

$$h = \int_{T_\infty}^{T} C_p dT \tag{5}$$

The reaction is represented on a molal basis, as follows

$$\nu_F'(\text{Fuel}) + \nu_O'(\text{Oxygen}) \rightarrow \nu_P''(\text{Products})$$

Stoichiometry then provides

$$\dot{w} = \dot{w}_i/(\nu_i'' - \nu_i')M_i = -\sum_i \dot{w}_i h_i^0/Q \tag{6}$$

where Q is the heat of reaction per ν_F' moles of fuel.

The boundary conditions far from the wall are the same in all regions

$$u = h = Y_F = 0,\ Y_O = Y_{O_\infty};\ y \rightarrow \infty \tag{7}$$

At the wall in all regions

$$u = 0;\ y = 0 \tag{8}$$

however, the remaining wall boundary conditions vary from region to region.

The wall boundary conditions for the pyrolysis zone are discussed by Kosden, et al. [1] and Kim, et al. [2] for both solid and liquid fuels. These conditions provide

$$\dot{m}'' = \rho v = \frac{\lambda}{LC_p}\frac{\partial h}{\partial y},\ \rho v(Y_{FT} - Y_F) = \frac{-\lambda}{C_p}\frac{\partial Y_F}{\partial y},\ h = h_{w_0};$$
$$0 < x < x_0,\ y = 0 \tag{9}$$

The wall temperature was assumed to be constant in the overfire region, which ignores the fact that the surface temperature increases from T_∞ far from the pyrolysis zone, to T_{w_0} near the end of the pyrolysis zone. The effect of this simplification will be examined by considering the two limits: $T_w = T_{w_0}$ and $T_w = T_\infty$. Condensation of fuel and product species on the wall was neglected, which implies that the concentration gradients of all species are zero at the wall. With these assumptions, the remaining boundary conditions may be formulated as follows

$$h = h_w,\ v = \frac{\partial Y_i}{\partial y} = 0;\ x_0 \leqslant x,\ y = 0 \tag{10}$$

The diffusion flame approximation also provides

$$Y_O = 0,\ x_0 \leqslant x \leqslant x_f;\ Y_F = 0,\ x_f \leqslant x;\ y = 0 \tag{11}$$

where the flame position is identified as the point where both $Y_O = Y_F = 0$, and x_f is the position where the flame returns to the wall.

In all regions, the heat flux to the wall is given by

$$\dot{q}'' = \frac{\lambda}{C_p}\frac{\partial h}{\partial y};\quad y = 0 \tag{12}$$

Variable Transformation. The terms involving enthalpy and concentrations are simplified by introducing the following Shvab-Zeldovich variables [9]:

$$\theta_{hO} = (h/L + (Y_O - Y_{O_\infty})Q/M_O\nu_O'L)/(h_{w_0}/L - Y_{O_\infty}Q/M_O\nu_O'L)$$
$$\theta_{hF} = (h/L + Y_F Q/M_F\nu_F'L)/(h_{w_0}/L + Y_{Fw_0}Q/M_F\nu_F'L)$$
$$\theta_{FO} = (Y_F/M_F\nu_F' - (Y_O - Y_{O_\infty})/M_O\nu_O')/(Y_{Fw_0}/M_F\nu_F' + Y_{O_\infty}/M_O\nu_O') \tag{13}$$

While only two of the θ_i are independent, it is convenient to use all three quantities in the overfire region, since wall boundary conditions are most easily expressed in terms of θ_{FO} and θ_{hO} for $x_0 \leqslant x \leqslant x_f$, and θ_{FO} and θ_{hF} for $x > x_f$.

A stream function is defined which satisfies equation (1)

$$\rho u = \rho_\infty \frac{\partial \psi}{\partial y},\ \rho v = -\rho_\infty \frac{\partial \psi}{\partial x} \tag{14}$$

The transformation of variables is completed by combining a Howarth-Dorodnitzyn transformation for variable properties with a local similarity transformation which reduces to the form used in [2] in the pyrolysis zone.

$$\xi = x/x_0,\ \eta = (\mathrm{Gr}_x{}^{*1/4}/x)\int_0^y \rho/\rho_\infty dy,\ \psi/\nu_\infty = 4\,\mathrm{Gr}_x{}^{*1/4} f(\eta, \xi) \tag{15}$$

Introducing equations (13)–(15) into equations (1)–(5) yields the following

$$f''' + 3ff'' - 2(f')^2 + F = 4\xi\left(f'\frac{\partial f'}{\partial \xi} - f''\frac{\partial f}{\partial \xi}\right) \quad (16)$$

$$\theta_i'' + 3\,\mathrm{Pr} f\theta_i' = 4\,\mathrm{Pr}\xi\left(f'\frac{\partial \theta_i}{\partial \xi} - \theta_i'\frac{\partial f}{\partial \xi}\right) \quad (17)$$

where partial derivatives with respect to η are denoted by primes. Since $Y_F = Y_O = 0$ at the flame, equation (13) yields the following criteria for the flame position

$$\theta_{FO_f} = r(B+1)/B(r+1) \quad (18)$$

where

$$B = Y_{O\infty}Q/M_O\nu_O'L - \tau_0; \quad r = Y_{O\infty}M_F\nu_F'/Y_{FT}M_O\nu_O' \quad (19)$$

The buoyancy term, F, has different forms inside and outside the flame, as follows:

$$F = B(1-\theta_{hO}) + \tau_0;\ \theta_{FO} \geqslant \theta_{FO_f}$$

$$F = (B+\tau_0)(\theta_{FO}/\theta_{FO_f}) - B\theta_{hO};\ \theta_{FO} \leqslant \theta_{FO_f} \quad (20)$$

The boundary conditions far from the wall are

$$f' = \theta_{hO} = \theta_{hF} = 0; \quad \eta \to \infty \quad (21)$$

while the wall boundary conditions, $\eta = 0$, become

$$f' = 0, f = B\theta_{hO}'/3\,\mathrm{Pr}, \theta_{hO} = \theta_{hF} = \theta_{FO} = 1; \xi \leqslant 1$$

$$f = f(0,1)\xi^{-3/4}, f' = \theta_{FO}' = 0; 1 < \xi$$

$$\theta_{hO} = 1 + (\tau_0 - \tau_1)/B; 1 < \xi < \xi_f$$

$$\theta_{hF} = \tau_1\theta_{FO_f}/(\tau_0 + \theta_{FO_f})B); \xi_f < \xi \quad (22)$$

In the pyrolysis zone, the boundary conditions are independent of ξ; and f and the θ_i are only functions of η. In the overfire region, the boundary condition for f at the wall, equation (22), depends upon ξ and the solution is no longer similar. The position ξ_f is found when $\theta_{FO} = \theta_{FO_f}$ at the wall.

The mass burning rate per unit area in the pyrolysis zone is given by

$$\dot{m}''x/\mu_\infty = -3\,\mathrm{Gr}_x{}^{*1/4}f(0); \xi \leqslant 1 \quad (23)$$

The heat flux to the wall is given by the following expressions

$$\dot{q}''x\mathrm{PrGr}_x{}^{*-1/4}/BL\mu_\infty = -\theta_{hO}'(0,\xi); \xi \leqslant \xi_f$$

$$\dot{q}''x\mathrm{PrGr}_x{}^{*-1/4}BL\mu_\infty = (\tau_0 + (1-\theta_{FO_f})B)\theta_{hF}'(0,\xi)/(B\theta_{FO_f}); \xi_f < \xi \quad (24)$$

If η is given, y can be determined from the following equation

$$(y/x)\mathrm{Gr}_x{}^{*1/4} = \int_0^\eta [1 + (LF/C_PT_\infty)]d\eta \quad (25)$$

Numerical Solution. The details of the calculations are discussed by Ahmad [8]. Briefly, the solution of equations (16)–(22) was obtained by the numerical procedure described by Hayday, et al. [5]. The solution in the pyrolysis region provided the initial condition, followed by step-wise integration in the overfire region. Present calculations in the pyrolysis zone agreed with results reported by Kim, et al. [2], within the accuracy of their plots.

Results and Discussion

Methanol, ethanol, and propanol were considered in both the calculations and the experiments. The properties employed for these materials, as well as the procedures used to determine property values, are summarized in Table 2.

Flow Development. The general characteristics of the overfire region are illustrated for a methanol fire in Figs. 3, 4, and 5. Since the flow is similar during pyrolysis, a single set of curves represents this entire region. Parametric values of ξ are considered for the nonsimilar overfire region.

Velocity profiles are illustrated in Fig. 3. In the lower portion of the overfire region, the peak in the velocity profile shifts toward the wall for a time as the effect of blowing due to mass transfer in the pyrolysis zone decays. At higher positions on the wall, the point of maximum velocity moves outward with increasing distance from the pyrolysis zone.

Concentration profiles are shown in Fig. 4. The position of the flame is indicated by $Y_F = Y_O = 0$. The flame moves toward the wall as ξ increases, reaching the wall at $\xi_f = 6.5$, which ends the combustion region. Above the combustion region, oxygen diffuses back to the wall.

Temperature profiles are shown in Fig. 5. During pyrolysis, the maximum temperature occurs in the flame, which is typical of combusting similar flows where the temperature peak generally coincides with the position of chemical energy release. In the nonsimilar overfire region, however, the temperature maximum occurs outside the flame position. In this region, the rate of reaction in the flame decreases as the concentration of fuel at the wall decreases; direct energy loss from the flame zone to the wall also increases as the flame position approaches the wall. As a result of both these effects, the wake-like decay of the high temperature region produced by reaction lower on the wall begins to dominate the characteristics of the temperature profile causing the peak temperature to be outside the flame position. Near the tip of the flame, the temperature at the flame position is relatively low, and quenching of the reaction could be important in this region. A chemical kinetic effect of this type is not treated in the present model. Beyond the tip of the flame the temperature profile continues to spread, similar to the velocity profile.

Table 2 Physical properties[a]

Property	Methanol	Ethanol	Propanol
Molecular weight[b]	32.04	46.07	60.09
Boiling temperature (K)	337.7	351.5	370.4
$L(kJ/kg)$[c]	1226	880	788
$C_p(kJ/kgK)$[c]	1.37	1.43	1.46
$Q(mJ/kg\text{-}molK)$[d]	675	1278	1889
$\mu_w \times 10^6(N\text{-}s/m^2)$[e]	18.0	20.8	21.6
ν_0' for $\nu_F = 1$	1.5	3.0	4.5
B	2.60	3.41	3.71
r	.154	.111	.096
τ_0	.044	.087	.134
Pr	.73	.73	.73

[a] Ambient conditions: air at 298 K, $Y_{O\infty} = .231$, $\nu_\infty = 15.3 \times 10^{-6}m^2/s$
[b] Molecular weight of oxygen = 32 kg/kg-mol
[c] Value for the fuel at the boiling temperature
[d] Lower heating value of the fuel at 298 K
[e] Dynamic viscosity of air at the boiling temperature of the fuel

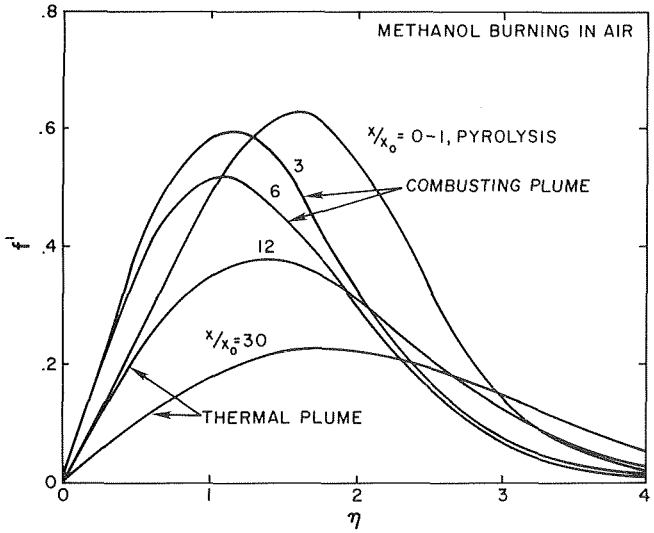

Fig. 3 Velocity profiles within a methanol-fueled wall fire burning in air

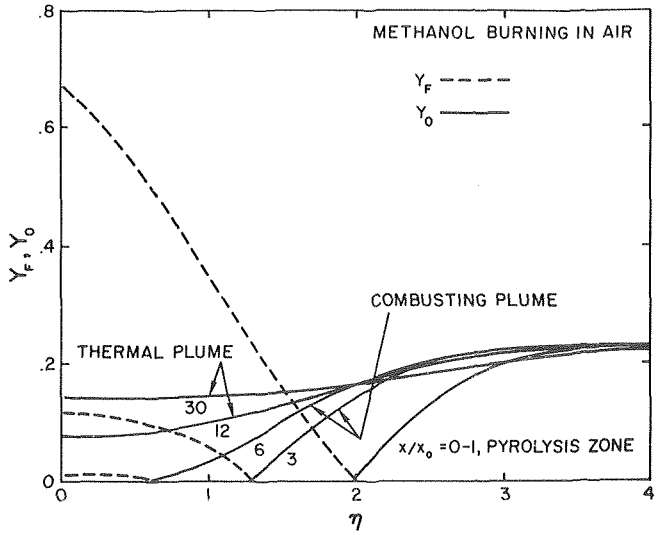

Fig. 4 Concentration profiles within a methanol-fueled wall fire burning in air

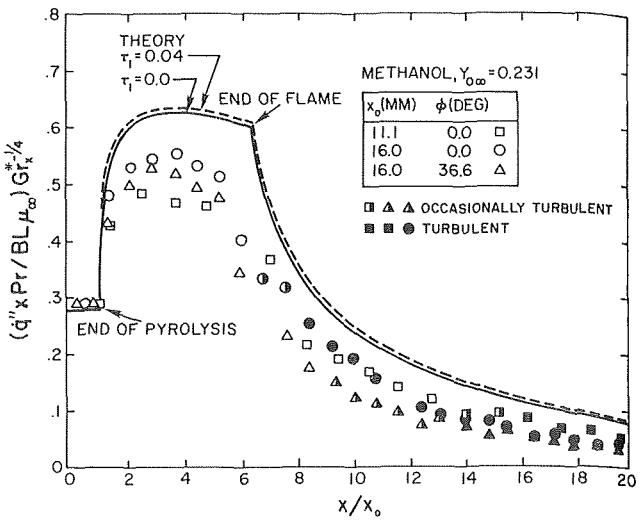

Fig. 6 Wall heat flux for a methanol-fueled wall fire burning in air

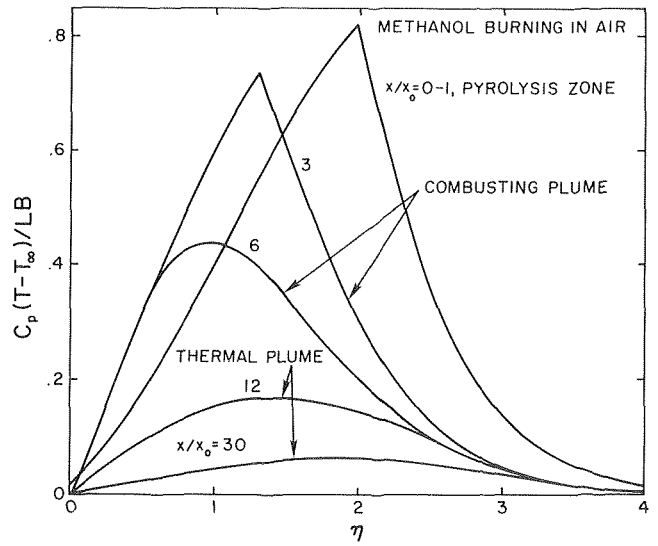

Fig. 5 Temperature profiles within a methanol-fueled wall fire burning in air

Comparision of Theory and Experiment. Fig. 6 presents predicted and measured wall heat flux values in the laminar region for methanol. The experimental results consider various pyrolysis zone lengths and wall angles up to 36.6 deg (facing downward).

The wall heat flux was obtained directly from the experiments in the overfire region. However, the heat flux was determined from the burning rate in the pyrolysis zone. During pyrolysis the wall heat flux is related to the burning rate as follows:

$$\dot{q}'' = L\dot{m}'' \tag{26}$$

Integration of equations (23) and (24) provides the following relationships between average values and values at x_0

$$\dot{q}''(x_0)/\dot{q}_{avg}'' = \dot{m}''(x_0)/\dot{m}_{avg}'' = 3/4 \tag{27}$$

which is typical for natural convection processes. Equations (26) and (27) relate the measured average burning rate to the heat flux at x_0, allowing determination of the heat flux parameter; these values have been arbitrarily placed in the region $0 \leqslant \xi \leqslant 1$ since they are theoretically independent of ξ in this region.

A rough correlation of the laminar burning rate measurements for methanol reported by Kim, et al. [2] is

$$\dot{m}_{avg}'' x_0/\mu_w = Gr_x'^{1/4} \tag{28}$$

for the range $5 \times 10^4 < Gr_x' < 10^8$. Equation (28) can be rewritten in terms of the present heat flux parameter as follows

$$\dot{q}'' x Pr Gr_x^{*1/4}/BL\mu_\infty = 0.23 \tag{29}$$

where the missing property values have been supplied from Table 2. The value from equation (29) is about 18 percent lower than the present measurements shown in Fig. 6 for the pyrolysis zone. This discrepancy is well within errors expected due to property uncertainties (in particular, the value of μ_{w0} used to reduce the data in [2] is not reported) and the scatter of the experiments.

The heat flux is low in the pyrolysis zone, due to the blowing effect of fuel evaporating at the wall. In the overfire region, the heat flux increases, within one pyrolysis zone length, to a relatively constant value which is maintained until the tip of the flame is approached. Beyond the end of the flame, the heat flux decreases rapidly once again. The experimental heat flux values start to decrease somewhat sooner than the predicted value of ξ_f.

Two wall conditions are illustrated for the predictions in Fig. 6; $\tau_1 = 0.044$, which implies that the entire wall is at the temperature of the fuel surface in the pyrolysis zone; and $\tau_1 = 0$, which implies that the wall temperature in the overfire region is equal to the ambient temperature. There is little difference between the two cases due to the high flame temperature and the low pyrolysis zone surface temperature for methanol. This finding helps justify the present transient method for measuring wall heat flux and the assumption of a constant wall temperature used in the analysis, since it indicates that low levels of wall heating do not substantially influence the results. For $\tau_1 = 0$, the wall heat flux is theoretically infinite at $\xi = 1$ due to the step-change in temperature, however the region of high heat flux values due to this effect is too small to be shown on the scale of Fig. 6. For $\tau_1 = 0.044$, the flow asymptotically approaches a natural convection process on a heated, isothermal wall, and the heat flux eventually becomes negative at large ξ.

Figs. 7 and 8 illustrate similar results for ethanol and propanol. Transition to turbulence in the combusting portions of the flow occurred in a shorter distance than for methanol, and a smaller pyrolysis zone length was required to measure the laminar heat flux at large ξ for these fuels.

The comparison between measured and predicted wall heat flux is similar for the three fuels. The agreement between theory and experiment is perhaps fortuitously good in the pyrolysis zone. In the

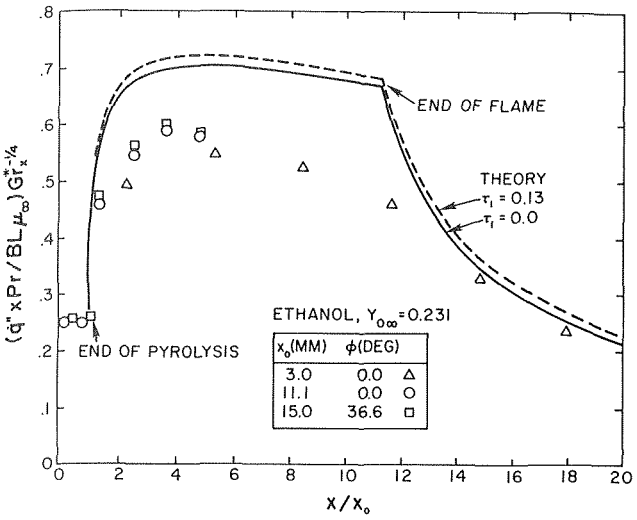

Fig. 7 Wall heat flux for an ethanol-fueled wall fire burning in air

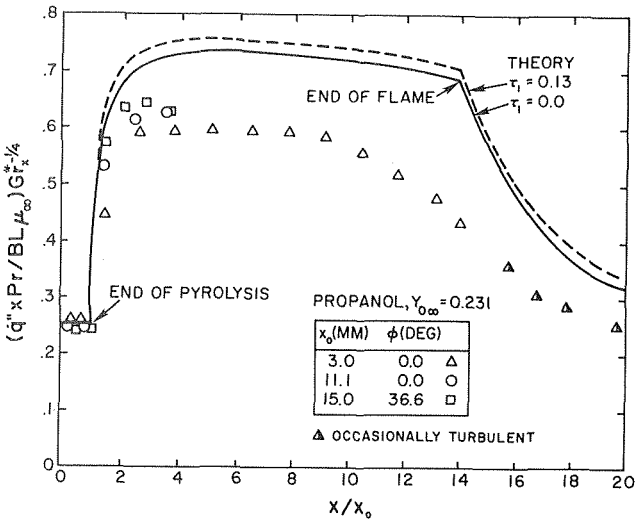

Fig. 8 Wall heat flux for a propanol-fueled wall fire burning in air

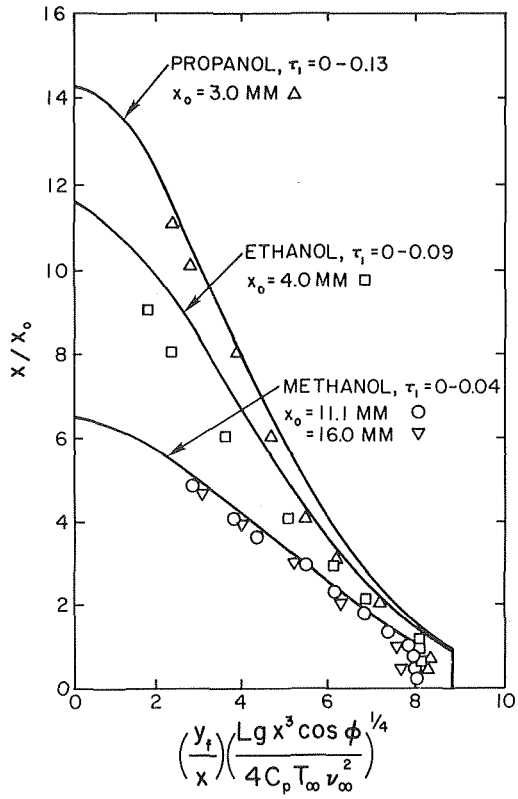

Fig. 9 Flame shapes for alcohol-fueled wall fires burning in air

overfire region, the measurements are generally only 15–20 percent lower than the predictions, except near the end of the flame where the discrepancy is somewhat greater.

Fig. 9 illustrates the flame position results for the three fuels. The data has been placed in the local similarity coordinate system in order to facilitate comparison with the theory. The values for the pyrolysis zone were measured near x_0; leading edge effects resulted in poorer comparison at lower values of x. The measurements are in reasonably good agreement with the predictions as far as they go; however, as illustrated in Fig. 2, the flame is not observed to return to the wall in the manner predicted by the diffusion flame theory. This is probably due to quenching of the reaction, as noted earlier. The heat flux results also support this view, since the measured heat flux consistently begins to decline sooner than predicted, suggesting a shorter length of active combustion.

There are a number of factors potentially responsible for the discrepancies between theory and experiment. In addition to quenching near the tip of the flame, chemical kinetic effects due to fuel decomposition, as the fuel diffuses to the reaction zone, and dissociation in high temperature regions are not treated by the model; all these effects would tend to reduce the heat flux to the wall from the value predicted by the model.

The present model is only a crude approximation of the variable property characteristics of the flow field of the test fuels. The treatment of multicomponent diffusion, and the effect of concentration variations on properties would be required for a more exact, and potentially more accurate, model.

Radiation losses from the flow could also be responsible for lower wall heat fluxes than the predictions. It is shown in the Appendix that the test wall absorbed only about one-fourth of the radiant energy lost by the flame which comprised about 12 percent of the wall heat flux at the worst condition. Therefore, it is conceivable that lower flame temperatures resulting from this radiant energy loss could cause wall heat fluxes lower than those predicted by a theory which neglects radiation.

Wall Heat Flux Calculations. When the behavior of the three test fuels is compared, it is evident that as B increases and r decreases, the length of the flame and the wall heat flux in the overfire region both increase. The effect of B and r is illustrated more systematically in Fig. 10. The major effect of reducing the value of r, for a constant value of B, is to increase the length of the flame; although the heat flux values increase somewhat as well. Increasing the value of B when r is constant causes a substantial increase in the wall heat flux and the length of the flame.

In natural fires, the ambient oxygen concentration for a given surface can vary due to oxygen consumption by neighboring burning elements. As the ambient oxygen concentration is reduced, both B and r decrease in value, which are counteracting effects from Fig. 10. The net result of varying the ambient oxygen concentration for methanol combustion is illustrated in Fig. 11. In this case, decreasing $Y_{O\infty}$ causes the heat flux to the wall to decrease and the flame length to increase. Even though the flame is shorter at higher values of $Y_{O\infty}$, the heat flux increases sufficiently so that the total heat transfer rate to the wall in the overfire region increases as $Y_{O\infty}$ increases, e.g., the total heat transfer rate is approximately twice as high in air as it is for $Y_{O\infty} = 0.1$. The effect of ambient oxygen concentration was similar for ethanol and propanol; this is a limited survey, however, and these trends might not be observed for all materials. The more rapid surface

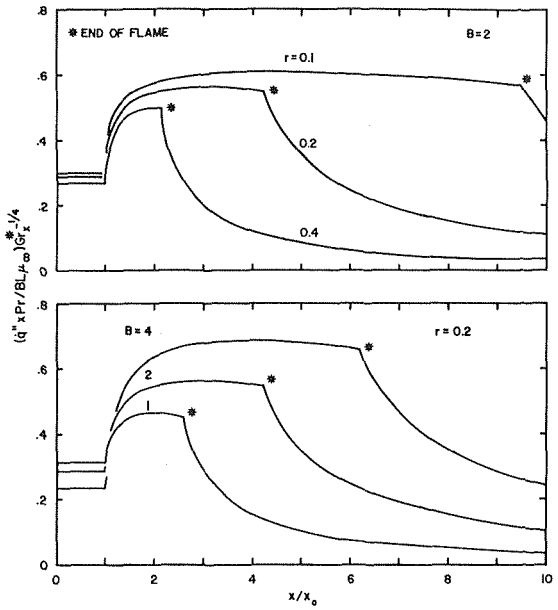

Fig. 10 Wall heat flux for various B and r values, Pr = 0.73, $\tau_0 = \tau_1 = 0$

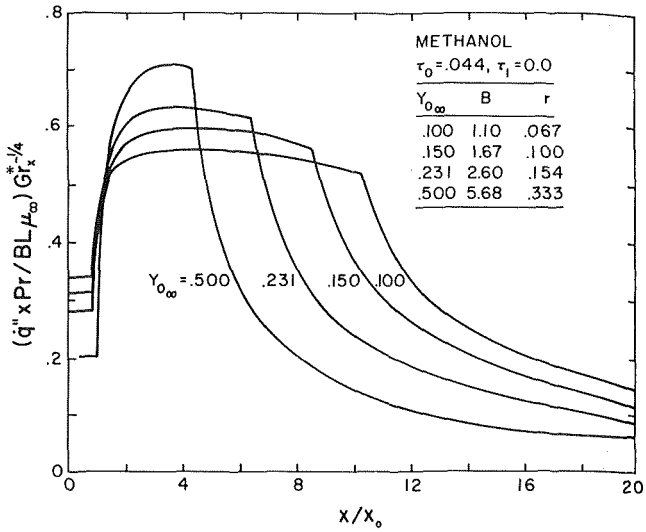

Fig. 11 Effect of ambient oxygen concentration on wall heat flux for methanol

heating rate at higher ambient oxygen concentrations implies a faster rate of upward flame propagation. This is generally observed in practice.

Transition to Turbulence. The shadowgraphs indicated the first appearance of turbulence at the outer edge of the boundary layer, with the turbulent region propagating toward the wall. The position of the first occurrence of turbulence oscillated up and down so that the flow was only turbulent a portion of the time at the lowest positions. The criteria for transition is different for the pyrolysis zone, the combusting plume region, and the thermal plume region. A full survey of transition conditions was not completed, however laminar flow was generally observed in the thermal plume region for $Gr_x' < .5 - 2 \times 10^8$.

While Gr_x' is well defined, it does not completely describe the conditions for transition. For example, transition is deferred somewhat for stable wall angles and occurs sooner for unstable angles, similar to the observations of Vliet and Ross [10]. Transition also occurred at lower values of Gr_x' as the point of transition approached the tip of the flame. Finally B and r control many of the processes of a wall fire, and there was a tendency for high B values and low r values to reduce the value of Gr_x' for transition. Therefore, the above criterion should be treated only as a rough guide.

Transition in the thermal plume region was not accompanied by a significant change in the variation of wall heat flux with distance, cf. Figs. 6 and 8. However, when transition occurred in the combusting portions of the overfire region, the wall heat flux was sharply reduced in the turbulent region. This effect is being examined more fully in current experiments.

Conclusions

Discrepancies between measured and predicted wall heat flux values and flame shapes were in the range 15–20 percent. The greatest errors were observed near the tip of the flame where wall quenching effects become important. Factors contributing to these discrepancies are: uncertainties in property values and the approximations of the variable property model, decomposition, dissociation and finite rate chemical effects in the flow field, and radiation. Further consideration of these phenomena would be desirable.

The heat flux to the wall increases just beyond the pyrolysis zone as the effect of blowing decays. However, the heat flux remains relatively constant throughout much of the combusting plume region. Therefore, the presence of the flame provides an extended zone of high wall heat flux, serving to heat the combustible.

Reduction of the ambient oxygen concentration increases the flame length, but for the fuels considered in this investigation, the wall heat flux decreases sufficiently so that the overall rate of preheating the combustible decreases as $Y_{O\infty}$ is reduced. Due to the high flame temperatures within the combusting region, there is little change in wall heat flux due to increased wall temperatures, at least for surface temperatures in the pyrolysis zone in the range of the present test fuels.

Conditions for transition in this flow are not fully resolved, however, for transition in the thermal plume region, the flow was generally laminar for $Gr_x' < 0.5 - 2 \times 10^8$. Transition is not completely described by Gr_x'; however, effects of fuel type, presence or absence of combustion, distance, and wall angle were also observed.

While the theoretical model yields satisfactory results, the method of solution is ponderous for direct use in flame spread analysis, or predictions of heat transfer in fires. For such applications integral models are more convenient, and the present results should be of value in checking their accuracy.

Acknowledgment

This research was supported by the United States Department of Commerce, National Bureau of Standards, Grant No. 5-9020, under the technical management of Dr. John Rockett of the Center for Fire Research.

References

1 Kosdon, F. J., Williams, F. A., and Buman, C., "Combustion of Vertical Cellulosic Cylinders in Air," *Twelfth Symposium (International) on Combustion,* The Combustion Institute, Pittsburgh, 1969, pp. 253–264.

2 Kim, J. S., deRis, J., and Kroesser, F. W., "Laminar Free-Convective Burning of Fuel Surfaces," *Thirteenth Symposium (International) on Combustion,* The Combustion Institute, Pittsburgh, 1971, pp. 949–961.

3 Yang, K-T., "Laminar Free-Convection Wake Above a Heated Vertical Plate," *ASME Journal of Applied Mechanics,* Vol. 31, 1964, pp. 131–138.

4 Pagni, P. J., and Shih, T-M., "Excess Pyrolyzate," *Sixteenth Symposium (International) on Combustion,* The Combustion Institute, Pittsburgh, 1977, pp. 1329–1343.

5 Hayday, A. A., Bowlus, D. A., and McGraw, R. A., "Free Convection From a Vertical Flat Plate with Step Discontinuities in Surface Temperature," ASME JOURNAL OF HEAT TRANSFER, Vol. 89, 1967, pp. 244–250.

6 Kim, J. S., de Ris, J., and Kroesser, F. W., "Laminar Burning Between Parallel Fuel Surfaces," *International Journal of Heat and Mass Transfer,* Vol. 17, 1974, pp. 439–451.

7 Blackshear, P. L., Jr., and Murty, K. A., "Some Effects of Size, Orientation, and Fuel Molecular Weight on the Burning of Fuel-Soaked Wicks," *Eleventh Symposium (International) on Combustion,* The Combustion Institute, Pittsburgh, 1967, pp. 545–552.

8 Ahmad, T., "Investigation of the Combustion Region of Fire-Induced Plumes Along Upright Surfaces," Ph.D. Thesis, The Pennsylvania State Uni-

versity, 1978.
9 Williams, F. A., *Combustion Theory*, Addison-Wesley, Reading, Ma, 1965, Chapter 1.
10 Vliet, G. C., and Ross, D. C., "Turbulent Natural Convection on Upward and Downward Facing Inclined Constant Heat Flux Surfaces," ASME JOURNAL OF HEAT TRANSFER, Vol. 97, 1975, pp. 549–555.
11 Edwards, D. K., and Balakrishnan, A., "Thermal Radiation by Combustion Gases," *International Journal of Heat and Mass Transfer*, Vol. 16, 1973, pp. 25–40.
12 Raznjevic, K., *Handbook of Thermodynamic Tables and Charts*, 1st ed., McGraw-Hill, New York, 1976.

APPENDIX

Radiation effects are most important in the region adjacent to the top of the pyrolysis zone, since the gas temperatures are high and the flow has the maximum thickness for the pyrolysis zone. Radiation was evaluated for the most conservative condition of the present experiments which involves the methanol flame with 16 mm pyrolysis zone length.

The theory provides the concentrations of fuel and oxygen, and the temperature, as illustrated in Figs. 4 and 5. In all regions of the flow, the concentration of nitrogen is

$$Y_N = Y_{N\infty}(1 - B\theta_{FO}/(1 + B)) \tag{30}$$

Two other relations are obtained by noting that H_2O and CO_2 are present in stoichiometric proportions under the present assumptions, and the sum of all mass fractions must be unity.

The flow field was divided into five increments, and the average temperature and concentration for each increment was determined. The emissivity of an increment was computed by adding individual band emissivities, ignoring band overlap [11]. For these calculations, methanol was assumed to have radiation properties equivalent to methane. Gas absorption was ignored, since less than two percent of the emitted radiation was found to be absorbed by intervening increments. The wall was somewhat tarnished and it was taken to be a gray body with an emissivity of 0.55 [12].

It was found that radiation absorbed by the wall was about 12 percent of the total wall heat flux at the top of the 16 mm pyrolysis zone. On the other hand, the flow absorbs little radiation and its total radiative loss is about four times larger than the increase in the wall heat flux due to radiation.

The effect of gas radiation is smaller at positions higher on the wall, due to increased rates of convection, lower fuel and product concentrations, and lower gas temperatures, cf. Figs. 4–6. Therefore, for the conditions of this experiment, direct radiative heat transfer to the wall is relatively small, although the high temperature portions of the flow are losing a significant amount of energy by radiation.

G. E. Myers

Professor of Mechanical Engineering,
The University of Wisconsin,
Madison, Wisc.
Mem. ASME

The Critical Time Step for Finite-Element Solutions to Two-Dimensional Heat-Conduction Transients

Computationally-useful methods of estimating the critical time step for linear triangular elements and for linear quadrilateral elements are given. Irregular nodal-point arrangements, position-dependent properties, and a variety of boundary conditions can be accommodated. The effects of boundary conditions and element shape on the critical time step are discussed. Numerical examples are presented to illustrate the effect of various boundary conditions and for comparison to the finite-difference method.

Introduction

The use of the finite-element method in solving heat-conduction problems is becoming widespread due to the ease with which irregular geometries can be approximated as compared with the older, more established finite-difference method. The reason for this is that in the finite-element method, irregular nodal-point locations can be handled with no more difficulty than uniformly-spaced nodal points. The finite-difference method, on the other hand, is fairly convenient to use when the nodal points are located in a regular pattern but it becomes rather awkward when the boundaries of the region do not conform to the nodal-point grid or when it is desirable to have some portions of the region more heavily populated with nodes than other portions.

The finite-element literature is fairly recent (1960s), and practically all of it is concerned with solving steady-state structural problems. Comparatively little has been written regarding the use of the finite-element method in solving transient heat-conduction problems.

One of the well known features of the finite-difference method for heat-conduction transients is that the selection of too large a time step can lead to a meaningless, oscillatory solution. This problem is touched upon in practically every heat-transfer textbook. The largest time step for which a Euler solution will be stable (and for which a Crank-Nicolson solution will be nonoscillatory) is called the critical time step ($\Delta\theta_c$). The familiar criterion for one-dimensional transients is that $\alpha\Delta\theta_c/(\Delta x)^2 = 1/2$. For two-dimensional problems using a square grid of nodal points, $\alpha\Delta\theta_c/(\Delta x)^2 = 1/4$. The ability to choose a stable time step ($\Delta\theta \leqq \Delta\theta_c$) in a computationally-convenient manner has previously been obtained and will be reviewed in this paper. Irregular nodal-point locations, position-dependent properties, and a variety of boundary conditions can be accommodated. A similar problem arises in the finite-element method, but it is more severe. The critical time step is smaller, and the knowledge of how to choose a stable time step in a computationally convenient manner is lacking.

Myers [1][1] mentions numerically-induced oscillations in one-dimensional finite-element problems but does not give any useful ways to cope with the problem. Lemmon and Heaton [2] derive a stability criterion for one-dimensional transients with uniform nodal-point spacing and uniform properties. For the finite-element method they found that $\alpha\Delta\theta_c/(\Delta x)^2 = 1/6$ as compared to the finite-difference value of $1/2$. One-dimensional problems are not too exciting as far as the finite-element method is concerned because they can be handled just as effectively by finite differences. The real utility of the finite-element method comes in treating two and three-dimensional problems with irregular regions and their concommitant irregular nodal-point arrangements.

Yalamanchili and Chu [3] use the von Neumann method to determine the critical time step for two-dimensional transients. For the finite-element method, using square elements, they report that $\alpha\Delta\theta_c/(\Delta x)^2 = 1/12$ as compared to the finite-difference value of $1/4$. As in the one-dimensional case, a more restrictive time step is found for the finite-element method. The von Neumann theory is strictly valid only for an infinite number of uniformly-spaced nodal points and uniform thermal properties, and it does not consider the boundary conditions. Yalamanchili reconsiders this problem in a more-recent

Contributed by the Heat Transfer Division for publication in the JOURNAL OF HEAT TRANSFER. Manuscript received by the Heat Transfer Division July 20, 1977.

[1] Numbers in brackets designate References at end of paper.

paper [4] but does not present any new information that would allow treatment of more general problems.

Up to this time, no computationally-useful method of estimating the critical time step has been reported for the finite-element method that is capable of treating general problems. The present paper provides such a method for linear triangular elements (equation (20)) and for linear quadrilateral elements (equation (24)). Furthermore the paper summarizes the theory necessary to provide a thorough understanding of the critical-time-step problem. The significance of the critical time step to the Crank-Nicolson scheme is discussed. The von Neumann theory is shown to overestimate $\Delta\theta_c$ in many situations and hence is not a safe technique to use in general. Numerical examples are given to illustrate the effect of various boundary conditions and to make comparisons with the finite-difference method. The theory is used to determine the optimum shape of triangular element.

Transient Equations

This paper is concerned with the general, two-dimensional, heat-conduction transient described by the partial differential equation

$$\rho(x, y)c(x, y)\frac{\partial t}{\partial \Theta} = \frac{\partial}{\partial x}\left[k(x, y)\frac{\partial t}{\partial x}\right] + \frac{\partial}{\partial y}\left[k(x, y)\frac{\partial t}{\partial y}\right] + g'''(x, y) \quad (1)$$

Observe that the thermal properties can be functions of position but not time or temperature in this paper. In addition, there will be no restriction to simple geometrical regions.

The conditions along the boundaries of the region may be any combination of adiabatic, convective, specified heat flux, or specified temperature as shown by equations (2) through (5).

$$\text{Adiabatic: } \frac{\partial t}{\partial n} = 0 \quad (2)$$

$$\text{Convective: } -k\frac{\partial t}{\partial n} = h(t_\infty - t) \quad (3)$$

$$\text{Specified heat flux: } -k\frac{\partial t}{\partial n} = q_s'' \quad (4)$$

$$\text{Specified temperature: } t = t_s \quad (5)$$

The parameters h, t_∞, q_s'', and t_s can vary with position around the boundary but may not depend upon time or temperature.

Finally, the initial condition is given by

$$t(x, y, 0) = t^{(0)}(x, y) \quad (6)$$

Equations (1–6) represent the exact mathematical description of the class of problems considered in this paper.

Spatially-Discrete Equations. The finite-element and the finite-difference methods for solving this problem both involve using a set of n nodal points to subdivide the region into a finite number of discrete regions. This discretizing process is discussed in [1] for both the finite-difference and finite-element methods. Both methods replace equations (1–5) by a system of first-order ordinary differential equations that can be compactly written in matrix notation as

$$\mathbf{C}\dot{\mathbf{t}} = -\mathbf{S}\mathbf{t} + \mathbf{r} \quad (7)$$

The initial condition, equation (6), is replaced by

$$\mathbf{t}(0) = \mathbf{t}^{(0)} \quad (8)$$

The temperature vector $\mathbf{t}$ contains the temperatures at the n nodal points. The capacitance matrix $\mathbf{C}$ describes the thermal-storage ability of the discretized problem. It involves the density, specific heat, and the area of each discrete region. The conductance matrix $\mathbf{S}$ contains the conductances between the various discrete regions and between the boundary and the ambient. Both $\mathbf{C}$ and $\mathbf{S}$ will be symmetric and, if the nodal points are numbered properly, they will be banded rather than full matrices. The input vector $\mathbf{r}$ contains the effects of energy generation, convective ambient temperature, specified boundary heat flux, and specified boundary temperature. The matrices $\mathbf{C}$, $\mathbf{S}$, and $\mathbf{r}$ will be constants (independent of time and temperature) for the class of problems considered in this paper.

The matrices $\mathbf{C}$, $\mathbf{S}$, and $\mathbf{r}$ obtained by the finite-element method will not in general be the same as one would obtain using the finite-difference method. Computationally, the most significant difference is that the finite-difference $\mathbf{C}$ will be diagonal, whereas it is not diagonal in the usual finite-element formulation. This difference is the underlying reason that the critical-time-step problem must be restudied for the finite-element method.

Nomenclature

a = shortest side of triangular element; L
$\mathbf{a}$ = constant vector in equation (11); T
A = area of finite element; L^2
b = longest side of triangular element; L
$\mathbf{b}$ = constant vector in equation (11); T/Θ
c = specific heat; E/MT
c = third side of triangular element; L
c_{ii} = diagonal entry in row i of $\mathbf{C}$; E/LT
$\mathbf{C}$ = capacitance matrix; E/LT
$\mathbf{D}$ = diagonal of $\mathbf{C}$; E/LT
E = dimension of energy; E
g''' = energy generation rate per unit volume; $E/\Theta L^3$
h = heat-transfer coefficient; $E/\Theta L^2 T$
H = Biot number, hL/k; none
k = thermal conductivity; $E/\Theta LT$
L = size of square region; L
L = dimension of length; L
M = dimension of mass; M
n = inward coordinate normal to boundary; L
n = total number of nodes; none
q = lower bound on β_1; none
q_s'' = specified boundary heat flux; $E/\Theta L^2$
$\mathbf{r}$ = input vector; $E/\Theta L$
s_{ii} = diagonal entry in row i of $\mathbf{S}$; $E/\Theta LT$
s_{ij} = off-diagonal entry in row i of $\mathbf{S}$; $E/\Theta LT$
$\mathbf{S}$ = conductance matrix; $E/\Theta LT$
t = temperature; T
t_s = specified boundary temperature; T
t_∞ = ambient temperature; T
$t^{(0)}$ = initial temperature; T
$\mathbf{t}$ = temperature vector; T
$\mathbf{t}^{(\nu)}$ = temperature vector at time $\theta^{(\nu)}$; T
$\dot{\mathbf{t}}$ = time derivative of temperature vector; T/θ
T = dimension of temperature; T
$\mathbf{u}$ = eigenvector; unspecified
$\mathbf{v}$ = eigenvector; unspecified
x = position coordinate; L
$\mathbf{x}$ = eigenvector; $\sqrt{LT/E}$
$\mathbf{X}$ = eigenvector matrix; $\sqrt{LT/E}$
$\mathbf{X}^T$ = transpose of eigenvector matrix; $\sqrt{LT/E}$
y = position coordinate; L
α = thermal diffusivity; L^2/Θ
β = angle between side c and x-axis; none
β = eigenvalue; none
β_1 = smallest eigenvalue of equation (35); none
$\Delta\theta$ = time-step size; Θ
$\Delta\theta_c$ = critical time step; Θ
$\Delta\theta_\infty$ = Toeplitz estimate of critical time step; Θ
$\Delta\theta_c^*$ = safe estimate of critical time step; Θ
$\Delta\theta_\infty^*$ = estimate of $\Delta\theta_\infty$; Θ
θ = time; Θ
$\theta^{(\nu)}$ = time at step number ν; Θ
Θ = dimension of time; Θ
κ = eigenvalue; $1/\Theta$
κ_n = largest eigenvalue of equation (33); $1/\Theta$
λ_i = i^{th} eigenvalue of equation (14); $1/\Theta$
λ_n = largest eigenvalue of equation (14); $1/\Theta$
$\mathbf{\Lambda}$ = diagonal eigenvalue matrix; $1/\Theta$
μ_i = i^{th} entry in $\mathbf{M}$; none
$\mathbf{M}$ = diagonal matrix in equation (11); none
ν = time-step number; none
ρ = density; M/L^3

Transient Solutions. The solution to equation (7) will approximate the solution to equation (1) with boundary conditions given by equations (2–5). In practical problems it is too much work to find the exact analytical solution to equation (7). Instead, step-by-step, time-marching schemes such as Euler or Crank-Nicolson are used to approximate the solution to equation (7).

In the Euler scheme, equation (7) is replaced by

$$\mathbf{C}\mathbf{t}^{(\nu+1)} = (\mathbf{C} - \mathbf{S}\Delta\theta)\mathbf{t}^{(\nu)} + \mathbf{r}\Delta\Theta \tag{9}$$

The Crank-Nicolson scheme replaces equation (7) by

$$\left(\mathbf{C} + \mathbf{S}\frac{\Delta\theta}{2}\right)\mathbf{t}^{(\nu+1)} = \left(\mathbf{C} - \mathbf{S}\frac{\Delta\theta}{2}\right)\mathbf{t}^{(\nu)} + \mathbf{r}\Delta\theta \tag{10}$$

In the finite-difference method $\mathbf{C}$ is diagonal and equation (9) can be solved explicitly for the new set of temperatures $\mathbf{t}^{(\nu+1)}$. In the finite-element method $\mathbf{C}$ is not diagonal and equation (9) does not give an explicit solution for $\mathbf{t}^{(\nu+1)}$. Rather, a system of algebraic equations must be solved at each time step (an implicit solution). The Crank-Nicolson scheme is implicit for both methods because $\mathbf{S}$ (which is not diagonal) has been introduced on the left-hand side of the equation. Consequently in the finite-element method one would normally use the more accurate Crank-Nicolson scheme since it can be carried out with no more computations than the Euler scheme, whereas in the finite-difference method one could choose Euler and avoid an implicit solution.

Reference [5] shows that the exact analytical solution to equation (7), the Euler solution, and the Crank-Nicolson solution can all be written as

$$\mathbf{t}^{(\nu+1)} = \mathbf{a} + \mathbf{b}\theta^{(\nu+1)} + \mathbf{X}\mathbf{M}^{\nu+1}\mathbf{X}^T\mathbf{C}(\mathbf{t}^{(0)} - \mathbf{a}) \tag{11}$$

where the vector $\mathbf{b}$ must satisfy

$$\mathbf{S}\mathbf{b} = \mathbf{0} \tag{12}$$

and the vector $\mathbf{a}$ must satisfy the equation

$$\mathbf{S}\mathbf{a} = \mathbf{r} - \mathbf{C}\mathbf{b} \tag{13}$$

The matrix $\mathbf{X}$ contains the eigenvectors $(\mathbf{x}_1, \mathbf{x}_2, \ldots, \mathbf{x}_n)$ of the generalized eigenproblem given by

$$\mathbf{S}\mathbf{X} = \mathbf{C}\mathbf{X}\Lambda \tag{14}$$

where Λ is a diagonal matrix containing the eigenvalues $(\lambda_1 \leqq \lambda_2 \leqq \ldots < \lambda_n)$.

The only place the three solutions represented by equation (11) differ is in the diagonal matrix $\mathbf{M}$. The diagonal entries, μ_i, in $\mathbf{M}$ for the exact analytical solution to equation (7) are given by

$$\mu_i = \exp(-\lambda_i\Delta\theta) \tag{15}$$

If these μ_i are substituted into equation (11) the exact analytical solution to equation (7) is seen to be the sum of n decaying exponentials (in addition to the linear leading terms). For the approximate Euler scheme, equation (9),

$$\mu_i = 1 - \lambda_i\Delta\theta \tag{16}$$

For the approximate Crank-Nicolson scheme, equation (10),

$$\mu_i = \frac{2 - \lambda_i\Delta\theta}{2 + \lambda_i\Delta\theta} \tag{17}$$

The Euler and Crank-Nicolson relations, equations (16) and (17), are approximations to the exact relation, equation (15). These three relations between μ_i and $\lambda_i\Delta\theta$ are compared in Fig. 1. Observe that the Crank-Nicolson relation is a much better approximation than the Euler relation. Thus for the same $\Delta\theta$ Crank-Nicolson will give a better approximation to the solution of equation (7) than Euler will. As $\Delta\theta$ goes to zero all three curves converge, but this is generally too small a time step to be practical.

The character of each of the three solutions is related to the numerical values of μ_i. Since $\mathbf{M}$ is diagonal, the entries in $\mathbf{M}^{\nu+1}$ in equation (11) will be $\mu_i{}^{\nu+1}$. Hence for values of μ_i between 0 and 1, $\mu_i{}^{\nu+1}$ will steadily decay to zero (e.g. $\frac{1}{2}, \frac{1}{4}, \frac{1}{8}, \frac{1}{16}, \ldots$). For values of μ_i between 0 and -1, $\mu_i{}^{\nu+1}$ will also decay to zero but will alternate sign (e.g. $-\frac{1}{2}, \frac{1}{4}, -\frac{1}{8}, \frac{1}{16}, \ldots$).These alternations in sign will propagate throughout the solution and give rise to "numerically-induced oscillations" in the temperature until they eventually die out. Finally, for values of μ_i less than -1, $\mu_i{}^{\nu+1}$ will not only alternate in sign but will grow in amplitude (e.g. $-2, 4, -8, 16, \ldots$). This behavior will produce unstable, numerically-induced oscillations in the temperature solution. Observe from Fig. 1 that the Euler scheme can exhibit all three kinds of behavior (steady decay, oscillatory decay, and oscillatory growth) if $\Delta\theta$ is large enough. The Crank-Nicolson scheme can only have steady decay and oscillatory decay. The exact analytical solution will only have a steady decay. It should be mentioned that in the finite-element method the exponentials in the exact analytical solution can add together in such a way as to produce some oscillatory behavior at small times [1] but this behavior should not be confused with numerically-induced oscillations.

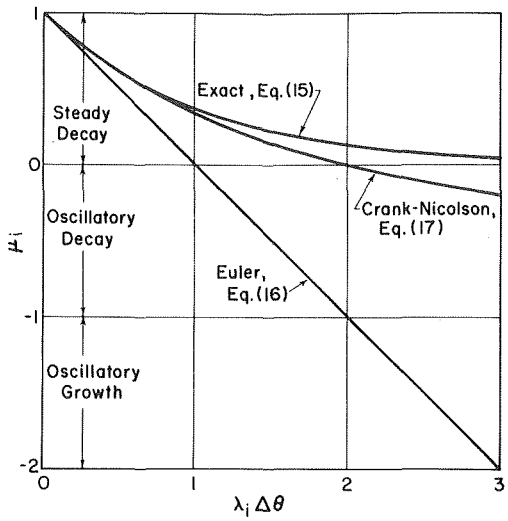

Fig. 1 Comparison of Euler and Crank-Nicolson values of μ_i to exact values

The larger the value of $\Delta\theta$ that is used, the more serious the numerically-induced oscillations become. Euler solutions can go out of control in a few time steps. Although the Crank-Nicolson scheme will never be unstable, the oscillations can make the solution useless. Thus the selection of a suitable time step is important for both the Euler and the Crank-Nicolson schemes.

The Critical Time Step

The value of $\Delta\theta$ beyond which the Euler solution would exhibit unstable oscillations is called the critical time step, $\Delta\theta_c$. A value of $\Delta\theta$ less than or equal to $\Delta\theta_c$ will ensure that none of the μ_i is less than -1. The most negative value of μ_i will be μ_n. It can be seen from Fig. 1, or equation (16), that $\mu_n = -1$ when $\lambda_n\Delta\theta = 2$. Thus the critical time step is given by

$$\Delta\theta_c = \frac{2}{\lambda_n} \tag{18}$$

The critical time step thus depends only upon the maximum eigenvalue of the generalized eigenproblem stated by equation (14). Therefore only the factors that determine the entries in $\mathbf{C}$ and $\mathbf{S}$ are important in determining the critical time step. Nodal-point locations, thermal properties (k, ρ, c, and h), and which nodal temperatures are specified are important. Factors such g''', q_s'', t_∞, and the actual value of a specified temperature, t_s, enter the problem only in the vector $\mathbf{r}$ and hence do not affect the critical time step. The initial condition, equation (6), is also unimportant.

Reference [5] discusses an important exception to equation (18). When there are specified-temperature nodes there will be an equal

number of eigenvalues that are directly associated with these nodes which will cancel out of the solution and hence will not influence the stability and oscillation characteristics. If any of these special eigenvalues is λ_n it can be disregarded. In this case λ_{n-1} should be used in equation (18) to determine the critical time step. That is, the largest eigenvalue not associated with a specified-temperature node should be used in equation (18).

It should also be observed from Fig. 1 that the critical time step defined by equation (18) is also the time step at which numerically-induced oscillations will begin to show up in the Crank-Nicolson solution. Thus a choice of $\Delta\theta \leqq \Delta\theta_c$ will also ensure that no numerically-induced oscillations will occur in a Crank-Nicolson solution. Since numerically-induced oscillations are unwelcome if they are too large, the critical time step is an important parameter in a Crank-Nicolson solution even though the solution will always be stable.

Although it is important to understand that the maximum eigenvalue determines the critical time step, precise evaluation of λ_n requires a major computational effort. It is not a convenient technique for finding $\Delta\theta_c$.

Safe Estimates. A "safe" estimate ($\Delta\theta_c^*$) of the critical time step is one which is less than or equal to the critical time step. An "unsafe" estimate of the critical time step is one that is larger than $\Delta\theta_c$. This would allow the possibility of choosing $\Delta\theta$ less than the unsafe estimate but greater than $\Delta\theta_c$ and hence obtain an unstable Euler solution or an oscillatory Crank-Nicolson solution. A safe estimate can be found by making an estimate of λ_n that is guaranteed to be too large and substituting it into equation (18) instead of λ_n.

There is a theorem by Gerschgorin [5, 6] that can be applied almost immediately in the finite-difference method since **C** is diagonal. The finite-difference result is that

$$\Delta\theta_c^* = 2 \min_{i=1}^{n} \left[\frac{c_{ii}}{s_{ii} + \sum_{\substack{j=1 \\ j\neq i}}^{n} |s_{ij}|} \right] \tag{19}$$

where c_{ii} and s_{ii} are the diagonal entries in row i of **C** and **S** and s_{ij} is an off-diagonal entry in **S** when $j \neq i$. The notation in front of the brackets means that the computation should be done for each of the n rows, and the minimum result should be taken as $\Delta\theta_c^*$. Reference [5] shows that rows corresponding to specified-temperature nodes may be excluded from this computation.

The development of a similar relation for the finite-element method is more involved since **C** is not diagonal. The proof depends upon the symmetry of **C** and **S** and upon the particular structure of **C** in addition to the Grsechgorin theorem as shown in the appendix at the end of the paper. For linear triangular elements the result is that

$$\Delta\theta_c^* = \min_{i=1}^{n} \left[\frac{c_{ii}}{s_{ii} + \sum_{\substack{j=1 \\ j\neq i}}^{n} |s_{ij}|} \right] \tag{20}$$

The only difference between the finite-element relation, equation (20), and the finite-difference result, equation (19), is the factor 2. However, since the entries in the finite-element **C** and **S** will in general be different than for finite differences, the estimates will not simply differ by a factor of two.

Equations (19) and (20) are quite general results. They may be used for problems with irregular nodal-point locations, position-dependent properties, and any combination of the boundary conditions given by equations (2–5). Equation (20) is a new result that is as convenient for the engineer to use in finite-element computations as equation (19) has been in the past for finite-difference computations. In finite-element practice a lumped-capacitance formulation is sometimes used. In this case **C** is diagonal and equation (19) should be used to estimate the critical time step.

Toeplitz Estimates. The Fourier method (separation of variables) used by Lemmon and Heaton [2] to estimate the critical time step and the von Neumann method used by Yalamanchili and Chu [3] are closely related. Both assume there are an infinite number of uniformly-spaced nodal points and that the thermal properties are uniform. Both methods ignore the boundary conditions of the problem. With all of these restrictions **C** and **S** will be infinitely-large Toeplitz matrices [7]. Analytical expressions for the eigenvalues of such matrices can be derived. If the largest eigenvalue, λ_∞, is substituted into equation (18), a "Toeplitz estimate" ($\Delta\theta_\infty$) is obtained. This result is the same as one obtains via the Fourier or von Neumann method. Toeplitz estimates as applied to finite differences and finite elements are elaborated on in [5].

Since the maximum Toeplitz eigenvalue is not necessarily greater than λ_n, the Toeplitz estimate ($\Delta\theta_\infty$) is not a safe estimate. Its relation to $\Delta\theta_c$ and $\Delta\theta_c^*$ will become apparent in the numerical examples of the next section. Toeplitz estimates can, however, be used to make interesting comparisons between various methods. For a square nodal-point grid, the Toeplitz estimate for triangular finite elements has been found [5] to be

$$\frac{\alpha\Delta\theta_\infty}{(\Delta x)^2} = \frac{2-\sqrt{3}}{2\sqrt{3}} = 0.0774 \tag{21}$$

For square finite elements, Yalamanchili and Chu [3] found that

$$\frac{\alpha\Delta\theta_\infty}{(\Delta x)^2} = \frac{1}{12} = 0.0833 \tag{22}$$

For finite differences,

$$\frac{\alpha\Delta\theta_\infty}{(\Delta x)^2} = \frac{1}{4} = 0.2500 \tag{23}$$

Observe that both finite-element methods are much more restrictive than the finite-difference method. Also note that triangular elements are slightly more restrictive than square elements.

Numerical Examples

The numerical examples presented in this section illustrate the behavior of the critical time step as a function of the nodal-point grid size and the boundary conditions. The relationship between $\Delta\theta_c$, $\Delta\theta_c^*$ and $\Delta\theta_\infty$ is discussed. Finite-difference results are incorporated for comparison.

Fig. 2 describes the region that will be examined. A uniform, square arrangement of nodal points will be used. Two finite-element arrangements will be considered—one will have all positive diagonals and will be indicated by a ⊕; the other will have all negative diagonals

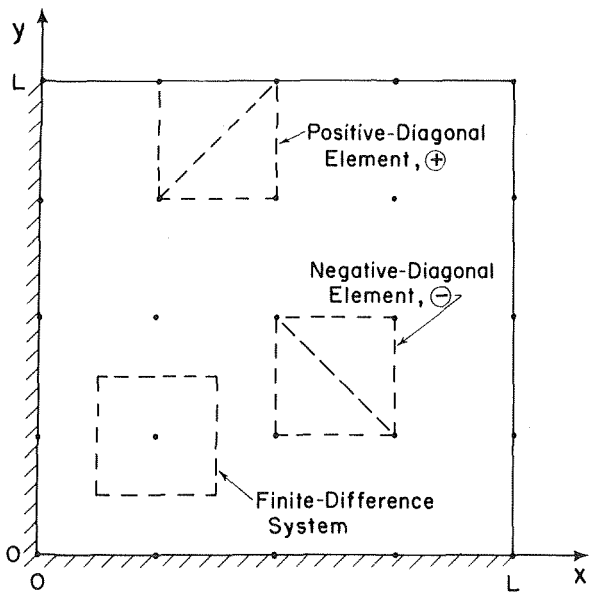

Fig. 2 Example problem

and be indicated by a Θ. The boundaries along $x = 0$ and along $y = 0$ will be adiabatic. The boundaries along $x = L$ and along $y = L$ will both be adiabatic, or convective, or have a specified temperature. Thermal properties will be uniform.

Exact Values. The exact values of the critical time step are shown in Fig. 3 for the various boundary conditions and element arrangements. These values are obtained by actually computing the maximum eigenvalues for equation (14) and substituting them into equation (18). The Toeplitz values, equations (21) and (23), are also shown.

Observe that for the finite-difference method the nondimensional critical time step for the completely adiabatic boundary ($H = 0$) is independent of the number of nodes and is the same as the Toeplitz estimate. For $H > 0$ it appears that the Toeplitz estimate is the limiting value as the number of nodes becomes infinite. This is reasonable since the assumptions behind the Toeplitz estimate are more nearly satisfied as the number of nodes increases. These observations do not appear to be true for the finite-element method however. Here it appears that the limiting value approached by all but the top curve is slightly below the Toeplitz estimate. This must be due to a boundary effect that is not accounted for by the Toeplitz theory. Consequently the Toeplitz estimate is hardly ever a safe one to use for triangular elements.

The effect of convection, for both finite differences and finite elements, is to reduce the critical time step. Thus the Toeplitz estimate is not a safe one to use for either method if there is a convective boundary. As H becomes large, $\Delta\theta_c$ goes to zero and an excessively large number of time steps would be required to complete a transient solution. However as H becomes large, the convective boundary may be satisfactorily modeled as a specified-temperature boundary. Observe that the critical time step for the specified-temperature boundary is less restrictive than the completely adiabatic boundary. Thus as H becomes large, one should think about changing the model from a convective boundary to a specified-temperature boundary to avoid being forced to take very small time steps.

Although the nondimensional critical time step increases (for $H > 0$) as the number of nodes increases, $\Delta\theta_c$ itself is decreasing since Δx is decreasing. In the limit a constant value (approximately the Toeplitz value) is approached, and then $\Delta\theta_c$ is proportional to $(\Delta x)^2$.

Estimates. Estimates of the critical time step (and of the Toeplitz value) based on equations (19) and (20) are shown in Fig. 4. The same qualitative behavior as Fig. 3 is observed. The finite-difference curves all approach the Toeplitz limit as the number of nodes increases whereas all but one of the finite-element curves approaches a limit of 1/24 which is below the Toeplitz limit.

The curves in Fig. 4 all fall below the corresponding curves in Fig. 3 as expected, but it is interesting to note that the difference between $\Delta\theta_c^*$ and $\Delta\theta_c$ is much less for the finite-difference method than for the finite-element method. The nondiagonal nature of the finite-element **C** has not permitted as good an estimate of λ_n as when **C** is diagonal.

Discussion

Previous investigations [2, 3] have used the Fourier or von Neumann method to study the critical-time-step problem. These techniques are seen in this paper as being related to Toeplitz matrix theory and simply provide a limiting-case solution as the number of nodal points becomes infinite. Although these techniques provide an interesting comparison between various discretization methods, they do not provide a computationally useful way to make a safe estimate of the critical time step in a general situation.

The major new result presented in this paper is equation (20) which gives a computationally convenient safe estimate of the critical time step for the finite-element method when using linear triangular elements. This result is applicable to problems with irregular nodal-point spacing, position-dependent properties, and a variety of boundary conditions. The engineer can now conveniently and safely estimate the critical time step.

The finite-element result, equation (20), cannot be expected to hold

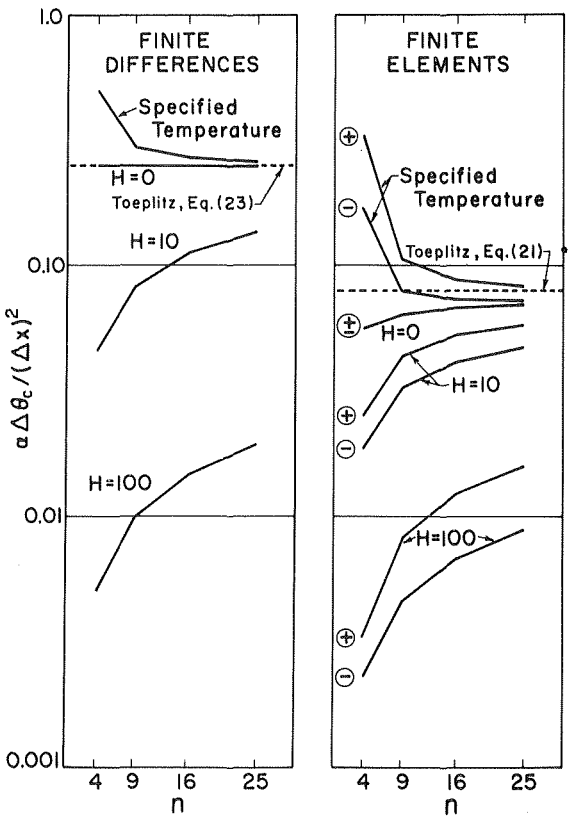

Fig. 3 Critical-time-step comparisons

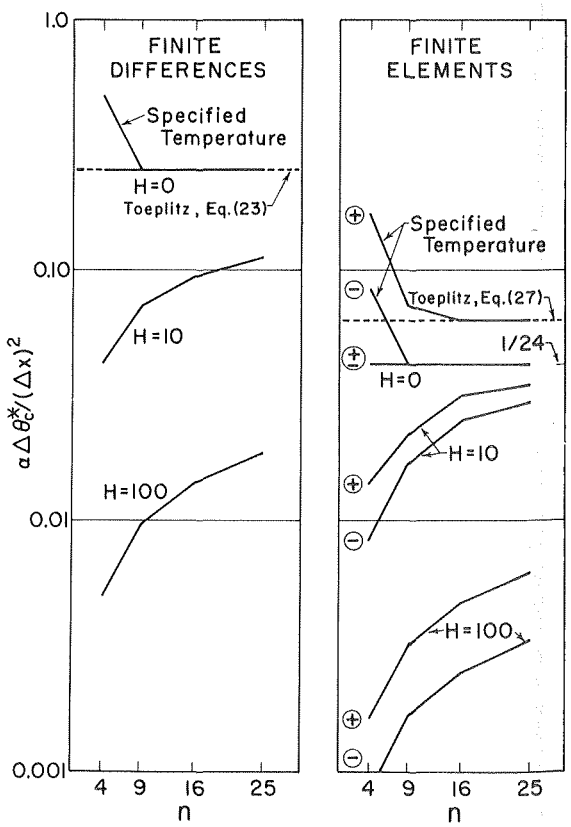

Fig. 4 Estimates of the critical time step

for non-triangular elements but it should be possible to derive similar results for other elements. As an example, it can be shown that for the linear quadrilateral element

$$\Delta\theta_c^* = \frac{1}{2} \operatorname*{Min}_{i=1}^{n} \left[\frac{c_{ii}}{s_{ii} + \sum_{\substack{j=1 \\ j \neq i}}^{n} |s_{ij}|} \right] \tag{24}$$

This equation replaces equation (20) for the quadrilateral elements. It is an extension of the comments of Yalamanchili and Chu [3] regarding square finite elements.

Comparisons of the critical time steps for the finite-element method with the finite-difference method show that the finite-element method is more restrictive. This is an interesting observation, but it will probably not govern the choice between using finite elements or finite differences. The superiority of the finite-element method at handling irregular geometries will probably override the disadvantage of being forced to take smaller time steps.

Convective boundary conditions have been shown to be an important factor in determining the critical time step. An alternative way to study this effect is shown in Fig. 5. Observe that as Δx decreases, $\alpha\Delta\theta_c^*/(\Delta x)^2$ for finite differences approaches 1/4 (the Toeplitz value) for all values of h. The corresponding limiting value for the finite-element curves is 1/24 (54 percent of the finite-element Toeplitz value, equation (21)). For large $h\Delta x/k$, each curve in Fig. 5 becomes linear. In this range $\Delta\theta_c^*$ is inversely proportional to the heat-transfer coefficient.

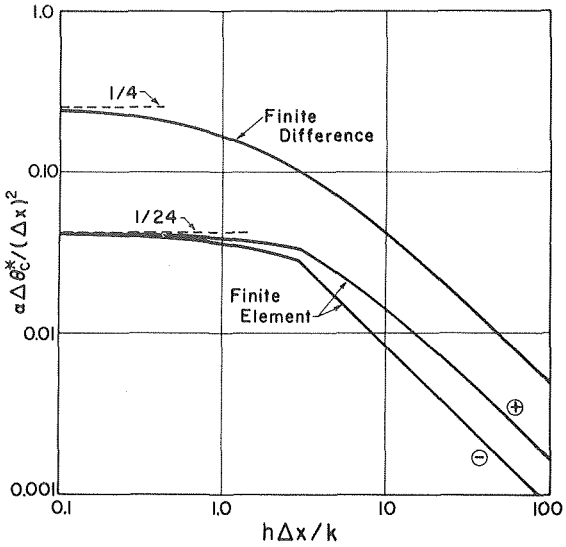

Fig. 5 Effect of convection on the critical time step

The effect of the shape of the triangular element can be studied by using Toeplitz estimates. The various triangular shapes may be parameterized as shown in Fig. 6. Although an analytical expression for the Toeplitz eigenvalues can be derived, it is not an easy task in general to find the maximum eigenvalue. Consequently an estimate ($\Delta\theta_\infty^*$), following equation (20), will be applied to the Toeplitz matrices. For triangular elements it can be shown [5] that

$$\frac{\alpha\Delta\theta_\infty^*}{\Delta x\,\Delta y} = \frac{\left(\frac{a}{c}\right)\sin\beta}{4\left[2\left(\frac{a}{c}\right)^2 + 2 + 3\left(\frac{a}{c}\right)\cos\beta + \left(\frac{a}{c}\right)\left|\cos\beta\right|\right]} \tag{25}$$

For comparison, the finite-difference result for $\beta = 90$ deg is given by[2]

$$\frac{\alpha\Delta\theta_\infty^*}{\Delta x\,\Delta y} = \frac{\left(\frac{a}{c}\right)}{2\left[1 + \left(\frac{a}{c}\right)^2\right]} \tag{26}$$

It should be mentioned that for the finite-difference result it happens that $\Delta\theta_\infty^* = \Delta\theta_\infty$. In both cases $\Delta\theta_\infty^*$ has been normalized using the product $\Delta x\,\Delta y$ which is twice the area of the triangle. Fig. 7 is a plot of equations (25) and (26). The angle β is an important factor for triangular elements. For a fixed value of a/c, $\Delta\theta_\infty^*$ increases as β increases until the maximum is attained when the triangle becomes isosceles. The optimum shape of isosceles triangle is the equilateral triangle ($a/c = 1$).

For the triangular elements used in arriving at equation (21), $\beta = 90$ deg, $a/c = 1$, and $\Delta x = \Delta y$. From equation (25) then,

$$\frac{\alpha\Delta\theta_\infty^*}{(\Delta x)^2} = \frac{1}{16} = 0.0625 \tag{27}$$

This is a more restrictive result than given by equation (21) because equation (25) was derived using an overestimate of the maximum

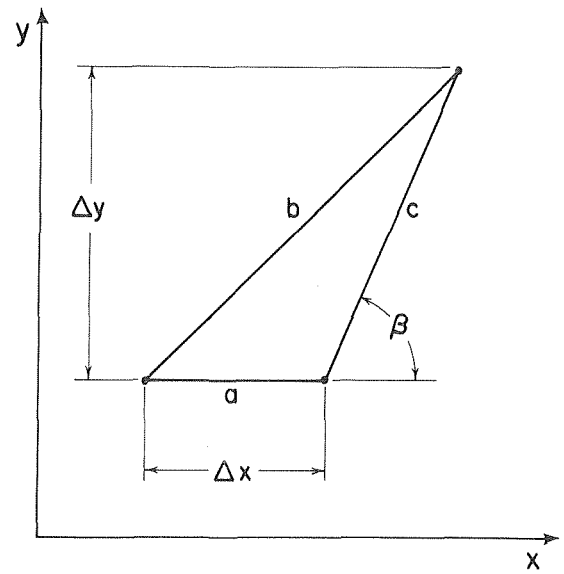

Fig. 6 Geometrical-shape parameters for triangular elements

Toeplitz eigenvalue, whereas equation (21) used the precise value. Similarly, the equilateral triangle result shown in Fig. 7 is $1/8\sqrt{3} = 0.0722$, whereas the precise value is $1/6\sqrt{3} = 0.0962$. Observe that this precise value for the equilateral triangle is less restrictive than the precise value, equation (22), which Yalamanchili and Chu [3] found for the square element, whereas the precise value for the right-triangular element, equation (21), is more restrictive.

Since the finite-element C is not diagonal, the Crank-Nicolson scheme should be used instead of Euler because it gives more accuracy with no additional computational effort. Since Crank-Nicolson is always stable, the critical time step can be exceeded without losing control of the solution. Numerically-induced oscillations will be introduced into the solution however. The larger the time step the more serious the oscillations. Wood and Lewis [8] show how this "noise" can be artificially damped by an averaging process.

Conclusions

The conclusions of this paper can be summarized as follows:

(1) The critical time step for linear triangular elements can be safely

[2] When $\beta \neq 90$ deg, the finite-difference expression is cumbersome to obtain for some of the same reasons that finite differences are cumbersome to program for irregular nodal locations.

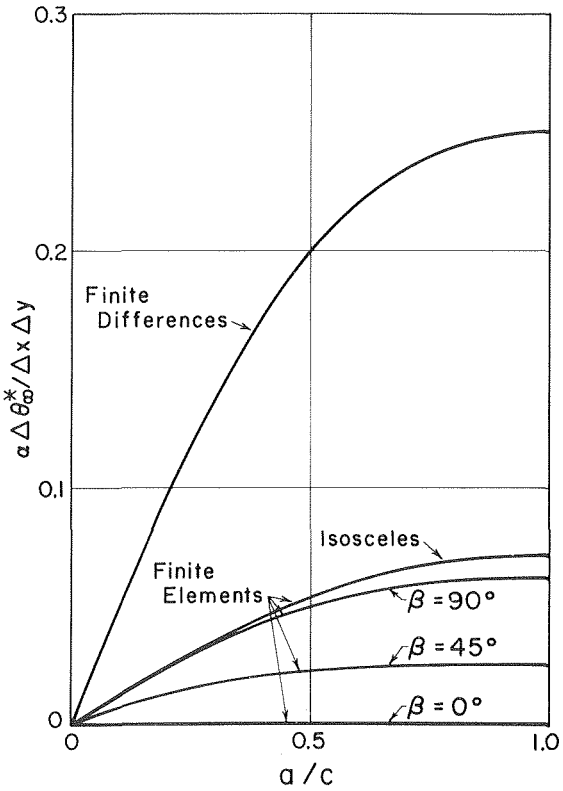

Fig. 7 Effect of element shape on $\Delta\theta^*_\infty$

estimated using equation (20). For linear quadrilateral elements equation (24) should be used.

(2) Relative to an adiabatic boundary, convection reduces the critical time step whereas a specified-temperature boundary will increase the critical time step.

(3) The equilateral triangle is the best shape of triangular element as far as the critical time step is concerned.

(4) Critical time steps for the finite-element method are smaller than for the finite-difference method.

Acknowledgments

This work was carried out under the sponsorship of the National Science Foundation under Grant GK-43429 and the Graduate School of the University of Wisconsin—Madison. A. Pincus of the University of Wisconsin Mathematics Research Center provided several key insights regarding the eigenvalue problem in this analysis. P. Nguyen and D. Bachelder carried out most of the computations.

References

1 Myers, G. E., *Analytical Methods in Conduction Heat Transfer*, McGraw-Hill, New York, 1971.

2 Lemmon, E. C., and Heaton, H. S., "Accuracy, Stability, and Oscillation Characteristics of Finite Element Method for Solving Heat Conduction Equation," ASME Paper No. 69-WA/HT-35.

3 Yalamanchili, R. V. S., and Chu, S. C., "Stability and Oscillation Characteristics of Finite-Element, Finite-Difference, and Weighted-Residuals Methods for Transient Two-Dimensional Heat Conduction in Solids," ASME, JOURNAL OF HEAT TRANSFER, Vol. 95, May 1973, pp. 235–239.

4 Yalamanchili, R., "Accuracy, Stability, and Oscillation Characteristics of Transient Two-Dimensional Heat Conduction," ASME Paper No. 75-WA/HT-85.

5 Myers, G. E., "Numerically-Induced Oscillation and Stability Characteristics of Finite-Element Solutions to Two-Dimensional Heat-Conduction Transients," Report 43, Engineering Experiment Station, University of Wisconsin-Madison, 1977.

6 Noble, B., *Applied Linear Algebra*, Prentice-Hall, Inc., Englewood Cliffs, NJ, 1969.

7 Grenander, U., and Szego, G., *Toeplitz Forms and Their Applications*, University of California Press, Berkeley, CA., 1958.

8 Wood, W. L., and Lewis, R. W., "A Comparison of Time Marching Schemes for the Transient Heat Conduction Equations," *International Journal for Numerical Methods in Engineering*, Vol. 9, 1975, pp. 679–689.

APPENDIX

An alternate statement of the eigenproblem given by equation (14) is

$$\mathbf{S}\mathbf{x} = \lambda\mathbf{C}\mathbf{x} \tag{28}$$

When $\mathbf{C}$ is diagonal as in finite differences or in the lumped-capacitance finite-element formulation, equation (28) can be premultiplied by $\mathbf{C}^{-1}$ and Gerschgorin's theorem [6] can be applied to obtain a meaningful bound on λ_n. This bound can then be substituted into equation (18) to obtain equation (19). When $\mathbf{C}$ is not diagonal, computation of $\mathbf{C}^{-1}$ is to be avoided due to the extensive computations and the additional computer storage requirements.

The first step in obtaining equation (20) is to define a diagonal matrix $\mathbf{D}$ as the diagonal of the matrix $\mathbf{C}$. Matrix $\mathbf{D}$ can be introduced into equation (28) to give

$$(\mathbf{D}^{-1/2}\mathbf{S}\mathbf{D}^{-1/2})\mathbf{D}^{1/2}\mathbf{x} = \lambda(\mathbf{D}^{-1/2}\mathbf{C}\mathbf{D}^{-1/2})\mathbf{D}^{1/2}\mathbf{x} \tag{29}$$

This is a new eigenproblem with the same eigenvalues as equation (28) and eigenvectors $\mathbf{D}^{1/2}\mathbf{x}$ instead of $\mathbf{x}$. The parenthesized matrices are symmetric.

There is a relatively well-known theorem [6] that can be applied to equation (29) to give

$$\lambda_n \leqq \frac{\kappa_n}{\beta_1} \tag{30}$$

where κ_n is the maximum eigenvalue of

$$(\mathbf{D}^{-1/2}\mathbf{S}\mathbf{D}^{-1/2})\mathbf{u}' = \kappa\mathbf{u}' \tag{31}$$

and β_1 is the minimum eigenvalue of

$$(\mathbf{D}^{-1/2}\mathbf{C}\mathbf{D}^{-1/2})\mathbf{v}' = \beta\mathbf{v}' \tag{32}$$

Premultiplying equation (31) by $\mathbf{D}^{-1/2}$ and introducing $\mathbf{u} = \mathbf{d}^{-1/2}\mathbf{u}'$ gives

$$\mathbf{D}^{-1}\mathbf{S}\mathbf{u} = \kappa\mathbf{u} \tag{33}$$

The Gerschgorin theorem [6] may be applied to $\mathbf{d}^{-1}\mathbf{s}$ to give an upper bound on κ_n as

$$\kappa_n \leqq \max_{i=1}^{n}\left[\frac{1}{c_{ii}}\left(s_{ii} + \sum_{\substack{j=1 \\ j\neq i}}^{n}\left|s_{ij}\right|\right)\right] \tag{34}$$

Premultiplying equation (32) by $\mathbf{D}^{1/2}$ and introducing $\mathbf{v} = \mathbf{d}^{-1/2}\mathbf{v}'$ gives

$$\mathbf{C}\mathbf{v} = \beta\mathbf{D}\mathbf{v} \tag{35}$$

Next a parameter q will be introduced by subtracting $q\mathbf{D}\mathbf{v}$ from both sides of equation (35) to give

$$(\mathbf{C} - q\mathbf{D})\mathbf{v} = (\beta - q)\mathbf{D}\mathbf{v}$$

It then follows [6] that

$$\beta_1 - q \geqq \frac{\text{minimum eigenvalue of } (\mathbf{C} - q\mathbf{D})}{\text{maximum eigenvalue of } \mathbf{D}}$$

or

$$\beta_1 \geqq q + \frac{\text{minimum eigenvalue of } (\mathbf{C} - q\mathbf{D})}{\text{maximum eigenvalue of } \mathbf{D}} \tag{36}$$

The value of q will be chosen as the largest value for which the minimum eigenvalue of $(\mathbf{C} - q\mathbf{D})$ can be guaranteed to be non-negative.

The matrix $(\mathbf{C} - q\mathbf{D})$ can be constructed as a sum of contributions, $(\mathbf{C}^{(e)} - q\mathbf{D}^{(e)})$, from each finite element. For triangular finite elements,

each $(\mathbf{C}^{(e)} - q\mathbf{D}^{(e)})$ will have $n - 3$ eigenvalues that are 0. The remaining 3 eigenvalues will be equal to the eigenvalues of the matrix

$$\frac{\rho cA}{12}\begin{bmatrix} 2-2q & 1 & 1 \\ 1 & 2-2q & 1 \\ 1 & 1 & 2-2q \end{bmatrix} \tag{37}$$

These eigenvalues are $\rho cA(1-2q)/12$, $\rho cA(1-2q)/12$, and $\rho cA(4-2q)/12$. The largest value of q that will ensure non-negative eigenvalues for $(\mathbf{C}^{(e)} - q\mathbf{D}^{(e)})$ is $q = 1/2$. Since, for this value of q, $(\mathbf{C} - q\mathbf{D})$ is the sum of matrices with non-negative eigenvalues, $(\mathbf{C} - q\mathbf{D})$ will also have only non-negative eigenvalues [6]. Hence equation (36) will give

$$\beta_1 \geqq \frac{1}{2} \tag{38}$$

Substitution of equations (34) and (38) into equation (30) will give a bound on λ_n which can then be substituted into equation (18) to yield equation (20).

The development of equation (24) for quadrilateral finite elements is the same as for triangular elements. The only difference is that the matrix (37) is replaced by

$$\frac{\rho cA}{36}\begin{bmatrix} 4-4q & 2 & 1 & 2 \\ 2 & 4-4q & 2 & 1 \\ 1 & 2 & 4-4q & 2 \\ 2 & 1 & 2 & 4-4q \end{bmatrix}$$

From which $q = 1/4$ and equation (24) will result.

Further details of the analysis presented in this paper can be found in a 180-page report by Myers [5]. Also discussed in this report is a modified form of equation (20) which can sometimes give better estimates of the critical time step. Discussions are also presented to explain the effects of heat-transfer boundary conditions upon the eigenvalues and hence upon the critical time step. This report may be obtained by writing to: Informational Resources Office, Engineering Experiment Station, University of Wisconsin—Madison, 1500 Johnson Drive, Madison, Wisconsin 53706.

A. Maewal
Postdoctoral Fellow,
Department of Applied Mechanics
and Engineering Science,
University of California, San Diego,
La Jolla, Calif.

G. A. Gurtman
Staff Scientist,
Systems, Science and Software,
La Jolla, Calif.

G. A. Hegemier
Professor,
Department of Applied Mechanics
and Engineering Science,
University of California, San Diego,
La Jolla, Calif.

A Mixture Theory for Quasi-One-Dimensional Diffusion in Fiber-Reinforced Composites[1]

A binary mixture theory is developed for heat transfer in unidirectional fibrous composites with periodic, hexagonal microstructure. The case treated concerns a class of problems for which heat conduction occurs primarily in the fiber direction. Model construction is based upon an asymptotic technique wherein the ratio of transverse-to-longitudinal thermal diffusion times is assumed to be small. The resulting theory contains information on the distribution of temperature and heat flux in individual components. Mixture accuracy is estimated by comparing transient solutions of the mixture equations with finite difference solutions of the Diffusion Equation for an initial boundary value problem. Excellent correlation between "exact" and mixture solutions is observed. The construction procedures utilized herein are immediately applicable to other diffusion problems—in particular, moisture diffusion.

Introduction

In this paper a continuum mixture theory for heat conduction in a fiber-reinforced composite is presented. As in the earlier work on diffusion in laminated composites [1, 2],[2] the technique used for construction of the continuum model follows an asymptotic method introduced by Hegemier [3] and successfully applied to the solution of wave-propagation problems [3–5]. The essential feature of the asymptotic technique is that it retains the heterogeneous character of the material, and yields, to a desired degree of approximation, information on temperature distribution in individual components of the composite.

It is, of course, possible to state the balance laws for composites directly in the form of a mixture theory by introducing partial heat flux quantities and an interaction term within the framework of general continuum theories of mixtures, as, for example, in [6]. Use of such an approach, however, leads to constitutive equations that involve mixture thermal properties which cannot be analytically determined even if the fiber and matrix are arranged in a periodic manner and their properties are known. On the other hand, use of the asymptotic technique described in [3–5] leads directly to a continuum theory in a mixture form involving composite material properties which can be determined from a knowledge of the geometrical arrangement and material properties of the individual constituents.

In the following, a mixture theory is constructed for the case in which heat conduction occurs primarily in a direction parallel to the fiber axis. An initial boundary value problem is solved, and results are compared using the mixture theory and a finite difference code solution of the Diffusion Equation.

A study of the problem class treated in this paper is important in many thermal protection applications, such as re-entry vehicle heat shields and nosetips in which the primary direction of heat flow is the fiber axis. Moreover, although the problems studied here can be directly solved by using numerical techniques, the reduction to one-dimensional problems leads to greater computational efficiency. This advantage becomes even more obvious when it is desired to analyze materials with temperature dependent properties. A study of such nonlinear effects will be the subject of a forthcoming paper.

Although the ensuing development is carried through for heat conduction problems, it is equally applicable to other diffusion phenomena which have recently attracted much attention, e.g. diffusion of moisture in composites [7, 8].

Formulation

Consider a periodic hexagonal array of circular cylindrical fibers (Constituent 1) embedded in a matrix (Constituent 2) as shown in Fig. 1. With respect to a polar cylindrical coordinate system $\bar{r}, \bar{\theta}, \bar{x}$, let the composite occupy the domain $0 \leq \bar{x} \leq \ell, 0 \leq \bar{r} \leq \infty, 0 \leq \bar{\theta} \leq 2\pi$. We assume that the temperature or heat flux boundary conditions on the boundaries at $\bar{x} = 0, \ell$ are such that the temperature distribution is similar in each hexagonal cell. As a consequence of this, the external boundary of the unit cell becomes a line of symmetry, and the component of the heat flux normal to the hexagonal boundary vanishes.

[1] Research was sponsored by Air Force Office of Scientific Research.

[2] Numbers in brackets designate References at end of paper.

Contributed by the Heat Transfer Division for publication in the JOURNAL OF HEAT TRANSFER. Manuscript received by the Heat Transfer Division April 4, 1977.

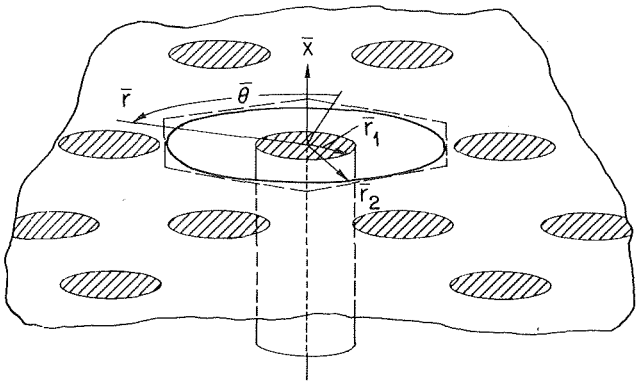

Fig. 1 Geometry and coordinate system

We further assume that there is no thermal resistance across the bond between the fiber and the matrix.

To describe heat conduction in a typical unit cell, the hexagonal boundary is approximated in the following development by a circle, as in the previous investigations of wave propagation [4, 5]. As a result of this approximation the temperature distribution within the cell is axisymmetric, with zero heat flux normal to the outer circular boundary of the matrix. Using the notation $\partial_t(\ ) \equiv \partial(\ )/\partial t$ etc., the initial boundary value problem that describes heat conduction in the cell is given by the following set of equations:

(a) Conservation of Energy

$$-\frac{1}{\bar{r}}\partial_{\bar{r}}(\bar{r}\bar{q}_{\bar{r}}^{(\alpha)}) - \partial_{\bar{x}}(\bar{q}_{\bar{x}}^{(\alpha)}) = \bar{\mu}^{(\alpha)}\partial_{\bar{t}}\bar{T}^{(\alpha)} \tag{1}$$

(b) Constitutive Equations

$$(\bar{q}_{\bar{x}}^{(\alpha)}, \bar{q}_{\bar{r}}^{(\alpha)}) = -\bar{k}^{(\alpha)}(\partial_{\bar{x}}, \partial_{\bar{r}})\bar{T}^{(\alpha)} \tag{2}$$

(c) Interface Condition

$$\bar{T}^{(1)}(\bar{x}, \bar{r}_1, \bar{t}) = \bar{T}^{(2)}(\bar{x}, \bar{r}_1, \bar{t}) \tag{3a}$$

$$\bar{q}_{\bar{r}}^{(1)}(\bar{x}, \bar{r}_1, \bar{t}) = \bar{q}_{\bar{r}}^{(2)}(\bar{x}, \bar{r}_1, \bar{t}) \tag{3b}$$

(d) Symmetry Condition

$$\bar{q}_{\bar{r}}^{(2)}(\bar{x}, \bar{r}_2, \bar{t}) = 0 \tag{4}$$

(e) Initial and boundary data.

The quantities $q_{\bar{r}}^{(\alpha)}$, $q_{\bar{x}}^{(\alpha)}$, $\bar{\mu}^{(\alpha)}$, $\bar{T}^{(\alpha)}$, $\bar{k}^{(\alpha)}$ in foregoing are, respectively, the heat flux vector components, heat capacity, temperature, and thermal conductivity of the α (≡1 or 2) constituent.

Nondimensionalization

To facilitate the analysis, the basic equations (1–4) are placed in a nondimensional form suggested by a subsequent assumption that a typical "macrodimension" ℓ is much larger than a "microdimension", say $\bar{r}_2$. Introduce the nondimensional quantities

$$\epsilon \equiv \bar{r}_2/\ell,\ x \equiv \bar{x}/\ell,\ r \equiv \bar{r}/\bar{r}_2$$
$$T^{(\alpha)} \equiv \bar{T}^{(\alpha)}/\bar{T}_0,\ q_x{}^{(\alpha)} \equiv \bar{q}_{\bar{x}}{}^{(\alpha)}/q_0$$
$$\epsilon q_r{}^{(\alpha)} \equiv \bar{q}_{\bar{r}}{}^{(\alpha)}/q_0,\ q_0 = k\bar{T}_0/\ell \tag{5}$$
$$t = \bar{t}/\bar{t}_0,\ \bar{t}_0 = \mu\ell^2/k,\ k_\alpha = \frac{\bar{k}^{(\alpha)}}{k},\ \mu_\alpha = \frac{\bar{\mu}^{(\alpha)}}{\mu}$$

where k, μ denote mixture conductivity and heat capacity to be defined later. It is noted here that (5) can be used to define the macrodimension ℓ in terms of characteristic time $\bar{t}_0$. The characteristic time $\bar{t}_0$ is also related to observation times in the sense that, following the application of a temperature or heat pulse to a composite, the mixture theory shall be able to yield meaningful results only after a time interval not too small compared to $\bar{t}_0$. Similarly, the theory shall yield reliable results only at observation stations whose distances from the boundaries $\bar{x} = 0$ or ℓ are not too small compared to ℓ. Thus, in the absence of any explicit choice of time scale $\bar{t}_0$ or length scale ℓ in a given application, one of these quantities can always be selected so as to reflect the fineness of the time or length scales to which the resolution of the temperature history is sought. In summary, therefore, a finite, nonzero macrodimension ℓ for the purpose of scaling can always be chosen to be one of the following: (i) actual length of the composite in the axial direction, (ii) a length associated with a time characteristic of the input pulse [from $t_0 = \mu\ell^2/k$, cf. (5)], (iii) an observation length and (iv) a length associated with an observation time scale.

Using (5), the basic equations (1–4) may be written as

(a) Conservation of Energy

$$-\frac{1}{r}\partial_r(rq_r{}^{(\alpha)}) - \partial_x(q_x{}^{(\alpha)}) = \mu_\alpha\partial_t T^{(\alpha)} \tag{6}$$

(b) Constitutive Equation

$$(q_x{}^{(\alpha)}, \epsilon^2 q_r{}^{(\alpha)}) = -k_\alpha(\partial_x, \partial_r)T^{(\alpha)} \tag{7}$$

(c) Interface Conditions

$$T^{(1)}(x, r_1, t) = T^{(2)}(x, r_1, t) \tag{8a}$$

$$q_r{}^{(1)}(x, r_1, t) = q_r{}^{(2)}(x, r_1, t) \tag{8b}$$

Nomenclature

$A^{(1)}, A^{(2)}$ = functions of x and t only
$B^{(1)}, B^{(2)}$ = functions of x and t only
$C^{(1)}, C^{(2)}$ = functions of x and t only
h = an arbitrary function denoting the dependent variables
$h_{(2n)}$ = n^{th} order term in the expansion of h
$\bar{k}_\alpha$ = thermal conductivity of α constituent
k_α = nondimensional thermal conductivity of α constituent
k = thermal conductivity of the mixture in the x direction
ℓ = typical macrodimension
n_α = volume fraction of α constituent
P = interaction term
$\bar{q}_r{}^{(\alpha)}, q_x{}^{(\alpha)}$ = components of heat flux vector in the α constituent
$q_r{}^{(\alpha)}, q_x{}^{(\alpha)}$ = components of nondimensional heat flux vector in the α constituent
$q_x{}^{(\alpha a)}$ = average heat flux in α constituent
$q_{r(0)}{}^{(\alpha)}, q_{x(0)}{}^{(\alpha)}$ = zeroth order terms in the expansion for $q_r{}^{(\alpha)}, q_x{}^{(\alpha)}$
q_0 = reference heat flux
Q^* = a mixture constant, equation (34)
$\bar{r}$ = radial coordinate
r = nondimensional radial coordinate
$\bar{r}_1$ = radius of the fiber cross-section
$\bar{r}_2$ = radius of the equivalent cell
r_1 = nondimensional radius of the fiber
$\bar{T}^{(\alpha)}$ = temperature of the α constituent
$\tilde{T}^{(\alpha)}$ = See equation (29)
$T^{(\alpha)}$ = nondimensional temperature of the α constituent
$T^{(\alpha a)}$ = average temperature in α constituent
$\bar{T}_0$ = reference temperature
$T_{(2n)}{}^{(\alpha)}$ = n^{th} order term in expansion for $T^{(\alpha)}$
$T^{(\alpha)*}$ = see equation (30)
$\bar{t}$ = time
t = nondimensional time
$\bar{t}_0$ = characteristic time
$\bar{x}$ = axial coordinate
x = nondimensional axial coordinate
$\alpha = \begin{cases} =1 \text{ for fiber} \\ =2 \text{ for matrix} \end{cases}$
β_1, β_2 = mixture constants, equation (37)
ϵ = nondimensional small parameter
$\bar{\theta}$ = angular coordinate
τ = interface temperature
$\bar{\mu}^{(\alpha)}$ = specific heat per unit volume of α constituent
$\mu^{(\alpha)}$ = nondimensional specific heat of α constituent
μ = mixture specific heat

(*d*) Symmetry Condition

$$q_r{}^{(2)}(x, r_1, t) = 0 \tag{9}$$

Asymptotic Expansions

The quantities $\mu\bar{r}_2{}^2/k$ and $\mu\ell^2/k$ represent, respectively, characteristic thermal diffusion times in the transverse and longitudinal (fiber axis) directions. The ratio of these diffusion times is $\bar{r}_2{}^2/\ell^2 = \epsilon^2$. In what follows, it is assumed that this ratio is small compared to unity.

The premise that $\epsilon^2 \ll 1$ suggests the following regular asymptotic expansion for all dependent variables:

$$h(x, r, t, \epsilon) = \sum_{n=0}^{\infty} \epsilon^{2n} h_{(2n)}(x, r, t) \tag{10}$$

If (10) is substituted into (6) through (9), an initial boundary value problem is obtained for each order of ϵ^2. The lowest order system is obtained by setting $\epsilon = 0$ and placing the subscript (0) on all dependent variables in (6) through (9).

It might be pointed out that implicit in the use of the asymptotic expansion procedure outlined here is the assumption that the nondimensional constituent properties k_α and μ_α that appear in (6) and (7) are of order unity. This condition can easily be satisfied for composites with achievable volume fractions through a proper choice of mixture properties k and μ used for scaling in (5). This is done in a subsequent section by using the definitions (40) for mixture thermal conductivity and heat capacity.

Mixture Theory

We wish to construct a mixture theory that will, as a minimum, incorporate the effect of microstructure to a predetermined degree of approximation. We begin by defining averaged quantities such that

$$(\ )^{(1a)} \equiv \frac{1}{n_1} \int_0^{r_1} 2r(\ )^{(1)} dr \tag{11a}$$

$$(\ )^{(2a)} \equiv \frac{1}{n_2} \int_{r_1}^{1} 2r(\ )^{(2)} dr \tag{11b}$$

where n_1, n_2 are the volume fractions of the two constituents, i.e.,

$$n_1 \equiv r_1{}^2, n_2 \equiv 1 - n_1 \tag{12}$$

Equation (6) is now averaged according to (11), so that on using the interface condition, equation (8b), we obtain

$$n_1[-\partial_x q_x{}^{(1a)} - \mu_1 \partial_t T^{(1a)}] = P \tag{13a}$$

$$n_2[-\partial_x q_x^{(2a)} - \mu_2 \partial_t T^{(2a)}] = -P \tag{13b}$$

where P is the so-called interaction term defined by

$$P \equiv 2r_1 q_r{}^{(1)}(x, r_1, t) \tag{14}$$

The primary object of the subsequent development in this section is to calculate the interaction term P in terms of $T^{(1a)}$ and $T^{(2a)}$ to "close" (13a) and (13b). As in [3, 4] the calculation is based on the two lowest order systems.

The first order system is, in part,

$$-\partial_x q_{x(0)}{}^{(\alpha)} - \frac{1}{r}\partial_r(r q_{r(0)}{}^{(\alpha)}) = \mu_\alpha \partial_t T_{(0)}{}^{(\alpha)}, \tag{15}$$

$$\partial_r T_{(0)}(\alpha) = 0, \tag{16}$$

$$q_{x(0)}{}^{(\alpha)} = -k_\alpha \partial_x {}^{(\alpha)}_{(0)} \tag{17}$$

From equations (16) and (17), it can be concluded that both $T_{(0)}{}^{(\alpha)}$ and $q_{x(0)}(\alpha)$ are independent of the radial coordinate; thus, equation (15) becomes

$$\frac{1}{r}\partial_r(r q_{r(0)}{}^{(\alpha)}) = -2A^{(\alpha)}(x, t) \tag{18}$$

where $A^{(\alpha)}$ is a function yet to be determined. Integration of (18) yields

$$q_{r(0)}{}^{(\alpha)} = -\left[A^{(\alpha)}(x, t) r + \frac{B^{(\alpha)}(x, t)}{r}\right] \tag{19}$$

Equation (19) is now substituted into the constitutive equation for $q_{r(0)}$ i.e., in

$$q_{r(0)}{}^{(\alpha)} = -k_\alpha \partial_r T_{(2)}{}^{(\alpha)} \tag{20}$$

From (20) the following expression for the temperature distribution $T_2{}^{(\alpha)}$ is obtained in terms of arbitrary functions of x and t only:

$$k_\alpha T_{(2)}{}^{(\alpha)} = A^{(\alpha)}(x, t)\frac{r^2}{2} + B^{(\alpha)}(x, t)\ell n r + C^{(\alpha)}(x, t) \tag{21}$$

The condition that temperature be finite at $r = 0$ leads to

$$B^{(1)} = 0 \tag{22}$$

Use of the symmetry condition, equation (9), furnishes

$$B^{(2)} = -A^{(2)} \tag{23}$$

Hence, the radial heat flux distribution in the cell is given by

$$q_{r(0)}{}^{(1)} = -A^{(1)}(x, t) r \tag{24a}$$

$$q_{r(0)}{}^{(2)} = -A^{(2)}\left[r - \frac{1}{r}\right] \tag{24b}$$

The second order temperature field in each constituent is, therefore, given by

$$k_1 T_{(2)}{}^{(1)} = A^{(1)}(x, t)\frac{r^2}{2} + C^{(1)}(x, t) \tag{25a}$$

$$k_2 T_{(2)}{}^{(2)} = A^{(2)}(x, t)\left[\frac{r^2}{2} - \ell n\, r\right] + C^{(2)}(x, t) \tag{25b}$$

The functions $A^{(\alpha)}$ are related to the interaction term P as follows: from (14) and the interface condition (8b) one has

$$\begin{aligned} P &= 2r_1 q_r{}^{(1)}(x, r_1, t) = 2r_1 q_r{}^{(2)}(x, r_1, t) \\ &= 2r_1 q_{r(0)}{}^{(1)}(x, r_1, t) + O(\epsilon^2) \\ &= 2r_1 q_{r(0)}{}^{(2)}(x, r_1, t) + O(\epsilon^2) \end{aligned} \tag{26}$$

If (24a) and (24b) are now substituted into (26), one obtains

$$A^{(1)} = -\frac{P}{2n_1}, \tag{27a}$$

$$A^{(2)} = \frac{P}{2n_2} \tag{27b}$$

Finally, use of (27) and (25) leads to the temperature distribution

$$T^{(1)} = \tilde{T}^{(1)} + \epsilon^2 T^{(1)*} r^2 + O(\epsilon^4) \tag{28a}$$

$$T^{(2)} = \tilde{T}^{(2)} + \epsilon^2 T^{(2)*}(r^2 - \ell n\, r^2) + O(\epsilon^4) \tag{28b}$$

where

$$\tilde{T}^{(\alpha)} = T_{(0)}{}^{(\alpha)} + \epsilon^2 C^{(\alpha)}(x, t), \tag{29}$$

$$T^{(1)*} = -\frac{P}{4n_2 k_2}, T^{(2)*} = \frac{P}{4n_2 k_2} \tag{30}$$

To obtain a minimal mixture theory that includes the effect of microstructure, it is necessary to satisfy the continuity of temperature at the interface up to and including terms of $O(\epsilon^2)$, thus

$$\begin{aligned} \tilde{T}^{(1)} + \epsilon^2 T^{(1)*} r_1{}^2 &= \tilde{T}^{(2)} + \epsilon^2 T^{(2)*}(r_1{}^2 - \ell n\, r_1{}^2) \\ &\equiv \tau(x, t, \epsilon), \end{aligned} \tag{31}$$

where τ is the interface temperature. Using equation (31), the temperature distribution given in (28) can be written in the form

$$T^{(1)} = \tau + \epsilon^2 T^{(1)*}(r^2 - n_1) \tag{32a}$$

$$T^{(2)} = \tau + \epsilon^2 T^{(2)*}\left(r^2 - n_1 - \ell n \frac{r^2}{n_1}\right) \tag{32b}$$

If (32) is now averaged according to (11), and if (30) is used to elimi-

nate $T^{(\alpha)*}$, one obtains

$$T^{(1a)} = \tau + \epsilon^2 \frac{P}{8k_1}, \tag{33a}$$

$$T^{(2a)} = \tau - \epsilon^2 \frac{P}{8k_2} Q^*, \tag{33b}$$

where

$$Q^* = -\frac{2}{n_2{}^2}\left[\frac{3}{2} + \frac{n_1{}^2}{2} - 2n_1 + \ell n\, n_1\right] \tag{34}$$

From (33) both the interaction term P and the interface temperature τ can be written in terms of average temperatures, thus

$$P = \frac{T^{(1a)} - T^{(2a)}}{\epsilon^2 \beta_1} \tag{35}$$

$$\tau = \frac{1}{2}\left\{(T^{(1a)} + T^{(2a)}) + \frac{\beta_2}{\beta_1}(T^{(1a)} - T^{(2a)})\right\} \tag{36}$$

where the constants β_1 and β_2 are given by

$$\beta_1 = \frac{1}{8}\left[\frac{1}{k_1} + \frac{Q^*}{k_2}\right] \tag{37a}$$

$$\beta_2 = \frac{1}{8}\left[\frac{Q^*}{k_2} - \frac{1}{k_1}\right] \tag{37b}$$

The foregoing analysis completes the construction of a binary mixture theory for the composite. The basic equations of the theory are the following:

$$n_1\{-\partial_x q_x{}^{(1a)} - \mu_1 \partial_t T^{(1a)}\} = P, \tag{13a}$$

$$n_2\{-\partial_x q_x{}^{(2a)} - \mu_2 \partial_t T^{(2a)}\} = -P, \tag{13b}$$

$$P = \frac{T^{(1a)} - T^{(2a)}}{\epsilon^2 \beta_1}, \tag{35}$$

$$q_x{}^{(\alpha a)} = -k_\alpha \partial_x T^{(\alpha a)}, \tag{38}$$

where the last equation follows directly from (7) and (11). To be appended to the above set are appropriate boundary and initial data.

It still remains to obtain expressions for mixture conductivity and specific heat to be used in (5). To do so, all dependent variables except $T^{(1a)}$ are eliminated from the mixture equations to obtain

$$\{(n_1k_1 + n_2k_2)\partial_x{}^2 - (n_1\mu_1 + n_2\mu_2)\partial_t + O(\epsilon^2)\}T^{(1a)} = 0 \tag{39}$$

Based on (39), the following definitions are introduced for the mixture properties:

$$k = n_1\bar{k}^{(1)} + n_2\bar{k}^{(2)} \tag{40a}$$

$$\mu = n_1\bar{\mu}^{(1)} + n_2\bar{\mu}^{(2)} \tag{40b}$$

With the definition (40), and in the limit as $\epsilon \to 0$, the mixture theory reduces to an elementary theory for heat conduction in a homogeneous material.

Numerical Results

To test the ability of the proposed theory to model diffusion in a composite, calculations have been conducted to determine the evolution of the temperature field in quiescent half-space $\bar{x} \geq 0$ subject to the boundary condition

$$\bar{T}(0, \bar{r}, \bar{t}) = \begin{cases} 1, 0 \leq \bar{t} \leq \bar{t}_0 \\ 0, \bar{t}_0 < \bar{t} \end{cases} \tag{41}$$

This boundary value problem has been solved by using (i) a finite-difference scheme for equations (13, 35 and 38) and (ii) a finite-difference scheme for equations (1–4). The finite-difference solution of equations (1–4)—the 'exact' solution—has been used as the correlating norm for estimating the accuracy of mixture theory solutions.

The material properties used for calculations are given in Table 1. Computations were carried out for $(a)\epsilon^2 = .111$, $(b)\epsilon^2 = .25$ and $(c)\epsilon^2 = 1$. Since there is no intrinsic axial length scale ℓ in the problem, the pulse duration $\bar{t}_0$ can be used for scaling in (5). Thus, with the same set of material and geometrical properties, an increase in ϵ^2 corresponds to a decrease in the pulse duration time and vice versa.

Figs. 2–4 illustrate the average temperature profiles in the two constituents after a short time following the termination of the temperature pulse. In Figs. 5 and 6, the evolution of average temperature is depicted at a given distance from the boundary. From these figures it can be seen that the agreement between the mixture theory results and the exact solutions is excellent for cases (a) and (b). In case (c), ϵ^2 has been chosen to be unity, clearly in violation of the basic premise that this parameter is much smaller than one. Thus, significant discrepancy is to be expected between mixture theory predictions and the exact solution, especially near a boundary or at times immediately following the application of a temperature pulse at the boundary.

Table I Material Properties Used for Computations

Thermal Conductivity Ratio	$\frac{\bar{k}^{(1)}}{\bar{k}^{(2)}} = 50$
Specific Heat Ratio	$\frac{\bar{\mu}^{(1)}}{\bar{\mu}^{(2)}} = 0.5$
Volume Fractions	$n_1 = .2$ (Fiber), $n_2 = .8$ (Matrix)

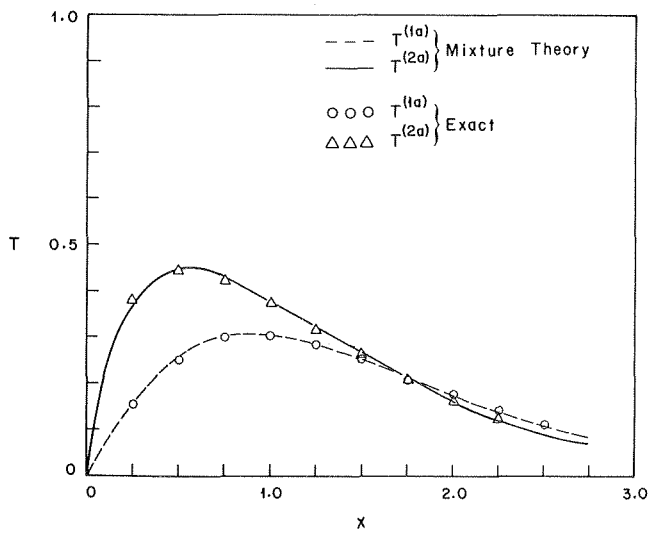

Fig. 2 Profile of average temperatures at $t = 1.2$ ($\epsilon^2 = 0.111$)

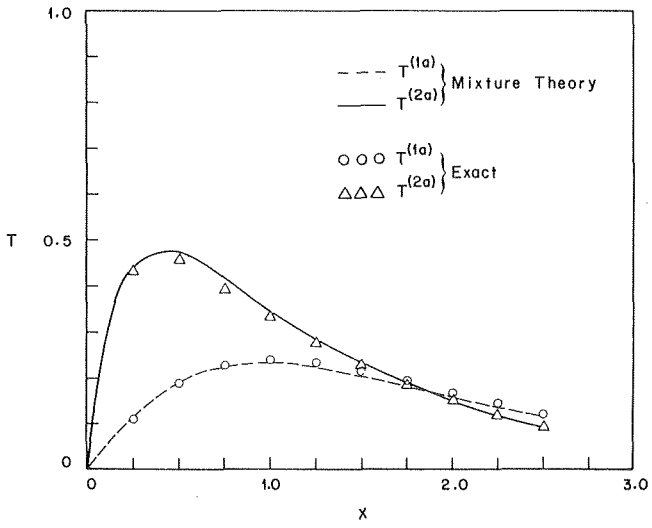

Fig. 3 Profile of average temperatures at $t = 1.2$ ($\epsilon^2 = 0.25$)

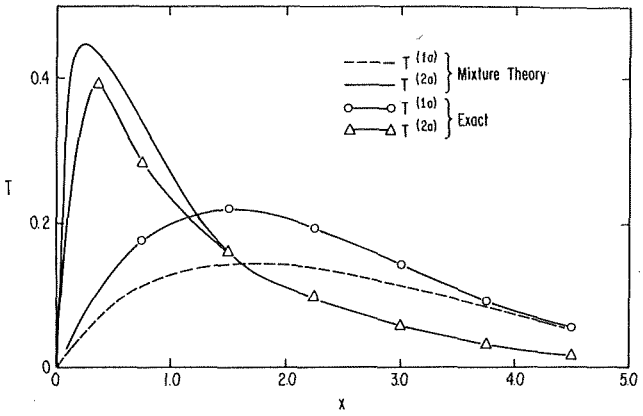

Fig. 4 Profile of average temperatures at $t = 1.2$ ($\epsilon^2 = 1.0$)

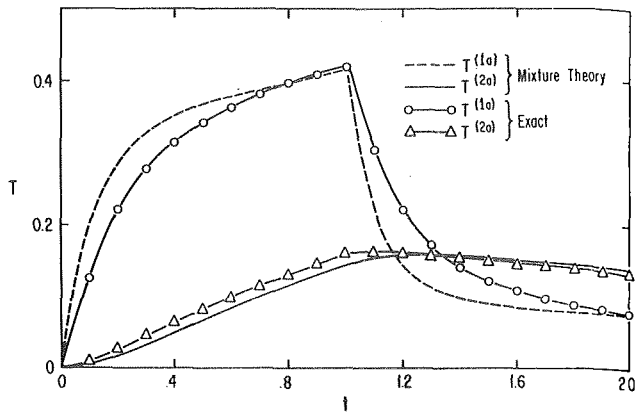

Fig. 6 Evolution of average temperature at $x = 1.5$ ($\epsilon^2 = 1.0$)

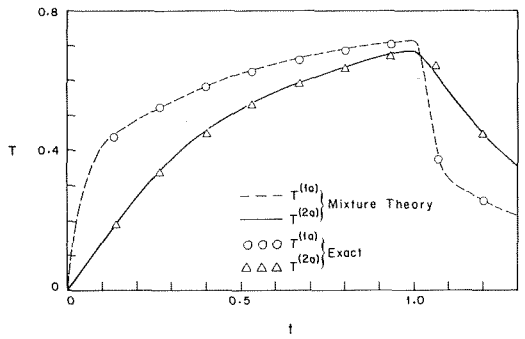

Fig. 5 Evolution of average temperature at $x = 0.5$ ($\epsilon^2 = 0.111$)

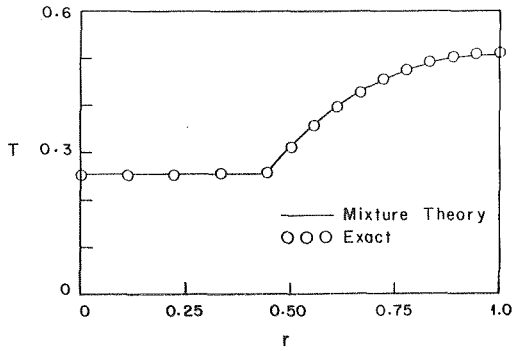

Fig. 7 Temperature microstructure at $x = 0.5$, $t = 1.2$ ($\epsilon^2 = 0.111$)

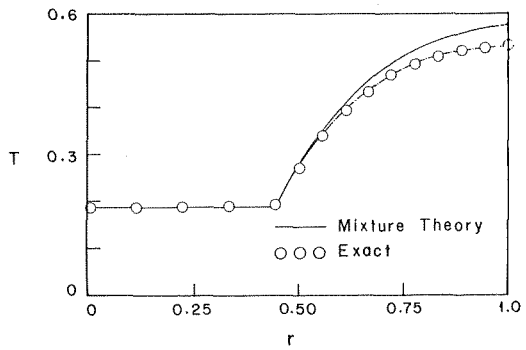

Fig. 8 Temperature microstructure at $x = 0.5$, $t = 1.2$ ($\epsilon^2 = 0.25$)

Thus this case is a very stringent test of our theory. However, even in this case, the mixture theory predictions become more accurate either at distances far from the boundary, or at long times compared to the input pulse duration, as can be seen in Figs. 4 and 6. The limitation of the theory for large values of ϵ^2 arises mainly from the outer nature of the solutions that it yields. However, the limitation is not a very serious one, since in most applications a typical macrodimension is indeed much larger than the cell dimension.

The ability of the mixture theory to predict the temperature microstructure is illustrated in Figs. 7 and 8. The radial distribution of temperature obtained from the mixture theory is almost identical to the exact solution. This feature of the theory proposed here is absent from most other continuum models of heat conduction in composites, e.g. [9].

Concluding Remarks

A mixture theory has been constructed for diffusion in a fiber-reinforced composite. The significant feature of the theory is that it converts what is essentially a three-dimensional problem to a problem involving a single spatial variable, without losing the essential details of local temperature distribution. Even if the mixture theory equations are solved numerically, their solution is much more economical than the use of a direct numerical strategy for the original problem. For example, for the problems treated in the last section, the solution of mixture equations was about fifty times faster than the solution of the original system. This computational efficiency is, of course, the result of the reduction in the number of spatial dimensions in the mixture theory equations. The excellent agreement between the mixture theory predictions and the exact solution of a boundary value problem indicates that the model proposed here can be effectively used for other problems of interest.

Acknowledgment

The authors wish to thank Dr. Kay Lie of Systems, Science and Software for performing the "exact" two-dimensional finite-difference calculations.

References

1 Maewal, A., Bache, T. C., and Hegemier, G. A., "A Continuum Model for Diffusion in Laminated Composite Media," ASME JOURNAL OF HEAT TRANSFER, Vol. 98, p. 133, 1976.

2 Nayfeh, A. H., "A Continuum Mixture Theory of Heat Conduction in Laminated Composites," *Journal Appl. Mech.*, Vol. 42, p. 399, 1975.

3 Hegemier, G. A., "Finite Amplitude Elastic Wave Propagation in Laminated Composites," *Journal Appl. Phys.*, Vol. 45, p. 4248, 1974.

4 Hegemier, G. A. and Gurtman, G. A., "Finite-Amplitude Elastic-Plastic Wave Propagation in Fiber-Reinforced Composited," *Journal Appl. Phys.*, Vol. 45, p. 4254, 1974.

5 Hegemier, G. A., Gurtman, G. A., and Nayfeh, A. H., "A Continuum

Mixture Theory of Wave Propagation in Laminated and Fiber-Reinforced Composites," *Int. J. Solids and Struct.*, Vol. 9, p. 395, 1973.
6 Green, A. E. and Naghdi, P. M., "A Theory of Mixtures," *Arch. Ratl. Mech. Anal.*, Vol. 24, p. 243, 1967.
7 Springer, G. S. and Shen, C. H., "Moisture Absorption and Desorption of Composite Materials," Air Force Materials Laboratory, Wright-Patterson Air Force Base, Ohio, 1976.
8 Augl, J. M. and Berger, A. M., "The Effect of Moisture on Carbon Fiber Reinforced Epoxy Composites I Diffusion," Naval Surface Weapons Center, White Oak, Silver Spring, Md., 1976.
9 Ben-Amoz, M. "Heat Conduction Theory for Composite Materials," *J. Appl. Math. Phys. ZAMP*, Vol. 27, p. 335, 1976.

R. J. Moffat
Professor of Mechanical Engineering,
Stanford University,
Stanford, Calif.

J. M. Healzer
Manager, Containment Methods,
Boiling Water Reactor Systems Department,
General Electric Company,
San Jose, Calif.

W. M. Kays
Professor of Mechanical Engineering,
Stanford University,
Stanford, Calif.

Experimental Heat Transfer Behavior of a Turbulent Boundary Layer on a Rough Surface With Blowing

Heat transfer measurements were made with a turbulent boundary layer on a rough, permeable plate with and without blowing. The plate was an idealization of sand-grain roughness, comprised of 1.25 mm spherical elements arranged in a most-dense array with their crests coplanar. Five velocities were tested, between 9.6 and 73 m/s, and five values of the blowing fraction, v_0/u_∞, up to 0.008. These conditions were expected to produce values of the roughness Reynolds number ($Re_\tau = u_\tau k_s/\nu$) in the "transitional" and "fully rough" regimes ($5 \leq Re_\tau \leq 70$, $Re_\tau > 70$).

With no blowing, the measured Stanton numbers were substantially independent of velocity everywhere downstream of transition. The data lay within ±7 percent of the mean for all velocities even though the roughness Reynolds number became as low as 14. It is not possible to determine from the heat transfer data alone whether the boundary layer was in the fully rough state down to Re = 14, or whether the Stanton number in the transitionally rough state is simply less than 7 percent different from the fully rough value for this roughness geometry.

The following empirical equations describe the data from the present experiments for no blowing:

$$\frac{C_f}{2} = 0.0036 \left(\frac{\theta}{r}\right)^{-0.25}$$

$$St = 0.0034 \left(\frac{\Delta}{r}\right)^{-0.25}$$

In these equations, r is the radius of the spherical elements comprising the surface, θ is the momentum thickness, and Δ is the enthalpy thickness of the boundary layer.

Blowing through the rough surface reduced the Stanton number and also the roughness Reynolds number. The Stanton number appears to have remained independent of free stream velocity even at high blowing; but experimental uncertainty (estimated to be ±0.0001 Stanton number units) makes it difficult to be certain. Roughness Reynolds numbers as low as nine were achieved.

A correlating equation previously found useful for smooth walls with blowing was found to be applicable, with interpretation, to the rough wall case as well:

$$\left.\frac{St}{St_0}\right|_\Delta = \left[\frac{\ell n(1+B)}{B}\right]^{1.25} (1+B)^{.25}$$

Here, St is the value of Stanton number with blowing at a particular value of Δ (the enthalpy thickness). St_0 is the value of Stanton number without blowing at the same enthalpy thickness. The symbol B denotes the blowing parameter, v_0/u_∞. St. The comparison must be made at constant Δ for rough walls, while for smooth walls it must be made at constant Re_Δ.

Contributed by the Heat Transfer Division for publication in the JOURNAL OF HEAT TRANSFER. Manuscript received by the Heat Transfer Division March 31, 1977.

The rough plate with blowing undergoes transition from a laminar to a turbulent boundary layer at approximately the same momentum thickness Reynolds number as does a smooth plate without blowing.

Introduction

There is considerable interest in protecting surfaces from high temperature environments by using transpiration or ablation. The ablating surface, in particular, frequently becomes mechanically rough during operation. It is important, from the designer's standpoint, to be able to predict the effects of roughness and blowing, in combination, on the heat transfer and friction behavior of the boundary layer. In addition, the combination of blowing and roughness offers a good opportunity to investigate some old concepts in a new situation, and thereby challenge our understanding.

Much of the present knowledge about rough surface hydrodynamics is based on ideas and results of the pipe-flow experiments by Nikuradse [1][1], who investigated flow through sand-grain-roughened tubes. The roughness elements for his experiments consisted of selected sand, carefully sieved and attached in maximum density to the tube walls. The roughness was described by a single parameter, k_s, the size of the sand-grain elements. The sand-grain measure of roughness became standard in skin friction studies; and it is still common practice to express the effects of an arbitrary roughness in terms of an "equivalent sand-grain roughness, k_s." Equivalent sand-grain roughness is defined as that sand-grain surface which would have had the same effect upon the flow as did the specimen surface.

Nikuradse's results showed three domains of behavior in terms of the "roughness Reynolds number," $\mathrm{Re}_\tau = u_\tau k_s/\nu$. For values less than five, the flow behaved as though the surface were smooth. For values greater than 70, the friction factor became independent of the pipe Reynolds number: a state described as "fully rough." The region between five and 70 defined a region of "transitional roughness." Prandtl and Schlichting [2] and von Kármán [3] used the Nikuradse results (in 1934) to predict the friction factor behavior of boundary layer flows over rough surfaces. These predictions indicated that a fully rough state of the boundary layer would be attained such that the friction factor would be a function only of x/k_s. These characterizations of boundary layer flows are still used, with the same values of roughness Reynolds number.

Two types of roughness are now identified in the literature: k and d-type. Nikuradse's classical sand-grain roughness is k-type. Two-dimensional roughness elements (ribs, rods, or grooves perpendicular to the flow) are referred to as "d-type." The two types have different characteristics though different authors have different opinions as to what constitutes the defining property. The present work is concerned with a k-type roughness (an idealization of sand-grain behavior).

[1] Numbers in brackets designate References at end of paper.

There have been several recent studies of the friction behavior of d-type roughness made by the addition of a regular array of transverse rods to a flat surface. Moore [4] studied a turbulent boundary layer in air flowing over such an array, using a fixed ratio between pitch and height. His data showed some evidence of fully rough behavior. Shortly thereafter, Liu [5] put a similar surface into a water table with a variable aspect ratio. Liu reported that the data could not be simply organized by an x-Reynolds number function. Perry and Joubert, et al. [6, 7] studied a similar rough surface in an adverse pressure gradient and reported no effect on the friction behavior due to the pressure gradient. This same study also attempted to simulate a change in roughness by changing the spacing between elements without changing their size. The results did not correspond as had been expected. It is the present consensus that closely spaced, regular, prismatic roughness elements behave differently from sand grains.

Grass [8] used a bubble technique to measure the instantaneous velocity distributions in a water tunnel above a sand-grain roughness and described the turbulent structure near the wall. Wu [9] used a floating element balance to measure skin friction in an air tunnel and showed fully rough behavior with good agreement between the measured values and the Prandtl-Schlichting predictions. Most recently, Tsuji and Iida [10] showed that the velocity profiles observed above a rough wall could be reasonably well predicted by a modified mixing-length approach, maintaining a non-zero value at the wall. The effect of an abrupt change from a smooth to a rough surface has been investigated by Antonia and Luxton [11], who detailed the velocity distributions. Townes, et al. [12, 13] have studied the structure of the turbulence in flow through a rough pipe.

Much less has been done in the field of heat transfer than has been done for friction. One of the first systematic rough surface heat transfer experiments was carried out by Nunner [14]. His experiments, using air flowing through rough pipes, were used to establish a simple empirical relationship between the increase in Nusselt number due to roughness and the increase in the skin friction. Several important heat transfer studies followed, notably by Dipprey and Sabersky [15], Owen and Thomson [16], and Gowen and Smith [17]. Dipprey and Sabersky studied pipe flows with four different roughnesses, each tested with four fluids of different Prandtl numbers. They showed that the rough wall heat transfer varied with the Prandtl number even in the fully rough regime where the molecular viscosity effects seemed unimportant. Owen and Thomson developed the idea of a "sublayer Stanton number" to correlate rough pipe heat transfer data and to account for the Prandtl number dependence. Gowen and Smith extended the Dipprey and Sabersky pipe flow heat transfer study to higher Prandtl numbers and confirmed the effect on heat transfer. The present state of the art of rough wall heat transfer is well sum-

Nomenclature

B = blowing parameter, $v_o/(u_\infty \mathrm{St})$
$C_f/2$ = friction factor, $g_c \tau_o/\rho_\infty u_\infty^2$
c = specific heat at constant pressure
F = blowing fraction, v_o/u_∞
g_c = gravitational constant
G = free stream mass velocity, $u_\infty \rho_\infty$
k = a measure of roughness size
k_s = the size of sand grains of equivalent roughness
$\dot{m}''$ = mass flux at the wall, $\rho_o v_o$
Re_θ = momentum thickness Reynolds number, $u_\infty \theta/\nu$
Re_Δ = enthalpy thickness Reynolds number, $u_\infty \Delta/\nu$
Re_τ = roughness Reynolds number, $u_\tau k_s/\nu$
r = radius of spherical surface elements
St = Stanton number, h/Gc
T_w = wall temperature
T_t = temperature of transpired fluid before reaching the test plate from below
u_τ = shear velocity, $u_\infty \sqrt{C_f/2}$
u_∞ = free stream velocity
v_0 = blowing velocity at the surface
x = distance in the streamwise direction
Δ = enthalpy thickness
θ = momentum thickness
τ_0 = surface shear stress
ρ_∞ = free stream density
ν = kinematic viscosity

marized by Sood and Jonsson [18], Norris [19], and Lakshman and Jayatilleke [20], who have collected the previous works in comparative studies and also present experimental results of their own.

Prediction methods generally follow close behind data; and rough wall heat transfer is no exception. Integral prediction schemes which include roughness effects have been described by Dvorak [21, 22] and Chen [23]. Nestler [24] has proposed a scheme which related the increase in Stanton number due to roughness to the increase in skin friction due to roughness and other boundary layer parameters. A recent study by Lawn [25] describes predictions of both skin friction and heat transfer in an annulus with its center cylinder roughened. Finite difference turbulence boundary layer prediction schemes which include roughness effects have been described by Lumsdaine, et al. [26] and by McDonald and Fish [27]. Each of these efforts modified the mixing-length distribution to introduce roughness effects.

In all of this large base of work, little has been done on boundary layer heat transfer with roughness and nothing on the problem including blowing. The experimental objective of the present program was to measure the heat transfer characteristics of a k-type rough surface with and without blowing, over a wide range of conditions. Velocity profiles and friction factor data were sought to complement the heat transfer data and to facilitate development of a prediction program.

The Rough, Porous Surface

The surface selected for this study is shown in Fig. 1. It consists of a regular array of spherical elements, 1.25 mm in diameter, arranged so that the crests of the spheres are all on the same plane. This idealization of k-type roughness is attractive because it is reproducible, porous, deterministic, and requires only one geometric length scale to describe it. It is more regular than sand grains, being geometrically describable, and yet is more like a sand-grain surface than are the "machined element" rough surfaces such as are used in other deterministic studies. An impermeable counterpart of the present surface is included in the library of surfaces reported by Schlichting [33], thus a baseline of "expected behavior" is available.

It should be borne in mind that the regularity of size and arrangement of the elements may affect the interaction between the flow and the surface and, indeed, there seems to be evidence of this in the mixing length variations needed to predict the data from this surface.

The Experimental Apparatus. The apparatus constructed for these tests is a closed-loop wind tunnel using air at essentially ambient conditions as both the transpired and the free-stream fluid. The basic design of the roughness rig was taken from the existing heat and mass transfer facility at Stanford described by Moffat and Kays [28].

Description of the Apparatus. The important features of the roughness rig are shown schematically in Fig. 2. The main air supply is an 8.3 m^3/s fan connected through return ducting to a heat exchanger. This is followed by a screen box to reduce mainstream velocity fluctuations, and then by a nozzle which delivers air to a test section 0.1 m high and 0.5 m wide. The main stream is held at ambient temperature plus or minus ½°C to minimize heat transfer within the nozzle. This keeps the enthalpy thickness near zero at the beginning of the rough surface. From the test section, the mainstream air exits through a 14 to 1 multistage diffuser back into the fan. The mainstream velocity in the test section can be varied from 9 m/s to over 70 m/s by changing the drive pulley and belting on the supply fan. When the tunnel is operating without transpiration, a small charging blower at the diffuser exit is used to maintain ambient pressure in the test section. The transpiration air system is separate. It delivers air through a separate heat exchanger to a header box and then to the plates which make up the test section through individual lines, each with its own control and metering systems.

The test section itself consists of fixed side walls, an adjustable top, and the rough-surfaced test plate assembly. The test plate assembly contains 24 separate porous plates, which together form a 2.4 m long test section. Each plate has its own transpiration air supply, instrumentation, and embedded electrical heater for temperature control. A cross section of a typical plate in the test section is shown in Fig. 3. Each working plate is supported by thin strips of phenolic to thermally isolate it from its neighbors and from the support casting. A sintered bronze pre-plate distributes the transpiration air beneath the porous surface plate. Plate heater wires are cemented into grooves on the bottom of the working plates, using a high-viscosity epoxy to reduce bleeding of the cement into the porous plate. The grooves were formed by leaving out one row of balls at each line where a heater was desired.

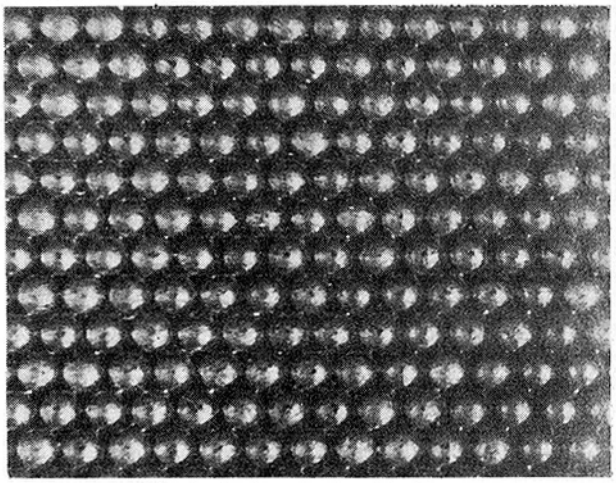

Fig. 1 Photograph of rough surface

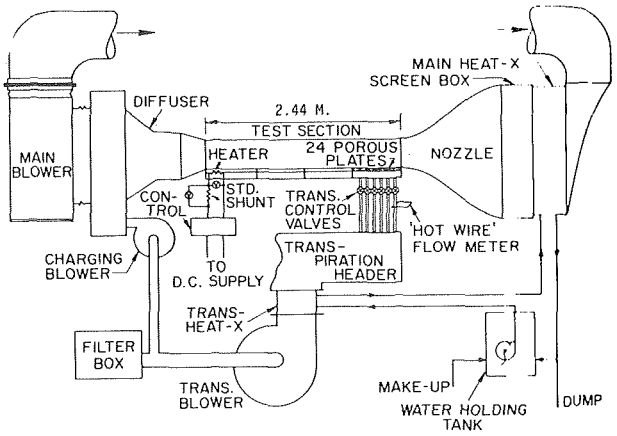

Fig. 2 Schematic of rough surface wind tunnel

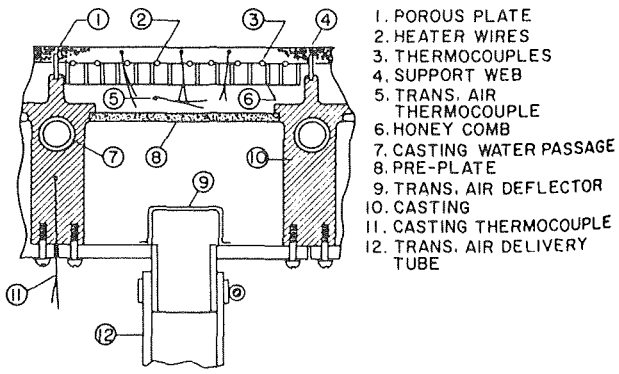

Fig. 3 Cross section of typical compartment

Plate temperatures are measured with five thermocouples embedded in each plate. A cross-shaped pattern is used to check the temperature distribution in the center of the plate. A sixth thermocouple is provided for each plate to measure the temperature of the transpiration air just before it enters the plate.

The plates are mounted in groups of six, one group in each of four aluminum castings. Alignment of the plates with each other and with the casting was assured by clamping the entire assembly to a surface plate during the assembly operation. The base castings have water passages for temperature control and the casting temperatures are monitored with thermocouples embedded in every second support web. These temperatures are used in correcting for conductive heat loss from the working plates.

The porous plates which form the test surface were fabricated by brazing together 1.25 mm dia O.F.H.C. copper balls, stacked in their most dense array. The final dimensions of each plate were 45.7 × 10.16 × 1.27 cm. The copper balls, 3.8 kg per plate, were supplied by a bearing manufacturer (dead soft copper ball bearings?). To provide a braze material, the balls were plated with 0.0127 mm of electroless nickel. They were then stacked, by hand, into rows inside copper molds in their most dense array and fired in an inert atmosphere furnace to just above the melting temperature of the plating. This brazed the pack into a uniformly porous plate. This method of fabrication, although tedious initially, provided a well-defined and uniformly porous plate. No subsequent machining was required.

Qualification Tests. The apparatus was tested in detail for reliability before being approved for use. The tests can be summarized as tests of the porous plates, tests of the mainstream condition, and energy-balance tests of the data-reduction program and instrumentation system.

Hot-wire anemometer surveys were made above the surface of the porous plate with only the transpiration flow present to check the uniformity of the plates. An unexpected phenomenon was found to exist in the flow just above the surface of the plate. Above a critical transpiration velocity, the flow formed a striated pattern of high and low-velocity regions. It was feared that these striations might affect the heat transfer by increasing the mixing in the boundary layer. This possibility was examined by a special series of tests in which Stanton number variations were recorded as a function of blowing (all other tunnel parameters being fixed) in a range of blowing values around the onset of the observed striations. No discernible discontinuity was found—the data passed smoothly through the "critical blowing velocity" without any anomaly. It was concluded that the striations were mainly a nuisance, interfering with the documentation of plate permeability. No evidence was found of any variations in plate permeability.

The mean velocity in the mainstream of the tunnel was found to be uniform within ±0.16 percent at 9 m/s and ±0.1 percent at 70 m/s. Free stream turbulence level was 0.4 percent at all velocities. Boundary layer momentum thicknesses were measured at five positions across the width of the tunnel, near the exit plane, and were uniform within 3 percent maximum to minimum.

Thermal qualification tests were conducted to evaluate heat losses from each test plate by conduction and radiation, and appropriate correction algorithms developed for each of the 24 plates. These correction algorithms allowed Stanton number values to be calculated by energy balance, from the power input and temperature data.

Any failure to close the energy balance under qualification conditions indicates a residual uncertainty in the values of Stanton number which will be recorded from that plate. Such a residual cannot be "subtracted out" unless one knows how the residual would vary as test conditions vary. When that is known, one has a correction algorithm and the residual disappears by definition. Residual uncertainty in the calculated value of Stanton number can be expressed in absolute units by normalizing the energy balance error using "average" conditions.

$$\Delta \mathrm{St} = \frac{\text{Plate Power} - \dot{m}''c(T_2 - T_t) - (\text{calculated losses})}{G_{\mathrm{typ}}c(T_w - T_\infty)_{\mathrm{typ}}} \quad (1)$$

Losses were calculated using analytical models for the processes involved, but using coefficients evaluated from separately conducted, special tests. After the correction algorithms had been developed, energy balance tests were conducted full-scale and repeated several times—in only four instances did even one plate out of the 24 show an energy balance closure error greater than 0.0001 Stanton number units, normalized with average conditions.

Experimental Results: No Blowing. All tests reported here were conducted with the free-stream temperature equal to the room temperature, and with the test plates uniform in temperature at a level 10–15°C above the free-stream temperature.

The first tests were hydrodynamic to establish the characteristics of the flow. Boundary layer momentum thickness measurements were made by integrating mean velocity profiles at several positions along the tunnel length. The momentum thicknesses were least-squares fit in log coordinates; and the derivative of this fit was used to find the friction factor. As a check, this procedure was first applied to the momentum thickness measurements by Simpson [29] and Andersen [30] on smooth plate boundary layers. Skin friction coefficients determined this way compared well with the results reported by the experimenters—in both cases within ±10 percent.

Mean velocity profiles for sand-grain roughened surfaces are described by Schlichting [33] in terms of the depression, Δu^+, of the log region for the rough profile beneath his recommended correlation for the smooth wall. The magnitude of Δu^+ can be used as a measure of the "equivalent sand-grain roughness" of a geometrically arbitrary surface. Measurements of Δu^+ from mean velocity profiles on the present apparatus yielded an equivalent sand-grain roughness size of between 0.60 and 0.63 times the diameter of the spheres comprising the surface. Schlichting quotes 0.625 for spherical elements. Thus the behavior of the mean profiles is as expected.

Schlichting defined the fully rough state as one in which the friction factor would be a function of "x" alone—not of free stream velocity. The data from the present apparatus showed this characteristic for all velocities above 9.6 m/s, to within the precision of the measurements of $C_f/2$.

Values of the friction factor from the present test lie about 20 percent below the correlation recommended by Schlichting for the fully rough state (that correlation presumedly being consistent with his tests of spherical elements).

No measurements were made of the characteristics of the turbulent structure. The regular, deterministic nature of the present surface may have had an effect on the structure but, if so, the effect seems not to have been pronounced, since most of the features of "sand-grain" surfaces have been reproduced.

Data presented in the present paper will be given in terms of momentum thickness (and enthalpy thickness) rather than x in deference to the current interest in local descriptors of boundary layer behavior. It can be shown that if $C_f/2$ is a function of x alone then, for a two-dimensional, zero-pressure gradient flow, it can be equally well described as a function of momentum thickness alone by means of the momentum integral equation. This choice seems more likely to be useful when blowing and acceleration are introduced into the problem.

Fig. 4 shows the measured momentum thicknesses versus distance along the test section for five different velocities. Also shown, for reference, is the expected behavior of a smooth plate for these same velocities. The measured momentum thickness distribution is independent of free stream velocity for all velocities above 9.6 m/s—the signature of a fully rough flow.

Introduction of the concept of a "virtual origin," as used in Fig. 4, has no effect on the validity of the conclusion that $d\theta/dx$ is a function of θ alone, since both are local descriptors—not dependent upon the value of x. At first glance, the fact that the data for 9.6 m/s lie beneath the other data seems to suggest transitionally rough behavior, since it appears that $C_f/2$ increased (at a fixed value of $x - x_o$) when U_∞ increased—behavior seen only in the regime of transitional roughness. No such conclusion can be firmly drawn without placing unjustifiable credence in the virtual origin assignment for the 9.6 m/s data. In terms of locally valid descriptors, the slope, $d\theta/dx$, of the 9.6 m/s data is lower for every value of θ, than for the data at higher velocities. While

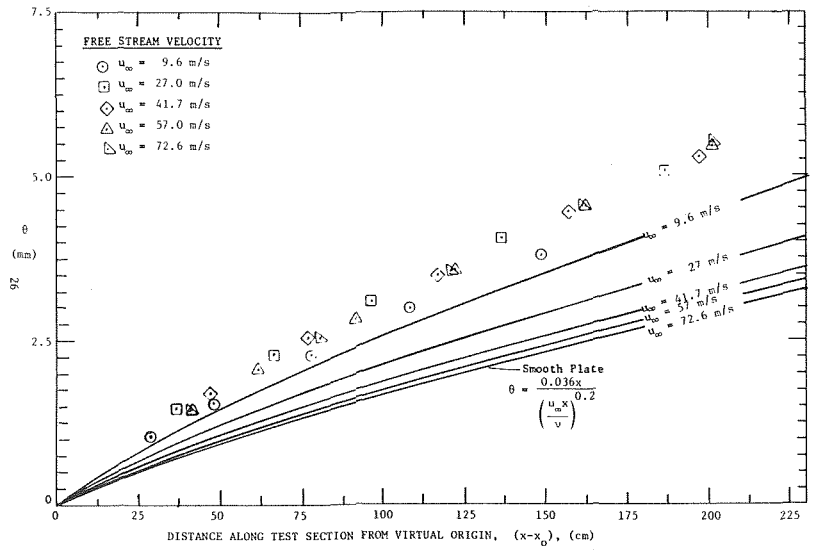

Fig. 4 Momentum thickness versus distance from boundary layer virtual origin

this is consistent with smooth-wall behavior, it is not proof. Without knowledge of the details of behavior of the present surface in the regime of transitional roughness, one cannot assign a definite meaning to the low values shown by the 9.6 m/s data.

Fig. 5 shows values of $C_f/2$ plotted against θ/r, the momentum thickness of the boundary layer made dimensionless using the radius of the balls. The data at the lowest velocity, 9.6 m/s, are somewhat low and there remains a suggestion of velocity dependence in the higher velocity data. But, considering the relatively unsophisticated method of determining $C_f/2$, the data strongly suggest that $C_f/2$ is a function of θ/r only and is independent of velocity.

The present apparatus was designed and developed primarily for heat transfer studies and the heat transfer data are believed to be more accurate than the friction factor data. No experimental baseline exists, however, against which to compare the rough surface heat transfer data even with no blowing. Comparisons of the present data with correlations recommended by Nunner [14] and Norris [19] showed good agreement even though both sources dealt with pipe flow data, not boundary layer data.

Success in representing the rough wall friction factor behavior in terms of the local value of momentum thickness suggested immediately that Stanton number be investigated in terms of enthalpy thickness, since for conditions of uniform free stream velocity and isothermal walls, the energy and momentum equations are similar.

Fig. 6 shows the Stanton number data for five different velocities plotted against enthalpy thickness. The data for 9.6, 27, and 41.7 m/s show the laminar/turbulent transition in differing degrees. This facet of the data is discussed in a later section of this paper. The present discussion centers around the turbulent region of the data. Of primary importance is the observation that the Stanton number data are well correlated on the basis of enthalpy thickness alone. The data for four of the five velocities are within ± three percent of the mean over the entire turbulent range, and even the 9.6 m/s data are less than ten percent off the mean, at worst. The fact that the data are compact in enthalpy thickness coordinates means that they would not be compact in any Reynolds number coordinate. From the heat transfer standpoint, the present data seem characteristic of fully rough behavior at all velocities tested including 9.6 m/s.

There is no sign of velocity dependence in the heat transfer data for velocities of 27 m/s and greater. Thus, one may infer that the slight dependence seen in the friction factor data may not have been real. The data for 9.6 m/s lie about seven percent above the mean near the transition; but as the boundary layer gets thicker, the data for 9.6 m/s converge to the mean, within three percent. The roughness Reynolds

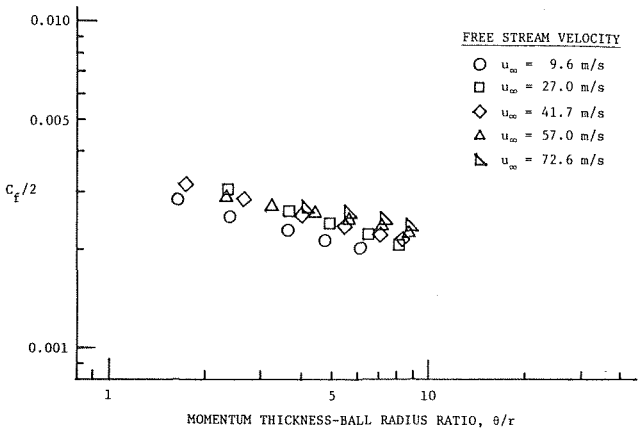

Fig. 5 Skin friction versus θ/r

number for the run at 9.6 m/s decreases from 29 to 23 as the boundary layer becomes thicker. If the overshoot of the 9.6 m/s data were due to an effect of transitional roughness, then the divergence should have increased, not decreased, as the roughness Reynolds number went down. The Stanton number data in the turbulent region are correlated well by the form

$$\mathrm{St} = 0.0034 \left(\frac{\Delta}{r}\right)^{-0.25} \tag{2}$$

The exponent in equation (2) was chosen, with some deference to tradition, to match the usual smooth-plate correlation exponent. In fact, the data show a tendency to level out as Δ/r increases, and no single exponent can accurately describe the entire curve.

The agreement between the 9.6 m/s data and those for higher velocities is surprising in view of the friction factor results. The roughness Reynolds number for the data at 9.6 m/s lies between 22 and 30, far below the usual boundary of fully rough behavior. The discovery that the Stanton number data correlated with the fully rough behavior, even at such low roughness Reynolds numbers, led to a special test aimed at creating a very low roughness Reynolds number. The free stream velocity was reduced to 5.6 m/s and the boundary layer thickness augmented by strong blowing ($F = 0.004$) through the first 0.6 m of the test section. Stanton number data taken in the last 1.8

m along the plate are compared with a reference set for 27 m/s in Fig. 7. Within 0.1 m after the blowing terminated, the Stanton number had risen to the unblown values corresponding to the existing boundary layer enthalpy thickness. It is noteworthy that the Stanton number data for the entire 1.8 m of unblown length on this run at 5.6 m/s lie exactly on the unblown data for 27 m/s. The roughness Reynolds number at the downstream end was only 14, as determined from hot-wire anemometer measurements of the shear stress near the surface, nearly "smooth" by the usual criteria. It seems clear that fully rough heat transfer behavior persists to much lower roughness Reynolds numbers, for the present surface geometry, than had been expected.

Experimental Results: Effects of Blowing. The identifying characteristic of the Stanton number for a fully rough turbulent boundary layer is its lack of dependence on free stream velocity. The present data clearly show this independence to be preserved, with blowing, down to values of the roughness Reynolds number at least as low as 17, and possibly preserved even lower, for the surface used in these tests. The evidence for this is found in Fig. 8.

Fig. 8 shows the Stanton number data with blowing up to $F = 0.008$ and with velocities from 9.6 to 74 m/s. To simplify the figure, only the turbulent portions are shown. The coherence is excellent, with data for all five velocities lying within ± five percent of the mean for each blowing level up to and including $F = 0.002$. The roughness Reynolds number was 17 for the last data point at $F = 0.002$ and 9.6 m/s, based on friction factors measured by means of the momentum integral equation with blowing (Healzer [31]).

No measurements were made of the friction factor for blowing greater than 0.002. Roughness Reynolds numbers for the conditions of heat transfer data of $F = 0.004$ and $F = 0.008$ can be estimated, however, by noting the relationship between $C_f/2$ and St in the present data. By either method, the lowest roughness Reynolds numbers for the data at 9.6 m/s were approximately 14 at $F = 0.004$, and 9 at $F = 0.008$. Examination of the Stanton number data for $F = 0.004$ shows a suggestion of velocity dependence. The "best fit" line through the 27 m/s data lies 20 percent below the line through the 9.6 m/s data, as would be predicted by a "smooth wall" correlation based on enthalpy thickness Reynolds number. To offset this, however, the data in Fig. 7 showed no sign of velocity dependence, again at a roughness Reynolds number of 14. The differences in measured Stanton numbers, in Fig. 8, for $F = 0.004$, are of the order of the uncertainties in energy balance closure (0.0001 Stanton number units). This suggests caution in assigning firm significance to the apparent velocity dependence. At $F = 0.008$, the data again show a 20 percent drop going from 9.6 to 27 m/s, as predicted by a smooth wall correlation. No other data were taken at roughness Reynolds number of nine.

There is strong evidence that the state of fully rough behavior persists to very low values of roughness Reynolds number for the surface used in these tests. The value of u_τ changes only slowly with distance along the test section; hence a line of constant velocity and constant F can be characterized reasonably well by a single "average" u_τ. There are larger differences in roughness Reynolds numbers between runs at the different velocities shown in Fig. 8 than there are along the individual lines; yet the data for all five velocities tested lie nicely along the same line. The roughness Reynolds numbers corresponding to the last Stanton number data point are in proportion to the free stream velocities—a 14-fold increase from 10 to 136 covering the range normally referred to as smooth up to fully rough, yet with

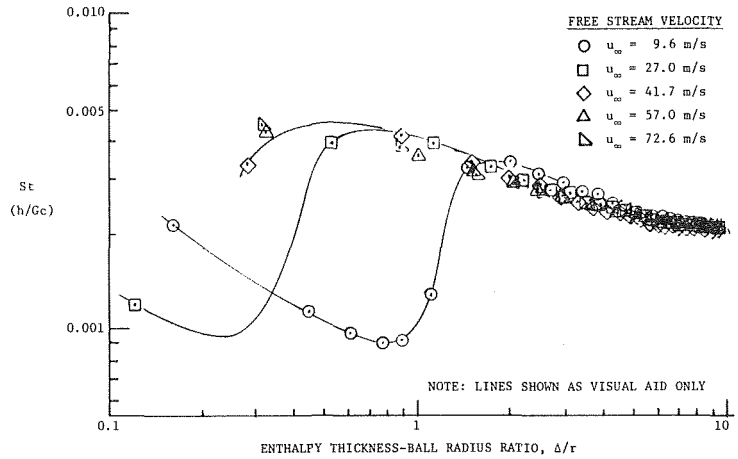

Fig. 6 Stanton number versus Δ/r

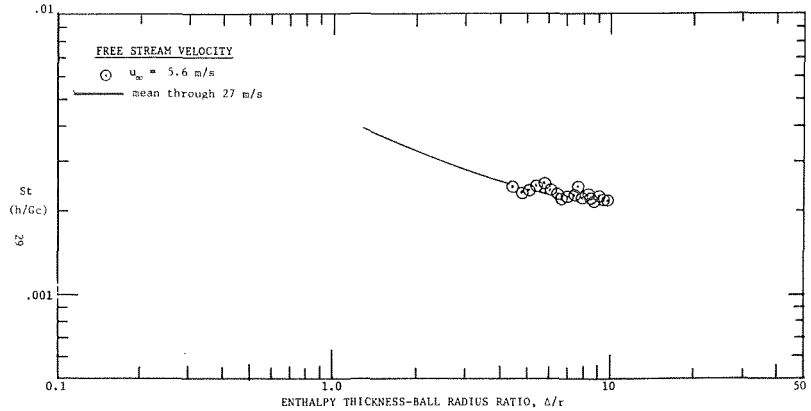

Fig. 7 Stanton number versus Δ/r at $u_\infty = 5.6$ m/s

the heat transfer behavior seemingly independent of velocity, at each value of F.

The effects of blowing on the Stanton number for a rough wall can be predicted by using an equation developed for smooth wall heat transfer (Kays and Moffat [32]) with only slight modifications. Blowing reduces the Stanton number of a turbulent boundary layer on a rough plate just as on a smooth plate; and the following equation predicts the effect within a few percent.

$$\left.\frac{\mathrm{St}}{\mathrm{St}_o}\right|_\Delta = \left[\frac{\ell n(1+B)}{B}\right]^{1.25}(1+B)^{0.25} \tag{3}$$

In this equation, St is the value of Stanton number with blowing, and St_o is the value without blowing, at the same enthalpy thickness, Δ. Note that the fully rough prediction is to be made at constant Δ, whereas the smooth plate prediction is done at constant Re_Δ. The agreement between predictions and data is good for all data lying more than 30 boundary layer thicknesses beyond the transition peak.

Experimental Results: The Effects of Roughness and Blowing on Transition. The unblown laminar boundary layers at 9.6 and 27 m/s began their transitions to turbulence at momentum thickness Reynolds numbers of about 400, as did most of the other data. The transition was marked by a hump in Stanton number which could be regarded either as an "overshoot" of the turbulent correlation or as a low Reynolds number effect. The peak value of Stanton number occurred at a momentum thickness Reynolds number of about 700 for both velocities.

Blowing through this rough surface does not drastically alter the onset of transition in momentum thickness Reynolds number coordinates, but it does advance the location markedly in x-Reynolds number.

Fig. 9 shows Stanton number data in the transition region for 9.6 m/s with five different values of blowing. Numbers near the onsets of transition are momentum thickness Reynolds number values.

Of primary importance is the fact that blowing through a rough

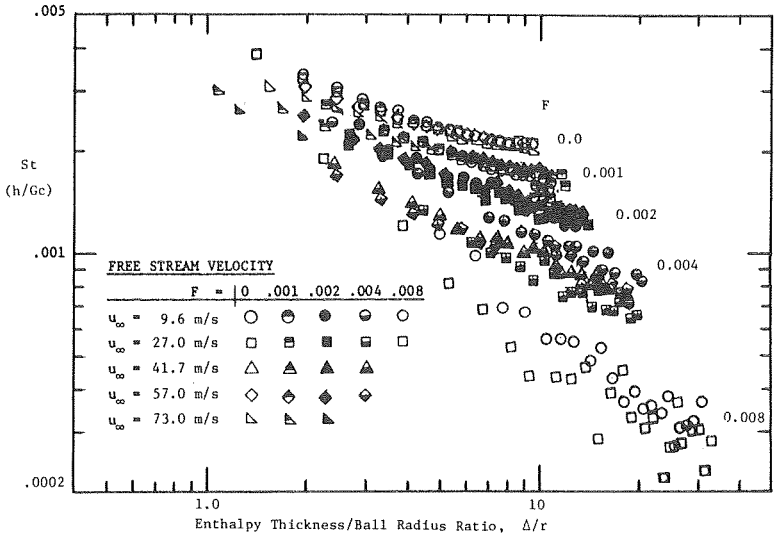

Fig. 8 Stanton number versus Δ/r at F = 0, .001, .002, .004, and .008

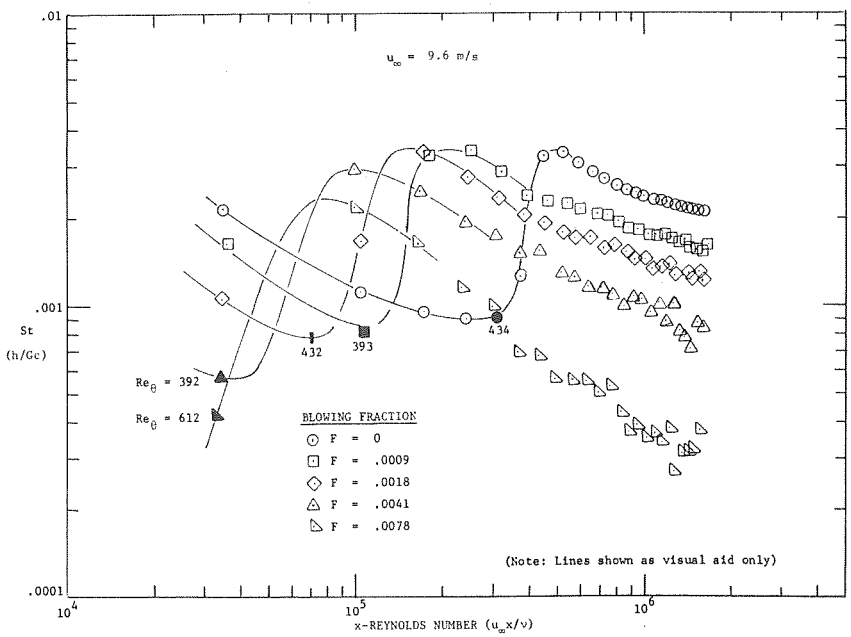

Fig. 9 Stanton numbers in the transition region with blowing, u_∞ = 9.6 m/s

surface does not make it more nearly smooth; in fact, blowing advances the transition in x-Reynolds number coordinates and exposes surface area to turbulent heat transfer which otherwise would have remained in the laminar regime. Turbulent heat transfer coefficients, even with strong blowing, are larger than the laminar, unblown values. As a result, the heat load to a structure could be increased drastically, instead of decreased, by premature blowing. The area enclosed between the curves for $F = 0.000$ and $F = 0.001$ represents the added heat load on a structure caused by blowing into an otherwise laminar region.

Roughness Reynolds Number. Heat transfer data from the present surface show fully rough behavior (i.e., Stanton number a function of enthalpy thickness only) at roughness Reynolds numbers as low as 14, far below the usually accepted threshold value of 70.

This may reflect the particular geometry used in these tests (regularly arranged spherical elements), although this geometry was included in the library of surfaces tested by Schlichting [33] and described by "equivalent sand grain" behavior. The region of transitionally rough behavior may be compressed when the roughness elements are of a single size and, in addition, the behavior of St and $C_f/2$ within the transitional region may be a function of the roughness geometry. For example, in $C_f/2$ versus Re_x coordinates, Schlichting [33] shows $C_f/2$ decreasing along the smooth line as Re_x increases, with a line of constant $C_f/2$ representing the fully rough state. For sand grain roughnesses, the values of $C_f/2$ in the transitional range are shown to dip below the fully rough asymptote and then approach it from below. For "commercially rough pipes," with less angular roughness elements, $C_f/2$ is shown to approach the fully rough asymptote from above, not from below, in the transitionally rough region. This latter characteristic has also been noted for d-type roughnesses.

If, in the present case, the transition range is compressed by the regularity, even if it were of the "approach from above" type of transition, it might well be impossible to detect transitionally rough behavior with measurements limited to ±0.0001 Stanton number units. The observed behavior might seem to be fully rough or fully smooth, but nothing in between. With the range of x-Reynolds numbers in the present test, the choices might seem to be, in fact, fully rough or laminar.

The local value of Stanton number is affected by the processes throughout the entire thickness of the boundary layer. As such, Stanton number is not the most critical test of the state of the boundary layer; it tends to average. It may well be that the low Reynolds number layers described here (Re_τ from 14 to 30) do, in fact, show some elements of transitionally rough behavior in their structures, but not in their Stanton number values.

There is another possible explanation for the apparent persistence of the fully rough behavior, not necessarily related to the specific geometry tested. If the threshold value of roughness Reynolds number is not constant but has even a slight dependence on boundary layer thickness, then a possibility exists that a boundary layer flow which is fully rough near the leading edge of the surface (or at transition) might remain fully rough as it progressed down the plate. Schlichting's [33] predictions of $C_f/2$ versus x-Reynolds number for sand-grain roughened surfaces show only a very slight convergence of the lines of constant roughness Reynolds number with the lines of constant $u_\infty k_s/\nu$. If these two lines were parallel, instead of weakly convergent, then a fully rough state would be persistent regardless of plate length. Alternatively, if the threshold value of roughness Reynolds number decreased as $\sqrt{C_f/2}$, then too, a fully rough state would be persistent. In the fully rough state, $C_f/2$ is a function of $\theta^{-.25}$, as shown by the present data. If the threshold value for the fully rough state varied with $\theta^{-.125}$, then the fully rough state would be persistent. Such a weak dependence could be detected only by tests covering a wide range of boundary layer thicknesses.

Friction Factor Correlation. The present data set offers much evidence of a fully rough state for heat transfer and shows an excellent correlation in terms of Stanton number versus enthalpy thickness. This suggests that a similar correlation can be offered for the friction factor behavior even though those data alone might not justify the form. It is proposed that:

$$\frac{C_f}{2} = 0.0036\left(\frac{\theta}{r}\right)^{-0.25}$$

Once again, the exponent was chosen to agree with a traditional value for this form. The present data set does not permit refinement of this equation because this general form was presumed to be valid in the data interpretation scheme used.

Conclusions

The conclusions which follow are based on experiments conducted on a permeable, rough surface of deterministic geometry in a variable-speed wind tunnel. The test conditions are summarized here to avoid tedious repetition of statements limiting the range of validity of the conclusions.

Turbulent boundary layer experiments were conducted on a rough, permeable plate made from spherical elements, each 1.25 mm in diameter, arranged in a most-dense array with the crests of the spheres coplanar. This plate was maintained at a uniform temperature, 10–15°C above the free stream. The thermal and velocity boundary layers originated very nearly at the upstream end of the rough surface. The test plate was 2.5 m long and 0.5 m wide. Two-dimensional behavior was verified. Stanton number values were calculated by energy balance means with corrections for heat loss. Skin friction values were calculated from measured values of the momentum thickness at sequential stations down the plate. Free stream velocity varied between 9.6 and 74 m/s. Transpiration values from $v_o/u_\infty = 0.0$ to 0.008 were tested, with v_o/u_∞ held uniform along the plate.

The conclusions which follow refer to this data set for the limits of their established validity but will likely allow some generalization.

- For the present surface, the Stanton number has been shown to be substantially independent of free stream velocity for values of the roughness Reynolds number as low as 14, without blowing. Stanton number values without blowing can be represented as a function of enthalpy thickness alone by the following equation, within ± seven percent, within the turbulent region:

$$\mathrm{St} = 0.0034\left(\frac{\Delta}{r}\right)^{-0.25}, \left(1 \le \frac{\Delta}{r} \le 10\right)$$

Friction factor data with no blowing, though displaying more scatter, can be represented by:

$$\frac{C_f}{2} = 0.0036\left(\frac{\theta}{r}\right)^{-0.25}, \left(1 \le \frac{\theta}{r} \le 10\right)$$

In these equations, r is the radius of the spheres comprising the surface, θ is the momentum thickness, and Δ the enthalpy thickness. For convenience, the forms were chosen to match traditional smooth-plate correlations.

- Blowing reduces the Stanton number and the roughness Reynolds number; but, again, for values of Re_τ greater than 14, Stanton number remains substantially independent of free stream velocity for the present surface. The data are reasonably well correlated by the following equation:

$$\left.\frac{\mathrm{St}}{\mathrm{St}_0}\right|_\Delta = \left[\frac{\ell n(1+B)}{B}\right]^{1.25}(1+B)^{0.25}$$

Here, St is the Stanton number with blowing and St_o is the Stanton number without blowing, evaluated at the same enthalpy thickness. The symbol B represents the blowing parameter, v_o/u_∞ St. This same form is used for smooth plate correlation but requires comparison at constant enthalpy thickness Reynolds number.

- The measured Stanton numbers are substantially independent of free-stream velocity for roughness Reynolds numbers as low as 14, both with and without blowing. This may be evidence that the fully rough state, for the present surface, persists to very low values of Re_τ. On the other hand, it may be that the boundary layer was in a transitionally rough state, but that the Stanton number was not measurably different from the fully rough value. The choice between these two cannot be made without studies of the turbulent structure within the boundary layers.

• Blowing through a rough, permeable surface advanced the x-location of transition; but the momentum thickness Reynolds number at which transition occurred was substantially the same as the expected value for a smooth plate with no blowing.

• Blowing through a rough surface which would otherwise have been covered by a laminar boundary layer can greatly increase the heat load on a structure by promoting an early transition. Turbulent boundary layer heat transfer on a rough surface, even with moderate blowing, is much higher than laminar heat transfer with no blowing.

Acknowledgments

The work reported here was supported by the Department of the Navy (Research Contract N00123-71-0-0372) and by the Office of Naval Research (Contract N00013-67-A-0112-0072). The authors wish to thank Dr. W. H. Thielbahr, of China Lake Naval Weapons Center, for his knowledgeable assistance in planning and evaluating the work, and Mr. James Patton, of the Office of Naval Research, for his continued support.

Access to the Data. The work summarized here is reported in detail in the dissertation of J. Healzer, Stanford University, June, 1974. Copies are available as Report HMT-18, through the office of the Thermosciences Division, Stanford University.

References

1 Nikuradse, J., "Strömungsgestze in rauhen Rohren," *VDI Forschungsheft*, No. 361, English translation, NACA TM, No. 1292, 1933.

2 Prandtl, L., and Schlichting, H., "Das Widerstandsgesetz rauher Platten," *Werft, Reederei, and Hafen*, 1934, p. 1.

3 von Karman, Th., "Turbulence and Skin Friction," *Jour. Aero. Sciences*, Vol. 1, No. 1, Jan., 1934.

4 Moore, W. L., "An Experimental Investigation of Boundary Layer Development along a Rough Surface," State University of Iowa, Ph.D. dissertation, Aug., 1951.

5 Liu, C. K., Kline, S. J., and Johnson, J. P., "An Experimental Study of Turbulent Boundary Layers on Rough Walls," Report MD-15, Dept. of Mechanical Engineering, Stanford University, July, 1966.

6 Perry, A. E., Schofield, W. H., and Joubert, P. H., "Rough Wall Turbulent Boundary Layers," *Journal of Fluid Mechanics*, Vol. 37, 1969, pp. 383–413.

7 Perry, A. E., and Joubert, P. H., "Rough Wall Boundary Layers in Adverse Pressure Gradients," *Journal of Fluid Mechanics*, Vol. 17, 1963, pp. 193–211.

8 Grass, A. J., "Structural Features of Turbulent Flow over Smooth and Rough Boundaries," *Journal of Fluid Mechanics*, Vol. 50, 1971, pp. 233–255.

9 Wu, J., "Flow in Turbulent Wall Layer over Uniform Roughness," ASME Paper 72-APM-U, to be published in *journal of Applied Mechanics*, TRANS. ASME.

10 Tsuji, Y., and Iida, S., "Velocity Distributions of Rough Wall Turbulent Boundary Layers Without Pressure Gradient," *Transactions of Japan Society of Aerospace Science*, Vol. 16, No. 31, 1973, pp. 60–70.

11 Antonio, R. A., and Luxton, R. T., "The Response of a Turbulent Boundary Layer to a Step Change in Surface Roughness. Part 1. Smooth to Rough," *Journal of Fluid Mechanics*, Vol. 48, Part 4, 1971, pp. 721–761.

12 Townes, H. W., Gow, J. L., Powe, R. E., and Weber, H., "Turbulent Flow in Smooth and Rough Pipes," *Journal of Basic Engineering*, TRANS. ASME, Series D, Vol. 94, No. 2, June 1972, pp. 353–362.

13 Townes, H. W., and Powe, R. E., "Turbulence Structure for Fully Developed Flow in Rough Pipes," *Journal of Fluids Engineering*, TRANS. ASME, Series I, Vol. 95, No. 2, pp. 255–261.

14 Nunner, W., "Heat Transfer and Pressure Drop in Rough Tubes," *VDI-Forschungsheft 455*, Series B, Vol. 22, 1956, pp. 5–39. English translation, A.E.R.E. Library, Transactions 786, 1958.

15 Dipprey, D. F., and Sabersky, R. H., "Heat and Momentum Transfer in Smooth and Rough Tubes at Various Prandtl Numbers," *International Journal of Heat and Mass Transfer*, Vol. 6, 1963, pp. 329–353.

16 Owen, P. R., and Thomson, W. R., "Heat Transfer across Rough Surfaces," *Journal of Fluid Mechanics*, Vol. 15, 1963, pp. 321–334.

17 Gowen, R. A., and Smith, J. W., "Turbulent Heat Transfer from Smooth and Rough Surfaces," *International Journal of Heat and Mass Transfer*, Vol. 11, 1968, pp. 1657–1673.

18 Sood, H. S., and Jonsson, V. K., "Some Correlations for Resistances to Heat and Momentum Transfer in the Viscous Sublayer at Rough Walls," JOURNAL OF HEAT TRANSFER, TRANS. ASME, Series C, Nov. 1969, pp. 488–499.

19 Norris, R. H., "Some Simple Approximate Heat Transfer Correlations for Turbulent Flow in Ducts with Surface Roughness," *Augmentation of Convective Heat and Mass Transfer*, published by the ASME, New York, 1971.

20 Lakshman, C., and Jayatilleke, V., "The Influence of Prandtl Number and Surface Roughness on the Resistance of the Laminar Sublayer to Momentum and Heat Transfer," *Progress in Heat and Mass Transfer*, Vol. 1, Pergamon Press, 1969, pp. 193–330.

21 Dvorak, F. A., "Calculation of Turbulent Boundary Layers on Rough Surfaces in Pressure Gradient," AIAA Journal, Vol. 7, No. 9, pp. 1752–1758, Sept. 1969.

22 Dvorak, F. A., "Calculations of Compressible Turbulent Boundary Layers with Roughness and Heat Transfer," AIAA Journal, Vol. 10, No. 11, pp. 1447–1451, Nov. 1973.

23 Chen, Karl K., "Compressible Turbulent Boundary Layer Heat Transfer to Rough Surfaces in Pressure Gradient," *AIAA Journal*, Vol. 10, No. 5, May, 1972, pp. 623–629.

24 Nestler, D. E., "Compressible Turbulent Boundary Layer Heat Transfer to Rough Surfaces," *AIAA Journal*, Vol. 9, No. 9, Sept. 1971.

25 Law, C. J., "The Use of an Eddy Viscosity Model to Predict the Heat Transfer and Pressure Drop Performance of Roughened Surfaces," *International Journal of Heat and Mass Transfer*, Vol. 17, 1974, pp. 421–428.

26 Lumsdaine, E., Wen, H. W., and King, F. K., "Influence of Surface Roughness and Mass Transfer on Boundary Layer and Friction Coefficient," *Developments in Mechanics*, Vol. 6, *Proceedings of the 12th Midwestern Mechanics Conference*, pp. 305–318.

27 McDonald, H., and Fish, R. W., "Practical Calculations of Transitional Boundary Layers," *International Journal of Heat and Mass Transfer*, Vol. 16, 1973, pp. 1729–1744.

28 Moffat, R. J., and Kays, W. M., "The Turbulent Boundary Layer on a Porous Plate: Experimental Heat Transfer with Uniform Blowing and Suction," *International Journal of Heat and Mass Transfer*, Vol. 11, 1968, pp. 1547–1566.

29 Simpson, R. L., Moffat, R. J., and Kays, W. M., "The Turbulent Boundary Layer on a Porous Plate: Experimental Skin Friction with Variable Injection and Suction," *International Journal of Heat and Mass Transfer*, Vol. 12, 1969, pp. 771–789.

30 Andersen, P. S., Kays, W. M., and Moffat, R. J., "The Turbulent Boundary Layer on a Porous Plate: An Experimental Study of the Fluid Mechanics for Adverse Free-Stream Pressure Gradients," Department of Mechanical Engineering, Stanford University, May, 1972.

31 Healzer, J. M., Moffat, R. J., and Kays, W. M., "The Turbulent Boundary Layer on a Rough Porous Plate: Experimental Heat Transfer with Uniform Blowing," Report HMT-18, Dept. of Mechanical Engineering, Stanford University, 1974.

32 Moffat, R. J., and Kays, W. M., "The Behavior of Transpired Turbulent Boundary Layers," in *Studies in Convection, Vol. 1: Theory, Measurement and Applications*, Academic Press, London, 1975. (Also published as HMT-20, Department of Mechanical Engineering, Stanford University, Apr. 1975.)

33 Schlichting, H., *Boundary Layer Theory* McGraw-Hill, New York, 6th ed., 1968, pp. 578–589, 610–620.

R. A. Seban
University of California at Berkeley, Berkeley, Calif.

A. Faghri
Arya Mehr University of Technology, Tehran, Iran

Wave Effects on the Transport to Falling Laminar Liquid Films

Existing data for the transport to falling liquid films are reviewed to show the effect of augmented transport by surface waves in the cases of heating of the film, absorption by the film from the surrounding gas, and evaporation from the film. It is shown that, while the effect of the waves can be partially rationalized, the nature of the waves themselves is not known exactly enough to provide a consistent specification for all of the available data.

Introduction

The effect of the waves that exist on the surface of a falling film in laminar motion has been demonstrated by numerous experiments for the cases of absorption of a gas, evaporation from the surface of the film, and of heating of the film by the wall. Here some of these results are reviewed to show the different effects of the waves on these three cases of transport. This is done by a comparison of the experimentally determined Nusselt number, $(h\delta/k)$, to the theoretical value for a Nusselt film of constant thickness, $\delta = 0.91\ (4\Gamma/\mu)^{1/3}(\nu^2/g)^{1/3}$, with velocity distribution $(u/u_m) = 3((y/\delta) - \frac{1}{2}(y/\delta)^2)$, these being the quantities associated with the Nusselt solution for the film. The theoretical dependence of Nusselt number on generalized length, $\xi = (x/\delta)(\alpha/u_m\delta)$ is available for absorption and for heating by the wall, but to obtain sufficient detail for values of ξ, for which the available eigenfunctions are insufficient, the relation was derived again by a numerical solution of the energy equation. This was done also for evaporation; this result has not so far been indicated.

Comparisons of the experimental and theoretical values of the transport should be supported by a specification of the nature of the waves, for it is through the interaction of the normal velocities produced by the waves and the distribution of the transported quantity that the additional transport arises. But this is complicated by the existence of an initial wave-free length, depending upon the way in which the film was formed by the liquid supply, and by a region of wave development which ostensibly culminates in a steady regime at a distance far enough down the height of the film. As an instance, Brauer [1][1] made measurements on water and mixtures of water and diethylene glycol at a distance of 1.3 m from the point of film initiation and found sinusoidal waves to begin at a Reynolds number, $(4\Gamma/\mu)$, of $1.2/(\mathrm{Ka})^{1/10}$, where $\mathrm{Ka} = (\nu^4\rho^3 g/\sigma^3)$ is the Kapitza number. The ratio of the crest height of the waves to the mean film thickness increased with Reynolds number to about twice this Reynolds number, then for higher Reynolds number this ratio remained the same up to a Reynolds number of $140/(\mathrm{Ka})^{1/10}$. Between these Reynolds numbers the waves were no longer sinusoidal but were distorted; above the higher Reynolds number were secondary, capillary waves on the surface. Throughout, up to $4\Gamma/\mu = 1600$, the average film thickness remains essentially that given by the Nusselt analysis. But in the range where the ratio of the crest height to the mean film thickness is almost constant, the wave frequency increases with Reynolds number to indicate a basis for a proportional increase in transport. Further, the realization of a steady wave regime at a given flow rate is still not defined. With water, Brauer [1] indicated, for one Reynolds number, a linear increase in the crest height with distance up to 1.8 m, so that a steady regime was not attained, and this development for other Reynolds and Kapitza numbers has apparently not yet been defined. Wilke [3] made similar measurements at a height of 2.2 m, with different Kapitza numbers, and his results for crest height do not check, relatively, with Brauer's measurements made at a height of 1.3 m.

Heating

Results for transport from the wall to the film have been obtained by Bays and McAdams' [2] and by Wilke [3] for heating, and by Iribarne, Gosman, and Spalding [4] for electrolytic mass transfer. Fig. 1 contains results for the heating case and shows the theoretical solution for the average Nusselt number for the cases of an isothermal wall and of constant heat flux at the wall; and for small values of ξ, the straight lines indicate the Leveque solution for these two cases.

The results of Bays and McAdams [2], obtained with film heights of 0.61 and 0.124 m for a Prandtl number of 1400 and with heights of 1.84 and 0.124 m for a Prandtl number of 51, are partially shown by representative points on Fig. 1. There they are slightly below the isothermal wall prediction, which condition should have been realized approximately by the steam heating used in these experiments. For $\xi > 0.10$, however, Bays' results, extending to $\xi = 0.5$, are in the region of the Leveque line extended and are unaccountably low. These anomalous results involve, partially, the greater film heights for both experiments, while the results for $\xi < 0.10$ are, in the main, associated with the smaller heights. For these runs, the Reynolds numbers ranged

[1] Numbers in brackets designate References at end of paper.

Contributed by the Heat Transfer Division for publication in the JOURNAL OF HEAT TRANSFER. Manuscript received by the Heat Transfer Division May 13, 1977.

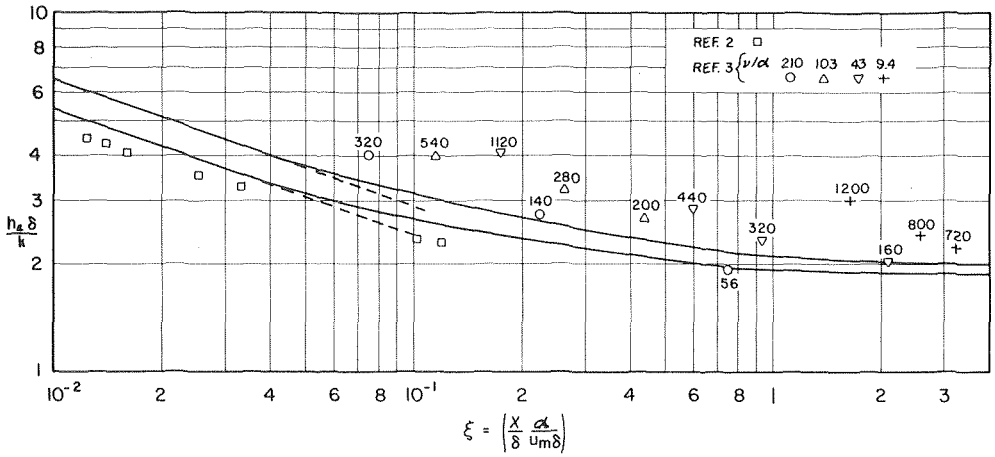

Fig. 1 Average Nusselt numbers for heating: The upper curve is the theoretical value for constant heat rate, the lower is for constant temperature. The tangent lines are the Leveque approximation. The Reynolds number for the data of reference [3] are indicated adjacent to the points

from 3.6 to 32 for the high Prandtl number and from 80 to 1000 for the low Prandtl number. The surface tension of the oils is unknown so that the Kapitza number cannot be evaluated, but in view of the high viscosity of the oils it is expected to be large, so that by the Brauer specification waves should have existed. In view of the subsequent results that are indicated for heating, it is possible that in this case the waves did not have sufficient time to develop.

Iribarne, et al. [4] obtained results for average Nusselt (Sherwood) numbers for Prandtl (Schmidt) numbers from 1400 to 18400, using a vertical tube with an "adiabatic" section 1 m long before the test section, which itself was relatively short. This, and the high Prandtl numbers, produced small values of ξ. At Pr = 1400, $(4\Gamma/\mu) = 400$, the value of ξ was 10^{-4}, so that, with a Prandtl number like that of Bays and McAdams', the value of ξ was much shorter. At a Prandtl number of 6350, lower Reynolds numbers were attained, yielding a maximum ξ of .0015. But in all cases the average Nusselt numbers agreed with the Leveque result, even though waves were observed. The implication is that there must have been a purely conduction layer near the wall through which the developing concentration layer could not penetrate to a significant degree, despite the fact that the Leveque penetration distance is $(y/\delta) = 0.14$ at $\xi = .0015$.

Wilke [3] obtained heating results for $9.4 < Pr < 210$ for a film on the outside of a 2.4 m high vertical tube, heated by water in counter flow on the inside of the tube. Local coefficients were evaluated by a measurement of the local mixed mean temperature along the film. These were averaged in the region in which the coefficient was nearly asymptotic, the results in an initial flow development length and part of the thermal entry length apparently not being considered. For sufficiently low Reynolds numbers, Wilke checked the predicted asymptotic value of 1.8 for the Nusselt number, but above a Reynolds number which he specified as $(4\Gamma/\mu)_u = 2460\ (\alpha/\nu)^{0.65}$, the asymptotic Nusselt number was higher, being given as

$$\frac{h_a\delta}{k} = .0292\left(\frac{4\Gamma}{\mu}\right)^{0.53}\left(\frac{\nu}{\alpha}\right)^{0.344} \tag{1}$$

This increase in the asymptotic value was implied as due to the waves, and the details of the initial local behavior were not given except in one case. It can be noted that for the fluids used by Wilke, the values of $(4\Gamma/\mu)_u$, which range from 20 to 143 for the Prandtl numbers from 210 to 9.4, can also be expressed as $(4\Gamma/\mu)_u = 9.6\ (\mathrm{Ka})^{-0.18}$. This indicates far greater spread of Reynolds number than implied by Brauer's formulation for the change in wave form and implies that it is the magnitude of an apparent diffusivity that is important. Chun [5] has noted that the Weber numbers, $(\sqrt{u^2\delta\rho/\sigma}) = (1/3.8)(\mathrm{Ka})^{1/6}(4\Gamma/\mu)^{5/6}$ are more nearly constant for this transition point, changing from 1.4 to 1 in the above range.

Fig. 1 contains the Nusselt numbers associated with $(4\Gamma/\mu) > (4\Gamma/\mu)_u$ plotted with ξ evaluated for the 2.4 m test length of the Wilke apparatus. The most conservative estimate of the undefined local behavior would be of a departure from the theoretical value of the local Nusselt number at the asymptotic value, and values of ξ for such a departure can be estimated by equating the local Nusselt number given by the Leveque solution to that specified by equation (1), to give:

$$\xi = \frac{18.5 \times 10^3}{\left(\frac{4\Gamma}{\mu}\right)^{1.59}\left(\frac{\nu}{\alpha}\right)^{1.03}} \tag{2}$$

For a given Reynolds number, this relation indicates smaller values of ξ as the Prandtl number increases. But this view is limited, for equation (2) implies a wave effect at very low ξ for very large Prandtl numbers when no such effect was found by Iribarne.

Absorption

Fig. 2 contains the theoretical result for the average Nusselt number for gas absorption and also contains a line for the penetration theory result (heat conduction into a semi-infinite medium) based on the interfacial velocity of the film.

Nomenclature

D = diffusion coefficient
g = gravity acceleration
h = local transfer coefficient; h_a, average coefficient
k = thermal conductivity
u_m = mean velocity in the film
x = distance along the film height
α = thermal diffusivity
Γ = film mass flow rate, per unit width
δ = film thickness
μ = dynamic viscosity
ν = kinetic viscosity
ρ = density
σ = surface tension

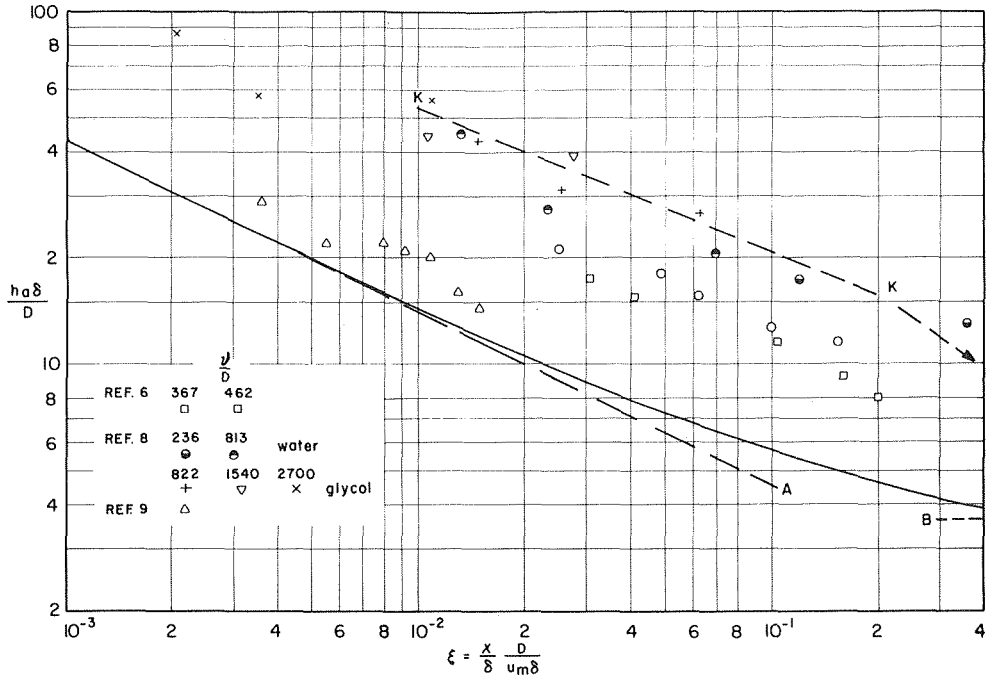

Fig. 2 Average Sherwood numbers for absorption: The curve is the theoretical solution with tangent A as the penetration solution and tangent B as the asymptotic value. Line K represents the Kamal results for Schmidt numbers from 280 to 813

Emmert and Pigford [6] used a water film 1.14 m high for the absorption of O_2 and CO_2 and obtained the average Sherwood numbers that are shown by points on the figure. They were the first to show definitely the augmentation by the waves, by adding a wetting agent to the water, whereby the results were reduced to values near the theoretical line, actually below it and near the penetration solution extended.

Kamei and Oishi [7] absorbed CO_2 into water film 2.50 m high, and by varying the water temperature obtained average Sherwood numbers for Schmidt numbers from 280 to 813. For Reynolds numbers from 200 to 2000, these results gave values of the Sherwood number that are represented fairly by the line shown on the figure. For $\xi > 0.20$, this line turns downward toward an intersection with the theoretical curve. There is no Schmidt number effect within the accuracy of the data, and in this respect the Emmert data also show little effect. But the results of Kamei are substantially higher than those of Emmert.

Chung and Mills [8] absorbed CO_2 into water and water-ethylene-glycol films 2.0 m high and obtained a small amount of data in the laminar range. Some of these are shown as points on Fig. 2, and they are reasonably close to the Kamei results.

All of the foregoing results are in the region of distorted waves as indicated by the Brauer specification, and even the break point for the Kamei data, which occurs at a Reynolds number of about 200, is not associated with the Brauer specification for the end of the sinusoidal wave regime, which is at $2.8/(\mathrm{Ka})^{1/10}$, or a Reynolds number of about 35. Rather, this magnitude is associated with the few data of Kamei that are near the theoretical line defined by the intersection of the extension of the line on Fig. 2.

The Weber numbers at the break in the Kamei curve are on the order of 0.35, and all data at lower values of ξ involve higher values of the Weber number. Chung's data is at Weber numbers greater than 1.8.

The Kamei data that are correlated fairly well by the line on Fig. 2 can also be correlated in terms of the Reynolds number, and the Prandtl number, because the film thickness δ that occurs in the abscissa of Fig. 2 depends upon the Reynolds number and upon the viscosity, and the Prandtl number depends primarily upon the viscosity. Thus these data can also be correlated by the relation

$$\frac{h_a\delta}{D} = 0.0368\left(\frac{4\Gamma}{\mu}\right)^{0.53}\left(\frac{\nu}{D}\right)^{0.475} \tag{3}$$

This serves also to specify fairly well the results of Chung and Mills. If it is estimated that the local transfer coefficient was fairly constant over the entire height of the film, then equation (3) might be expected to have some relation to equation (1), despite the difference in boundary conditions. The exponent of the Reynolds number is the same, but that of the Prandtl number differs. The exponent of the Prandtl number in equation (1) is of the order of expectation for a linear velocity distribution near the wall, and that of equation (3) is near the value of one-half that is associated with the relatively uniform velocity distribution in the outer part of the film.

The results of Emmert are not correlated by equation (3), but they demonstrate a similar Reynolds number dependence but are 20 percent lower for a Schmidt number of 462 and show a slightly greater Prandtl number dependence. The difference is possibly due to the shorter film height. In this respect, the assumption of truly laminar behavior initially, followed by an immediate transition to a constant coefficient, as given by equation (3), enables the specification of average Nusselt numbers like those found by Emmert by assuming a transition at about one-third of the film height. With such a length, for a film height of 2.5 m, like that of Kamei, there would be predicted results only 6 percent lower than given by equation (3). Thus the difference in the Kamei and the Emmert results might be ascribed to an initial wave-free region. But this interpretation is tenuous, and there is still no assurance that equation 3 defines truly asymptotic performance.

Fig. 2 also contains data obtained by Javdani [9] for the absorption of CO_2 into oil, the Reynolds number being on the order of 4 and the Schmidt number of the order of 90000, with nearly sinusoidal waves produced by the vibration of a wire in the film. The Weber number was about 0.25 and the local limit for sinusoidal waves is indicated by Brauer to be at a Reynolds number of 2.8.

Javdani indicated that a hydrodynamic solution for the sinusoidal waves could be used to produce an eddy diffusivity which varied approximately linearly with distance inward from the free surface, and

he used this in a penetration model of the transport equation to predict approximately the results for values of ξ on the order of those for which his results are shown in Fig. 2. The theory fails for larger values of ξ and tends to give too large a dependence of the transfer coefficient on the Reynolds number, but it is representative of what can be done theoretically when the waves are sinusoidal.

Evaporation

Chun [10] obtained data for evaporation from a film of water, heated at a constant rate, flowing down the outside of a tube 0.61 m high, with the initial 0.30 m being adiabatic, with local coefficients measured at 0.076, 0.13, 0.18, and 0.23 m along the heated length. The trend of the local values implied that those at the final stations were asymptotic and these were reported by Chun and Seban [5] and shown to agree with a "wavy laminar" prediction derived from condensation results. In Fig. 3 all of the local values are shown in comparison to the theoretical prediction for the local Nusselt numbers.

In some of these runs, the subcooling of the feed was as much as 4.8°C, but by a calculation of the heating of the liquid by condensation of the vapor according to the theoretical line of Fig. 2, the subcooling of the mean temperature at the position where heating began should have been about 0.20°C, and less if any augmentation due to waves is considered. But the theory indicates that the subcooling of the fluid at the wall would have been greater than that of the mean temperature, and could have been as much as 0.26°C. Thus the high initial Nusselt numbers may have been due to initial subcooling and, taking the ratio of the feed subcooling to the wall to saturation temperature difference at the asymptotic location, this ratio was on the order of unity for runs 1 through 4 and on the order of one-half for runs 5 and 6. The higher local coefficients in the thermal development region for the former runs indeed may have been due to liquid heating prior to evaporation, and the local coefficients for runs 5 and 6, which tend to depart from the theoretical line, with a subsequent almost constant values, at $\xi \approx 0.02$, may be the only ones that truly reveal the effect of the waves.

The inset of Fig. 3 is a plot of the asymptotic values of the Nusselt number, this being a repetition of the representation of reference [5] with more detail, and containing points at higher Reynolds number than does the basic figure. It shows the wavy laminar prediction and the turbulent correlation of [5] for Prandtl numbers of 2.9, 5.1, and 5.9, and by solid lines it shows, for Prandtl numbers of 2.9 and 5.1, the Wilke relation, equation (1), with its coefficient changed to 0.0255, to fit the few available data for a Prandtl number of 5.1 that apparently indicate a transition from the wavy laminar to the turbulent regime. The data that are shown for the other Prandtl numbers is too sparse to be definitive, but the point for a Prandtl number of 2.9, at a Reynolds number of 1450, does indicate a wavy laminar situation at just about the location at which the transition to the solid line is indicated. This intersection occurs at Weber numbers of 1.0 and 1.13 for the respective Prandtl numbers of 5.1 and 2.9, and the Reynolds numbers at the intersection are less than those indicated by $Re = 140\ Ka^{-1/10}$, so that the flow is implied to be within the regime of distorted waves. Further, the intersection of the solid lines with the turbulent predictions is in the region of a Reynolds number of 1600.

The values of the Nusselt number for Reynolds numbers truly in the wavy laminar regime correspond to situations for which Wilke measured asymptotic Nusselt numbers for heating that indicated no augmentation. Thus the augmented Nusselt numbers for evaporation imply an additional transport effect localized on the outer part of the film where the effect of the additional transport for heating would be small because of the reduced heat flux in the outer part of the film in the case of heating.

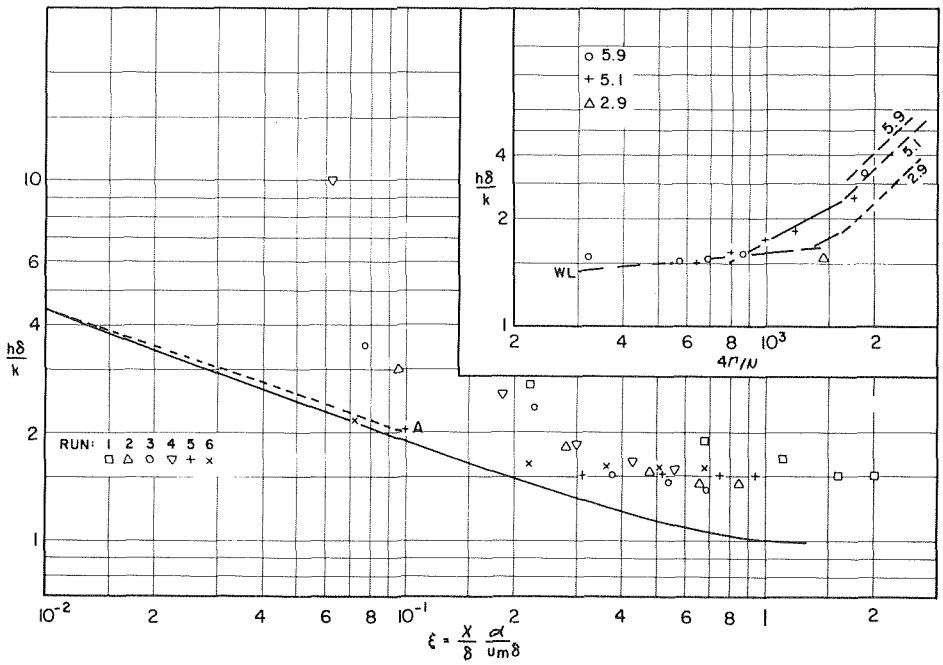

Fig. 3 Local Nusselt number for Evaporation: The curve is the theoretical solution for constant heat rate. A is the Leveque solution for heating with this wall condition. Values for the runs are

Run	1	2	3	4	5	6
Re	320	574	696	860	626	800
Pr	5.9	5.9	5.9	5.9	5.1	5.1
Feed Subcooling, °C	1.9	4.8	4.5	4.7	2.5	2.1

The inset shows the final Nusselt number, taken to be asymptotic, for the indicated Prandtl numbers. The dashed lines are the wavy laminar prediction and the turbulent correlation, reference [5], and the solid lines are equation (2), with a coefficient of 0.0255.

Summary

The augmentation of transfer to laminar falling films has been demonstrated by a review of existing results for the cases of heating, absorption, and evaporation, to indicate the relative effects which must be explained by the as yet unavailable models for such transport when the waves are distorted and are no longer of sinusoidal form. The comparisons of the data with expectation for a film of constant thickness are impeded, moreover, both by the lack of data for local Nusselt numbers and by the inability to characterize definitively the nature of the waves, particularly in regard to the height required for wave development. Nevertheless, the examination of the data for the three cases does provide some estimates about the nature of the transport.

With heating, when the Reynolds numbers are sufficiently large, there is apparently no effect of the waves until the temperature field penetrates a region near the wall in which there is little augmentation of the transport, but data for local Nusselt numbers are lacking for the precise definition of the end of this region. When it ends there is apparently a rapid change of the Nusselt number to a nearly constant, value which depends on the Reynolds number, because the transport augmentation, where it exists in the region away from the wall, is so dependent.

With absorption there is always an augmentation of the transport because the nature of the transport in the region near the wall is relatively unimportant in this case. For the regime of distorted waves, those of the existing results that have been obtained with large heights imply an early attainment of asymptotic Sherwood numbers which have a Reynolds number dependence like the asymptotic Nusselt numbers found for heating.

With evaporation, the one set of local Nusselt numbers that are available appear to be affected by initial subcooling, but they do indicate an ultimate asymptotic behavior. These asymptotic values are about 50 percent greater than for a film of constant thickness in the domain where the heating results reveal no wave effect, and in the domain where the heating results do record such an effect, the limited results for evaporation indicate an increased augmentation which then follows the trand of the results for heating.

References

1 Brauer, H., "Stromung and Warmenbergang bei Rieselfilmen," VDI Forschunsheft, 457, Dusseldorf 1956.

2 Bays, G., and McAdams, W., "Heat Transfer Coefficients in Falling Film Heaters: Streamline Flow," *Ind. Eng. Chemistry*, Vol. 29, 1973 pp. 1240–46.

3 Wilke, W., "Warmenbergang an Rieselfilme," VDI Forschunsheft 490, Dusseldorf 1962.

4 Iribarne, A., Gosman, A., and Spalding, D., "A Theoretical and Experimental Investigation of Diffusion Controlled Electrolytic Mass Transfer between a Falling Liquid Film and a Wall," *International Journal of Heat and Mass Transfer*, Vol. 10, 1967 pp. 1661 to 1676.

5 Chun, K., and Seban, R., "Heat Transfer to Evaporating Liquid Films" ASME, JOURNAL OF HEAT TRANSFER, Vol. 91, 1971, pp. 391–396.

6 Emmert, R., and Pigford, R., "A Study of Gas Absorption in Falling Liquid Films," *Chem. Eng. Progress*, Vol. 50, 1954, p. 87.

7 Kamei, S., and Oishi, J., "Mass and Heat Transfer in a Falling Liquid Film of Wetted Wall Tower," Mem. Fac. of Engineering, Kyoto Univ., Vol. 17 1956, pp. 277–289.

8 Chung, D., and Mills, A., "Experimental Study of Gas Absorption into Turbulent Falling Films of Water and Ethylene Glycol Mixtures, *International Journal of Heat and Mass Transfer*, Vol. 19, 1976, pp. 51–60.

9 Javdani, K., "Mass Transfer in Wavy Liquid Films," *Chemical Engineering Science*, Vol. 29, 1974, pp. 61–69.

10 Chun, K., "Evaporation From Thin Liquid Films," Ph.D. dissertation, University of California at Berkeley, 1969.

J. Szego
F. W. Schmidt

Mechanical Engineering Department,
The Pennsylvania State University,
University Park, Pa.

Transient Behavior of a Solid Sensible Heat Thermal Storage Exchanger

The transient response characteristics of a solid sensible heat storage exchanger which interacts with two energy transporting fluids are presented. The storage unit is composed of a series of large aspect ratio rectangular channels for the fluids, separated by slabs of the heat storage material. The hot and cold fluids flow in counter current fashion, in alternate channels so that each slab of storage material is in contact with both fluids. The entire system is considered to be initially in equilibrium at a uniform temperature, a step change in the inlet temperature of one of the fluids is imposed, and the thermal response of the unit is predicted until steady state conditions are reached. The response of the storage exchanger to an arbitrary time variation of one of the fluids' inlet temperature may be obtained using superposition.

Introduction

The design of an economically attractive industrial or commercial energy system requires that all possible sources of energy, including waste heat, be effectively utilized to satisfy the energy demands of the system. The matching of energy supplies and demands may impose difficulties because, frequently, they don't coincide timewise. Consequently, a more efficient utilization of the available energy is achieved if thermal energy storage capabilities are incorporated into the system.

The importance of energy storage was emphasized when the Energy Research and Development Administration (ERDA) requested that the National Research Council conduct a study on the potential of energy storage systems. The report [1][1] recognized the wide range of potential applications and indicated that the storage system selected would be dependent on its ability to respond to the demands required by the specific application.

The thermal energy is usually transported from one location to another by streams of liquids or gases. A heat exchanger can be used to enable the thermal energy to be transferred between the flowing streams. The amount of heat transfer, for steady-state operation, is easily calculated using conventional techniques described in basic heat transfer textbooks. Standard heat exchangers employ thin walls to separate the fluid streams, and thus have negligible heat storage capabilities. If it is desired, at certain periods, to remove a larger amount of the energy from the hot stream than required by the thermal load, or conversely, the thermal energy demand is higher than the energy being added to the system at that particular period of time, it becomes necessary to incorporate storage capabilities into the system. The easiest way to accomplish this is by replacing the usual thin metallic wall in the heat exchanger with a thick layer of a material having good heat storage characteristics. A sketch of a typical sensible heat storage exchanger is given in Fig. 1(a). The outlet temperatures of both fluid streams will be time dependent, and in many applications the inlet temperatures of one or both fluids may vary with time.

The transient response of heat exchangers has been the topic of a number of papers. A summary of these studies has been presented by Schmidt [2]. Most investigators were mainly concerned with the response of the energy transporting fluids, and the heat capacity of the separating wall was either neglected or serious restrictions were imposed when accounting for its contribution to the response of the heat exchanger.

Studies that have taken the heat capacity of the wall into consideration are described by Cima and London [3] and London, et al. [4]. The heat exchanger's walls were subdivided in the direction of flow. Each subdivision was considered to be at a uniform temperature and to have a heat capacity equal to its mass times the specific heat of the material. The conductive resistance to the transfer of heat offered by the material was divided in half and each half was added to the resistance offered by the convective film at the exchanger's surfaces. Axial conduction in the metal was neglected. Solutions obtained using an electrical analog system were presented for the transient response of a direct transfer counterflow regenerator for gas turbine applications.

A recent study by Schmidt and Szego [5] used a finite difference technique to predict the transient response of a two fluid heat storage exchanger for a solar energy system; but no general analysis of the

[1] Numbers in brackets designate References at end of paper.

Contributed by the Heat Transfer Division for publication in the JOURNAL OF HEAT TRANSFER. Manuscript received by the Heat Transfer Division April 7, 1977.

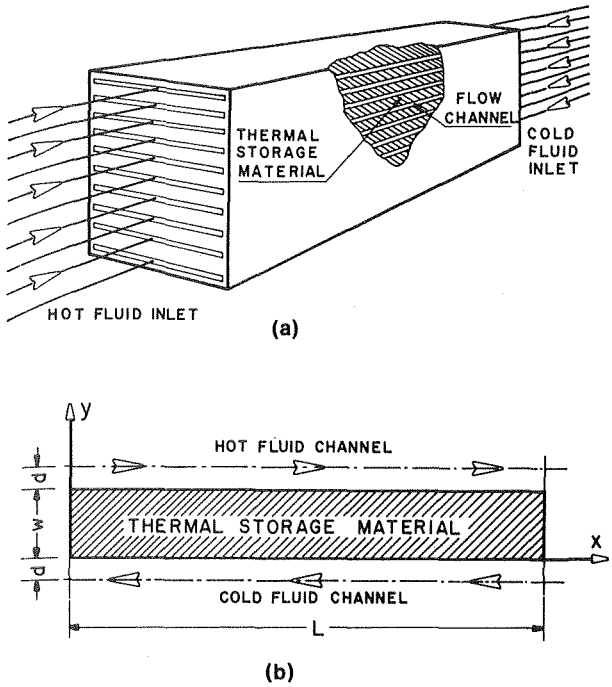

Fig. 1 Heat storage exchanger; (*a*) schematic of typical heat storage exchanger unit (*b*) cross section considered in the analysis

response characteristics of these units was reported. The present study will utilize these techniques to determine the response of a counter-flow heat storage exchanger unit under a variety of operating conditions.

Analysis of the Response of the Heat Storage Exchanger

The heat storage exchanger system to be considered is composed of a series of large aspect ratio rectangular cross-sectional channels for the energy transporting fluids. The hot and cold fluids flow in a counter current fashion, in alternate channels, so that each slab of the storage material is in contact with both fluids (Fig. 1(a)). Planes of symmetry were assumed to exist at the mid-locations of the flow channels, restricting the analysis to the section shown in Fig. 1(b).

The following idealizations were used in establishing the mathematical model describing the physical system under consideration:

(a) constant fluid and material properties
(b) uniform convective film coefficients
(c) two-dimensional conduction within the storage material
(d) constant fluid mean velocities
(e) uniform initial temperature distribution in the storage material
(f) process initiated by a step change in the inlet temperature of the hot fluid.

Based upon these assumptions, the differential equations relating the temperatures in the system are the two-dimensional transient heat conduction equation for the storage material, coupled to the one-dimensional conservation of energy equations for the energy transporting fluids. The resulting equations express the temperatures in the fluids and the storage material as a function of the two spacial coordinates, x and y, and time, θ:

cold fluid

$$\rho_c C_c A_c \left[\frac{\partial t_c}{\partial \theta} - v_c \frac{\partial t_c}{\partial x}\right] = h_c P_c (t_{wc} - t_c) \tag{1}$$

storage material

$$\frac{1}{\alpha}\frac{\partial t_m}{\partial \theta} = \frac{\partial^2 t_m}{\partial x^2} + \frac{\partial^2 t_m}{\partial y^2} \tag{2}$$

and hot fluid

$$\rho_h C_h A_h \left[\frac{\partial t_h}{\partial \theta} + v_h \frac{\partial t_h}{\partial x}\right] = h_h P_h (t_{wh} - t_h) \tag{3}$$

The associated initial and boundary conditions are:

$$\theta = 0 \quad t_m = t_c = t_h = t_o$$

$$\theta > 0 \quad x = 0 \quad t_h = t_{hi} \quad \frac{\partial t_m}{\partial x} = 0 \text{ for } 0 < y < w$$

$$x = \mathrm{L} \quad t_c = t_{ci} \quad \frac{\partial t_m}{\partial x} = 0 \quad \text{for } 0 < y < w$$

$$y = 0 \quad k\frac{\partial t_m}{\partial y} = h_c(t_m - t_c) \quad \text{for } 0 \le x \le L$$

$$\text{and } y = \mathrm{w} \qquad k\frac{\partial \mathrm{t_m}}{\partial \mathrm{y}} = -\mathrm{h_h}(\mathrm{t_m} - \mathrm{t_h}) \quad \text{for } 0 \le x \le L.$$

For greater generality the equations were nondimensionalized by introducing the following dimensionless parameters:

$$\text{Biot numbers:} \quad \mathrm{Bi}_h \equiv \frac{h_h w}{k}, \quad \mathrm{Bi}_c \equiv \frac{h_c w}{k};$$

Nomenclature

A = flow cross-sectional area
C = specific heat at constant pressure
d = semi-width of flow channels
E = fluid heat capacity
h = convective film coefficient
k = thermal conductivity of storage material
K = constant defined in equation (10)
L = length of unit
$\dot{m}$ = mass rate of flow
P = heated perimeter of flow channel
Q = amount of heat stored
R = convective resistance ratio
S = heat transfer surface area
t = temperature
$\bar{t}_w$ = mean temperature of the wall averaged over its thickness
T = dimensionless temperature
$\overline{T}_m$ = mean storage material dimensionless temperature averaged over its volume
U = overall heat transfer coefficient
v = fluid velocity
V = volume of storage material
w = thickness of storage material
x = axial coordinate
y = transverse coordinate
ρ = density
θ = time

θ_d = dwell time = $\dfrac{L}{v}$

α = thermal diffusivity of storage material

Subscripts

c = cold fluid
ci = cold fluid entering
co = cold fluid leaving
h = hot fluid
hi = hot fluid entering
ho = hot fluid leaving
m = storage material
o = initial condition
wc = wall temperature cold fluid side
wh = wall temperature hot fluid side

Superscript

ss = steady state condition

Fourier number: $\mathrm{Fo} \equiv \dfrac{\alpha\theta}{w^2}$;

dimensionless temperature: $T \equiv \dfrac{t - t_{ci}}{t_{hi} - t_{ci}}$;

dimensionless flow length: $X \equiv \dfrac{x}{L}$;

dimensionless transverse coordinate: $Y \equiv \dfrac{y}{w}$

thickness/length ratio: $V^+ \equiv \dfrac{w}{L}$;

capacity rate ratio for fluids: $C^+ \equiv \dfrac{\rho_c v_c A_c C_c}{\rho_h v_h A_h C_h} = \dfrac{\dot{m}_c C_c}{\dot{m}_h C_h} = \dfrac{E_c}{E_h}$;

convective resistance ratio: $R^+ \equiv \dfrac{\dfrac{1}{P_c L h_c}}{\dfrac{1}{P_h L h_h}} = \dfrac{\mathrm{Bi}_h P_h}{\mathrm{Bi}_c P_c} = \dfrac{\mathrm{Bi}_h}{\mathrm{Bi}_c}$;

and $G_c{}^+ = \dfrac{P_c k}{E_c}$, $G_h{}^+ = \dfrac{P_h k}{E_h}$.

The equations for the fluids become:

$$-\frac{\alpha}{w v_c V^{+2}}\frac{\partial T_c}{\partial Fo} + \frac{\partial T_c}{\partial X} - \frac{G_c{}^+ \mathrm{Bi}_c}{V^+}[T_c - T_{wc}] = 0 \tag{4}$$

and

$$\frac{\alpha}{w v_h V^{+2}}\frac{\partial T_h}{\partial Fo} + \frac{\partial T_h}{\partial X} + \frac{G_c{}^+ \mathrm{Bi}_c R^+ C^+}{V^+}[T_h - T_{wh}] = 0. \tag{5}$$

From an order of magnitude analysis to evaluate the importance of each term in the above equations (4) and (5), it was concluded that a negligible error is introduced if the transient term in the fluid equation is abandoned. This assumption, which implies neglecting the heat capacities of the fluids, was previously discussed in [6] and can be further substantiated by the findings of Cima and London [3].

The complete set of governing equations in nondimensional form becomes:

cold fluid

$$\frac{\partial T_c}{\partial X} - \frac{G_c{}^+ \mathrm{Bi}_c}{V^+}[T_c - T_{wc}] = 0, \tag{6}$$

storage material

$$V^{+2}\frac{\partial^2 T_m}{\partial X^2} + \frac{\partial^2 T_m}{\partial Y^2} = \frac{\partial T_m}{\partial \mathrm{Fo}}, \text{ and} \tag{7}$$

hot fluid

$$\frac{\partial T_h}{\partial X} + \frac{G_c{}^+ \mathrm{Bi}_c R^+ C^+}{V^+}[T_h - T_{wh}] = 0 \tag{8}$$

with the initial condition

$$\mathrm{Fo} = 0, \quad T_m = T_c = T_h = T_0$$

and the boundary conditions

$$X = 0 \quad T_h = T_{hi} = 1 \quad \frac{\partial T_m}{\partial X} = 0 \quad \text{for } 0 < Y < 1$$

$$X = 1 \quad T_c = t_{ci} = 0 \quad \frac{\partial \mathrm{T_m}}{\partial \mathrm{X}} = 0 \quad \text{for } 0 < Y < 1$$

$$Y = 0 \quad \frac{\partial T_m}{\partial Y} = \mathrm{Bi}_c(T_{wc} - T_c) \quad \text{for } 0 \le X \le 1$$

and

$$Y = 1 \quad \frac{\partial T_m}{\partial Y} = -\mathrm{Bi}_h(T_{wh} - T_h) \quad \text{for } 0 \le X \le 1.$$

Equations (6), (7), and (8) form a coupled set and must therefore be solved simultaneously. This is accomplished by means of a numerical solution using a digital computer. The thermal storage material is subdivided in the X and Y directions, establishing a grid pattern. Equation (7) is rewritten in finite-difference form, using backward differences for the time derivatives and central differences for the spacial derivatives. Third order orthogonal polynomials are fitted by least squares to T_{wh} and T_{wc} along the flow channels. These polynominals are then substituted into equations (6) and (8) allowing for an exact solution of the resulting equations for the fluids. The conduction equation is solved by finite difference techniques, but an iterative procedure is needed to match equations and boundary conditions. A detailed outline of this numerical solution is presented in the appendix to [6]. The reader must keep in mind that in the present investigation two fluid equations must be solved rather than the one equation used in [6] for the single-fluid case; the general procedure is, however, essentially the same.

Discussion of Results and Conclusions

Transient Response Parameters. The transient response of a thermal storage exchanger, initially in equilibrium at a uniform temperature, to a step change in the inlet temperature of one of the fluids will be discussed. Results will be presented for the case of a step change in the inlet temperature of the hot fluid, although they are equally valid if the step change in inlet temperature occurred in the cold fluid. This would require the replacement of "heat stored" by "heat retrieved," "hot" for "cold", and vice-versa in the final results. Three new time dependent dimensionless parameters are introduced as follows:

$$\epsilon_h = \frac{\left[\begin{array}{c}\text{rate of heat transfer from hot}\\ \text{fluid at time } \theta\end{array}\right]}{\left[\begin{array}{c}\text{heat transfer rate from hot}\\ \text{fluid at steady state}\end{array}\right]} = \frac{E_h[t_{hi} - t_{ho}]}{E_h[t_{hi} - t_{ho}{}^{ss}]}$$

$$\epsilon_c = \frac{\left[\begin{array}{c}\text{rate of heat transfer from cold}\\ \text{fluid at time } \theta\end{array}\right]}{\left[\begin{array}{c}\text{heat transfer rate from cold}\\ \text{fluid at steady state}\end{array}\right]} = \frac{E_c[t_{ci} - t_{co}]}{E_c[t_{ci} - t_{co}{}^{ss}]}$$

and

$$Q^+ = \frac{[\text{amount of heat stored at time } \theta]}{[\text{amount of heat stored at steady state}]} = \frac{Q}{Q^{ss}} = \frac{\overline{T}_m}{\overline{T}_m{}^{ss}}.$$

This set of dependent parameters was formulated since it has simple physical significance and is convenient for graphical presentation of the transient behavior of the heat storage exchanger. The basic analysis was carried out with the complete set of governing equations, equations (6-8), and associated boundary conditions. The results obtained indicated that for the cases of practical interest, the effects of longitudinal heat conduction are negligible and the first term on the left hand side of equation (7) can be neglected. Thus it is possible to combine G^+ and V^+ into one single parameter, namely G^+/V^+, since these parameters appear only as the indicated ratio. The steady-state quantities that are used in the definitions of ϵ_h, ϵ_c, and Q^+ can be obtained exactly, as shown in the Appendix. For all the cases under consideration in this study the intial uniform temperature of the storage material is equal to the incoming temperature of the cold fluid, $T_o = T_{ci} = 0$, since the step change is imposed on the inlet temperature of the hot stream alone.

Performing an overall energy balance for the entire system without heat losses to the surroundings gives:

$$\frac{dQ}{d\theta} = E_h(t_{hi} - t_{ho}) + E_c(t_{ci} - t_{co}) \tag{9}$$

Rearranging this equation and introducing the previously defined parameters yield a simple expression relating the three dependent variables:

$$K\frac{dQ^+}{dFo} = \epsilon_h - \epsilon_c \tag{10}$$

where

$$K = \left(\frac{G^+}{V^+}\right)_c C^+ \left(\frac{\overline{T}_m{}^{ss}}{1 - T_{ho}{}^{ss}}\right),$$

$\overline{T}_m{}^{ss}$ and $T_{ho}{}^{ss}$ are given by equations (A9) and (A7). The dependent variables ϵ_h, ϵ_c, and Q^+ are each functions of the five independent variables Bi_c, $(G^+/V^+)_c$, C^+, R^+ and Fo.

In order to allow a reasonably compact graphical presentation of the results, an additional restriction became necessary. It was assumed that both the energy transporting fluids have equal physical properties and that the flow channels have the same dimensions. Under these conditions and considering turbulent flow, the convective resistance ratio reduces to the ratio of the mean velocities of the two fluids raised to some exponent. The exponent commonly employed by most correlations is 0.8, and the relation obtained is

$$R^+ = (C^+)^{-0.8} \tag{11}$$

Therefore only four independent dimensionless parameters are required.

A more convenient way of presenting results was obtained by plotting ϵ_h, ϵ_c and Q^+ against $Fo/(G^+/V^+)_{max}$. The maximum G^+/V^+ was selected for the presentation of the results, since it involves the minimum fluid heat capacity. In addition, the commonly used steady-state parameter NTU proved to be useful as one of the variables. The final results show ϵ_h, ϵ_c and Q^+ as functions of Bi_c, C^+, NTU, $Fo/(G^+/V^+)_{max}$. The following relationships between the variables hold:

$$\mathrm{Bi}_h = \frac{\mathrm{Bi}_c}{C^{+0.8}}, \tag{12}$$

$$\mathrm{NTU} = \frac{SU}{E_{min}} = \left(\frac{G^+}{V^+}\right)_{max}\left[\frac{1}{\mathrm{Bi}_c} + \frac{1}{\mathrm{Bi}_h} + 1\right]^{-1} \tag{13}$$

$$\text{and}\quad \frac{Fo}{(G^+/V^+)_{max}} = \frac{E_{min}}{(\rho CV)_m}\theta. \tag{14}$$

where k has cancelled out in equation (14). It is noteworthy that the latter two variables have already been employed by Cima and London [3] to correlate their results.

Results—Step Change in One Inlet Fluid Temperature. From the definitions of ϵ_c and Q^+ it is evident that both quantities range from a magnitude of zero at the beginning of the process, $\theta = 0$, to a value of unity as steady state operation is approached. Moreover, ϵ_h starting from some value larger than one will also approach unity at steady state. The mathematical model described previously in the analysis does not account for the events which take place from the sudden increase of the inlet temperature of the hot fluid to the moment when the first heated particles leave the system. However, this time interval is typically very small compared to characteristic time for the overall process. Having in mind the specified initial conditions, it is apparent that the disturbance will be felt at the outlet of the hot stream exactly a dwell time, θ_d, later, and that the first fluid particles will have viewed a constant temperature wall as they moved through the unit. Solving equation (8) with a constant wall temperature, $T_{wh} = T_o = 0$, gives:

$$T_{ho} = \exp\left[-\mathrm{Bi}_c\left(\frac{G^+}{V^+}\right)_c C^{+0.2}\right] \text{ for } \theta = \theta_d, \tag{15}$$

while $T_{ho} = 0$ for $0 < \theta < \theta_d$. Thus it follows that an abrupt change in the hot fluid outlet temperature will occur. A listing of T_{ho} at $\theta = \theta_d$ is presented in Table 1. Fig. 2 shows a typical plot of the results to illustrate the foregoing conclusions. The area bounded by the curves for ϵ_h and ϵ_c, and $Fo/(G^+/V^+)_{max}$ varying from zero and some speci-

C^+	NTU	Bi_c	T_{co}^{ss}	T_{ho}^{ss}	$\overline{T}_m^{ss}$	$T_{ho}(\theta_d)$
0.1	0.1	0.1	0.095	0.990	0.838	0.924
		1.0			0.706	0.872
		10.			0.557	0.797
	1.0	0.1	0.619	0.938	0.871	0.452
		1.0			0.785	0.256
		10.			0.688	0.001
	3.0	0.1	0.939	0.906	0.920	0.092
		1.0			0.876	0.017
		10.			0.827	0.000
1.0	0.1	0.1	0.091	0.909		0.810
		1.0				0.741
		10.				0.301
		100.				0.000
	1.0	0.1	0.500	0.500	0.5	0.122
		1.0				0.050
		10.				0.000
		100.				0.000
	3.0	0.1	0.750	0.250		0.002
		1.0				0.000
		10.				0.000
		100.				0.000
10.	0.1	0.1	0.0095	0.905	0.139	0.889
		1.0			0.175	0.876
		10.			0.333	0.760
		100.			0.455	0.182
	1.0	0.1	0.062	0.381	0.114	0.308
		1.0			0.138	0.267
		10.			0.241	0.064
		100.			0.320	0.000
	3.0	0.1	0.094	0.061	0.072	0.029
		1.0			0.084	0.019
		10.			0.136	0.000
		100.			0.177	0.000

Table 1 Operating characteristics of heat storage exchangers

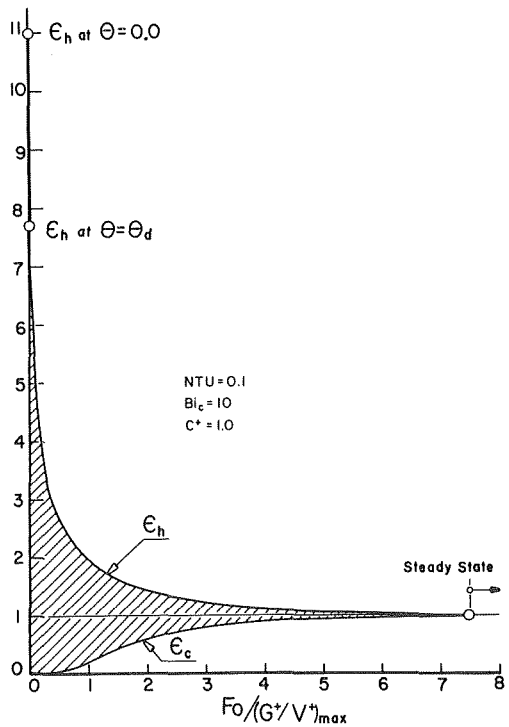

Fig. 2 Typical representation of the results

fied value is given by $KQ^+/(G^+/V^+)_{max}$, as can be inferred by integrating equation (10). Since at steady state conditions Q^+ approaches the value of one, the shaded area in Fig. 2 is equal to $K/(G^+/V^+)_{max}$.

Figs. 3-10 represent the final results of the present investigation. Fig. 3 shows ϵ_h and ϵ_c for $C^+ = 1.0$. The transient response of the hot fluid, represented by ϵ_h is shown to be strongly dependent upon Bi_c for NTU = 0.1, but as the NTU is increased this dependency tends to disappear completely. In fact, for NTU = 3, the curves for Bi_c equal to 0.1, 1.0 and 10 coincide. It will also be noted that for specified values of C^+ and NTU, the value of the abscissa, $Fo/(G^+/V^+)_{max}$, where steady state is reached is nearly independent of Bi_c. The response of the cold fluid, ϵ_c seems to be a weak function of Bi_c for $C^+ = 1.0$. Figs. 4 and 5 show analogous curves for $C^+ = 0.1$ and $C^+ = 10$. While for $C^+ = 10$ the trends are similar to those for $C^+ = 1.0$, the results for $C^+ = 0.1$ show that as the NTU is changed, the curves tend to keep their general shape indicating that the influence of Bi_c is equally detectable for the range of NTUs examined.

The results for a constant NTU, varying Bi_c and C^+, are shown in Figs. 6 and 7. The trends are similar for the two NTUs considered, NTU = 1.0 and NTU = 3.0. The lines representing ϵ_c for the various cases tend to overlap, but there is a clear distinction between the lines for ϵ_h, namely that larger values of ϵ_h were obtained for the smaller C^+s. The influence of the Bi_c over these results is similar to that discussed previously in conjunction with Figs. 3–5.

The next three Figs., 8, 9, and 10, are the representation of the fraction of the steady-state heat storage as a function of $Fo/(G^+/V^+)_{max}$. For all cases, the constant NTU curves shift to the right as the NTU decreases. As the Biot number increases, the curves shift to the left. It is important to realize that these results cover a wide range of possible physical situations. The amount of heat stored and the transient fluid outlet temperatures can be evaluated employing the steady-state quantities used in the definition of ϵ_h, ϵ_c and Q^+. Table 1 shows these steady-state parameters for the range of variables covered in this study.

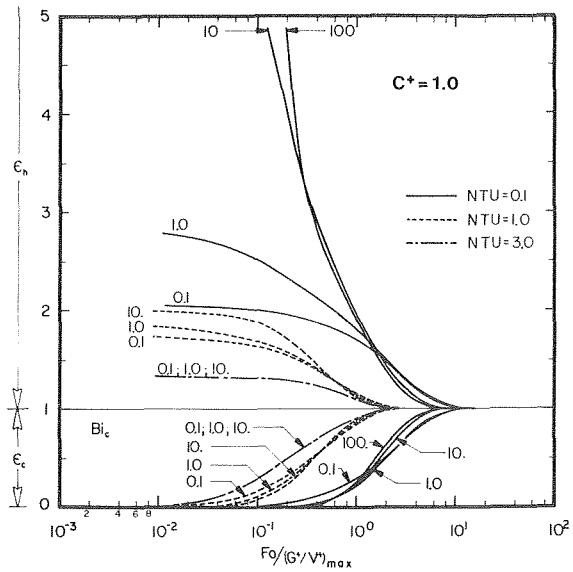

Fig. 3 Response of heat storage exchanger — $C^+ = 1.0$

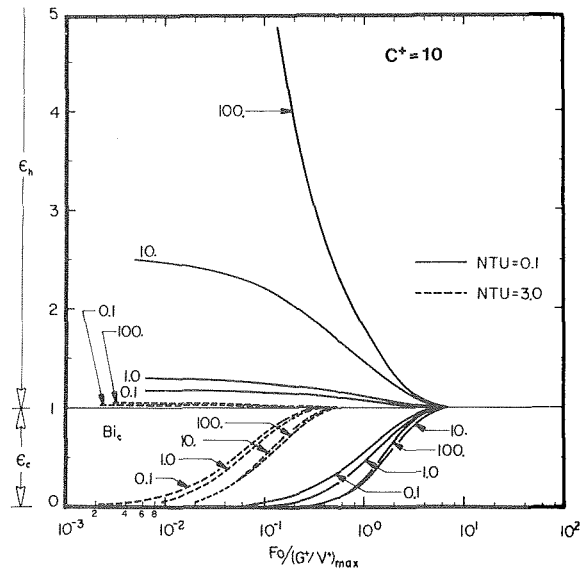

Fig. 5 Response of heat storage exchanger — $C^+ = 10$

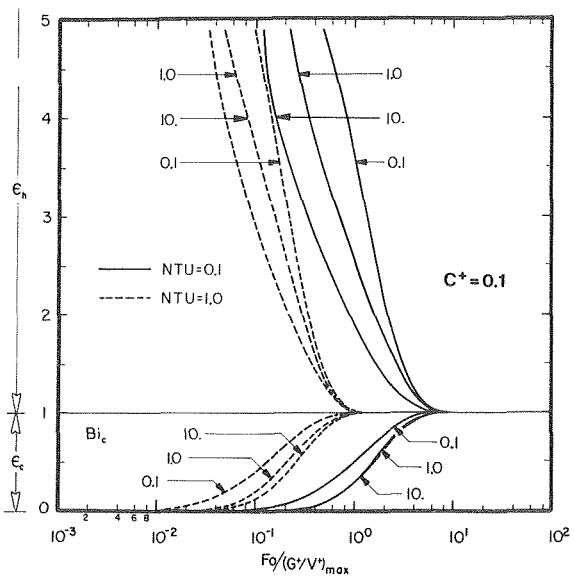

Fig. 4 Response of heat storage exchanger — $C^+ = 0.1$

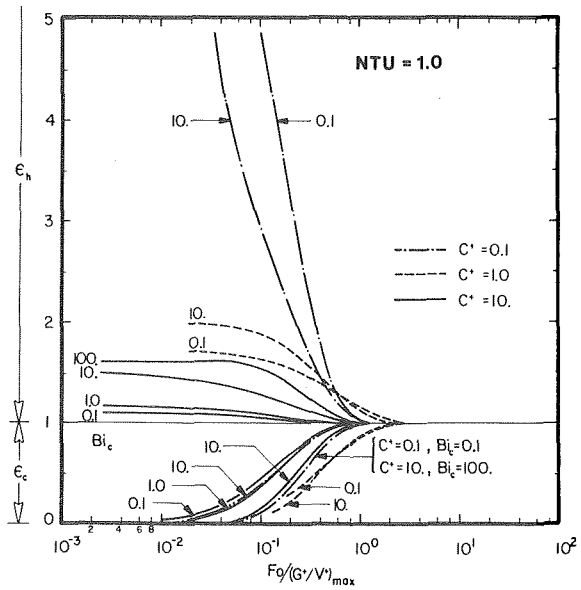

Fig. 6 Response of heat storage exchanger — NTU = 1.0

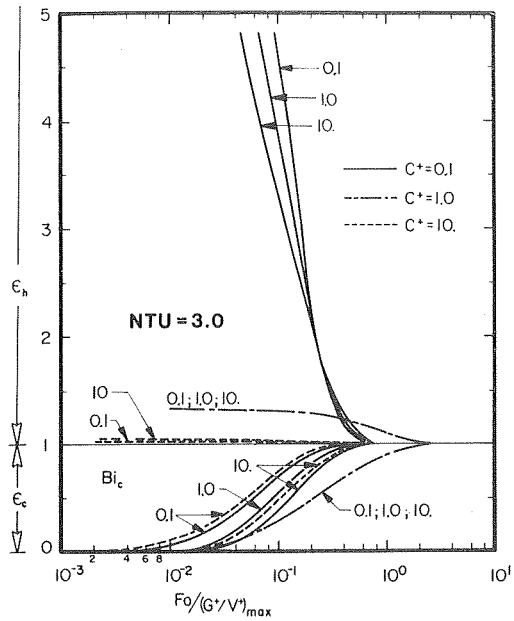

Fig. 7 Response of heat storage exchanger — NTU = 3.0

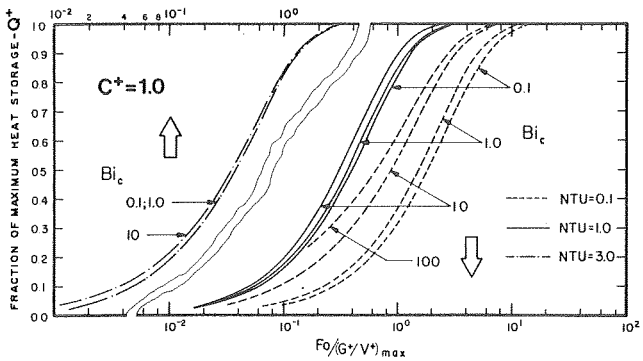

Fig. 8 The fraction of the steady-state heat storage — $C^+ = 1.0$

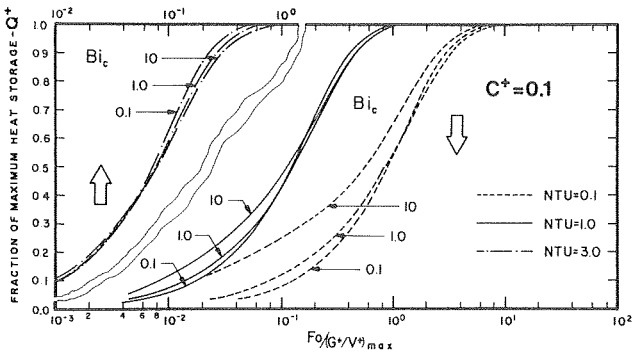

Fig. 9 The fraction of the steady-state heat storage — $C^+ = 0.1$

Arbitrary Time Variations in Fluid Inlet Temperature. A very important extension of these results is possible because of the linear nature of the governing differential equations and associated boundary conditions. The procedure, usually referred to as Duhamel's method, can be employed to predict the transient response of a heat storage exchanger to an arbitrary time variation of the hot fluid inlet

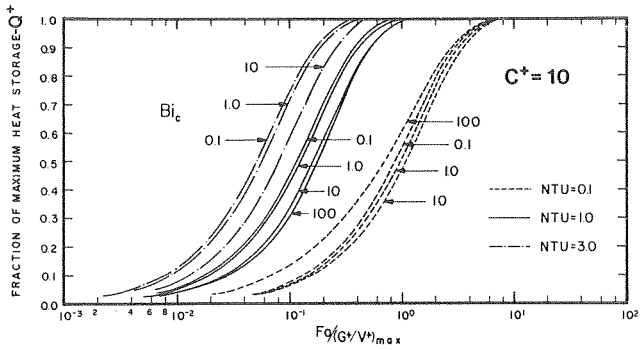

Fig. 10 The fraction of the steady-state heat storage — $C^+ = 10$

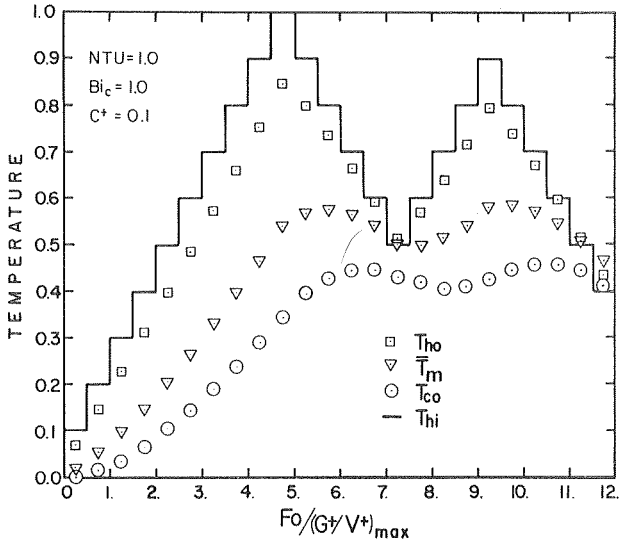

Fig. 11 Response of the heat storage exchanger to a time variation in the hot fluid inlet temperature

temperature. In order to use the present step function solutions for superposition, the arbitrary variation of the hot fluid inlet temperature must be approximated by the sum of a finite number of steps. Next, the steady-state quantities have to be calculated to enable us to evaluate T_{ho} and T_{co} utilizing the values of ϵ_h and ϵ_c obtained for a single step change, recalling that the inlet temperature of the cold fluid remains constant throughout the process. The actual transient response, T_{ho}, T_{co} and $\overline{T}_m$, to the specified time dependent hot fluid inlet temperature will be, at each instant of time, the sum of the contribution of all the step changes up to that moment. Fig. 11 is an illustration of this procedure for the case of $C^+ = 0.1$, $\mathrm{Bi}_c = 1.0$ and NTU = 1.0.

Conclusions

A wide range of possible practical applications for heat storage exchangers exist, however there must be a compromise between the amount of available energy to be transferred to the cold fluid and the desired amount stored in the storage material. If it is desired to store a considerable portion of the energy being transported by the hot fluid it is necessary to operate at low values of C^+. On the other hand, for small C^+, T_{ho} tends to be large, indicating that only a small fraction of the available energy has been used. As we go to larger C^+s the amount of heat stored, for a constant geometry, decreases, but better use of the available energy is made. It becomes apparent that each proposed application has to be examined on its own merits, and the results of this present investigation should be used as a guide to allow

the designer to establish the best configuration suitable for the application in hand.

Acknowledgments

The authors wish to acknowledge that this work was performed under NSF-RANN Grant AER 75-16216. The technical oversight of this grant is provided by ERDA, Division of Conservation, Oak Ridge, Tennessee.

References

1 Committee on Advanced Energy Storage Systems, "Criteria for Energy Storage R & D," ISBN 0-309-02530-3, National Academy of Science, Washington, D. C., 1976.

2 Schmidt, F. W., "Numerical Simulation of the Thermal Behavior of Convective Heat Transfer Equipment," *Heat Exchanger: Design and Theory Sourcebook*, N. Afgan and E. U. Schlunder ed., McGraw Hill, New York, 1974, pp. 491–524.

3 Cima, R. M., and London, A. L., "The Transient Response of a Two Fluid Counterflow Heat Exchanger—The Gas Turbine Regenerator," TRANSACTIONS ASME, Vol. 80, 1958, pp. 1169–1179.

4 London, A. L., Sampsell, D. F., and McGowan, J. G., "The Transient Response of Gas Turbine Plant Heat Exchangers—Additional Solutions for Regenerators of the Periodic and Direct Transfer Types," *Journal of Engineering for Power*, TRANS. ASME, Series A, Vol. 86, 1964, pp. 127–135.

5 Schmidt, F. W., and Szego, J., "Transient Behavior of Solid Sensible Heat Thermal Storage Units for Solar Energy Systems," 1975 International Seminar, "Future Energy Production—Heat and Mass Transfer Problems," Yugoslavia, 1975.

6 Schmidt, F. W., and Szego, J., "Transient Response of Solid Sensible Heat Thermal Storage Units—Single Fluid," ASME JOURNAL OF HEAT TRANSFER, August 1976, pp. 471–477.

APPENDIX

Evaluation of Steady State Parameters

In order to calculate the numerical values of the dependent variables, ϵ_h, ϵ_c, and Q^+, used to present the final results of this study, three steady-state quantities must be evaluated. Under the assumptions of steady-state and negligible longitudinal heat conduction, the temperature distribution in the storage material in the y direction becomes linear at each location x along the flow channels (Fig. 1(b)). Hence, a mean wall temperature $\bar{t}_w$ is used and effective heat-transfer coefficient, R_h and R_c, are specified by combining heat transfer coefficient with the convective contributions of each of the energy transporting fluids. The energy conservation equations become:
hot fluid

$$E_h \frac{dt_h}{dx} + R_h P_h (t_h - \bar{t}_w) = 0; \tag{A1}$$

cold fluid

$$E_c \frac{dt_c}{dx} - R_c P_c (t_c - \bar{t}_w) = 0; \tag{A2}$$

storage material

$$R_h P_h (t_h - \bar{t}_w) + R_c P_c (t_c - \bar{t}_w) = 0; \tag{A3}$$

and for the entire system

$$-R_c P_c L (t_c - \bar{t}_w) = R_h P_h L (t_h - \bar{t}_w) = US(t_h - t_c). \tag{A4}$$

Eliminating $\bar{t}_w$ from the above equations gives:

$$E_h \frac{dt_h}{dx} + \frac{US}{L}(t_h - t_c) = 0, \text{ and} \tag{A5}$$

$$E_c \frac{dt_c}{dx} + \frac{US}{L}(t_h - t_c) = 0. \tag{A6}$$

Introducing the dimensionless parameters defined in the text and solving the resulting equations yield the steady-state temperature distributions in the fluids and the storage material. This latter must be integrated over the volume of the storage material to obtain $\overline{T}_m{}^{ss}$. The final results are:

$$T_{ho}{}^{ss} = \frac{C^+ e^M - e^M}{C^+ - e^M} \text{ for } C^+ \neq 1;$$

$$T_{ho}{}^{ss} = \frac{1}{\text{NTU} + 1} \text{ for } C^+ = 1 \tag{A7}$$

$$T_{co}{}^{ss} = \frac{1 - e^M}{C^+ - e^M} \text{ for } C^+ \neq 1;$$

$$T_{co}{}^{ss} = \frac{\text{NTU}}{\text{NTU} + 1} \text{ for } C^+ = 1 \tag{A8}$$

$$\overline{T}_m{}^{ss} = \frac{1}{2} \frac{\left[e^M \left(\frac{N}{M} - 2 \right) - \frac{N}{M} \right]}{C^+ - e^M} \text{ for } C^+ \neq 1;$$

$$\overline{T}_m{}^{ss} = \frac{1}{2} \left[1 + \frac{\text{N}^*}{\text{NTU} + 1} \right] \text{ for } C^+ = 1 \tag{A9}$$

where

$$M = \text{NTU}\,(1 - C^+) \text{ for } C^+ < 1$$

$$M = \text{NTU} \left(\frac{1 - C^+}{C^+} \right) \text{ for } C^+ > 1$$

$$N = (C^+ + 1) + (C^+ - 1)N^*$$

$$N^* = \frac{\frac{1}{\text{Bi}_c} - \frac{1}{\text{Bi}_h}}{\frac{1}{\text{Bi}_c} + \frac{1}{\text{Bi}_h} + 1}.$$

P. C. Wayner, Jr.

Department of Chemical and Environmental Engineering,
Rensselaer Polytechnic Institute,
Troy, N. Y.

The Effect of the London-Van Der Waals Dispersion Force on Interline Heat Transfer

A theoretical procedure to determine the heat transfer characteristics of the interline region (junction of liquid-solid-vapor) from the macroscopic optical and thermophysical properties of the system is outlined. The analysis is based on the premise that the interline transport processes are controlled by the London-van der Waals dispersion force between condensed phases (solid and liquid). Numerical values of the dispersion constant are presented. The procedure is used to compare the relative size of the interline heat sink of various systems using a constant heat flux mode. This solution demonstrates the importance of the interline heat flow number, $\overline{A}h_{fg}\nu^{-1}$, which is evaluated for various systems.

Introduction

It is well known that the vapor pressure over an adsorbed film of a nonpolar liquid is a function of the temperature and the London-van der Waals dispersion force of attraction between the solid and liquid (e.g., references [1–4][1] are of particular relevance). This fact can be used to predict the interline heat transfer coefficient and the heat sink capability of a stable evaporating wetting film of liquid [5–7]. These heat transfer characteristics are of major importance to the analysis of the rewetting of a hot spot, the heat transfer rate from an evaporating meniscus, falling thin film evaporation, and boiling. The analyses presented in [6, 7] demonstrate the importance of the group of properties, $\overline{A}h_{fg}/\nu$, which we call the interline heat flow number, in which $\overline{A}$ is a dispersion constant, h_{fg} is the heat of vaporization of an adsorbed film and ν is the kinematic viscosity. For example, a constant heat flux model of the evaporating interline [6] shows that the theoretical interline heat sink for a unit length of interline, Q, is given by

$$Q = [2\overline{q} \ln \eta]^{0.5} [h_{fg}\overline{A}/\nu]^{0.5} \tag{1}$$

in which $\overline{q}$ is the heat flux and η is a dimensionless thickness. Herein, methods for predicting the value of the interline heat flow number and, therefore, the size of the interline heat sink are presented and used. In essence, a theoretical procedure to determine the interline heat sink capability of an evaporating thin film from the macroscopic optical properties and thermophysical properties of the system is outlined.

Evaluation of $\overline{A}$

Assuming that bulk values can be used to approximate the values of the heat of vaporization and the kinematic viscosity, the problem of predicting the value of the interline heat flow number, $\overline{A}\,h_{fg}/\nu$, is reduced to the critical one of evaluating a dispersion constant, $\overline{A}$. Since $\overline{A}$ is important to many fields, considerable literature concerning its determination is available. Basically, there are two methods of calculating the dispersion force between condensed bodies. The microscopic approach starts with the interaction between individual atoms or molecules and postulates their additivity. The attractive force between the liquid and solid is then calculated by integration over all atoms and molecules [8]. The result is a purely geometrical term and the Hamaker constant, $A_{s\ell v}$, which is a function of the interacting materials. The macroscopic approach uses the macroscopic optical properties of the interacting materials and calculates the London-van der Waals dispersion force from the imaginary part of the complex dielectric "constants" [1]. It is generally accepted in the literature that the macroscopic approach is more satisfying than the microscopic approach. Presently we are concerned with a first order approximation of the effect of the dispersion force on heat transfer. Therefore, we will use the results of both methods in order to obtain maximum use of the prior literature.

A good physical description of the microscopic approach is given by Sheludko [2]. Using the microscopic procedure, the equation for the temperature independent dispersion constant is

$$\overline{A} = \frac{A_{\ell s} - A_{\ell\ell}}{6\pi} \approx -\frac{A_{s\ell v}}{6\pi} \tag{2}$$

with

$$A_{\ell\ell} = \frac{\pi^2 \beta_{\ell\ell}}{\overline{v}_\ell{}^2} \quad \text{and} \quad A_{\ell s} = \frac{\pi^2 \beta_{\ell s}}{\overline{v}_\ell \overline{v}_s}$$

where $\overline{v}_i{}^{-1}$ is the number of atoms or molecules per unit volume and β_{ij} is the constant in London's equation for the attraction between

[1] Numbers in brackets designate References at end of paper.

Contributed by the Heat Transfer Division for publication in the JOURNAL OF HEAT TRANSFER. Manuscript received by the Heat Transfer Division September 22, 1977.

two atoms. If the force of attraction between the liquid and solid (represented by $A_{\ell s}$) is greater than the force of attraction between two liquid molecules (represented by $A_{\ell\ell}$) the liquid wets the solid and a decrease in the vapor pressure occurs.

Using the macroscopic procedure, an equivalent Hamaker constant, $A_{s\ell v}$ can be obtained from the Lifshitz-van der Waals constant, $\hbar\bar{\omega}_{s\ell v}$:

$$A_{s\ell v} = \frac{3\hbar\bar{\omega}_{s\ell v}}{4\pi} \tag{3}$$

Using this definition to relate both approaches through an equivalent Hamaker constant, the two procedures can be unified and compared. For the purpose of this report the Lifshitz-van der Waals constant can be calculated using the following approximate formula [1]:

$$\bar{\omega}_{s\ell v} = \int_0^\infty \frac{[\epsilon_\ell(i\xi) - \epsilon_s(i\xi)]\,[\epsilon_\ell(i\xi) - 1]}{[\epsilon_\ell(i\xi) + \epsilon_s(i\xi)]\,[\epsilon_\ell(i\xi) + 1]}\, d\xi \tag{4}$$

where ϵ_s, ϵ_v, ϵ_ℓ are the frequency dependent dielectric constants of the solid, vapor ($\epsilon_v = 1$), and liquid evaluated along the imaginary frequency axis, $i\xi$. (The assumptions associated with deriving this equation from a more general formulation are presented in [1].) In turn these imaginary frequency dependent dielectric constants can be calculated from the imaginary part of the complex dielectric constant which can be experimentally measured. The dielectric constant, $\epsilon(\omega)$, is a complex function of the frequency, ω.

$$\epsilon(\omega) = \epsilon'(\omega) + i\epsilon''(\omega) \tag{5}$$

The function $\epsilon(\omega)$ is related to the complex index of refraction, $\hat{n}$, the refractive index, n, and the absorption constant, k, by

$$\sqrt{\epsilon(\omega)} = \hat{n} = n(\omega) + ik(\omega) \tag{6}$$

$$\epsilon'(\omega) = n^2(\omega) - k^2(\omega) \tag{7}$$

$$\epsilon''(\omega) = 2n(\omega)k(\omega) \tag{8}$$

For the purpose of analysis, it is useful to consider the frequency, ω, to be a complex variable:

$$\omega = \omega' + i\xi \tag{9}$$

As presented above, the dispersion force depends on the value of the dielectric constant on the imaginary frequency axis, $\epsilon(i\xi)$. The function is always positive and is related to the dissipation of energy in an electromagnetic wave propagated in the medium. $\epsilon(i\xi)$ is a real quantity which decreases monotonically from ϵ_0 (the electrostatic dielectric constant, $\epsilon_0 = \hat{n}^2 > 1$) for dielectrics or from $+\infty$ for ideal metals at $\omega = i0$ to 1 at $\omega = i\infty$ for all materials [9]. Without the need for a specific model, equation (10) can be used to calculate $\epsilon(i\xi)$ from the imaginary part of the dielectric constant, $\epsilon''(\omega)$, [9].

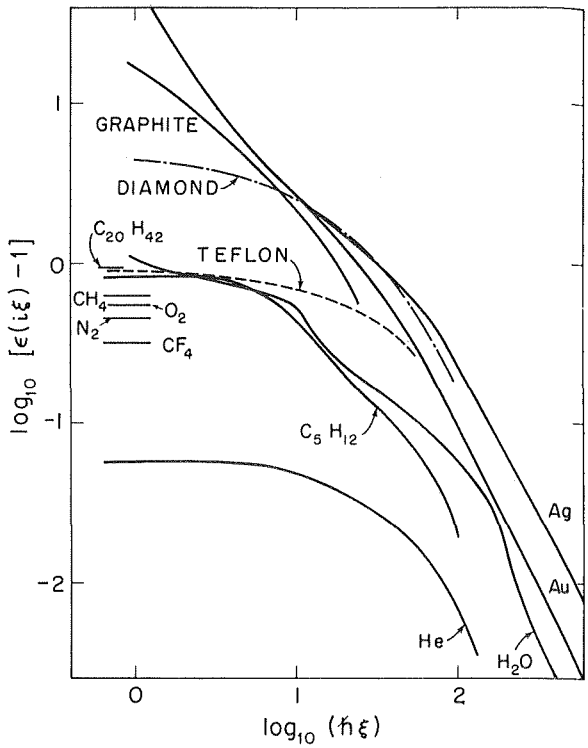

Fig. 1 Plot of $\log_{10}[\epsilon(i\xi) - 1]$ as a function of $\log_{10}(\hbar\xi)$ for various materials

$$\epsilon(i\xi) = 1 + \frac{2}{\pi}\int_0^\infty \frac{X\epsilon''(X)}{(X^2 + \xi^2)}\, dX \tag{10}$$

where ξ and X are angular frequencies of the electromagnetic field. Therefore, $\epsilon(i\xi)$ can be obtained directly from experimental data on the refractive index and absorption constant. However, due to the lack of sufficient data for the frequency dependent optical constants, semi-empirical models are usually used.

Equation (4) demonstrates that a thin wetting film of adsorbed liquid on a solid surface will be stable if the dielectric constant of the solid along the imaginary frequency axis is greater than that of the liquid, $\epsilon_s(i\xi) > \epsilon_\ell(i\xi)$. Therefore, it is instructive to compare the values of $\epsilon(i\xi)$ for various materials. In Fig. 1, the $\log_{10}[\epsilon(i\xi) - 1]$ is presented as a function of the energy associated with an electromagnetic wave in electron volts, $\log_{10}(\hbar\xi)$. The source of the individual values are given in the Appendix. For nonpolar dielectric materials, the static

Nomenclature

$\bar{A}$ = dispersion constant [J]
A = Hamaker constant [see equation (2)] [J]
D = mean separation between close packed planes [m]
$\hbar 2\pi$ = Planck's constant [$J{\cdot}s$]
h_{fg} = heat of vaporization [$J{\cdot}kg^{-1}$]
k = thermal conductivity [$W{\cdot}m^{-1}{\cdot}K^{-1}$]
k = absorption constant
n = refractive index
0 = heat transferred [$W{\cdot}m^{-1}J$]
q = heat flux [$W{\cdot}m^{-2}$]
s = solid thickness [m]
T = temperature [K]
U = overall heat transfer coefficient, [$W{\cdot}m^{-2}{\cdot}K^{-1}$]
β = see equation (2)
γ = interfacial free energy, [$J{\cdot}m^{-2}$]
δ = film thickness [m]
η = dielectric constant, $\epsilon = \epsilon' + i\epsilon''$
ϵ = dimensionless film thickness, δ/δ_0
ν = kinematic viscosity [$m^2{\cdot}s^{-1}$]
ξ = imaginary part of complex frequency [$rad{\cdot}s^{-1}$]
$\bar{\omega}$ = defined by equation (4) [$rad{\cdot}s^{-1}$]
ω = angular frequency [$rad{\cdot}s^{-1}$]

Subscripts

ℓ = liquid phase
ℓ_v = liquid-vapor interface
s = solid
o = evaluated at interline
v = vapor phase

Superscripts

d = dispersion
- = averaged
^ = complex index of refraction

dielectric constant, ϵ_0, can be obtained using the Maxwell relation, $\epsilon_0 = n^2$, in which the index of refraction, n, can be obtained in the visible range of frequencies. It is a measure of the induced polarization. The n-alkanes and diatomic molecules are representative of these materials. Curves for pentane and helium are presented in Fig. 1. For comparison, limiting values of nitrogen, oxygen, methane and carbon-tetrafluoride are also given.

Polar molecules have, in addition to the induced polarization, an orientation polarization. As a result, the dielectric constant is not constant in the frequency range below the visible. The alcohols and water are representative of this group. The curve for water in Fig. 1 stops at $\hbar\xi = 1$. At $\xi = 0$, the dielectric constant for water has a value of $\epsilon_0 = 81$. At $\hbar\xi = 3.16$, $\epsilon \approx 1.75$. At most frequencies the dielectric constant for pentane is less than that for water. Experimentally, pentane has been observed to form a thin wetting film on a water substrate [10]. Films of octane on water are marginally stable. A theoretical study of hydrocarbon adsorption on water surfaces that describes and confirms this phenomenon has been done using Lifshitz's theory [11]. The values of $\epsilon(i\xi)$ for ideal metals (smooth and clean surfaces free from oxides and contaminants) are also presented in Fig. 1. Since the complex part of the dielectric constant, $2nk$, is large for metals, $\epsilon(i\xi)$ also has a relatively large value. In practical heat transfer equipment these values cannot be reached since nonidealities (oxides and adsorbed contaminates) are usually present. However, they do represent an upper limit for $\epsilon(i\xi)$. Experimentally, the important value is the measured value of $2nk = \epsilon''$ which characterizes the surface being used. These results also emphasize the fact that metals are high energy surfaces which are easily wetted and easily contaminated. The dielectric properties of polytetrafluoroethylene (Teflon) fall above but close to those of pentane. Pentane wets Teflon since its surface tension ($\gamma^d = 0.016\ J/m^2$) is less than the critical surface tension for the wetting of Teflon ($0.0185\ J/m^2$).

Churaev used equation (4) to calculate the Hamaker constant for various systems [14] which are presented in Table 1. Since the dielectric constants for metals are larger than that for water, which, in turn, is larger than that for pentane, the absolute value of the Hamaker constants for the alkane $\simeq$ metal systems are larger than that for the pentane $\simeq$ water system. For comparison, the Hamaker constant for the $He\text{-}CaF_2$ system is $A_{s\ell v} \approx -3.8 \times 10^{-21}\ J$. [15]. The lower values of the dielectric constants for helium and CaF_2 result in a relatively low value of $A_{s\ell v}$. The refractive index of CaF_2 is approximately $n \approx 1.4$. The approximate value of the Hamaker constant, $A_{s\ell v}$, can be obtained using

$$A_{s\ell v} = A_{\ell\ell} - A_{s\ell} \tag{11}$$

A good approximation for the Hamaker constant, $A_{s\ell}$, is $(A_{ss}\, A_{\ell\ell})^{0.5}$ [16]. Therefore, we can calculate the approximate value of $A_{s\ell v}$ from the more readily available values of A_{ss} and $A_{\ell\ell}$. Calculated values for $A_{s\ell v}$ obtained using equation (11) are presented in Table 2. The values for $A_{\ell\ell}$ were obtained using

$$A_{\ell\ell} = 24\pi D^2 \gamma \tag{12}$$

Israelachvili [17] successfully compared the surface tension of a number of saturated hydrocarbons calculated on the basis of equation (12) with experimental data. In Table 3, a list of values for A_{ss} is given. Due to limitations in the availability, interpretation and use of the optical data, there is a degree of inconsistency in the values of these constants. For example, recent data on the adsorption of alkanes on Teflon [4] indicate the value of A_{ss} obtained by Vassilieff and Ivanov [12] is probably too high. As a result of these inconsistencies, the theoretical results based on these initial values of the Hamaker constant are obviously approximate. However, the relative values calculated using the same set of assumptions are very instructive. The refinement of the procedures and the availability of more extensive optical data will lead to more consistent results in the future.

Table 1

Calculated values of $A_{s\ell v}$ for wetting films [14]

Liquid, substrate	$-A_{s\ell v}\cdot 10^{20}$ J	Liquid, substrate	$-A_{s\ell v}\cdot 10^{20}$ J
Water on quartz	1.12	Pentane on water	0.74
Octane on quartz	1.67	Hexane on water	0.63
Decane on quartz	1.57	Decane on water*	0.34
Tetradecane on quartz	1.34	Octane on steel	19.2
Benzene on quartz	0.91	Decane on steel	18.9
CCl_4 on quartz	0.56	Decane on gold	23.1
		Water on gold	11.2

* The results in [10] indicate that decane does not form a stable film on water.

Predicted Values of the Interline Heat Flow Number, $\bar{A}\, h_{fg}/\nu$

Predicted values of the interline heat flow number obtained using bulk values for the heat of vaporization and the kinematic viscosity are presented in Table 4. The gold-alkane system and the Teflon-alkane system are two ideal systems for comparison since the solids

Table 2

Values of $A_{s\ell v}$ calculated using equations (11) and (12)

$A_{ss}\cdot 10^{20}$ references [16 & 12]	$A_{\ell\ell}\cdot 10^{20}$ J	$-A_{s\ell v}\cdot 10^{20}$ J
Gold : 45	Methane : 3.95	9.4
Gold : 45	Pentane : 5.04	10.0
Gold : 45	Hexane : 5.48	10.2
Gold : 45	Heptane : 5.82	10.4
Gold : 45	Octane : 6.08	10.5
Gold : 45	n-Dodecane : 6.75	10.7
Gold : 45	Nitrogen : 2.49	8.1
Teflon : 10.5	Methane : 3.95	2.5
Teflon : 10.5	Octane : 6.08	1.9
Teflon : 10.5	Nitrogen : 2.49	2.6

Table 3

Calculated values of A_{ii} from [12]

Material	$A_{ii}\cdot 10^{20}$ J	Material	$A_{ii}\cdot 10^{20}$ J
Decane	6.7	Polypropylene	9.05
Diamond	41.4	Teflon	10.5
Hydrocarbon II	7.7	Quartz	8.65
Polyethylene	10.5	Water	6.05
Polystyrene	11.1		

Table 4

Theoretical values of the interline heat flow number, $h_{fg}\bar{A}\ \nu^{-1}$

Liquid—Substrate	$(h_{fg}\, A\ \nu^{-1})\cdot 10^9$ Watts		$\bar{A}$ Source
Methane—Gold	9.76	(111.4K)[2]	Table (2)
Pentane—Gold	5.26	(293K)	Table (2)
Hexane—Gold	4.22	(293K)	Table (2)
Heptane—Gold	3.33	(293K)	Table (2)
Octane—Gold	2.62	(293K)	Table (2)
Dodecane—Gold	1.12	(293K)	Table (2)
Nitrogen—Gold	4.17	(77K)	Table (2)
Decane—Steel	2.90	(293K)	Ref. [14]
Decane—Steel	4.14	(447K)[3]	Ref. [14]
Decane—Gold	3.50	(293K)	Ref. [14]
Methane—Teflon	2.60	(111.4K)	Table (2)
Octane—Teflon	0.26	(293K)	Table (2)
Nitrogen—Teflon	1.53	(77K)	Table (2)
CCl_4—Quartz	0.105	(293K)	Ref. [14]
CCl_4—Quartz	0.497	(350K)[3]	Ref. [14]
Octane—Quartz	0.418	(293K)	Ref. [14]

[2] h_{fg} and ν are evaluated at this temperature.
[3] Reference [14] values for $\bar{A}$ were adjusted for temperature using equations (11) and (12).

have been extensively studied and the alkanes are simple nonpolar fluids. More importantly, these systems represent a broad range, since gold is a very high surface energy material and Teflon a very low surface energy material. The value of the interline heat flow number for methane-gold is 9.76×10^{-9} W versus 2.6×10^{-9} W for methane-Teflon. Increasing the molecular weight of the fluid gives $h_{fg}\overline{A}/\nu = 2.62 \times 10^{-9}$ W or octane-gold. This decrease occurs because the ratio h_{fg}/ν decreases faster than $\overline{A}$ increases. For all practical purposes these numbers bracket the range for simple fluids. The inconsistencies present in the table values for the interline heat flow number result from the inconsistencies in the values of $\overline{A}$ in the literature. For a finite contact angle system, the "interline region" as defined herein vanishes and the thin film starts with a finite thickness. Polar fluids and liquid metals are not addressed herein.

The Theoretical Interline Heat Sink, Q, and Interline Length, x.

The above results can be used to estimate various characteristics of the interline evaporation process. The theoretical interline heat sink for a unit length of interline, Q, is obtained using equation (1). The length of the interline region of thickness range $\eta > 1$, x, is [6]

$$x = [2\,\ell n\,\eta]^{0.5}\,[\overline{q}]^{-0.5}\,[h_{fg}\overline{A}/\nu]^{0.5} \tag{13}$$

These equations are presented in Figs. 2 and 3 for $\eta = 10$. In Fig. 2 some of the values of $\overline{A}h_{fg}/\nu$ listed in Table (4) are marked on the theoretical curve. Obviously an increase in the interline heat flow number gives an increase in the theoretical heat sink, Q, and the length of the interline region, x. Two of the systems, decane-steel and carbon tetrachloride-glass are given in more detail in Fig. 3. Curve (1a) represents the decane-steel system at 293K, and Curve (1b) represents the system at 447K. Curves (2a and 2b) represent the carbon tetrachloride system st 293K and 350K. The results predict that the interline heat sink, Q, for the decane-steel system is approximately three times larger than that for the carbon tetrachloride system at the same heat flux and $P_v = 1.01 \times 10^5\ N{\cdot}m^{-2}$. This results from the increased length of the evaporating thin film, x, of thickness $1 < \eta \leq 10$, which is a function of the interline heat flow number. The increase of Q with temperature results from the substantial decrease in the kinematic viscosity in this temperature range. This increase will not continue, since the dispersion constant will decrease substantially at higher temperatures. For the carbon tetrachloride-quartz system, both the dispersion constant and the reciprocal of the kinematic viscosity increase with temperature at this temperature level (note the effect of the relative size of $A_{\ell\ell}$ on $A_{s\ell v}$ in equation (11)).

As presented in [6], the equation for the interline heat sink can be written as

$$Q = [2\,\ln\,(\eta)k_s(T_s - T_v)\,S^{-1}]^{0.5}\,[\overline{A}h_{fg}\,\nu^{-1}]^{0.5} \tag{14}$$

thereby defining an effective overall heat transfer coefficient, U_{eff}, as

$$U_{\text{eff}} = [2k_s\overline{A}h_{fg}/\nu S(T_s - T_v)]^{0.5} \tag{15}$$

for

$$Q = U_{\text{eff}}\,[\ell n\,\eta]^{0.5}\,[T_s - T_v] \tag{16}$$

If the temperature in the solid, T_s, at the distance, S, from the surface is known, equation (14) can be used to obtain Q using the values of $\overline{A}\,h_{fg}/\nu$ presented herein.

Discussion

A theoretical procedure to determine the interline heat sink capability of an evaporating thin film using the macroscopic optical properties and the thermophysical properties of the system has been outlined above. This procedure significantly increases our understanding of the interline and shows how the level of the interline transport processes is controlled by the dispersion forces resulting from the interaction of the solid and liquid. The procedure can be used to predict the relative size of the interline heat sink and, thereby, enhance the development of heat transfer equipment which use the evaporating interline region. Due to the basic nature of the equations, their current level of development and the limited availability of optical data, the use of ideal systems (e.g., neglecting surface roughness) has been emphasized. However, this does not detract from the significance of the results, since ideal systems give an order of magnitude approximation and enhanced understanding of real systems, and reveal the basic mechanisms involved in the transport processes.

The constant heat flux model explicitly demonstrated the importance of the interline heat flow number [6]. Using theoretical values of the interline heat flow number, the relative size of the interline heat sink and the interline length can be determined. The absolute upper limit of the interline heat sink cannot be determined using only these procedures because the important questions of interline stability and the transition from the thin film to the meniscus region have not been addressed herein. However, these concepts do describe why the interline heat sink of a system like decane-steel should be greater than that of a system like carbon tetrachloride-quartz. A procedure is now available whereby various systems can be theoretically compared.

By necessity, there are aspects of the above theoretical results which

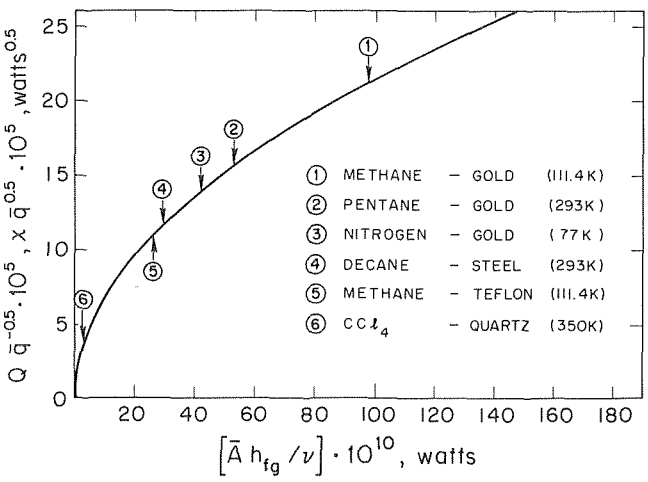

Fig. 2 Graphical representation of equations (1) and (13) for $\eta = 10$

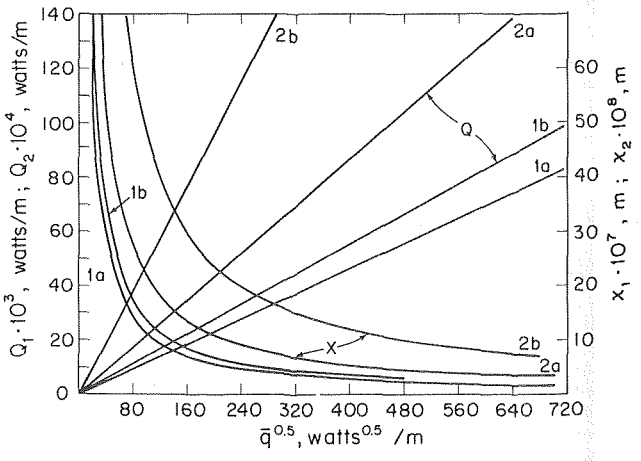

Fig. 3 Heat sink capability, Q, and interline length, x, for $\eta = 10$: (1a) decane-steel at 293 K; (1b) decane-steel at 447 K; (2a) CCl_4-quartz at 293 K; (2b) CCl_4-quartz at 350 K

need experimental evaluation, refinement, and extension because of the assumptions in the models. These results indicate that this can be accomplished by measuring the interline stability and the interline length, x, as a function of heat flux and the interline heat flow number.

References

1 Dzyaloshinskii, I. E., Lifshitz, E. M., and Pitaevskii, L. P., "The General Theory of Van der Waals Forces," *Adv. Physics* vol. 10, 1959, pp. 165–208.

2 Sheludko, A., *Colloid Chemistry,* Elsevier Pub. Co., New York, N.Y., 1966.

3 Deryagin, B. V., and Zorin, A. M., "Optical Study of the Adsorption and Surface Condensation of Vapors in the Vicinity of Saturation on a Smooth Surface," in *Proc. 2nd Int. Congr. Surface Activity* London, Vol. 2, 1957, pp. 145–152.

4 Hu, P., and Adamson, A. W., "Adsorption and Contact Angle Studies," *J. Colloid and Interface Science,* Vol. 59, No. 3, 1977, pp. 605–613.

5 Potash, M. L., Jr., and Wayner, P. C. Jr., "Evaporation from a Two-dimensional Extended Meniscus," *International Journal of Heat and Mass Transfer* vol. 15, 1972, pp. 1851–1863.

6 Wayner, P. C., Jr., "A Constant Heat Flux Model of the Evaporating Interline Region," to be published in the *International Journal of Heat and Mass Transfer.*

7 Wayner, P. C., Jr., Kao, Y. K., and LaCroix, L. V., The Interline Heat-Transfer Coefficient of an Evaporating Wetting Film, *International Journal of Heat and Mass Transfer* vol. 19, 1976, pp. 487–491.

8 Hamaker, H. C., *Physica* (Utrecht) vol. 4, 1058 (1937).

9 Landau, L. D., and Lifshitz, E. M., *Electrodynamics of Continuous Media,* Pergamon Press, New York, N.Y. 1960, pp. 247–268.

10 Hauxwell, F., and Ottewill, R. H., "A Study of the Surface of Water by Hydrocarbon Adsorption," *J. Colloid Interface Sci.* vol. 34, 1970, p. 473.

11 Richmond, P., Ninham, W., and Ottewill, R. H., "A Theoretical Study of Hydrocarbon Adsorption on Water Surfaces Using Lifshitz Theory," *J. Colloid Interface Sci.* Vol. 45, 1973, pp. 69–80.

12 Vassilieff, Chr. St., and Ivanov, I. B., "Simple Semiempirical Method of Calculating van der Waals Interactions in Thin Films from Lifshitz Theory," *Zeit. für Naturforsch.* Vol. 31a, 1976, pp. 1584–1588.

13 Alexander, G., and Rutten, G. A. F. M., "Surface Characteristics of Treated Glasses for the Preparation of Glass Capillary Columns in Gas-Liquid Chromatography," *Journal of Chromatography* Vol. 99, 1974, pp. 81–101.

14 Churaev, N. V., "Molecular Forces in Wetting Films of Non-Polar Liquids," *Kolloidnyi Zhurnal* Vol. 36, 1974, pp. 323–327.

15 Richmond, P., and Ninham, B. W., "Calculations of Van der Waals Forces Across Films of Liquid Helium Using Lifshitz Theory," *Journal of Low Temperature, Physics* Vol. 5, 1971, pp. 177–189.

16 Krupp, H., Schnabel, W., and Walter, G., "The Lifshitz-Van der Waals Constant, Computation of the Lifshitz-Van der Waals Constant on the Basis of Optical Data," *Journal Colloid and Interface Science* Vol. 39, 1972, pp. 421–423.

17 Israelachvili, J. N., "Van der Waals Dispersion Forces Contribution to Works of Adhesion and Contact Angle on the Basis of Macroscopic Theory," *Journal of Chemical Soc.,* Faraday Trans. II Vol. 69, 1973, pp. 1729–1738.

18 Krupp, H., "Particle Adhesion Theory and Experiment," *Advan. Colloid Interface Sci.* Vol. 1, 1967, pp. 111–239.

19 Muller, V. M., and Churaev, N. V., "Use of the Macroscopic Theory of Molecular Forces to Calculate the Interaction of Particles in a Metal Hydrosol," *Kolloidnyi Zournal* Vol. 36, 1974, pp. 492–497.

Acknowledgment

The support of NASA(AMES) P.O. #A-38597-B(DG) entitled "The Effect of the Liquid-Solid System Properties on the Interline Heat Transfer Coefficient" is gratefully acknowledged.

APPENDIX

Determination of Values of $\epsilon(i\xi)$ Used in Fig. (1)

There are various procedures to obtain spectral graphs of $\epsilon(i\xi)$ from the limited experimental data. One of the most useful makes use of the following empirical formula [18]:

$$\frac{\epsilon(i\xi) - 1}{\epsilon(i\xi) + 1} = a \exp(-b\xi) \tag{A-1}$$

This equation was used to obtain the curves for graphite, diamond and Teflon. The constants and references are given in Table A-1.

Table A-1
Constants and references for equation (A-1)

Substance	a	$b \cdot 10^{17}$, s/rad	Reference
Graphite	0.948	3.9	18
Diamond	0.705	1.5	12
Polyethylene	0.420	2.1	12
Polypropylene	0.390	2.1	12
Teflon	0.317	1.2	12
Polystyrene	0.433	2.1	12

The curve for pentane was obtained from [11]. The dielectric constant is essentially constant ($\epsilon = n^2$) from zero frequency through to an ultraviolet frequency, ω_{uv}, which they chose to be the first ionization potential. For frequencies less than ω_{uv} they used the following equation:

$$\epsilon(i\xi) = 1 + \frac{n^2 - 1}{1 + (\xi/\omega_{uv})^2} \tag{A-2}$$

For frequencies higher than the plasma frequency, ω_p, they used equation (A-3) with straight line interpolation in between

$$\epsilon(i\xi) = 1 + \omega_p{}^2/\xi^2 \tag{A-3}$$

The curve for helium was obtained from [15], in which a similar procedure was used.

The data for nitrogen, oxygen, methane and carbon tetrafluoride were obtained using

$$\epsilon = n^2 \tag{A-4}$$

and standard values for the index of refraction. The values for gold and silver were obtained from [19].

journal of heat transfer

technical notes

This section consists of contributions of 1500 words or equivalent. In computing equivalence, a typical one-column figure or table is equal to 250 words. A one-line equation is equal to 30 words. The use of a built-up fraction or an integral sign or summation sign in a sentence will require additional space equal to 10 words. Technical notes will be reviewed and approved by the specific division's reviewing committee prior to publication. After approval such contributions will be published as soon as possible, normally in the next issue of the journal.

Predictive Capabilities of Series Solutions for Laminar Free Convection Boundary Layer Heat Transfer

F. N. Lin[1] and B. T. Chao[2]

Nomenclature

a,b = semidiameters of elliptical cylinder
g = gravitational acceleration
Gr = Grashof number, $g\beta|T_w - T_\infty|L^3/\nu^2$
k = thermal conductivity
L = reference length
Nu = Nusselt number, $q_w L/(T_w - T_\infty)k$
Pr = Prandtl number
q_w = wall heat flux
$\bar{r}$ = radial distance from axis of symmetry to a surface element, $r = \bar{r}/L$
T = temperature; T_w and T_∞ refer to surface and undisturbed ambient temperature, respectively
$\bar{u}$ = velocity component in $\bar{x}$-direction; $u = \bar{u}L/(\nu\,\mathrm{Gr}^{1/2})$
$\bar{v}$ = velocity component in $\bar{y}$-direction; $v = \bar{v}L/(\nu\,\mathrm{Gr}^{1/4})$
$\bar{x}$ = streamwise coordinate; $x = \bar{x}/L$
$\bar{y}$ = coordinate normal to $\bar{x}$; $y = \mathrm{Gr}^{1/4}\bar{y}/L$
α = angle defined in Fig. 1
β = thermal expansion coefficient
θ = dimensionless temperature, $(T - T_\infty)/(T_w - T_\infty)$
ν = kinetmatic viscosity
ϕ = sin α
ψ = stream function in (x,y) coordinates; $ru = \partial\psi/\partial y$ *and* $rv = -\partial\psi/x$

Introduction

A number of series solutions for the prediction of laminar, free convection boundary layer heat transfer over isothermal and nonisothermal bodies are available in the literature. Chiang and Kaye [1][3] used a Blasius series expansion to determine local Nusselt number for horizontal circular cylinders with prescribed surface temperature or surface heat flux expressed as polynomials of distances from the stagnation point. The same procedure was used by Chiang, Ossin, and Tien [2] for spheres. Koh and Price [3] devised transformations for the cylinder equations used in [1] to remove their dependence on the coefficients that appear in the polynomial surface condition. Fox [4] proposed a further generalization of the results given in [2, 3] for treating bodies of arbitrary shape. More recently, Harpole and Catton [5] extended the Blasius series method to low Prandtl number fluids.

Saville and Churchill [6] used a Görtler-type series for analyzing two-dimensional, planar and axisymmetrical boundary layer flows over smooth isothermal bodies of fairly arbitrary contours. When applied to horizontal circular cylinders or spheres, the series converge faster than the corresponding Blasius series. The Görtler-type series has been used by Wilks [7] and by Lin [8] for two-dimensional boundary layers over bodies of uniform heat flux. Kelleher and Yang [9] also employed a Görtler-type series for treating free convection over a nonisothermal vertical plate. The class of problems considered in [6] was treated by Lin and Chao [10] using a series expansion of the form proposed by Merk [11] and later corrected by Chao and Fagbenle [12].

When assessing the usefulness of the various proposed methods, the investigators usually made comparisons with experiments and/or prior published calculations. However, such comparison was almost always limited to horizontal circular cylinders or spheres. The main purpose of this note is to show that conclusions based on circular cylinders or spheres cannot be assumed to have general validity. The radius of convergence of the various series is strongly dependent on the body configuration and, to a much less extent, on the Prandtl number and the coordinate system involved.

Görtler Series, S-I and S-II

Investigations of two Merk-type series by the present authors [10, 13] showed that their radius of convergence depends, among other things, on the coordinate system used for the transformed momentum and energy boundary layer equations. Since the Görtler series has the advantage of requiring significantly less tabulation of universal functions than the other series solution methods, it was decided to develop the Görtler series, using the same two sets of coordinate system employed in [10, 13]. One of them closely resembles that of Saville and Churchill [6].

To be definite, we consider two-dimensional or rotationally symmetrical bodies of uniform surface temperature T_w immersed in an infinite ambient fluid of undisturbed temperature T_∞ as illustrated in Fig. 1. The governing conservation equations are well known and were given in dimensionless form by equations (10), (11), and (12) in [10]. The analysis of [13] makes use of the coordinate pair:

$$\tilde{\xi} = 4\int_0^x (r^4\phi)^{1/3}dx,\quad \tilde{\eta} = (r\phi)^{1/3}\tilde{\xi}^{-1/4}y, \tag{1a,b}$$

a stream function $\tilde{f}(\tilde{\xi},\tilde{\eta}) = \tilde{\xi}^{-3/4}\psi(x,y)$ and a temperature function $\tilde{\theta}(\tilde{\xi},\tilde{\eta}) = \theta(x,y)$ to obtain

$$\tilde{f}''' + 3\tilde{f}\tilde{f}'' - \lambda(\tilde{f}')^2 + \tilde{\theta} = 4\tilde{\xi}\frac{\partial(\tilde{f}',\tilde{f})}{\partial(\tilde{\xi},\tilde{\eta})} \tag{2}$$

$$\mathrm{Pr}^{-1}\tilde{\theta}'' + 3\tilde{f}\tilde{\theta}' = 4\tilde{\xi}\frac{\partial(\tilde{\theta},\tilde{f})}{\partial(\tilde{\xi}\tilde{\eta})} \tag{3}$$

---

[1] Formerly Principal Engineer, Planning Research Corp., Kennedy Space Center, Fla. Now at NASA, White Sands Test Facility, Las Cruces, N.Mex.
[2] Professor, University of Illinois at Urbana-Champaign, Urbana, Ill. Fellow, ASME.
[3] Numbers in brackets designate References at end of technical note.

Contributed by the Heat Transfer Division of THE AMERICAN SOCIETY OF MECHANICAL ENGINEERS. Manuscript received by the Heat Transfer Division July 20, 1977.

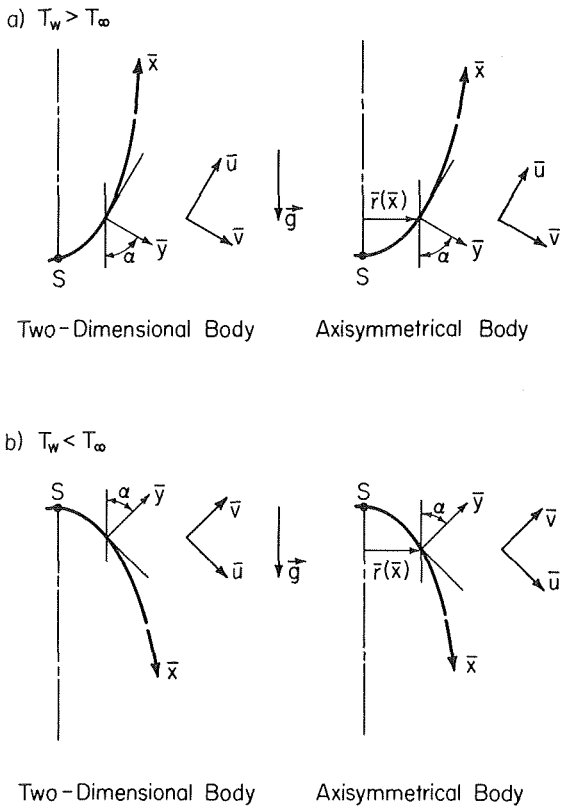

Fig. 1 Physical model and coordinate system

with boundary conditions:

$$\tilde{f}(\tilde{\xi},0) = \tilde{f}'(\tilde{\xi},0) = 0, \tilde{\theta}(\tilde{\xi},0) = 1 \quad (4a,b,c)$$

$$\tilde{f}'(\tilde{\xi},\infty) \to 0, \tilde{\theta}(\tilde{\xi},\infty) \to 0. \quad (5a,b)$$

In the foregoing, the prime denotes $\partial/\partial\eta$ and $\partial(\ ,\ )/\partial(\tilde{\xi},\tilde{\eta})$ is the Jacobian. The configuration function λ is given by

$$\lambda = 2 + \frac{1}{3}\frac{\tilde{\xi}}{(r^4\phi)^{1/3}}\frac{d}{dx}\ell n\ (\phi/r^2). \quad (6)$$

The Görtler series solution based on (2) and (3) is herein designated as S-I. Alternately, the coordinate-pair employed in [10] is:

$$\xi = \int_0^x r^2 U dx,\ \eta = rU(2\xi)^{-1/2}y \quad (7a,b)$$

where

$$U = \left[2\int_0^x \phi dx\right]^{1/2}. \quad (7c)$$

Upon introducing a stream function $f(\xi,\eta) = (2\xi)^{-1/2}\psi(x,y)$ and a temperature function $\theta(\xi,\eta)$ identically defined as $\tilde{\theta}(\tilde{\xi},\tilde{\eta})$, the momentum and energy equations become

$$f''' + ff'' + \Lambda[\theta - (f')^2] = 2\xi\frac{\partial(f',f)}{\partial(\xi,\eta)} \quad (8)$$

$$\mathrm{Pr}^{-1}\theta'' + f\theta' = 2\xi\frac{\partial(\theta,f)}{\partial(\xi,\eta)} \quad (9)$$

wherein the configuration function is

$$\Lambda = 2\xi\frac{d}{d\xi}\ell n\ U = 2\frac{\phi\xi}{r^2U^3}. \quad (10)$$

The boundary conditions are the same as those prescribed by (4) and (5). The Görtler series based on (8) and (9) is designated as S-II. When the body contour is such that λ or Λ is a constant, the boundary layer flow becomes self-similar. Under such condition, $\lambda = 3\Lambda$ as has been pointed out in [13]. In the more general case of nonsimilar flows, λ and Λ are expanded in series as follows:

$$\lambda(\tilde{\xi}) = \sum_{i=0}^{\infty}\lambda_i\tilde{\xi}^{i\gamma} \quad (11)$$

$$\Lambda(\xi) = \sum_{i=0}^{\infty}\Lambda_i\xi^{i\Gamma} \quad (12)$$

The quantities λ_0 and γ depend only on the class of body shape, not on the details of the contour. So do Λ_0 and Γ. For round-nosed cylinders, $\lambda_0 = 3$, $\gamma = 3/2$ and $\Lambda_0 = 1$, $\Gamma = 1$. For round-nosed axisymmetric bodies, $\lambda_0 = 3/2$, $\gamma = 3/4$, and $\Lambda_0 = 1/2$, $\Gamma = 1/2$.

The appropriate S-I series solutions are

$$\tilde{f}(\tilde{\xi},\tilde{\eta}) = \sum_{i=0}^{\infty}\tilde{f}_i(\tilde{\eta})\tilde{\xi}^{i\gamma} \quad (13)$$

$$\tilde{\theta}(\tilde{\xi},\tilde{\eta}) = \sum_{i=0}^{\infty}\tilde{\theta}_i(\tilde{\eta})\tilde{\xi}^{i\gamma} \quad (14)$$

from which the following equation sets can be readily established:

$$\tilde{f}'''_0 + 3\tilde{f}_0\tilde{f}''_0 - \lambda_0(\tilde{f}'_0)^2 + \tilde{\theta}_0 = 0 \quad (15)$$

$$\mathrm{Pr}^{-1}\tilde{\theta}''_0 + 3\tilde{f}_0\tilde{\theta}'_0 = 0 \quad (16)$$

with

$$\tilde{f}_0(0) = \tilde{f}'_0(0) = 0, \tilde{\theta}_0(0) = 1 \quad (17a,b,c)$$

$$\tilde{f}'_0(\infty) \to 0, \tilde{\theta}_0(\infty) \to 0; \quad (18a,b)$$

$$\tilde{f}'''_1 + 3\tilde{f}_0\tilde{f}''_1 - 2(\lambda_0 + 2\gamma)\tilde{f}_0\tilde{f}'_1 + (3+4\gamma)\tilde{f}''_0\tilde{f}_1 + \tilde{\theta}_1 = \lambda_1(\tilde{f}'_0)^2 \quad (19)$$

$$\mathrm{Pr}^{-1}\tilde{\theta}''_1 + 3\tilde{f}_0\tilde{\theta}_1' - 4\gamma\tilde{f}'_0\tilde{\theta}_1 + (3+4\gamma)\tilde{\theta}'_0\tilde{f}_1 = 0 \quad (20)$$

with

$$\tilde{f}_1(0) = \tilde{f}'(0) = 0, \tilde{\theta}_1(0) = 0 \quad (21a,b,c)$$

$$\tilde{f}'_1(\infty) \to 0, \tilde{\theta}_1(\infty) \to 0, \quad (22a,b)$$

etc.

The equation pair for the zeroth-order functions, (15) and (16), is identical to that of the Merk series reported in [13] when λ_0 is replaced by λ. The equations for the higher order functions can be made independent of the λ_i's ($i \geq 1$) by introducing

$$\left.\begin{aligned}\tilde{f}_1(\tilde{\eta}) &= \lambda_1\tilde{F}_1(\tilde{\eta})\\ \tilde{\theta}_1(\tilde{\eta}) &= \lambda_1\tilde{H}_1(\tilde{\eta})\end{aligned}\right\} \quad (23)$$

$$\left.\begin{aligned}\tilde{f}_2(\tilde{\eta}) &= \lambda_1^2\tilde{F}_{21}(\tilde{\eta}) + \lambda_2\tilde{F}_{22}(\tilde{\eta})\\ \tilde{\theta}_2(\tilde{\eta}) &= \lambda_1^2\tilde{H}_{21}(\tilde{\eta}) + \lambda_2\tilde{H}_{22}(\tilde{\eta})\end{aligned}\right\}, \text{etc.} \quad (24)$$

The functions, $\tilde{F}_1$, $\tilde{H}_1$, $\tilde{F}_{21}$, etc., are universal in the sense that they are independent of parameters associated with the details of the body contours, since $\gamma = 3/2$ for *all* round-nosed cylinders and $\gamma = 3/4$ for *all* round-nosed axisymmetric bodies as has already been pointed out.

The local heat transfer coefficient can be calculated from

$$\frac{\mathrm{Nu}}{\mathrm{Gr}^{1/4}} = \frac{(r\phi)^{1/3}}{\tilde{\xi}^{1/4}}\left[-\frac{\partial\tilde{\theta}}{\partial\tilde{\eta}}(\tilde{\xi},0)\right] \quad (25a)$$

where

$$\frac{\partial\tilde{\theta}}{\partial\tilde{\eta}}(\tilde{\xi},0) = \tilde{\theta}'_0(0) + \lambda_1\tilde{H}'_1(0)\,\tilde{\xi}^{\gamma} + [\lambda_1^2\tilde{H}'_{21}(0) + \lambda_2\tilde{H}'_{22}(0)]\tilde{\xi}^{2\gamma} + \cdots \quad (25b)$$

Similar expressions have been developed for the S-II series but we shall refrain from presenting the details.

The first three sets of coupled ordinary differential equations governing the universal functions $\tilde{f}_0$, $\tilde{\theta}_0$, $\tilde{F}_1$, $\tilde{H}_1$, $\tilde{F}_{21}$, $\tilde{H}_{21}$, $\tilde{F}_{22}$, and $\tilde{H}_{22}$ for S-I and a similar set for S-II have been numerically integrated for Pr ranging from 0.004 to 100 and for both round-nosed axisymmetric and two-dimensional bodies. Tables of their wall derivatives are available.

Comparison of Results

Recently, Merkin [14] presented data for local heat transfer coefficient over horizontal cylinders of circular and elliptical cross section for Pr = 0.70 and 1.0. These data were calculated by a finite difference numerical technique. A comparison of the dimensionless heat transfer parameter, expressed in terms of Nu $Gr^{-1/4}$ and obtained from various methods for a circular cylinder, is shown in Table 1. Since only the first two terms of the Blasius series for Pr = 0.70 are available, all series expansion results are based on two terms. In the case of both Merk and Görtler series, the second term is very small, being two to four orders of magnitude smaller than the first. The Blasius series has a constant first term which corresponds to the value at the stagnation point. The data of Table 1 indicate that the Merk series of [10] gives the best agreement with the finite difference calculation and the Blasius series is better than either Görtler series. It may also be stated that all series expansion results are acceptable, perhaps with the exception of the Görtler series at θ = 150 degrees. Had three terms been used, the Görtler series would yield 0.280 for S-I and 0.311 for S-II; thus, some improvement is obtained.

From a purely theoretical standpoint, it may be argued that the validity of a series solution should be examined within its radius of convergence and not be judged from the truncated series. In practice, however, when only a limited number of terms can be calculated as are all cases considered in the paper, the method of comparison used is quite acceptable on the basis of the semidivergent nature of the series and the relative magnitude of the available terms.

The results for an elliptical cylinder in slender configuration are shown in Fig. 2. The Merk series based on the coordinate system used in [10][4] gives excellent agreement with Merkin's data although some deterioration is observable when the ellipse eccentric angle measured from the stagnation point S exceeds 140 deg ($\bar{x}/2a$ = 0.9230). On the other hand, both Görtler series, S-I and S-II, and the Blasius series are completely useless except in the region very close to S. For example, at $\bar{x}/2a$ = 0.09624 which corresponds to the eccentric angle of 30 deg, the first three terms of the S-I series for Nu $Gr^{-1/4}$ are 0.6298 + 0.1043 − 0.7189 and the first two terms of the Blasius series are 0.8898 − 1.3983.

Fig. 3 summarizes the results for an elliptical cylinder in blunt configuration. The Merk series in [10] again agrees well with the finite difference data. Some minor discrepancies are noted in the region where the curve exhibits the maximum. The two Görtler series give good predictions only in the region when the eccentric angle is less than 70 deg ($\bar{x}/2a$ = 1.027), beyond which their usefulness rapidly deteriorates. The two-term Blasius series yields a monotonously increasing value of Nu $Gr^{-1/4}$ as $\bar{x}/2a$ increases and is judged to be unacceptable.

The predictive capability of the Görtler series, when applied to elliptical cylinders of both slender (a/b = 4) and blunt (a/b = 0.5) configuration, has also been extensively studied for Pr = 0.001, 0.01,

[4] Results obtained by Merk series based on the coordinate system of [13] are not as satisfactory.

Table 1 Local heat transfer parameter, Nu/$Gr^{1/4}$, for isothermal, horizontal, circular cylinder evaluated by various predictive methods (Pr = 0.70)

θ, deg.	Finite Difference [14]	Merk Series [10]	Blasius Series [1,3]	Görtler Series S-I	Görtler Series S-II
0	0.4402	0.4402	0.4402	0.4402	0.4402
30	0.4348	0.4346	0.4350	0.4351	0.4396
60	0.4190	0.4186	0.4192	0.4187	0.4241
90	0.3922	0.3913	0.3930	0.3898	0.3992
120	0.3532	0.3508	0.3563	0.3449	0.3664
150	0.2986	0.2923	0.3091	0.2740	0.3273

θ is the angle measured from the stagnation point; the reference length in Nu and Gr is cylinder diameter. Data under S-I are identical to those evaluated from [6].

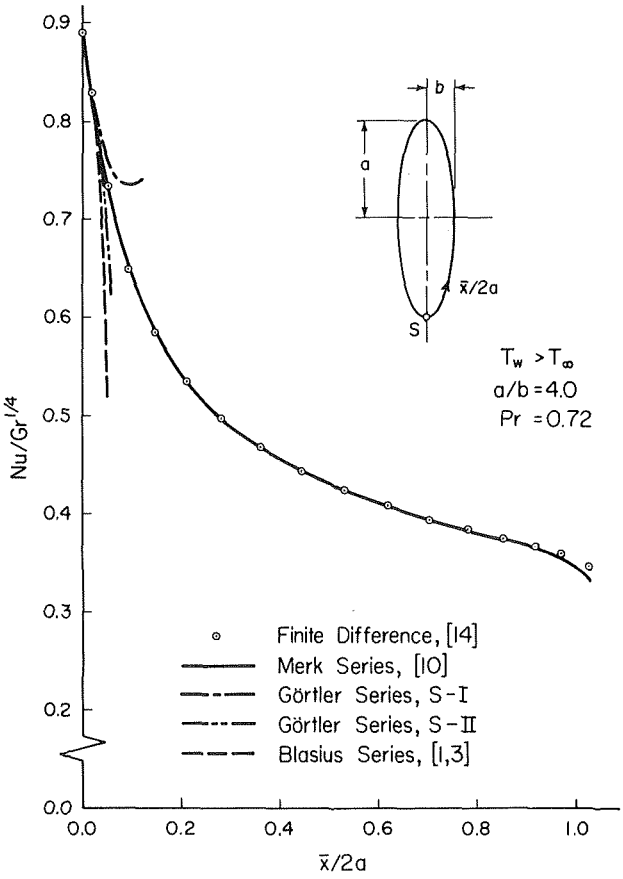

Fig. 2 Heat transfer over isothermal, horizontal, elliptical cylinder in slender configuration (reference length in Nu and Gr is 2a)

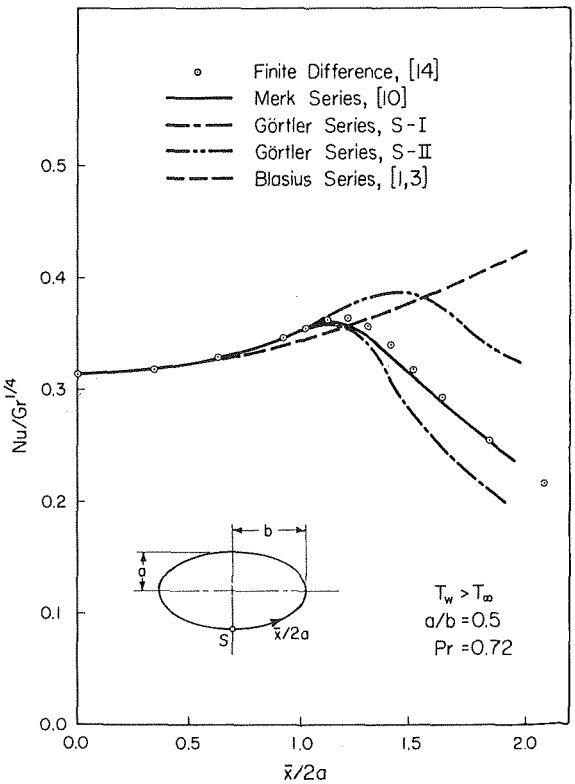

Fig. 3 Heat transfer over isothermal, horizontal, elliptical cylinder in blunt configuration (reference length in Nu and Gr is 2a)

10, and 100. The serious handicap just noted for Pr = 0.72 and illustrated in Figs. 2 and 3 generally persists. Details will not be given here since finite difference data are not available for comparison. Based on the examination of the first three terms of the series, it can be inferred that the inability of both Görtler series to be a predictive tool worsens progressively as Prandtl number decreases from 0.72 to 0.01 and 0.004. Some improvement is noted for Pr = 100 but not enough to justify their use.

We have also examined the predictive capability of the Blasius series for Pr = 0.004 and 0.01 using the wall derivatives of the appropriate universal functions recently given by Harpole and Catton [5]. Good results are obtained for circular cylinders. When applied to elliptical cylinders, the results are woefully disappointing. To illustrate, we cite here some computed data for an elliptical cylinder of $a/b = 4$. At the eccentric angle of 30 deg ($\bar{x}/2a = 0.09624$), which is not far from the stagnation point, the first three terms of the series for $\mathrm{Nu}\,\mathrm{Gr}^{-1/4}$ (with $2a$ as the reference length) read: 0.08965 − 0.12238 + 0.80699 for Pr = 0.004, and 0.13938 − 0.19207 + 1.2859 for Pr = 0.01.

The universal functions associated with the Merk series in [10] have not been computed for Pr = 0.01 and 0.004. Consequently, definitive conclusions will not be stated at this time. However, judging from the information obtained in this and earlier studies, the authors see no obvious reason why it will not perform well even though the predictions may not be as good as those for moderate or large Prandtl numbers.

References

1 Chang, T., and Kaye, J., "On Laminar Free Convection from a Horizontal Cylinder," *Proceedings, Fourth National Congress of Applied Mechanics*, University of California, Berkeley, June 1962, pp. 1213–1219.

2 Chiang, T., Ossin, A., and Tien, C. L., "Laminar Free Convection from a Sphere," ASME, JOURNAL OF HEAT TRANSFER, Vol. 86, 1964, pp. 537–542.

3 Koh, J. C. Y., and Price, J. F., "Laminar Free Convection from Nonisothermal Cylinder," ASME, JOURNAL OF HEAT TRANSFER, Vol. 87, 1965, pp. 237–242.

4 Fox, J., Discussion of References [2] and [3].

5 Harpole, G. M. and Catton, I., "Laminar Natural Convection about Downward Facing Heated Blunt Bodies to Liquid Metals," ASME, JOURNAL OF HEAT TRANSFER, Vol. 98, 1976, pp. 208–212.

6 Saville, D. A., and Churchill, S. W., "Laminar Free Convection in Boundary Layers near Horizontal Cylinders and Vertical Axisymmetric Bodies," *Journal Fluid Mech.*, Vol. 29, 1967, pp. 391–399.

7 Wilks, G., "External Natural Convection about Two-dimensional Bodies with Constant Heat Flux," *Internal Journal Heat Mass Transfer*, Vol. 15, 1972, pp. 351–354.

8 Lin, F. N., "Laminar Free Convection over Two-dimensional Bodies with Uniform Surface Heat Flux," *Letters in Heat and Mass Transfer*, Vol. 3, 1976, pp. 59–68.

9 Kelleher, M., and Yang, K. T., "A Görtler-type Series for Laminar Free Convection along a Non-isothermal Vertical Plate," *Quart. J. Mech. and Appl. Math.*, Vol. 25, 1972, pp. 447–457.

10 Lin, F. N. and Chao, B. T., "Laminar Free Convection over Two-Dimensional and Axisymmetric Bodies of Arbitrary Contour," ASME, JOURNAL OF HEAT TRANSFER, Vol. 96, 1974, pp. 435–442.

11 Merk, H. J., "Rapid Calculations for Boundary-Layer Transfer using Wedge Solutions and Asymptotic Expansions," *Journal of Fluid Mechanics*, Vol. 5, 1959, pp. 460–480.

12 Chao, B. T., and Fagbenle, R. O., "On Merk's Method of Calculating Boundary Layer Transfer," *Int. J. Heat Mass Transfer*, Vol. 17, 1974, pp. 223–240.

13 Chao, B. T., and Lin, F. N., "Local Similarity Solutions for Free Convection Boundary Layer Flows," ASME, JOURNAL OF HEAT TRANSFER, Vol. 97, 1975, pp. 294–296.

14 Merkin, J. H., "Free Convection Boundary Layers on Cylinders of Elliptic Cross Section," submitted for publication in ASME, JOURNAL OF HEAT TRANSFER, Vol. 99, 1977, pp. 453–457.

Nonsimilar Laminar Free Convection Flow Along a Nonisothermal Vertical Plate

B. K. Meena[1]
G. Nath[2]

Nomenclature

f = dimensionless stream function
g = dimensionless temperature
$\bar{g}$ = gravitational acceleration
$g'(s, 0)$, $g'(\xi, 0)$ = surface heat transfer parameters
G_w = Grashof number
G_{w0} = value of G_w at the leading edge
$G_{w\bar{x}}$ = local Grashof number
h, h_s = local convective heat-transfer coefficients
h_0 = value of h based on uniform surface temperature
k = thermal conductivity
L = characteristic length of the plate
p = surface temperature variation exponent
$\mathrm{Nu}_{\bar{x}}$ = local Nusselt number
Pr = Prandtl number
R = function of s
R_1 = ratio of heat transfer coefficients, h/h_0
s = ratio of Grashof numbers
T = temperature
T_w = surface temperature depending on $\bar{x}$
T_∞ = ambient temperature
u, v = dimensionless velocity components along $\bar{x}$ and $\bar{y}$ directions, respectively
$\bar{u}, \bar{v}$ = dimensional velocity components along $\bar{x}$ and $\bar{y}$ directions, respectively
$\bar{x}, \bar{y}$ = distances along and perpendicular to the plate, respectively
x, y = dimensionless distances along and perpendicular to the plate, respectively
β = parameter depending on s
β_1 = coefficient of volumetric expansion
ϵ = a positive constnat
η, ξ = transformed coordinates
ν = kinematic viscosity
ψ = dimensional stream function

Subscripts

s, x, y = partial derivatives
w = surface conditions

Superscript

′ (prime) = differentiation with respect to η

Introduction

The free convection problem on a nonisothermal vertical plate under boundary layer approximations has been studied by several authors [1–3][3] using approximate methods such as integral and series

[1] Research Student, Department of Applied Mathematics, Indian Institute of Science, Bangalore, India.

[2] Associate Professor, Department of Applied Mathematics, Indian Institute of Science, Bangalore, India.

Contributed by the Heat Transfer Division of THE AMERICAN SOCIETY OF MECHANICAL ENGINEERS. Manuscript received by the Heat Transfer Division June 30, 1977.

[3] Numbers in brackets designate References at end of technical note.

10, and 100. The serious handicap just noted for Pr = 0.72 and illustrated in Figs. 2 and 3 generally persists. Details will not be given here since finite difference data are not available for comparison. Based on the examination of the first three terms of the series, it can be inferred that the inability of both Görtler series to be a predictive tool worsens progressively as Prandtl number decreases from 0.72 to 0.01 and 0.004. Some improvement is noted for Pr = 100 but not enough to justify their use.

We have also examined the predictive capability of the Blasius series for Pr = 0.004 and 0.01 using the wall derivatives of the appropriate universal functions recently given by Harpole and Catton [5]. Good results are obtained for circular cylinders. When applied to elliptical cylinders, the results are woefully disappointing. To illustrate, we cite here some computed data for an elliptical cylinder of $a/b = 4$. At the eccentric angle of 30 deg ($\bar{x}/2a = 0.09624$), which is not far from the stagnation point, the first three terms of the series for $\mathrm{Nu}\,\mathrm{Gr}^{-1/4}$ (with $2a$ as the reference length) read: 0.08965 − 0.12238 + 0.80699 for Pr = 0.004, and 0.13938 − 0.19207 + 1.2859 for Pr = 0.01.

The universal functions associated with the Merk series in [10] have not been computed for Pr = 0.01 and 0.004. Consequently, definitive conclusions will not be stated at this time. However, judging from the information obtained in this and earlier studies, the authors see no obvious reason why it will not perform well even though the predictions may not be as good as those for moderate or large Prandtl numbers.

References

1 Chang, T., and Kaye, J., "On Laminar Free Convection from a Horizontal Cylinder," *Proceedings, Fourth National Congress of Applied Mechanics*, University of California, Berkeley, June 1962, pp. 1213–1219.

2 Chiang, T., Ossin, A., and Tien, C. L., "Laminar Free Convection from a Sphere," ASME, JOURNAL OF HEAT TRANSFER, Vol. 86, 1964, pp. 537–542.

3 Koh, J. C. Y., and Price, J. F., "Laminar Free Convection from Nonisothermal Cylinder," ASME, JOURNAL OF HEAT TRANSFER, Vol. 87, 1965, pp. 237–242.

4 Fox, J., Discussion of References [2] and [3].

5 Harpole, G. M. and Catton, I., "Laminar Natural Convection about Downward Facing Heated Blunt Bodies to Liquid Metals," ASME, JOURNAL OF HEAT TRANSFER, Vol. 98, 1976, pp. 208–212.

6 Saville, D. A., and Churchill, S. W., "Laminar Free Convection in Boundary Layers near Horizontal Cylinders and Vertical Axisymmetric Bodies," *Journal Fluid Mech.*, Vol. 29, 1967, pp. 391–399.

7 Wilks, G., "External Natural Convection about Two-dimensional Bodies with Constant Heat Flux," *Internal Journal Heat Mass Transfer*, Vol. 15, 1972, pp. 351–354.

8 Lin, F. N., "Laminar Free Convection over Two-dimensional Bodies with Uniform Surface Heat Flux," *Letters in Heat and Mass Transfer*, Vol. 3, 1976, pp. 59–68.

9 Kelleher, M., and Yang, K. T., "A Görtler-type Series for Laminar Free Convection along a Non-isothermal Vertical Plate," *Quart. J. Mech. and Appl. Math.*, Vol. 25, 1972, pp. 447–457.

10 Lin, F. N. and Chao, B. T., "Laminar Free Convection over Two-Dimensional and Axisymmetric Bodies of Arbitrary Contour," ASME, JOURNAL OF HEAT TRANSFER, Vol. 96, 1974, pp. 435–442.

11 Merk, H. J., "Rapid Calculations for Boundary-Layer Transfer using Wedge Solutions and Asymptotic Expansions," *Journal of Fluid Mechanics*, Vol. 5, 1959, pp. 460–480.

12 Chao, B. T., and Fagbenle, R. O., "On Merk's Method of Calculating Boundary Layer Transfer," *Int. J. Heat Mass Transfer*, Vol. 17, 1974, pp. 223–240.

13 Chao, B. T., and Lin, F. N., "Local Similarity Solutions for Free Convection Boundary Layer Flows," ASME, JOURNAL OF HEAT TRANSFER, Vol. 97, 1975, pp. 294–296.

14 Merkin, J. H., "Free Convection Boundary Layers on Cylinders of Elliptic Cross Section," submitted for publication in ASME, JOURNAL OF HEAT TRANSFER, Vol. 99, 1977, pp. 453–457.

Nonsimilar Laminar Free Convection Flow Along a Nonisothermal Vertical Plate

B. K. Meena[1]
G. Nath[2]

Nomenclature

f = dimensionless stream function
g = dimensionless temperature
$\bar{g}$ = gravitational acceleration
$g'(s, 0)$, $g'(\xi, 0)$ = surface heat transfer parameters
G_w = Grashof number
G_{w0} = value of G_w at the leading edge
$G_{w\bar{x}}$ = local Grashof number
h, h_s = local convective heat-transfer coefficients
h_0 = value of h based on uniform surface temperature
k = thermal conductivity
L = characteristic length of the plate
p = surface temperature variation exponent
$\mathrm{Nu}_{\bar{x}}$ = local Nusselt number
Pr = Prandtl number
R = function of s
R_1 = ratio of heat transfer coefficients, h/h_0
s = ratio of Grashof numbers
T = temperature
T_w = surface temperature depending on $\bar{x}$
T_∞ = ambient temperature
u, v = dimensionless velocity components along $\bar{x}$ and $\bar{y}$ directions, respectively
$\bar{u}, \bar{v}$ = dimensional velocity components along $\bar{x}$ and $\bar{y}$ directions, respectively
$\bar{x}, \bar{y}$ = distances along and perpendicular to the plate, respectively
x, y = dimensionless distances along and perpendicular to the plate, respectively
β = parameter depending on s
β_1 = coefficient of volumetric expansion
ϵ = a positive constnat
η, ξ = transformed coordinates
ν = kinematic viscosity
ψ = dimensional stream function

Subscripts

s, x, y = partial derivatives
w = surface conditions

Superscript

$'$ (prime) = differentiation with respect to η

Introduction

The free convection problem on a nonisothermal vertical plate under boundary layer approximations has been studied by several authors [1–3][3] using approximate methods such as integral and series

[1] Research Student, Department of Applied Mathematics, Indian Institute of Science, Bangalore, India.

[2] Associate Professor, Department of Applied Mathematics, Indian Institute of Science, Bangalore, India.

Contributed by the Heat Transfer Division of THE AMERICAN SOCIETY OF MECHANICAL ENGINEERS. Manuscript received by the Heat Transfer Division June 30, 1977.

[3] Numbers in brackets designate References at end of technical note.

expansion methods. Recently, Sparrow and co-workers [4–6] presented an approximate method known as the local nonsimilarity method, for solving nonsimilar boundary-layer problems, which gives more accurate results than the series and integral methods. More recently, Kao and Elrod [7] have developed another approximate method for the solution of nonsimilar boundary layer problems. The results are found to be slightly more accurate than those of the local nonsimilarity method. Further, Kao, et al. [8] have applied this technique to study the free convection problem on a vertical flat plate with sinusoidal and exponential wall temperature variations and linearly varying and exponentially increasing heat flux. They have compared their results with those of the difference-differential method and found them in excellent agreement.

In the present note, an implicit finite-difference technique [9] has been applied to study laminar free convection boundary-layer flow along a vertical flat plate with power-law distribution of wall temperature. It may be noted that Kao, et al. [8] have not studied this type of wall temperature variation. The results have been compared with those of the difference-differential, series, integral, and local nonsimilarity methods. Furthermore, the comparison has also been made with the results obtained by use of the asymptotic method developed by Kao and Elrod [7] and Kao, et al. [8].

Governing Equations. The equations governing the steady laminar boundary-layer free convection flow along a vertical nonuniformly heated flat plate can be expressed in the dimensionless form as [3, 8]

$$f''' + [3 - 2\beta(s)]ff'' - 2f'^2 + g = 4R(f'f_s' - f''f_s) \quad (1)$$

$$\mathrm{Pr}^{-1}g'' + [3fg' - 2\beta(s)(fg' + 2gf')] = 4R(f'g_s - g'f_s) \quad (2)$$

with boundary conditions

$$f(s, o) = f'(s, o) = f'(s, \infty) = g(s, \infty) = 0, g(s, o) = 1 \quad (3)$$

Here, the surface temperature has been assumed to be of the form [3]

$$\mathrm{G}_w/\mathrm{G}_{w0} = s = 1 + \epsilon x^p \quad (4)$$

where

$$\mathrm{G}_w = \bar{g}\beta_1 L^3(T_w - T_\infty)/\nu^2 \quad (5a)$$

$$\xi = \int_0^x \mathrm{G}_w dx = (s - 1)^{1/p}(p + s)(1/\epsilon)^{1/p}(p + 1)^{-1}\mathrm{G}_{w0} \quad (5b)$$

$$\eta = y[\mathrm{G}_w{}^2/(4\xi)]^{1/4}, \psi = \mathrm{G}_w(4\xi/\mathrm{G}_w{}^2)^{3/4}f(\xi, \eta) \quad (5c)$$

$$g(\xi, \eta) = (T - T_\infty)/(T_w - T_\infty), R = s\beta(s) \quad (5d)$$

$$\beta = (d\mathrm{G}_w/dx)\mathrm{G}_w{}^{-2}\int_0^x \mathrm{G}_w dx = p(p + s)(p - 1)^{-1}(s - 1)s^{-2} \quad (5e)$$

$$u = \bar{u}L/\nu = \psi_y, v = \bar{v}L/\nu = -\psi_x \quad (5f)$$

The local Nusselt number is given by [3]

$$\mathrm{Nu}_{\bar{x}}/(\mathrm{G}_{w\bar{x}})^{1/4} = -[x\mathrm{G}_w/(4\xi)]^{1/4}g'(\xi, 0) = -(2)^{-1/2}[s(p + 1)(p + s)^{-1/4}]^1.g'(s, o) \quad (6)$$

where

$$\mathrm{Nu}_{\bar{x}} = h\bar{x}/k, h = -k\,\partial T/\partial\bar{y})_w/(T_w - T_\infty) \quad (7a)$$

$$\mathrm{G}_{w\bar{x}} = \bar{g}\beta_1\bar{x}^3(T_w - T_\infty)/\nu^2, x = \bar{x}/L, y = \bar{y}/L \quad (7b)$$

It may be remarked that equations (1) and (2) have been written after correcting some minor printing mistakes in the equations given in reference [3] and they are same as those in reference [8].

Results and Discussion

Equations [1] and [2] under the boundary conditions of equation (3) have been solved numerically using an implicit finite-difference scheme. Since this method is treated in great detail in reference [9], for the sake of brevity, it is not repeated here. The velocity and temperature profiles are shown in Fig. 1. In accordance with the usual practice in free convection problems, the results in the form of the Nusselt number have been depicted in Fig. 2 which also contains the corresponding results of the integral solution [1], series solution [3], and local nonsimilarity (3-equation model) solution [4–6, 10]. In addition, Fig. 2 also contains the results obtained by use of the asymptotic method developed by Kao and Elrod [7] and Kao, et al. [8]. It is evident from Fig. 2 that the Nusselt number $\mathrm{Nu}_{\bar{x}}$ increases with s and p. The results are found to be in good agreement with those of the series method, local nonsimilarity method, and asymptotic method of references [7–8]. We have also compared our results with those of the difference-differential method [11–12] and found that they agree at least up to 3-decimal place. Hence, it is not shown in Fig. 2. The finite-difference or difference-differential method gives accurate solution for larger values of s as compared to other approximate methods. It may be noted that the local nonsimilarity solution method gives more accurate results than the series method whereas the asymptotic method of references [7–8] is found to give slightly better results than the local nonsimilarity method for large distances from the leading edge of the flat plate.

In order to compare our results with those of the integral method of reference [1], we introduce the ratio h/h_s given by [3]

$$h/h_s = [s^{1/2}\mathrm{Nu}_{\bar{x}}/\mathrm{G}_{w\bar{x}}{}^{1/4}]/[0.508\{\mathrm{Pr}^2/(0.952 + \mathrm{Pr})\}^{1/4}R_1] \quad (8)$$

where h_s is given by the integral method of reference [1], R_1 is also known from reference [1], and $\mathrm{Nu}_{\bar{x}}/\mathrm{G}_{w\bar{x}}{}^{1/4}$ is given by equation (6). The ratio h/h_s is shown in Fig. 2. As in reference [3], it is found that the integral solution overestimates the rates of heat transfer.

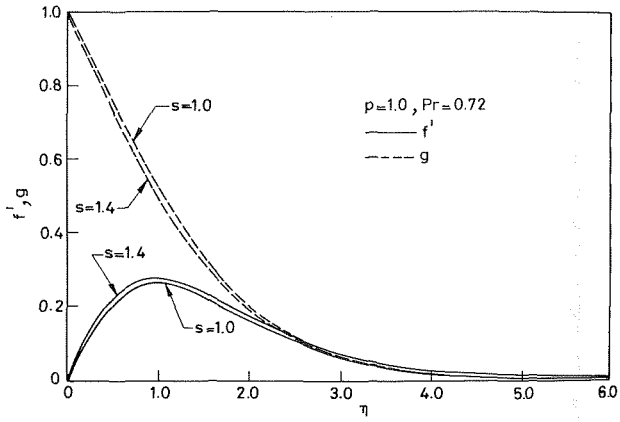

Fig. 1 Velocity and temperature profiles

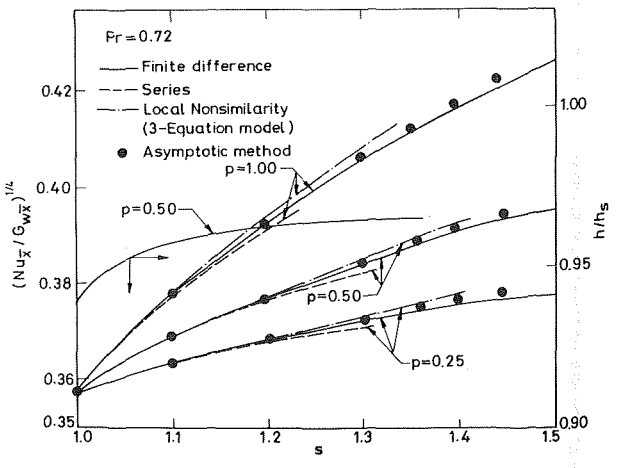

Fig. 2 Heat transfer distribution

Conclusions

The heat transfer increases along the flat plate. This conclusion is based upon limited study of the wall temperature distribution. The heat transfer may not increase along the plate if other wall temperature distributions are considered. The finite-difference results are almost the same as those of the difference-differential method and they are also in good agreement with those of the local nonsimilarity method and the asymptotic method of Kao and Elrod. However, the local nonsimilarity method gives more accurate results than the series method and the asymptotic method is found to be more accurate than the local nonsimilarity method for large distances from the leading edge. The integral solution overestimates the rates of heat transfer.

Acknowledgments

One of the authors (G. Nath) would like to thank the Council for International Exchange of Scholars, Washington, for the award of a fellowship and the Ohio State University for providing the facilities.

References

1 Sparrow, E. M., "Laminar Free Convection on a Vertical Plate with Prescribed Nonuniform Wall Heat Flux or Prescribed Nonuniform Wall Temperature," NACA Technical Note, No. 3508, 1955.

2 Kuiken, H. K., "General Series Solution for Free Convection Past a Nonisothermal Vertical Flat Plate," *Applied Scientific Research*, Vol. 20A, Nos. 2–3, Feb. 1969, pp. 205–215.

3 Kelleher, M., and Yang, K. T., "A Görtler-Type Series for Laminar Free Convection Along a Nonisothermal Vertical Plate," *Quarterly Journal of Mechanical and Applied Math.*, Vol. 25, Part 4, Nov. 1972, pp. 447–457.

4 Sparrow, E. M., Quack, H. and Boerner, C. J., "Local Nonsimilarity Boundary-Layer Solutions," *AIAA Journal*, Vol. 8, No. 11, Nov., 1970, pp. 1936–1942.

5 Sparrow, E. M., and Yu, H. S., "Local Nonsimilarity Thermal Boundary Layer Solutions," ASME, JOURNAL OF HEAT TRANSFER, Vol. 93, No. 4, Nov. 1971, pp. 328–334.

6 Minkovyez, W. J. and Sparrow, E. M., "Local Nonsimilarity Solution for Natural Convection on a Vertical Cylinder," ASME, JOURNAL OF HEAT TRANSFER, Vol. 96, No. 2, May 1974, pp. 178–183.

7 Kao, T., and Elrod, H. G., "Laminar Shear Stress Pattern in Nonsimilar Boundary Layers," *AIAA Journal*, Vol. 12, No. 10, Oct. 1974, pp. 1401–1408.

8 Kao, T., Domoto, G. A., and Elrod, H. G., "Free Convection Along a Nonisothermal Vertical Flat Plate," ASME, JOURNAL OF HEAT TRANSFER, Vol. 99, No. 1, Feb. 1977, pp. 72–78.

9 Marvin, J. G., and Sheaffer, Y. S., "A Method for Solving Nonsimilar Boundary Layer Equations Including Foreign Gas Injection," NASA Technical Note, No. D-5516, 1969.

10 Nath, G., "Nonsimilarity Solutions of a Class of Free Convection Problems," *Proceedings of Indian Academy of Science*, Vol. 84A, No. 3, Sept. 1976, pp. 114–123.

11 Smith, A. M. O. and Clutter, D. W., "Solution of Incompressible Laminar Boundary Layer Equations," *AIAA Journal*, Vol. 1, No. 9, Sept. 1963, pp. 2062–2071.

12 Smith, A. M. O., and Clutter, D. W., "Machine Calculation of Compressible Laminar Boundary Layers," *AIAA Journal*, Vol. 3, No. 4, Apr. 1965, pp. 639–647.

A Local Nonsimilarity Analysis of Free Convection From a Horizontal Cylindrical Surface

M. A. Muntasser[1] and J. C. Mulligan[1]

Nomenclature

Gr_w = Grashof number, $r^3g\beta(T_w - T_\infty)/\nu^2$
Nu = Nusselt number, hr/k
T_w = temperature of cylinder surface
T_∞ = ambient temperature of the fluid
x^* = actual coordinate along surface of cylinder
x = dimensionless angle from lower stagnation point, x^*/r
y^* = actual coordinate normal to cylinder surface
y = dimensionless normal coordinate, $y^*Gr_w{}^{1/4}/r$
$\phi_1(x), \phi_2(x)$ = azimuthal scaling functions, equation (1)
ψ^* = actual stream function
ψ = dimensionless stream function, $\psi^*/\nu Gr_w{}^{1/4}$

Introduction

The laminar, steady-state, free-convective heat transfer from an isothermal horizontal cylinder has been treated analytically in the literature many times with varying degrees of success. Approximate similarity transformations [1],[2] approximate series and integral procedures [2, 3, 4], and numerical finite difference methods [5] have all been employed in obtaining solutions of the thermal boundary-layer equations in this particular nonsimilar application. Unfortunately, the numerical results of these studies are not entirely consistent. In this paper, an analysis of this problem using the method of local nonsimilarity [6, 7, 8] is presented in an effort to reconcile the differences in these previous solutions, as well as to demonstrate the utility of the method in nonsimilar applications characterized by streamwise curvature. The technique of local nonsimilarity, in general, offers to nonsimilar convective heat transfer problems many of the advantages of similarity analysis while, at the same time, providing a direct and accurate alternative to the more laborious series methods. Also, in the present application, the technique facilitates a systematic elimination of the basic approximations of local similarity and coefficients invariance involved implicitly in Hermann's [1] classical approximate similarity procedure, while avoiding altogether the algebraic approximations necessarily utilized by Hermann in uniquely evaluating coordinate scaling functions.

Formulation

The basic conservation equations for the free convection from a horizontal cylinder are first simplified by introducing the similarity type transformations

$$\eta = y\phi_1(x),\ \psi = \phi_2(x)F(\eta,x),\ \Theta(\eta,x) = (T - T_\infty)/(T_W - T_\infty) \quad (1)$$

where ϕ_1 and ϕ_2 are unknown scaling functions. In terms of these variables, the transformed momentum and energy equations become

$$d\left(\frac{\partial^3 F}{\partial\eta^3}\right) + cF\left(\frac{\partial^2 F}{\partial\eta^2}\right) - (b + c)\left(\frac{\partial F}{\partial\eta}\right)^2 + \Theta = d(\phi_2/\phi_1)\left\{\frac{\partial F}{\partial\eta}\frac{\partial^2 F}{\partial x\,\partial\eta} - \frac{\partial F}{\partial x}\frac{\partial^2 F}{\partial\eta^2}\right\} \quad (2)$$

$$\frac{\partial^2\Theta}{\partial\eta^2} + a\,(\mathrm{Pr})\,F\frac{\partial\Theta}{\partial\eta} = \mathrm{Pr}(\phi_2/\phi_1)\left\{\frac{\partial F}{\partial\eta}\frac{\partial\Theta}{\partial x} - \frac{\partial\Theta}{\partial\eta}\frac{\partial F}{\partial x}\right\} \quad (3)$$

with $F = \partial F/\partial\eta = 0$ and $\Theta = 1$ at $\eta = 0$, and $\partial F/\partial\eta = 0$ and $\theta = 0$ as $\eta \to \infty$. The coefficient functions are defined by

$$\phi_2'/\phi_1 = a,\ \phi_2{}^2\phi_1\phi_1' = b \cdot \sin x \quad (4)$$

$$\phi_1{}^2\phi_2\phi_2' = c \cdot \sin x,\ \phi_2\phi_1{}^3 = d \cdot \sin x \quad (5)$$

where $\phi_1(x = 0)$ = constant and $\phi_2(x = 0) = 0$. The latter conditions follow from the flow pattern which must exist at $x = 0$.

It can be shown that of the functions a, b, c, and d, only one combination of two will yield a solution of equations (4) and (5) which is

[1] Mechanical and Aerospace Engineering Department, North Carolina State University, Raleigh, N. C.

[2] Numbers in brackets designate References at end of technical note.

Contributed by the Heat Transfer Division of THE AMERICAN SOCIETY OF MECHANICAL ENGINEERS. Manuscript received by the Heat Transfer Division June 13, 1977.

Conclusions

The heat transfer increases along the flat plate. This conclusion is based upon limited study of the wall temperature distribution. The heat transfer may not increase along the plate if other wall temperature distributions are considered. The finite-difference results are almost the same as those of the difference-differential method and they are also in good agreement with those of the local nonsimilarity method and the asymptotic method of Kao and Elrod. However, the local nonsimilarity method gives more accurate results than the series method and the asymptotic method is found to be more accurate than the local nonsimilarity method for large distances from the leading edge. The integral solution overestimates the rates of heat transfer.

Acknowledgments

One of the authors (G. Nath) would like to thank the Council for International Exchange of Scholars, Washington, for the award of a fellowship and the Ohio State University for providing the facilities.

References

1 Sparrow, E. M., "Laminar Free Convection on a Vertical Plate with Prescribed Nonuniform Wall Heat Flux or Prescribed Nonuniform Wall Temperature," NACA Technical Note, No. 3508, 1955.

2 Kuiken, H. K., "General Series Solution for Free Convection Past a Nonisothermal Vertical Flat Plate," *Applied Scientific Research*, Vol. 20A, Nos. 2–3, Feb. 1969, pp. 205–215.

3 Kelleher, M., and Yang, K. T., "A Görtler-Type Series for Laminar Free Convection Along a Nonisothermal Vertical Plate," *Quarterly Journal of Mechanical and Applied Math.*, Vol. 25, Part 4, Nov. 1972, pp. 447–457.

4 Sparrow, E. M., Quack, H. and Boerner, C. J., "Local Nonsimilarity Boundary-Layer Solutions," *AIAA Journal*, Vol. 8, No. 11, Nov., 1970, pp. 1936–1942.

5 Sparrow, E. M., and Yu, H. S., "Local Nonsimilarity Thermal Boundary Layer Solutions," ASME, JOURNAL OF HEAT TRANSFER, Vol. 93, No. 4, Nov. 1971, pp. 328–334.

6 Minkovyez, W. J. and Sparrow, E. M., "Local Nonsimilarity Solution for Natural Convection on a Vertical Cylinder," ASME, JOURNAL OF HEAT TRANSFER, Vol. 96, No. 2, May 1974, pp. 178–183.

7 Kao, T., and Elrod, H. G., "Laminar Shear Stress Pattern in Nonsimilar Boundary Layers," *AIAA Journal*, Vol. 12, No. 10, Oct. 1974, pp. 1401–1408.

8 Kao, T., Domoto, G. A., and Elrod, H. G., "Free Convection Along a Nonisothermal Vertical Flat Plate," ASME, JOURNAL OF HEAT TRANSFER, Vol. 99, No. 1, Feb. 1977, pp. 72–78.

9 Marvin, J. G., and Sheaffer, Y. S., "A Method for Solving Nonsimilar Boundary Layer Equations Including Foreign Gas Injection," NASA Technical Note, No. D-5516, 1969.

10 Nath, G., "Nonsimilarity Solutions of a Class of Free Convection Problems," *Proceedings of Indian Academy of Science*, Vol. 84A, No. 3, Sept. 1976, pp. 114–123.

11 Smith, A. M. O. and Clutter, D. W., "Solution of Incompressible Laminar Boundary Layer Equations," *AIAA Journal*, Vol. 1, No. 9, Sept. 1963, pp. 2062–2071.

12 Smith, A. M. O., and Clutter, D. W., "Machine Calculation of Compressible Laminar Boundary Layers," *AIAA Journal*, Vol. 3, No. 4, Apr. 1965, pp. 639–647.

A Local Nonsimilarity Analysis of Free Convection From a Horizontal Cylindrical Surface

M. A. Muntasser[1] and J. C. Mulligan[1]

Nomenclature

Gr_w = Grashof number, $r^3g\beta(T_w - T_\infty)/\nu^2$
Nu = Nusselt number, hr/k
T_w = temperature of cylinder surface
T_∞ = ambient temperature of the fluid
x^* = actual coordinate along surface of cylinder
x = dimensionless angle from lower stagnation point, x^*/r
y^* = actual coordinate normal to cylinder surface
y = dimensionless normal coordinate, $y^*Gr_w{}^{1/4}/r$
$\phi_1(x), \phi_2(x)$ = azimuthal scaling functions, equation (1)
ψ^* = actual stream function
ψ = dimensionless stream function, $\psi^*/\nu Gr_w{}^{1/4}$

Introduction

The laminar, steady-state, free-convective heat transfer from an isothermal horizontal cylinder has been treated analytically in the literature many times with varying degrees of success. Approximate similarity transformations [1],[2] approximate series and integral procedures [2, 3, 4], and numerical finite difference methods [5] have all been employed in obtaining solutions of the thermal boundary-layer equations in this particular nonsimilar application. Unfortunately, the numerical results of these studies are not entirely consistent. In this paper, an analysis of this problem using the method of local nonsimilarity [6, 7, 8] is presented in an effort to reconcile the differences in these previous solutions, as well as to demonstrate the utility of the method in nonsimilar applications characterized by streamwise curvature. The technique of local nonsimilarity, in general, offers to nonsimilar convective heat transfer problems many of the advantages of similarity analysis while, at the same time, providing a direct and accurate alternative to the more laborious series methods. Also, in the present application, the technique facilitates a systematic elimination of the basic approximations of local similarity and coefficients invariance involved implicitly in Hermann's [1] classical approximate similarity procedure, while avoiding altogether the algebraic approximations necessarily utilized by Hermann in uniquely evaluating coordinate scaling functions.

Formulation

The basic conservation equations for the free convection from a horizontal cylinder are first simplified by introducing the similarity type transformations

$$\eta = y\phi_1(x),\ \psi = \phi_2(x)F(\eta,x),\ \Theta(\eta,x) = (T - T_\infty)/(T_W - T_\infty) \quad (1)$$

where ϕ_1 and ϕ_2 are unknown scaling functions. In terms of these variables, the transformed momentum and energy equations become

$$d\left(\frac{\partial^3 F}{\partial\eta^3}\right) + cF\left(\frac{\partial^2 F}{\partial\eta^2}\right) - (b + c)\left(\frac{\partial F}{\partial\eta}\right)^2 + \Theta = d(\phi_2/\phi_1)\left\{\frac{\partial F}{\partial\eta}\frac{\partial^2 F}{\partial x\,\partial\eta} - \frac{\partial F}{\partial x}\frac{\partial^2 F}{\partial\eta^2}\right\} \quad (2)$$

$$\frac{\partial^2\Theta}{\partial\eta^2} + a\,(\mathrm{Pr})\,F\frac{\partial\Theta}{\partial\eta} = \mathrm{Pr}(\phi_2/\phi_1)\left\{\frac{\partial F}{\partial\eta}\frac{\partial\Theta}{\partial x} - \frac{\partial\Theta}{\partial\eta}\frac{\partial F}{\partial x}\right\} \quad (3)$$

with $F = \partial F/\partial\eta = 0$ and $\Theta = 1$ at $\eta = 0$, and $\partial F/\partial\eta = 0$ and $\theta = 0$ as $\eta \to \infty$. The coefficient functions are defined by

$$\phi_2'/\phi_1 = a,\ \phi_2{}^2\phi_1\phi_1' = b \cdot \sin x \quad (4)$$

$$\phi_1{}^2\phi_2\phi_2' = c \cdot \sin x,\ \phi_2\phi_1{}^3 = d \cdot \sin x \quad (5)$$

where $\phi_1(x = 0)$ = constant and $\phi_2(x = 0) = 0$. The latter conditions follow from the flow pattern which must exist at $x = 0$.

It can be shown that of the functions a, b, c, and d, only one combination of two will yield a solution of equations (4) and (5) which is

[1] Mechanical and Aerospace Engineering Department, North Carolina State University, Raleigh, N. C.

[2] Numbers in brackets designate References at end of technical note.

Contributed by the Heat Transfer Division of THE AMERICAN SOCIETY OF MECHANICAL ENGINEERS. Manuscript received by the Heat Transfer Division June 13, 1977.

consistent with the above boundary conditions on ϕ_1 and ϕ_2. In terms of a and c/a, the result is

$$\phi_1 = (c/a)^{1/3} (\sin x)^{1/3} \left[\frac{4}{3} a\,(c/a)^{1/3} \int_0^x (\sin \xi)^{1/3}\, d\xi \right]^{-1/4} \quad (6)$$

$$\phi_2 = \left[\frac{4}{3} a\,(c/a)^{1/3} \int_0^x (\sin \xi)^{1/3}\, d\xi \right]^{3/4}, \mathrm{d} = \mathrm{c/a} \quad (7)$$

$$b(x) = \frac{4}{9} (c/a)\, a\, (\sin x)^{-4/3} \times \cos x \int_0^x (\sin \xi)^{1/3}\, d\xi - \frac{1}{3} a(c/a) \quad (8)$$

To be consistent with the analysis of Hermann, the arbitrary functions a and (c/a) are chosen as 3 and 1, respectively. Thus, equations (6–8) determine a consistent set of values for $\phi_1(x)$, $\phi_2(x)$, and $b(x)$. The overall solution then follows from equations (2) and (3).

In Hermann's classical approximate similarity procedure, the right-hand sides of equations (2) and (3) are neglected at the outset and $b(x)$ assumed to be -1 for all x. The functions ϕ_1 and ϕ_2 are then determined approximately. From equation (8) it can be shown that $b(x)$ is actually -1 only at $x = \pi/2$, and that a rapid and substantial decrease occurs beyond $x = \pi/2$. Interestingly, even though $b(x)$ varies considerably, the values of the scaling functions ϕ_1 and ϕ_2, computed from equations (6) and (7), actually deviate only slightly from Hermann's algebraically approximate evaluation.

Local Similarity and Local Nonsimilarity Analysis

Local similarity is not new in boundary layer theory and, in essence, involves suppressing streamwise derivatives such as $\partial F/\partial x$, $\partial^2 F/\partial x\,\partial\eta$, *and* $\partial\theta/\partial x$, which occur in the right hand terms of equations (2) and (3). Such an analysis of the present problem thus involves the equations

$$F''' + 3FF'' - [b(x) + 3]\,(F')^2 + \theta = 0 \quad (9)$$

$$\theta'' + 3\,(\mathrm{Pr})\,F\theta' = 0 \quad (10)$$

where the primes denote differentiation with respect to η and $b(x)$ is determined from equation (8). If $b(x)$ is chosen as -1 for all x, the equations become the same as Hermann's, thus illustrating the two distinctly separate and partially compensating approximations involved in Hermann's procedure.

When the correct $b(x)$ function is employed along with local similarity, a high degree of error can be expected at large streamwise locations because of the deletions in the governing equations. To avoid this, the deletions are systematically transferred to coupled higher order equations by changes of variable. The procedure is, inherently, one of successive approximation and is known as the method of local nonsimilarity. In the present problem the technique avoids the $b(x)$ approximation as well as the local similarity approximation. First, the new functions $E(\equiv \partial F/\partial x)$ and $H(\equiv \partial\theta/\partial x)$ are defined and substituted into the right hand sides of equations (2) and (3), yielding two equations involving the four unknowns F, θ, E, and H. A second set of two equations, of higher level, are then obtained by differentiating with respect to x and subsequently deleting the terms $(\phi_2/\phi_1)\partial(F'E' - F''E)/\partial x$ and $(\mathrm{Pr})(\phi_2/\phi_1)\partial(F'H - \theta'E)/\partial x$. Thus, the complete system of equations for the local nonsimilarity, second level approximation become

$$F''' + 3FF'' - (b(x) + 3)(F')^2 + \theta = (\phi_2/\phi_1)(F'E' - F''E) \quad (11)$$

$$\theta'' + 3(\mathrm{Pr})\,F\theta' = \mathrm{Pr}(\phi_2/\phi_1)(F'H - \theta'E) \quad (12)$$

$$E''' + 3FE'' - (b(x) + 9)\,F'E' - (b(x) - 6)\,F''E - (F')^2 b'(x) + H = 0 \quad (13)$$

$$H'' + 3\,\mathrm{Pr}\,FH' + \mathrm{Pr}(b(x) - 3)\,F'H - \mathrm{Pr}(b(x) - 6)\,\theta'E = 0 \quad (14)$$

with the boundary conditions $F = F' = E = E' = H = 0$ and $\theta = 1$ when $\eta = 0$, and $F' = E' = \theta = H = 0$ as $\eta \to \infty$.

A third level analysis involving a total of six equations could be developed in the same manner, thus displacing the approximation even further from the fundamental energy and momentum equations. This added computation, however, was not found to be necessary in the present application.

The numerical evaluation of $\phi_1(x)$, $\phi_2(x)$, and $b(x)$ from equations (6, 7), and (8) is straightforward. An implicit finite difference numerical method [9] known as "accelerated successive replacement", which has been found to be particularly suited for the solution of some types of ordinary differential equations, was used in solving the equations comprising both the first level (local similarity) as well as the second level (local nonsimilarity) systems. Hermann's results provided a convenient starting point for the implicit computation.

Results and Discussion

Numerical results were obtained for Prandtl numbers of 0.72, 0.733, 1.0, 5.0, and 10.0. The ratio of the local Nussett number Nu_x and $\mathrm{Gr}_w^{1/4}$, $\mathrm{Nu}_x/\mathrm{Gr}_w^{1/4} = -\phi_1(x)\,\theta'(x, \eta = 0)$, are plotted in Fig. 1 for a Prandtl number of 1.0 and various locations x, along with local values obtained by other investigators using other methods. The first level results agree very well with Merkin's finite difference data on the lower side of the cylinder and up to $x = 120$ deg, where the variation is not more than 1.87 percent. But, as expected, the computations begin to deviate appreciably at $x > 120$ deg, with the error reaching 30 percent at 150 deg.

It can be seen that the difference between the first and the second level computations are negligible on the forward side of the cylinder. The second level solution corrected the rear-side deviation from Merkin's data to less than one percent at 150 deg. The deviation between the second level and Hermann's result, however, is as high as nine percent at the larger angles ($x = 150$ deg), and as low as 0.04 percent at $x = 90$ deg. Hermann's result is clearly most accurate in the neighborhood of $x = 90$ deg.

The difference between the second level and the Gortler series solution is as high as nine percent at $x = 150$ deg although negligible on the forward side. It can also be seen that the second level solution is closer to the finite-difference solution than any of the other approximate results presented in Fig. 1, whereas Hermann's results are low by as much as eight percent. Surprisingly, the Blasius series solution appears to be the most accurate of the previously available solutions.

Table 1 shows the results of computations of $\mathrm{Nu}_x/\mathrm{Gr}_w^{1/4}$ for various

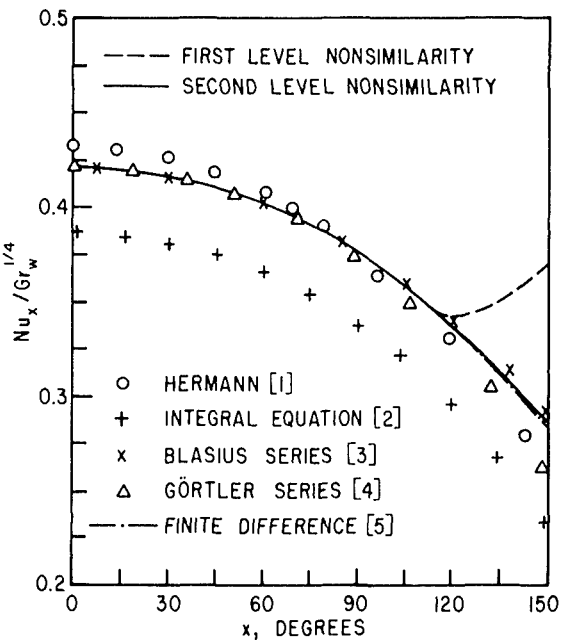

Fig. 1 Peripheral variation of the local convective heat transfer from a horizontal cylinder for Pr = 1.0

Table 1 The ratio of the local Nusselt number and Grashof number, $Nu_x/Gr_w^{1/4}$, for various azimuthal angles x and Prandtl numbers.

Pr / x	0.72		0.733		1.0		5.0		10.0	
	First Level	Second Level	First Level	Second Level	First Level	Second Level	First Level	Second Level	First Level	Second Level
0	0.3743	0.3745	0.3768	0.3770	0.4216	0.4214	0.7169	0.7142	0.8821	0.8822
30	0.3697	0.3700	0.3722	0.3724	0.4164	0.4162	0.7075	0.7051	0.8703	0.8699
60	0.3565	0.3567	0.3588	0.3590	0.4013	0.4010	0.6798	0.6790	0.8356	0.8350
90	0.3347	0.3344	0.3368	0.3365	0.3762	0.3753	0.6330	0.6325	0.7765	0.7753
120	0.3062	0.3020	0.3081	0.3039	0.3427	0.3379	0.5665	0.5617	0.6912	0.6877
150	0.3424	0.2598	0.3442	0.2611	0.3704	0.2853	0.5276	0.4485	0.6163	0.5435
Arithmetic Mean	0.3473	0.3329	0.3500	0.3350	0.3881	0.3729	0.6386	0.6235	0.7787	0.7656
Jodlbauer [4]*	0.3330		0.3354		0.3789		0.6512		0.7435	
Churchill and Chu [11]	0.3040		0.3060		0.3397		0.5813		0.7150	
Morgan [10]	0.3718		0.3734		0.4036		0.6035		0.7178	
Hermann [1]*	0.3106		0.3128		0.3534		0.6073		0.7401	

*Data corrected for Prandtl number using interpolation formula of Merk and Prins [2].

values of the Prandtl number and at various locations x. Also, the arithmatic mean, $(Nu_m/Gr_w^{1/4})$, is compared with the mean value computed from the empirical correlations of Morgan [10], Churchill and Chu [11], and the corrected data of Jodlbauer [4]. Interestingly, the present results for the arithmetic mean computed from the second level are as much as nine percent higher than those of Churchill and Chu, deviate by as much as ten percent from Morgan's, yet are only four percent from Jodlbauer's corrected data. Thus, in the intermediate Prandtl number range of interest here, it appears the empirical data of Jodlbauer, corrected using the Prandtl number interpolation formula of Merk and Prins [2], is the most accurate. Hermann's analytical result for the mean value of the ratio $Nu/Gr_w^{1/4}$, corrected for Prandtl number, deviates from the second level by as much as 6.6 percent.

Conclusions

The method of local nonsimilarity was found to be a simple, direct, and accurate procedure in reducing the partial differential equations of streamwise nonsimilar free convection to a format of ordinary differential equations. When coupled with a computer routine for solving ordinary differential equations, such as the method of accelerated successive replacement, accurate and inexpensive boundary-layer computations are readily carried out. Moreover, the technique preserves many of the advantages inherent in similarity analysis. In the present formulation, for example, the functions ϕ_1, ϕ_2, and $b(x)$ are only geometry dependent and, after the geometry is specified, cases of various boundary conditions with various conditions of dissipation or radiation can be considered with little modification. Local computations are readily carried out without the need for streamwise numerical iteration (discretization).

For the case of the isothermal horizontal cylinder, it was found that only two levels of computation produced results significantly more accurate than either series or integral procedures and within one percent of those obtained by finite difference computation, thus corroborating for the first time the correctness of these data. In addition, it was shown that the commonly held notion that Hermann's classical solution is accurate everywhere except at the upper and lower stagnation points is not entirely correct. It is, essentially, a solution which is accurate only in the immediate neighborhood of $x = 90$ deg.

Acknowledgment

This research was supported by the National Science Foundation, NSF Grant No. ENG 75-14616, and the support is gratefully acknowledged.

References

1 Hermann, R., "Heat Transfer by Free Convection from Horizontal Cylinders in Diatomic Gases," NACA Technical Member, 1366, 1954.

2 Merk, H. J., and Prins, J. A., "Thermal Convection in Laminar Boundary Layers, III," *Journal of Applied Scientific Research*, Sec. A, Vol. 4, 1953, pp. 207–220.

3 Chiang, T., and Kaye, J., "On Laminar Free Convection from a Horizontal Cylinder," *Proceedings of the Fourth National Congress of Applied Mechanics*, 1962, pp. 1213–1219.

4 Saville, D. A., and Churchill, S. W., "Laminar Free Convection in Boundary Layers Near Horizontal Cylinders and Vertical Axisymmetric Bodies," *Journal Fluid Mechanics*, Vol. 29, 1967, pp. 391–399.

5 Merkin, J. H., "Free Convection Boundary Layer on an Isothermal Horizontal Cylinder," ASME Paper No. 76-HT-16, Presented at ASME-AICHE Heat Transfer Conference, St. Louis, Mo., Aug. 9–11, 1976.

6 Sparrow, E. M., Quack, H., and Boerner, C. J., "Local Nonsimilarity Boundary-Layer Solutions," *AIAA Journal*, Vol. 8, 1970, pp. 1936–1942.

7 Sparrow, E. M., and Yu, H. S., "Local Nonsimilarity Thermal Boundary-Layer Solutions," JOURNAL OF HEAT TRANSFER, TRANS. ASME, Series C, Vol. 93, 1971, pp. 328–334.

8 Minkowycz, W. J., and Sparrow, E. M., "Local Nonsimilar Solutions for Natural Convection on a Vertical Cylinder," JOURNAL OF HEAT TRANSFER, TRANS ASME, Series, C, Vol. 96, 1974, pp. 178–183.

9 Lew, H. G., "Method of Accelerated Successive Replacement Applied to Boundary-Layer Equations," *AIAA Journal*, Vol. 6, 1968, pp. 929–931.

10 Morgan, V. T., "The Overall Convective Heat Transfer from Smooth Circular Cylinders," *Advances in Heat Transfer*, Vol. 11, 1975, pp. 199–264.

11 Churchill, S. W., and Chu, H. H. S., "Correlating Equations for Laminar and Turbulent Free Convection from a Horizontal Cylinder," *International Journal Heat Mass Transfer*, Vol. 18, 1975, pp. 1049–1053.

Transient Temperature Profile of a Hot Wall Due to an Impinging Liquid Droplet

M. Seki[1]
H. Kawamura[2]
K. Sanokawa[3]

An experiment was made to investigate the heat transfer to a liquid drop impinging on a hot surface. The transient temperature of the heater surface was measured by a thin-film thermometer. The surface temperature fell to a contact temperature immediately after contact with the drop. The contact temperature increased with increasing initial surface temperature T_0. In the case of the water drop, however, it was approximately constant for $200°C \lesssim T_0 \lesssim 300°C$; and it increased again for $T_0 \gtrsim 300°C$. The surface temperature at the turning point, i.e., $T_0 \sim 300°C$, roughly coincided with the Leidenfrost point.

Introduction

Knowledge of heat transfer from a hot wall to an impinging liquid droplet is required for analysis of spray cooling, quenching, cool down of a cryogenic pump, etc.

When a drop falls on a solid surface at a temperature higher than the Leidenfrost point, a vapor layer forms beneath the drop immediately. The drop is then said to be in the spherodial state. Many studies ([1],[4] for example) have been made of the heat transfer to a drop in the spherodial state, but only a few studies [2, 3] have been made of the formation process of the vapor layer. The purpose of the present study is to measure the rapid change of the temperature of the hot surface during the formation of the vapor layer below a liquid drop.

[1] Research scientist, Japan Atomic Energy Research Institute, Tokai-mura, Ibaraki-ken, Japan.

[2] Research scientist, Japan Atomic Energy Research Institute, Tokai-mura, Ibaraki-kem, Japan.

[3] Principal scientist, Chief of Heat Transfer Lab, Japan Atomic Energy Research Institute, Tokai-mura, Ibaraki-ken, Japan.

[4] Numbers in brackets designate References at end of technical note.

Contributed by the Heat Transfer Division of THE AMERICAN SOCIETY OF MECHANICAL ENGINEERS. Manuscript received by the Heat Transfer Division.

Table 1 The ratio of the local Nusselt number and Grashof number, $Nu_x/Gr_w^{1/4}$, for various azimuthal angles x and Prandtl numbers.

Pr / x	0.72		0.733		1.0		5.0		10.0	
	First Level	Second Level	First Level	Second Level	First Level	Second Level	First Level	Second Level	First Level	Second Level
0	0.3743	0.3745	0.3768	0.3770	0.4216	0.4214	0.7169	0.7142	0.8821	0.8822
30	0.3697	0.3700	0.3722	0.3724	0.4164	0.4162	0.7075	0.7051	0.8703	0.8699
60	0.3565	0.3567	0.3588	0.3590	0.4013	0.4010	0.6798	0.6790	0.8356	0.8350
90	0.3347	0.3344	0.3368	0.3365	0.3762	0.3753	0.6330	0.6325	0.7765	0.7753
120	0.3062	0.3020	0.3081	0.3039	0.3427	0.3379	0.5665	0.5617	0.6912	0.6877
150	0.3424	0.2598	0.3442	0.2611	0.3704	0.2853	0.5276	0.4485	0.6163	0.5435
Arithmetic Mean	0.3473	0.3329	0.3500	0.3350	0.3881	0.3729	0.6386	0.6235	0.7787	0.7656
Jodlbauer [4]*	0.3330		0.3354		0.3789		0.6512		0.7435	
Churchill and Chu [11]	0.3040		0.3060		0.3397		0.5813		0.7150	
Morgan [10]	0.3718		0.3734		0.4036		0.6035		0.7178	
Hermann [1]*	0.3106		0.3128		0.3534		0.6073		0.7401	

*Data corrected for Prandtl number using interpolation formula of Merk and Prins [2].

values of the Prandtl number and at various locations x. Also, the arithmatic mean, $(Nu_m/Gr_w^{1/4})$, is compared with the mean value computed from the empirical correlations of Morgan [10], Churchill and Chu [11], and the corrected data of Jodlbauer [4]. Interestingly, the present results for the arithmetic mean computed from the second level are as much as nine percent higher than those of Churchill and Chu, deviate by as much as ten percent from Morgan's, yet are only four percent from Jodlbauer's corrected data. Thus, in the intermediate Prandtl number range of interest here, it appears the empirical data of Jodlbauer, corrected using the Prandtl number interpolation formula of Merk and Prins [2], is the most accurate. Hermann's analytical result for the mean value of the ratio $Nu/Gr_w^{1/4}$, corrected for Prandtl number, deviates from the second level by as much as 6.6 percent.

Conclusions

The method of local nonsimilarity was found to be a simple, direct, and accurate procedure in reducing the partial differential equations of streamwise nonsimilar free convection to a format of ordinary differential equations. When coupled with a computer routine for solving ordinary differential equations, such as the method of accelerated successive replacement, accurate and inexpensive boundary-layer computations are readily carried out. Moreover, the technique preserves many of the advantages inherent in similarity analysis. In the present formulation, for example, the functions ϕ_1, ϕ_2, and $b(x)$ are only geometry dependent and, after the geometry is specified, cases of various boundary conditions with various conditions of dissipation or radiation can be considered with little modification. Local computations are readily carried out without the need for streamwise numerical iteration (discretization).

For the case of the isothermal horizontal cylinder, it was found that only two levels of computation produced results significantly more accurate than either series or integral procedures and within one percent of those obtained by finite difference computation, thus corroborating for the first time the correctness of these data. In addition, it was shown that the commonly held notion that Hermann's classical solution is accurate everywhere except at the upper and lower stagnation points is not entirely correct. It is, essentially, a solution which is accurate only in the immediate neighborhood of $x = 90$ deg.

Acknowledgment

This research was supported by the National Science Foundation, NSF Grant No. ENG 75-14616, and the support is gratefully acknowledged.

References

1 Hermann, R., "Heat Transfer by Free Convection from Horizontal Cylinders in Diatomic Gases," NACA Technical Member, 1366, 1954.

2 Merk, H. J., and Prins, J. A., "Thermal Convection in Laminar Boundary Layers, III," *Journal of Applied Scientific Research*, Sec. A, Vol. 4, 1953, pp. 207–220.

3 Chiang, T., and Kaye, J., "On Laminar Free Convection from a Horizontal Cylinder," *Proceedings of the Fourth National Congress of Applied Mechanics*, 1962, pp. 1213–1219.

4 Saville, D. A., and Churchill, S. W., "Laminar Free Convection in Boundary Layers Near Horizontal Cylinders and Vertical Axisymmetric Bodies," *Journal Fluid Mechanics*, Vol. 29, 1967, pp. 391–399.

5 Merkin, J. H., "Free Convection Boundary Layer on an Isothermal Horizontal Cylinder," ASME Paper No. 76-HT-16, Presented at ASME-AICHE Heat Transfer Conference, St. Louis, Mo., Aug. 9–11, 1976.

6 Sparrow, E. M., Quack, H., and Boerner, C. J., "Local Nonsimilarity Boundary-Layer Solutions," *AIAA Journal*, Vol. 8, 1970, pp. 1936–1942.

7 Sparrow, E. M., and Yu, H. S., "Local Nonsimilarity Thermal Boundary-Layer Solutions," JOURNAL OF HEAT TRANSFER, TRANS. ASME, Series C, Vol. 93, 1971, pp. 328–334.

8 Minkowycz, W. J., and Sparrow, E. M., "Local Nonsimilar Solutions for Natural Convection on a Vertical Cylinder," JOURNAL OF HEAT TRANSFER, TRANS ASME, Series, C, Vol. 96, 1974, pp. 178–183.

9 Lew, H. G., "Method of Accelerated Successive Replacement Applied to Boundary-Layer Equations," *AIAA Journal*, Vol. 6, 1968, pp. 929–931.

10 Morgan, V. T., "The Overall Convective Heat Transfer from Smooth Circular Cylinders," *Advances in Heat Transfer*, Vol. 11, 1975, pp. 199–264.

11 Churchill, S. W., and Chu, H. H. S., "Correlating Equations for Laminar and Turbulent Free Convection from a Horizontal Cylinder," *International Journal Heat Mass Transfer*, Vol. 18, 1975, pp. 1049–1053.

Transient Temperature Profile of a Hot Wall Due to an Impinging Liquid Droplet

M. Seki[1]
H. Kawamura[2]
K. Sanokawa[3]

An experiment was made to investigate the heat transfer to a liquid drop impinging on a hot surface. The transient temperature of the heater surface was measured by a thin-film thermometer. The surface temperature fell to a contact temperature immediately after contact with the drop. The contact temperature increased with increasing initial surface temperature T_0. In the case of the water drop, however, it was approximately constant for $200°C \lesssim T_0 \lesssim 300°C$; and it increased again for $T_0 \gtrsim 300°C$. The surface temperature at the turning point, i.e., $T_0 \sim 300°C$, roughly coincided with the Leidenfrost point.

Introduction

Knowledge of heat transfer from a hot wall to an impinging liquid droplet is required for analysis of spray cooling, quenching, cool down of a cryogenic pump, etc.

When a drop falls on a solid surface at a temperature higher than the Leidenfrost point, a vapor layer forms beneath the drop immediately. The drop is then said to be in the spherodial state. Many studies ([1],[4] for example) have been made of the heat transfer to a drop in the spherodial state, but only a few studies [2, 3] have been made of the formation process of the vapor layer. The purpose of the present study is to measure the rapid change of the temperature of the hot surface during the formation of the vapor layer below a liquid drop.

[1] Research scientist, Japan Atomic Energy Research Institute, Tokai-mura, Ibaraki-ken, Japan.

[2] Research scientist, Japan Atomic Energy Research Institute, Tokai-mura, Ibaraki-kem, Japan.

[3] Principal scientist, Chief of Heat Transfer Lab, Japan Atomic Energy Research Institute, Tokai-mura, Ibaraki-ken, Japan.

[4] Numbers in brackets designate References at end of technical note.

Contributed by the Heat Transfer Division of THE AMERICAN SOCIETY OF MECHANICAL ENGINEERS. Manuscript received by the Heat Transfer Division.

Experiment

The hot surface was an upper surface of the stainless steel cylinder 32 mm in diameter (see Fig. 1). It was finished with number 1000 emery papers. Heat was supplied by a sheathed heater wound around the cylinder. A liquid drop of distilled water or ethanol was dropped from a needle held 20 mm over the surface. The weight of a drop was 10.8 mg for water and 3.75 mg for ethanol. The initial temperature of a drop was nearly 20°C. A thin-film thermometer was employed to measure the rapid change of the surface temperature. A shape of the evaporated film is shown in Fig. 1. Silicon monoxide (SiO) was evaporated on the hot surface as an electric insulator; then nickel was deposited on it. SiO was evaporated again over the nickel film to protect it from oxidation at high temperatures. The thickness of the SiO layer was on the order of 0.1 μm and that of the nickel was about 0.5 μm. The drop made contact within a very small area; so the nickel film was designed to measure the local temperature just beneath the drop. Potential terminals C and D were fitted in addition to current terminals A and B. A constant current was supplied from A to B. Resistance change was detected by the change of the potential difference between C and D. Then, the surface temperature in the area bounded by C and D (0.9 mm × 1.2 mm) could be measured.

Results and Discussion

Typical temperature traces are shown in Fig. 2. Immediately after the contact with a liquid drop, the hot surface temperature suddenly dropped to the "contact" temperature (T_c). The sudden drop was followed by an oscillatory variation. These oscillatory changes probably indicate nucleate boiling. Liquid-solid contact was studied by Bradfield [4] and other investigators. It was found that the contact was nearly periodic for a bouncing droplet. However, the period of the present temperature oscillation was random and much shorter than that of the bouncing. Therefore, the oscillation is attributable to the boiling.

The boiling became more vigorous as the surface temperature increased. When the initial surface superheat ΔT_0 reached about 170 K, the water drop obtained the spheroidal state. For 170 K $\lesssim T_0 \lesssim$ 200 K, however, some oscillation is still in evidence suggesting that the drop then wets the surface intermittently. For $T_0 \gtrsim$ 200 K, the temperature drop suddenly and recovers smoothly; no oscillation can be observed in the traces (see Fig. 2-a-4). In this case, the minimum surface temperature was reached within ten ms. For an ethanol drop, the amplitude of temperature oscillation was smaller and the frequency higher than for the water drop.

The behavior of the liquid drop changed with the initial surface temperature. When T_0 was low, the drop was quiescent and the formation of a large single bubble was repeated (Fig. 2-a-1). The boiling became vigorous as the increase of the surface temperature and explosive vapor generation sometimes scattered the drop (Figs. 2-a-2 and 2-b-2). The bouncing occurred at a relatively high temperature near the Leidenfrost point (Fig. 2-a-3). When the temperature exceeded the Leidenfrost point, the drop obtained the spheroidal state and moved about.

Total vaporization time for $T_0 \gtrsim$ 200°C was measured with a stopwatch using a slightly concave heating surface. The effect of the SiO film on the vaporization time was tested, and the results are shown in Fig. 3. The vaporization time obtained here agrees well with Baumeister's correlation [1]. The data indicate that the Leidenfrost

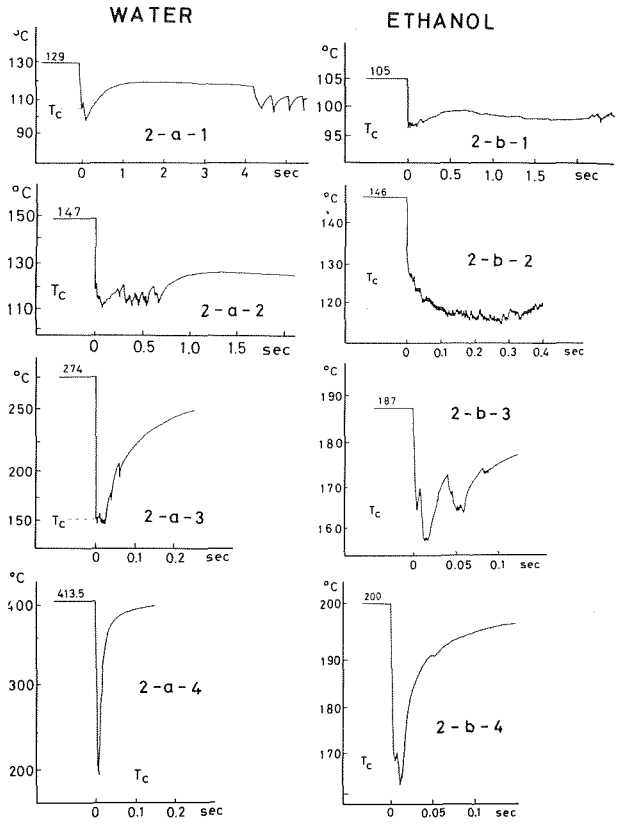

Fig. 2 Typical temperature traces, surface temperature versus time

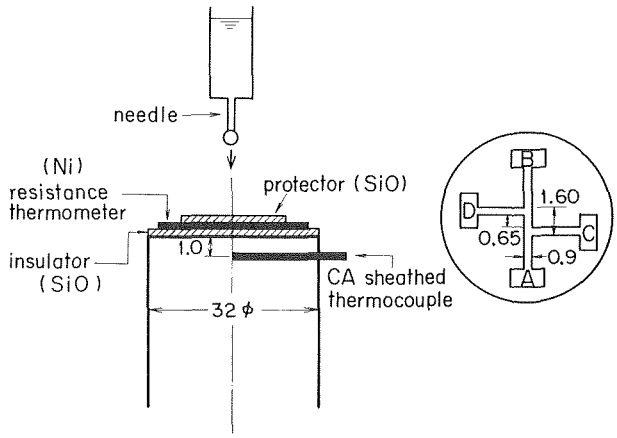

Fig. 1 Experimental apparatus

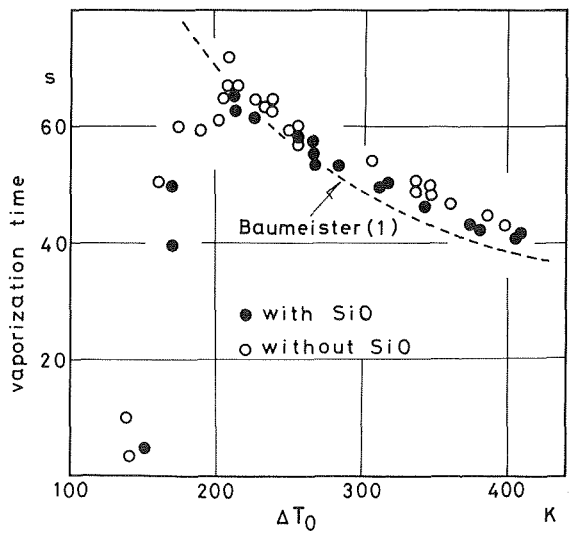

Fig. 3 The total vaporization time of a water drop on the surfaces with and without the SiO film

temperature in this study is about 300°C and that the SiO film has only a small effect on the vaporization time.

The contact temperature is plotted against the initial surface superheat in Fig. 4. The contact temperature can be expressed in "superheat", $\Delta T_C = T_C - T_{sat}$. This will be called "contact superheat" hereafter. Let us assume that two solids, initially at different temperatures T_1 and T_2, are suddenly brought into contact. Then the temperature at the contact surface is given by $T_C^* = (T_1\beta_1 + T_2\beta_2)/(\beta_1 + \beta_2)$ [5]. Here, β is $\sqrt{\rho ck}$, and ρ, c, and k represent density, specific heat, and thermal conductivity, respectively. The contact superheat $\Delta T_C^* = (T_C^* - T_{sat})$ is shown by the broken lines for water and ethanol in Fig. 4.

Water Drop. For $\Delta T_0 \lesssim 70$ K, the contact superheat ΔT_C increases with the increasing initial surface superheat. It is in fair agreement with the theoretical ΔT_C^*. So, the boiling does not occur at the moment of the initial contact. For 100 K $\lesssim \Delta T_0 \lesssim$ 200 K, ΔT_C is approximately constant (about 50 K) and is far below ΔT_C^*. The nucleate boiling starts during the initial decrease of the surface temperature. When $\Delta T_0 \gtrsim 200$ K, ΔT_C increases again with the increasing initial superheat. In this case, the vapor layer forms at T_C (Fig. 2-a-4); film boiling occurs; and the drop obtains the stable spheroidal state. The initial surface temperature when this just occurs, roughly coincides with the Leidenfrost point.

Ethanol Drop. The experimental contact superheat ΔT_C agrees roughly with the theoretical ΔT_C^* for all the surface superheat tested. The contact superheat increases linearly with increasing T_0; no range of T_0 is observed where ΔT_C is held constant. Nucleate boiling apparently did not occur immediately on contact in the present experimental range; there was always some delay. There was, however, no observable delay in the case of water. The difference is similar to the one found in the study of transient boiling [6]. The reason for the difference is not known for the transient boiling either.

Conclusions

The thin-film thermometer was manufactured to measure the transient temperature variation of the hot surface when the liquid drop impacted it.

For the water drop, the contact temperature was approximately constant for 100 K $\lesssim \Delta T_0 \lesssim$ 200 K; for $\Delta T_0 \gtrsim$ 200 K, it increased again. The turning point, that is $\Delta T_0 \sim$ 200 K, roughly coincided with the Leidenfrost temperature.

For the ethanol drop, the contact temperature increased linearly with the increasing T_0.

References

1 Baumeister, K. J., and Simon, F. F., "Leidenfrost Temperature Its Correlation for Liquid Metals, Cryogens, Hydro carbons, and Water," JOURNAL OF HEAT TRANSFER, TRANS. ASME, Series, C. Vol. 95, 1973, pp. 166–173.

2 Wachters, L. H. J., and Westering, N. A. J., "The Heat Transfer from a Hot Wall to Impinging Water Drops in the Spheroidal State," *Chemical Engineering Science*, Vol. 21, 1966, pp. 1047–1056.

3 Nishi-o, S., and Hirata, K., "A Study on the Leidenfrost Temperature," *Proceedings of JSME Meeting*, No. 760-19, 1976, pp. 115–122.

4 Bradfield, W. S., "Liquid-Solid Contact in Stable Film Boiling," *I&EC Fundamentals*, Vol. 5, 1966, pp. 200–204.

5 Carslaw, H. S., and Jaeger, J. C., *Conduction of Heat in Solids*, Oxford University Press, Oxford, second ed., 1959, p. 88.

6 Sympson, H. C., and Walls, A. S., "A Study of Nucleation Phenomena in Transient Pool Boiling," *Proceedings of Institution of Mechancial Engineers*, Vol. 180, Pt 3G, 1965–66.

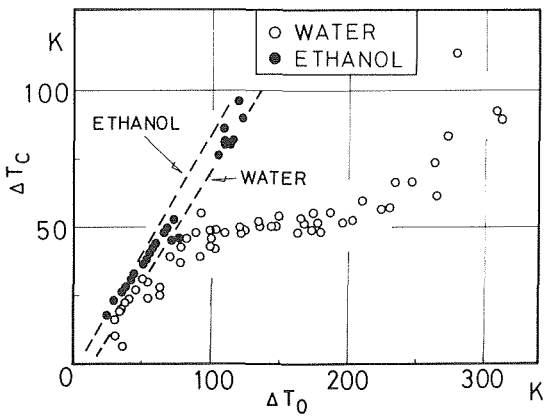

Fig. 4 The contact temperature versus initial surface temperature for water and ethanol drops

Combined Conduction-Radiation Heat Transfer Through an Irradiated Semi-transparent Plate

R. Viskanta[1] and E. D. Hirleman[1]

Nomenclature

Bi = Biot number, $\tilde{h}t/k$
F = radiative flux
F = incident flux
$\tilde{h}$ = effective (convective + radiative) heat transfer coefficients
k = thermal conductivity
n = index of refraction
q = total (conductive plus radiative) heat flux
q^* = dimensionless heat flux, $q/[k(T_{a2} - T_{a1})/t]$
T = temperature
t = plate thickness
Γ = dimensionless parameter, $(\mu^\circ F_b^\circ + F_d^\circ)/[k(T_{a2} - T_{a1})/t]$
Θ = dimensionless temperature, $(T - T_{a1})/(T_{a2} - T_{a1})$
κ = absorption coefficient
μ = $\cos\theta$, where θ is the refracted angle in the material
ξ = dimensionless distance, x/t
ρ = reflectivity of an interface
τ = transmissivity of an interface
τ_o = optical thickness of the medium, κt
Φ = dimensionless radiative flux, $F/(\mu^\circ F_b^\circ + F_d^\circ)$

Subscripts

a = refers to ambient conditions
b = refers to the beam (collimated) component
d = refers to the diffuse component
λ = refers to the wavelength
1 = refers to side 1
2 = refers to side 2

Superscript

° = refers to the medium of incidence (air)

Introduction

There are a large number of physical and technological systems which use semi-transparent solids such as glass, plastics, and others as thermal/structural elements. Examples of such systems include architectural windows [1],[2] cover plates for flat-plate solar collectors [2], windows for metallurgical and other furnaces [3], cover tubes for

[1] School of Mechanical Engineering, Purdue University, West Lafayette, Ind.

[2] Numbers in brackets designate References at end of technical note.

Contributed by the Heat Transfer Division of THE AMERICAN SOCIETY OF MECHANICAL ENGINEERS. Manuscript received by the Heat Transfer Division, March 28, 1977.

temperature in this study is about 300°C and that the SiO film has only a small effect on the vaporization time.

The contact temperature is plotted against the initial surface superheat in Fig. 4. The contact temperature can be expressed in "superheat", $\Delta T_C = T_C - T_{sat}$. This will be called "contact superheat" hereafter. Let us assume that two solids, initially at different temperatures T_1 and T_2, are suddenly brought into contact. Then the temperature at the contact surface is given by $T_C^* = (T_1\beta_1 + T_2\beta_2)/(\beta_1 + \beta_2)$ [5]. Here, β is $\sqrt{\rho ck}$, and ρ, c, and k represent density, specific heat, and thermal conductivity, respectively. The contact superheat $\Delta T_C^* = (T_C^* - T_{sat})$ is shown by the broken lines for water and ethanol in Fig. 4.

Water Drop. For $\Delta T_0 \lesssim 70$ K, the contact superheat ΔT_C increases with the increasing initial surface superheat. It is in fair agreement with the theoretical ΔT_C^*. So, the boiling does not occur at the moment of the initial contact. For 100 K $\lesssim \Delta T_0 \lesssim$ 200 K, ΔT_C is approximately constant (about 50 K) and is far below ΔT_C^*. The nucleate boiling starts during the initial decrease of the surface temperature. When $\Delta T_0 \gtrsim 200$ K, ΔT_C increases again with the increasing initial superheat. In this case, the vapor layer forms at T_C (Fig. 2-a-4); film boiling occurs; and the drop obtains the stable spheroidal state. The initial surface temperature when this just occurs, roughly coincides with the Leidenfrost point.

Ethanol Drop. The experimental contact superheat ΔT_C agrees roughly with the theoretical ΔT_C^* for all the surface superheat tested. The contact superheat increases linearly with increasing T_0; no range of T_0 is observed where ΔT_C is held constant. Nucleate boiling apparently did not occur immediately on contact in the present experimental range; there was always some delay. There was, however, no observable delay in the case of water. The difference is similar to the one found in the study of transient boiling [6]. The reason for the difference is not known for the transient boiling either.

Conclusions

The thin-film thermometer was manufactured to measure the transient temperature variation of the hot surface when the liquid drop impacted it.

For the water drop, the contact temperature was approximately constant for 100 K $\lesssim \Delta T_0 \lesssim$ 200 K; for $\Delta T_0 \gtrsim 200$ K, it increased again. The turning point, that is $\Delta T_0 \sim 200$ K, roughly coincided with the Leidenfrost temperature.

For the ethanol drop, the contact temperature increased linearly with the increasing T_0.

References

1 Baumeister, K. J., and Simon, F. F., "Leidenfrost Temperature Its Correlation for Liquid Metals, Cryogens, Hydro carbons, and Water," JOURNAL OF HEAT TRANSFER, TRANS. ASME, Series, C. Vol. 95, 1973, pp. 166–173.

2 Wachters, L. H. J., and Westering, N. A. J., "The Heat Transfer from a Hot Wall to Impinging Water Drops in the Spheroidal State," *Chemical Engineering Science*, Vol. 21, 1966, pp. 1047–1056.

3 Nishi-o, S., and Hirata, K., "A Study on the Leidenfrost Temperature," *Proceedings of JSME Meeting*, No. 760-19, 1976, pp. 115–122.

4 Bradfield, W. S., "Liquid-Solid Contact in Stable Film Boiling," *I&EC Fundamentals*, Vol. 5, 1966, pp. 200–204.

5 Carslaw, H. S., and Jaeger, J. C., *Conduction of Heat in Solids*, Oxford University Press, Oxford, second ed., 1959, p. 88.

6 Sympson, H. C., and Walls, A. S., "A Study of Nucleation Phenomena in Transient Pool Boiling," *Proceedings of Institution of Mechancial Engineers*, Vol. 180, Pt 3G, 1965–66.

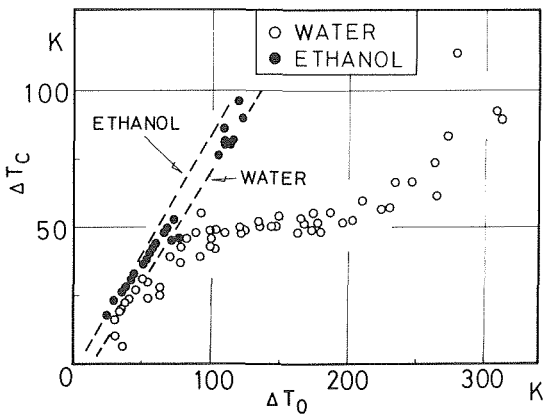

Fig. 4 The contact temperature versus initial surface temperature for water and ethanol drops

Combined Conduction-Radiation Heat Transfer Through an Irradiated Semi-transparent Plate

R. Viskanta[1] and E. D. Hirleman[1]

Nomenclature

Bi = Biot number, $\tilde{h}t/k$
F = radiative flux
F = incident flux
$\tilde{h}$ = effective (convective + radiative) heat transfer coefficients
k = thermal conductivity
n = index of refraction
q = total (conductive plus radiative) heat flux
q^* = dimensionless heat flux, $q/[k(T_{a2} - T_{a1})/t]$
T = temperature
t = plate thickness
Γ = dimensionless parameter, $(\mu^\circ F_b^\circ + F_d^\circ)/[k(T_{a2} - T_{a1})/t]$
Θ = dimensionless temperature, $(T - T_{a1})/(T_{a2} - T_{a1})$
κ = absorption coefficient
μ = $\cos\theta$, where θ is the refracted angle in the material
ξ = dimensionless distance, x/t
ρ = reflectivity of an interface
τ = transmissivity of an interface
τ_o = optical thickness of the medium, κt
Φ = dimensionless radiative flux, $F/(\mu^\circ F_b^\circ + F_d^\circ)$

Subscripts

a = refers to ambient conditions
b = refers to the beam (collimated) component
d = refers to the diffuse component
λ = refers to the wavelength
1 = refers to side 1
2 = refers to side 2

Superscript

° = refers to the medium of incidence (air)

Introduction

There are a large number of physical and technological systems which use semi-transparent solids such as glass, plastics, and others as thermal/structural elements. Examples of such systems include architectural windows [1],[2] cover plates for flat-plate solar collectors [2], windows for metallurgical and other furnaces [3], cover tubes for

[1] School of Mechanical Engineering, Purdue University, West Lafayette, Ind.

[2] Numbers in brackets designate References at end of technical note.

Contributed by the Heat Transfer Division of THE AMERICAN SOCIETY OF MECHANICAL ENGINEERS. Manuscript received by the Heat Transfer Division, March 28, 1977.

parabolic solar concentrators [4], and many others. In these systems, the semi-transparent materials are irradiated from some thermal radiation source at high temperature and heat transfer though the material occurs by combined conduction and radiation. The problem is of current practical interest as heat transfer through semitransparent materials is relevant to solar energy utilization systems [2]. Heat transfer through semitransparent materials at low temperature on which there is incident thermal radiation is predicted by ignoring the interaction of conduction with radiation [2–4]. This is accomplished by assuming that conduction predominates over radiation, and in a plane layer of material with a constant thermal conductivity, for example, the temperature profile is linear. This is an oversimplification of a physical situation and may result in errors when predicting the heat transfer rate. An extensive review of heat transfer through radiating and nonradiating semi-transparent solids is available [5].

The purpose of this note is to present an analytical solution for the steady-state temperature distribution in a plate of semi-transparent solid which is irradiated on one side by beam (collimated) and diffuse fluxes. The validity of neglecting the interaction of conduction with radiation in the solid is examined by comparing the heat transfer rates predicted with those based on an approximate approach.

Analysis

Physical Model and Assumptions. Consider steady-state heat transfer by combined conduction and radiation through a plane layer of semi-transparent material such as glass which is irradiated uniformly on one side from some external source. The physical thickness of the layer t is much greater than the wavelength of radiation λ so that wave interference effects can be neglected. The interfaces are assumed to be optically smooth and parallel to each other. Thus, the radiation reflection and transmission characteristics are predicted from Fresnel's equations. The material is assumed to be isotropic and homogeneous with negligible scattering compared to absorption. The temperature of the medium is sufficiently low so that internal emission can be neglected in comparison to the absorption of external radiation. For the sake of convenience and ease of analysis, the radiation field incident on the layer is resolved into a beam (collimated) ($F_b°$) and a diffuse ($F_d°$) component.

The steady-state conservation equation for the problem is

$$\frac{d}{dx}\left(-k\frac{dT}{dx}+\mathrm{F}\right)=0 \tag{1}$$

or

$$q(x)=-k\frac{dT}{dx}+\mathrm{F}(x)=\text{constant} \tag{2}$$

where the local radiative flux $\mathrm{F}(x)$[3] is given by [5]

$$\mathrm{F}(x)=\int_0^\infty \{\tau_{1\lambda}(\mu°)\mu°F_{b\lambda}°e^{-\kappa_\lambda x/\mu}[1-\rho_{2\lambda}(\mu)e^{-2(\tau_{o\lambda}-\kappa_\lambda x)/\mu}]/ \beta(\tau_{o\lambda},\mu)+2F_{d\lambda}{}^0[T_3(\kappa_\lambda x)-\mathrm{R}_3(2\tau_{o\lambda}-\kappa_\lambda x)]\}d\lambda \tag{3}$$

where

$$T_3(x)=\int_0^1 \tau_1(\mu')e^{-x/\mu}(\mu')^{n-2}d\mu'/\beta(\tau_{o\lambda},\mu) \tag{4}$$

$$\mathrm{R}_3(x)=\int_0^1 \tau_1(\mu')\rho_2(\mu)e^{-x/\mu}(\mu')^{n-2}d\mu'/\beta(\tau_{o\lambda},\mu) \tag{5}$$

and

$$\beta(\tau_{o\lambda},\mu)=[1-\rho_1(\mu)\rho_2(\mu)\exp(-2\tau_{o\lambda}/|\mu|)] \tag{6}$$

The factor β accounts for multiple interreflections between the two interfaces. Setting this factor to unity is not always justifiable. This is expected to be particularly true for oblique angles of incidence ($\mu \to 0$) when both $\rho_1(\mu)$ and $\rho_2(\mu)$ approach unity and when the optical path, $\tau_{o\lambda}/|\mu|$, is small such that $\exp(-2\tau_{o\lambda})/|\mu|) \approx 1$.

Solution. If dimensionless variables are introduced, the energy equation (2) becomes

$$-\frac{d\Theta}{d\xi}+\Gamma\Phi(\xi)=q^* \tag{6}$$

Assuming that the total (convective plus radiative) heat transfer from the plate to a fluid at ambient temperature T_a can be expressed by Newton's cooling law, energy balances at the two interfaces yield the boundary conditions

$$\frac{d\Theta}{d\xi}+\mathrm{Bi}_1=0 \text{ at } \xi=0$$

and

$$-\frac{d\Theta}{d\xi}+\mathrm{Bi}_2(\Theta-1)=0 \text{ at } \xi=1 \tag{7}$$

The solution of equation (6) with the imposed boundary conditions is

$$\Theta=(1-\mathrm{Bi}_1\xi)(1/\mathrm{Bi}_1)/D+\Gamma\left\{[(1-\xi)-1/\mathrm{Bi}_2](1/\mathrm{Bi}_1)\Phi(0)+(1-\mathrm{Bi}_1\xi)(1/\mathrm{Bi}_1\mathrm{Bi}_2)\Phi(1)+D\int_0^\xi\Phi(\eta)d\eta-(1-\mathrm{Bi}_1\xi)(1/\mathrm{Bi}_1)\int_0^1\Phi(\eta)d\eta\right\}/D \tag{8}$$

where

$$D=[(1/\mathrm{Bi}_1)+(1/\mathrm{Bi}_2)-1]^{-1} \tag{9}$$

Equation (8) shows that, as expected, in the absence of interaction between conduction and radiation ($\Gamma=0$) the temperature profile is determined by pure conduction. The integration of $\Phi(\xi)$ over ξ (i.e., dummy integration variable η) indicated that equation (8) can be carried out analytically, and there results

$$\int_0^\xi\Phi(\eta)d\eta=\left(\frac{1}{\mu°F_b°+F_d°}\right)\int_0^\infty\left\{\tau_{1\lambda}(\mu°)\mu°F_{b\lambda}°\left(\frac{\mu}{\tau_{o\lambda}}\right)[1-e^{-(\tau_{o\lambda}/\mu)\xi}+\rho_{2\lambda}(\mu)e^{-2\tau_{o\lambda}/\mu}[1-e^{(\tau_{o\lambda}/\mu)\xi}]]/\beta(\tau_{o\lambda},\mu)+2(F_{d\lambda}°/\tau_{o\lambda})[\tilde{T}_4(0)-\tilde{T}_4(\tau_{o\lambda}\xi)+\tilde{\mathrm{R}}_4(2\tau_{o\lambda})-\tilde{\mathrm{R}}_4(2\tau_{o\lambda}-\tau_{o\lambda}\xi)]\right\}d\lambda \tag{10}$$

where

$$\tilde{T}_4(x)=\int_0^1\tau_1(\mu')\mu'\mu e^{-x/\mu}d\mu'/\beta(\tau_o,\mu) \tag{11}$$

and

$$\tilde{\mathrm{R}}_4(x)=\int_0^1\tau_1(\mu')\rho_2(\mu)\mu'\mu e^{-x/\mu}d\mu'/\beta(\tau_o,\mu) \tag{12}$$

The sum of the conductive and radiative fluxes at the surface 1, $\xi=0$, is obtained from equations (6) and (8),

$$q_1^*=\left[-\frac{d\theta}{d\xi}+\Phi(\xi)\right]_{\xi=0}=1/D+\Gamma\left[\Phi(0)/\mathrm{Bi}_1+\Phi(1)/\mathrm{Bi}_2-\int_0^1\Phi(\eta)d\eta\right]/D \tag{13}$$

Because of the rather complex form of equation (13), it is difficult to draw general conclusions regarding the effect of internal absorption of radiation on the total heat transfer rate. The various special cases follow immediately from the general solution presented and will be examined next.

Special Cases. For the special case of negligible convective resistance at the two faces of the plate ($1/\mathrm{Bi}_1=1/\mathrm{Bi}_2=0$) the temperature distribution, equation (8), reduces to

[3] The error in equations (55) and (58) of reference [5] has been corrected.

$$\theta = \xi + \Gamma\left[\int_0^{\xi}\Phi(\eta)d\eta - \xi\int_0^1\Phi(\eta)d\eta\right] \quad (14)$$

The temperature gradient at the surface ($\xi = 0$) is obtained from equations (14) and (10) resulting in

$$\left.\frac{d\theta}{d\xi}\right|_0 = 1 + \frac{\Gamma}{(\mu^\circ F_b^\circ + F_d^\circ)}\int_0^\infty \left\{\tau_{1\lambda}(\mu^\circ)\mu^\circ F_{b\lambda}^\circ\left[1 - \rho_{2\lambda}(\mu)e^{-2\tau_{o\lambda}/\mu} - \left(\frac{\mu}{\tau_{o\lambda}}\right)(1 - e^{-\tau_{o\lambda}/\mu})(1 - \rho_{2\lambda}(\mu)e^{-\tau_{o\lambda}/\mu})\right]\Big/\beta(\tau_{o\lambda},\mu) + 2F_{d\lambda}^\circ[T_3(0) - R_3(2\tau_{o\lambda})] - 2F_{d\lambda}^\circ[\tilde{T}_4(0) - \tilde{T}_4(\tau_{o\lambda}) + R_4(2\tau_{o\lambda}) - R_4(\tau_{o\lambda})]/\tau_{o\lambda}\right\} d\lambda \quad (15)$$

Examination of this equation reveals that radiation always increases the temperature gradient and hence the conductive flux at the surface $\xi = 0$. The total heat flux at the surface follows from equation (13) yielding

$$q_1^* = -1 + \Gamma\int_0^1\Phi(\eta)d\eta \quad (16)$$

Since the integral in this equation is always positive, the result indicates that internal absorption of radiation always decreases the heat transfer rate at the irradiated surface when $T_2 - T_1 > 0$ and increases the rate when $T_2 - T_1 < 0$.

For a gray medium, $\kappa_\lambda = \bar{\kappa}$ = constant, the wavelength independent radiation surface characteristics, and the integration over wavelength indicated in equations (12) and (16) are eliminated.

For example, when only a beam component of the radiative flux ($F_d^\circ = 0$) is incident on the plate, the medium is gray with wavelength independent transmission and reflection characteristics of the interfaces and there is negligible convective resistance at the surfaces ($1/\mathrm{Bi}_1 = 1/\mathrm{Bi}_2 = 0$), the temperature distribution becomes

$$\theta = \xi + \Gamma\tau_1(\mu^\circ)(\mu/\tau_o)\{(1 - e^{-(\tau_o/\mu)\xi}) + \rho_2(\mu)e^{-2\tau_o/\mu}(1 - e^{(\tau_o/\mu)\xi}) - \xi[(1 - e^{-\tau_o/\mu}) + \rho_2(\mu)e^{-2\tau_o/\mu}(1 - e^{\tau_o/\mu})]\}/\beta(\tau_o,\mu) \quad (17)$$

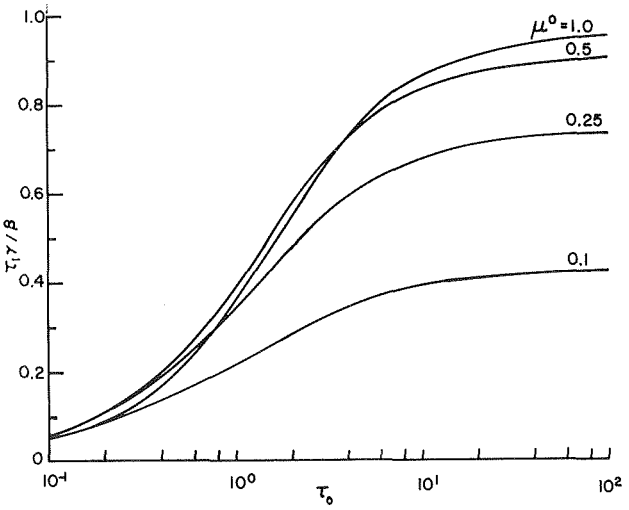

Fig. 1 Variation of function $\tau_1\gamma/\beta$ with the optical thickness τ_o

and the dimensionless surface heat flux at $\xi = 0$ simplifies to

$$q_1^* = -1 - \Gamma\{[\tau_1(\mu^\circ)/\beta(\tau_o,\mu)][\gamma(\tau_o,\mu) - \phi(\tau_o,\mu)]\} \quad (18)$$

where

$$\gamma(\tau_o,\mu) = 1 - \rho_2(\mu)e^{-2\tau_o/\mu} - \left(\frac{\mu}{\tau_o}\right)(1 - e^{-\tau_o/\mu})[1 - \rho_2(\mu)e^{-\tau_o/\mu}] \quad (19)$$

and

$$\phi(\tau_o,\mu) = [1 - \rho_2(\mu)e^{-2\tau_o/\mu}] \quad (20)$$

Example

Sample results are presented in Fig. 1 and Table 1 for a semitransparent material having a wavelength independent absorption coefficient and negligible convective resistances at the surfaces such that $T_{a1} = T_1$ and $T_{a2} = T_2$. In the analysis the surfaces were assumed to be optically smooth and the radiation characteristics were calculated from the Fresnel [6] equations. The angle of incident θ° outside the medium was related to the angle of refraction inside the medium by Snell's law, $n^\circ \sin\theta^\circ = n \sin\theta$. The results of Fig. 1 show that $\tau_1\gamma/\beta$ increases with the optical thickness $\tau_o = \bar{\kappa}t$ and approaches an asymptotic value as τ_o becomes large. The results of this figure together with equation (18) indicate that absorption of radiation in the material increases the conductive heat flux at the surface. Since the parameter Γ can become greater than unity when either $(\mu^\circ F_b^\circ + F_d^\circ)$ is large and/or $k(T_2 - T_1)/t$ is small, one can envision may physical situations where presence of radiation would increase significantly the conductive flux. As a practical example, consider a plate of glass ($k = 0.75$ W/mK) having thickness $t = 0.3$ cm and a temperature difference $T_2 - T_1 = 1$ K across it which is irradiated with a total flux $\mu^\circ F_b^\circ + F_d^\circ = 500$ W/m^2. The interaction parameter Γ has a value of 2.

The parameter $\tau_1\phi/\beta$ represents the dimensionless radiative flux inside the medium at $\xi = 0$. Since the reflectivity, $\rho_2(\mu)$, is relatively small, the dependence of $\tau_1\phi/\beta$ on the optical thickness τ_o is much weaker than that on the direction (μ°) of the incident beam of radiation. At $\mu^\circ = 0$ all of the incident radiation is reflected and hence $\tau_1\phi/\beta = 0$.

If it is assumed that the radiation absorbed by a plate of semitransparent material is distributed uniformly, then for the special case of gray material and a beam of radiation ($F_d^\circ = 0$) incident on the surface an approximate expression for the heat flux can be obtained. The analysis yields that the dimensionless heat flux at the surface ($\xi = 0$) is given by

$$q^*_{1,\mathrm{approx}} = -1 - \Gamma[\tau_1(\mu^\circ)/\beta(\tau_o,\mu)]\{(1 - e^{-\tau_o/\mu})[1 + \rho_2(\mu)e^{-\tau_o/\mu}]\} \quad (21)$$

Examination of Table 2 reveals that a significant loss in accuracy will result in the prediction of the heat transfer rate if equation (18) is used. There is even a change in sign of the ratio $q_1^*/q^*_{1,\mathrm{approx}}$ for large values of the optical thickness τ_o of the material.

References

1 "Solar Radiation Considerations in Building Planning and Design," National Academy of Sciences, Washington, D. C., 1976.

Table 1 Variation of function $\tau_1\phi/\beta$ with the optical thickness τ_0 and the cosine of the angle of incidence μ deg

	$n/n^\circ = 1.5$				$n/n^\circ = 2.0$			
$\tau_0\backslash\mu^\circ$	1.0	0.5	0.25	0.10	1.0	0.5	0.25	0.10
0.01	0.9238	0.8381	0.5863	0.2786	0.8018	0.7245	0.5211	0.2612
0.1	0.9298	0.8525	0.6195	0.3213	0.8163	0.7458	0.5535	0.2992
1.0	0.9550	0.9044	0.7253	0.4210	0.8770	0.8262	0.6664	0.3974
10	0.9600	0.9108	0.7358	0.4284	0.8889	0.8386	0.6816	0.4076
100	0.9600	0.9108	0.7358	0.4284	0.8889	0.8386	0.6816	0.4076

Table 2 Comparison of heat transfer rates Q_1^*/Q_1^*, approx for F_d° = 0, n/n° = 1.5, $1/Bi_1 = 1/Bi_2 = 0$, and $\Gamma = 10$

$\tau_o \backslash \mu^\circ$	1.0	0.5	0.25	0.1
0.01	1.000	0.985	0.959	0.961
0.1	0.999	0.985	0.962	0.964
1.0	0.911	0.868	0.844	0.835
2.0	0.710	0.615	0.579	0.566
4.0	0.356	0.254	0.223	0.214
10.0	0.000	−0.046	−0.059	−0.063
100.0	−0.225	−0.230	−0.231	−0.231

2 Duffie, J. A., and Beckman, W. A., *Solar Thermal Processes*, John Wiley and Sons, New York, 1974.

3 Siegel, R., and Hussain, N. A., "Combined Radiation, Convection and Conduction for a System with a Partially Transmitting Wall," NASA Technical Note TN D-7985, Washington, D. C., 1975.

4 Ahmazadeh, J., and Gascoigne, M., "Efficiency of Solar Collectors," Energy Conversion, Vol. 16, 1976, pp. 13–21.

5 Viskanta, R., and Anderson, E. E., "Heat Transfer in Semi-transparent Solids," in *Advances in Heat Transfer*, Vol. 11, Academic Press, New York, 1975, pp. 317–441.

6 Siegel, R., and Howell, J. R., *Thermal Radiation Heat Transfer*, McGraw-Hill, New York, 1972.

Transient Conduction in a Slab With Temperature Dependent Thermal Conductivity

J. Sucec[1]
S. Hedge[2]

Nomenclature

$Bi = hL/k_e$ Biot number
$F = \alpha_e t/L^2$ Fourier number
h = surface coefficient of heat transfer
j = subscript indicating x location of nodes
k, k_i, k_e = thermal conductivity at any temperature, at initial temperature T_i, and at fluid temperature T_e, respectively
K_{j-1}, K_{j+1} = $1 + \gamma(\phi_{j-1}{}^n + \phi_j{}^n)/2$, $1 + \gamma(\phi_{j+1}{}^n + \phi_j{}^n)/2$, respectively
L = half thickness of slab
n = number of time increments
N = denotes node at surface
t = time
T, T_i, T_e = slab temperature, initial slab temperature, and fluid temperature, respectively
x = space coordinate measured from slab center
$X = x/L$ nondimensional space coordinate
α_e = thermal diffusivity of solid at temperature T_e
γ = defined by equation (6)
$\phi = (T - T_e)/(T_i - T_e)$ temperature excess ratio
ϕ_c, ϕ_X = value of ϕ at center and at any nondimensional position, respectively
$\Delta Bi = h\Delta x/k_e$
$\Delta F = \alpha_e \Delta t/\Delta x^2$
Δx = node spacing in x direction
Δt = time increment

Introduction

Considerable attention has been devoted to the problem of transient heat conduction in solids with variable thermal conductivity. Most of the efforts employ a thermal conductivity which linearly depends upon temperature because this is a realistic approximation for many materials of interest. Friedmann [1][3] summarizes the work done prior to 1958, gives linearized solution bounds for specified boundary temperature, and presents some analog solutions for constant temperature and constant heat flux boundaries. Yang [2] effects a solution to the semi-infinite slab by use of a similarity transformation, while Goodman [3] and Koh [4] utilize approximate integral methods. Dowty and Haworth [5] solve the infinite slab case by finite difference methods, but the results are limited to certain temperature ranges and the case of heating only. A two-dimensional transient is dealt with by Hays and Curd [6] by use of a restricted variational principle. A finite element formulation of the general problem and a few representative results are given by Aguirre-Ramirez and Oden [7], while Vujanovic [8] and Mastanaiah and Muthunayagam [9] apply the method of optimal linearization. Integral method techniques are applied by Krajewski [10] and by Chung and Yeh [11] while, most recently, Mehta [12] used an iterative technique, based on a modified constant property solution, to yield solutions to the variable thermal conductivity problem.

In all of the previous work on the variable thermal conductivity problem, numerical results are presented only for the case of specified temperature or specified flux on the surface of the solid, and not for the more frequently encountered situation in practice, namely, the convective type boundary condition. In addition, none of the available numerical results are in a comprehensive, easy to use, form for the designer. It is the intent of this technical note to solve the problem by finite difference methods with a convective type boundary condition when the thermal conductivity varies linearly with temperature, and to present these results in such a form that they serve as approximate correction factors (with a certain error band) for the constant property Heisler charts, as given, for instance, in [13].

Analysis

The problem to be considered is a slab, of half thickness L, whose thermal conductivity is a linear function of the temperature, which is initially at constant temperature T_i throughout, when, suddenly, it is subjected to a fluid at constant temperature T_e with a constant surface coefficient of heat transfer h between the fluid and the slab. In the absence of generation and radiation, the slab's temperature distribution in space x and time t is required. The mathematical statement of the problem, in nondimensional form, is given as follows:

$$\frac{\partial}{\partial X}\left\{[1 + \gamma\phi]\frac{\partial \phi}{\partial X}\right\} = \frac{\partial \phi}{\partial F} \tag{1}$$

$$\phi = 1 \text{ at } F = 0 \text{ for } 0 \le X \le 1$$

$$\frac{\partial \phi}{\partial X} = 0 \text{ at } X = 0 \text{ for } F > 0$$

$$-[1 + \gamma\phi]\frac{\partial \phi}{\partial X} = Bi\phi \text{ at } X = 1 \text{ for } F > 0$$

The nonlinearity in equation (1), when coupled with the type of boundary conditions for the slab, precludes, at present, an exact analytical solution; so finite difference methods were chosen to solve equation (1). Explicit difference equations were derived for the various interior nodes by making an energy balance on the material associated with the nodes, and the result is, for the j^{th} interior node,

[1] Professor of Mechanical Engineering, University of Me., Orono, Maine. Mem. ASME.

[2] Engineer, West Coast Paper Mills, Dandeli, India. Formerly, Graduate Student, University of Maine at Orono.

Contributed by the Heat Transfer Division for publication in the JOURNAL OF HEAT TRANSFER. Manuscript received by the Heat Transfer Division May 27, 1977.

[3] Numbers in brackets designate References at end of technical note.

Table 2 Comparison of heat transfer rates Q_1^*/Q_1^*, approx for F_d° = 0, n/n° = 1.5, $1/Bi_1 = 1/Bi_2 = 0$, and $\Gamma = 10$

$\tau_o \backslash \mu^\circ$	1.0	0.5	0.25	0.1
0.01	1.000	0.985	0.959	0.961
0.1	0.999	0.985	0.962	0.964
1.0	0.911	0.868	0.844	0.835
2.0	0.710	0.615	0.579	0.566
4.0	0.356	0.254	0.223	0.214
10.0	0.000	−0.046	−0.059	−0.063
100.0	−0.225	−0.230	−0.231	−0.231

2 Duffie, J. A., and Beckman, W. A., *Solar Thermal Processes*, John Wiley and Sons, New York, 1974.

3 Siegel, R., and Hussain, N. A., "Combined Radiation, Convection and Conduction for a System with a Partially Transmitting Wall," NASA Technical Note TN D-7985, Washington, D. C., 1975.

4 Ahmazadeh, J., and Gascoigne, M., "Efficiency of Solar Collectors," Energy Conversion, Vol. 16, 1976, pp. 13–21.

5 Viskanta, R., and Anderson, E. E., "Heat Transfer in Semi-transparent Solids," in *Advances in Heat Transfer*, Vol. 11, Academic Press, New York, 1975, pp. 317–441.

6 Siegel, R., and Howell, J. R., *Thermal Radiation Heat Transfer*, McGraw-Hill, New York, 1972.

Transient Conduction in a Slab With Temperature Dependent Thermal Conductivity

J. Sucec[1]
S. Hedge[2]

Nomenclature

$Bi = hL/k_e$ Biot number
$F = \alpha_e t/L^2$ Fourier number
h = surface coefficient of heat transfer
j = subscript indicating x location of nodes
k, k_i, k_e = thermal conductivity at any temperature, at initial temperature T_i, and at fluid temperature T_e, respectively
K_{j-1}, K_{j+1} = $1 + \gamma(\phi_{j-1}{}^n + \phi_j{}^n)/2$, $1 + \gamma(\phi_{j+1}{}^n + \phi_j{}^n)/2$, respectively
L = half thickness of slab
n = number of time increments
N = denotes node at surface
t = time
T, T_i, T_e = slab temperature, initial slab temperature, and fluid temperature, respectively
x = space coordinate measured from slab center
$X = x/L$ nondimensional space coordinate
α_e = thermal diffusivity of solid at temperature T_e
γ = defined by equation (6)
$\phi = (T - T_e)/(T_i - T_e)$ temperature excess ratio
ϕ_c, ϕ_X = value of ϕ at center and at any nondimensional position, respectively
$\Delta Bi = h\Delta x/k_e$
$\Delta F = \alpha_e \Delta t/\Delta x^2$
Δx = node spacing in x direction
Δt = time increment

Introduction

Considerable attention has been devoted to the problem of transient heat conduction in solids with variable thermal conductivity. Most of the efforts employ a thermal conductivity which linearly depends upon temperature because this is a realistic approximation for many materials of interest. Friedmann [1][3] summarizes the work done prior to 1958, gives linearized solution bounds for specified boundary temperature, and presents some analog solutions for constant temperature and constant heat flux boundaries. Yang [2] effects a solution to the semi-infinite slab by use of a similarity transformation, while Goodman [3] and Koh [4] utilize approximate integral methods. Dowty and Haworth [5] solve the infinite slab case by finite difference methods, but the results are limited to certain temperature ranges and the case of heating only. A two-dimensional transient is dealt with by Hays and Curd [6] by use of a restricted variational principle. A finite element formulation of the general problem and a few representative results are given by Aguirre-Ramirez and Oden [7], while Vujanovic [8] and Mastanaiah and Muthunayagam [9] apply the method of optimal linearization. Integral method techniques are applied by Krajewski [10] and by Chung and Yeh [11] while, most recently, Mehta [12] used an iterative technique, based on a modified constant property solution, to yield solutions to the variable thermal conductivity problem.

In all of the previous work on the variable thermal conductivity problem, numerical results are presented only for the case of specified temperature or specified flux on the surface of the solid, and not for the more frequently encountered situation in practice, namely, the convective type boundary condition. In addition, none of the available numerical results are in a comprehensive, easy to use, form for the designer. It is the intent of this technical note to solve the problem by finite difference methods with a convective type boundary condition when the thermal conductivity varies linearly with temperature, and to present these results in such a form that they serve as approximate correction factors (with a certain error band) for the constant property Heisler charts, as given, for instance, in [13].

Analysis

The problem to be considered is a slab, of half thickness L, whose thermal conductivity is a linear function of the temperature, which is initially at constant temperature T_i throughout, when, suddenly, it is subjected to a fluid at constant temperature T_e with a constant surface coefficient of heat transfer h between the fluid and the slab. In the absence of generation and radiation, the slab's temperature distribution in space x and time t is required. The mathematical statement of the problem, in nondimensional form, is given as follows:

$$\frac{\partial}{\partial X}\left\{[1 + \gamma\phi]\frac{\partial \phi}{\partial X}\right\} = \frac{\partial \phi}{\partial F} \tag{1}$$

$$\phi = 1 \text{ at } F = 0 \text{ for } 0 \le X \le 1$$

$$\frac{\partial \phi}{\partial X} = 0 \text{ at } X = 0 \text{ for } F > 0$$

$$-[1 + \gamma\phi]\frac{\partial \phi}{\partial X} = Bi\phi \text{ at } X = 1 \text{ for } F > 0$$

The nonlinearity in equation (1), when coupled with the type of boundary conditions for the slab, precludes, at present, an exact analytical solution; so finite difference methods were chosen to solve equation (1). Explicit difference equations were derived for the various interior nodes by making an energy balance on the material associated with the nodes, and the result is, for the j^{th} interior node,

[1] Professor of Mechanical Engineering, University of Me., Orono, Maine. Mem. ASME.

[2] Engineer, West Coast Paper Mills, Dandeli, India. Formerly, Graduate Student, University of Maine at Orono.

Contributed by the Heat Transfer Division for publication in the JOURNAL OF HEAT TRANSFER. Manuscript received by the Heat Transfer Division May 27, 1977.

[3] Numbers in brackets designate References at end of technical note.

$$\phi_j^{n+1} = \Delta F K_{j-1}\phi_{j-1}^{n} + \Delta F K_{j+1}\phi_{j+1}^{n} + [1 - \Delta F K_{j-1} - \Delta F K_{j+1}]\phi_j^{n} \quad (2)$$

However, an explicit equation derived in this fashion for the surface node N led to, in some cases, a severe stability criterion which would cause excessive machine run time. This was overcome by implicitizing at the boundary node, so that the stability limit shifted back to the interior nodes. This gives the following boundary node equation

$$\phi_N^{n+1} = \{\phi_N^{n} + 2\Delta F K_{N-1}\phi_{N-1}^{n+1}\}/\{1 + 2K_{N-1}\Delta F + 2\Delta F \Delta B_i\} \quad (3)$$

Because of the one-dimensionality of the problem, equation (3) is actually implicit in ϕ_N^{n+1}, since one can solve for ϕ_{N-1}^{n+1} from equation (2) and use it in equation (3).

It was found that equations (2) and (3) were consistent with the governing partial differential equation and with the convective type boundary condition as long as $\Delta t/\Delta x \to 0$, as Δt and Δx approach zero. The fact that the finite difference lattice must be refined in this restricted fashion does not present any difficulty, since the conditional stability requirement for the set of equations (2) and (3) is that

$$\Delta F \leqq 1/(K_{j-1} + K_{j+1}) \quad (4)$$

Since ΔF is proportional to $\Delta t/\Delta x^2$, the usual type of lattice refinement which takes place at constant ΔF insures that $\Delta t/\Delta x \to 0$. Numerical experimentation indicated that the use of 31 nodes was sufficient for convergence of the finite difference solution.

The finite difference solution was checked by comparison to available limiting cases. For the constant conductivity situation, the results were compared to those of Heisler [14] and satisfactory agreement noted. Such was also the case when a comparison with Krajewski's [10] approximate solutions for $B_i \to \infty$ was made. Graphs of the response functions for the slab center are given in [15], from which much of the present work was drawn.

When this work was begun, it was reasoned that the most logical form of the linear thermal conductivity relation should be the following:

$$k = k_i[1 + \epsilon(1 - \phi)] \quad (5)$$

the reason for this initial choice being that the slab at some time, namely $t = 0$, would be at a nondimensional temperature which would allow it to have the reference conductivity k_i. Solutions were found and graphed for ϕ versus F when equation (5) was used, and it was noted that the curves for different values of ϵ exhibited quite a bit of spread among themselves. This spread seemed also to be thwarting efforts to correlate the curves with the constant property results of Heisler's charts. Because of this, the following alternate representation of the conductivity versus temperature relation was tried:

$$k = k_e[1 + \gamma\phi] \quad (6)$$

It was found that the use of equation (6) greatly reduced the spread of the curves of different γ and hence was used in all of the work being presented here. To illustrate, the use of equation (6) rather than (5) reduced the spread of the curves over much of the F range by a factor of at least two, when $B_i = \infty$ and $X = 1$.

Development of Approximate Relations for Design Use

The finite difference solution results, even when put into the form of charts, are cumbersome, to say the least, because of the large number of charts needed. For every curve on Heisler's [14] chart for $X = 0.0$ (which is a curve of $\gamma = 0$), one would need a minimum of four other curves from the present work, namely, curves for $\gamma = +0.5, +0.3, -0.3$, and -0.5. In addition, preliminary attempts to find a simple equivalent of Heisler's auxiliary, or position correction ratio, chart for the variable conductivity case were unsuccessful. Hence, effort was directed toward the establishment of an easy to use approximate correlation of these finite difference results with the results of Heisler's charts. Sought first was a relationship between the temperature excess ratio at any X, ϕ_X, and the temperature excess ratio at the center, ϕ_c, at the same time, by attempting to collapse the curves of ϕ_X/ϕ_c, at various γ, on to the $\gamma = 0$ curves of Heisler's auxiliary chart. This collapsing factor must equal zero when $\gamma = 0$, must approach unity as F gets large for all γ, and would, in general, depend on B_i and on X. Guided by these constraints, a trial and error process resulted in the following two factors. For $\gamma \geqq 0$

$$C_F = \frac{1 - \gamma \exp\{-1.55(1 - \gamma) + 12X/(4.05 + 1.0/B_i)\}}{16 \exp\{3.1F(0.5 - 0.1/B_i)\}} \quad (7)$$

For $\gamma \leqq 0$

$$C_F = \frac{1 - \gamma \exp\{-1.55\gamma + 12X/(4.05 + 1.0/B_i)\}}{43 \exp\{3.1F(0.5 - 0.1/B_i)\}} \quad (8)$$

The collapsing factors, C_F, are the ratio of the ordinate of Heisler's auxiliary (position correction) chart, at the value of X and B_i of interest, to the actual temperature excess ratio ϕ_X/ϕ_c for the γ of interest in the variable conductivity case. Or, viewed another way, the ordinate of Heisler's position correction chart is interpreted as being $C_F[\phi_X/\phi_c]$ where the ϕ_X/ϕ_c in this product is the one for the variable thermal conductivity situation. These correction factor correlations were made using the following parameter values; $\gamma = 0.5$ to -0.5 in 0.1 increments, $X = 0.2, 0.4, 0.5, 0.6, 0.8$, and 1.0, $B_i = \infty$, 20.0, 10.0, 5.0, 2.4, 1.0, 0.625, 0.4, and 0.2, F = 0.30 to whatever value is needed for all ϕ to be less than 0.01. The error in ϕ_X/ϕ_c due to use of this correction factor is, in most cases, less than three percent with a maximum error of five percent in a few cases. For $B_i < 0.2$ and $-0.5 \leq \gamma \leq 0.5$, Heisler's charts can be used directly with little error; for then the temperature distribution is almost lumped in the space coordinate, and the precise value of the thermal conductivity is of little consequence because of the convection controlled heating or cooling.

The next step was to attempt a correlation between the center temperature excess ratio, ϕ_c, for $\gamma \neq 0$ and the corresponding quantity for $\gamma = 0$, as portrayed in Heisler's main chart. Guided by some of the same considerations as were used to develop the C_F expressions and also by the form of the solution function for certain steady state problems with variable conductivity, the following generalized center temperature excess ratios, $\phi_c{}^*$, were devised. For $\gamma \geqq 0$

$$\phi_c{}^* = \phi_c\{1 + 0.575\gamma(1 - \phi_c)[1 - \exp(-0.5705\ B_i)]\} \quad (9)$$

For $\gamma \leqq 0$

$$\phi_c{}^* = \phi_c\{1 + 0.595\gamma(1 - \phi_c + 0.45\ \phi_c{}^2)[1 - \exp(-0.79\ B_i)]\} \quad (10)$$

The correlations (9) and (10) have the following meaning: $\phi_c{}^*$ is the ordinate of Heisler's main chart at the values of F and B_i of interest, while ϕ_c is the actual temperature excess ratio at the slab center at the value of γ for the problem. Alternately, the right hand sides of equations (9) and (10) can be viewed as the ordinate value of Heisler's main chart for the slab. For $F \geqq 0.30$, the equations (9) and (10) are accurate to within 3.8 percent, with the usual accuracy being closer to two percent, except for some cases at low values of ϕ_c where small errors, in the temperature excess ratio, such as 0.001 to 0.002, get magnified on a percent basis because of division by the small ϕ_c.

Hence, as long as small error can be tolerated, equations (7) through (10), in conjunction with Heisler's [14] main chart and auxiliary chart for the slab, allow a rapid, easy solution to the transient conduction problem with thermal conductivity a linear function of temperature.

Sample Problem

Consider a two percent tungsten steel slab, initially at 730°C throughout, which is to be cooled in a 26.7°C fluid environment. If the cooling is done such that $B_i = 5$, it is required to find the nondimensional time F for the center temperature excess ratio, ϕ_c, to reach 0.237 and the surface temperature excess at this time. A plot of the thermal conductivity values from [16] yields a straight line that can be represented as follows for the specific conditions of this problem:

$$k = k_e(1 + \gamma\phi) = 61.25(1 - 0.5\phi)\ W/m°C \quad (11)$$

(It is important to bear in mind that γ is *not* the slope of the k versus

T curve but, rather, is the slope multiplied by $(T_i - T_e)/k_e$).

This sample problem will be solved using the average conductivity $\bar{k}$ with Heisler's charts (the solution mode normally used for variable conductivity problems by the engineer in industry), and then by using the appropriate correlation equations from the set (7)-(10) with Heisler's charts. Both solutions will be compared with the finite difference solution of [15]. $\bar{\phi} = (1 + 0.237)/2 = 0.6185$, hence, using (11), $\bar{k} = 42.3\ W/m°C$ and $\bar{B}_i = hL/\bar{k} = 7.239$. At $1/\bar{B}_i = 0.138$ and $\phi_c = 0.237$, one reads from Heisler's charts, as given in [17], that $\bar{F} = 0.88$ and $\phi_{X=1}/\phi_c = 0.18$. Changing the basis of $\bar{F}$ from $\bar{k}$ to k_c, for later comparison, gives the following solution to the problem using the method of "average" conductivity:

$$F = 1.27 \text{ and } \phi_{X=1}/\phi_c = 0.18$$

Now, solving by the correlation equations given in this paper, one gets from equation (10), using $B_i = 5$, $\gamma = -0.5$, and $\phi_c = 0.237$, that $\phi_c{}^* = 0.182$. Using this as the ordinate on Heisler's main chart along with $1/B_i = 0.2$ gives, from [17], $F = 1.12$. From equation (8), $C_F = 1.08$ so that the ordinate of Heisler's position correction chart is taken to be $1.08[\phi_{X=1}/\phi_c]$. This ordinate value from the auxiliary chart in [17] is 0.26 at $1/B_i = 0.2$, hence $1.08[\phi_{X=1}/\phi_c] = 0.26$ or $\phi_{X=1}/\phi_c = 0.241$. Thus, the solution to this problem using the correlation equations of this paper gives, $F = 1.12$ and $\phi_{X=1}/\phi_c = 0.241$. The finite difference solution, for this case, in [15] yields $F = 1.10$ and $\phi_{X=1}/\phi_c = 0.237$. So the error in F and in the surface temperature excess ratio by using the average conductivity technique is 15.8 and 24 percent, respectively. The corresponding errors using the correlation equations of this work are 1.82 and 1.6 percent.

Concluding Remarks

Correlation equations have been developed which allow the engineer to easily and rapidly solve the conduction transient in a slab with linearly temperature-dependent thermal conductivity and convection-type boundary conditions. This is carried out by using the correlation equations, together with the corresponding constant conductivity solution, as embodied in Heisler's (or equivalent) charts. A sample problem was shown where the concept of using an average conductivity in Heisler's charts gave rise to considerable error, whereas the correlation equation approach gave an error that would normally be acceptable. Calculations indicate that the proposed approach is easier and faster than finite difference solutions for problems requiring only relatively few values of temperatures and times to be found, when no use is made of a programable calculator, and, also, for problems where intermediate numbers of temperatures and times are needed to be found, in which case the four algebraic equations of this note must be programed and the computed correction factors combined with readings of Heisler's charts. In the case where extremely large numbers of temperatures and times are needed, then, in all probability, one would not even choose to use Heisler's charts for constant conductivity problems but, rather, would evaluate the infinite series solution numerically for these, and would employ finite differences for the variable conductivity situations. Also presented are the finite difference equations whose solution forms the basis of the resulting correlation equations and which can be programed for situations in which additional accuracy is deemed important.

Acknowledgments

The authors thank the Computing and Processing Services Department of the University of Maine at Orono for their donation of computer time.

References

1 Friedmann, N. E., "Quasilinear Heat Flow," TRANS. ASME, Vol. 80, 1958, pp. 635-645.

2 Yang, K. T., "Transient Conduction in a Semi-Infinite Solid with Variable Thermal Conductivity," *Journal of Applied Mechanics*, TRANS. ASME, Vol. 80, 1958, pp. 146-147.

3 Goodman, T. R., "The Heat Balance Integral—Further Considerations and Refinements," JOURNAL OF HEAT TRANSFER, TRANS. ASME, Series C, Vol. 83, Feb., 1961, pp. 83-86.

4 Koh, J. C. Y., "One-Dimensional Heat Conduction with Arbitrary Heating Rate and Variable Properties," *Journal of the Aerospace Sciences*, Vol. 28, 1961, pp. 989-990.

5 Dowty, E. L., and Haworth, D. R., "Solution Charts for Transient Heat Conduction in Materials with Variable Thermal Conductivity," ASME Paper No. 65-WA/Ht-29, 1965.

6 Hays, D. F., and Curd, H. N., "Heat Conduction in Solids: Temperature Dependent Thermal Conductivity," *International Journal of Heat and Mass Transfer*, Vol. 11, 1968, pp. 285-295.

7 Aguirre-Ramirez, G., and Oden, J. T., "Finite Element Technique Applied to Heat Conduction in Solids with Temperature Dependent Thermal Conductivity," *International Journal for Numerical Methods in Engineering*, Vol. 7, 1973, pp. 345-355.

8 Vujanovic, B., "Application of the Optimal Linearization Method to the Heat Transfer Problem," *International Journal of Heat and Mass Transfer*, Vol. 16, 1973, pp. 1111-1117.

9 Mastanaiah, K., and Muthunayagam, A. E., "Transient Conduction in a Finite Slab with Variable Thermal Conductivity," *AIAA Journal*, Vol. 13, No. 7, 1975, pp. 954-956.

10 Krajewski, B., "On a Direct Variational Method for Nonlinear Heat Transfer," *International Journal of Heat and Mass Transfer*, Vol. 18, 1975, pp. 495-502.

11 Chung, B. T. F., and Yeh, L. T., "Analysis of Heat Transfer in Slabs with Variable Properties Subjected to Radiation and Convection," ASME Paper No. 75-WA/HT-67, 1975.

12 Mehta, T. C., "On the Solution of Transient Conduction with Temperature Dependent Thermal Conductivity," JOURNAL OF HEAT TRANSFER, TRANS. ASME, Series C, Vol. 99, 1977, pp. 137-139.

13 Kreith, F., *Principles of Heat Transfer*, 3rd Edition, Intext Educational Publishers, New York, 1973.

14 Heisler, M. P., "Temperature Charts for Induction and Constant Temperature Heating," TRANS. ASME, Vol. 69, 1947, pp. 227-236.

15 Hegde, S. "The Transient Temperature Distribution in a Slab with Temperature Dependent Thermal Conductivity and Convection Boundary Condition Using Finite Differences," MS Thesis, University of Maine at Orono, 1976.

16 Rohsenow, W. M., and Hartnett, J. P., eds., *Handbook of Heat Transfer* McGraw-Hill, New York, 1973.

17 Sucec, J., *Heat Transfer* Simon and Schuster, New York, 1975.